Development and characterisation of novel therapeutic and biotechnological molecules

Thesis submitted to the University of Kent for the degree of Doctor of Philosophy (Ph.D.) in Biochemistry.

Nyasha Allen

University of Kent
School of Biosciences

2020

Declaration.

No part of this thesis has been submitted in support of an application for any degree or qualification of the University of Kent or any other University or Institute of learning.

Signed:
Nyasha Allen.

Acknowledgments

Firstly, I would like to express my deepest gratitude to my supervisors Prof. Dan Mulvihill and Dr. Jen Hiscock for their continued guidance and support throughout this project. I would also like to thank the past and current members of the Mulvihill, Geeves, Goult, and Hiscock laboratories for the friendship, the valued time spent together, assistance, and motivation provided throughout my time here. In addition, I would like to thank the individuals at Public Health England, in particular Charlotte Hind and Mark Sutton, who have collaborated with me and provided advice and assistance concerning this project.

Thank you to my husband, Max Allen for your love, encouragement, and technical support throughout this process. Without his tremendous support and understanding, it would have been impossible to complete my studies. I would like to thank the Manyanya and Allen families, in particular my dad, Gilbert Manyanya, who has supported and encouraged me throughout my education. And finally, I would like to extend a special thanks to my church family at King's Chatham, and my friends, in particular Lisa and Lynet Nyoni, who have provided unwavering support and encouragement throughout my education.

Abstract

The cell membrane, made up of a complex arrangement of proteins and lipids, is an integral component of cells and functions as a protective barrier around cells. Interactions with cell membranes can impact the membrane dynamics, integrity and morphology and therefore have biological consequences. The study of these interactions allows a deeper understanding of fundamental biological processes, particularly the vast number of membrane related proteins whose physiological function is still currently unknown. This information may also allow us to determine the pathogenesis of diseases associated with these membrane related proteins. It can be utilised in the development of effective therapeutic agents against these diseases, such as bacterial infections, due to the significance of membranes in cell survival.

Thus, this project is focused on understanding the interactions between biotechnological and therapeutic molecules with cell membranes through the use of synthetic liposomes, and a range of membrane binding assays. In the first part of this project, the antimicrobial activity of a series of membrane binding supramolecular self-associating amphiphiles (SSAs) was determined. Stepwise modifications were made to these molecules to ascertain their structure-activity relationships which were then utilised to produce second generation antimicrobials with improved *E. coli* activity. The anionic geometry of SSAs heavily influenced the acidity of the molecules and subsequent intermolecular interactions, which in turn impacted the antimicrobial activity observed. Lipid binding of SSAs was confirmed through the use of a competitive binding microscopy assay and fluorescence anisotropy experiments. The second-generation antimicrobials were found to gelate in salt solutions; thus, fluorescence microscopy was employed to characterise the gelation properties of these SSAs.

In the second part of this study, the lipid binding properties of the membrane related protein alpha synuclein (α-Syn), which has been implicated in Parkinson's Disease (PD) was investigated. In addition, the impact of the post-translational modifications acetylation and phosphorylation was also explored. Unacetylated and Nt-acetylated α-Syn exhibited high affinities to CL and PE lipids in the thermal shift assays conducted. Further, fluorescence anisotropy binding experiments revealed binding of acetylated and unacetylated α-Syn to POPA, a key signalling lipid. Additionally, unacetylated α-Syn exhibited increased lipid binding activities in comparison to acetylated α-Syn, suggesting negative regulation of α-Syn by Nt-acetylation. The final part of this project was concerned with the lipid binding interactions of the C-*elegans* myosin 1 homolog, Hum-1, specifically its TH1 domain. Hum-1 TH1 was found to predominantly interact with anionic lipids, and phosphorylation of Hum-1 TH1 increased binding to PA lipids. This project demonstrated the value of investigating

membrane lipid interactions in order to further understand the native roles and regulation of membrane proteins and improve the activity of membrane binding therapeutic molecules.

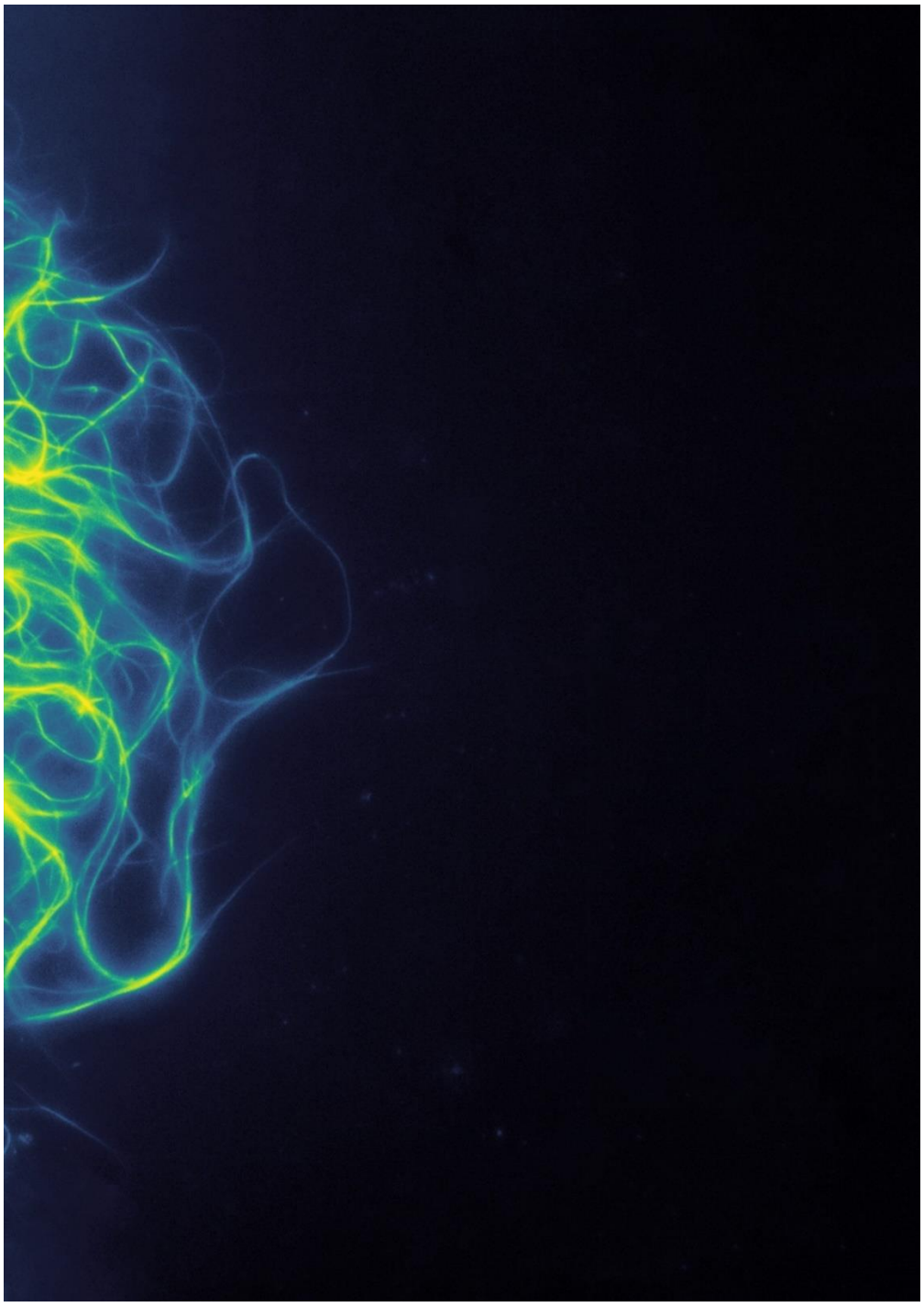

Title image: Widefield fluorescence microscopy image showing the gel strands formed by SSA 85 (5mg/mL) in $NaNO_3$ (0.505 M). Scale = 15 µm.

Table of Contents

Abbreviations used **8**
Table of Figures **10**
List of Tables **23**
List of equations **24**
Chapter 1: Introduction **25**
6.1. Cells and growth 25
6.1.1. Cell membranes 25
6.1.2. Phospholipids 25
1.1.3. Diffusion and osmosis 33
1.1.4. Membrane Proteins 35
1.2. Prokaryotes 37
1.2.1. Bacterial life cycle 38
1.2.2. Bacterial Pathogenesis 39
1.2.3. Antimicrobial Resistance 40
1.2.4. Advances in antimicrobial development 41
1.2.5. Supramolecular Chemistry and antimicrobial research 41
1.2.6. Bacterial Membranes 42
1.2.7. Bacterial Membrane lipid composition 44
1.2.8. Membrane Targeting 45
1.3. Eukaryotes 46
1.3.1. The eukaryotic life cycle 46
1.3.2. Cytoskeleton 48
1.3.3. Molecular motor proteins 50
1.3.4. Myosin 50
1.3.5. Endocytosis 51
1.3.6. Post-translational modifications 52
1.3.7. Alpha synuclein 54
1.3.8. The project 55
Aims of the project 56
2.1. Software **59**
2.2. Buffers & media recipes **60**
2.3. Biological Techniques **63**
2.3.1. Preparation of Luria Broth (LB) Agar plates 63
2.3.2. Preparation of Bacterial Plates 63

2.3.3. Preparation of Overnight Cultures 63
2.3.4. Preparation of Secondary cultures 63
2.3.5. Antibiotic Concentrations 63
2.3.6. DNA Preparation 63
2.3.7. *E. coli* Transformation 64
2.3.8. Nickel Column Preparation 64
2.3.9. Nickel Column Protocol 64
2.3.10. VNp and αS expression[98] 64
2.3.11. VNp and αS Nickel Purification[98] 65
2.3.12. Protein Dialysis 65
2.3.13. Protein Concentration Calculation 65
2.3.14. Hum1 TH1 Expression 66
2.3.15. Hum1 Native Purification 66
2.3.16. Hum1 Denaturing Purification 67
2.3.17. Hum1 Desalting 67
2.3.18. SDS PAGE 67
2.3.19. PIP Strip Protocol 68
2.4. Antimicrobial Assays[113] **69**
2.4.1. Preparation of the 0.5 McFarland Standard 69
2.4.2. Preparation of 5 % EtOH 69
2.4.3. Preparation of Antimicrobial Compounds for Screening 70
2.4.4. Preparation of Antimicrobial Compounds for MIC_{50} Calculations 70
2.4.5. Preparation of Cell Suspension 70
2.4.6. Preparation of 96 well Microplate for screening 70
2.4.7. Preparation of 96 well Microplate for MIC_{50}s 71
2.4.8. Growth Curves and MIC_{50} Calculation 71
2.4.9. Calculation of Growth rate 71
2.4.10. Compound Co-Drug Studies[66] 72
2.4.11. Agar well diffusion assay[116] 72
2.4.12. Agar surface diffusion assay[116] 73
2.4.13. Zone of inhibition measurements in ImageJ.[106] 74
2.5. Microscopy **75**
2.5.1. Competitive Binding Assay 75
2.5.2. Sample Preparation 75
2.5.3. Quantitative Fluorescence analysis 76

2.5.4. Gel Microscopy 76
2.6. Liposome Studies **77**
2.6.1. Liposome preparation 77
2.6.2. Co-sedimentation Assay under a density gradient 77
2.6.3. Fluorescence Anisotropy (protein) 78
2.6.4. Fluorescence Anisotropy (compound) 78
2.6.5. Thermal Shift Assay[118] 78
2.7. Novel Compound Characterisation **79**
2.7.1. SSA 82 Synthesis 79
2.7.2. SSA 83 Synthesis 79
2.7.3. Infrared (IR) measurements 80
2.7.4. Dynamic Light Scattering (DLS) Studies 80
2.7.5. Zeta Potential Measurements 80
2.7.6. Melting Point Measurements 81
2.7.7. NMR Spectroscopy 81
2.7.8. Mass Spectrometry 81
2.7.9. Single crystal X-ray diffraction studies 81
2.7.10. Tensiometry studies 82
2.7.11. Inversion test 82
2.8. Statistical analysis **82**
Chapter 3: Investigating the structure-activity relationships of novel antimicrobial compounds **83**
3.1. Introduction **83**
3.2. Supramolecular self-associating amphiphiles (SSAs) **86**
3.3. Aims and hypothesis **87**
3.4. Antimicrobial Activity Assays **89**
3.4.1. Structures of SSAs 89
3.4.2. SSA 32 90
3.4.3. Initial Antimicrobial Screening 91
3.4.4. Determining Solvent toxicity 91
3.4.5. Analysis of Growth dynamics and kinetics 92
3.4.6. MIC_{50} determination 107
3.5. Structure-Activity Relationships of SSA 1 – 50 ..... **110**
3.5.1. Increased growth of bacteria 110
3.5.2. Urea and Thiourea functionalities 110
3.5.3. Increasing the thio(urea) anion spacer 111

3.5.4. Exchanging the counter cation 113
3.5.5. Altering the sulfonyl group 117
3.5.6. R groups on the aromatic ring 118
3.5.7. Removal of the phenyl ring 121
3.5.8. Extension of the aromatic ring system 123
3.5.9. Antimicrobial gel plate testing 126
3.5.10. Combinatory effects of aromatic compounds 129
3.6. Mode of Action Determination 131
3.6.1. Fluorescence Microscopy 132
3.6.2. Fluorescence Anisotropy and membrane binding 144
3.7. Summary 149
Chapter 4: The characterisation and optimisation of novel antimicrobial compounds 152
4.1. Introduction 152
4.1.1. Aim of studies 152
4.2. Molecular Design 153
4.3. Physicochemical Studies 154
4.3.1. Low level *in silico* modelling 154
4.3.2. Synthesis 157
4.3.3. Single-crystal x-ray diffraction 158
4.3.4. Gas-phase mass spectrometry 161
4.3.5. Solution state studies 163
4.3.5.1. Dynamic Light Scattering (DLS) 164
4.3.5.2. Surface tension and CMC 168
4.3.5.3. ^{1}H DOSY NMR 169
4.3.5.4. Quantitative NMR 171
4.3.5.5. Zeta potential 174
4.3.5.6. ^{1}H NMR Dilution studies 175
4.4. Antimicrobial studies 177
4.4.5.1. Analysis of Growth dynamics and kinetics 177
4.3.1.1. MIC_{50} determination 181
4.4. Gel Characterisation 183
4.4.2. Inversion test and MGC 183
4.4.3. Rheology 187
4.5. Microscopy studies 190
4.5.1. Gel fibre characterisation 191

4.5.2. Measurement of gel fibres 193
4.5.3. Microscopy summary Tables 195
4.5.4. The fibre formation of SSAs 82, 83, and 85 gels 197
4.5.4. Antimicrobial Studies 208
4.6. Summary 213
Chapter 5: Exploring the lipid binding properties of membrane-related proteins 217
5.1. Introduction 217
5.1.1. Aim of studies 218
5.2. Recombinant protein synthesis and purification 219
5.3. Fluorescence anisotropy 221
5.4. Melting temperature 231
5.5. Myosin 1 238
5.5.2. Aim of studies 239
5.5.3. Protein expression 239
5.6. Hum-1 TH1 Purification and Refolding 240
5.7. Hum-1 TH1 lipid binding 243
5.8. Summary 252
Chapter 6: Discussion 255
6.1. The development of multifunctional SSAs to tackle antimicrobial resistance . 255
6.2. Investigating the role of post-translational modifications on lipid interactions. 258
6.3. Conclusion 261
Screening growth curves 296
Escherichia coli (*E. coli*) 296
USA 300 Methicillin-resistant Staphylococcus aureus (MRSA) 302
Antimicrobial gel plates 308
Quantitative Microscopy Analysis 312
E. coli at 30 minutes 313
E. coli at 4 hours 326
MRSA at 30 minutes 342
MRSA at 4 hours 352
Physicochemical studies conducted on second generation SSAs 367
Gelation studies 376
Antimicrobial gel plates: second generation SSAs 383
Lengths of gel fibres used to determine long and short strands 385
Gel fluorescence microscopy images 386

Statistics 404

Zones of inhibition 404

WT ANOVA 406

VNp ANOVA 409

Lz ANOVA 417

Hum1 Fluorescence 420

Abbreviations used

AMR – antimicrobial resistance

AMPs – antimicrobial peptides

ATP – Adenosine triphosphate

αS – Alpha Synuclein

A.U – Arbitrary unit

CMC – critical micelle concentration

CL – Cardiolipin

DPPE – 1,2-dipalmitoyl-sn-glycero-3-phosphoethanolamine

DSPG – 1,2-distearoyl-sn-glycero-3-phospho-(1'-rac-glycerol) (sodium salt)

EtOH – Ethanol

E. coli – *Escherichia coli*

HBD – hydrogen bond donator

HBA – hydrogen bond acceptor

HUM – Human unconventional myosin

IPTG – Isopropyl-β-D-1 thiogalactopyranoside

LMW – Low molecular weight

MRSA – Methicillin-resistant *Staphylococcus Aureus*

mCer3 – mCerulean3

mNg – mNeongreen

OD_{600} – Optical density at 600 nm

OGP – Octyl β-D-glucopyranoside

PA – Phosphatidic acid

PC - Phosphatidylcholine

PE – Phosphatidylethanolamine

PG – Phosphatidylglycerol

POPA – 1-palmitoyl-2-oleoyl-sn-glycero-3-phosphate (sodium salt)

POPC – 1-palmitoyl-2-oleoyl-glycero-3-phosphocholine

POPG - 1-palmitoyl-2-oleoyl-sn-glycero-3-phospho-(1'-rac-glycerol) (sodium salt)

PH – Pleckstrin homology domain

SSAs – Supramolecular Self-associating Amphiphiles

TMA - Tetramethylammonium

TEA – Tetraethylammonium

TPA – Tetrapentylammonium

TBA – Tetrabutylammonium

TH – Tail-homology domain

T_m – Mid-point melting temperature

WT – Wild type

Table of Figures

Figure 1. Types of amphiphiles. 26
Figure 2. Schematic illustrations of the critical micelle concentration. 27
Figure 3. Packing parameter (*p*) equation. 28
Figure 4. Amphiphile geometries 29
Figure 5. Sphingolipid and Sterol structures. 30
Figure 6. Chemical diversity of glycerophospholipids. 31
Figure 7. Prosed lipid migration during cell fission. 33
Figure 8. Routes for cytosolic entry. 34
Figure 9. Types of membrane proteins. 35
Figure 10. Graphical representation of the bacterial four-phase growth pattern. 38
Figure 11. Gram positive vs Gram negative cell walls 43
Figure 12. The stages of the eukaryotic life cycle. 47
Figure 13. Actin polymerisation. 48
Figure 14. Intermediate filaments. 49
Figure 15. The basic structure of Myosin 1. 50
Figure 16.Clathrin-mediated endocytosis. 52
Figure 17. Chemical groups added to proteins in regulation. 53
Figure 18. Structure of alpha synuclein. 54
Figure 19. PIP Strip layout. 100 picomoles of lipid per spot.[112] 69
Figure 20. Zone of inhibition measurements using the length function in ImageJ.[106] 74
Figure 21. Amphiphilic antimicrobials. 84
Figure 22. Use of self-associative molecules. 85
Figure 23. Use of self-associating molecules in antimicrobial research. 86
Figure 24. General structures of SSAs by developed by Hiscock et al., 2018.[154] 87
Figure 25. Structures of SSAs discussed in this chapter. 90
Figure 26. A representation of the dimerisation of SSA 32. 91
Figure 27. Determining solvent toxicity. 92
Figure 28. Growth curves of *E. coli* demonstrating compound aggregation. 95
Figure 29. Growth curves of *E. coli* demonstrating minimal inhibition. 96
Figure 30. Growth Curves MRSA demonstrating reversible inhibition. 97
Figure 31. Growth curves of MRSA demonstrating partial inhibition. 98
Figure 32. Growth curves of MRSA demonstrating partial inhibition. 99
Figure 33. Growth curves of MRSA demonstrating partial inhibition. 99
Figure 34. Example growth curves of *E. coli* demonstrating delayed inhibition. 100
Figure 35: Example growth curves of *E. coli* demonstrating delayed inhibition. 102
Figure 36 – Graphical representation of the growth rates presented in Table 6. 104
Figure 37. Graphical representation of the MIC_{50} values presented in Table 9. 109
Figure 38. MRSA Growth curves. 113
Figure 39. Crystal structures of SSAs 32 and 38. 114
Figure 40. Structure of the anionic component in SSA 32. 118
Figure 41. Growth curves of *E. coli*. 122
Figure 42. Comparative *E. coli* growth curves in the presence of SSAs 70 and SSA 34. 125
Figure 43. Comparison between the methods used in the antimicrobial gel assays. 126
Figure 44. Antimicrobial studies conducted using 1:1 molar mixes of SSAs 66 – 68. 130
Figure 45. Structures of (A) SSA 69 and (B) SSA 70. 132
Figure 46. Widefield fluorescence microscopy images. 132

Figure 47. Widefield fluorescence microscopy Images. 133
Figure 48. Fluorescence Microscopy Images. 134
Figure 49. Fluorescence Microscopy images. 134
Figure 50 – Fluorescence microscopy images of MRSA and *E. coli.* 135
Figure 51. Fluorescence Microscopy Images of MRSA and E. coli in a 1:1 heterogeneous mix. 136
Figure 52. Transmitted Light images of *E. coli*. 137
Figure 53. Transmitted Light Images of MRSA. 137
Figure 54. Quantitative microscopy image analysis. 139
Figure 55. Competitive binding microscopy assay. 140
Figure 56. Quantitative Analysis of Fluorescence Microscopy Images. 141
Figure 57. Combined Fluorescence Microscopy Images. 142
Figure 58. Quantitative Analysis of Fluorescence Microscopy Images. 143
Figure 59. Diagram showing the principles of fluorescence anisotropy. 144
Figure 60. Fluorescence anisotropy and intensity measurements. 146
Figure 61. Structures of molecules discussed within this chapter. 153
Figure 62. Electrostatic potential map calculated for SSA 82. 155
Figure 63. Electrostatic potential maps calculated for SSA 83. 156
Figure 64. Single-crystal X-ray structures of SSA 82. 159
Figure 65. Single-crystal X-ray structures of SSA 83. 160
Figure 66. High-resolution ESI spectra of SSA 82 162
Figure 67. High-resolution ESI spectrum of SSA 83 163
Figure 68. Average intensity particle size distribution. 166
Figure 69. Average intensity particle size distribution. 167
Figure 70. Average intensity particle size distribution. 167
Figure 71. Average intensity particle size distribution. 168
Figure 72. ^{1}H NMR DOSY. 171
Figure 73. ^{1}HNMR spectra of (A) SSA 82 and (B) SSA 83 with a delay of 60 s. 172
Figure 74. ^{1}HNMR spectra of (A) SSA 82 and (B) SSA 83 with a delay of 60 s. 173
Figure 75. Downfield Chemical Shift Graph. 176
Figure 76. Example growth curves of MRSA demonstrating complete inhibition. 179
Figure 77. Example growth curves of *E. coli* demonstrating partial/delayed and partial inhibition of SSAs 82 and 83, respectively. 180
Figure 78. Comparison between the structures of SSAs (A) 70 and (B) 85. 180
Figure 79. Results from the inversion tests. 185
Figure 80. Results from the inversion tests. 185
Figure 81. Results from the inversion tests. 186
Figure 82. Results from the inversion tests. 186
Figure 83. Results from the inversion tests. 187
Figure 84. Graphical representation of the amplitude sweep experiments. 188
Figure 85. Example graph of amplitude sweep experiments conducted on SSA 82 (5 mg/mL) in (A) $NaNO_3$ and (B) in Na_2SO_4. 189
Figure 86. Example graph of amplitude sweep experiments conducted on SSA 83 (5 mg/mL) in NaCl. 190
Figure 87. Example images used to define packing density of gel fibres. 192
Figure 88. Example fluorescence microscopy images showing gel strand sharpening using the 'unsharp mask' filter. 193
Figure 89. Example widefield fluorescence microscopy images showing further gel strand definition using the 'difference of gaussians' filter. 194
Figure 90. Widefield fluorescence microscopy. 197
Figure 91. Widefield fluorescence microscopy. 198

Figure 92. Widefield fluorescence microscopy. 199
Figure 93. Widefield fluorescence microscopy. 199
Figure 94. Widefield fluorescence microscopy. 200
Figure 95. Widefield fluorescence microscopy. 200
Figure 96. Widefield fluorescence microscopy. 201
Figure 97. widefield fluorescence microscopy. 201
Figure 98. widefield fluorescence microscopy images. 202
Figure 99. Widefield fluorescence microscopy. 203
Figure 100. Widefield fluorescence microscopy. 204
Figure 101. Widefield fluorescence microscopy. 205
Figure 102. Widefield fluorescence microscopy. 205
Figure 103. Widefield fluorescence microscopy. 206
Figure 104. Widefield fluorescence microscopy. 207
Figure 105. *E. coli* surface diffusion assay. 209
Figure 106. Means plot reporting the zones of inhibition for SSAs 70, 82 and 83 used in determining statical significance. 211
Figure 107. SDS PAGE gel showing the expression and purification of VNp-mNg. 220
Figure 108. SDS PAGE gel showing the expression and purification α-syn-mCer3. 221
Figure 109. Background anisotropy curve. 222
Figure 110. Unacetylated α-syn-mCer3 change in anisotropy curves. 223
Figure 111. Acetylated α-syn-mCer3 anisotropy binding curves. 224
Figure 112. Acetylated α-syn-mCer3 anisotropy binding curves. 225
Figure 113. Acetylated α-syn-mCer3 Anisotropy binding curves. 226
Figure 114. Anisotropy binding curves. 227
Figure 115. VNp-mNg anisotropy binding curves 228
Figure 116. Anisotropy binding curves. 230
Figure 117. Melting curves of unacetylated α-syn-mCer3 alone. 232
Figure 118. Thermal shift melting curves. 234
Figure 119. SDS PAGE expression gel. 240
Figure 120. SDS PAGE purification gels. 241
Figure 121. SDS PAGE desalting gels. 242
Figure 122. SDS PAGE of co-sedimentation experiments. 242
Figure 123. Hum-1 TH1-mNg SDS PAGE gels. 243
Figure 124. PIP Strip binding assay. 244
Figure 125. Average fluorescence intensity values obtained from the density gradient co-sedimentation assay. 246
Figure S126 - E. coli DH10B growth curves created from an average of 6 absorbance readings in the presence of SSAs **32, 35**, **37**, **46**, **55**, **56**, **66**, **69, 70** and **77**. 296
Figure S127 - E. coli DH10B growth curves created from an average of 6 absorbance readings in the presence of SSAs **33** and **36.** 296
Figure S128 - E. coli DH10B growth curves created from an average of 6 absorbance readings in the presence of SSAs **34** and **42.** 297
Figure S129 **-** E. coli DH10B growth curves created from an average of 6 absorbance readings in the presence of SSAs **38**, **39**, **47**, **48**, **49**, **53**, **57** and **65**. 297
Figure S130 - E. coli DH10B growth curves created from an average of 6 absorbance readings in the presence of SSAs **40** and **41.** 298
Figure S131 - E. coli DH10B growth curves created from an average of 6 absorbance readings in the presence of SSAs **52**, **52**, **58**, and **63**. 298
Figure S132 - E. coli DH10B growth curves created from an average of 6 absorbance readings in the presence of SSAs **50**, **67**, **78**, **75** and **51.** 299

Figure S133 - E. coli DH10B growth curves created from an average of 6 absorbance readings in the presence of SSAs **60, 64** and **71.** MIC not calculated for compound **33** due to solubility of compound. 299
Figure S134 **-** E. coli DH10B growth curves created from an average of 6 absorbance readings in the presence of SSAs **72**, **73**, **74** and **76**..... 300
Figure S135 - E. coli DH10B growth curves created from an average of 6 absorbance readings in the presence of SSAs **79**, **80** and **81**. 300
Figure S136 - E. coli DH10B growth curves created from an average of 6 absorbance readings in the presence of SSA **68**..... 301
Figure S137 - E. coli DH10B growth curves created from an average of 6 absorbance readings in the presence of SSA **61**..... 301
Figure S138 - MRSA growth curves created from an average of 6 absorbance readings in the presence of SSAs **32, 35**, **36**, **46**, **54**, **55**, **56**, **69** and **70**. 302
Figure S139 **-** MRSA growth curves created from an average of 6 absorbance readings in the presence of SSAs **33, 36,** and **61** and **64**..... 302
Figure S140 **-** MRSA growth curves created from an average of 6 absorbance readings in the presence of SSAs **34** and **42.** 303
Figure S141 - MRSA growth curves created from an average of 6 absorbance readings in the presence of SSAs **38**, **39**, **48**, **49,** and **63**..... 303
Figure S142 **-** MRSA growth curves created from an average of 6 absorbance readings in the presence of SSAs **40 and 41**..... 304
Figure S143 **-** MRSA growth curves created from an average of 6 absorbance readings in the presence of SSAs **19, 20, 44** and **47**..... 304
Figure S144 **-** MRSA growth curves created from an average of 6 absorbance readings in the presence of SSAs **52**, **53**, **57**, **58**, **68** and **77**..... 305
Figure S145 **-** MRSA growth curves created from an average of 6 absorbance readings in the presence of SSAs **72**, **73**, **74**, **76**, **79**, **80** and **81**..... 305
Figure S146 **-** MRSA growth curves created from an average of 6 absorbance readings in the presence of SSAs **60** and **71**. 306
Figure S147 - MRSA growth curves created from an average of 6 absorbance readings in the presence of SSA **47**..... 306
Figure S148 **-** MRSA growth curves created from an average of 6 absorbance readings in the presence of SSAs **66**, **67** and **68**. Screening conducted at 3.75 mM as part of a separate study..... 307
Figure S210 – Surface diffusion assay using the SSA **70** (5 mg/mL) gel on MRSA inoculated agar plates..... 308
Figure S211 – Surface diffusion assay using the SSA **70** (5 mg/mL) gel on E. coli inoculated agar plates..... 308
Figure S212 – Well diffusion assay using the SSA **70** (5 mg/mL) gel on MRSA inoculated agar plates..... 308
Figure S213 – Well diffusion assay using the SSA **70** (5 mg/mL) gel on E. coli inoculated agar plates..... 309
Figure S214 – Well diffusion assay using the Ampicillin (5 mg/mL) on MRSA inoculated agar plates..... 309
Figure S215 – Well diffusion assay using Ampicillin (5 mg/mL) gel on E. coli inoculated agar plates..... 310
Figure S216 – Surface diffusion assay using the co-formulated SSA **70** and ampicillin gel (5 mg/mL) on MRSA inoculated agar plates..... 310
Figure S217 – Well diffusion assay using the co-formulated SSA **70** and ampicillin gel (5 mg/mL) on MRSA inoculated agar plates..... 310

Figure S218 – Surface diffusion assay using the co-formulated SSA **70** and ampicillin gel (5 mg/mL) on E. coli inoculated agar plates. 311
Figure S219 – Well diffusion assay using the co-formulated SSA **70** and ampicillin gel (5 mg/mL) on E. coli inoculated agar plates. 311
Figure S220 – *E. coli* transmitted image and fluorescence image at 450 nm used in fluorescence intensity calculations in the absence of both SSA **70** and FM4-64 at T = 30 minutes. Transmitted image used to locate cells on fluorescence image. Scale bar = 10 µM. 313
Figure S221 – *E. coli* transmitted image and fluorescence image at 605 nm used in fluorescence intensity calculations in the absence of both SSA **70** and FM4-64 at T = 30 minutes. Transmitted image used to locate cells on fluorescence image. Scale bar = 10 µM. 313
Figure S222 – *E. coli* transmitted image and fluorescence image at 450 nm images used in fluorescence intensity calculations in the absence of both SSA **70** and FM4-64 at T = 30 minutes. Transmitted image used to locate cells on fluorescence image at 450 nm. Scale bar = 10 µM. 314
Figure S223 – *E. coli* transmitted image and fluorescence image at 605 nm used in fluorescence intensity calculations in the absence of both SSA **70** and FM4-64 at T = 30 minutes. Transmitted image used to locate cells on fluorescence image. Scale bar = 10 µM. 314
Figure S224 – *E. coli* transmitted image and fluorescence image at 450 nm used in fluorescence intensity calculations in the absence of both SSA **70** and FM4-64 at T = 30 minutes. Transmitted image used to locate cells on Fluorescence image at 450 nm. Scale bar = 10 µM. 315
Figure S225 – *E. coli* transmitted image and fluorescence image at 605 nm used in fluorescence intensity calculations in the absence of both SSA **70** and FM4-64 at T = 30 minutes. Transmitted image used to locate cells on fluorescence image. Scale bar = 10 µM. 315
Figure S226 – *E. coli* transmitted image and fluorescence image at 450 nm used in fluorescence intensity calculations in the presence of SSA **70** at T = 30 minutes. Scale bar = 10 µM. 316
Figure S227 – *E. coli* transmitted image and fluorescence image at 450 nm used in fluorescence intensity calculations in the presence of SSA **70** at T = 30 minutes. Scale bar = 10 µM. 316
Figure S228 – *E. coli* transmitted image and fluorescence image at 605 nm used in fluorescence intensity calculations in the presence of SSA **70** at T = 30 minutes. Scale bar = 10 µM. 317
Figure S229 – *E. coli* transmitted image and fluorescence image at 450 nm used in fluorescence intensity calculations in the presence of SSA **70** at T = 30 minutes. Scale bar = 10 µM. 317
Figure S230 – *E. coli* transmitted image and fluorescence image at 605 nm used in fluorescence intensity calculations in the presence of SSA **70** at T = 30 minutes. Scale bar = 10 µM. 318
Figure S231 – *E. coli* transmitted image and fluorescence image at 450 nm used in fluorescence intensity calculations in the presence of SSA **70** at T = 30 minutes. Scale bar = 10 µM. 318
Figure S232 – *E. coli* transmitted image and fluorescence image at 605 nm used in fluorescence intensity calculations in the presence of FM4-64 at T = 30 minutes. Scale bar = 10 µM. 319

Figure S233 – *E. coli* transmitted image and fluorescence image at 605 nm used in fluorescence intensity calculations in the presence of FM4-64 at T = 30 minutes. Scale bar = 10 µM. 319
Figure S234 – *E. coli* transmitted image and fluorescence image at 605 nm used in fluorescence intensity calculations in the presence of FM4-64 at T = 30 minutes. Scale bar = 10 µM. 320
Figure S235 – *E. coli* transmitted image and fluorescence image at 450 nm used in fluorescence intensity calculations in the presence of FM4-64 at T = 30 minutes. Fluorescence image at 605 nm used to locate cells on fluorescence image at 450 nm. Scale bar = 10 µM. 321
Figure S236 – *E. coli* transmitted image and fluorescence image at 450 nm used in fluorescence intensity calculations in the presence of FM4-64 at T = 30 minutes. Fluorescence image at 605 nm used to locate cells on fluorescence image at 450 nm. Scale bar = 10 µM. 322
Figure S237 – *E. coli* transmitted image and fluorescence image at 450 nm used in fluorescence intensity calculations in the presence of both SSA **70** and FM4-64 at T = 30 minutes. Scale bar = 10 µM. 323
Figure S238 – *E. coli* transmitted image and fluorescence image at 605 nm used in fluorescence intensity calculations in the presence of both SSA **70** and FM4-64 at T = 30 minutes. Fluorescence image at 450 nm and transmitted image used to locate cells on fluorescence image at 605 nm. Scale bar = 10 µM. 323
Figure S239 – *E. coli* transmitted image and fluorescence image at 450 nm used in fluorescence intensity calculations in the presence of both SSA **70** and FM4-64 at T = 30 minutes. Scale bar = 10 µM. 324
Figure S240 – *E. coli* transmitted image and fluorescence image at 605 nm used in fluorescence intensity calculations in the presence of both SSA **70** and FM4-64 at T = 30 minutes. Fluorescence image at 450 nm and transmitted image used to locate cells on fluorescence image at 605 nm. Scale bar = 10 µM. 324
Figure S241 – *E. coli* transmitted image and fluorescence image at 450 nm used in fluorescence intensity calculations in the presence of both SSA **70** and FM4-64 at T = 30 minutes. Scale bar = 10 µM. 325
Figure S242 – *E. coli* transmitted image and fluorescence image at 605 nm used in fluorescence intensity calculations in the presence of both SSA **70** and FM4-64 at T = 30 minutes. Fluorescence image at 450 nm and transmitted image used to locate cells on fluorescence image at 605 nm. Scale bar = 10 µM. 325
Figure S243 – *E. coli* transmitted image and fluorescence image at 450 used in fluorescence intensity calculations in the absence of both SSA **70** and FM4-64 at T = 4 hrs. Transmitted image used to locate cells on fluorescence image. Scale bar = 10µM. 326
Figure S244 – *E. coli* transmitted image and fluorescence image at 605 nm used in fluorescence intensity calculations in the absence of both SSA **70** and FM4-64 at T = 4 hrs. Transmitted image used to locate cells on fluorescence image. Scale bar = 10µM. 326
Figure S245 – *E. coli* transmitted image and Fluorescence image at 450 nm used in fluorescence intensity calculations in the absence of both SSA **70** and FM4-64 at T = 4 hrs. Transmitted image used to locate cells on fluorescence image. Scale bar = 10µM. 327
Figure S246 – *E. coli* transmitted image and fluorescence image at 605 nm used in fluorescence intensity calculations in the absence of both SSA **70** and FM4-64 at T = 4 hrs. Transmitted image used to locate cells on fluorescence image. Scale bar = 10µM. 327
Figure S247 – *E. coli* transmitted image and fluorescence image at 450 nm used in fluorescence intensity calculations in the absence of both SSA **70** and FM4-64 at T = 4 hrs. Transmitted image used to locate cells on fluorescent image. Scale bar = 10µM. 328

Figure S248 – *E. coli* transmitted image and fluorescence image at 605 nm used in fluorescence intensity calculations in the absence of both SSA **70** and FM4-64 at T = 4 hrs. Transmitted image used to locate cells on fluorescence image. Scale bar = 10µM. 328
Figure S249 – *E. coli* transmitted image and fluorescence image at 450 nm used in fluorescence intensity calculations in the presence of SSA **70** at T = 4 hours. Scale bar = 10µM. 329
Figure S250 – Z-slice image used in combination with above figure to obtain more accurate fluorescence intensity calculations. Fluorescence image at 450 nm of *E. coli* in the presence of SSA **70** at T = 4 hours. Scale bar = 10µM. 329
Figure S251 – *E. coli* transmitted image and fluorescence image at 450 nm used in fluorescence intensity calculations in the presence of SSA **70** at T = 4 hours. Scale bar = 10µM. 330
Figure S252 – Different z-slices used in combination with figure above to obtain more accurate fluorescence calculations. Fluorescence images at 450 nm of *E. coli* in the presence of SSA **70** at T = 4 hours. Scale bar = 10µM. 331
Figure S253 – *E. coli* transmitted image and fluorescence image at 450 nm used in fluorescence intensity calculations in the presence of SSA **70** at T = 4 hours. Scale bar = 10µM. 332
Figure S254 – Different z-slices used in combination to obtain more accurate fluorescence calculations. Fluorescence image at 450 nm of *E. coli* in the presence of SSA **70** at T = 4 hours. Scale bar = 10µM. 333
Figure S255 – (Above) *E. coli* transmitted image and fluorescence image at 605 nm used in fluorescence intensity calculations in the presence of SSA **70** at T = 4 hours. (Below) fluorescent images at 450 used in combination with transmitted images to locate cells on fluorescence image at 605 nm. Scale bar = 10µM. 334
Figure S256 – *E. coli* transmitted image and fluorescence image at 605 nm used in fluorescence intensity calculations in the presence of FM4-64 at T = 4 hours. Scale bar = 10µM. 335
Figure S257 – *E. coli* transmitted image and fluorescence image at 605 nm used in fluorescence intensity calculations in the presence of FM4-64 at T = 4 hours. Scale bar = 10µM. 335
Figure S258 – *E. coli* transmitted image and fluorescence image at 605 nm used in fluorescence intensity calculations in the presence of FM4-64 at T = 4 hours. Scale bar = 10µM. 336
Figure S259 – (Above) *E. coli* transmitted image and fluorescence image at 450 nm used in fluorescence intensity calculations in the presence of FM4-64 at T = 4 hours. (Below) Fluorescence image at 605 nm used to locate cells on fluorescence image at 450 nm. Scale bar = 10µM. 337
Figure S260 – (Above) *E. coli* transmitted image and fluorescence image at 450 nm used in fluorescence intensity calculations in the presence of FM4-64 at T = 4 hours. (Below) Fluorescence image at 605 nm used to locate cells on fluorescence image at 450 nm. Scale bar = 10µM. 338
Figure S261 – *E. coli* transmitted image and fluorescence image at 450 nm used in fluorescence intensity calculations in the presence of both SSA **70** and FM4-64 at T = 4 hours. Scale bar = 10µM. 339
Figure S262 – *E. coli* transmitted image and fluorescence image at 605 nm used in fluorescence intensity calculations in the presence of both SSA **70** and FM4-64 at T = 4 hours. Fluorescence image at 450nm (Figure S658) and transmitted image used in combination with the fluorescence image at 605 nm to locate cells on fluorescence image at 605 nm. Scale bar = 10µM. 339

Figure S263 – *E. coli* transmitted image and fluorescence image at 450 nm used in fluorescence intensity calculations in the presence of both SSA **70** and FM4-64 at T = 4 hours. Scale bar = 10µM. 340
Figure S264 – *E. coli* transmitted image and fluorescence image at 605 nm used in fluorescence intensity calculations in the presence of both SSA **70** and FM4-64 at T = 4 hours. Fluorescence image at 450 nm (Figure S684) and transmitted images used to locate cells on fluorescence image at 605 nm. Scale bar = 10µM. 340
Figure S265 – *E. coli* transmitted image and fluorescence image at 450 nm used in fluorescence intensity calculations in the presence of both SSA **70** and FM4-64 at T = 4 hours. Scale bar = 10µM. 341
Figure S266 – *E. coli* transmitted image and fluorescence image at 605 nm used in fluorescence intensity calculations in the presence of both SSA **70** and FM4-64 at T = 4 hours. Figure S710 and transmitted images used in combination with fluorescence image at 605 nm for accurate fluorescence intensity calculations. Scale bar = 10µM. 341
Figure S267 – MRSA transmitted image and fluorescence image at 450nm used in fluorescence intensity calculations in the absence of both SSA **70** and FM4-64 at T = 30 minutes. Transmitted image used to locate cells on fluorescence image. Scale bar = 10µM 342
Figure S268 – MRSA transmitted image and fluorescence image at 605nm used in fluorescence intensity calculations in the absence of both SSA **70** and **FM4-64** at T = 30 minutes. Transmitted image used to locate cells on fluorescence image. Scale bar = 10µM 342
Figure S269 – MRSA transmitted image and fluorescence image at 605 nm used in fluorescence intensity calculations in the absence of both SSA **70** and **FM4-64** at T = 30 minutes. Transmitted image used to locate cells on fluorescence image. Scale bar = 10µM 343
Figure S270 – MRSA transmitted image and fluorescence image at 605 nm used in fluorescence intensity calculations in the absence of both SSA **70** and **FM4-64** at T = 30 minutes. Transmitted image used to locate cells on fluorescence image. Scale bar = 10µM 343
Figure S271 – MRSA transmitted image and fluorescence image at 450 nm used in fluorescence intensity calculations in the presence of SSA **70** only at T = 30 minutes. Scale bar = 10µM 344
Figure S272 – MRSA transmitted image and fluorescence image at 450 nm used in fluorescence intensity calculations in the presence of SSA **70** only at T = 30 minutes. Scale bar = 10µM 344
Figure S273 – MRSA transmitted image and fluorescence image at 450 nm used in fluorescence intensity calculations in the presence of SSA **70** only at T = 30 minutes. Scale bar = 10µM 345
Figure S274 – MRSA transmitted image and fluorescence image at 450 nm used in fluorescence intensity calculations in the presence of SSA **70** only at T = 30 minutes. Scale bar = 10µM 345
Figure S275 – MRSA transmitted image and fluorescence image at 605 nm used in fluorescence intensity calculations in the presence of SSA **70** only at T = 30 minutes. Fluorescence image at 450 nm used to locate cells on fluorescence image at 605 nm. Scale bar = 10µM 346
Figure S276 – MRSA transmitted image and fluorescence image at 605 nm used in fluorescence intensity calculations in the presence of **FM4-64** only at T = 30 minutes. Scale bar = 10µM 347

Figure S277 – MRSA transmitted image and fluorescence image at 605 nm used in fluorescence intensity calculations in the presence of **FM4-64** only at T = 30 minutes. Scale bar = 10μM 347
Figure S278 – MRSA transmitted image and fluorescence image at 605 nm used in fluorescence intensity calculations in the presence of **FM4-64** only at T = 30 minutes. Scale bar = 10μM 348
Figure S279 – MRSA transmitted image and fluorescence image at 450 nm used in fluorescence intensity calculations in the presence of both SSA **70** and **FM4-64** at T = 30 minutes. Scale bar = 10μM 348
Figure S280 – MRSA transmitted image and fluorescence image at 605 nm used in fluorescence intensity calculations in the presence of both SSA **70** and **FM4-64** at T = 30 minutes. Transmitted image used to locate cells on fluorescence image. Scale bar = 10μM 349
Figure S281 – MRSA transmitted image and fluorescence image at 450 nm used in fluorescence intensity calculations in the presence of both SSA **70** and **FM4-64** at T = 30 minutes. Scale bar = 10μM 349
Figure S282 – MRSA transmitted image and fluorescence image at 605 nm used in fluorescence intensity calculations in the presence of both SSA **70** and **FM4-64** at T = 30 minutes. Transmitted image used to locate cells on fluorescence image. Scale bar = 10μM 350
Figure S283 – MRSA transmitted image and fluorescence image at 450 nm used in fluorescence intensity calculations in the presence of both SSA **70** and **FM4-64** at T = 30 minutes. Scale bar = 10μM 350
Figure S284 – MRSA transmitted image and fluorescence image at 605 nm used in fluorescence intensity calculations in the presence of both SSA **70** and **FM4-64** at T = 30 minutes. Transmitted image used to locate cells on fluorescence image. Scale bar = 10μM 351
Figure S285 – MRSA transmitted image and fluorescence image at 450 nm used in fluorescence intensity calculations in the presence of both SSA **70** and **FM4-64** at T = 30 minutes. Scale bar = 10μM 351
Figure S286 – MRSA transmitted image and fluorescence image at 605 nm used in fluorescence intensity calculations in the presence of both SSA **70** and **FM4-64** at T = 30 minutes. Transmitted image used to locate cells on fluorescence image. Scale bar = 10μM 352
Figure S287 – MRSA transmitted image and fluorescence image at 605 nm used in fluorescence intensity calculations in the absence of both SSA **70** and **FM4-64** at T = 4 hours. Transmitted image used to locate cells on fluorescence image. Scale bar = 10μM . 352
Figure S288 – MRSA transmitted image and fluorescence image at 605 nm used in fluorescence intensity calculations in the absence of both SSA **70** and **FM4-64** at T = 4 hours. Transmitted image used to locate cells on fluorescence image. Scale bar = 10μM . 353
Figure S289 – MRSA transmitted image and fluorescence image at 605 nm used in fluorescence intensity calculations in the absence of both SSA **70** and **FM4-64** at T = 4 hours. Transmitted image used to locate cells on fluorescence image. Scale bar = 10μM . 353
Figure S290 – MRSA transmitted image and fluorescence image at 450nm used in fluorescence intensity calculations in the absence of both SSA **70** and **FM4-64** at T = 4 hours. Transmitted image used to locate cells on fluorescence image. Scale bar = 10μM . 354
Figure S291 – MRSA transmitted image and fluorescence image at 450nm used in fluorescence intensity calculations in the absence of both SSA **70** and **FM4-64** at T = 4 hours. Transmitted image used to locate cells on fluorescence image. Scale bar = 10μM . 354

Figure S292 – MRSA transmitted image and fluorescence image at 450 nm used in fluorescence intensity calculations in the presence of SSA **70** only at T = 4 hours. Scale bar = 10μM 355
Figure S293 – MRSA transmitted image and fluorescence image at 450 nm used in fluorescence intensity calculations in the presence of SSA **70** only at T = 4 hours. Scale bar = 10μM 355
Figure S294 – MRSA transmitted image and fluorescence image at 450 nm used in fluorescence intensity calculations in the presence of SSA **70** only at T = 4 hours. Scale bar = 10μM 356
Figure S295 – MRSA transmitted image and fluorescence image at 605 nm used in fluorescence intensity calculations in the presence of SSA **70** only at T = 4 hours. Fluorescence image taken 450 nm used to locate cells on fluorescence image 605 nm. Scale bar = 10μM 357
Figure S296 – MRSA transmitted image and fluorescence image at 605 nm used in fluorescence intensity calculations in the presence of **FM4-64** only at T = 4 hours. Scale bar = 10μM 358
Figure S297 – MRSA transmitted image and fluorescence image at 605 nm used in fluorescence intensity calculations in the presence of **FM4-64** only at T = 4 hours. Scale bar = 10μM 358
Figure S298 – MRSA transmitted image and fluorescence image at 605 nm used in fluorescence intensity calculations in the presence of **FM4-64** only at T = 4 hours. Scale bar = 10μM 359
Figure S299 – MRSA transmitted image and fluorescence image at 605 nm used in fluorescence intensity calculations in the presence of **FM4-64** only at T = 4 hours. Scale bar = 10μM 359
Figure S300 – MRSA transmitted image and fluorescence image at 450 nm used in fluorescence intensity calculations in the presence of **FM4-64** only at T = 4 hours. Transmitted image used to locate cells on fluorescence image. Scale bar = 10μM 360
Figure S301 – MRSA transmitted image and fluorescence image at 450 nm used in fluorescence intensity calculations in the presence of both SSA **70** and **FM4-64** at T = 4 hours. Scale bar = 10μM 360
Figure S302 – MRSA transmitted image and fluorescence image at 605 nm used in fluorescence intensity calculations in the presence of both SSA **70** and **FM4-64** only at T = 4 hours. Transmitted image used to locate cells on fluorescence image. Scale bar = 10μM . 361
Figure S303 – MRSA transmitted image and fluorescence image at 450 nm used in fluorescence intensity calculations in the presence of both SSA **70** and **FM4-64** at T = 4 hours. Scale bar = 10μM 361
Figure S304 – MRSA transmitted image and fluorescence image at 605 nm used in fluorescence intensity calculations in the presence of both SSA **70** and **FM4-64** only at T = 4 hours. Transmitted image used to locate cells on fluorescence image. Scale bar = 10μM . 362
Figure S305 – MRSA transmitted image and fluorescence image at 450 nm used in fluorescence intensity calculations in the presence of both SSA **70** and **FM4-64** at T = 4 hours. Scale bar = 10μM 362
Figure S306 – MRSA transmitted image and fluorescence image at 605 nm used in fluorescence intensity calculations in the presence of both SSA **70** and **FM4-64** only at T = 4 hours. Transmitted image used to locate cells on fluorescence image. Scale bar = 10μM . 363
Figure S307 – MRSA transmitted image and fluorescence image at 450 nm used in fluorescence intensity calculations in the presence of both SSA **70** and **FM4-64** at T = 4 hours. Scale bar = 10μM 363

Figure S308 – MRSA transmitted image and fluorescence image at 605 nm used in fluorescence intensity calculations in the presence of both SSA **70** and **FM4-64** only at T = 4 hours. Transmitted image used to locate cells on fluorescence image. Scale bar = 10µM . 364
Figure S309 – Hydrogen bond distances and angles observed for 3, calculated from the single-crystal X-ray structure shown of SSA **82**. 367
Figure S310 – Hydrogen bond distances and angles observed for 3, calculated from the single crystal X-ray structure shown of SSA **83**. 367
Figure S311 – ^{1}H NMR of SSA **82** in DMSO-*d*$_6$ conducted at 298.15 K. 368
Figure S312 –^{1}H NMR of SSA **83** in DMSO-*d*$_6$ conducted at 298.15 K. 368
Figure S313 – ^{13}C NMR of SSA **82** in DMSO-d_6 conducted at 298.15 K. 368
Figure S314 – ^{13}C NMR of SSA **83** in DMSO-d_6 conducted at 298.15 K. 369
Figure S315 – ^{1}H DOSY NMR spectrum of SSA **82** (55.56 mM) in DMSO-*d6* at 298 K and a table reporting the diffusion constants calculated for each peak used to determine the hydrodynamic diameter of the anionic and cationic components of SSA **82**. 370
Figure S316 – ^{1}H NMR spectrum of SSA **83** (55.56 mM) in DMSO-*d*6 at 298 K and a table reporting the diffusion constants calculated for each peak used to determine the hydrodynamic diameter of the anionic and cationic components of SSA **83**. 371
Figure S317 –^{1}H NMR stack plot of SSA **82** in DMSO-d_6 0.5 % H2O solution. Samples were prepared in series with an aliquot of the most concentrated solution undergoing serial dilution. 372
Figure S318 –1H NMR stack plot OF SSA **83** in DMSO-d_6 0.5 % H2O solution. Samples were prepared in series with an aliquot of the most concentrated solution undergoing serial dilution. 372
Figure S319 – Graph illustrating the ^{1}H NMR down-field change in chemical shift of urea NH resonances with increasing concentration of SSA **82** in DMSO-d_6 0.5 % H_2O (298.15 K). Equal K / dimerisation model: http://app.supramolecular.org/bindfit/view/e2d9a602-610c-4841-ae02-013b689f35c3 ; CoEK model: http://app.supramolecular.org/bindfit/view/ce54a853-3245-4e75-9754-66b20f4dd1e6 372
Figure S320 – Graph illustrating the ^{1}H NMR down-field change in chemical shift of urea NH resonances with increasing concentration of SSA **83** in DMSO-d_6 0.5 % H_2O (298.15 K). Equal K / dimerisation model: http://app.supramolecular.org/bindfit/view/38e6a72c-f700-47aa-b043-cfc3b3c3137e , CoEK model: http://app.supramolecular.org/bindfit/view/69d9124c-f2d4-4042-be5e-7fd0064909f8 373
Figure S321 – Correlation function data for 10 DLS runs of SSA **82** (0.56 mM) in an EtOH:H2O (1:19) solution at 298 K. 374
Figure S322 – Correlation function data for 10 DLS runs of SSA **82** (5.56 mM) in an EtOH:H2O (1:19) solution at 298 K. 374
Figure S323 – Correlation function data for 10 DLS runs of SSA **83** (0.56 mM) in an EtOH:H2O (1:19) solution at 298 K. 375
Figure S324 – Correlation function data for 10 DLS runs of SSA **83** (5.56 mM) in an EtOH:H2O (1:19) solution at 298 K. 375
Figure S325 – Calculation of CMC (28.95 mM) for SSA **82** in an EtOH: H2O 1:19 mixture using surface tension measurements. 375
Figure S326 – Calculation of CMC (28.95 mM) for SSA **83** in an EtOH: H2O 1:19 mixture using surface tension measurements. 376
Figure S327 – Results of the amplitude sweep experiments. For SSA **82** in the presence of NaCl (0.505 M). 376
Figure S328 – Results of the amplitude sweep experiments. For SSA **82** in the presence of KCl (0.505 M) 377
Figure S329 – Results of the amplitude sweep experiments. For SSA **82** in the presence of NaH_2PO_4 (0.505 M). 377

Figure S330 – Results of the amplitude sweep experiments. For SSA **82** in the presence of Na_2SO_4 (0.505 M). Sol to gel transition likely caused by experimental conditions. 378
Figure S331 – Results of the amplitude sweep experiments. For SSA **82** in the presence of $NaNO_3$ (0.505 M) 378
Figure S332 – Results of the amplitude sweep experiments. For SSA **82** in the presence of NaCl (0.505 M) 379
Figure S333 – SSA **82**(5 mg/mL) inversion test in the presence of NaCl (0.505 M). 379
Figure S334 – SSA **82**(5 mg/mL) inversion test in the presence of KCl (0.505 M) 380
Figure S335 – SSA **82**(5 mg/mL) inversion test in the presence of NaH_2PO_4 (0.505 M) 380
Figure S336 – SSA **82**(5 mg/mL) inversion test in the presence of Na_2SO_4 (0.505 M) 380
Figure S337 – SSA **82**(5 mg/mL) inversion test in the presence of $NaNO_3$ (0.505 M) 381
Figure S338 – SSA **82**(5 mg/mL) inversion test in the presence of NaOBz (0.505 M). 381
Figure S339 – SSA **83** (5 mg/mL) inversion test in the presence of NaCl (0.505 M). 381
Figure S340 – SSA **83** (5 mg/mL) inversion test in the presence of KCl (0.505 M) 382
Figure S341 – SSA **83** (5 mg/mL) inversion test in the presence of NaH_2PO_4 (0.505 M) 382
Figure S342 – SSA **83** (5 mg/mL) inversion test in the presence of Na_2SO_4 (0.505 M) 382
Figure S343 – SSA **83** (5 mg/mL) inversion test in the presence of $NaNO_3$ (0.505 M) 383
Figure S344 – SSA **83** (5 mg/mL) inversion test in the presence of NaOBz (0.505 M). 383
Figure S345 – Surface diffusion assay using the SSA **82** (5 mg/mL) gel on E. coli inoculated agar plates. 383
Figure S346 – Surface diffusion assay using the SSA **82** (5 mg/mL) gel on MRSA inoculated agar plates. 384
Figure S347 – Surface diffusion assay using the SSA **83** (5 mg/mL) gel on E. coli inoculated agar plates. 384
Figure S348 – Surface diffusion assay using the SSA **83** (5 mg/mL) gel on MRSA inoculated agar plates. 384
Figure S349 – Surface diffusion assay using the SSA 85 (5 mg/mL) gel on MRSA inoculated agar plates. 385
Figure S350 – Surface diffusion assay using the SSA 85 (5 mg/mL) gel on E. coli inoculated agar plates. 385
Figure S351. Fluorescence microscopy images showing the gel formation process of SSA **70** (5 mg/ mL) in NaCl (0.505 mM). 386
Figure S352 - Fluorescence microscopy images showing the gel formation process of compound **85** (5 mg/ mL) in NaCl (0.505 mM). Majority of strands formed were long, curled, and resultant gel was made up of layers of densely packed curled fibres and layers of loosely packed curled fibres. 387
Figure S353 – Fluorescence microscopy images showing the gel formation process of compound **82** (5 mg/ mL) in NaCl (0.505 mM). Long straight strands form initially which then branch off at bright spots (nodes), and pack closer together. The resultant gel is made up of a network of straight, branching fibres. 388
Figure S354 – Fluorescence microscopy images showing the gel formation process of compound **83** (5 mg/ mL) in NaCl (0.505 mM). Long strands formed and curled as they elongated, multiple strands branched off at bright spots (nodes). Gel fibres then aggregated together. The resultant gel was made up of densely packed non-uniform fibers. 389
Figure S355 – Fluorescence microscopy images showing the gel formation process of compound **85** (5 mg/ mL) in KCl (0.505 mM). Branching strands, gel made up of long, non-uniform strands with layers that were loosely packed and layers that were more closely packed. 390
Figure S356 – Fluorescence microscopy images showing the gel formation process of compound **82** (5 mg/ mL) in KCl (0.505 mM). Long unidirectional strands that were straighter and branching/connecting at bright spots 391

Figure S357 – Fluorescence microscopy images showing the gel formation process of compound **83** (5 mg/ mL) in KCl (0.505 mM). Regions of short straight fibres formed between regions of compound that hadn't formed strands yet. These regions of compound that hadn't formed strands yet became smaller over time, connecting the shorter strands together in multiple directions, resulting in a more geometric 'star' pattern. 392
Figure S358 – Fluorescence microscopy images showing the gel formation process of compound **85** (5 mg/ mL) in NaH_2PO_4 (0.505 mM). However, at 5mg/mL, aggregates formed, and the structures formed quickly. Then, small, fragile gel clumps formed which easily broke up and the resulting structures were indiscernible. Due to movement of these clumps. (Some of the last images captured using the NDsnap feature) 393
Figure S359 – Fluorescence microscopy images showing the gel formation process of compound **82** (5 mg/ mL) in NaH_2PO_4 (0.505 mM). Small aggregates formed and the larger structures formed, however no gel fibres formed. 394
Figure S360 – Fluorescence microscopy images showing the gel formation process of compound **83** (5 mg/ mL) in NaH_2PO_4 (0.505 mM). No gel fibers observed 395
Figure S361 – Fluorescence microscopy images showing the gel formation process of compound **82** (5 mg/ mL) in Na_2SO_4 (0.505 mM). Majority of strands were short straight fibres in a geometric pattern, however random longer curled fibres were also present..... 396
Figure S362 – Fluorescence microscopy images showing the gel formation process of compound **83** (5 mg/ mL) in Na_2SO_4 (0.505 mM). The long, curled strands from earlier form a more geometric pattern later on. 397
Figure S363 – Fluorescence microscopy images showing the gel formation process of compound **85** (5 mg/ mL) in $NaNO_3$ (0.505 mM). Compound aggregates formed then fibres, potentially using the aggregates to elongate. Resulting gel was made up of loosely packed, long, and curled strands..... 398
Figure S364 – Fluorescence microscopy images showing the gel formation process of compound **82** (5 mg/ mL) in $NaNO_3$ (0.505 mM). The final gel was made up of regions of densely packed gel fibres and regions of solvent. The resulting gel also 'floated' within the solvent. 399
Figure S365 – Fluorescence microscopy images showing the gel formation process of compound **83** (5 mg/ mL) in $NaNO_3$ (0.505 mM). Initial aggregates, then short straight strands formed. The strands got longer, and as they were elongated, they began to curl into themselves. Aggregated together in an almost cross-hatched manner and became more and more densely packed..... 400
Figure S366 – Fluorescence microscopy images showing the gel formation process of compound **85** (5 mg/ mL) in NaOBz (0.505 mM). Strands formed quickly from bright spots (aggregates) and randomly. Resulting gel was made up of densely packed disorganised strands..... 401
Figure S367 – Fluorescence microscopy images showing the gel formation process of compound **82** (5 mg/ mL) in NaOBz (0.505 mM). The resulting gel had regions of long curled strands and regions of shorter straighter strands separated by solvent..... 402
Figure S368 – Fluorescence microscopy images showing the gel formation process of compound **83** (5 mg/ mL) in NaOBz (0.505 mM). Initially long curled fibres formed, branching off at bright spots. The resulting gel was made up of regions of densely packed non-uniform gel strands 'floating' in solvent and constantly moving. 403

List of Tables

Table 1: Table highlighting the differences in the membrane lipid compositions of different bacterial species. 45
Table 2. Materials, reagents, and chemicals used in this thesis 57
Table 3. Plasmids and bacterial strains and used in this thesis 58
Table 4. The extinction coefficients and molecular weights of proteins used in this thesis. 66
Table 5. Volumes of reagents used in 10 % SDS PAGE gel preparation. 67
Table 6: Growth rates (*k*) of MRSA and *E. coli* in the presence of SSAs 32 – 81 in minutes. 94
Table 7: Type of inhibition exhibited by SSAs 32 – 81 against *E. coli* and MRSA. 105
Table 8. Antimicrobial screening results for SSAs 32 – 81. 106
Table 9. MIC_{50} values obtained for SSAs 32 – 81. 108
Table 10: The zone of inhibition. 127
Table 11. Phospholipid profiles.[196] 147
Table 12. Hydrogen bond angles and distances involved in hydrogen bonded self-association. 161
Table 13. DLS Data 165
Table 14. Critical micelle concentrations. 169
Table 15. Calculated d_H. 170
Table 16. Summary of the apparent percentage 'loss'. 174
Table 17. Summary zeta potential measurements. 175
Table 18. Summary Self-association constants. 177
Table 19: Growth parameters. 178
Table 20: MIC_{50} values obtained for SSAs 82 – 85. 181
Table 21: Minimum gelation concentrations obtained from inversion tests. 184
Table 22. Gel fibres summary Table. 195
Table 23. Gel fibres summary Table. 196
Table 24. Zones on inhibition measured using ImageJ.[106,246] 210
Table 26. Thermal shift assay. 233
Table 27. Statistical analysis summary Table. 233
Table 28. Thermal shift assay. 236
Table 29. Statistical analysis summary Table 236
Table 30. Thermal shift assay. 238
Table 31. Summary of statistical analysis for the negative controls. 247
Table 32. Statistical analysis comparing mean FM4-64 fluorescence values. 247
Table 33. Statistical analysis comparing mean mNg fluorescence values. 248
Table 34. Statistical analysis comparing mean FM4-64 fluorescence values. 249
Table 35. Statistical analysis comparing mean mNg fluorescence values. 249
Table 36. Statistical analysis comparing mean FM4-64 fluorescence values. 250
Table 37. Statistical analysis comparing mean mNg fluorescence values. 250
Table S38**.** Fluorescence intensities (FI) of *E. coli* at T=30 min and T= 4 hours under various conditions. Cells n_{total} = total number of cells analyzed for that condition. DAPI (450 nm) and mCherry (605 nm) filters used. 312
Table S39. Fluorescence intensities (FI) of MRSA at T=30 min and T= 4 hours under various conditions. Cells n_{total} = total number of cells analyzed for that condition. DAPI (450 nm) and mCherry (605 nm) filters used. 312
Table 40. [a] = larger than field of view, [b] = unable to discern individual fibres, [c] = no gel fibres observed 385

List of equations

Equation 1. Exponential phase growth rate equation. 71
Equation 2. Doubling time equation (T_d). 72
Equation 3. Growth rate (k) 72
Equation 4. The Stokes-Einstein equation. 164

Chapter 1: Introduction

6.1. Cells and growth

Over 10 million species are estimated to exist on earth, yet despite their differences, they all share the same fundamental life processes.[1–3] All are made up of fundamental building blocks called cells which contain all the genetic information defining the species. Some organisms are made up entirely of a single cell, whilst others are made up of intricate systems of specialised cells linked by complex communication. Regardless, the construction of a new organism begins with cells, which universally possess three distinct features: the cytoplasm, which is the solution inside of a cell, genetic material, and a cell membrane.[2]

6.1.1. Cell membranes

All cells contain a barrier, called a membrane, that defines the cell contents and allows regulated movement of substances between the external and internal environment of the cell.[3–5] The fluid mosaic model, introduced in 1972 by Singer and Nicolson, explains the structure of the membrane. While this model has evolved over time, the fundamental principles still hold true. This model describes the plasma membrane as a dynamic fluid combination of molecules, which allows controlled exchange of substances between the cells and the environment.[6] Membranes are an integral feature of the cell, responsible for maintaining the cell structure, function, and survival, and they comprise of phospholipids and membrane related proteins, that allow the cells to carry out specialised functions.[7]

6.1.2. Phospholipids

Phospholipids are amphiphilic molecules that make up a large proportion of the cell membranes. Amphiphiles are molecules containing hydrophobic components, with greater affinity to non-polar solvents, and hydrophilic components, with greater affinity to polar solvents.[8] Classification of amphiphiles is dependent on the nature of the polar head group. Cationic amphiphiles contain a positively charged head group, anionic amphiphiles contain a negatively charged head group, non-ionic amphiphiles contain a head group with no net charge and zwitterionic amphiphiles contain both a positive and negative charge in the head

group (Figure 1).[8] Low molecular weight amphiphiles can also be called ‘surfactants’, owing to their surface-active properties.

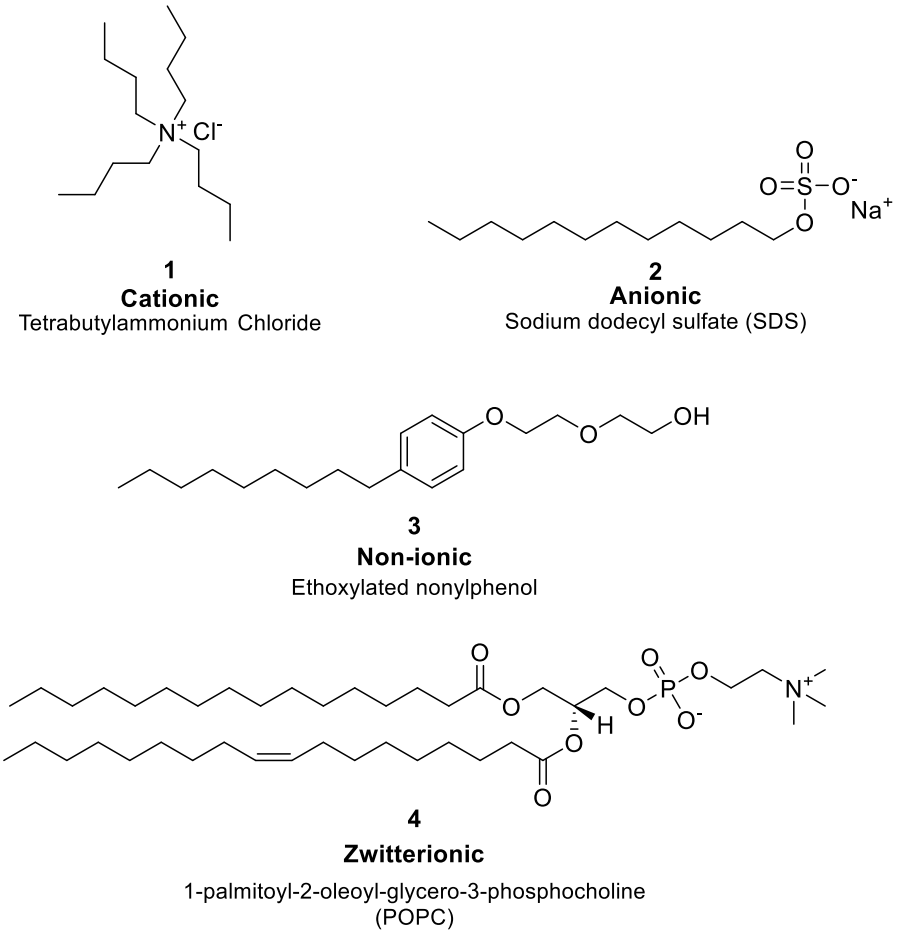

Figure 1. Types of amphiphiles.

Example amphiphiles categorised by the head group. **1** – cationic amphiphile tetrabutylammonium chloride, **2** – anionic surfactant SDS, **3** – nonionic emulsifier ethoxylated nonylphenol, and **4** – zwitterionic phospholipid POPC (1-palmitoyl-2-oleoyl-glycero-3-phosphocholine).[9–12]

At concentrations below the critical micelle concentration (CMC), amphiphiles in an aqueous environment, orient themselves at the air-water interface, so that the hydrophilic region is in contact with water and the hydrophobic portion is in contact with the air.[8,13] This lowers the surface tension, which can be manipulated for a range of uses such as detergents, adhesives, emulsifiers, and drug delivery vehicles.[14] As the concentration increases, the

surface becomes saturated, and eventually, the molecules begin to form self-associated structures, and the point the formation of these structures begins is the CMC.[8,13] The CMC therefore, as defined by Holmberg et al 2002, is the concentration of molecule above which self-assembled structures called micelles, are spontaneously formed (Figure 2).[13]

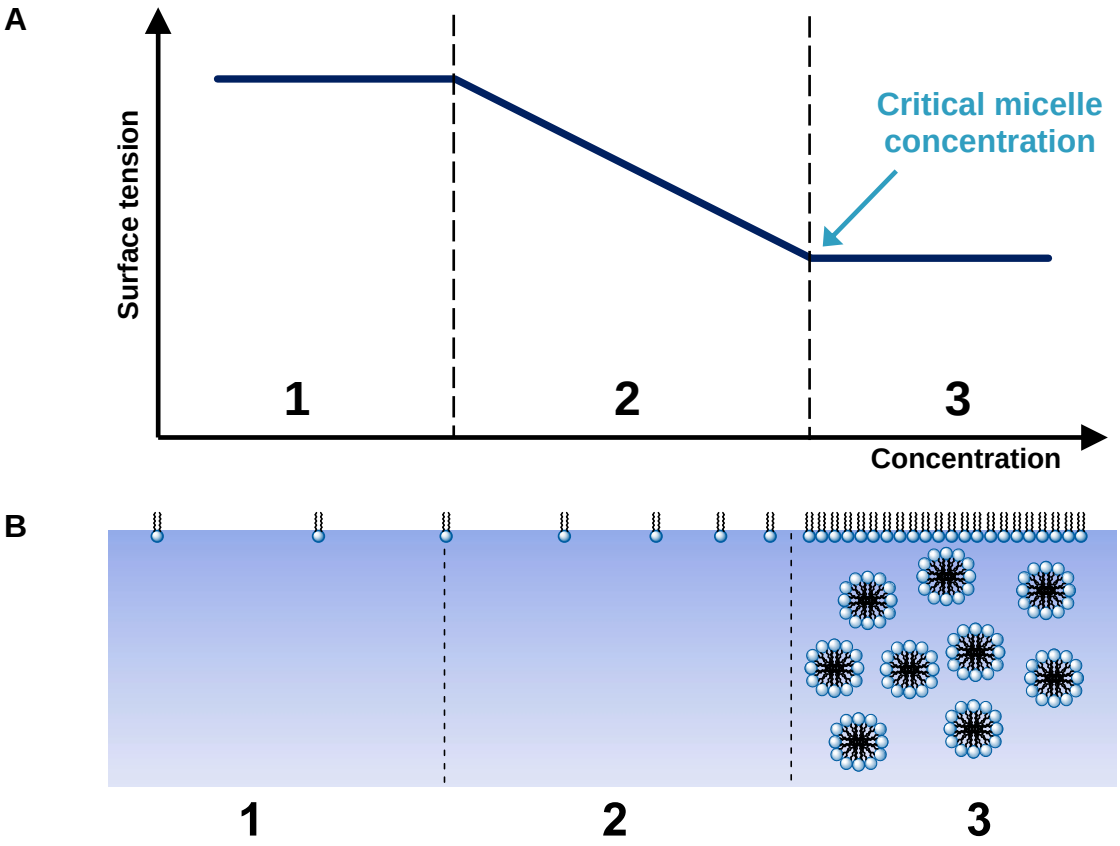

Figure 2. Schematic illustrations of the critical micelle concentration.

(A) graphical representation and **(B)** pictorial representations of the CMC.[15]

The solvent environment surrounding amphiphilic molecules drives their nanostructure formation through solvophobic interactions. In aqueous environments, hydrophilic regions interact with the water molecules, while the hydrophobic groups migrate to the center of the self-associated structure, away from the water molecules, forming a range of aggregates. The geometry and packing properties of the monomeric units also impact the resulting aggregate formation. The ratio of the area occupied by the hydrophilic and hydrophobic regions, termed the packing parameter or shape factor (***p***), is often used to predict the morphology of the resulting aggregate (Figure 3).[8,13,16]

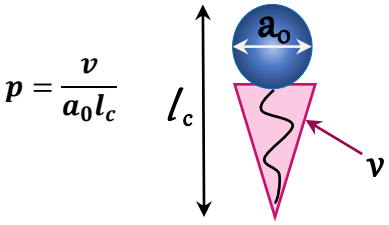

Figure 3. Packing parameter (*p*) equation.

The packing parameter equation and schematic diagram for determining amphiphile assembly morphologies: where v = volume of the hydrophobic segment, a_0 = contact area of polar head group, and l_c = length of the hydrophobic segment.[8,13,16]

Spherical micelle formation is more probably where $p < 1/3$, which is the case for molecules with strong polar or ionic head groups as well as non-ionic molecules with comparatively larger head groups (Figure 4a). Cylinder or rod formation occurs when $1/3 < p < ½$, which is characteristic of single-chain ionic monomers with either strongly bound counterions or added electrolytes, and with non-ionic molecules with either intermediately sized head groups or a head group similar in size to the tail region (Figure 4b). Double-chain amphiphiles, such as phospholipids, and non-ionic amphiphiles with shorter head groups tend to form lamellar structures, and their p values fall in the range of ½ - 1 (Figure 4c and 4d). If p >1, reversed structures are formed, as observed with the continued addition of electrolytes to ionic amphiphiles or with amphiphiles in microemulsions (Figure 4e).[8,13,16–18]

Surprisingly, cell membranes are not solely comprised of bilayer forming lipids. Non-bilayer lipids such as phosphatidylethanolamine (PE) and diaglycerol (DAG) are vital membrane constituents, with roles such as mediating proteolipid interactions within the bilayer and increasing membrane plasticity.[19,20] In fact, bilayers in cell membranes typically exhibit lateral heterogeneity; different combinations of lipids are arranged asymmetrically.[19]

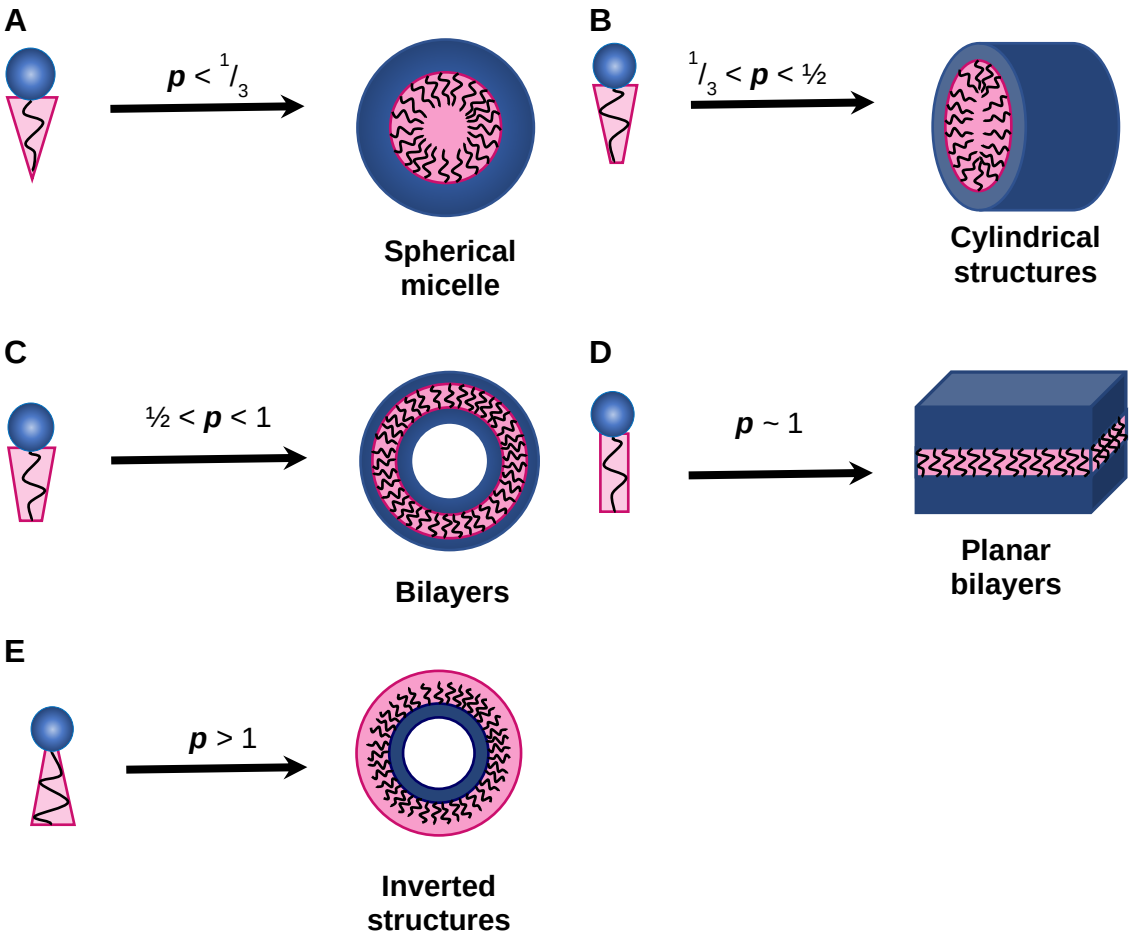

Figure 4. Amphiphile geometries

Example amphiphile geometries and the resultant aggregates that can be predicted using the packing parameter (*p*). **(A)** spherical micelle formation, **(B)** cylindrical or rod structure formation, **(C)** bilayer formation, **(D)** planar bilayer formation, and (**E**) inverted or reversed structure formation.[8,13,16–18]

Each individual lipid constituting the membrane plays an essential role that is regulated by proteins, contributing to a stable membrane. Functions of these lipids include their use in protein recruitment, signaling, and aiding in membrane structure and curvature.[21] These roles are dependent on the individual lipid structures, which impact the physicochemical properties.[21] Therefore, it is nearly impossible to understand the membrane and its related interactions without first understanding the lipids that constitute it.[22] Membrane lipids can be classified into three categories: sphingolipids, sterols, and glycerophospholipids (GPLs).

Sphingolipids are a subgroup of lipids containing a hydrophilic head group and a hydrophobic region, within which is a sphingosine backbone (Figure 5).[22,23]

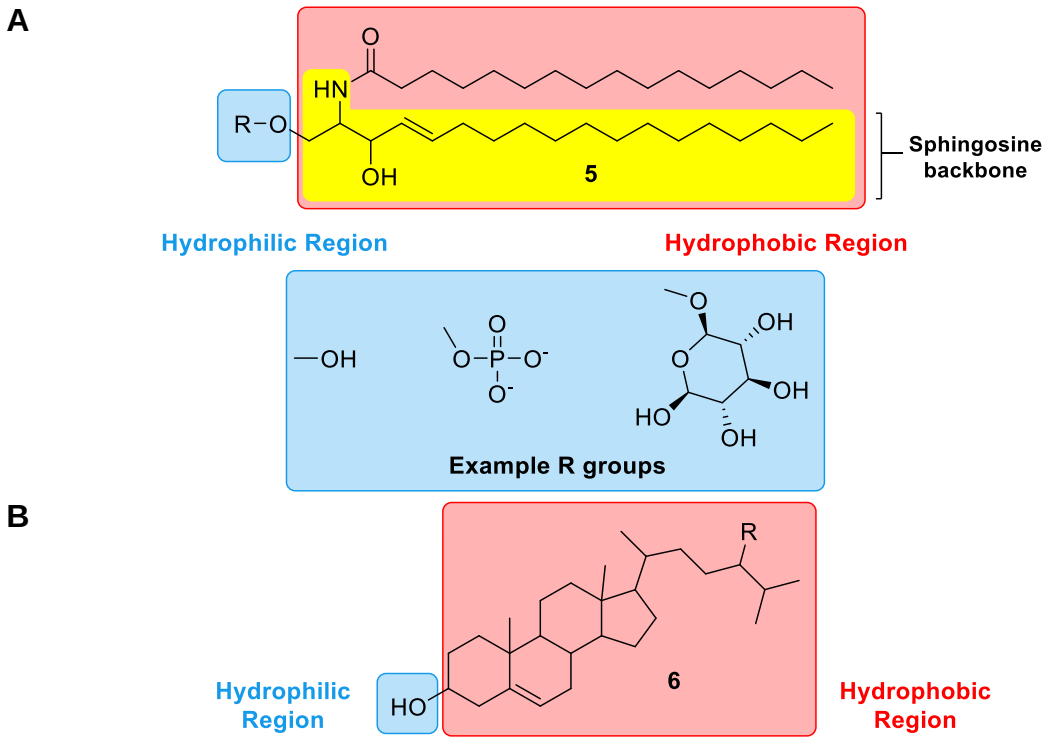

Figure 5. Sphingolipid and Sterol structures.

(A) An example of a sphingolipid comprising of a hydrophilic region (blue) and a hydrophobic region (red) made up of a sphingosine backbone (yellow) and a fatty acid chain; **(B)** an example sterol, comprising of a hydrophobic region made up of tetracyclic steroid core and hydrocarbon side chains, and a hydrophilic alcohol group.[22,24,25]

Sterols are a subgroup of lipids that contain a steroidal tetracyclic region, hydrophobic alkyl chains, and a hydrophilic alcohol group (Figure 5B).[25,26] While sphingolipids and sterols tend to constitute a smaller proportion of membranes, in comparison to glycerophospholipids, they perform a variety of essential biological functions including regulation of membrane structure, cytoskeletal reorganisation, and cell signalling.[22,23,25]

Glycerophospholipids (GPLs), on the other hand, are the most abundant membrane lipids. Their structure is similar to that of sphingolipids in that they contain a hydrophobic headgroup

and hydrophilic chains, however, GPLs are built on a glycerol backbone as opposed to sphingosine (Figure 6A).[27]

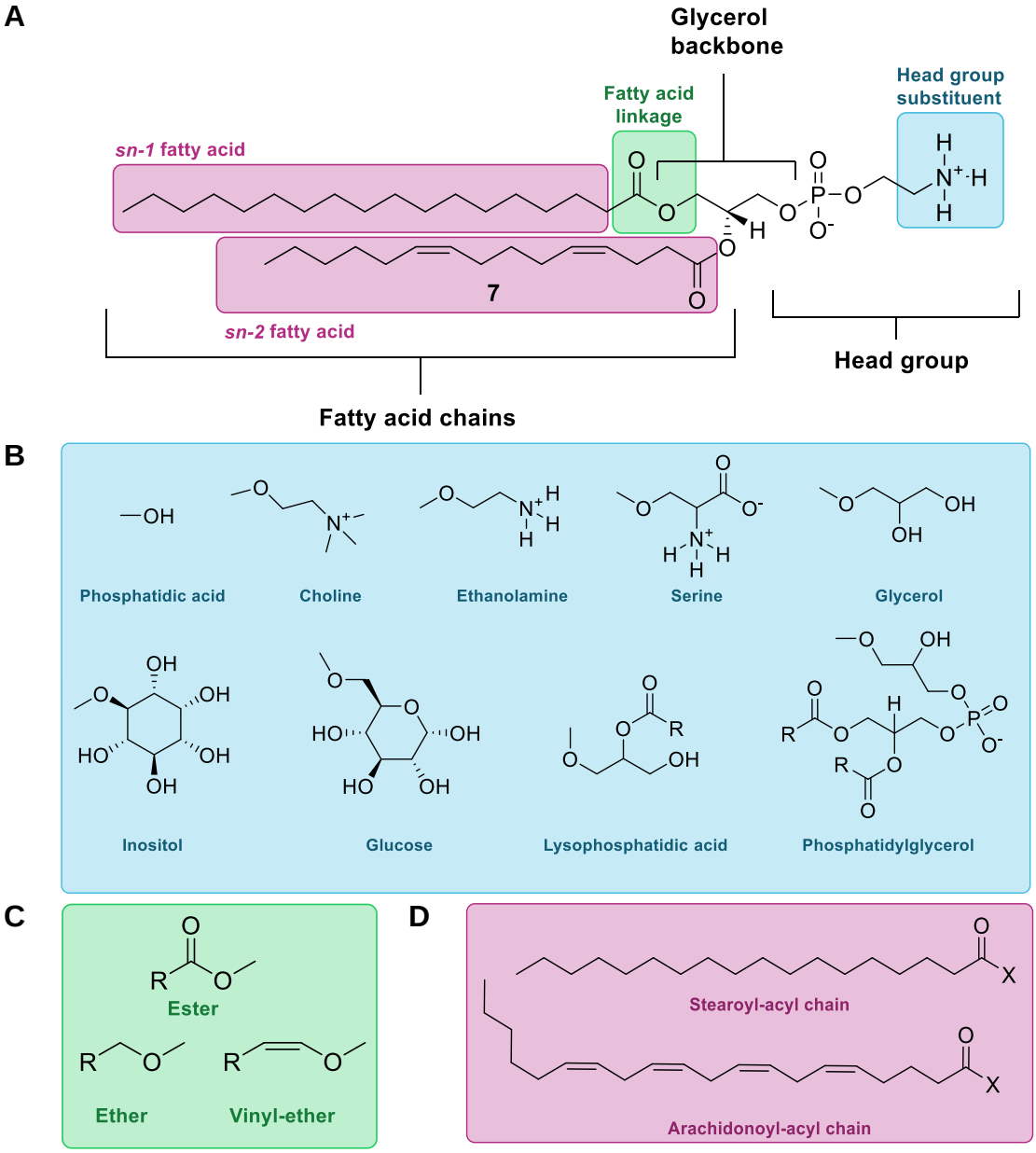

Figure 6. Chemical diversity of glycerophospholipids.

(A) The general structure of glycerophospholipids. Regions of variation include the *sn-1* and *sn-2* fatty acid chains (**purple)**, fatty acid linker (**green**), and head group substituent (**blue**). Structures of **(B)** head group substituents, **(C)** fatty acid linkers, and **(D)** example fatty acid chains.[21,27–29]

Diversity in GPLs arises from variations within the head group, the fatty acid chains, and the fatty acid linker (Figure 6A).[21,27–29]

Typically, the fatty acids are attached to the first two carbons of the glycerol backbone through various fatty acid linkers. While fatty acids can vary in chain length, double bond number, and position, the *sn*-1 fatty acid is usually a saturated or monounsaturated acyl chain, such as a stearoyl chain, and *sn*-2 fatty acid tends to be an unsaturated or polyunsaturated chain such as an arachidonoyl chain (Figure 6D).[27] Variation in the fatty acid chain is thought to influence membrane fluidity. Long saturated chains tend to reduce fluidity due to tighter packing and stronger lipid-lipid interactions, whereas unsaturated chains prevent tighter packing and reduce lipid-lipid interactions thereby increasing fluidity.[27]

GPL head group variation allows for a wide range of functions, as the headgroup present can determine the interactions and behaviour of the lipid (Figure 6B).[30,31] Variation in the head group can influence the overall charge of the lipid, which in turn impacts membrane rigidity, lipid orientation, and determine lipid interactions.[32–34] For example, negatively charged headgroups such as PA or PS may induce membrane curvature in the presence of excess ions due to charge repulsion, and more lamellar structures in the absence of ions.[35]

As previously discussed, the ratio between the sizes of the head and tail groups can drive the resulting bilayer formation. This has multiple implications in cell membrane structures and processes, one of these being membrane curvature.[19,27] When lipids with similar shapes cluster together, known as phase separation, the monolayer will adopt the spontaneous curvature of the lipids. Consequently, the bilayer adopts a curvature equal to the difference between the curvatures of its inner and outer monolayers. Phosphatidylcholine (PC) and phosphatidylserine (PS) are cylindrical lipids, thus tend to form flat layers, whereas lipids such as PE, cardiolipin (CA), and phosphatidic acid (PA) impose negative curvature on membranes, owing to their smaller comparative head size that results in a conical shape.[20,27] Conversely, lipids with larger headgroups such as those containing the lysophosphatidic acid

(LPA) head group or phosphoinositides (PI) tend to bend the membrane into a positive curvature, due to their inverted conical shape.[27] Specific proteins regulate the migration and distribution of lipids in the membrane at various stages. For example, during membrane remodeling or processes such as cell fission, non-bilayer forming lipids may migrate to the required site and impose membrane curvature to aid membrane deformation (Figure 7).[21,36]

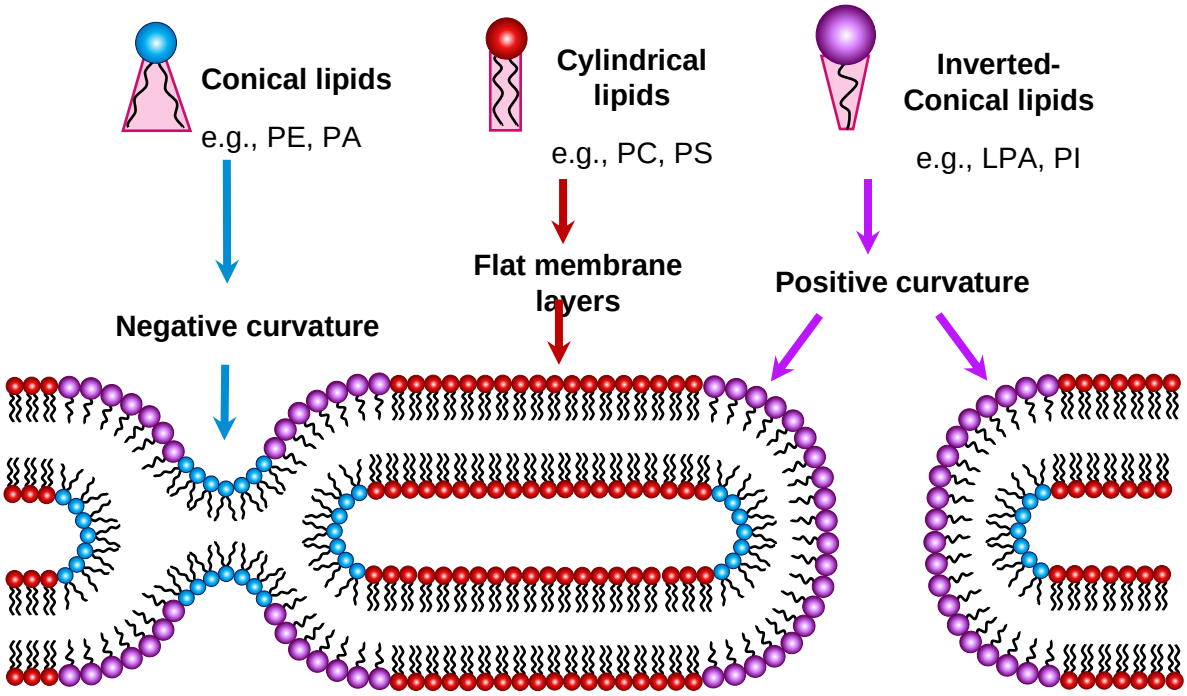

Figure 7. Prosed lipid migration during cell fission.

Imposed membrane curvature by asymmetrical lipids allows cells to bend during cell fission.[21,36]

1.1.3. Diffusion and osmosis

The internal homeostasis of the cell can be maintained by controlling the movement of molecules across the membrane. The transportation of molecules in and out of cells occurs in two main ways: passive transport and active transport (Figure 8).[2,5]

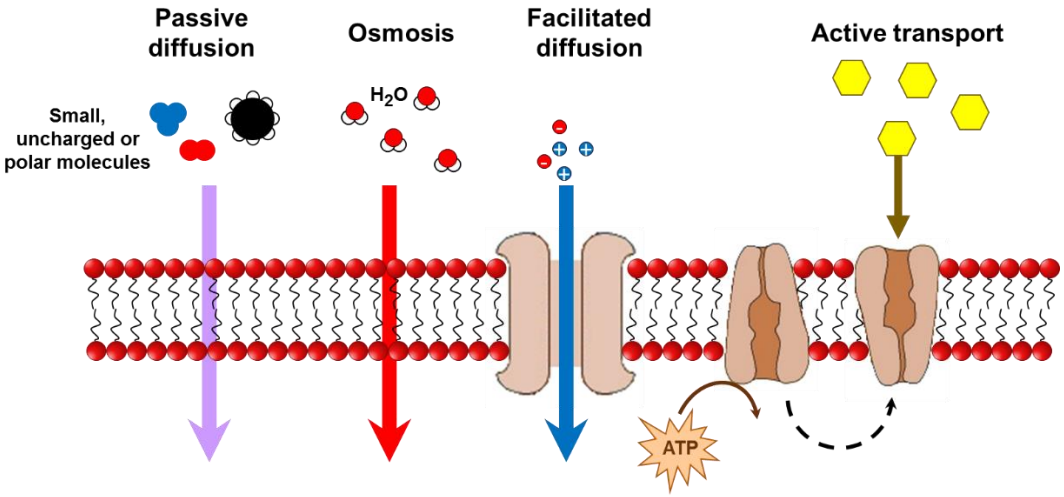

Figure 8. Routes for cytosolic entry.

Small, uncharged, polar or water molecules, in the case of osmosis, can passively diffuse across the membrane along a concentration gradient; some molecules are assisted by proteins to diffuse along a concentration gradient; larger molecules are transported by active transport and require energy (typically ATP hydrolysis) to do so. Adapted from G.M. Cooper (2002).[7]

Passive transport can involve the diffusion of molecules along a concentration gradient. Energy is not required for this process, as small, uncharged molecules can freely diffuse across the membrane.[5,7] Osmosis is a form of passive transport that involves the movement of water molecules along a concentration gradient, which is utilised when the membrane is not permeable to the solute.[5,7] Facilitated diffusion involves the movement of molecules along a concentration gradient through the use of carrier proteins or pores in the membranes which aid their transportation.[5,7] Larger molecules and charged molecules cannot freely diffuse across membranes and require additional mechanisms to enable transportation, one of these being active transport.[2,5] Active transport involves the movement of molecules against a concentration or electrochemical gradient through the use of chemical reactions, such as ATP hydrolysis. To carry out active transport, the cell utilises a variety of proteins that act as controlled passages between the intracellular and extracellular environments.[26]

1.1.4. Membrane Proteins

While the basic structure of cells is mainly provided by the phospholipid bilayer, associated with the membrane are a range of proteins that carry out the majority of membrane functions and provide membranes with characteristic functional properties.[2,5,7] The complement of proteins associated with the membrane varies depending on cell type, function, and localisation, and the way a protein is associated with the membrane can indicate its function (Figure 9).[2,7]

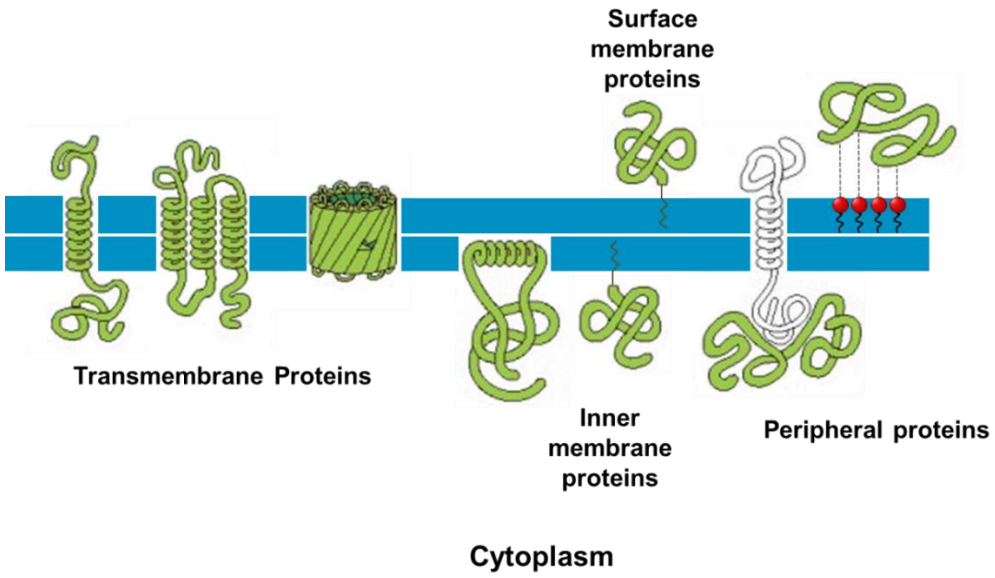

Figure 9. Types of membrane proteins.

The ways membrane proteins can associate with the lipid bilayer; transmembrane proteins span across the bilayer; inner membrane proteins are covalently linked to the inner membrane leaflet; surface membrane proteins covalently linked to the outer membrane leaflet; peripheral proteins are not directly linked to the membrane but associate with the membrane through interactions with other proteins or non-covalent interactions with phospholipid headgroups. Adapted from Alberts et al., 2002.[2]

Peripheral proteins, for example, are proteins that are not directly associated with the membrane but interact with the membrane through covalent or non-covalent interactions with other membrane proteins and phospholipid head groups. These proteins do not directly

interact with the hydrophobic core of the bilayer and tend to be hydrophilic enabling their role in cell signalling processes and cell interactions.[2,5,7]

Conversely, integral proteins contain several sections that are directly embedded in the bilayer. Integral proteins tend to be amphiphilic, to enable anchoring within the hydrophobic core of the bilayer.[2,5,7] Some integral proteins, however, can be completely hydrophobic and provide additional structural support to the membrane by embedding in the hydrophobic core only. Integral proteins on the external cell surface can interact with peripheral proteins, acting as cell surface receptors and can aid in cell signalling and interaction processes.[2,5,7]

Transmembrane proteins are integral proteins that span across the lipid bilayer, with both ends exposed on the cytoplasmic side and the external surface.[2,5,7] Similar to surface proteins, transmembrane proteins are amphipathic, anchoring them to the membrane and enabling interactions with both the intracellular and extracellular environments.[2,5,7] This is particularly useful in active transport, as it allows the passage of molecules that would otherwise be impermeable to the membrane. An example of a transmembrane transportation protein is the sodium-potassium ion pump in neuronal cells.[5,37] The sodium-potassium pump channels Na^+ ions out of the cell and K^+ ions into the cell, against the concentration gradients, which allows the cells to maintain a higher concentration of K^+ within the cell and a high concentration of Na^+ outside the cell.[5,37] An example of this is seen with neurons, which utilise sodium-potassium pumps to maintain a negative resting membrane potential and osmotic equilibrium.[5,37] Transportation proteins involved in transportation do not remain permanently open. Instead, they can exist in closed or open states which can be triggered by external or internal signals in a heavily regulated process.[5,37]

Inner membrane proteins are integral proteins that associate with the inner membrane leaflet of the bilayer. Proteins linked to a monolayer of the membrane are often involved in intracellular signalling roles and in anchoring the eukaryotic cytoskeleton.[5,7] Cytosolic membrane proteins are soluble and not covalently linked to the membrane at all, however,

these proteins are recruited to the membrane by specific signalling lipids such as phosphatidic acid (PA) or by inner membrane proteins.[5,7] The recruitment of cytosolic membrane proteins is seen in cell movement and deformation processes like cytokinesis and endocytosis. These proteins can function by aiding actin polymerisation and disassembly, signalling cell division sites, or facilitating membrane deformation. [5,7,38,39]

Membrane proteins are not always free to move within the membrane. Cells can confine proteins to specific locations, thereby creating protein and lipid domains in the membrane.[2] Membrane lipids and proteins influence a range of processes within the cell. The specific types of protein associated with the membrane and the lipid composition are largely dependent on the type of organism the cells belong to, and all the cells that make up these organisms can be classified into two groups; prokaryotic cells and eukaryotic cells.[2,5,26]

1.2. Prokaryotes

Prokaryotes represent the simplest form of life that share many similar characteristics. As their name suggests, (*pro* meaning before, *karyon* meaning nucleus), they do not contain membrane-bound genetic information.[4,5,40] Their genetic material instead is typically a single molecule of double-stranded DNA within the cytoplasm.[41] Prokaryotic cells are also defined by their simplified internal structure in comparison to eukaryotic cells; they lack internal organelles, and their smaller sizes (1 - 5µm).[3,41] Despite the simplicity of prokaryotes, exposure to a far harsher environment has led to the development of additional protective measures. Furthermore, functional specialisation and optimisation have diversified prokaryotes and resulting in a further subdivision.[4,40] The most recognizable and well classified unicellular prokaryotes are bacteria.[42] As their classification suggests, bacteria lack membrane bound organelles and a membrane defined nucleus, genetic material in bacteria is stored in a singular large circular chromosome instead. Variation only occurs through the number of copies of this nucleoid, which changes depending on the life cycle stage of the cell.[4,42]

1.2.1. Bacterial life cycle

Bacterial reproduction is exclusively asexual and only limited by nutrient availability in the environment, allowing bacteria to reproduce faster than multicellular organisms.[40,41,43] Bacterial growth in liquid media can be described by a well-characterised four-phase pattern (Figure 10).

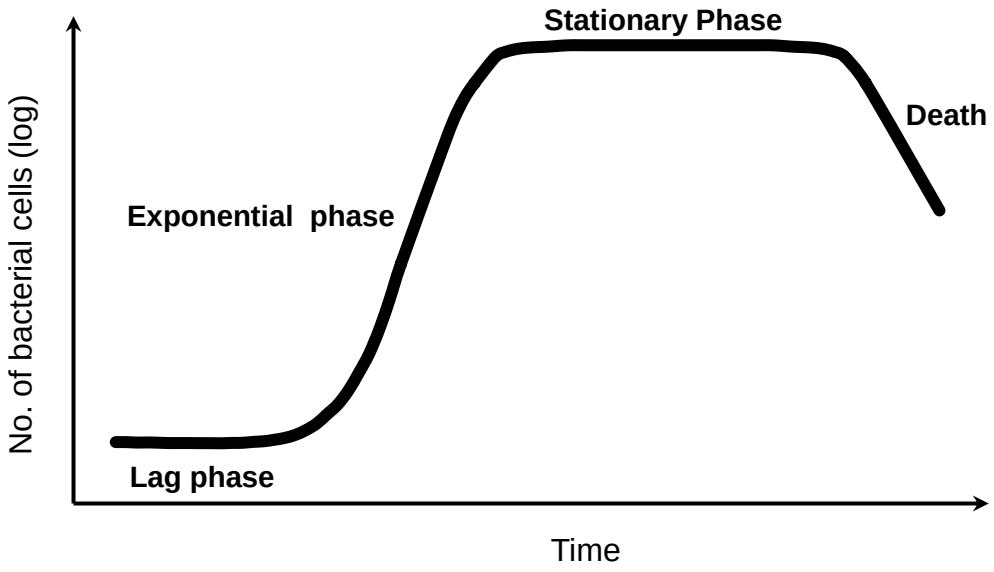

Figure 10. Graphical representation of the bacterial four-phase growth pattern.
Lag phase – cells acclimatise and prepare for division; exponential phase – rapid division through binary fission; stationary phase – cell death equals replication resulting in a plateau; death phase – cell death exceeds replication resulting in population decline.

Initially, cells begin in lag phase where they acclimatise to the new environment.[44,45] During lag phase, cells begin to prepare for replication by increasing their size, replicating DNA replication, and assembling division-related molecules such as the bacterial cytoskeletal protein FtsZ. Accumulation of FtsZ triggers cell division due to the protein self-assembling into a contractile ring structure at mid cell under the membrane – the site of division.[42,44,45] The FtsZ ring constricts at the leading edge of the invaginating membrane simultaneously with cell wall synthesis and the cell divides to form two daughter cells. This process is called

binary fission.[4,44] When cells start replicating, they enter the log or exponential phase of growth. During log phase, cells rapidly divide through binary fission, and the cell culture reaches its maximal growth rate.[45] If nutrient depletion occurs, bacterial growth plateaus as the number of cells diving is equal to those dying. This is called the stationary phase. The death phase occurs when bacteria lose the ability to divide and the number of dying cells exceeds that of living cells. Bacterial growth in this four-phase pattern is typically depicted in a growth curve.[45] While growth in a controlled culture tends to follow this four-phase growth pattern, bacterial growth in the environment can differ significantly due to environmental conditions, and availability of nutrients. Additionally, the bacterial cell cycle does not have distinct stages in the same way eukaryotes do, the various processes can overlap with one another. Thus, cells can alter the length of their cycle stages in response to the environmental and nutrient conditions. It is this adaptability that gives rise to a multitude of bacterial infections.[4]

1.2.2. Bacterial Pathogenesis

Bacterial infections occur through the invasion of a host organism by bacterial cells, leading to various illnesses ranging in severity. The capacity for bacteria to cause diseases (their pathogenesis) provides a basis for their organisation into three main groups. Primary pathogens are organisms that are the primary cause of infection e.g., *salmonella spp.*, opportunistic infections infect hosts with compromised defenses e.g., *Serratia marcescens,* and non-pathogens rarely or never cause infections e.g., *Lactobacillus acidophilus*.[42] The pathogenicity of an organism can be measured by virulence, which is affected by multiple factors including route of entry, host defenses, and the number of infecting bacteria. Bacterial growth is favoured in most cases due to their faster growth rate, high mutation rate, short generation time, and faster adaptability in comparison to eukaryotes.[42] Bacteria have adopted a host of defense mechanisms to evade the host's defense systems. Some bacteria have adapted to acquire the necessary nutrients without too much damage to the host, as the death of the host tends to result in the death of the organism. While the host immune

system can be sufficient in defending the host against the infection, where the defense systems fail, other methods are required to treat the infection.[42]

In 1928 Alexander Fleming discovered the first of a class of molecules capable of killing bacteria, through a mould contaminated agar plate.[46,47] Since then, a multitude of drugs have been developed to aid in the treatment of bacterial infections, called antibiotics. Fleming's discovery of Penicillin in 1928 kickstarted what is now termed as the golden era of antibiotic discovery.[48] An antimicrobial or antibiotic is a drug or molecule that inhibits the growth or kills microorganisms, specifically bacteria.[49] Antimicrobials can target bacteria through the inhibition of specific pathways or enzymes which then results in deficits in the targeted cell and may lead to cell death. An example is seen with beta-lactam antibiotics, such as penicillin, and glycopeptides such as vancomycin, which inhibit peptidoglycan synthesis, resulting in a compromised cell wall and ultimately cell death.[49–51] Upon receiving his Nobel prize in 1945, Fleming warned that the overuse of these drugs may lead to resistant bacterial forms. His concerns were justified, as over 70 years later, antimicrobial resistance (AMR) now threatens the prevention and treatment of bacterial infections and is projected to overtake the deaths attributed to cancer by 2050.[52–54]

1.2.3. Antimicrobial Resistance

Drug resistance is a natural phenomenon that occurs when a bacterial population is exposed to an antibacterial drug.[50,55] If a few members within the population already possess intrinsic resistance to this drug, selective pressures allow resistant bacteria to survive and susceptible bacteria to die.[56] If the bacterial population is exposed to the drug at sublethal concentrations, bacteria may be able to rapidly adapt due to the high mutation rate and relatively short life cycle and survive any toxic effects the drug may have had. While naturally occurring, the overuse and misuse of antibiotics have resulted in the acceleration of this process, resulting in multiple drug-resistant strains of bacteria.[50,56] Consequently, infections that have previously been relatively simple to treat now require last antibiotics. Furthermore,

the majority of antibiotics in use today were discovered during the golden era of antibiotics. Since then, few antimicrobials have been successful in overcoming drug-resistant bacteria. Thus, a combination of novel antimicrobial discovery, effective diagnostic procedure development, and better stewardship of current antimicrobials are required to overcome resistance.[57]

1.2.4. Advances in antimicrobial development

In 2017, the WHO published a priority list of pathogens that have developed resistance to the majority of current antimicrobials, including some last-line antimicrobials, to focus drug discovery efforts on those pathogens. Since then, a multitude of approaches have been employed to tackle AMR.[57] Paul Ehrlich by 1990 had conducted extensive systematic screenings of potentially antimicrobial compounds in his search for therapeutic agents with high affinities for pathogens and low host toxicity, describing them as ‘magic bullets’.[58] This ideology and the systematic method of screening are still used as a basis for antimicrobial drug discovery, albeit with newer technology. Molecules used in these systematic screenings tend to be isolated from natural sources, such as marine environments or plants, as many organisms produce highly effective toxins to outcompete bacteria that are less likely to exhibit mammalian toxicity.[48,59] Advances in technology have allowed for more effective systematic screenings to be conducted, as the potential for a molecule to be antimicrobial can be more accurately predicted. Furthermore, as bacterial genomes continue to be further understood, molecules to accurately target specific processes or pathways can be developed more efficiently. More recently, supramolecular chemistry has been utilised in the development of novel antimicrobials.

1.2.5. Supramolecular Chemistry and antimicrobial research

Supramolecular chemistry is a multidisciplinary field concerned with intermolecular interactions and self-assembly processes.[60,61] The design of self-associated molecules in drug design has become a focus due to their capacity for a range of applications, such as

drug delivery systems, medicinal gels, and therapeutic agents.[62–64] Supramolecular chemistry has also been utilised in extending the shelf life of established antimicrobials and for combination therapies.[48,65,66]

Molecular self-assembly is the spontaneous ordered aggregate formation through the use of non-covalent interactions, such as hydrogen bonding or electrostatic interactions. These self-association events are dependent on a multitude of factors including molecular geometries, intermolecular interactions, hydrophobic/hydrophilic interactions with solvent environments.[61] Self-association is at the heart of a range of essential life processes including protein folding, membrane bilayer formation, and DNA structure.[2,5,7] This is an attractive property for antimicrobial molecules as self-association may allow for active and specific targeting, alleviates many bioavailability barriers and can achieve high local concentrations of drug to a specific region.[62,64] The use of small self-associating molecules may also enable customisable architectures and simpler optimisation through stepwise molecular changes.[64]

One of the hindrances in antimicrobial discovery is the identification of new targets in bacteria. The majority of current antibiotics target similar cell processes, such as components of cell wall synthesis and DNA/RNA metabolism, and targeting these processes decreases the likelihood of effective antimicrobial activity.[67,68] Thus, bacterial membranes have become attractive targets, as there is a lower propensity for bacteria to gain resistance and may provide ways to target bacterial species with high specificity. In order to effectively target bacterial membranes, an understanding of the components of bacterial membranes is required.

1.2.6. Bacterial Membranes

The application of a gram stain allows for bacteria to be subdivided into two groups; gram-positive bacteria that retain the dye, and gram-negative bacteria that do not.[4,41] This distinction highlights a significant difference in the cell wall architecture between the two groups .[4] Bacterial cell walls functions to protect the integrity of the cell and allow bacteria to

interact with the environment in a heavily regulated manner.[4] In gram-positive bacteria, a thick layer of peptidoglycan and other wall polymers such as teichoic acids constitute a large proportion of the membrane, which surrounds the cytoplasmic membrane (Figure 11).[4,41]

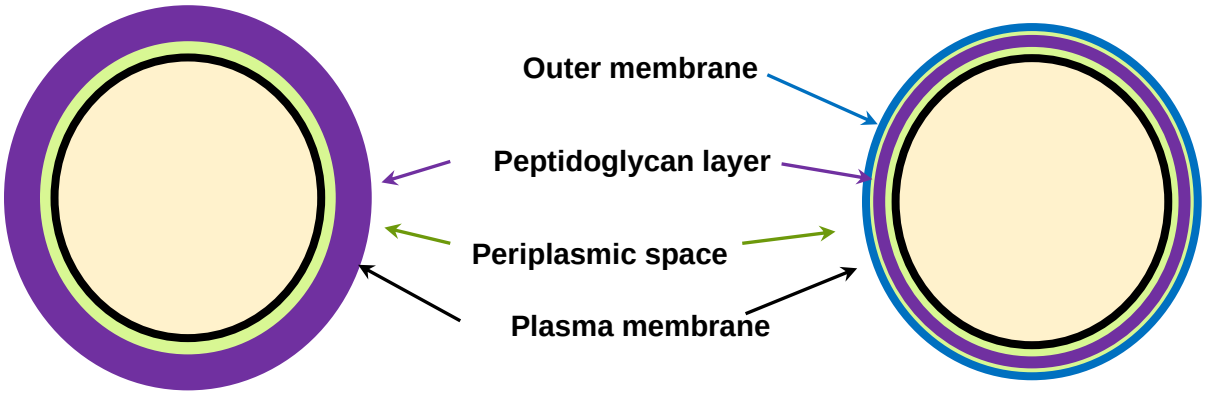

Figure 11. Gram positive vs Gram negative cell walls

A pictorial representation of bacterial cell wall structures, highlighting the differences between gram-positive and gram-negative bacteria. Gram-positive bacteria contain a thicker peptidoglycan layer, and gram-negative bacteria contain an additional outer membrane.

Wall teichoic acids are charged anionic polyol phosphates, which give the gram-positive cell wall a net negative charge.[4] Conversely, the gram-negative bacterial envelope is comprised of 3 layers. A cytoplasmic membrane, a thinner peptidoglycan layer in the periplasm, and an additional outer membrane.[4,41] Gram-negative bacteria also contain a range of periplasmic proteins that aid in a variety of processes such as toxin removal, transportation of molecules, and intracellular signalling.[4,69] The outer membrane of gram-negative bacteria is integral, as it acts as a selectively permeable barrier.

Bacterial plasma membranes carry out some of the functions that organelles in eukaryotes would carry out. For example, DNA replication and subsequent protein synthesis can occur almost simultaneously at the membrane, as a continual connection exists between DNA and membranes. To facilitate their multifunctional properties, proteins, and lipids within bacterial membranes are arranged in a 1:3 lipid-protein ratio.[4]

1.2.7. Bacterial Membrane lipid composition

E. coli membranes are well characterised and have previously been used as the model to understand bacterial membranes. Within *E. coli* are three major membrane lipids: PE (~75%), and anionic lipids PG and CL (~20%).[70,71] The membrane composition in *E. coli* is not representative of the diversity in membrane lipids present in other bacteria, as some species have more complex lipid compositions, as illustrated in Table 1. [70]

Lipid composition between species can vary drastically and can occur through the use of different lipids as well as lipid derivatives. For example, PE derivatives, such as monomethyl-PE (MMPE) or dimethyl-PE (DMPE) are common constituents in many bacterial species, which can either be intermediates in the synthesis of other lipids such as PC or can constitute a large proportion of a membrane.[70] Similarly, the PG head group can be modified through the addition of the amino acids lysine (in LPG), alanine (in alanyl-PG), or arginine (in arginyl-PG) which are present in some gram-positive species such as *Staphylococcus aureus* and *Bacillus subtilis*.[70] Some gram-negative bacteria, such as m*ycobacterium tuberculosis* can also synthesise PI, typically a eukaryotic membrane lipid. Phospholipids are not the only lipids that can constitute bacterial membranes, as DAG (diacylglycerol) lipids, sphingolipids, sulfolipids, and ornithine lipids, some of which are only present in prokaryotic membranes.[70,71]

Table 1: Table highlighting the differences in the membrane lipid compositions of different bacterial species.

PG – phosphatidylglycerol; CL – cardiolipin; PE – phosphatidylethanolamine; PC – phosphatidylcholine; OL – ornithine lipid; APG – alanyl-phosphatidylglycerol; PI – phosphatidylinositol; PIM – phosphatidylinositol mannoside; LPG – lysyl phosphatidylglycerol; GPL – glycophospholipid; GL – glycolipid; MMPE – monomethyl-PE; DMPE – dimethyl-PE. Adapted from Sohlenkamp & Geiger 2015.[70]

Membrane lipid compositions of different bacteria	
Bacteria	Membrane lipid composition
Escherichia coli	PG, CL, PE
Pseudomonas aeruginosa	PG, CL, PE, PC, OL, APG
Vibrio cholerae	PG, CL, PE, OL
Mycobacterium tuberculosis	PG, CL, PE, PI, PIM, OL
Bacillus subtilis	PG, CL, PE, LPG, GL, GPL
Staphylococcus aureus	PG, CL, LPG, GPL
Streptococcus pneumoniae	PG, CL, GL
Legionella pneumophila	PG, CL, PE, MMPE, DMPE, PC

1.2.8. Membrane Targeting

Although bacterial lipids make up a comparatively smaller proportion of bacterial membranes, they have a range of vital roles within cells. Membrane lipids can directly or indirectly influence certain cell processes such as cell signalling, cell division, and the regulation of cell shape and size.[7,72] Furthermore, as some membrane lipids and isoforms can be species-specific, lipid targeting provides an effective way of targeting bacteria with minimal mammalian toxicity. Membrane targeting antibiotics are thought to influence specific membrane properties that can result in cell death.[50] For example, some membrane antibiotics cause changes to the distribution of lipids on a membrane by causing clustering of lipids in one region. This prevents those lipids from taking part in essential interactions, which could therefore limit vital cell processes.[50] Gram-negative bacteria are notoriously more

resistant to antimicrobials, as previously mentioned, due to the additional membrane. While this membrane may provide additional protection against membrane targeting antimicrobials, damage to the outer membrane of gram-negative bacteria can result in significant bacterial toxicity, as it allows an influx of other larger molecules into the cell space.[50] Furthermore, the use of combinatory methods utilising membrane-targeting antibiotics and antimicrobials with secondary targets could be promising novel antimicrobial research routes.

1.3. Eukaryotes

Eukaryotic cells, as their name suggests (*Eu = true or well, karyon meaning nucleus)* are defined by the presence of a well-defined nucleus. Within this nucleus, eukaryotic DNA is arranged in linear chromosomes that vary in number and size depending on the organism.[3] Typically, eukaryotic cells are larger in comparison to prokaryotes and contain extensive internal compartments called organelles, all with distinct roles.[3] Reproduction of eukaryotic cells occurs in a more controlled manner through complex pathways and specific cell signals and responses, as defects in these responses lead to uncontrolled growth.[73]

1.3.1. The eukaryotic life cycle

Unlike prokaryotes, the eukaryotic cell cycle has four defined and heavily regulated phases, these being gap 1 (G1), gap 2 (G2), synthesis (S) phase, which collectively make up interphase, and mitosis (Figure 12).[2,74,75]

While the length of time spent in each stage varies between organisms, the fundamental processes remain the same. Following cytokinesis, the cell enters G1 phase, where the cell is metabolically active and continuously growing.[7,75] The initiation of DNA replication marks the beginning of S-phase, and once complete the cell then enters G2 phase, where the cell continues to grow and prepares for mitosis by synthesizing the relevant proteins, organelles, and membrane material for two daughter cells. Once the cell is ready, mitosis begins.[7,75]

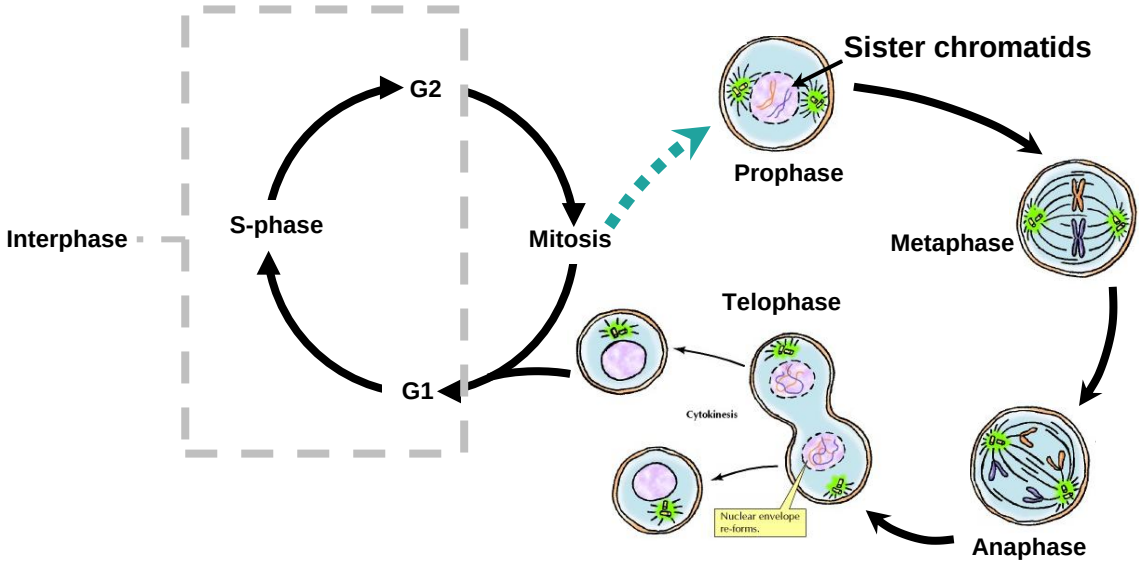

Figure 12. The stages of the eukaryotic life cycle.

Cells start in G1; "S"-phase is where DNA replication occurs; G2 stage where the cell prepares for division; Mitosis, which is further divided into distinct stages; prophase, metaphase, anaphase, and telophase where cytokinesis occurs. Adapted from Cooper (2000).[7]

Mitosis can be further divided into four distinct stages: prophase, metaphase, anaphase, and telophase. Prophase is defined by the condensing of newly replicated connected chromosomes (sister chromatids), nuclear envelope break down, and spindle microtubules formation. During metaphase, microtubules connect to the kinetochore of condensed sister chromatids and are oriented on opposite sides of the chromosomes, lining them up for cell division.[7] During anaphase sister chromatids are separated by the spindle microtubules, which pull each chromosome to opposite poles. Microtubules that are not attached to chromosomes also widen the gap between chromosomes and elongate the cell. Mitosis then ends with telophase, where nuclear envelopes re-form and chromosomes decondense, then the cell divides (cytokinesis) resulting in two daughter cells, starting the cycle once again.[7]

1.3.2. Cytoskeleton

The cytoskeleton is an extensive network of protein filaments involved in the maintenance of cell shape and polarity.[5,39,76] Its main substituent, actin, is one of the most highly conserved and abundant eukaryotic proteins.[77] The actin monomer (G-actin) is a globular protein, made up of 4 subdomains and a nucleotide-binding pocket. At critical concentrations and in the presence of specific ions, actin can self-assemble into polymerised helical filaments (F-actin), in a reversible process known as actin polymerisation.[5] F-actin is a polar filament, with two ends known as the barbed and pointed ends and this polarity defines the direction of myosin movement.

During actin polymerisation, G-actin initially aggregates to form an unstable oligomer, which acts as the nucleus for the subsequent elongation.[5] The actin filament is formed through the addition of ATP-bound G-actin at the barbed end of the filament.[2,76] The wide range of actin structures observed, including the actin cytoskeleton, are formed from this basic filament through the use of a plethora of actin-binding proteins (Figure 13).[2,7,78]

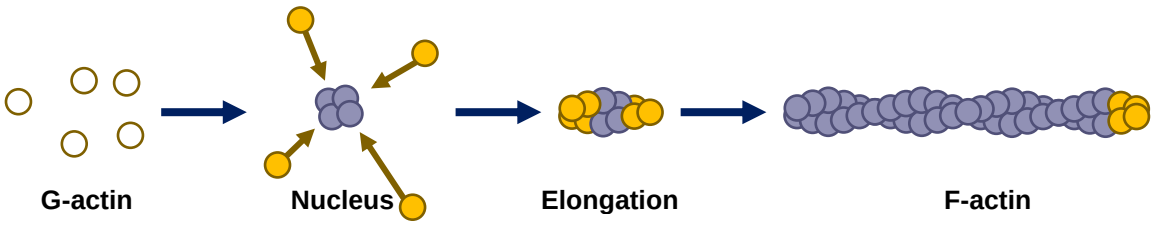

Figure 13. Actin polymerisation.

G- actin initially oligomerizes to form a nucleus, then the continued addition of G-actin results in an F-actin filament.

The second major component of the cytoskeleton is microtubules.[2,7] Microtubules are rigid polymers, composed of a dimeric protein called tubulin. Similar to actin, tubulin dimers polymerise through GTP (an ATP analogue) binding to form protofilaments, which in turn assemble in a head-to-tail arrangement into microtubules around a hollow core. Microtubules are also polar structures, with a fast-growing end and a slow-growing end, similar to the

barbed and pointed ends of actin. Disassembly of microtubules occurs through GTP hydrolysis which weakens the binding affinity of tubulin.[7]

Over 50 different proteins have been identified as constituents of intermediate filaments. Despite this diversity, intermediate filaments share the same basic structure; an amino terminus, an alpha-helical rod domain, and a C-terminus (Figure 14A).[7]

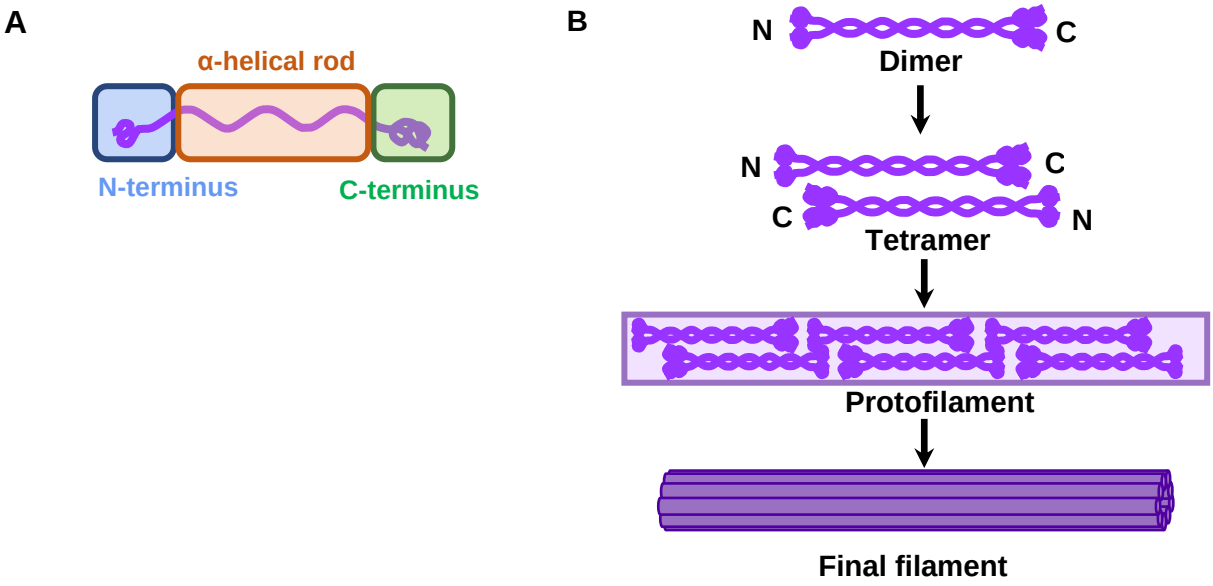

Figure 14. Intermediate filaments.

(A) the basic structure for protein units that make up intermediate filaments **(B)** intermediate filament assembly; proteins dimerise, then dimers assemble to form tetramers, tetramers assemble into protofilaments and protofilaments assemble into the final intermediate filament. Adapted from Cooper (2002).[7]

Filament assembly initially occurs through the alpha-helical rod domains of two proteins interacting with each other, resulting in dimers (Figure 14B).[7] Following this, dimers aggregate to form tetramers, then form protofilaments by assembling in an end-to-end arrangement.[7] The final intermediate filament, made up of up to eight protofilaments, is a rope-like filament of proteins. Intermediate filaments are apolar, and as such are not directly involved in cell movement, but instead provide structural support to cells.[63,79]

1.3.3. Molecular motor proteins

The movement of microtubules and pulling apart of sister chromatids during anaphase and division of cells to form two daughter cells are driven by a group of molecular motors called motor proteins.[2] Molecular motor proteins possess the ability to convert chemical energy, typically ATP hydrolysis, into movement of some kind. Three main superfamilies of motor proteins exist, which are the dynein family, the kinesin family, and perhaps the most recognisable, the myosin family.[2,80]

1.3.4. Myosin

Myosins are ATP and actin-binding motor proteins, implicated in numerous cellular processes such as muscle contraction, cell adhesion, and cytokinesis.[78] All myosins exhibit the same basic structure a catalytic head domain, a light chain binding neck region, and a tail domain.[7,78] Myosins can be categorised into 15 classes (Myosin 1-15), or more loosely classified as either conventional myosins, which are two-headed muscle myosins, and unconventional myosins. The most abundant and thoroughly studied unconventional myosin is Myosin 1 (Figure 15) .[81]

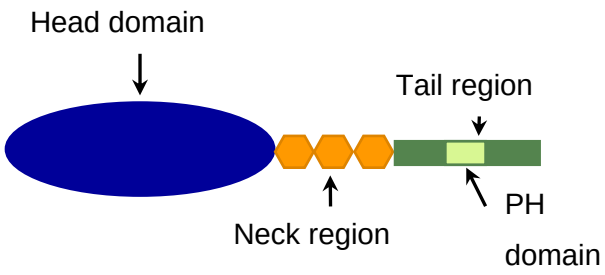

Figure 15. The basic structure of Myosin 1.

Like other myosins, Myosin 1 contains an actin-binding head domain, a light chain binding neck region, and a C-terminal tail domain with a pleckstrin homology (PH) domain within.[78,81]

Within the monomeric head domain of Myosin 1 proteins is an ATP binding site, which upon binding to actin couples ATP hydrolysis with motion. The actin activation of myosin ensures ATPase activity only operates at its maximal rate when bound to actin and slowly hydrolyses

ATP when actin is absent.[5] ATP hydrolysis provides sufficient energy for the transportation of cargo along actin filaments and may also be utilised to link actin bundles to plasma membranes.[5,7] Attached to the head domain is an alpha-helical neck region, thought to regulate myosin activity through calmodulin binding in response to Ca2+ signals.[78,81] All myosins are regulated by Ca2+ in some capacity, however, the responses to the Ca2+ signal differs between myosins depending on function. The C-terminal tail domains determine the specific function and localisation of myosin, as it contains specific binding sites. [81,82] Myosin 1 tends to localise to cell membranes, which is thought to be due to the presence of the pleckstrin homology (PH) domain, which is known to interact with phospholipids.[83–85] While the mechanisms behind their localisation and specific interactions are not fully characterised, myosin 1 proteins are thought to be involved in many transportation and cell deformation processes.[86–88] One of the deformation processes myosin 1 proteins are thought to be involved in is cell motility, which is also reliant on the dynamic properties of the cytoskeleton.[2]

1.3.5. Endocytosis

While channel proteins exist on cell membranes for the transportation of small molecules, eukaryotic cells also have a mechanism for the internalisation of larger molecules, such as proteins or signalling molecules. [7] This distinct process, called endocytosis, has a variety of functions including the detection of environmental changes, nutrient uptake, elimination of pathogens, cell-cell communication.[89] Eukaryotes utilise many endocytic pathways for cargo uptake, a prime example being clathrin-mediated endocytosis (Figure 16). [7,89] During clathrin-mediated endocytosis, the cargo to be internalised arrives at the cell surface and binds to cell surface receptors in regions called clathrin-coated pits (Figure 16A). A clathrin coat assembles at the membrane, and multiple membrane binding and scaffold proteins are recruited to the site (Figure 16 B & C).[7] Actin polymerisation then drives the invagination of the membrane around the cargo (Figure 16 D), forming a clathrin-coated vesicle which then buds off from the membrane (Figure 16 E).[7] Clathrin-coated vesicles are internalised through

actin polymerisation (Figure 16 E), then the clathrin coat is dissembled (Figure 16 F) and the components recycled while cargo is directed to the relevant region of the cell (Figure 16 G).

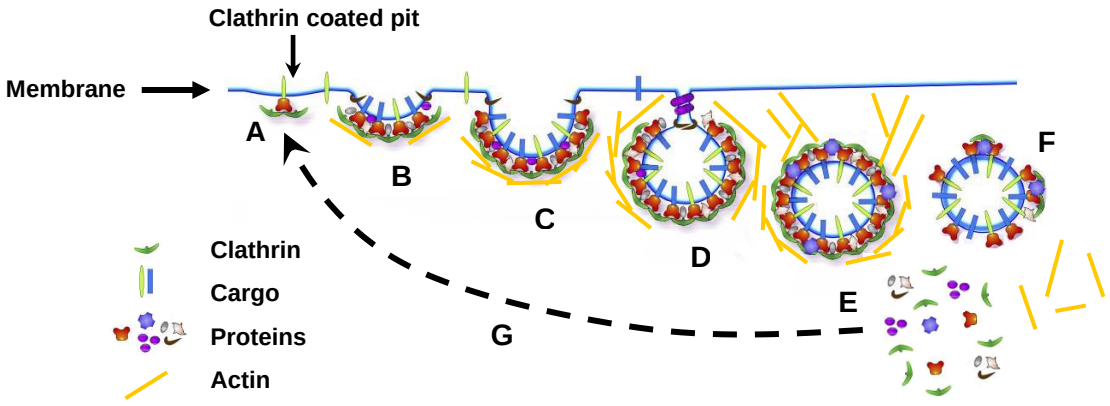

Figure 16.Clathrin-mediated endocytosis.

(A) Cargo arrives at membrane surface; **(B)** Clathrin coat forms and various proteins are recruited to the site; **(C & D)** Actin drives invagination of membrane; **(E)** vesicle buds off and is internalised; **(F)** clathrin coat disassembles; **(G)** clathrin coat components are recycled. Adapted from Schmidt (2017) and Mettlen et al., (2018).[90,91]

Clathrin-mediated endocytosis, like many processes within the cell, is very heavily regulated through conformational changes and post-translational modifications on associated proteins.[91]

1.3.6. Post-translational modifications

Translation is the process by which protein synthesis occurs and modifications made to the protein past this point are termed post-translational modifications.[2,5] Post-translational modifications can reversibly or irreversibly alter protein structure and function, enabling eukaryotic cells to dynamically regulate proteins. Almost all cellular events involve post-translational modifications to some degree, including cell-cell communication, endocytosis, gene expression.[2,5,92] Post-translational modifications can occur through protein cleavage (proteolysis), or through the addition of peptides, complex molecules, or chemical groups to a

protein. Three main chemical group additions are typically utilised in protein regulation: methylation, acetylation, and phosphorylation (Figure 17). [2,5,92]

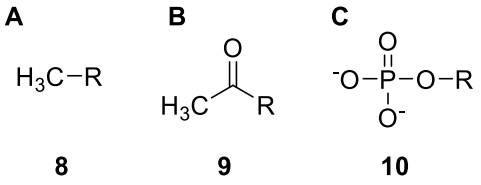

Figure 17. Chemical groups added to proteins in regulation.

(A) methyl group in methylation; **(B)** acetyl group in acetylation; **(C)** phosphate group in phosphorylation.

While methylation is more frequently seen in the regulation of DNA and gene expression, proteins can also be regulated through this mechanism.[92–94] Specific methyltransferases add methyl groups to protein, thereby regulating key cell processes. One of the most well-known cell processes regulated by methylation is transcription, where the addition of methyl groups to lysine or arginine residues can modulate RNA-protein interactions.[92–94]

The most common post-translational modification is phosphorylation. Phosphorylation is the addition of phosphate groups to a polar group, catalysed by protein kinases and phosphatases.[95,96]. In proteins, the polar group can be a serine, threonine, tyrosine, or histidine residue. The addition of a phosphate group results in a more hydrophilic protein, inducing conformational changes, thereby impacting the structure and subsequent interactions. Protein phosphorylation has been implicated in a broad range of cellular processes, in particular cell signalling, where phosphorylation status is reversible, and rapidly affects protein activity and levels.[97]

Protein acetylation is a highly specific post-translational modification that involves the addition of acetyl groups to proteins through the use of acetyltransferases.[98,99] Acetylation can be subdivided into three main types. Nα-acetylation, where the acetyl group is irreversibly added to the N-terminus, Nε-acetylation, where the acetyl group is reversibly added to a lysine residue and O-acetylation, where the acetyl group is added to a tyrosine, serine or threonine hydroxyl group.[99] Acetylation is a major regulator of transcription and has also been implicated in protein folding, mitochondrial function, and membrane interactions.[99]

As cells rely on proteins for all of their physiological functions, the misregulation of proteins can have catastrophic effects. Defects in post-translational regulation have frequently been shown to result in dysregulation of genes and abnormal protein structure and function, resulting in numerous disease states.[2,5] An example of this is seen with alpha synuclein.

1.3.7. Alpha synuclein

Alpha synuclein (αSyn) is a presynaptic neuronal protein coded by the SNCA gene, thought to contribute to the pathogenesis of Parkinson's disease (PD).[100–102] In aqueous solutions, αSyn is known to be natively unfolded, however upon binding to anionic lipids has been observed forming alpha-helical structure.[100,102] Similar to other members of the synuclein family, αSyn is composed of three distinct regions: an amino terminus containing lipid-binding motifs, a hydrophobic central 'NAC' region with a propensity to form beta-sheets, and a highly unstructured negatively charged C-terminus (Figure 18).[100,102] The central NAC region separates αSyn from other members of the synuclein family. αSyn is predominantly expressed in neuronal cells, making up 1% of total cytosolic proteins, and is also expressed in erythrocytes and platelets.[100,102] While its physiological function has not yet been fully characterised, it has been implicated in modulating synaptic transmission through interactions with synaptic vesicles. [100,102]

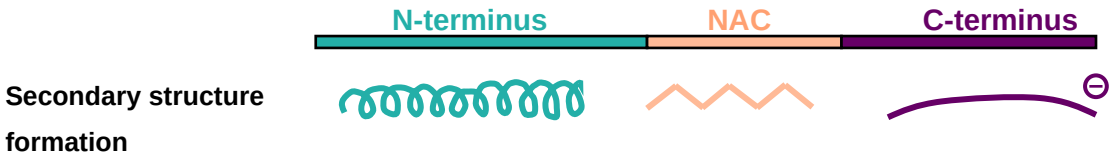

Figure 18. Structure of alpha synuclein.

αSyn consists of an amino terminus capable of forming an alpha-helical structure; a central NAC region capable of forming β-sheets, and an unstructured negatively charged C-terminus.

αSyn contains sites for post-translational modifications to occur, thus it has been suggested that misfolding or misregulation of αSyn may result in the formation of aggregated protein

structures called Lewy bodies, the hallmark of PD.[103] Understanding the roles of these post-translational modifications and may provide an insight into the function of αSyn and its involvement in PD pathogenesis.

1.3.8. The project

The function and interactions of individual membrane components has been the focus for a large amount of research for several decades.[104] While a great deal of information has been uncovered, much information surrounding membranes remains undiscovered and further research is required to fully understand their complexity. Membrane interactions influence a wide range of cell functions, thus once properly understood may provide a way of understanding and treating diseases. Additionally, these interactions may be manipulated for the creation of new therapeutics. This thesis seeks to investigate membrane lipid interactions in order to better understand membranes and to utilise that knowledge in the creation of therapeutics.

Aims of the project

This project aims to:

1. Identify and characterise the relationships between the structures of a group of self-associating amphiphiles and their antimicrobial activity. This information can then be utilised in the development of multifunctional antimicrobials with high efficacy against gram-negative bacteria in particular.
2. Understand the membrane binding properties of the molecules through the use of synthetic liposomes.
3. Identify the specific lipid interactions of membrane binding proteins myosin 1 and alpha synuclein, to ascertain their physiological functions and localisation.
4. Explore the impact of phosphorylation and acetylation on these lipid interactions to determine their role in protein regulation.

Chapter 2: Materials and Methods

Table 2. Materials, reagents, and chemicals used in this thesis

Materials	Source	Identifier
DPPE (1, 2-dipalmitoyl-sn-glycero-3-phosphoethanolamine)	Avanti Polar lipids	850705
DSPG (1, 2-distearoyl-sn-glycero-3-phospho-(1'-rac-glycerol) (sodium salt))	Avanti Polar Lipids	840465
POPA (1-palmitoyl-2-oleoyl-sn-glycero-3-phosphate (sodium salt))	Sigma-Aldrich	840857P
POPC (1-palmitoyl-2-oleoyl-glycero-3-phosphocholine)	Avanti Polar Lipids	850457
POPG (2-Oleoyl-1-palmitoyl-sn-glycero-3-phospho-rac-(1-glycerol) sodium salt)	Sigma-Aldrich	63371
Total lipid extract (*E. coli*)	Sigma-Aldrich	100500P
Polar lipid extract (*E. coli*)	Sigma-Aldrich	100600P
Cardiolipin (*E. coli*) (sodium salt)	Sigma-Aldrich	841199P
Octyl β-D-glucopyranoside (OGP)	Sigma-Aldrich	O8001
HisPur™ Ni-NTA Resin	Thermo Fisher	88221
PageRuler™ Unstained Protein Ladder	Thermo Fisher	26614
Coomassie Brilliant blue	Thermo Fisher	20278
QIAprep Spin Miniprep Kit **Print**	Qiagen	27106
HisPur™ Ni-NTA Resin	Thermo-Fisher	88223
Invitrogen FM4-64	Thermo-Fisher	T13320
Echelon Biosciences, PIP Strips™ Membranes	Thermo Fisher	P23750
Desalting Prepacked Gravity Flow Columns	Biorad	7322010
Invitrogen™ Empty Gel Cassettes, mini, 1.0 mm	Thermo Fisher	11549156

Table 3. Plasmids and bacterial strains and used in this thesis

Lab Stock number	Strain/Plasmid name	Antibiotic Selection
2353	*E. coli* DH10β	-
2757	USA300 MRSA	-
-	BL21 DE3	-
-	BL21 NatB	Chloramphenicol
-	BL21 Cam 1 Rosetta plysS	Chloramphenicol
V696	**Alpha-Synuclein-Cerulean3** (pDUET-1alpha-Synuclein-Cerulean3)	Kanamycin
V833	**Hum1 TH1** (pET151/D-TOPO-Nde1-Hum-1-TH1-SalI)	Ampicillin
V867	**Hum-1-TH1 D-mutant** (pET151DTOPO_myo1TH1-S782D)	Ampicillin
V884	**Neon green Hum1 TH1** (pET151DTOPO_NcoImNeongreen-Nde1hum1TH1(717-912)BamH1)	Ampicillin
V886	**Neon green Hum1 TH1 S734D** (pET151DTOPO_NcoImNeongreen-Nde1hum1TH1(717-912) S734D BamH1)	Ampicillin
V953	**VNp** (pRSFDuet-α-Syn Nt1-38-mNeonGreen-GGSG-Kpn1-His6)	Kanamycin

2.1. Software

- Fiji (ImageJ) software. US National Institutes of Health, Bethesda MA USA.[105,106]
- Origin (Pro), version 2020. OriginLab Corporation, Northampton MA USA.
- SkanIt Software version 6.0. Thermo Scientific, Waltham MA USA.
- MetaMorph Software. Molecular Devices, Sunnyvale, CA, USA.
- Mars Data Analysis Software. BMG Labtech, Ortenberg Germany.
- IBM SPSS Statistics for Windows, version 27.0. IBM Corp, Armonk NY: IBM Corp.
- Compass Data Analysis software version 4.1. Bruker, Billerica MA USA.
- ShelXT & ShelXS structure solution programs, Olex2 was used as an interface for all ShelX programs. G. M. Sheldrick, Universität Göttingen.[107–109]
- ACD Labs version 2019. Advanced Chemistry Development Inc., Toronto Canada, *www.acdlabs.com, 2020.*
- MestReNova version 14.2.0. Mestrelab, Santiago de Compostela, Spain.[110]
- Topspin NMR data analysis software version 4.0. Bruker, Billerica MA USA.
- Kalliope particle analysis software v1.2.0. Anton-Paar, Graz, Austria.
- IRsolution FTIR software v1.40. Shimadzu, Kyoto Japan.
- BindFit version 0.5. Supramolecular, OpenDataFit, P. Thordarson, J. Wilmot, and V. Efremova, CBNS & UNSW, Sydney Australia.[111]

2.2. Buffers & media recipes

Luria-Bertani (LB) Media

5 g Yeast Extract

10 g Tryptone

10 g Sodium Chloride

1 L dH_2O

Once prepared, the LB solution was autoclaved

αSyn Binding Buffer

0.05 M Tris·Cl

0.5 M NaCl

1 % Triton x100

10 mM Imidazole

pH 7.8

PMSF to a final concentration of 1 mM was then added prior to use

Ni-NTA Buffer A

0.05 M NaH_2PO_4

0.3 M NaCl

0.01 M Imidazole

pH 8.0

Ni-NTA Buffer B

0.05 M NaH_2PO_4

0.3 M NaCl

0.02 M Imidazole

pH 8.0

αSyn Wash Buffer

0.05 M Tris·Cl

0.5 M NaCl

1 % Triton x100

pH 6.0

Ni-NTA Buffer C

0.05 M NaH_2PO_4

0.3 M NaCl

0.5 M Imidazole

pH 8.0

αSyn Elution Buffer

0.05 M Tris·Cl

0.5 M NaCl

0.3 M Imidazole

pH 6.0

Denaturing Lysis Buffer

7 M Urea

0.1 M NaH_2PO_4

0.1 M Tris·Cl

pH 8.0

Column Storage Buffer

0.02 M MES

0.03 M NaCl

pH 5.0

αSyn Buffer A

0.02 M Tris·Cl

0.05 M NaCl

pH 7.0

αSyn Buffer B

0.02 M Tris·Cl

pH 7.0

Vesicle Buffer A

0.005 M NaH_2PO_4

0.5 M NaCl

pH 7.2

Vesicle Buffer B

0.1 M NaH_2PO_4

0.1 M Tris·Cl

pH 7.2

Denaturing Wash buffer

8 M Urea

0.1 M NaH_2PO_4

0.1 M Tris·Cl

pH 6.3

Denaturing Elution buffer

8 M Urea

0.1 M NaH_2PO_4

0.1 M Tris·Cl

pH 4.5

Desalting Buffer A

0.1 M NaH_2PO_4

0.1 M Tricl·Cl

pH 5.0

Desalting Buffer B

0.1 M NaH_2PO_4

0.1 M Tricl·Cl

pH 7.2

High Salt Buffer A

0.02 M Tris·Cl

0.4 M NaCl

pH 7.0

Vesicle Buffer C

0.1 M NaH_2PO_4

0.1 M Tris·Cl

0.5 M NaCl

pH 7.2

Tris Running Buffer

25 mM Tris·Cl

192 mM Glycine

3.5 mM SDS

pH 8.3

PIP Strip Detection Buffer

Must be made fresh each time

0.1 M NaCl

0.1 M Tris·Cl pH 9.6

5 mM $MgCl_2$

De-stain

500 mL Methanol

140 mL Acetic Acid

1360 mL dH_2O

PIP Strip Protein Buffer

PBS

0.1 % Tween 20

3 % BSA

0.1 %Coomassie Brilliant blue

0.75 g Coomassie R-250

400 mL Methanol

100 mL Acetic Acid

This was stirred for 15 minutes and then filtered through filter paper then 500 mL dH_2O was added

PBS

137 mM NaCl

2.7 mM KCl

10 mM Na_2HPO_4

1.76 mM KH_2PO_4

pH 7.4

PIP Strip Blocking Buffer

PBS

0.1 % v/v Tween 20

3 % BSA

PIP Strip Wash Buffer

PBS

0.1 % Tween 20

2.3. Biological Techniques

2.3.1. Preparation of Luria Broth (LB) Agar plates

Agar (6 g) was added to LB (400 mL) and autoclaved. Once cool, the LB Agar was poured into sterile Petri dishes under sterile conditions and allowed to set. LB plates were stored at 4 ºC until use.

2.3.2. Preparation of Bacterial Plates

Sterile LB agar plates were streaked using the desired bacteria (either *E. coli* or MRSA within this thesis), then incubated at 25°C overnight.

2.3.3. Preparation of Overnight Cultures

Overnight cultures were created by inoculating LB media (5 mL) with at least 4 single colonies of the desired bacteria from a bacterial plate under sterile conditions and incubated at 37°C overnight.

2.3.4. Preparation of Secondary cultures

Secondary cultures were prepared using LB (5 mL) inoculated with 50 µl from an overnight culture, then incubated at 37°C until the culture had reached an optical density of 0.4 at 600 nm unless otherwise stated.

2.3.5. Antibiotic Concentrations

Antibiotics were used to achieve plasmid selection at final concentrations of 50 µg/mL (Ampicillin & Kanamycin) or 25 µg/mL (Chloramphenicol).

2.3.6. DNA Preparation

Plasmid DNA from *E. coli* DH10β was extracted using the Qiagen miniprep kit (based on the alkaline lysis method) following the manufacturer's instructions.

2.3.7. *E. coli* Transformation

Aliquots of competent cells were thawed on ice then 2 µL plasmid DNA was added to the cells, mixed gently, and incubated on ice for 30 minutes. Cells were then heat shocked for 90 seconds at 42°C and returned to the ice for 2 minutes. LB (100 µL) was added to the cells and allowed to recover for 1 hour at 37°C before being plated onto an LB plate containing the appropriate antibiotic.

2.3.8. Nickel Column Preparation

A 10 mL syringe with the plunger removed was fixed onto a clamp stand. Sterile glass wool was added to the bottom of the syringe to prevent the nickel beads from pouring through. The nickel bead slurry was resuspended and pipetted (2-3 mL) into the column. Once the beads had settled the appropriate binding buffer (5 times of the resin volume was used to equilibrate the column by gently pipetting along the inside of the column, ensuring beads were not disturbed. A cap was used to stop the flow of buffer whenever necessary.

2.3.9. Nickel Column Protocol

To run a nickel column, the soluble-cleared cell extract was loaded onto the column, and the flow-through was collected to ensure any excess protein was not lost. Once the protein had bound to the nickel column, the column was washed using 5x the resin volume of the appropriate wash buffer. The protein was then eluted using the appropriate elution buffer, collecting 1 mL fractions until all the protein was removed from the column. The presence of the protein was then confirmed by SDS PAGE.

2.3.10. VNp and αS expression[98]

VNp or αS plasmids were transformed into calcium competent BL21 DE3 and BL21 NatB[98] in order to make acetylated and unacetylated versions of this protein. A single colony was used in LB (5 mL) and grown overnight at 37 °C. The overnight culture (1 mL) was used to inoculate LB (1 L) with the appropriate antibiotics and incubated at 37 °C, with shaking, until

an optical density of 0.4-0.6 was reached. IPTG was then added to a final concentration of 20 ug/mL, to induce the protein under the T7 promoter, and induced for 2-3 hours. Cells were then harvested by centrifugation at 1800 rcf for 20 minutes and the resulting pellets were frozen at -20°C until purification.

VNp-mNeongreen = ~ 32.4 kDa

αS-mNeongreen = ~42.55 kDA

2.3.11. VNp and αS Nickel Purification[98]

Frozen cell pellets were defrosted on ice and then resuspended in **αS binding buffer** (16 mL). Cells were then sonicated for 2 minutes; 20 second pulses and a 59 second gap between them. The suspension was then centrifuged at 4400 rcf for 30 minutes and the supernatant was kept for purification. A nickel column was set up and run as described previously, using **αS binding buffer** for equilibration, **αS wash buffer** for the wash steps, and **αS elution buffer** for the elution steps.

2.3.12. Protein Dialysis

Protein was placed into a cellulose membrane dialysis tubing with a molecular weight cut off point of 14,000 Da. The cellulose tubing was securely sealed at both ends and placed into 5 L **αS buffer B** which was then placed on a magnetic stirrer at 4 °C. The buffer was changed at least 3 times over a 24-48-hour period, divided into aliquots, and flash frozen using liquid nitrogen. Aliquots were stored at -80°C until the day of use.

2.3.13. Protein Concentration Calculation

Protein concentrations were calculated using absorbance measurements at 280 nm (A_{280}), the extinction coefficients and molecular weights listed in Table 4.

Table 4. The extinction coefficients and molecular weights of proteins used in this thesis.

	Extinction coefficients, ε (Mol^{-1} cm^{-1})	Molecular weight Daltons (Da)
VNp-mNeongreen	44350	32546
VNp-Lz-mNeongreen	45840	36483
αS-mCerulean	30495	42551
Hum 1 TH1	15025	27452
Hum 1 TH1-mNeongreen	57885	51340

2.3.14. Hum1 TH1 Expression

Plasmids were transformed into the appropriate calcium competent cells. A single colony was used in LB (5 mL) and grown overnight at 37°C. The overnight culture (1 mL) was used to inoculate LB (1 L) with the appropriate antibiotics and incubated at 37°C, with shaking, until an optical density of 0.4-0.6 was reached. IPTG was then added to a final concentration of 20 ug/mL, to induce the protein under the T7 promoter, and induced overnight at 25°C. Cells were then harvested by centrifugation at 1800 rcf for 20 minutes and then the resulting pellets were frozen at -20°C until purification.

2.3.15. Hum1 Native Purification

Frozen cell pellets were defrosted on ice and then resuspended in **Ni-NTA buffer A** (16 mL). Cells were then sonicated for 2 minutes; 20 second pulses and a 59 second gap between them. The suspension was then centrifuged at 4400 rcf for 30 minutes and the supernatant was kept for purification. A nickel column was prepared and run as described previously, using **Ni-NTA buffer A** for equilibration, **Ni-NTA buffer B** for the wash steps, and **Ni-NTA buffer C** for the elution steps.

2.3.16. Hum1 Denaturing Purification

Frozen cell pellets were defrosted on ice and then resuspended in **denaturing buffer A** (16 mL) and incubated at 25 °C with shaking for 1 hour, then centrifuged at 10,000 rpm for 20-30 minutes at 25 °C. The supernatant was then kept for purification. A nickel column was prepared as described previously, using **denaturing buffer A** for equilibration, **denaturing wash buffer** for the wash steps, and **denaturing elution buffer** for the elution steps.

2.3.17. Hum1 Desalting

Urea removal from denatured purified protein samples was conducted using the Biorad gravity desalting column according to the manufacturer's instructions using **desalting buffers A, B & C**.

2.3.18. SDS PAGE

2.3.18.1. **Gel preparation**

The resolving gel was prepared using the volumes in **Table 5** and pipetted into the gel cassettes, then isopropanol (1 mL) was pipetted to create a level gel interface. Once set, the isopropanol was removed and thoroughly washed with water. The stacking gel was then prepared using the volumes in **Table 5**, then pipetted on top of the resolving gel, and a comb was gently inserted before being allowed to set in the 37°C incubator.

Table 5. Volumes of reagents used in 10 % SDS PAGE gel preparation.

	Resolving Gel	**Stacking Gel**
dH_2O	2.55 mL	7 mL
1.5 M Tris (pH 8.8)	3.75 mL	-
1 M Tris (pH 6.8)	-	1.25 mL
10 % w/v SDS	100 µL	50 µL
30 % Acrylamide	3.2 mL	1.7 mL
10 % w/v APS	100 µL	50 µL
TEMED	15 µL	15 µL

2.3.18.2. Sample preparation

Loading buffer was added to all protein samples ($^1/_5{}^{th}$ of the volume of protein sample) then heated to 90°C for 10 minutes before being loaded into wells of the SDS PAGE gel.

2.3.18.3. SDS PAGE gel protocol

The PageRuler© unstained ladder was used as the protein standard on all gels. Gels were run at 120 V for 90 minutes in **Tris running buffer**. Then gels were stained with 0.1 % Coomassie brilliant blue for at least 1 hour then fully unstained using **de-stain.**

2.3.19. PIP Strip Protocol

PIP strip membranes developed by Echelon Biosciences (Salt Lake, UT) were purchased ThermoFisher Scientific (Table 2).

PIP strip membranes were kept wet throughout all the steps and gentle agitation was used where shaking was required. Membranes were placed in a petri dish and covered with PIP Strip blocking buffer (5-10 mL) then gently agitated for 1 hour at 25 °C or overnight at 4 °C. The PIP Strip blocking buffer was then discarded, and the protein of interest was added (0.5 µg/mL) in PIP Strip protein buffer (5-10 mL) and incubated for 1 hour at room temperature with gentle agitation. The protein solution was discarded, and membranes were washed with PIP Strip wash buffer (5 mL) with gentle agitation at 25°C for 10 minutes and repeated three times. The desired primary antibody was added (1:2000 in the blocking buffer) and the membranes were incubated for 1 hour at 25 °C with gentle agitation. Membranes were then washed three times with PIP Strip wash buffer (5 mL) with gentle agitation at 25 °C for 10 minutes. The wash buffer was discarded, and the desired secondary antibody was added (1:2000 in Blocking Buffer), then incubated for 1 hour at 25 °C or overnight at 4 °C with gentle agitation. The membranes were washed with the PIP Strip wash buffer three times, and the buffer was discarded. PIP Strip detection buffer was added to fully cover the

membranes and allowed to rest for 5 minutes. Membranes were removed and placed in an empty petri dish and washed over with 1 mL of enzyme substrate until spots could be visualised, then rinsed with sterile water. Membranes were then imaged, and results were compared to the PIP Strip layout (Figure 19) to determine which phospholipids had bound.

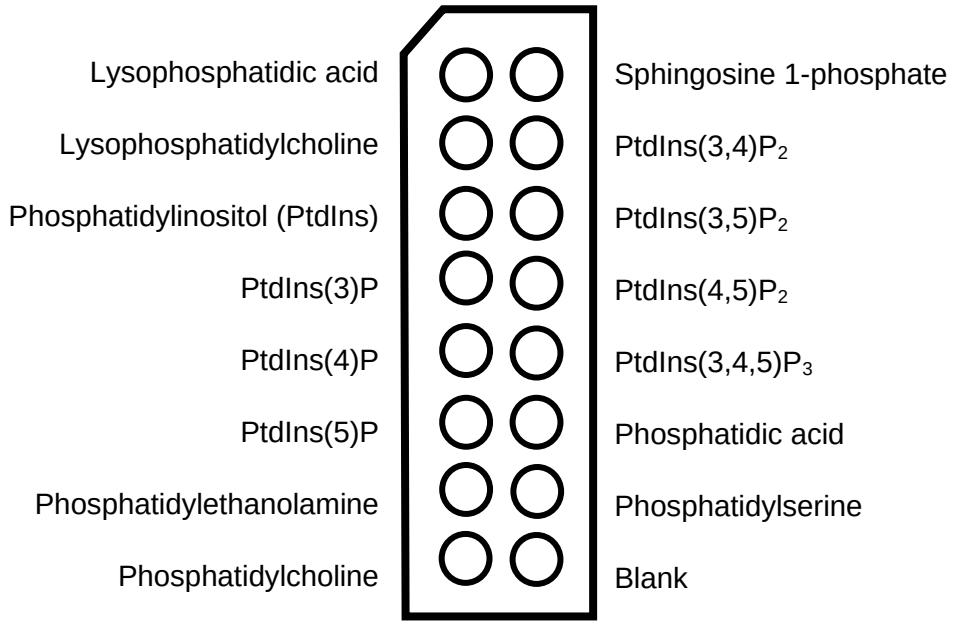

Figure 19. PIP Strip layout. 100 picomoles of lipid per spot.[112]

2.4. Antimicrobial Assays[113]

2.4.1. Preparation of the 0.5 McFarland Standard

Barium chloride (1 %, 50 µL) was added to sulfuric acid (1 %, 9.95 mL) and mixed. The optical density was recorded at 600 nm.

2.4.2. Preparation of 5 % EtOH

Unless otherwise stated, 5 % EtOH was prepared in H_2O

2.4.3. Preparation of Antimicrobial Compounds for Screening

Stock compound solutions were made on the day of the experiment at 20 mM in 5 % ethanol and sterile dH_2O.

2.4.4. Preparation of Antimicrobial Compounds for MIC_{50} Calculations

Compound solutions were made on the day of the experiment at eight appropriate concentrations, determined by the screening, in 5 % ethanol and sterile dH_2O.

2.4.5. Preparation of Cell Suspension

A secondary culture was created and grown to an optical density of 0.4 at 600 nm, then its density was adjusted using sterile dH_2O to equal 0.5 McFarland Standard (10^7 – 10^8 cfu/mL). McFarland standards are standard solutions used to standardise bacterial suspensions so an approximate number of bacteria can be determined. A 1:10 dilution was carried out using sterile dH_2O (900 µL) and the McFarland adjusted suspension (100 µL). A final dilution (1:100) was carried using the 1:10 suspension (150 µL) and LB (14.85 mL) before use to achieve a final cell concentration of 10^5 cfu/mL.

2.4.6. Preparation of 96 well Microplate for screening

A 20 mM compound solution was prepared using 5 % ethanol in sterile dH_2O. A cell suspension prepared as described previously (10^5 cfu/mL, 150 µL) was pipetted into each well of a 96 well sterile plate, then the compound solution (20 mM, 30 µL) was added into 6 wells on the plate, to give a final screening concentration of 3.3 mM within each well. This was repeated for all compounds to be screened. Absorbance values were obtained using the Thermo Scientific Multiscan Go 1510-0318C plate reader and recorded using the SkanIt Software 4.0. Values were taken at 600nm, every 15 minutes for 25 hours at 37 ºC, then used to generate growth curves.

Compounds that showed inhibited growth by 10 % or more were taken forward for MIC calculations.

2.4.7. Preparation of 96 well Microplate for MIC_{50}s

A cell suspension was created as described previously, then dispensed into individual wells of a 96 well sterile plate under sterile conditions (10^5 cfu/mL, 150 µL). Compounds (30 µL) were added to the wells to equal a total volume of 180 µL within the wells ensuring that there are six repeats of each concentration of every compound on the plate. The plates were sealed using Parafilm, and absorbance values were obtained using the Thermo Scientific Multiscan Go 1510-0318C plate reader and recorded using the SkanIt Software 4.0. Absorbance values were taken at 600 nm (OD_{600}), every 15 minutes for 18-25 hours at 37 ºC, then used to generate growth curves.

2.4.8. Growth Curves and MIC_{50} Calculation

Growth curves were plotted from OD_{600} absorbance readings using Microsoft Excel.

OD_{600} absorbance readings at 900 minutes for each SSA concentration were plotted in Origin. The resultant curve was normalised and fitted using the Boltzmann equation to define the MIC_{50} values for each drug.

2.4.9. Calculation of Growth rate

12 consecutive OD600 values were taken from the exponential phase of a plotted growth curve and plotted against time. The growth rates were then calculated using the equations described by Fattah et al. (2018) and Stensjøen et al. (2015) below.[114,115]

$y = Ae^{Bx}$ (where A and B are numbers)

Equation 1. Exponential phase growth rate equation.

$$y = Ae^{Bx} \rightarrow \ln\frac{(y \div A)}{B}$$

$$when\ y = 1, x1 = \frac{\ln(1 \div A)}{B},\ when\ y = 2, x2 = \frac{\ln(2 \div A)}{B}$$

$$T_d = x2 - x1 = \frac{[(\ln 2 - \ln A) - (\ln 1 - \ln A)]}{B} \ln 1 = 0$$

$$T_d = \frac{\ln 2}{B} = \frac{0.693}{B}$$

Equation 2. Doubling time equation (T_d).

$$r = \frac{ln2}{T_d}$$

Equation 3. Growth rate (k)

2.4.10. Compound Co-Drug Studies[66]

A cell suspension was created as described previously, then dispensed into individual wells of a 96 well sterile plate under sterile conditions (10^5 cfu/mL, 90 µL). Compound **35** - **37** (90 µL) were either added alone or in 1:1 compound mixtures of these compounds were added into wells (90 µL). The plates were sealed using Parafilm then absorbance values were obtained using the Thermo Scientific Multiscan Go 1510-0318C plate reader and recorded using the SkanIt Software 4.0. Absorbance values were taken at 600 nm, every 15 minutes for 18-25 hours at 37 ºC, then used to generate growth curves. Each experiment was repeated on a different day to ensure reproducibility. Growth curves were then plotted and MIC_{50}s were calculated as previously described.

2.4.11. Agar well diffusion assay[116]

An overnight culture was prepared as previously described. On the following day, a secondary culture was prepared using the overnight culture, then incubated at 37 °C

it had reached an optical density of 0.5-0.6 at 600 nm. LB Agar was prepared and once autoclaved, the molten agar was placed in a 50 °C water bath and maintained at this temperature. The molten agar was then inoculated using the secondary culture (15 mL), then swirled to mix. The inoculated agar was added to sterile Petri dishes (6 mL) and allowed to set under sterile conditions. A sterile cutter was used to remove a disk from the inoculated agar, creating a well in the plate, and the bottom was sealed using fresh agar (5 µL). Compound gel solutions were prepared and heated, the gel solutions were then pipetted (50 µL) into the wells and allowed to set. Sodium chloride was pipetted (50 µL) into the wells of the appropriate plates. All the plates were then placed into a 37 °C incubator over 18 hours then imaged using the ESPON perfection V750 PRO scanner.

2.4.12. Agar surface diffusion assay[116]

An overnight culture was prepared as previously described. On the following day, a secondary culture was prepared using the overnight culture, then incubated at 37 °C it had reached an optical density of 0.5-0.6 at 600 nm. LB Agar was prepared and once autoclaved, the molten agar was placed in a 50°C water bath maintained at this temperature. The molten agar was then inoculated using the secondary culture (15 mL) and swirled to mix. The inoculated agar was added to 60 mm x 15 mm sterile Petri dishes (6 mL) then allowed to set under sterile conditions. A compound gel solution (50 µL) was pipetted onto a sterile agar plate and allowed to set. Once set, the gel domes were carefully lifted using a spatula and placed in the center of the agar plate. Sodium chloride was pipetted straight onto the agar plate as a control. All the plates were then placed into a 37 °C incubator over 18 hours then imaged using the ESPON perfection V750 PRO scanner.

2.4.13. Zone of inhibition measurements in ImageJ.[106]

Gel plate images were opened in ImageJ,[106] and the scale was set based on the measurements of the agar plates (*d* = 60 mm). 4 zones of inhibition measurements were subsequently taken using the “measure length” function (Figure 20), and the average zone of inhibition was calculated for each plate. The final zone of inhibition reported is the average of 3 plates and the standard deviation was used as the error value.

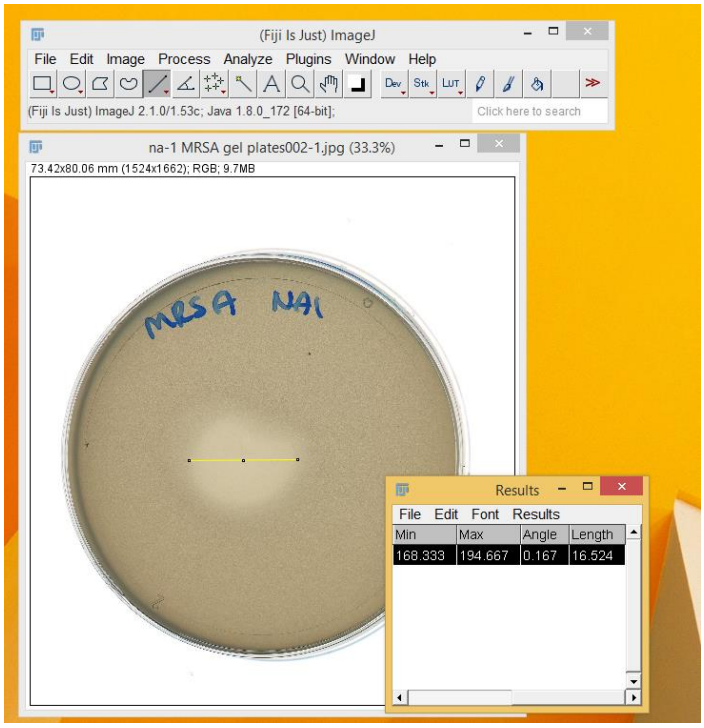

Figure 20. Zone of inhibition measurements using the length function in ImageJ.[106]

Four measurements were taken (red lines) and an average was calculated for each plate.

2.5. Microscopy

2.5.1. Competitive Binding Assay

An overnight culture was prepared as previously described. On the following day, a secondary culture was prepared using the overnight culture, then incubated at 37 °C it had reached an optical density of 0.4 at 600 nm. The culture (500 µL) and LB (100 µL) were pipetted into each sterile Eppendorf under sterile conditions. Different conditions were set up as follows; solvent alone: 5 % EtOH (100 µL) was added; compound alone: the compound (5 mM, 100 µL) was added; FM4-64 alone: 5 % EtOH (100 µL) and FM4-64 (0.7 µL) were added and FM4-64 & compound: the compound (5 mM, 100 µL) and FM4-64 (0.7 µL) were added. Samples were incubated at room temperature for 30 minutes then cells were mounted onto the agarose LB pads under coverslips[117]. Samples were visualised using an Olympus IX71 microscope with UAPON 150x 1.45 NA Widefield fluorescence lens mounted on a PIFOC z-axis focus drive (Physik Instrumente, Karlsruhe, Germany), and illuminated using LED light sources (Cairn Research Ltd, Faversham, UK) with appropriate filters (Chroma, Bellows Falls, VT) using a Zyla 4.2 CMOS camera (Andor). The system was controlled with Metamorph software (Molecular Devices). Images were subsequently analysed using Metamorph and ImageJ software[105].

2.5.2. Sample Preparation

Samples were prepared as described by Mulvihill (2017)[117]. 2 % agarose was placed in a 90 °C hot plate until molten. Molten agarose (50 µL) was pipetted into a microscope slide and then a pro-former was used to flatten the agarose pads. Once set, samples (6-10 µL) were pipetted onto the agarose pads and allowed to almost dry under sterile conditions when necessary. A coverslip was then placed onto the microscope slide and sealed on two sides.

2.5.3. Quantitative Fluorescence analysis

Images were analysed using ImageJ software[105]. Line scans were created by drawing a line through the width of the cell using the line tool in image J. The same selection was made on all the corresponding images and an intensity profile of the line was created using the plot profile option. The background fluorescence was determined and subtracted from the maximum fluorescence. The fluorescence intensities for ~30 – 100 cells were measured for each condition and an average fluorescence was used to create a bar chart from these data. Error bars show the variation in fluorescence within that condition.

2.5.4. Gel Microscopy

Samples were visualised using an Olympus IX71 microscope with UAPON 150x 1.45 NA Widefield fluorescence lens mounted on a PIFOC z-axis focus drive (Physik Instrumente, Karlsruhe, Germany), and illuminated using LED light sources (Cairn Research Ltd, Faversham, UK) with appropriate filters (Chroma, Bellows Falls, VT) using a Zyla 4.2 CMOS camera (Andor).

A chamber was created by placing a coverslip on a microscope slide and taping on three sides of the coverslip. The appropriate salt solution (1 mL, 0.505 M) was added to 5 mg of the compound in a glass vial and heated to 60 °C. The microscope slide was placed onto the microscope stage and the gel solutions were pipetted into the chamber. The gelation process was then imaged as the gel was setting and analysed in imageJ[105].

2.6. Liposome Studies

2.6.1. Liposome preparation

A solution of desired lipids (5 mL, 1 mM) was prepared in chloroform. The chloroform was removed on a rotary evaporator to create a thin film of lipid on the flask, then left under vacuum overnight to remove trace chloroform. The thin film was then rehydrated using buffer B that was at 10 °C above the phase transition temperature of each lipid and sonicated to ensure all of the lipid was in solution. For lipid mixes, the highest transition temperature was used. Liquid nitrogen and a water bath set 10 °C above the phase transition temperature of the desired lipid, were used to conduct nine freeze-thaw cycles. Lipids were then extruded before use at 10 °C above the Phase transition temperature, then diluted to the concentration required for the assay. These liposomes were then used in all assays.

2.6.2. Co-sedimentation Assay under a density gradient

Liposomes were prepared as described previously (100 µL, 1 mM) and added to a microcentrifuge tube with WT Hum-1 TH1-mNg protein in 30% sucrose (100 µL, 1 mg/mL). The protein-lipid mixture was incubated at 37°C for 1 hour to allow binding. A 25% sucrose solution (250 µL) was carefully pipetted over the top of the protein-lipid mixture in the microcentrifuge tube, which was then followed by αS buffer B (50 µL). Samples underwent centrifugation at 18,0000 *xg* for 1 hour at 20°C, with a slower deceleration. Fractions of 160 µL were carefully extracted and pipetted into separate centrifuge tubes. 80 µL from each fraction was pipetted into the wells of a 96 well black plate, and FM4-64 (0.8 µL) was added to the wells. These would be the lipid detection wells. The remaining 80 µL from each fraction was pipetted into separate wells, which would be the protein (mNg) fluorescence detection wells. 3 Fluorescence intensity at nm in the FM4-64 wells and nm in the mNg well were measured using the

BMG Clariostar microplate reader. The final fluorescence values were an average from two independent experiments and the standard deviation was used as the error value. Protein in the presence of solvent alone was used as the protein control, and FM4-64 in the presence of solvent alone was used as the FM4-64 control.

2.6.3. Fluorescence Anisotropy (protein)

Liposomes were prepared as described previously in **αS buffer B**. Serial dilutions of protein from 2.5 mg/mL were prepared in the **αS buffer B**. Protein solutions (10 µL) and the desired vesicle solutions at (50 µL, 1 mM) were pipetted into a 96 well black plate, allowed to bind for 30 minutes at room temperature, then anisotropy readings were measured using the **BMG Clariostar** microplate reader with appropriate filters and **MARS data analysis software**.

2.6.4. Fluorescence Anisotropy (compound)

Liposomes were prepared as described above in 5 % ethanol in dH_2O. Serial dilutions of compounds from 5 mM were prepared in the 5 % ethanol in dH_2O. The desired compound solution (10 µL) and the desired liposome suspension (50 µL, 1 mM) were pipetted into a 96 well black plate, allowed to bind for 30 minutes at room temperature, then anisotropy readings were measured using **BMG Clariostar** microplate reader with appropriate filters and **MARS data analysis software**.

2.6.5. Thermal Shift Assay[118]

The assay is based on the method developed by Hattori et al., 2012 and Nji et al., 2018.[27,118] PCR tubes comprising of the desired protein (65 µL 3 mg/mL), the desired lipid (65 µL, 1 mM), **αS Buffer B** (5 µL), and OGP (15 µL, 10 %) were prepared. The tubes were labeled with the desired temperatures, with three repeats of each temperature to be tested. Tubes were heated using a gradient PCR at the chosen temperatures for 10 minutes, centrifuged at 18,000 *xg*, then the supernatant was

carefully removed and pipetted into a 96 well black plate. Fluorescence values were obtained using the **BMG Clariostar** microplate reader. Fluorescence values were normalised and used to create a melting curve, where the melting temperature (T_m) was calculated using Origin labs. The final T_m value reported was an average of the three repeats. One-way ANOVA was conducted on the resulting T_m values using **IBM statistics software**.

2.7. Novel Compound Characterisation

2.7.1. SSA 82 Synthesis

Tetrabutylammonium (TBA) hydroxide (1N) in methanol (4 mL, 4 mM) was added to 2-aminoethane-1-sulfonic acid (0.25 g, 2.0 mM) and taken to dryness. Triphosgene (0.309 g, 1 mM) was added to a stirring solution of 4-(6-methylbenzothiazol)aniline (0.5 g, 2 mM) in ethyl acetate (30 mL) and the mixture heated at reflux for 4 hours. The TBA salt was then dissolved in ethyl acetate (10 mL) and added to the reaction mixture and heated at reflux overnight, filtered and the solid washed with ethyl acetate (10 mL). Impurities were removed through precipitation in methanol with ethyl acetate, the solids filtered, and the filtrate taken to dryness to give the pure product as a pale yellow solid.

2.7.2. SSA 83 Synthesis

Tetrabutylammonium (TBA) hydroxide (1N) in methanol (4 mL, 4.0 mM) was added to 3-aminopropane-1-sulfonic acid (0.28 g, 2.0 mM) and taken to dryness. Triphosgene (0.309 g, 1 mM) was added to a stirring solution of 4-(6-methylbenzothiazol) aniline (0.5 g, 2 mM) in Chloroform (30 mL) and the mixture heated at reflux for 4 hours. The TBA salt was then dissolved in Chloroform (10 mL) and added to the reaction mixture and heated at reflux overnight, filtered and the solid washed with chloroform (10 mL). Impurities were removed by precipitation in methanol with chloroform, the solids

filtered, and the filtrate taken to dryness to give the pure product as a pale yellow solid.

2.7.3. Infrared (IR) measurements

Infrared spectra of SSAs **82** and **83** were obtained using a Shimadzu IR-Affinity-1 model Infrared spectrometer. The data are analysed in wavenumbers (cm^{-1}) using IRsolution software.

2.7.4. Dynamic Light Scattering (DLS) Studies

SSAs **82** and **83** to be tested (5.56 mM) were prepared in filtered 5 % ethanol (1 mL) then underwent an annealing process in which they were heated at 40 °C before being allowed to cool to 25 °C. A series of 10 particle size experiments were carried out on the sample using the Anton Paar LitesizerTM 500 at 25 °C then processed using Kalliope^{TM} Professional DLS. The sample was removed from the DLS and diluted to 0.56 mM, then underwent the annealing process in which it was heated to 40 °C and cooled to 25 °C. Another series of 10 particle size experiments were carried out for these samples. The final hydrodynamic aggregate diameters reported is an average of each peak maxima obtained from the average particle size distributions from each experiment and the standard error of the mean (SEM) was used as the error value.

2.7.5. Zeta Potential Measurements

Solvents used were filtered to remove any particulates that may interfere with the results. Studies for SSAs **32**-**81** were conducted by another member of the lab whilst compounds **82** and **83** were conducted by me. Compounds (5.56 mM) were dissolved in filtered 5 % ethanol (1 mL) and underwent an annealing process in which they were heated at 40 °C before being allowed to cool to 25 °C. A series of 10 zeta potential measurements were conducted out using the Anton Paar LitesizerTM 500 at

25 °C then processed using Kalliope™ Professional DLS. The final zeta potential value reported is an average of the experiments conducted and the standard error of the mean (SEM) was used as the error value.

2.7.6. Melting Point Measurements

The melting points for SSAs **82** and **83** were measured using the Stuart SMP10 melting point apparatus.

2.7.7. NMR Spectroscopy

The NMR spectra of SSAs **82** and **83** were obtained using a Bruker AV2 400 MHz or AVNEO 400 MHz spectrometer. The data was processed using ACD Labs, MestReNova, or Topspin software. NMR Chemical shift values are reported in parts per million (ppm) and calibrated to the center of the residual solvent peak set (s = singlet, br = broad, d = doublet, t = triplet, q = quartet, m = multiplet).

2.7.8. Mass Spectrometry

Compounds **82** and **83** experiments were conducted by Rebecca Ellaby. High-resolution mass spectrometry (Electrospray ionization negative -ESI^-) was performed using a Bruker microTOF-Q mass spectrometer and spectra were recorded and processed using Bruker's Compass Data Analysis software.

2.7.9. Single crystal X-ray diffraction studies

Single crystals of SSAs **82** and **83** were prepared from the slow evaporation of alcohol: water solutions. Single crystal structures were obtained by Dr. Hiscock. A suitable single crystal of each molecule was selected and mounted on a Rigaku Oxford Diffraction Supernova diffractometer. Data were collected using Cu Kα radiation at 100 K or 150 K as necessary due to crystal instability at lower temperatures. Structures were solved with the ShelXT or ShelXS structure solution

programs via Direct Methods and refined with ShelXL by Least Squares minimisation.[107,108] Olex2 was used as an interface to all ShelX programs.[109]

2.7.10. Tensiometry studies

SSAs **82** and **83** were prepared in an EtOH:H_2O (1:19) solution, then underwent an annealing process in which they were heated to 40°C before being allowed to cool to 25°C. Serial dilutions of the SSA solutions were then prepared using the annealed sample. Three surface tension measurements for each sample at a given concentration were obtained using the pendant drop method. Average values were then used to calculate the critical micelle concentration (CMC).

2.7.11. Inversion test

SSAs **82** and **83** (5 mg) were dissolved in the appropriate salt solution (1 mL, 0.505 M) in glass vials. SSA solutions were subsequently heated to ~40°C then allowed to cool to 25°C, to allow gel formation. Once cooled, glass vials were upturned and imaged. The presence of a stable gel was determined by reproducible *n=3* inversion tests.

2.8. Statistical analysis

Paired-samples t-tests and one-way ANOVA were performed using IBM statistics software.

Chapter 3: Investigating the structure-activity relationships of novel antimicrobial compounds

3.1. Introduction

The rise of antimicrobial resistance (AMR) within bacterial populations is rapidly becoming an increased risk to public health, projected to account for higher deaths per year than the combined total of cancer and aids-related diseases by the year 2050.[53,119] Moreover, the increased risk to the global economy due to increased costs of available treatments, healthcare, diagnostics tests, and disease surveillance means that new methods in the management and treatment of microbial diseases are imperative.[52,53,120–123] This concern has driven a variety of strategies to tackle antimicrobial resistance, including increasing global awareness;[124] conducting research to improve current diagnostic techniques;[125] increased development of novel antimicrobial compounds;[68] and reduced distribution of unnecessary antibiotics in the environment.[52,53,68,125,126]

Amphiphiles, such as antimicrobial peptides (AMPs), are versatile molecules composed of hydrophilic regions and hydrophobic regions.[127,128] These molecules have been at the forefront of recent antimicrobial discovery, as AMPs have been shown to interact with anionic bacterial membranes, which is desirable as there is a reduced propensity for developing resistance and these interactions can lead to broad-spectrum activity.[120,121,129] Amphiphilic molecules have the potential to exhibit bacteriostatic and bactericidal activities and their facial amphiphilicity allows for them to effectively insert into bacterial membranes through interactions with membrane lipids, which may cause cell death due to the loss of membrane integrity.[119,120,129] As amphiphilic antimicrobials tend to be based on or inspired by naturally occurring molecules, they tend to have lower toxicity to mammalian cells, as observed by Rahman et al., whose cholic acid-derived amphiphiles exhibited potent activity against gram-negative bacteria and low mammalian cell toxicity (Figure 21).[120,130] Furthermore, Chrom et al., through the use of AP3 peptide derived analogues, linked the ability to bind and permeabilise bacterial membranes to their

antimicrobial activity and showed the low cytotoxicity exhibited by their amphiphilic analogues.[131]

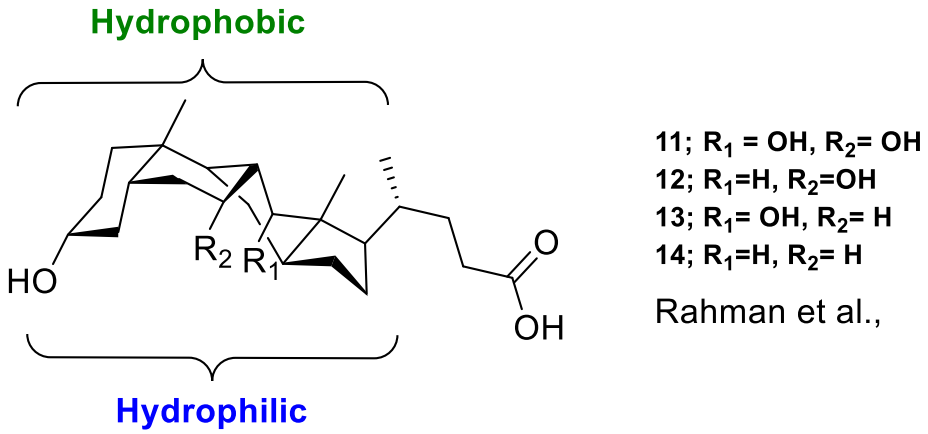

Figure 21. **Amphiphilic antimicrobials.**

The use of amphiphiles as antimicrobial compounds demonstrated by the work of Rahman et al., 2018.[120]

As previously discussed, molecular self-association is an essential process that drives a variety of regulatory, binding, organisation, and stabilising processes.[132–135] These self-association processes occur through the formation of non-covalent interactions that are influenced by solvent interactions and the hydrogen bonding accepting or donating (HBA/HBD) groups present within the molecules.[136,137] The use of self-associative molecules, in particular those that incorporate hydrogen bonding, has increased due to their versatility. Specific examples include the work of Supuran et al, whose urea-based molecules exhibited activity against M. *tuberculosis* H37Rv,[138] (Figure 22a), Gale et al., who incorporated thio(urea) functionalities into their structures to encourage hydrogen-bonded coordination (Figure 22b).[139] This is further explored by Zhou et al., who utilised hydrogen-bonded amphiphiles for the development of novel drug delivery systems (Figure 22c).[140]

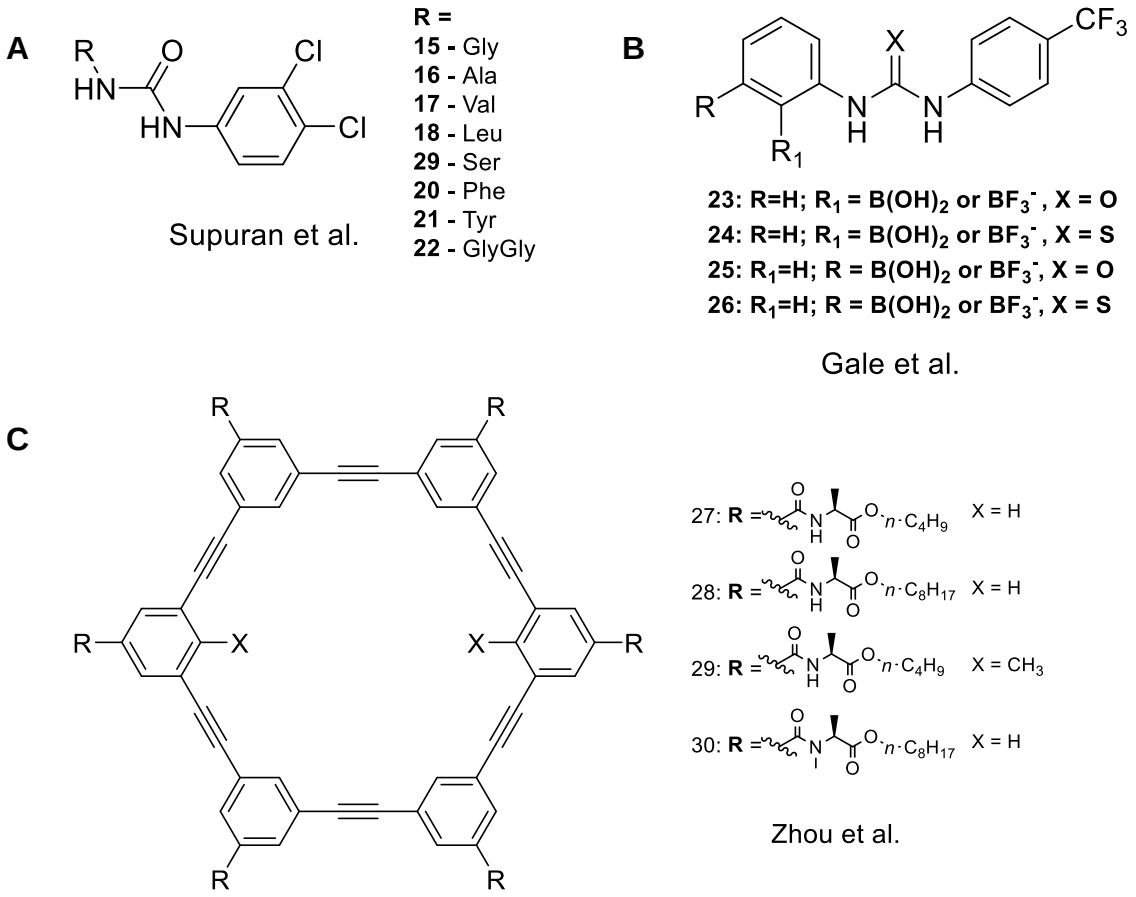

Figure 22. **Use of self-associative molecules.**

Example structures of molecules showing the diverse use of self-associative thio(urea) derived molecules as demonstrated by **(A)** Supuran et al.,[138] **(B)** Gale et al.,[139] **(C)** Zhou et al.,[140]

Understanding the structure-activity relationships of the molecules and their antimicrobial activity has proven to be invaluable for the development of novel antimicrobial compounds. Stepwise modifications to a generic structure and physicochemical studies conducted with the resultant structures can be utilised for accurate optimisation of therapeutics and the determination of structure-activity relationships.[141,142] Linking the chemical structure of an antimicrobial molecule to its biological activity may allow us to predict the activity of future compounds in a more cost-effective and time-efficient manner.[142,143]

Antibiotics with a singular target are far less effective than those with multiple targets, as bacteria cannot as easily develop resistance mechanisms with the latter.[144–146] Consequently, coformulations have become more desirable in drug discovery, as they provide a way of reviving previously effective molecules, may allow for broad-spectrum activity, and improve efficacy.[144,147,148] An example of this is the work of Ganewatta et al., whose quaternary amine containing compounds not only exhibited biocidal activity but were able to form micelles in water which allowed for the encapsulation of ampicillin, thereby greatly improving ampicillin activity (Figure 23).[149]

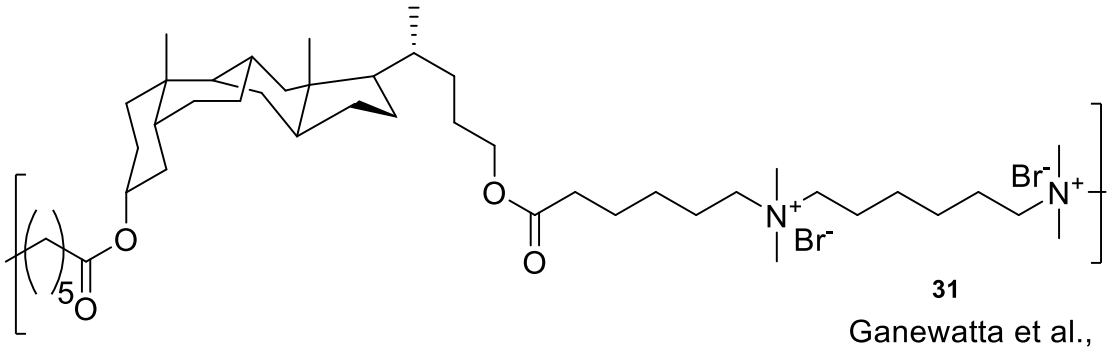

Figure 23. **Use of self-associating molecules in antimicrobial research.**
Example structure of quaternary amine containing compounds developed by Ganewatta et al., used in the encapsulation of ampicillin.[149]

3.2. Supramolecular self-associating amphiphiles (SSAs)

Drawing from the work conducted by Gale et al.,[139,150–152], Zhou et al.,[140] Supuran et al.,[138], Rahman et al.,[120] and Ganewatta et al.,[149] Hiscock et al.,[153] created a series of supramolecular self-associating amphiphiles (SSAs) with antimicrobial properties, hypothesised to interact with membranes.[154] These molecules consist of an anionic hydrogen accepting group, a thio(urea) hydrogen accepting/donating region, and a hydrophobic region as shown in Figure 24. The SSAs contain two hydrogen bond

accepting sites (the thio(urea) and sulfonate functionalities), and one hydrogen bond donating (HBD) site (the amines in the thio(urea) functionality).

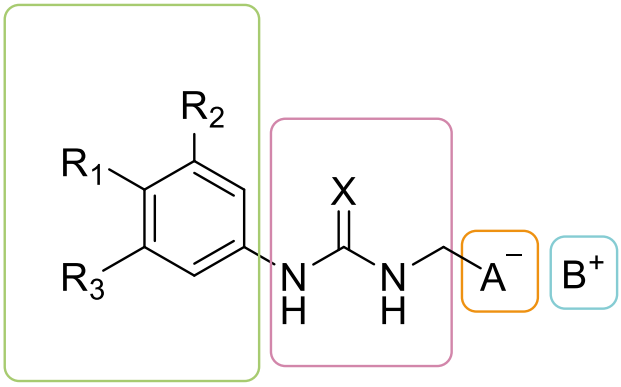

Figure 24. General structures of SSAs by developed by Hiscock et al., 2018.[154]

A schematic of the regions that made up the SSAs developed by Hiscock et al.,[66,153,155,156]. Green = hydrophobic region, pink = thio(urea) functionality, yellow = hydrophilic group, blue = counter cation.

This allows the molecules to self-associate through the formation of intermolecular hydrogen bonds. A combination of ^{1}H NMR dilution studies, DLS, and Zeta potential measurements confirmed the presence of self-associated aggregates, ranging from 100 – 550 nm, with few exceptions.[153,154] It is hypothesised that the dimerisation of these molecules is directly correlated to their antimicrobial activity, and thus enhancing the molecules' hydrogen bonding capacity will allow for improved self-association, which in turn improves antimicrobial activity.

3.3. Aims and hypothesis

This chapter will explore the structure-activity relationships of this novel class of antimicrobial compounds in relation to their microbial activity. It is hypothesised that the antimicrobial activity of these molecules is dependent on the conformation of the self-associated structures formed. Furthermore, the antimicrobial activity of these molecules is attributed to electrostatic interactions with membrane phospholipids, which form pores in bacterial membranes leading to a loss of membrane integrity and resulting in cell

death[119]. As such, this chapter will explore the impact of stepwise modifications made to SSA **32** on antimicrobial activity, the mode of action and membrane-binding properties of these molecules, and this chapter will demonstrate how the compounds can be used in combination with other therapeutic agents as adjuvants in response to the decline in novel antimicrobial development.[119]

The data discussed in this chapter has been published in the following articles:

Allen, N., White, L.J., Boles, J.E., Williams, G.T., Chu, D.F., Ellaby, R.J., Shepherd, H.J., Ng, K.K.L., Blackholly, L.R., Wilson, B., Mulvihill, D.P. and Hiscock, J.R. (2020), *Towards the Prediction of Antimicrobial Efficacy for Hydrogen-Bonded, Self-Associating Amphiphiles*. ChemMedChem, 15, 2193. **doi:10.1002/cmdc.202000533**

White, L. J., Wells, N. J., Blackholly, L. R., Shepherd, H. J., Wilson, B., Bustone, G. P., … Hiscock, J. R. (2017). *Towards quantifying the role of hydrogen bonding within amphiphile self-association and resultant aggregate formation*. Chemical Science, 8(11), 7620–7630. **https://doi.org/10.1039/c7sc03888g**

Tyuleva, S. N., Allen, N., White, L. J., Pépés, A., Shepherd, H. J., Saines, P. J., … Hiscock, J. R. (2019). *A symbiotic supramolecular approach to the design of novel amphiphiles with antibacterial properties against MSRA*. Chemical Communications, 55(1), 95–98. **https://doi.org/10.1039/c8cc08485h**

White, L., Boles, J., Allen, N., Alesbrook, L., Sutton, J., Hind, C., Hilton, K., Blackholly, L., Ellaby, R., Williams, G., Mulvihill, D. and Hiscock, J. (2020). *Controllable hydrogen bonded self-association for the formation of multifunctional antimicrobial materials*. Journal of Materials Chemistry B. Royal Society of Chemistry, 8 (21), 4694-4700. **doi: 10.1039/D0TB00875C**

3.4. Antimicrobial Activity Assays

3.4.1. Structures of SSAs

Synthesis and characterisation of SSAs **32** – **81** were conducted by Lisa J. White.

SSA 32

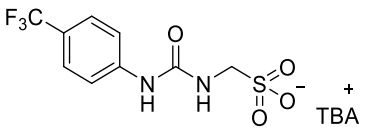

SSA 33

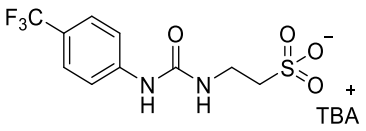

SSA 34

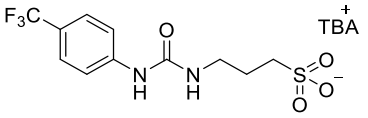

SSA 35

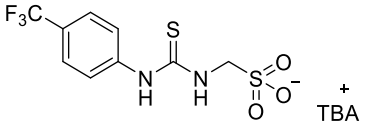

SSA 36

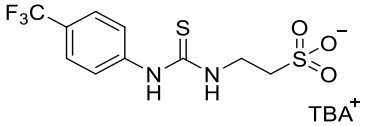

SSA 37

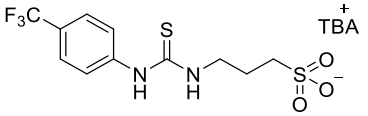

SSA 38

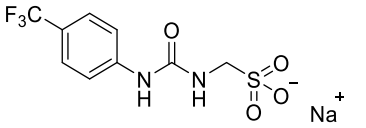

SSA 39

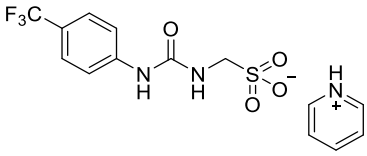

SSA 40

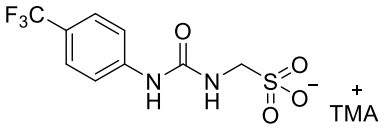

SSA 41

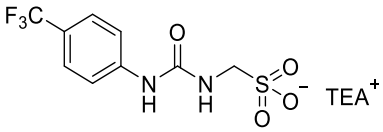

SSA 42

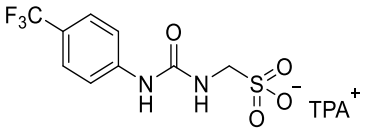

SSA 43

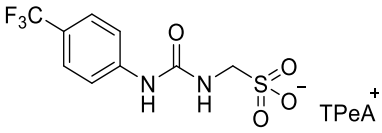

SSA 44

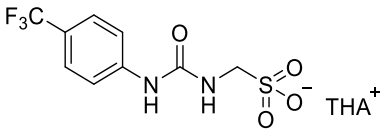

SSA 45

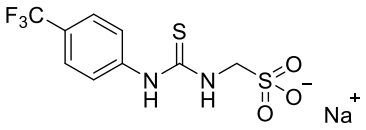

SSA 46

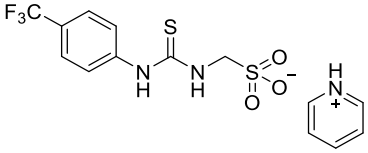

SSA 47

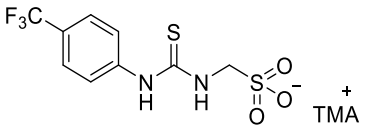

SSA 48

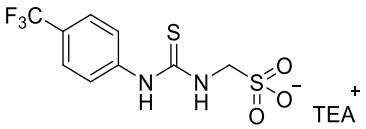

SSA 49

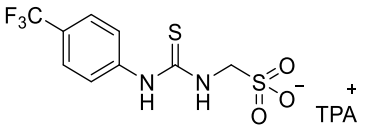

SSA 50

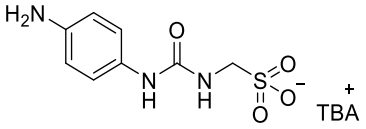

SSA 51

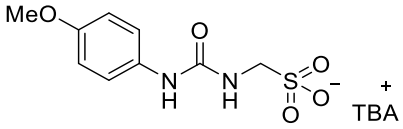

SSA 52

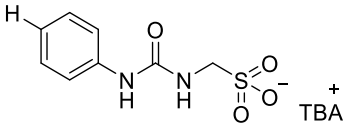

SSA 53

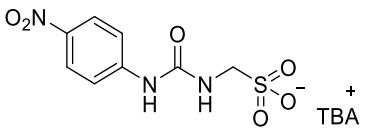

SSA 54

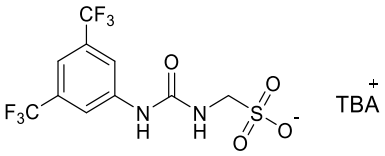

SSA 55

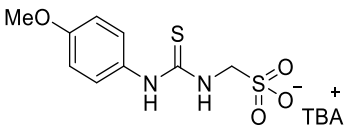

SSA 56

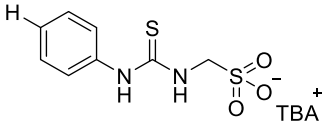

SSA 57

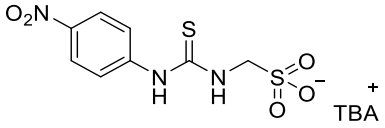

SSA 58

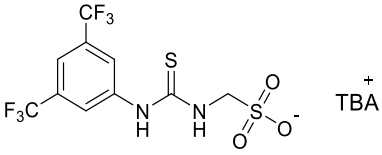

SSA 59

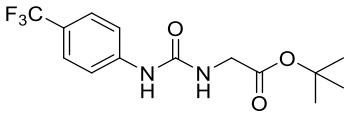

SSA 60

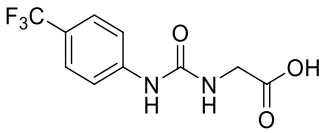

SSA 61

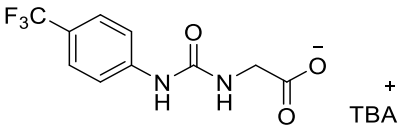

SSA 62

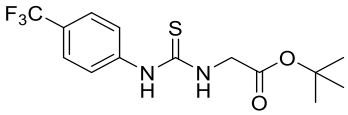

SSA 63

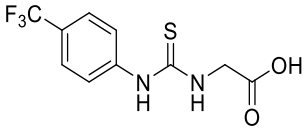

SSA 64

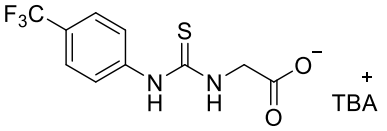

SSA 65

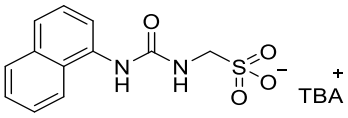

SSA 66

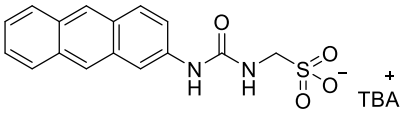

SSA 67

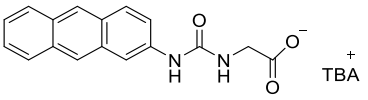

SSA 68

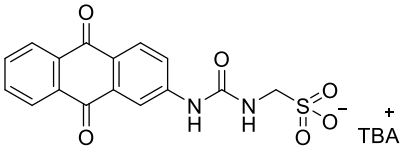

SSA 69

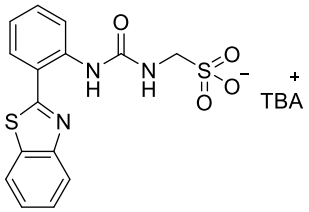

SSA 70

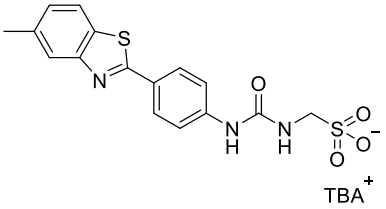

SSA 71

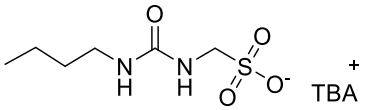

SSA 72

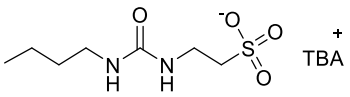

SSA 73

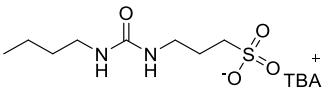

SSA 74

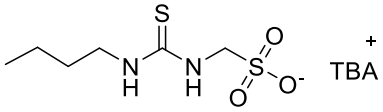

SSA 75

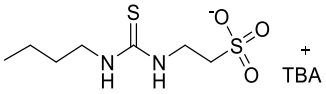

SSA 76

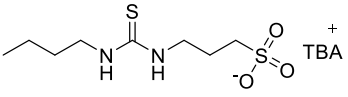

SSA 77

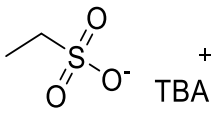

SSA 78
Tetramethylammonium chloride

SSA 79
Tetraethylammonium chloride

SSA 80
Tetrapentylammonium chloride

SSA 81
Tetrabutylammonium chloride

Figure 25. **Structures of SSAs discussed in this chapter.**

3.4.2. SSA 32

SSA **32** contains a urea functionality, two NH functionalities, and a sulfonate hydrophilic region, which enable the molecule to self-associate through four hydrogen bonds as demonstrated in Figure 26.

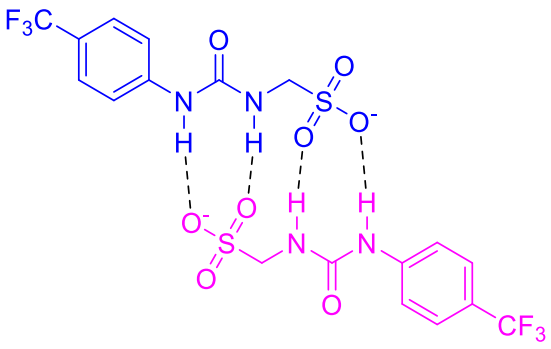

Figure 26. **A representation of the dimerisation of SSA 32.**

Hydrogen bonds formed between the oxygens of the sulfonate group of one molecule and the amine groups on the urea group of the other molecule. Purple = monomer 1, blue = monomer 2, dashed lines indicate hydrogen bonds.

Stepwise modifications made to SSA **32**, forming SSAs **33 – 76** (Figure 25), could alter hydrogen bonding modes exhibited by the molecules, impacting dimerisation and antimicrobial activity. To determine how each modification would alter the antimicrobial activity, I carried out antimicrobial activity analysis on SSAs **32** – **81**.

3.4.3. Initial Antimicrobial Screening

Antimicrobial screenings are often carried out as part of the early drug discovery process to provide an initial assessment of activity, allowing for the identification of suitable candidates against test organisms and the removal of ineffective molecules.[55,157,158] Thus, I conducted an initial screening of SSAs **32** – **81** was against *E. coli* DH10β and MRSA USA100. These data was used to compare the effects of the compounds on gram-negative and gram-positive bacteria, respectively. Antimicrobial screening was carried out as described in section **2.4.3** and **2.4.6** of the materials and methods. Briefly, SSAs were added to a final concentration of 3.3 mM to mid-log phase cells at a concentration of 10^5 cfu/mL in a 96 well plate. OD values were then recorded every 15 minutes over 24 hours.

3.4.4. Determining Solvent toxicity

SSAs were dissolved in EtOH: H_2O (1:19), (5 % EtOH), to aid their solubility in water, so we needed to ensure that the final concentration of ethanol within the experiment would

have a minimal impact on growth. As such, bacterial growth in 5 % EtOH was compared to growth in LB media, and toxicity was determined by a reduction in bacterial growth, determined by the final OD values obtained. If the reduction in growth was ≤ 10%, the toxicity was considered minimal. The results of these studies are presented in Figure 27. These growth curves revealed a reduction of *E. coli* growth was by 9% and MRSA growth by 10%. As the impact of 5 % EtOH on *E. coli* and MRSA growth was considered minimal, the antimicrobial screening was conducted.

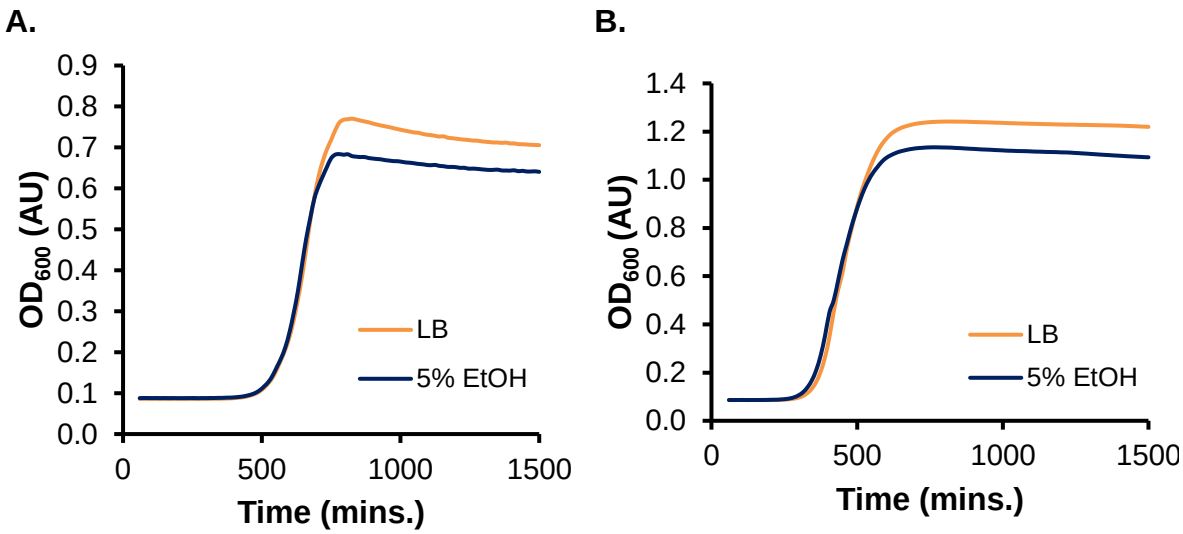

Figure 27. Determining solvent toxicity.

Growth curves comparing bacterial growth in LB and 5 % EtOH at the same concentration as experimental conditions. **(A)** *E. coli*; 9% reduction in growth observed in 5 % EtOH **(B)** MRSA; 10 % reduction in growth observed.

3.4.5. Analysis of Growth dynamics and kinetics

As previously described, bacterial growth in closed culture follow a discernible growth pattern that has been well characterised in literature.[43,45,159] This pattern is made up of 4 distinct phases: a lag phase, where bacteria acclimatise to the new environment; an exponential growth phase, where cells replicate exponentially; a stationary phase, where the rates of division and cell death are balanced; and a death phase, where the rate of cell death is greater that of division.

Recording OD values at regular intervals throughout the growth process allows for the creation of growth curves, which in turn allows for the examination of microbial growth dynamics in the presence of these molecules. [49,160] Further, parameters such as growth rate (*k*) can then be calculated, which are essential in providing a full evaluation of the activity of these molecules. Initial indications of the mode of action may be evident in the growth curves obtained in the presence of each SSA. Consequently, an analysis of the growth curves generated using the screening data was performed and the growth rates (*k*) of both MRSA and *E. coli* in the presence of SSAs **32** – **81** were calculated. These were conducted using the exponential phase of the bacterial growth curves in the presence of each SSA (Table 6), as described by Fattah et al. (2018) and Stensjøen et al. (2015), [section in **2.4.9** materials and methods].[114,115] These rates were compared to the growth rate of the bacteria without compound present.

Table 6: Growth rates (*k*) of MRSA and *E. coli* in the presence of SSAs 32 – 81 in minutes.

[a] - growth rate assumed to be zero due to lack of growth, [b] – SSAs screened at 3.75 mM, [c]– growth control; the growth rate of bacteria in the presence of EtOH: H_2O (1:19) only.

Average Growth Rate (*k*)					
	***k* (mins.)**			***k* (mins.)**	
	E. coli	**MRSA**		***E. coli***	**MRSA**
32	106.38 ± 4.64	NA[a]	***58***	90.32 ± 1.12	NA[a]
33	95.04 ± 3.36	NA[a]	***60***	72.97 ± 3.49	118.71 ± 28.38
34	89.87 ± 2.15	NA[a]	***61***	98.70 ± 2.10	NA[a]
35	91.34 ± 4.26	NA[a]	***63***	105.06 ± 2.29	NA[a]
36	98.70 ± 2.10	NA[a]	***64***	84.87 ± 3.99	249.52 ± 90.90
37	91.54 ± 2.05	NA[a]	***65***	97.13 ± 8.61	84.75 ± 5.13
38	89.16 ± 1.09	79.85 ± 4.60	***66[b]***	193.08 ± 41.37	91.82 ± 1.28
39	84.02 ± 0.59	NA[a]	***67[b]***	331.79 ± 26.01	106.78 ± 4.36
40	115.57 ± 2.41	83.54 ± 20.79	***68[b]***	93.70 ± 2.07	168.49 ± 7.09
41	113.65 ± 1.67	145.91 ± 1.77	***69***	90.46 ± 4.33	208.78 ± 9.35
42	84.04 ± 1.43	NA[a]	***70***	85.77 ± 1.55	NA[a]
46	82.52 ± 0.80	72.77 ± 0.73	***71***	90.53 ± 3.53	64.40 ± 1.25
47	90.03 ± 0.95	87.39 ± 28.83	***72***	92.45 ± 2.01	363.24 ± 39.40
48	90.92 ± 1.49	NA[a]	***73***	89.45 ± 1.14	738.53 ± 433.59
49	92.42 ± 0.00	23239.34 ± 39902.57	***74***	96.99 ± 2.31	414.1 ± 12.74
50	123.53 ±16.04	630.13 ± 0	***75***	114.12 ± 1.79	93.40 ± 2.33
51	99.91 ± 4.83	NA[a]	***76***	102.59 ± 6.19	375.31 ± 82.69
52	109.19 ± 2.22	201.12 ± 7.53	***77***	90.69 ± 3.19	168.03 ± 20.89
53	106.31 ± 3.37	180.85 ± 13.91	***78***	109.16 ± 0.99	779.79 ± 100.04
54	89.52 ± 3.01	NA[a]	***79***	87.48 ± 1.38	78.99 ± 0.45
55	100.51 ± 2.66	328.61 ± 114.95	***80***	88.30 ± 0.65	70.37 ± 0.41
56	91.83 ± 1.57	130.28 ± 10.55	***81***	92.83 ± 3.63	163.30 ± 6.66
57	94.63 ± 0.64	72.21 ± 1.08	***Control[c]***	78.57 ± 7.61	65.10 ± 1.12

While the molecules were structurally related, the impact on bacterial growth varied significantly, which led to a classification of the type of inhibition exhibited by the SSAs on *E. coli* and MRSA. Screening growth curves were used in this characterisation. The categories used in this classification were: minimal inhibition, reversible inhibition, partial inhibition, delayed inhibition, and complete inhibition.

Minimal inhibition was defined by a reduction in growth that was ≤ 10% and uninterrupted bacterial growth stages that mirrored the growth control, as exhibited by SSA **67** in Figure 28.

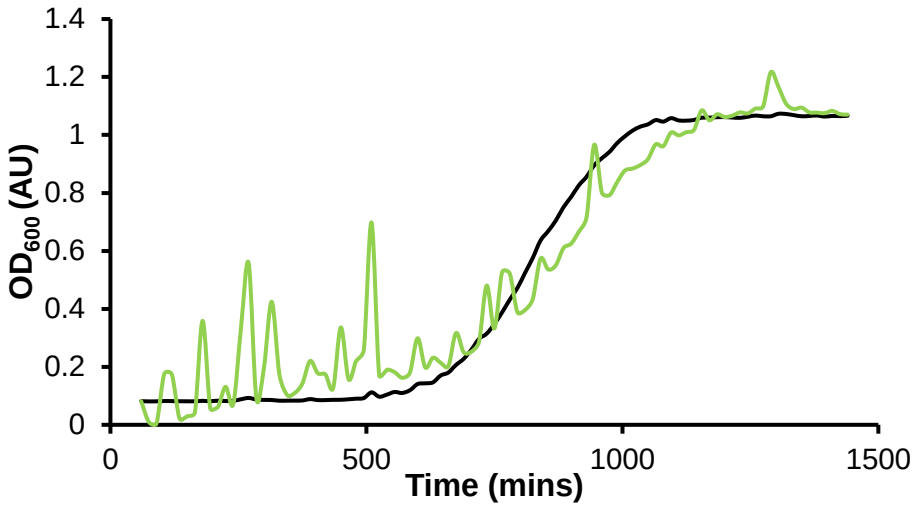

Figure 28. Growth curves of *E. coli* demonstrating compound aggregation.

Growth curves comparing *E. coli* growth in the presence of SSA **67** (green) at 3.3 mM compared to the 5 % EtOH growth control (black).

Initially, the growth rate of *E. coli* in the presence of SSA **67** was calculated to be 830.11 ± 987.14 minutes, which was significantly higher than the growth control. However, the large variation prompted further examination of the growth curve produced in the presence of SSA **67**, which revealed fluctuating OD values. As the fluctuation was present from the start of the observation period, this was attributed to compound aggregates forming which may be due to low solubility in solution. While SSA **67** may have been initially soluble in 5 % EtOH, its stability decreased significantly and resulted in the decreased solubility. Further, when compared to the growth control, while growth was indeed slower in the presence of this SSA, it was not as significant as the initial calculated growth rate suggested and exhibited minimal inhibition to *E. coli* growth. This highlighted the importance of pairing growth rate calculations with growth curve analysis, as in this case, this growth rate may have suggested a greater efficacy than the SSA's true activity. Therefore, the growth rate for SSA **67** reported in Table 6 is the recalculated

growth rate of 331.79 ± 26.01 minutes, which accounts for the compound aggregation. Minimal inhibition was further demonstrated by *E. coli* growth in the presence of SSA **46** (Figure 29).

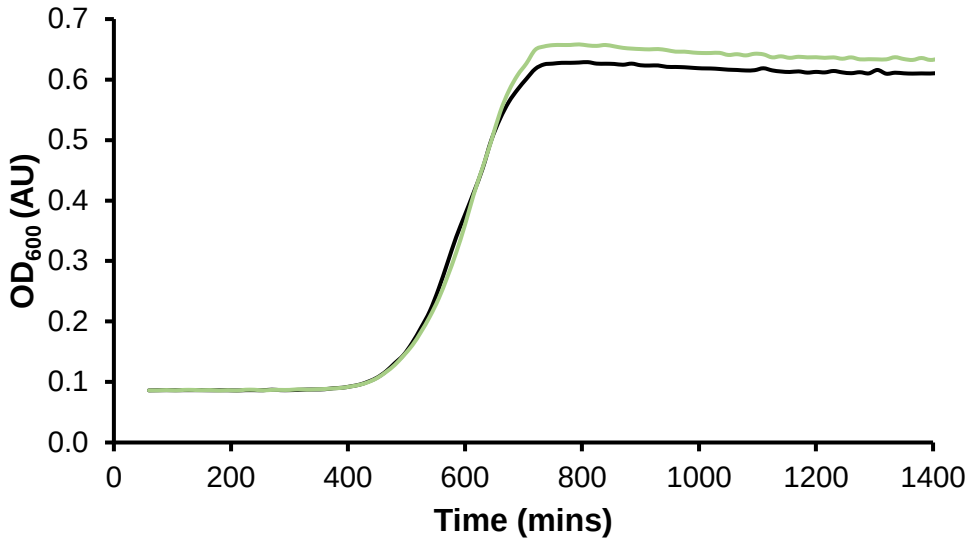

Figure 29. Growth curves of *E. coli* demonstrating minimal inhibition.

OD_{600} growth curves of *E. coli* growth in the presence of SSA **46** at 3.3 mM (green), in comparison to the 5 % EtOH growth control (black).

The growth stages in the presence of SSA **46** appeared to be uninterrupted. Further, the growth rate in the presence of **46** was 82.52 minutes, which while higher than the growth control (78.57 minutes), the growth curve produced revealed this to not be significant (Figure 29). Finally, the culture was able to reach a higher final OD value than the growth control, indicating improved *E. coli* growth. Thus, SSAs **67** and **46,** along with any other molecule that demonstrated a similar impact on bacterial growth, were classified as producing minimal inhibition.

SSAs that exhibited an elongated lag phase, followed by a recovery, shown by the presence of an exponential phase that resulted in the final OD value either being ≥ 10 % lower or an OD value that was higher than that of the growth control, were deemed to exhibit reversible inhibition. An example of this is seen with SSA **38** against MRSA (Figure 30).

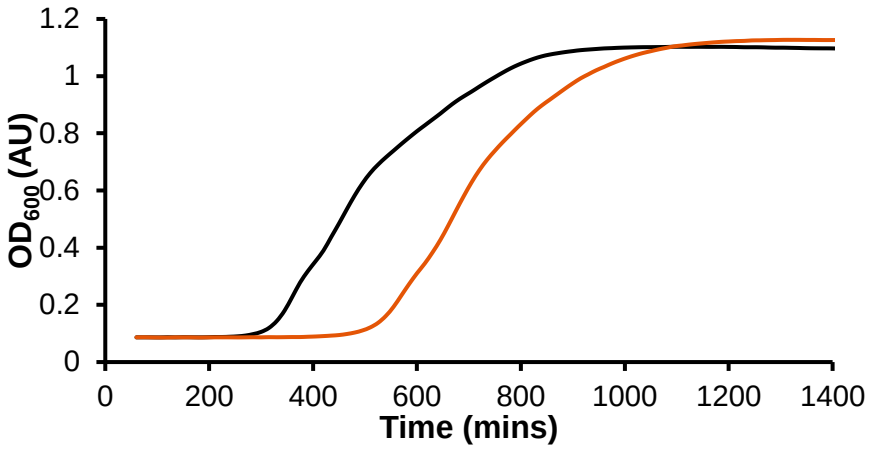

Figure 30. Growth Curves MRSA demonstrating reversible inhibition.

OD_{600} growth curves showing MRSA growth in the presence of SSA **38** (orange) at 3.3 mM in comparison to the growth control (5 % EtOH) (black).

While the exponential phase began at ~ 500 minutes, 200 minutes later than the growth control, and the growth rate (89.16 minutes) was higher than that of the growth control (65.10 minutes), the cells recovered and were able to reach a greater population density than the growth control. It has been established that subinhibitory doses of antimicrobials allow cells to develop resistance against those SSAs, resulting not only in recovery from any initial inhibition that may have taken place but improved growth in the presence of that SSA.[161] The extended lag phase exhibited in the presence of SSA **38** indicates an initial inhibition, and the OD value being higher than the growth control suggests both recovery and improved growth, which are indications of resistance. As such, SSA **38** and any other SSAs that impacted bacterial growth in this way, were deemed to produce reversible inhibition.

SSAs were classified as exhibiting partial inhibition when an exponential phase was observed with the SSA present, however, the final OD value was > 10% lower than the growth control. This could involve an extended lag phase, as demonstrated by SSA **69** (Figure 31), which entered the exponential phase 400 minutes later than the growth control.

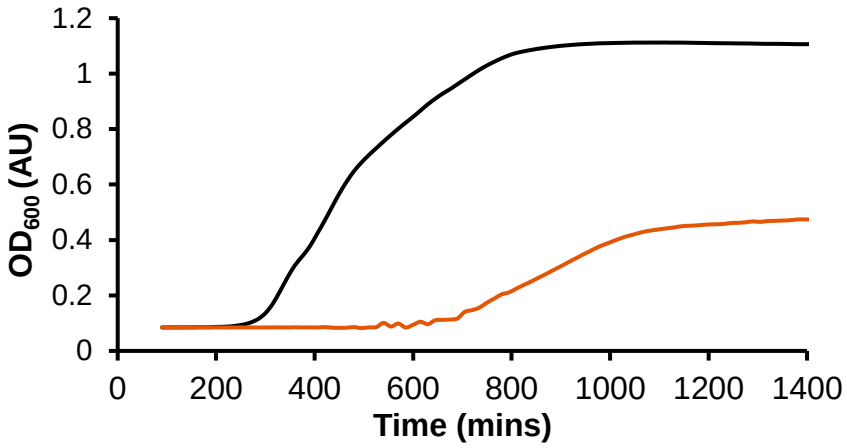

Figure 31. Growth curves of MRSA demonstrating partial inhibition.

Growth curves showing MRSA growth in the presence of SSA **69** (orange) at 3.3 mM in comparison to the growth control (5 % EtOH, black).

And while cells were able to recover, the growth rate was considerably higher (208.78 minutes) than the growth control (65.10 minutes) and the final OD value reached was significantly lower than that of the growth control. Additional examples of this are shown in the MRSA growth curves produced by SSAs **55** and **56** (Figure 32). Growth stages in the presence of SSA **55** were severely disrupted. The lag phase was elongated marginally, and a brief but rapid exponential phase was observed at ~ 300 minutes. However, while the exponential phase continued, it was extended and considerably slower, resulting in a growth rate of 328.61 minutes, which was significantly higher than that of the growth control. Similarly, SSA **56** exhibited an elongated lag phase, followed by a brief exponential phase, which appears to stop between ~400 minutes and 1200 minutes. Following this, another exponential phase was observed at 1200 minutes onward, which obtained a lower growth rate of 130.28 minutes, compared to **55**. However, the final OD value was still significantly lower than the growth control, hence its classification in this category.

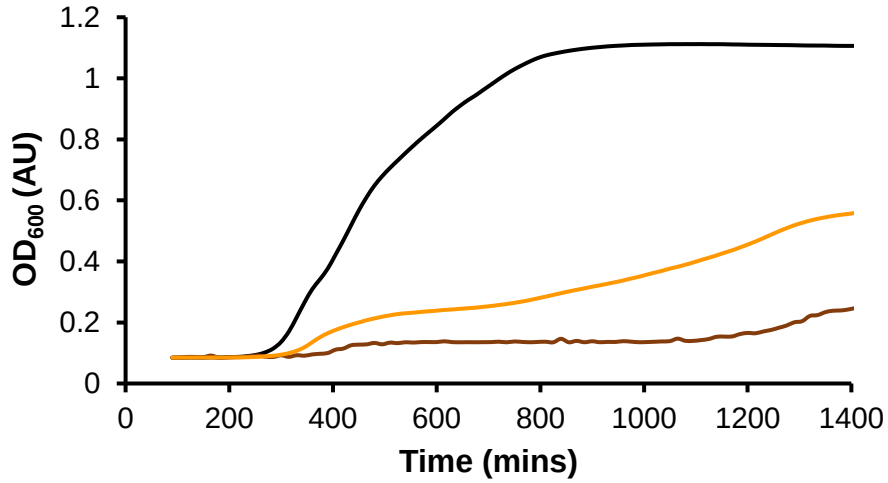

Figure 32. Growth curves of MRSA demonstrating partial inhibition.

Growth curves showing MRSA in the presence of SSAs **55** (brown) and **56** (orange) at 3.3 mM in comparison to the growth control (5 % EtOH, black).

This was further demonstrated by MRSA in the presence of SSA **49**, shown in Figure 33.

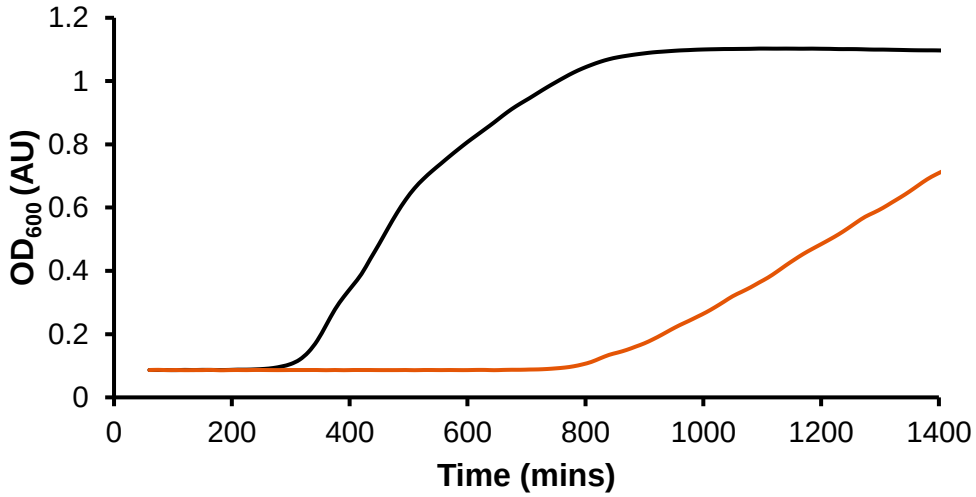

Figure 33. Growth curves of MRSA demonstrating partial inhibition.

Growth curves showing MRSA growth in the presence of SSA **49** (orange) at 3.3 mM in comparison to the growth control (5 % EtOH, black).

A significantly elongated lag phase was observed, which ended at ~ 500 minutes later than that of the growth control. And while cells were able to recover, the growth rate was considerably higher, at 92.42 minutes, resulting in a final OD value that was lower than that of the growth control. SSAs that resulted in growth displaying these characteristics

were classified as exhibiting partial inhibition. Partial inhibition was undesirable as this increases the propensity for bacteria to develop resistance to the SSAs. SSAs were classified as exhibiting delayed inhibition if bacterial death was observed in the later stages of growth, such as mid-log phase and stationary phase, shown by a decline in OD values. This was the case for SSAs **55** and **66** in the presence of *E. coli* (Figure 34). A decline in absorbance values was observed from ~ 800 minutes, with the decline exhibited by SSA **55** being faster than that of SSA **66.** This decline in bacterial growth was a direct result of the compounds' presence, as demonstrated by SSA **35** (Figure 34). While the final OD value reached in the presence of this compound was lower than that of the growth control, a death phase was not observed. Interestingly, while the growth pattern of *E. coli* in the presence of SSAs **66** and **55** was similar, the growth rates differed significantly; **66** = 193.08 minutes, **55** = 100.51 minutes.

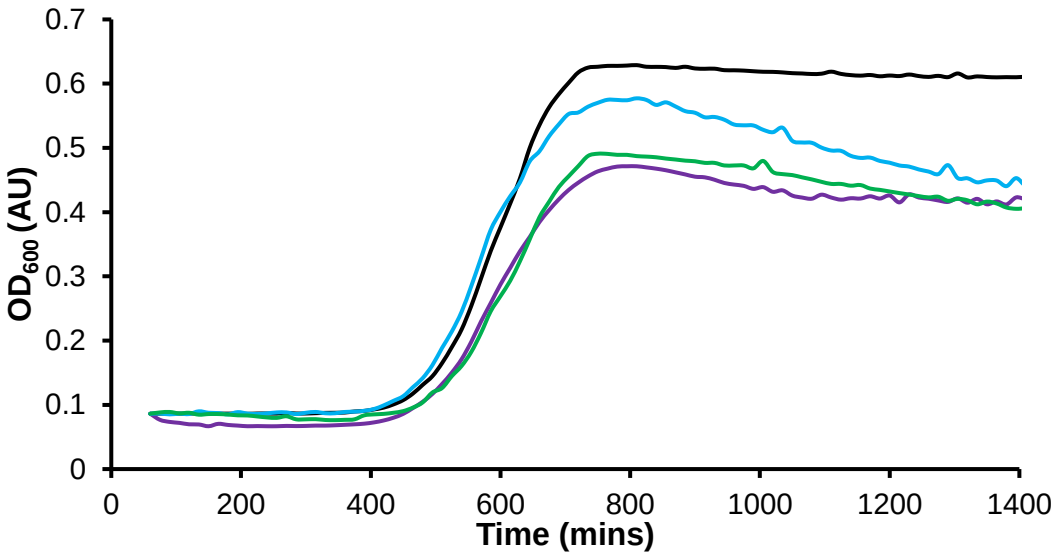

Figure 34. Example growth curves of *E. coli* demonstrating delayed inhibition.

Growth curves showing *E. coli* growth in the presence of SSAs **35** (purple), **55** (blue) and **66** (green) at 3.3 mM, in comparison to the 5 % EtOH growth control.

Further, an elongated lag phase was observed by SSA **66** which was not detected in the presence of SSA **55**. This observation combined with the more rapid death phase observed with SSA **55** than with SSA **66**, suggests that the compounds were affecting

different stages in growth. SSA **66** had a more prominent effect at earlier stages in growth, indicated by the later lag phase, whereas SSA **66** impacted the stationary phase more prominently, indicated by the more rapid death phase. During bacterial growth, multiple changes are made to the phospholipids that make up the membrane during the transition from the exponential phase to the stationary phase, which are thought to protect against phospholipid degradation and improve stability.[162,163] These changes include increases in cardiolipin (CL), decreases in phosphatidylglycerol (PG), and increases in cyclopropane fatty acids.[71,163] As the SSAs are hypothesised to interact with bacterial membranes, the activity observed at different stages of growth may indicate specific lipid binding. If the lipids are more prevalent during the stationary phase, then this would allow the SSAs to impact the stationary more significantly than the other phases.

Delayed inhibition is further demonstrated by *E. coli* in the presence of SSAs **34** and **37** (Figure 35). A delayed lag phase was observed with compound **34**, (Figure 35a), and the *E. coli* growth rate was 89.87 minutes, which was marginally higher than the growth control, suggesting a minimal impact on growth in the exponential phase. However, at ~600 minutes, a rapid death phase was observed followed by fluctuated OD values, and the final OD values were close to those observed in the lag phase, suggesting total cell death. The growth curve for SSA **37** (Figure 35B) revealed an unhindered lag phase, and a marginally impacted exponential phase, indicated by a growth rate of 91.54 minutes (Table 6). However, a far more prominent death phase was observed, followed by a fluctuation in OD values. The death phase appears to slow down from 1100 minutes, which may indicate the cells recovering or adjusting to the presence of this compound, which was not detected with SSA **34**.

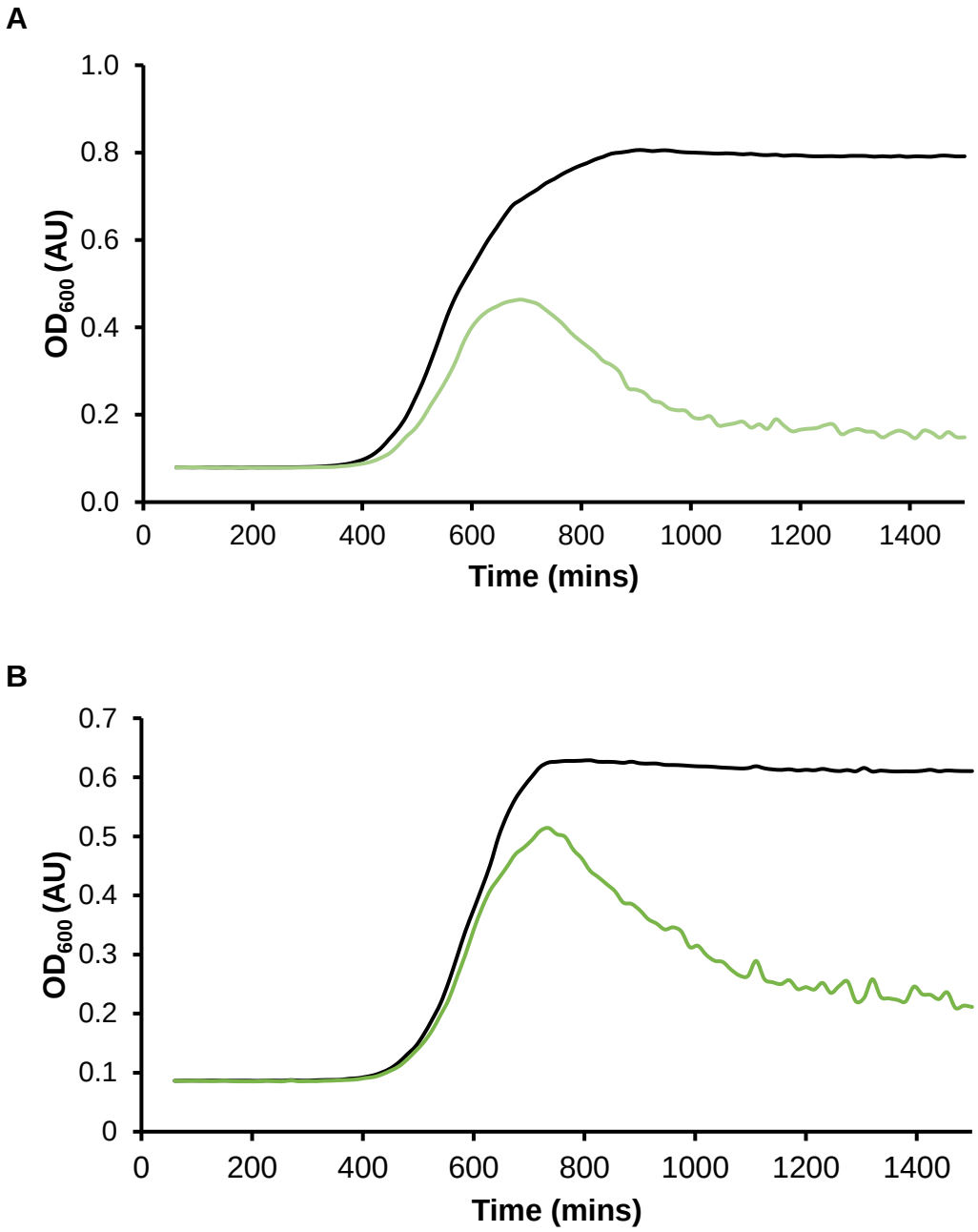

Figure 35: **Example growth curves of *E. coli* demonstrating delayed inhibition.**

Growth curves should *E. coli* growth in the presence of **(A)** SSA **34** and **(B)** SSA **37** at 3.3 mM compared to the 5 % growth control (black).

This is further confirmed with the growth curves exhibited by SSAs **55** and **56**, which suggested different compounds impacting different stages of growth. The fluctuation observed with SSAs **34** and **37** was only observed either during or after the death phase and not during the lag phase. While compound aggregation was still possible, the

aggregation was only present within the death phase, decreasing the likelihood of that being the case. It was hypothesised that the fluctuation could either be due to bacterial aggregation caused by the loss of membrane integrity or due to the compound aggregating lipids, as observed with other amphiphilic antimicrobials.[164] However, a deeper analysis into the membrane-binding properties of the SSAs would allow us to determine whether this was the case.

Lastly, SSAs that resulted in OD values remaining the same as the lag phase OD values throughout the growth period were defined as exhibiting complete inhibition. This suggested a lack of growth in the presence of those SSAs. SSAs that produced this type of inhibition did not have a growth rate calculated, as growth was not detected during the growth period.

E. coli growth rates remained relatively consistent compared to MRSA, which fluctuated greatly, as shown in the graphical representations of the growth rates in Figure 36. Further, none of the SSAs tested produced complete inhibition against *E. coli*, whereas ~ 30% of SSAs tested appeared to completely inhibit MRSA, showing a greater impact on MRSA than *E. coli*. Gram-negative bacteria, like *E. coli*, have an extra outer lipid membrane, which creates an additional obstacle for the SSAs to overcome that isn't present in MRSA, which is gram-positive. As such, a greater impact on MRSA produced by the SSAs was expected.

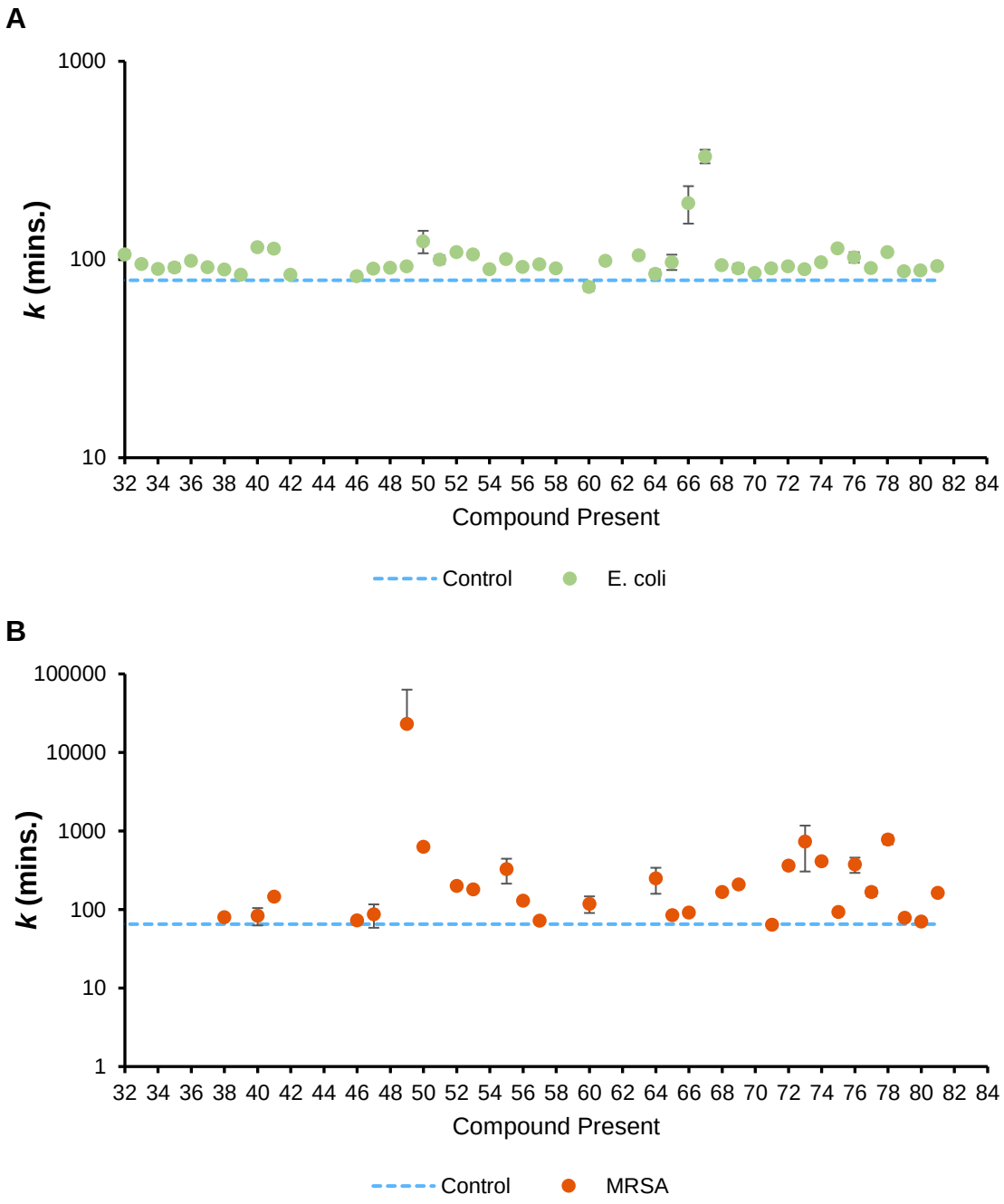

Figure 36 – Graphical representation of the growth rates presented in Table 6.

Growth rates (*k*) of **(A)** *E. coli* and **(B)** in the presence of SSAs **32** – **81** (minutes). Blue line = growth rate in 5 % EtOH growth control.

Table 7 provides a summary of the types of inhibition exhibited by MRSA and *E. coli* in the presence of the SSAs.

Table 7: Type of inhibition exhibited by SSAs 32 – 81 against *E. coli* and MRSA.

	E. coli	MRSA		*E. coli*	MRSA
32	Delayed	Complete	***58***	Minimal	Partial
33	Delayed	Complete	***60***	Minimal	Reversible
34	Delayed	Complete	***61***	Partial/Delayed	Complete
35	Partial	Complete	***63***	Minimal	Complete
36	Delayed	Complete	***64***	Partial/Delayed	Complete
37	Delayed	Complete	***65***	Partial/Delayed	Partial
38	Minimal	Reversible	***66[b]***	Partial	Partial
39	Minimal	Complete	***67[b]***	Minimal	Partial
40	Minimal	Partial	***68[b]***	Minimal	Partial
41	Minimal	Partial	***69***	Partial	Partial
42	Partial	Complete	***70***	Delayed	Complete
46	Minimal	Minimal	***71***	Minimal	Minimal
47	Minimal	Reversible	***72***	Partial/Delayed	Partial
48	Minimal	Complete	***73***	Partial/Delayed	Partial
49	Minimal	Partial	***74***	Partial/Delayed	Partial
50	Minimal	Partial	***75***	Minimal	Partial
51	Minimal	Complete	***76***	Partial/Delayed	Partial
52	Partial/Delayed	Partial	***77***	Partial	Partial
53	Partial	Partial	***78***	Minimal	Minimal
54	Minimal	Partial	***79***	Minimal	Minimal
55	Partial	Partial	***80***	Minimal	Minimal
56	Partial	Partial	***81***	Partial/Delayed	Partial
57	Partial/Delayed	Partial			

Following the growth curve analysis, OD values at the end of the growth period were taken for each SSA and a percentage change was calculated using the OD values of the growth control (5 % EtOH) as a comparison. This would allow us to differentiate between effective and ineffective antimicrobial SSAs. Effective SSAs were characterised by a > 10 % inhibition of bacterial growth, thereby passing the screening, whereas SSAs that exhibited a ≤ 10 % inhibition failed the screening process and were not taken forward for any further antimicrobial testing. Additionally, as 3.3 mM was a high concentration compared to the MICs obtained for commercially available antimicrobials,[165,166] SSAs that were not soluble in 5 % EtOH at 3.3 mM were considered ineffective molecules, and consequently, antimicrobial studies were not conducted. These SSAs are included within

this chapter to provide a thorough comparative analysis. The screening results and percentage change in growth produced by each SSA are presented in Table 8.

Table 8. Antimicrobial screening results for SSAs 32 – 81.

SSAs were screened at 3.3 mM against both *E. coli* and MRSA. **F** – failed the screening, **P** – passed the screening. Percentage change calculated using OD values at the end of the growth period: **+** indicates that this value is a percentage increase, all other values percentage values were a percentage decrease compared to the 5 % EtOH growth control. [a] – SSA was not soluble under experimental conditions, [b] – compound decomposes over time.

Antimicrobial Screening for SSAs 32 - 81									
	Screening Result		**Percentage Change (%)**			**Screening Result**		**Percentage Change (%)**	
	E. coli	**MRSA**	***E. coli***	**MRSA**		***E. coli***	**MRSA**	***E. coli***	**MRSA**
32	P	P	73.86	100.00	***57***	P	P	28.28	17.31
33	P	P	73.18	99.36	***58***	F	P	7.57	97.63
34	P	P	90.34	100.00	***59[a]***	-	-	-	-
35	P	P	37.81	99.12	***60***	F	F	+ 3.71	+ 5.74
36	P	P	62.56	99.98	***61***	P	P	88.77	100.00
37	P	P	73.39	100.00	***62[a]***	-	-	-	-
38	F	F	7.80	+ 2.84	***63***	P	P	12.66	99.88
39	F	P	4.18	100.00	***64***	P	P	33.25	87.57
40	F	P	9.20	63.52	***65***	P	P	27.70	22.77
41	F	P	7.32	54.86	***66***	P	P	37.00	100
42	P	P	31.43	100.00	***67***	F	P	+ 3.04	100
43[a]	-	-	-	-	***68***	F	P	+2.49	100
44[a]	-	-	-	-	***69***	P	P	19.44	62.00
45[b]	-	-	-	-	***70***	P	P	27.12	99.00
46	F	F	+ 4.50	+ 2.70	***71***	F	F	+ 0.05	+ 2.00
47	F	F	4.40	1.91	***72***	P	P	31.76	93.00
48	F	P	7.26	100.00	***73***	P	P	15.38	85.00
49	F	P	4.27	44.20	***74***	P	P	39.26	96.00
50	F	P	+ 1.52	80.02	***75***	F	P	+ 1.75	40.00
51	F	P	+ 1.64	97.61	***76***	P	P	26.36	78.00
52	P	P	46.36	93.00	***77***	P	P	22.83	70.00
53	P	P	54.12	66.23	***78***	F	F	3.01	+ 12.00
54	F	P	5.97	81.73	***79***	F	F	2.04	+ 1.00
55	P	P	30.70	85.41	***80***	F	F	1.68	+ 2.00
56	P	P	20.49	55.02	***81***	P	P	29.84	78.00

3.4.6. MIC_{50} determination

The MIC_{50} represents the concentration of a drug that inhibits 50 % of isolates in a test population.[167,168] MIC_{50} values were calculated for the SSAs that passed the screening process; those that inhibited bacterial growth > 10 %. Further, as compounds that exhibited 100% decreases in growth could not be compared using the screening results, their MIC_{50} values were used for comparison.

MIC_{50} values were obtained as described in section **2.4.4, 2.4.7,** and **2.4.8** of the materials and methods. Briefly, SSA solutions were created in 5 % EtOH, using the screening results as a basis for selecting the concentrations tested. The concentrations were selected so that the highest concentration would produce total cell death, or as close to this as possible, and the lowest concentration would have a minimal impact on bacterial growth. The SSA solutions were then added to mid-log cells at a diluted concentration of 10^5 cfu/mL, then incubated at 37 °C in a microplate reader. OD values were recorded every 15 minutes for 18 hours, then MIC_{50} values were calculated using the OD values at 900 minutes from each concentration. These values are presented in Table 9. Further, $1/MIC_{50}$ is displayed in Figure 37 to better visualise the most effective SSAs.

Table 9. MIC_{50} values obtained for SSAs 32 – 81.

MIC_{50} values calculated for SSAs that passed the screening process, [a] – compound was not soluble under experimental conditions, [b] – compound breaks down over time, [c] – unable to calculate an MIC_{50} value due to crystallisation of compound, [d] – compound failed the screening process, * - predicted endpoint used to calculate MIC_{50} due to solubility of the compound under experimental conditions.

MIC_{50} values obtained for SSAs 32 – 81.

	MIC_{50} (mM)			**MIC_{50} (mM)**	
	E. coli	**MRSA**		***E. coli***	**MRSA**
32	3.85*	0.46	***58***	NA[d]	1.10
33	3.93*	0.98	***61***	1.25	1.14
34	1.48*	NA[b, c]	***63***	NA[a]	0.83
35	NA[a]	3.03	***64***	NA[d]	0.77
36	NA[a]	0.25	***65***	4.30*	2.96
37	1.85*	1.08	***66***	NA[a]	0.46
39	NA[d]	0.35	***67***	NA[d]	0.61
39	NA[d]	2.17	***68***	NA[d]	0.71
40					
41	NA[d]	2.85	***69***	3.57*	0.99
42	5.96*	0.42	***70***	5.00*	0.93
48	NA[d]	0.92	***71***	NA[d]	4.41
49	NA[d]	5.10	***72***	5.67*	2.85
50	NA[d]	3.00	***73***	NA[a]	5.78
51	NA[d]	2.18	***74***	6.03*	3.07
52	NA[a]	0.98	***75***	NA[d]	2.78
53	NA[a]	2.59	***76***	6.91*	8.99
54	NA[d]	1.65	***77***	6.26*	3.12
55	8.65*	1.96	***81***	6.36*	3.18
56	7.37*	2.24			

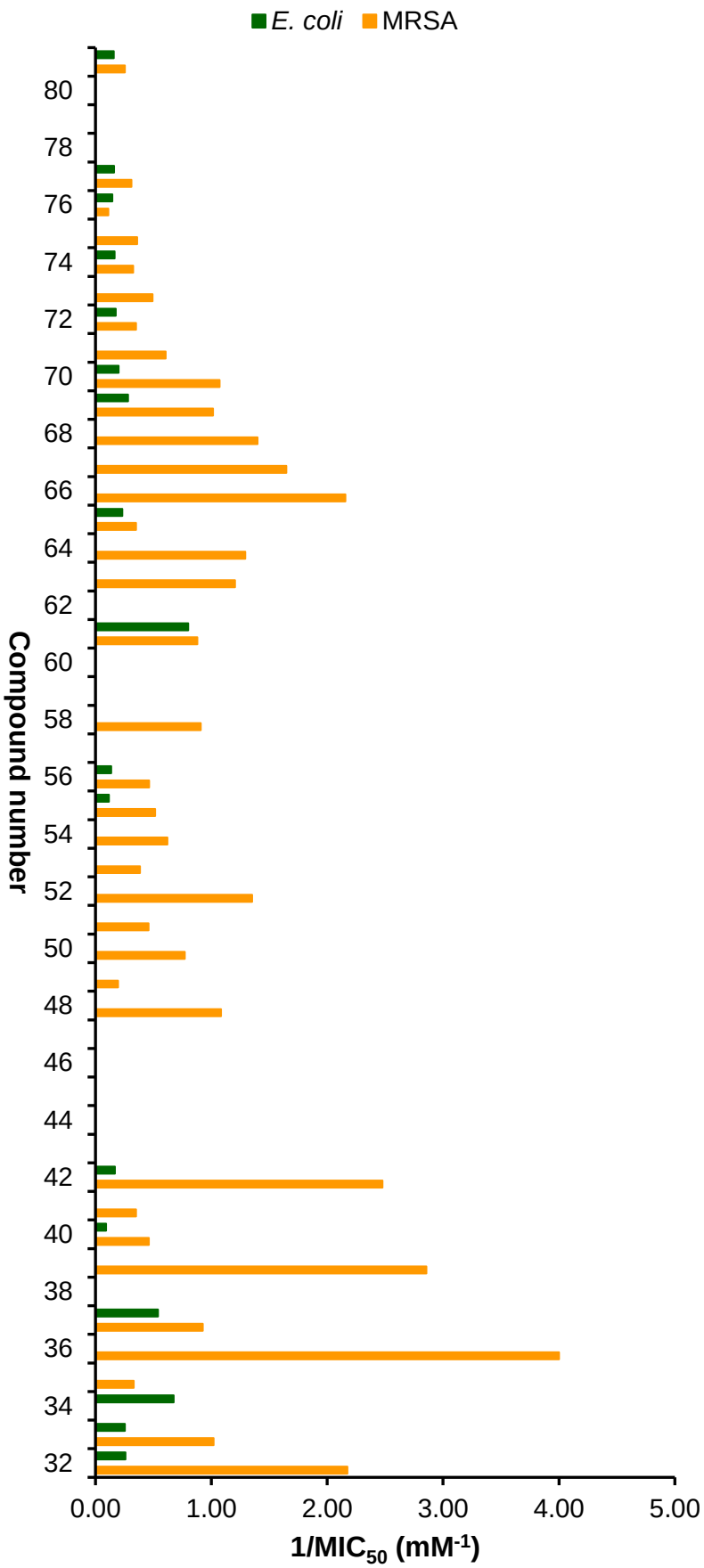

Figure 37. Graphical representation of the MIC_{50} values presented in Table 9.

Antimicrobial efficacy of SSAs **32** – **81** against *E. coli* and MRSA, determined by MIC_{50} values (mM). $1MIC_{50}$ (mM^{-1}) is displayed to better visualise the MIC_{50} values. The larger the bar, the smaller the MIC value.

3.5. Structure-Activity Relationships of SSA 1 – 50

The data discussed in this section corresponds to the data presented in Tables 6 to 9 and Figures 36 and 37. Any physicochemical studies discussed were conducted by Lisa White.[153,154]

3.5.1. Increased growth of bacteria

The addition of some of the SSAs to bacteria led to increased bacterial growth in comparison to their respective growth controls. These SSAs were **46** (+4.53%),**50** (+0.95%), **51** (+0.97%), **60** (+3.59%), **67** (+0.39%) and **75** (+3.97%) for *E. coli* and for **38** (+2.92%), **46** (+2.45%), **60** (+8.81%), **71** (+1.92%), **78** (+7.87%), **79** (+1.55%) and **80** (+1.31%), for MRSA. Bacteria can rapidly adapt to different environments and utilise their environment to improve growth.[169,170] As previously mentioned, exposing bacteria to sublethal concentrations of antimicrobials can improve growth which may be due to the development of resistance and increased nutrient uptake, leading to increased growth. Further, the cells may be able to break down and utilise the SSAs to promote growth. Therefore, any SSAs that increased bacterial growth were considered ineffective antimicrobials.

3.5.2. Urea and Thiourea functionalities

Thiourea and urea derived compounds are widely used for a range of purposes, and particularly known for their biological activities such as their antiparasitic, anticancer, antioxidant, antibacterial, and antifungal properties.[171–173] Within these molecules are two HBD amine groups,[174] which enable self-association events to occur. Whilst structurally similar, the change from an oxygen atom to a sulphur atom alters the physicochemical properties of the molecule. Polarity exists within the thio(urea) functionality due to the electronegativity of the sulphur (S) and oxygen (O) atoms, which results in a partial negative charge on the S/O atoms and a partial positive charge on the NH hydrogen atoms. However, the sulphur atom is a less electronegative atom so polarises the bond less in comparison to the oxygen atom. Thus the NH hydrogens are less acidic in the

thiourea functionality than in the urea functionality, allowing the urea to form stronger hydrogen-bonded complexes.[175–179] However, as the sulphur atom is larger in size than the oxygen atom, the partial negative charge is dispersed over a larger area, allowing thiourea to be more lipophilic. The thiourea-based molecules were predicted to perform better as antimicrobials than urea-based molecules, due to the greater lipophilicity which was predicted to allow the molecule to pass through bacterial membranes with greater ease than the urea-based molecules. Consequently, the urea functionality was changed to a thiourea, giving rise to SSA **35**. Rather than increased antimicrobial efficacy, however, SSA **35** had considerably less activity than SSA **32.** Reduction in bacterial growth was 73.86 % for SSA **32** but 37.81% for SSA **35** against *E. coli*. And although a marginal difference between percentage reduction in MRSA growth for SSAs **32** and **35**, (100.00% and 99.12%, respectively), the MIC_{50} value for SSA **35** (3.03 mM) was considerably higher than that of SSA **32** (0.64 mM). A comparison was made using the other molecules containing urea and thiourea functionalities which revealed a decrease in efficacy with the thiourea counterparts for the vast majority of molecules. Furthermore, the substitution to the thiourea functionality reduced the stability of SSA **45** (compared with SSA **38**), which we were unable to test as a result of this modification. These observations were consistent with the majority of SSAs, where the urea and thiourea functionalities were compared, and thus we concluded that the urea functionality played an integral role in the antimicrobial action and was more effective than the thiourea functionality. This may be due in part to the higher electronegativity of the oxygen atom and increased acidity of the urea functionality which may have resulted in stronger hydrogen bonded complexes, in comparison to the thiourea functionality.

3.5.3. Increasing the thio(urea) anion spacer

Increasing the connective alkyl chain between the sulfonate group and the amine groups and the sulfonate group, from n=1 to n=2, resulted in SSAs **33** and its thiourea counterpart, SSA **36**. Regarding SSA **33**, this change decreased antimicrobial efficacy drastically against MRSA. Whilst screening results only reveal a minor decrease in

activity against MRSA growth, decreasing growth by 99.36% in comparison to the 100% reduction in growth by SSA **32**, it is with the compound's MIC_{50} against MRSA that we truly see this. The MIC_{50} for SSA **33** (0.98 mM) was more than twice the MIC of SSA **32** (0.46 mM) against MRSA. Antimicrobial activity against *E. coli* was not as drastically different; screening results revealed a 0.68% difference in their effect on growth and while slightly lower for SSA **33**, the MIC_{50} for SSAs **32** and **33** against *E. coli* were similar (3.85 mM and 3.93 mM) respectively. Solution state studies conducted on SSA **33** revealed a lower association constant, in comparison to those obtained for the other SSAs.[154] Further, solid-state studies revealed SSA **33** spent the majority of time forming an intramolecular hydrogen bond between the sulfonyl group one of the urea amine groups, which is proposed to reduce intermolecular self-association events.

Increasing the alkyl chain further from n= 2 to n=3 increased antimicrobial activity, especially against *E. coli*. A comparison between SSAs **32** – **34** revealed a reduction in *E. coli* growth of 90.34 % by SSA **34** (n=3), which was higher than that of SSA **32** (n=1), (90.34 %) and SSA **33** (n=2), (73.18 %). Further, the MIC_{50} of SSA **34** (1.48 mM) was significantly lower than SSAs **32** (3.85 mM) and **33** (3.93 mM), which was the second lowest MIC_{50} against *E. coli.* Improved efficacy against MRSA was also observed with SSA **34**, compared to SSA **33**, decreasing growth by 100% in comparison to **33**, which decreased growth by 99.36%. An MIC_{50} could not be calculated for SSA **34** against MRSA, however, as consistent results could not be obtained. MRSA growth curves produced in the presence of SSA **34** varied drastically, which was not observed with *E. coli* (Figure 38).

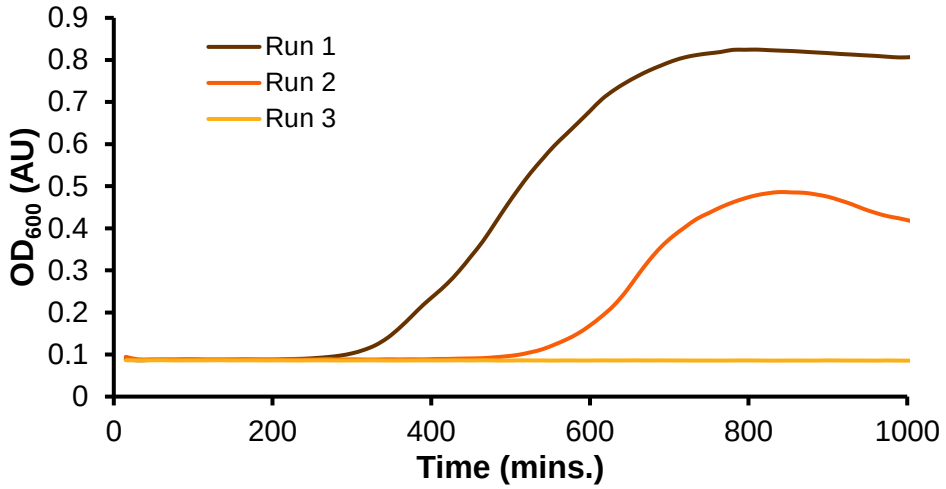

Figure 38. MRSA Growth curves.

Growth curves showing the variation of MRSA growth in the presence of SSA **34** at 1.67 mM.

This was hypothesised to be a result of the SSAs tendency to crystallise, which may have had a more pronounced effect at lower concentrations, and given the high efficacy against MRSA, this would produce inconsistent results. The thiourea counterparts (SSA **35** – **37**) mirror this increase in efficacy when the alkyl chain was increased n=3, with the major difference being the improved stability of SSA **37**, in comparison to SSA **34** against MRSA.

An investigation of the structures of SSAs **34** and **37** revealed the molecules did not spend as much time forming the intramolecular bond observed with SSA **33.** This may allow both the sulfonyl group and both central NH groups to form hydrogen bonds more freely, which we hypothesised may be integral to the antimicrobial activity of these compounds.

3.5.4. Exchanging the counter cation

Hydrogen bond complexation events can be negatively impacted by the presence of competitive ion-ion pairs, thus TBA counter cations are more favourable due to low coordination. SSAs **38** – **49** were used to investigate how this would impact the antimicrobial activity. It was hypothesised that ion-ion pair effects would hinder self-associative hydrogen bond events, impacting dimer formation and therefore reducing

antimicrobial activity. The cations selected were tested alone to determine their own antimicrobial activity (SSAs **78** – **81**). SSAs **78** – **80** had minimal impact on growth, with the highest activity being that of **78**, which decreased growth by 3.01%. Whilst SSA **81** had antimicrobial activity on its own, as documented in literature[11,180–182], its higher MIC_{50} values against *E. coli* (6.36 mM) and MRSA (3.18 mM) in comparison to those of SSA **32** (*E. coli;* 3.85 mM and MRSA; 0.46 mM), as well as the majority of compounds containing TBA suggested that the antimicrobial activity could not solely be attributed to TBA. Rather, the combination of the anion and the TBA cation produced the antimicrobial activity observed. Following this, the compound screening and MIC_{50} calculations for SSAs **38** – **49** were conducted. The sodium counter cation was first selected as it would be more strongly co-ordinating to the anion than the TBA cation. Crystal structures of the resulting structures formed by SSAs **38** and **45** suggested disrupted dimer formation caused by the sulfonate group no longer involved in self-association processes, but urea-urea stacking was observed instead (Figure 39).[154,183]

A **B**

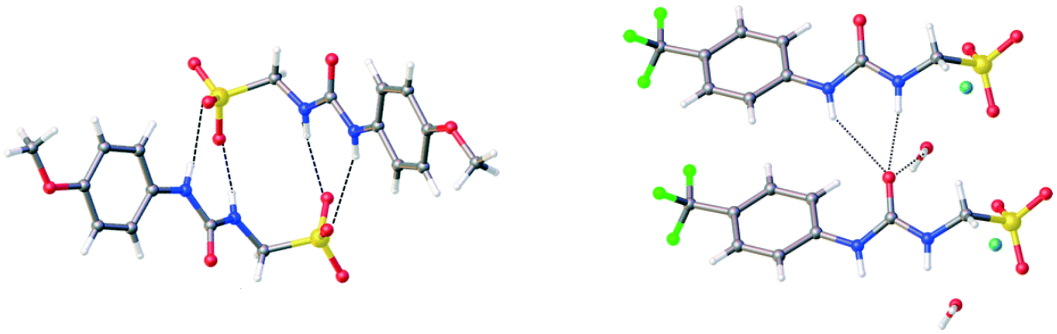

Figure 39. Crystal structures of SSAs 32 and 38.

Crystal structures showing **(A)** the dimerisation of SSA **32** in comparison to **(B)** the urea-urea stacking observed with SSA **38**.[183]

Further, in the solution state, dilution studies conducted on **38** revealed ion-ion pair effects.[154] This was reflected in the activity of these two SSAs, which were compared to

SSAs **32** and **35,** respectively. SSA **38** revealed a drastic reduction in antimicrobial activity during the screening process, only decreasing bacterial growth by 7.80% against *E. coli* and increasing MRSA growth by 2.84%, and thereby failing the screening. Its thiourea counterpart, **45,** was unstable during the synthesis process so could not be taken forward for any antimicrobial activity analysis.

Charge diffusion and steric hindrance as the cations increased in size would result in weaker coordination to the anionic component, in comparison to the sodium ion. The pyridinium cation was slightly less coordinated to the anionic component, and the impact of this was next examined through the use of SSAs **39** and **46** which were compared to SSAs **32** and **35**, respectively. While SSA **39** decreased activity against *E. coli* (4.18% decrease was observed for SSA **39**, thereby failing the screening process), activity against MRSA increased, with a drastically lower MIC_{50} of 0.35 mM. Its thiourea counterpart (**46**), however, failed the screening process against both bacteria. Next, the effect of the TMA cation was observed through SSAs **40** and **47**. These molecules exhibited improved activity in comparison to SSAs **38** and **45,** respectively. While it still failed the screening process, SSA **40** decreased *E. coli* growth by 9.20 %, which was higher than that of SSA **38** (7.80 %). MRSA activity significantly increased, shown by SSA **40** decreasing growth by 63.52% and producing an MIC_{50} value of 2.17 mM, in comparison to SSA **38** activity, which failed the screening process. The thiourea counterpart, SSA **47**, failed screening against both bacteria, however, was more stable than SSA **45** and able to undergo antimicrobial testing.

The necessity of maintaining hydrophilicity at the sulfonate portion of the molecule could be observed using the TEA cation present in SSAs **41** and **48**. TEA was not as strongly coordinating in comparison to the sodium, pyridinium, and TMA cations, as shown by the solution state studies.[154] However, it is hypothesised to not be hydrophilic enough to remain at the hydrophilic portion of the molecule (the sulfonate group) and not be hydrophobic enough to remain at the hydrophobic (benzene ring) portion of the molecule, which could result in a loss of self-associative structures.[153,154] This is reflected in the

screening results and MIC_{50} values obtained for SSA **41**. SSA **41** exhibited lower antimicrobial activity compared to SSAs **38**, **40,** and **42** against both *E. coli* and MRSA, decreasing *E. coli* growth by 7.32% and MRSA growth by 58.86%. Further, within this urea-based group of compounds (SSAs **38** - **42**), SSA **41** had the highest MIC_{50} value against MRSA. This suggested that maintaining hydrophilicity around the sulfonate region was essential to the antimicrobial activity, and the counter cation played an integral role in this.

Conversely, the thiourea counterparts did not follow this pattern. A comparison between SSAs **47** and **48** revealed SSA **48** had higher antimicrobial activity in comparison to SSA **47**, as the TMA failed the screening process whereas the TEA decreased growth by 100%. Furthermore, the comparison between SSAs **48** and **49** revealed SSA **48** was significantly more effective than **49**, as shown by their MIC_{50} values of 0.92 mM and 5.10 mM respectively against MRSA. These observations could be a result of multiple factors and suggested more complex interactions taking place, which would require further analysis for a viable hypothesis to be made.

The TPA cation present in SSAs **42** and **49**, was less coordinated to the anionic component than the TEA cation. This was reflected in the drastically improved antimicrobial activity exhibited by SSA **42** against both *E. coli* and MRSA, with MIC_{50} values of 5.96 mM and 0.42 mM, respectively, which were the lowest and second lowest MIC_{50} values within this group of compounds. Its thiourea counterpart (**49**), however, was not as effective, as it failed the screening against *E. coli* and had a higher MIC_{50} against MRSA (5.10 mM) compared to SSAs **47** and **48**. The TBA cation was the least coordinating cation tested, and this was reflected in the MIC_{50} for SSA **32** against *E. coli* (3.85 mM) being far lower than those obtained for SSAs **38 – 42**. Interestingly, the pyridinium cation proved to be the most effective cation against MRSA within this group of compounds, as it had the lowest MIC_{50} of 0.35 mM. The thiourea counterparts (SSAs **35**, **45** – **49**) revealed the TEA counter cation was the most effective with respect to MRSA activity, as it produced the lowest MIC_{50} of 0.40 mM against MRSA.

Therefore, *E. coli* activity was improved by the selection of a weakly coordinating cation, such as TBA. However, competitive hydrophobicity of the cation impacts the molecule's ability to solubilise in an aqueous environment, as observed with SSAs **43** and **44**, which were not tested due to their insolubility under these experimental conditions. MRSA activity, however, appeared to favour the pyridinium cation, as observed with the drastically higher activity exhibited by SSAs **39** and **48**.

3.5.5. Altering the sulfonyl group

Testing the sulfonyl group alone (SSA **77**), allowed for the determination of its importance to the antimicrobial activity. SSA **77** had an MIC_{50} of 6.26 mM against *E. coli* and 3.12 mM against MRSA. This suggested that the activity of SSA **32** could be attributed in part to the presence of this group, due to the significantly higher MIC_{50} values obtained with SSA **77**.

SSAs **59** – **64** demonstrate the impact of changing the sulfonyl group to a neutral carboxylic acid group (**60** and **63**) or to a carboxylate functionality (**61** and **64**) on the antimicrobial activity, which were then compared to SSAs **32** and **35**. SSAs **59** and **62** were both insoluble under experimental conditions, most likely due to their lower capability to form hydrogen bonds at the sulfonate end of the molecule. The carboxylic acid group exhibited lower activity against *E. coli* compared to the carboxylate group and the sulfonyl group. SSA **60** failed the screening process and SSA **63** decreased growth by 12.66%, whereas SSAs **61** and **64** decreased growth by 88.77% and 33.25% respectively. Solution state studies, through the use of zeta potential measurements, revealed self-associated structures formed by **60** were unstable.[154] The modification from the sulfonyl (SSA **32**) to the carboxylate (**SSA 61**) increased *E. coli* activity. SSA **30** produced the lowest MIC_{50} against *E. coli* (1.25 mM) out of all the compounds tested.

Similarly, when observing MRSA activity, SSA **60**, which failed the screening process, was far less effective than SSA **61**, which not only passed the screening but also had an MIC_{50} of 1.14 mM. However, SSA **32** activity was still higher than that of SSAs **60** and **61,**

shown by its MIC_{50} of 0.46 mM. This was further demonstrated by their thiourea counterparts, SSAs **63** and **64,** which produced MIC_{50} values of 0.83 mM and 0.77 mM respectively, both being lower than SSA **35**.

These data provide evidence of the anion geometry directly impacting antimicrobial activity due to the shape of the resultant aggregates formed, demonstrated by the carboxylate group improving *E. coli* efficacy. The sulfonyl group is tetrahedral, whereas the carboxylate group is trigonal planar, which impacts the resultant complexes formed. The carboxylate forms a planar 6-membered ring system, whereas the angles present in the sulfonate group prevents this. Further, solution-state studies on SSA **61** revealed a higher association constant, attributed to comparatively increased basicity of the anionic component of the molecule. This suggested higher order complex formation, which may be beneficial for *E. coli* activity. However, the sulfonyl group produced far greater MRSA activity than the carboxylate and carboxylic acid groups, suggesting differing binding modes or targets for MRSA and *E. coli* activity.

3.5.6. R groups on the aromatic ring

As determined previously, maintaining hydrophilicity at the sulfonate end of the molecule was essential to the antimicrobial activity of these molecules. Therefore, the next step was to determine the importance of maintaining hydrophobicity at the phenyl ring portion of the molecules. Attached to the benzene ring of SSA **32** is a CF_3 group (Figure 40) which is hydrophobic and also electron-withdrawing, thus making the NHs in the (thio)urea functionalities more acidic.

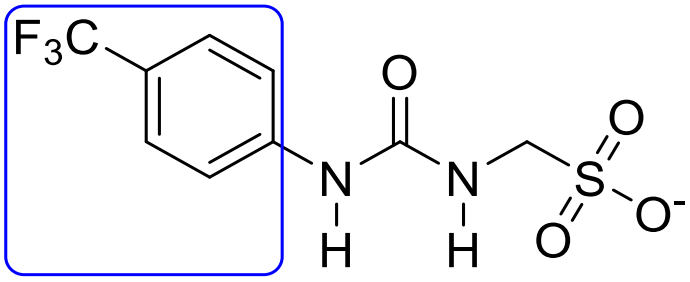

Figure 40. Structure of the anionic component in SSA 32. Structure highlighting the region where r-groups were modified. Blue = phenyl ring and associated R-group, CF_3

It was hypothesised that maintaining this acidity played a key role in the antimicrobial activity of these molecules, due to its impact on the resultant complexes formed, and changing the R – group associated with the phenyl ring would impact this. A more electron-withdrawing group would make them more acidic, and a more electron-donating group would make the NHs less positive. Therefore, to determine this, specific functionalities were selected; NH_2 (**50**), MeO (**51** and **55**), H (**52** and **56**), NO_2 (**53** and **57**), and two CF_3 groups in the meta positions on the benzene ring (**54** and **58**).

The NH_2 functionality present in SSA **50** is a hydrophilic, electron-donating group, causing lower lipophilicity at the phenyl ring and less acidity in the NH groups at the urea functionality, in comparison to SSA **32**, resulting in weaker hydrogen bond formation by the urea NHs. This is reflected in the antimicrobial activity of SSA **50,** which failed the screening process against *E. coli*, and had a significantly higher MIC_{50} value against MRSA of 3.00 mM. Following this, we examined the impact of the MeO group present in SSA **51**. This is an electron-donating group that is less hydrophilic than the NH_2 group but less hydrophobic than the CF_3 group. Again, antimicrobial activity against *E. coli* was lower than that of SSA **32**, as SSA **51** failed the screening process and had a higher MIC_{50} of 2.18 mM against MRSA. SSA **51** was more effective than SSA **50**, however, this suggested that increasing hydrophobicity was beneficial to antimicrobial activity. This was further explored through the analysis of SSA **52**, which has a H atom attached to the phenyl ring that is neither electron-withdrawing nor donating but is more hydrophilic than SSAs **50** and **51**. This may allow for the formation of stronger hydrogen bonds by the urea NHs, in comparison to **50** and **51**. This could explain the antimicrobial activity of SSA **52** being higher in comparison to SSAs **50** and **51**. SSA **52** passed the screening process, decreasing *E. coli* growth by 46.36% and the MIC_{50} values against MRSA was significantly lower (0.98 mM) than those of SSAs **50** and **51**. The NO_2 functionality present in SSA **53**, revealed a further increase in antimicrobial activity against *E. coli*, which decreased growth by 54.12%, however antimicrobial activity against MRSA decreased, with the MIC_{50} value of 2.59 mM, in comparison to SSAs **50** – **52**. The NO_2

functionality is electron-withdrawing, increasing the acidity of the urea NHs, and the improved activity compared to SSAs **50** – **52** may be attributed to this. However, the NO_2 group is also more hydrophilic, reflected by its lower activity against *E. coli*, in comparison to SSA **32**. The reduced activity against MRSA suggests that despite the increase in acidity of the central NHs, this wasn't enough to combat the increased hydrophilicity of the phenyl ring, further solidifying the hypothesis that both hydrophobicity in the phenyl region and increased acidity in the central NH region are required for effective antimicrobial activity.

SSA **54** had two CF_3 groups on the phenyl ring, in the meta positions, which are more electron-withdrawing than the singular CF_3 in SSA **32**, and more hydrophobic. This significantly reduced activity against *E. coli*, decreasing growth by 5.97%, thereby failing the screening process. While SSA **54** performed better than SSAs **50** and **51**, it had significantly lower activity than SSAs **52** and **53**. Similarly, SSA **54** was more effective against MRSA, shown by its MIC_{50} value of 1.65 mM, than SSAs **50** and **51** (3.00 mM and 2.18 mM, respectively) which had more electron-donating R groups at the phenyl ring, and was more effective than SSA **53** (2.59 mM), which had more hydrophilic groups. However, SSA **52,** which was hydrophilic but neither electron-donating or withdrawing, exhibited higher efficacy than **54** against MRSA, as the MIC_{50} value for **52** was 0.98 mM, significantly lower than that of **54**. This is further demonstrated by the significantly higher activity exhibited by SSA **32** (0.46 mM), whose singular CF_3 was hydrophobic at the phenyl ring system and also electron-withdrawing, thereby increasing the acidity of the urea NHs, allowing stronger hydrogen bond complexation.

A comparison using the thiourea counterparts of SSAs **50** – **54**, (**55** – **58**), reveals improved activity when the thiourea functionality was present, with the exception of SSA **56** against *E. coli*. SSA **56** had reduced activity against *E. coli,* with an MIC_{50} value of 7.37 mM than SSAs **55** which produced an MIC_{50} value of 8.65 mM, consistent with the prior comparisons made between urea/thiourea-based molecules. Conversely, MRSA

activity was reversed, with SSA **56** producing a higher MIC_{50} value (2.24 mM) than SSA **55** (1.96 mM). The improved activity exhibited by the thiourea counterpart may be attributed to the increased hydrophobicity of the thiourea in comparison to the urea functionality, and also the increased electronegativity of the sulphur in the thiourea, than the oxygen present in the urea. This is further demonstrated by the comparison between SSAs **51** and **55**, which were the more electron-donating groups, in comparison to SSAs **32** and **35**. SSA **51** had lower activity against *E. coli* than SSA **55**, as SSA **51** failed the screening process but SSA **55** produced an MIC_{50} of 8.65 mM. Further, **55** produced a lower MIC_{50} value (1.96 mM) than **51** (2.18 mM), thus the presence of the thiourea may have 'rescued' the antimicrobial activity.

These data provide evidence that maintaining hydrophobicity at the phenyl ring and whilst also using an electron-withdrawing group to ensure the amine group in the thio(urea) functionality remained acidic was essential in the activity of these molecules. A balance was required, however, as observed with SSAs **54** and **58**, which though containing more hydrophobic R – groups at the phenyl ring, produced significantly lower antimicrobial activity, thus a singular CF_3 functionality provided that balance whilst also maintaining the acidity of the urea NHs.

3.5.7. Removal of the phenyl ring

Having determined the role of the R – groups associated with the phenyl ring, the next step was to determine how the removal of the ring would impact the antimicrobial activity, giving rise to SSAs **71** – **76**, which were compared to SSAs **32** and **35**.

A significant decrease in activity was observed with SSA **71**, which increased both *E. coli* and MRSA growth by 0.05% and 2.00% respectively, failing the screening process. Its thiourea counterpart, SSA **74**, while higher, produced an MIC_{50} of 3.07 mM against MRSA, which was close to that of SSA **35** (3.03 mM). Increasing the alkyl chain had improved activity against *E. coli*, as shown by the comparison of SSAs **32** – **34**, and therefore, the alkyl chain was extended from n=1 in SSA **71** to n=2 in SSA **72** and n= 3 in

SSA **73.** Unlike SSAs **32** – **34**, SSA **72** exhibited better antimicrobial activity against both *E. coli* and MRSA than SSA **73** (n=3). The MIC_{50} values obtained for SSA **72** were 5.67 mM against *E. coli* and 2.85 mM against MRSA. Whereas the MIC_{50} value of SSA **73** against MRSA was 5.78, significantly higher than **72**, and an MIC_{50} value could not be calculated against *E. coli*, as it was higher than the solubility of the compound under experimental conditions (Figure 41). Similarly, their thiourea counterparts exhibited better antimicrobial activity against MRSA when the alkyl chain was increased to n=2, with the lowest MIC_{50} within this subgroup of compounds being that of SSA **75** (2.78 mM), which was even lower than SSA **35**. However, a comparison between SSAs **74** – **76** against *E. coli* revealed that SSA **74**, which produced an MIC_{50} value of 6.03 mM, was the most effective SSA out of these three molecules, as SSA **75**, increased *E. coli* growth by 1.75 %, and SSA **76** produced an MIC_{50} of 6.91 mM.

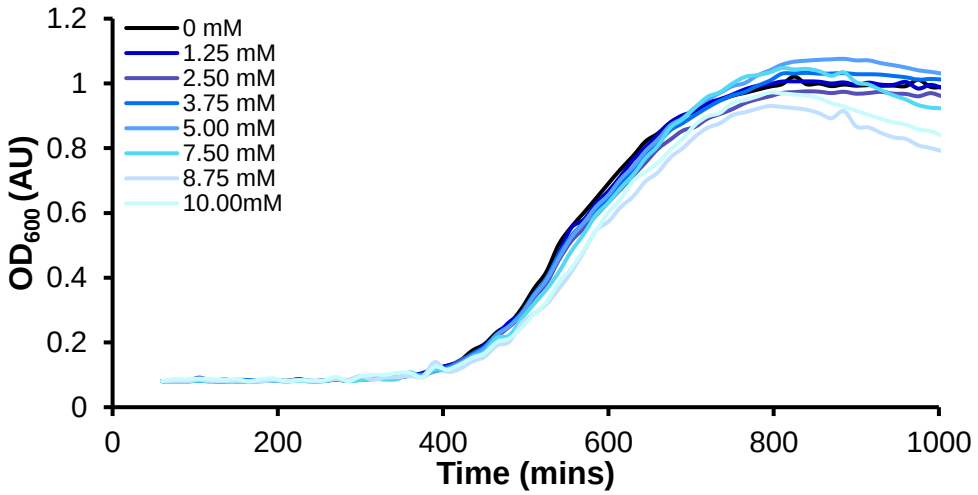

Figure 41. Growth curves of *E. coli*.

Growth curves showing *E. coli* growth in the presence of SSA **73** at varying concentrations. An MIC_{50} value could not be obtained due to compound solubility under experimental conditions.

Overall, the removal of the phenyl ring drastically reduced activity. This is demonstrated by the comparison between SSAs **32** which obtained MIC_{50} values of 3.85 mM against *E. coli* and 0.46 mM against MRSA, in comparison to SSA **71** which failed screening against *E. coli* and produced an MIC_{50} against MRSA of 4.41 mM. This is consistently observed

when structurally related compounds, only differing in the presence or absence of the phenyl ring, were compared. SSA **33**, which produced an MIC_{50} of 3.93 mM against *E. coli* and 0.98 mM against MRSA, was more effective than SSA **72**, which produced MIC_{50} values of 5.67 mM and 2.85 mM against *E. coli* and MRSA, respectively. Furthermore, SSA **37**, which produced MIC_{50} values of 1.85 mM and 1.08 mM against *E. coli* and MRSA respectively, was more effective than SSA **76**, which produced MIC_{50} values of 6.91 mM and 8.99 mM against *E. coli,* respectively. These data provides evidence of the significance of the phenyl ring to the antimicrobial activity of the molecules, as molecules containing the phenyl ring exhibited greater antimicrobial activity than those without.

3.5.8. Extension of the aromatic ring system

Having established the importance of the phenyl ring to the antimicrobial activity, specifically for the urea-based molecules, we then sought to determine whether increasing the number of aromatic rings would improve activity, giving rise to SSAs **65** – **70**.

Thiourea counterparts were not created for these molecules. By extending the aromatic ring system, we increased the propensity of our molecules to self-associate through the formation of pi-pi interactions. The addition of a singular aromatic ring (SSA **65**) decreased activity against both *E. coli* and MRSA, with the MIC_{50} values increasing to 4.30 mM and 2.96 mM, respectively, in comparison to those of SSA **32**, which were 3.85 mM against *E. coli* and 0.46 mM against MRSA. Whilst increasing this ring system further, forming SSA **66**, decreased *E. coli* activity, MRSA activity remained the same, as seen with its MIC_{50} value of 0.46 mM. The carboxylate functionality present in SSA **61** was previously shown to improve *E. coli* activity, so SSA **67** was created to determine whether this would improve activity against *E. coli*. However, this had the opposing effect, as SSA **67** failed the screening process against *E. coli* and its MIC_{50} value of 0.61 mM against MRSA was higher than that of SSAs **32** and SSA **66**. Exchanging the electron-rich anthracene group in SSA **66** to the electron-poor anthraquinone group present in

SSA **68** decreased antimicrobial efficacy against *E. coli*, as this molecule failed screening against *E. coli*, increasing growth by 2.49%, and produced a higher MIC_{50} value of 0.71 against MRSA. Therefore, it was concluded that increasing the ring system decreased efficacy against *E. coli*, whereas MRSA activity was initially hindered by the addition of a singular ring, however, when this ring was further extended to form SSA **66**, antimicrobial activity improved significantly, obtaining the same MIC_{50} value as SSA **32**. Solution state studies conducted by Tyuleva et al., 2019 revealed stronger dimer formation due to increased acidity of the urea amine groups in SSA **68**, compared to SSAs **66**.[66] Despite this, the replacement of the anthracene in SSA **66** to the anthraquinone group in SSA **68** significantly reduced antimicrobial activity.

The R – groups present in SSAs **69** and **70** are identical, however, the position of the benzothiazole ring system is different. SSA **69** has the benzothiazole group in the ortho position whereas SSA **70** has this group in the para position. Similar to SSA **33**, the crystal structure of SSA **69** revealed a greater propensity to form an intramolecular bond between the benzothiazole ring system and one of the urea NH groups, which may result in disrupted dimer formation due to reduced hydrogen bonding, compared to **70**. The antimicrobial activity exhibited against MRSA provides evidence for this, as the MIC_{50} value for SSA **70** was lower than that of **69**. Conversely, with respect to *E. coli* activity, the MIC_{50} value for SSA **69** was lower than that of SSA **70**, even though the percentage decrease was higher for SSA **70**. Further analysis of the growth curves produced by SSA **70** revealed variation in OD values in the presence of SSA **70** after 1000 minutes, which was not observed with other SSAs, even those that exhibited aggregation at the later stages of growth, such as SSA **34** (Figure 42). It was later discovered that SSA **70** gelated in the presence of sodium salt solutions, in particular sodium chloride, which was present in the LB media used in these assays. It was therefore likely that SSA **70** was either forming a gel within the wells or similar aggregates, resulting in the variation in OD values obtained. The formation of these gel fibres within the wells prompted the

exploration of other methods for testing the antimicrobial efficacy for SSA **70**, and any other gelating molecules.

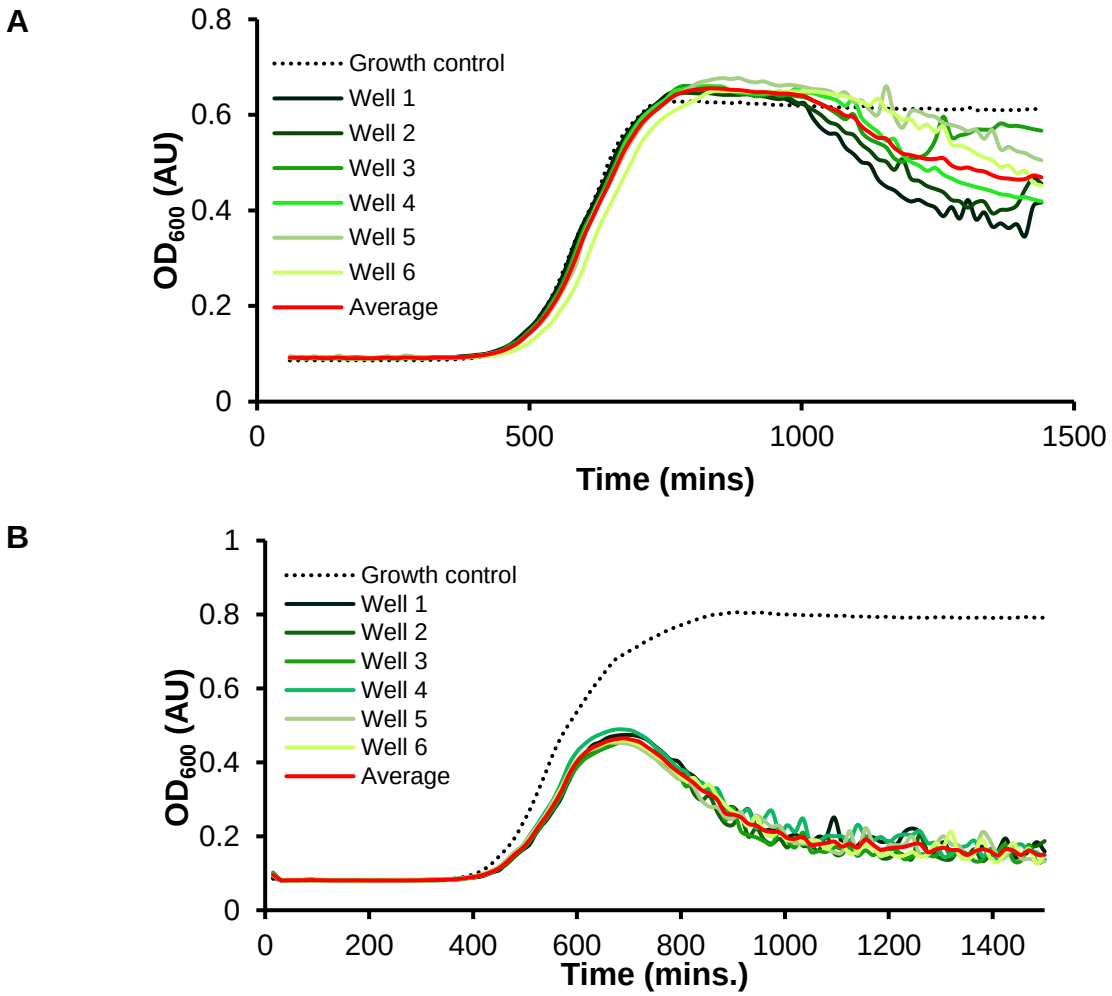

Figure 42. Comparative *E. coli* growth curves in the presence of SSAs 70 and SSA 34.

Growth curve depicting the variation of *E. coli* growth between wells on the same 96 well plate. **(A)** Variation of growth in the presence of SSA **70** at 3.3 mM in different wells on the same plate. **(B)** Variation of growth in the presence of SSA **34** at 3.3 mM in different wells on the same plate. *Black dotted line* – growth control; 5% EtOH added in place of compound. *Green lines* – growth curves of different wells, the darkest being the first well, the lightest being the last well. *Red line* – Average of the green curves.

3.5.9. Antimicrobial gel plate testing

The antimicrobial studies discussed within this section of the thesis were performed in collaboration with Jess Boles.[155]

The gelation of SSA **70** in sodium salts prompted the use of gel-based antimicrobial testing to provide a comparison with the solution-based antimicrobial testing. To determine the activity of SSA **70** in its gelated form, agar well diffusion assays were conducted, as described in section **2.4.11** of the materials and methods. Briefly, LB agar was inoculated with either *E. coli* or MRSA and poured into sterile Petri dishes. Once set, wells were created using a sterile well cutter in the centre of the inoculated agar plate, and 50 µL of molten gel solution was pipetted into the well. Plates were incubated at 37°C for 18 hours and imaged using a scanner. This would ensure the gel was undisturbed and only the effects of the gel could be observed. To also determine whether any differences could be observed when the gel was placed directly on the surface of the gel, surface diffusion assays were conducted (Figure 43), as described in section **2.4.12** of the materials and methods.

A **B**

Figure 43. Comparison between the methods used in the antimicrobial gel assays.

(A) Well diffusion assay: a well was created in the centre of the well, using a sterile cutter, and compound solutions were pipetted into the well, then allowed to set where applicable. **(B)** Surface diffusion assay: set gels were carefully placed in the centre of the inoculated agar plate.

Similar to the well diffusion assay, inoculated agar plates were created, however, instead of adding the gel solution to a cut well, we carefully placed a 50 µL aliquot of gel on the surface of the inoculated agar plate, then incubated the plates at 37°C for 18 hours and scanned the plates. Additionally, it was hypothesised that the SSA **70** gel could be used in combination with other antimicrobials, as previously shown by Ganewatta et al., who encapsulated ampicillin with their AMPs.[149] Therefore, a co-formulated ampicillin gel was created by adding ampicillin sodium salt to SSA **70** at 5 mg/mL and conducting the well and surface diffusion assays on the resulting gel. The activity of ampicillin alone was as a comparison. Zones of inhibition were measured by Dr. George Williams (Table 10) and statistical analysis was conducted by me.

Table 10: The zone of inhibition.

The measured zones of inhibition by SSA **70**, ampicillin, and the two in combination against *E. coli* and MRSA under these experimental conditions: [a] – surface diffusion, [b] – well diffusion.

	Zone of inhibition (mm)	
	E. coli	**MRSA**
70 [a]	15 ± 2.65	15.67 ± 1.53
Ampicillin and 70 [a]	59.33 ± 0.58	23.33 ± 1.53
70 [b]	17.67 ± 4.16	13.67 ± 1.15
Ampicillin and 70 [b]	53.33 ± 1.53	17.00 ± 1.00
Ampicillin [b]	52.67 ± 2.89	15.33 ± 1.15

While antimicrobial testing of the SSA **70** gel alone revealed the zones of inhibition measured using the surface diffusion method were generally numerically larger than those obtained using the well diffusion method, we needed to determine whether the values obtained were statistically significantly different. As such, paired-samples t-tests were performed to compare how different the two methods affected the zones of inhibitions created by the SSA **70** gel and the co-formulated ampicillin-**70** gel against both bacteria.[184–188]

When the zones of inhibition created by SSA **70** gel alone were analysed, it was determined that there was not a statistically significant difference in the zones measured using the surface diffusion method (*M* = 15.00, SD = 2.65) and the well diffusion method (*M* = 17.67, SD = 4.16) against *E. coli*; t (2) = -1.835, *p* =.208. similarly, there was not a statistically significant difference when the zones created against MRSA using the surface diffusion method (*M* = 15.67, SD =1.53) and the well diffusion method (*M* =13.67, SD =1.15) were observed; t (2) =3.464, *p* =.074. These results suggest that the method selected had little effect on the zone of inhibition observed, and either method could be used when the SSA was tested alone. When co-formulated with ampicillin, however, a statistically significant difference in the zones of inhibitions measured was observed using the surface diffusion method (*M* =59.33, SD =.58) and the well diffusion method (*M* =53.33, SD =1.53) against *E. coli*; t (2) = 5.196, *p* =.035. Similarly, a significant difference was seen between the surface diffusion method (*M* =23.33, SD =1.53) and the well diffusion method (*M* = 17.00, SD =1.00) when tested against MRSA; t (2) =4.359, *p* =.049. The zones of inhibition measured using the surface diffusion method were statistically significantly larger than those measured using the well diffusion method. It was therefore determined that as the zones of inhibition using ampicillin were larger, the difference between the two methods was more clearly seen, and therefore antimicrobial analysis of compound gels would be carried out using the surface diffusion method as opposed to the well diffusion method.

In order to determine how the efficacy of ampicillin was impacted by its coformulation with **70** in a gel, a comparison was made between the zones of inhibition created in the presence of ampicillin alone and those created in the presence of the co-formulated ampicillin gel. To provide a thorough examination, a paired samples t-test was performed on these zones of inhibition measured.[184–188]

While the co-formulated ampicillin gel produced zones of inhibition that were numerically larger than the ampicillin alone, there was not a statistically significant difference between

E. coli in the presence of ampicillin alone (*M* = 52.67, SD =2.89) and in the presence of the co-formulated ampicillin gel (*M* =53.33, SD =1.53); t (2) =-.277, *p* =.808. Similarly, there was not a statistically significant difference between MRSA in the presence of ampicillin alone (*M* =17.00, SD =1.00) and in the presence of the co-formulated ampicillin gel (*M* =15.33, SD =1.15); t (2) =1.890, *p* =.199. Therefore, little enhanced antimicrobial efficacy was observed with the co-formulated ampicillin gel, in comparison to the ampicillin alone. However, these data also revealed that co-formulating ampicillin in a gel with SSA **70** did not significantly hinder its activity, thereby providing another method of administering antimicrobials. Furthermore, using the structure-activity relationships detailed within this chapter to enhance the antimicrobial activity of SSA **70** and then co-formulating this enhanced molecule with other antimicrobial compounds, could be effective in tackling antimicrobial resistance by reactivating molecules that have become less effective over time.

3.5.10. Combinatory effects of aromatic compounds

SSAs **66** – **68** were synthesised and had their physicochemical properties were determined by Stilyana N. Tyuleva and Lisa J. White, while the antimicrobial testing of these compounds was carried out by Stilyana N. Tyuleva and me.

This sub-group of molecules allowed for the determination of the antimicrobial properties as independent species as well as in combination with one another, to ascertain the possibility of co-formulations with other molecules and enabling us to predict future interactions with other molecules. As such, 1:1 molar mixes of SSAs **66** – **68** were created (Figure 44A), then taken through the antimicrobial testing process in the same way as the singular compounds. As the antimicrobial screening results revealed a 100% decrease in MRSA growth, MIC_{50} values, and an additional screen at 0.375 mM were used for the comparison (Figure 44B).

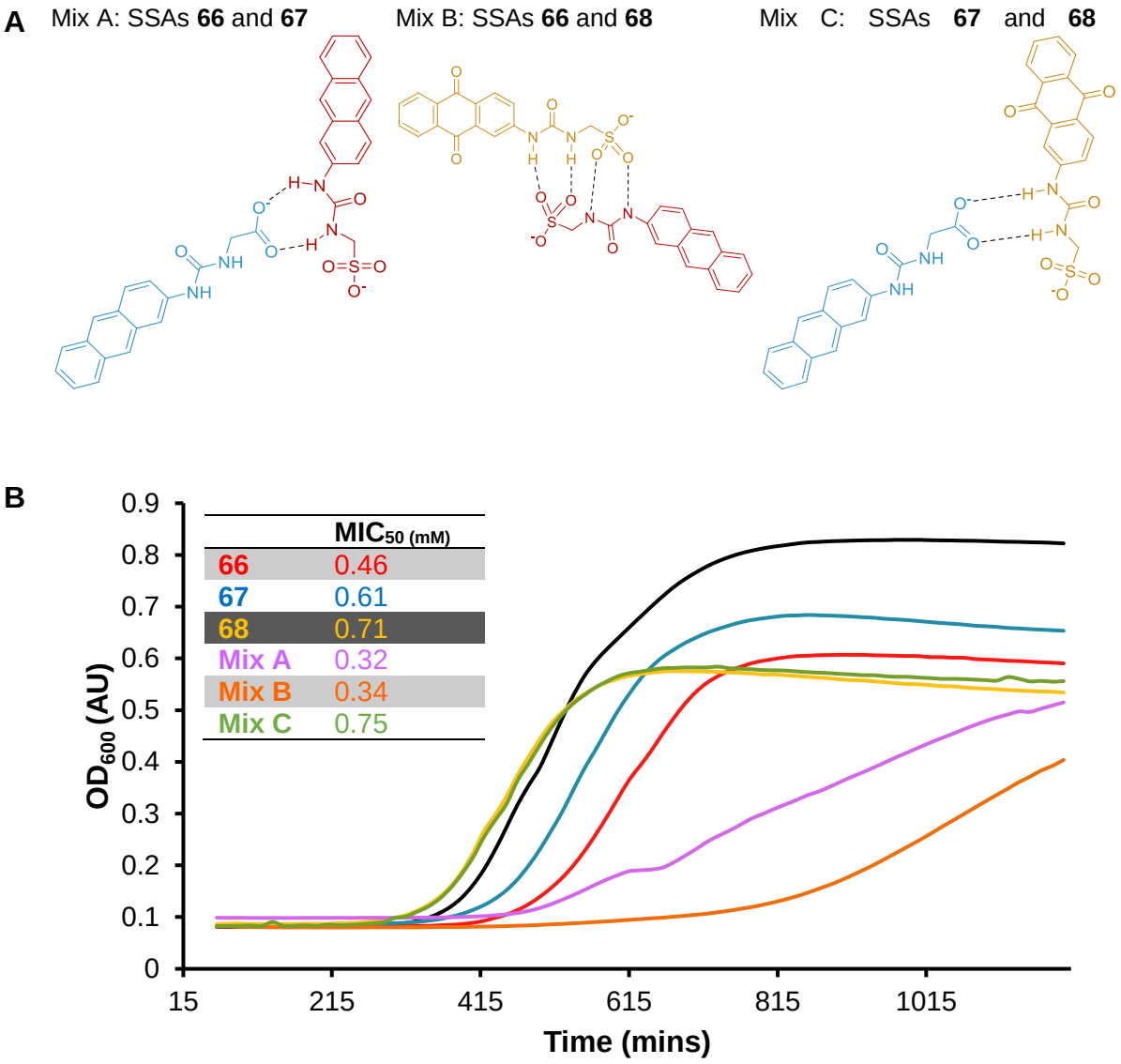

Figure 44. Antimicrobial studies conducted using 1:1 molar mixes of SSAs 66 – 68. **(A)** Heterogenous compound mixes used for this study and the hypothesised hydrogen binding modes predicted. **(B)** MRSA growth comparison at 3.75 mM and MIC_{50} values for homogeneous solutions of SSAs **66** (Red), **67** (blue), **68** (yellow), as well as 1:1 heterogeneous mixes A (purple), B (orange) and C (green). Black = MRSA growth in the absence of compound. Values for the compound mixes represent the total molar concentration.

SSA mix C had the highest MIC_{50} value of 0.75 mM, which was higher than those obtained for SSAs **67** (0.61 mM) and **68** (0.71 mM), suggesting antagonism between these two molecules. When observing the potential hydrogen bonding modes, it was

hypothesised that a differing hydrogen-bonding mode could be exhibited by SSA **67** and any compound mixtures it would create, due to the substituted carboxylate group (Figure 44). The resulting complexes formed were hypothesised to be weaker, and thus lowering the antimicrobial efficacy of SSA **67** and the compound mix formed with SSA **68**. Where SSA **66** was present, the MIC_{50} values were significantly reduced by almost half. SSA **67** alone produced an MIC_{50} of 0.61 mM, however, in a 1:1 mix with SSA **66** this was reduced to 0.36 mM. Similarly, SSA **68** produced an MIC_{50} value of 0.71 mM alone, however, in a compound mix with **66** this was drastically reduced to 0.34 mM. Further, SSA **66** alone produced an MIC_{50} of 0.46 mM, however, this MIC_{50} value decreased when used in combination with SSA **67** (0.32). These data provide evidence for the use of these molecules, in particular, SSA **66** in combination therapies, as the combination of two molecules decreased the MIC_{50} values significantly. Further, as mentioned before, SSA **68** formed stronger hydrogen-bonded complexes, and should theoretically perform better than SSA **66**. However, SSA **68** had the highest MIC_{50} value out of the independent SSAs and the second highest overall.

3.6. Mode of Action Determination

In an effort to discern the mode of action of these SSAs, several methods were utilised. Increasing the ring system of these molecules caused the compounds to be intrinsically fluorescent, and a number of fluorescence assays could then be employed to investigate the binding properties of these molecules. Therefore, fluorescence microscopy, using *E. coli* and MRSA, and fluorescence anisotropy, using the fluorescent molecules with liposomes, were conducted.

3.6.1. Fluorescence Microscopy

While SSAs **65** – **70** were all fluorescent, the most amenable for imaging were SSAs **69** and **70** (Figure 45).

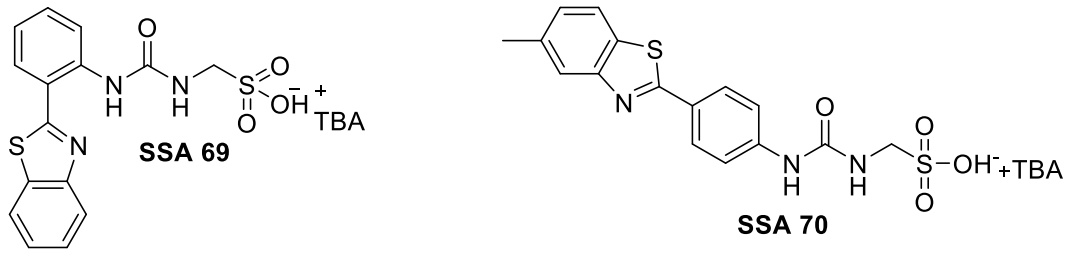

Figure 45. Structures of (A) SSA 69 and (B) SSA 70.

Preliminary microscopy experiments consisted of adding SSAs **69** and **70** to *E. coli* cells at 0.6 mM and comparing the images obtained. In these preliminary experiments, SSA **70** provided clearer images than SSA **69,** and also appeared to exhibit stronger membrane binding, as all cells displayed membrane fluorescence in the presence of **70**, which was not the case for SSA **69** (Figure 46).

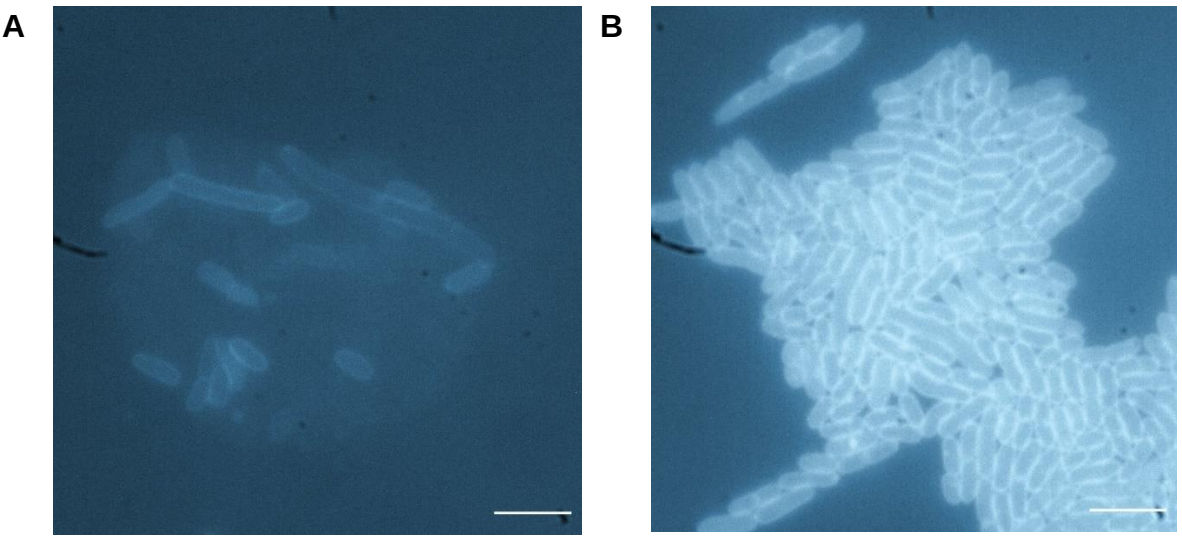

Figure 46. Widefield fluorescence microscopy images.

Comparative fluorescence of *E. coli* in the presence of SSA **(A) 69** and **(B) 70** at 0.6 mM. Scale = 10 µm.

As such, all microscopy analysis was conducted using SSA **70**, supplied in a 5 % EtOH solution. To visualise the localisation and morphology of bacteria in the presence of this

compound, *E. coli* and MRSA were grown to mid-log phase, as determined by their OD values, then incubated in the presence of SSA **70** at a final concentration of 0.6 mM for 30 minutes before imaging. Once imaging samples had been taken, the cultures were then further incubated for 4 hours then imaged. To compare membrane binding and internalisation, control cultures in the absence of compound were grown alongside those with the compound and imaged at the same time points.

The images presented in Figure 47 demonstrate the membrane fluorescence exhibited by MRSA and *E. coli* in the presence of SSA **70** after 30 minutes of incubation. SSA **70** appeared to be evenly distributed around the *E. coli* membrane, with no internalisation visualised at this time point, whereas in, MRSA brighter regions were observed both around the membrane and within the cytoplasm, suggesting internalisation.

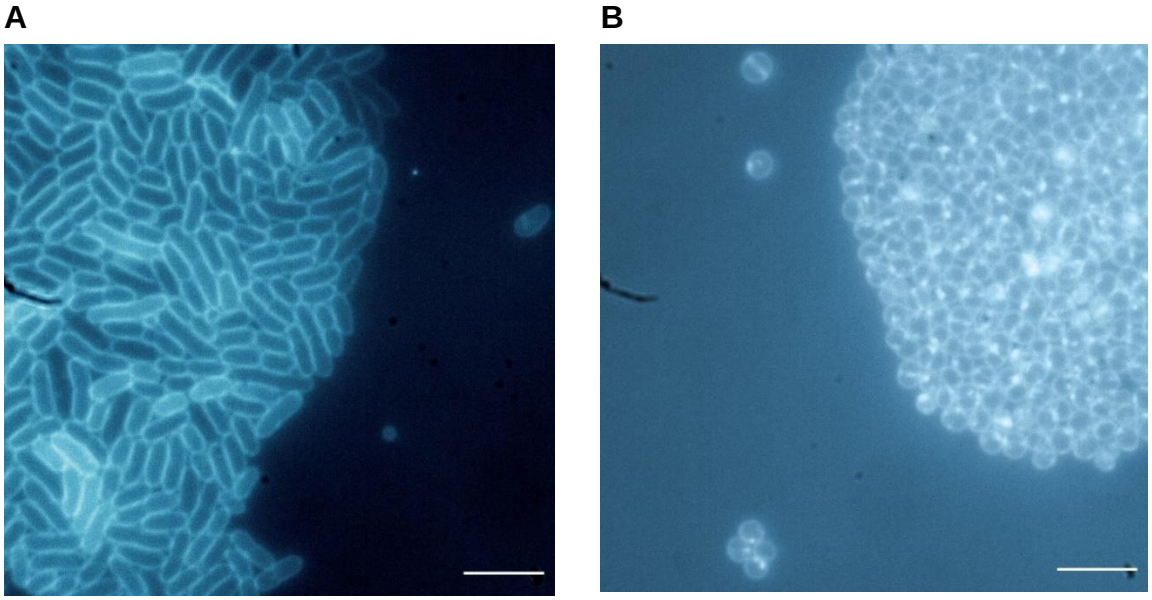

Figure 47. **Widefield fluorescence microscopy Images.**

Microscopy mages showing SSA **70** localization after 30 minutes of incubation with **(A)** *E. coli* cells and **(B)** MRSA cells. Scale = 10 µm.

The images presented in Figure 48 show SSA **70** localisation after 4 hours of incubation with *E. coli* and MRSA.

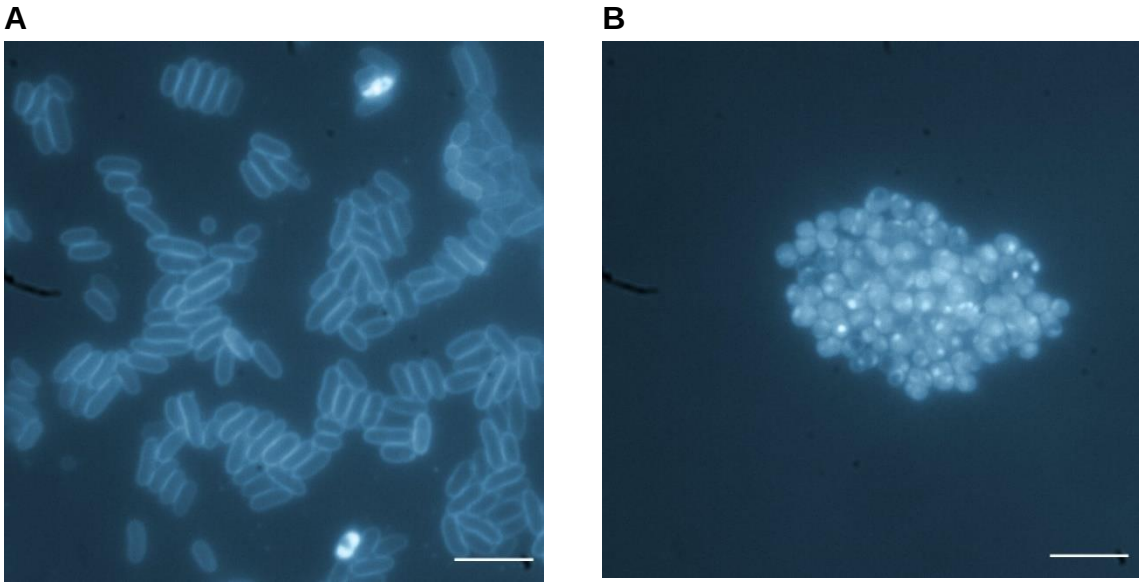

Figure 48. **Fluorescence Microscopy Images.**

Microscopy images showing SSA **70** localization after 4 hours of incubation with **(A)** *E. coli* cells and **(B)** MRSA cells. Scale = 10 µm

4 hours after the initial addition of SSA **70**, internalisation could be observed in all MRSA cells, with bright spots in the cytosol, and little discernible membrane binding was observed (Figures 48). However, for *E. coli*, while internalisation was observed, this was not the case for all cells, as shown in Figure 48. Where internalisation of SSA **70** in *E. coli* was observed, this was consistently non-uniform and similar to MRSA, there were more defined brighter regions, which suggested a secondary target within cells (Figure 49).

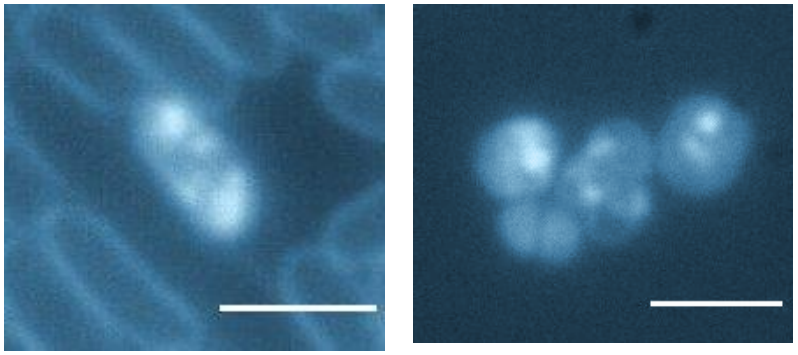

Figure 49. Fluorescence Microscopy images.
Images showing the internalisation of SSA **70** at 0.6 mM in **(A)** *E. coli* and **(B)** MRSA after a 4-hour incubation. Bright spots indicate a secondary target. Scale = 5 µm

To further characterise the comparative binding and internalisation of SSA **70** between *E. coli* and MRSA, a 1:1 heterogeneous culture of mid-log phase *E. coli* and MRSA was created, then SSA **70** at 0.6 mM was added. Images were taken 30 minutes, 1 hour, and then 4 hours after the initial addition of SSA **70**. These images are presented in Figure 50.

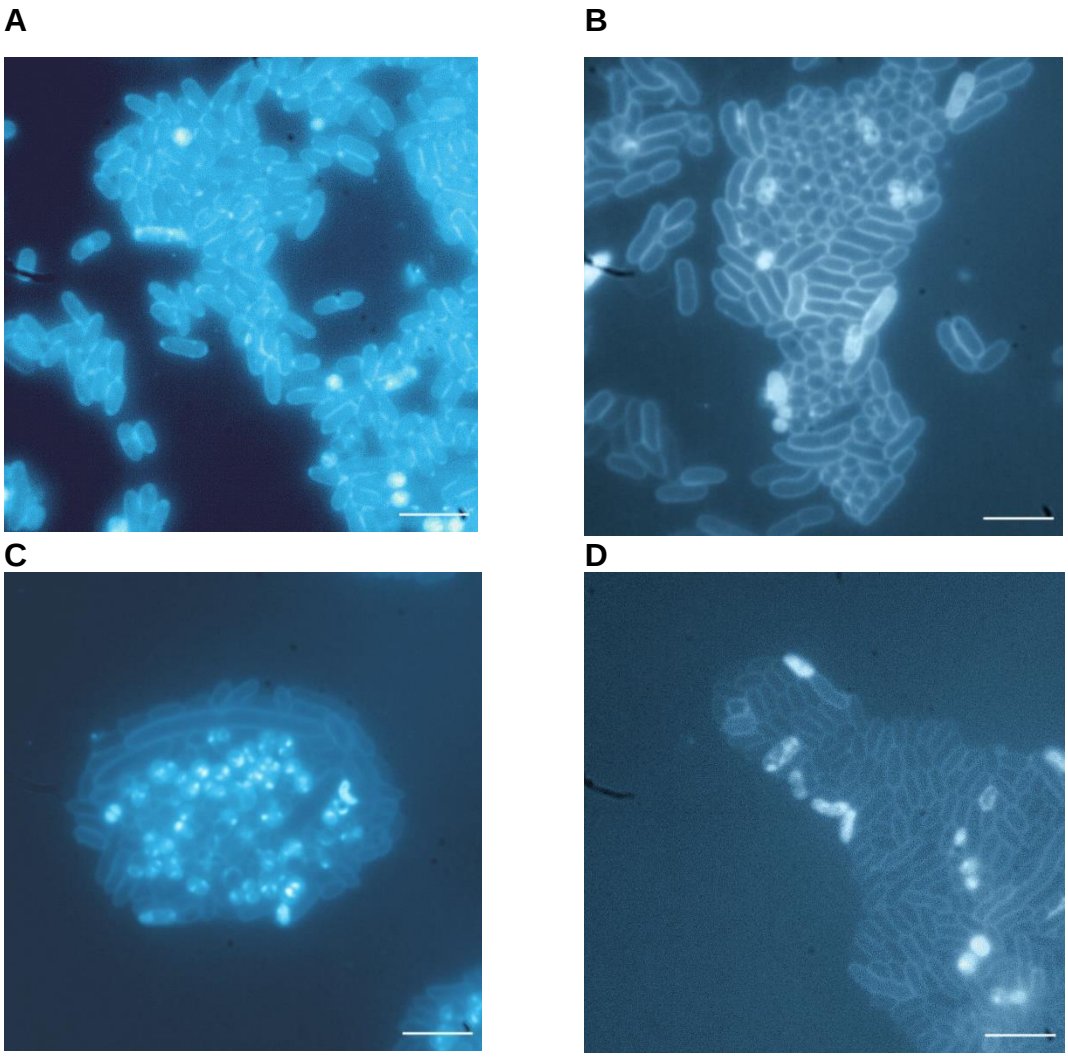

Figure 50 – Fluorescence microscopy images of MRSA and *E. coli.*

Bacteria in a 1:1 heterogeneous mix **(A)** 30 minutes **(B)** 1 hour and **(C & D)** 4 hours after the addition of SSA **70** at 0.6 mM. Scale = 10 µm

Figure 50 shows SSA **70** being predominantly membrane-bound to *E. coli* after 30 minutes, with few cells having internalised compound. A greater proportion of SSA **70** was observed to be internalised in *E. coli* after 1 hour, however, the majority of cells exhibited membrane fluorescence only, even at 4 hours (Figure 50D). Conversely,

internalisation of SSA **70** was significantly more prevalent and rapid in MRSA than in *E. coli*; (Figure 50) cytoplasmic fluorescence of MRSA cells was observed from 30 minutes to 4 hours. Examination of the morphology of the cells in the 1:1 mix revealed abnormal fluorescent shapes present 4 hours after the addition of SSA **70**, as shown in Figure 51. These compound-filled masses were hypothesised to be depolarised cells due to the activity of the compound, and so these images were compared to those of the homogenous bacterial cultures, shown in Figures 47 and 48.

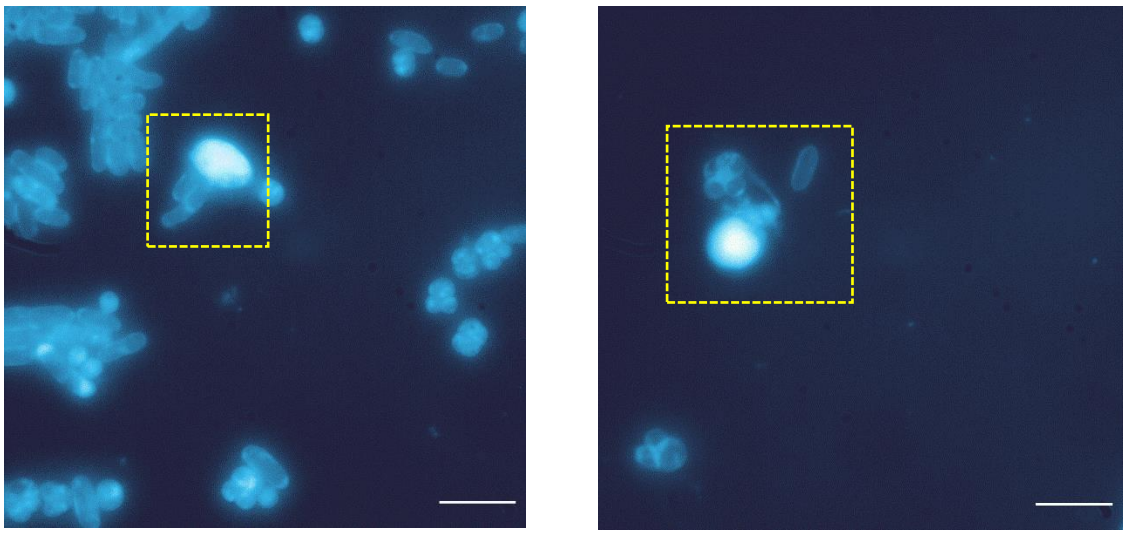

Figure 51. Fluorescence Microscopy Images of MRSA and E. coli in a 1:1 heterogeneous mix.

Images were captured 4 hours after the addition of SSA **70** at 0.6 mM. Large compound-filled masses are highlighted in yellow. Scale bar = 10µM.

A comparison between the transmitted images obtained of *E. coli* cells in the presence and absence of SSA **70** present revealed the vast majority of *E. coli* cells in the presence of **70** were similar to the untreated cells (Figure 52). However, where SSA **70** had internalised (Figure 50B), membrane deformation was observed.

A **B**

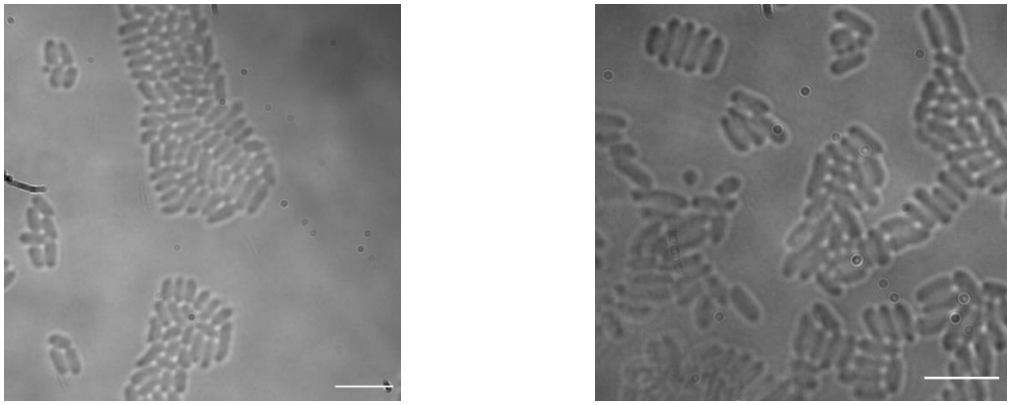

Figure 52. Transmitted Light images of *E. coli*.

Images comparing the morphology of *E. coli* in the **(A)** absence and **(B)** the presence of SSA **70** at 0.6 mM after a 4-hour incubation. Scale = 10µm.

A more pronounced change in morphology was observed with MRSA cell after 4 hours of incubation with SSA **70** when the images in Figure 50 were compared to those in Figure 48. More irregular shapes and a loss of individual cell definition were observed which was not present in untreated cells, as shown in Figure 54.

A **B**

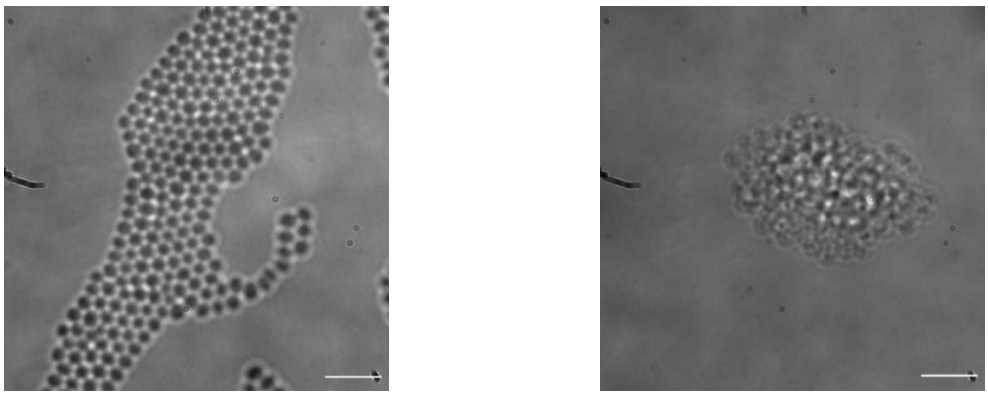

Figure 53. Transmitted Light Images of MRSA.

Images showing the morphological changes of MRSA in the **(A)** absence and **(B)** presence of **70** at 0.6 mM. Scale = 10 µM.

However, while these morphological changes occurred, changes in the sizes of the individual cells were not observed in any images obtained for MRSA. Therefore, it was hypothesised that these abnormal shapes may have been depolarised *E. coli* cells due to the action of SSA **70**.

To further confirm these observations and better understand the extent of the lipid binding properties of SSA **70**, a lipid binding microscopy assay was conducted, using FM4-64, a non-specific lipid binding molecule.

SSA **70** and FM4-64 fluoresce at different wavelengths, allowing both molecules to be observed under the microscope independently of one another, using a 450 nm emission filter to observe SSA **70** fluorescence and a 605 nm filter to observe FM4-64 fluorescence. Colocalization of these molecules would be consistent with lipid binding, which if absent, would suggest other targets on the membranes. *E. coli* and MRSA at mid-log phase were incubated in the presence of either 5 % EtOH alone, SSA **70** alone, FM4-64 alone, or the combination of **70** and FM4-64, as described in section **2.5.1** of the materials and methods. Samples were imaged at 30 minutes and 4 hours; then quantitative analysis was performed on the subsequent images to obtain average fluorescence intensities from between 30 and 100 cells in each experimental condition. Quantitative analysis was conducted by generating line scans across individual cells, then obtaining the fluorescence intensity profile of that line scan using Fiji (ImageJ), as shown in Figure 54.[105,106,189] The background fluorescence from the intensity profiles was subtracted from the maximum fluorescence, which was then used as the final fluorescence value (Figure 54).

A **B**

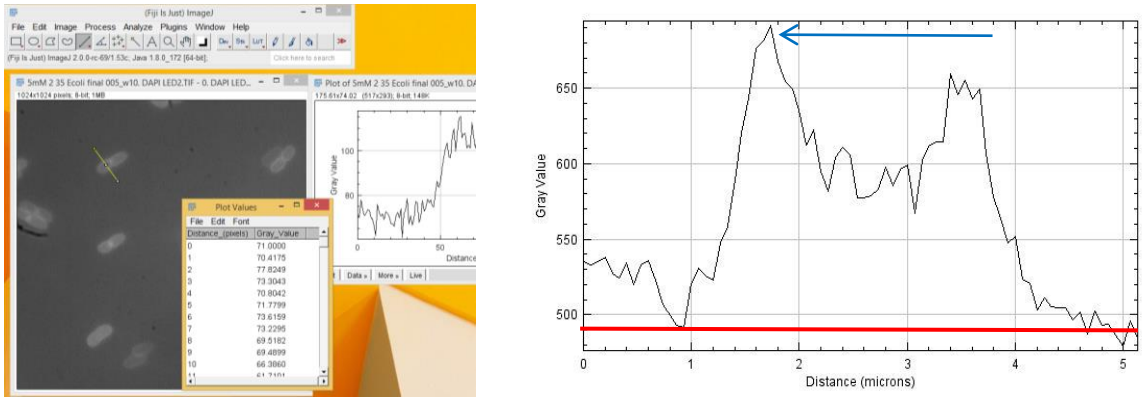

Figure 54. Quantitative microscopy image analysis.

(A) line scans generated across the width of the cell, then intensity profiles of the line scans were then obtained using the "Plot profile" function in ImageJ.[105,106] **(B)** Values used in fluorescence calculation: *red line* = background fluorescence, *blue line* = maximum fluorescence.

After 30 minutes, FM4-64 fluorescence was seen to drop significantly, almost to background level, in the presence of SSA **70** (Figure 55). This was confirmed by the quantitative analysis, which revealed FM4-64 fluorescence for *E. coli* dropped by 80 % when **70** was present and by 86 % for MRSA (Figure 56). And while the fluorescence of **70** in the presence of *E. coli* was lower with FM4-64 present, this was not as significant or as prominent as with FM4-64 (Figure 56). In contrast, the MRSA analysis at 30 minutes revealed SSA **70** fluorescence was higher in the presence of FM4-64, while FM4-64 fluorescence decreased significantly (Figure 56).

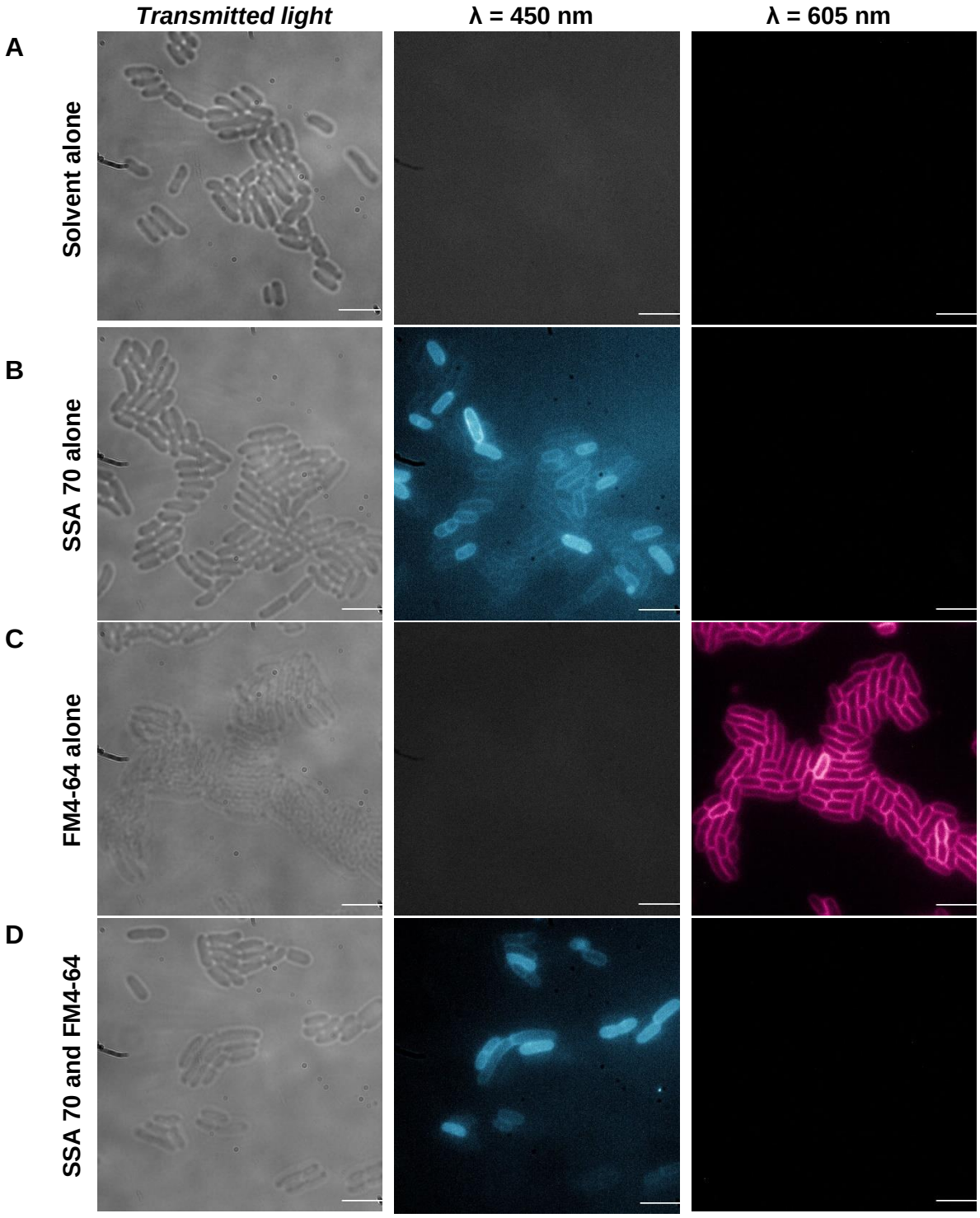

Figure 55. Competitive binding microscopy assay.

Fluorescence images of *E. coli* in the presence of **(A)** solvent alone **(B)** SSA **70** alone **(C)** FM4-64 alone and **(D)** a combination of FM4-64 and SSA **70**. T = 30 minutes. Fluorescence images obtained using 450 and 605 nm filters to observe SSA **70** (blue) and FM4-64 (magenta) fluorescence, respectively. Scale = 10 µm.

A

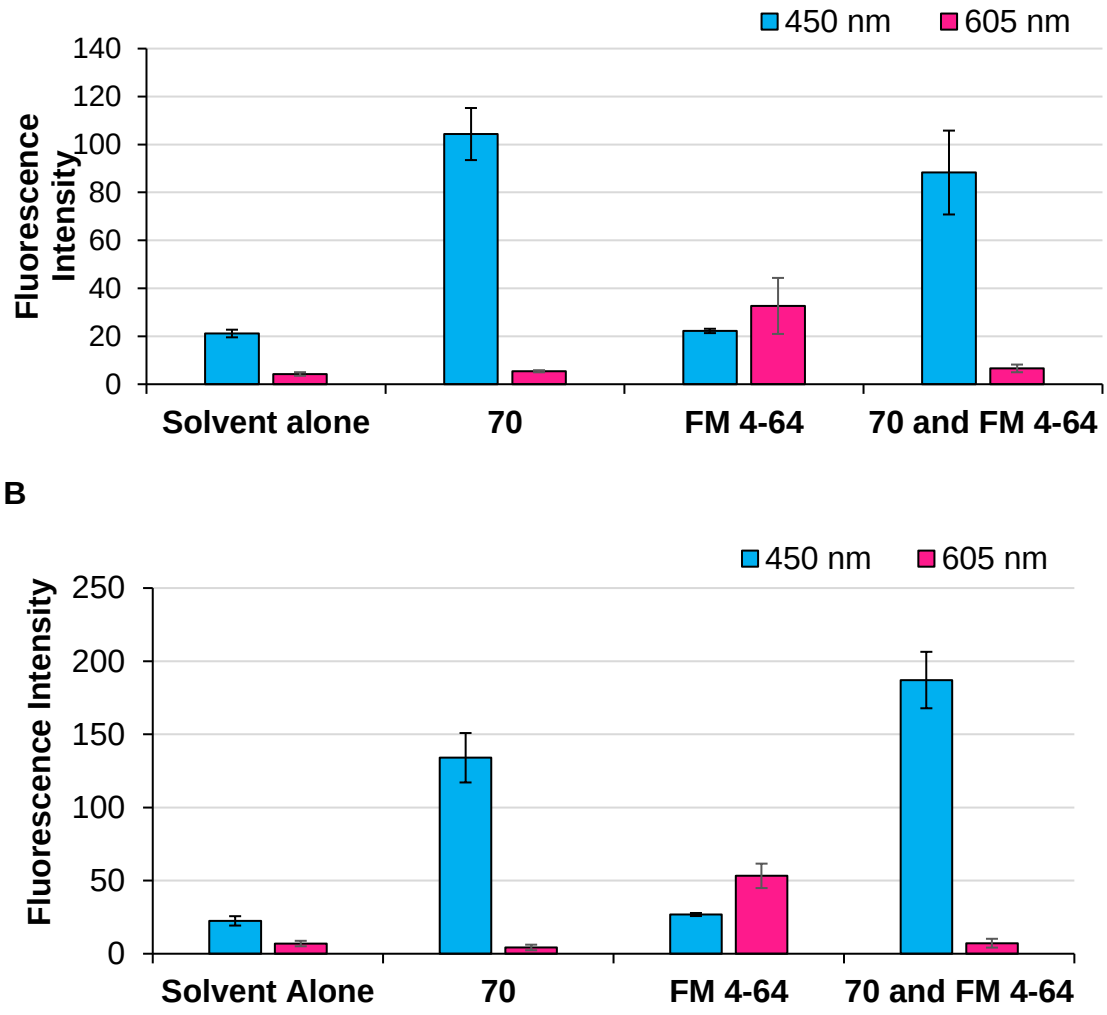

Figure 56. Quantitative Analysis of Fluorescence Microscopy Images.

Graphs showing the average fluorescence intensity of between 30 and 100 cells: **(A)** *E. coli* after 30 minutes in the presence of solvent alone, SSA **70**, FM4-64 and a combination of both **70** and FM4-64 and **(B)** MRSA after 30 minutes in the presence of SSA **70**, FM4-64 and a combination of both **70** and FM4-64.

After 4 hours, in *E. coli* cells with internalised SSA **70**, FM4-64 fluorescence was detected in cells where both **70** and FM4-64 was present (Figure 57).

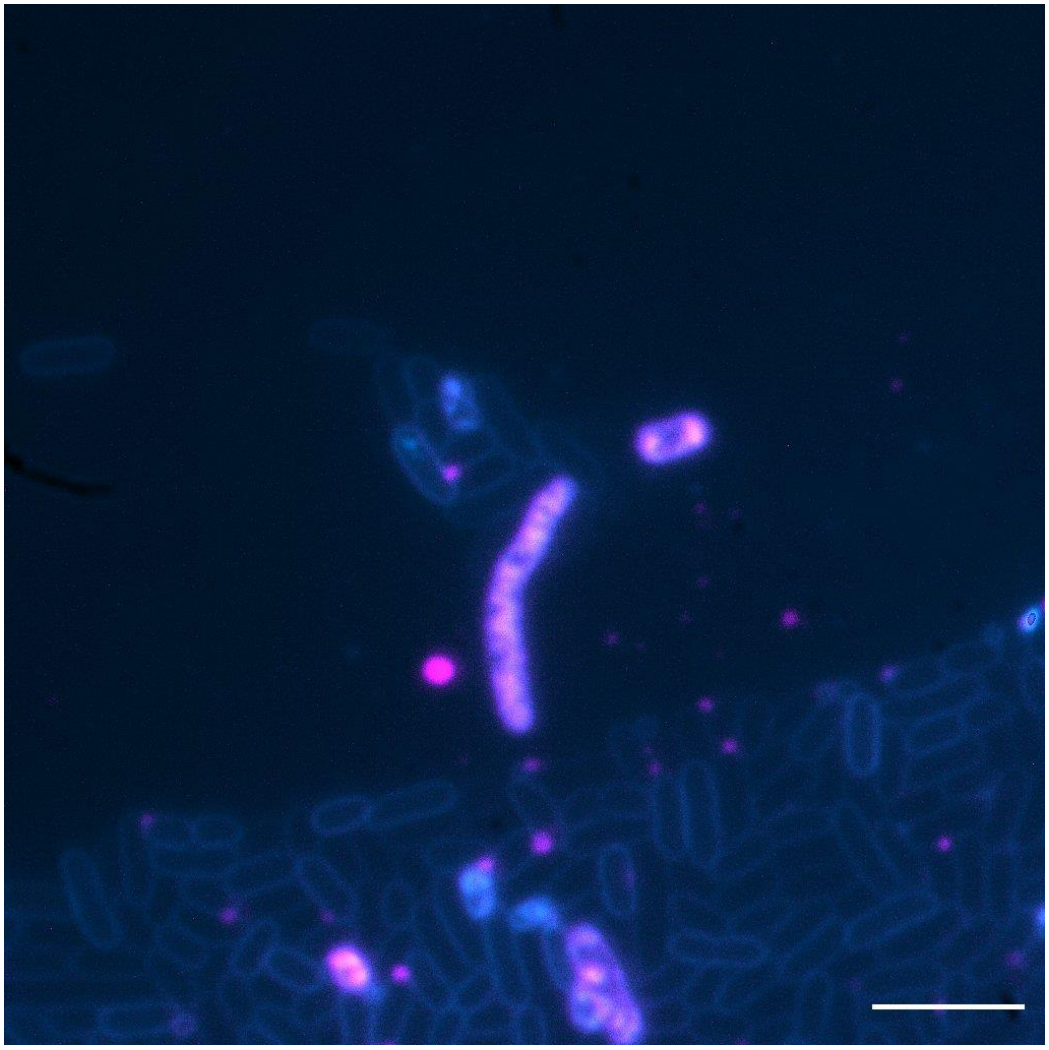

Figure 57. Combined Fluorescence Microscopy Images.

Images showing SSA **70** fluorescence (blue) and FM4-64 fluorescence (magenta) and regions of co-localisation (white). Scale bar = 10 µm.

Quantitative analysis, shown in Figure 58, reveals an increase in FM4-64 fluorescence of 77% at 4 hours when compared to the fluorescence at 30 minutes. This was not observed with MRSA, however, as FM4-64 remained at background level in the presence of **70** after 4 hours.

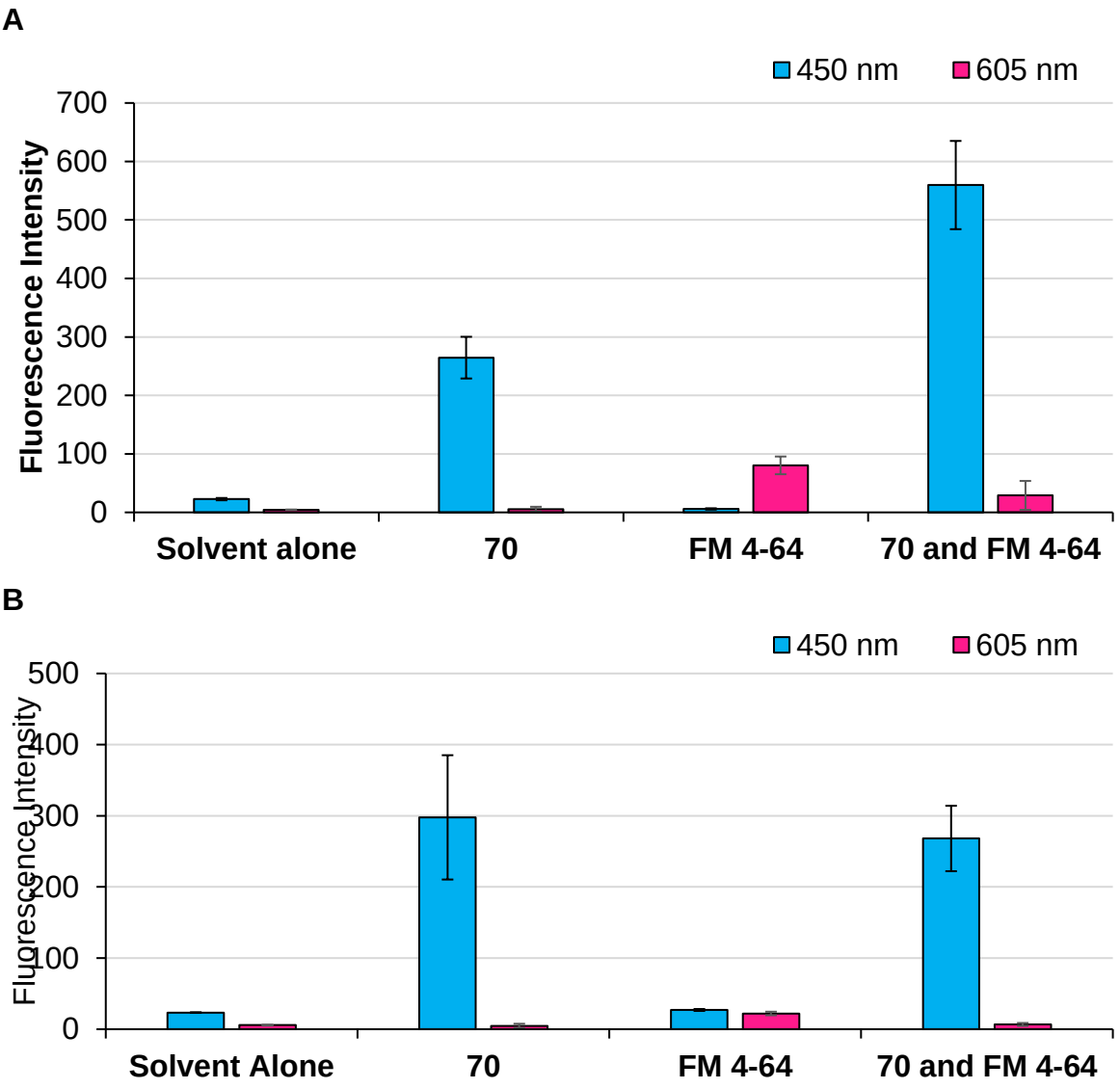

Figure 58. Quantitative Analysis of Fluorescence Microscopy Images.

Graphs showing the average fluorescence intensity of between 30 and 100 cells: **(A)** *E. coli* after 4 hours in the presence of solvent alone, SSA **70**, FM4-64 and a combination of both **70** and FM4-64 and **(B)** MRSA after 4 hours in the presence of SSA **70**, FM4-64 and a combination of both **70** and FM4-64.

The large variation observed when SSA **70** was present after 4 hours was due to the brighter regions observed after its internalisation, as these bright regions were not uniform or present in every cell, in the case of *E. coli.* These data provide evidence to suggest SSA **70** and FM4-64 binding to the same region on the membrane. FM4-64 binds non-specifically to lipids, and SSA **70** outcompeting FM4-64, confirmed that SSA **70** was binding to lipids. This was further solidified by the data obtained at 4 hours, as FM4-

64 was only detected in *E. coli* in cells where the compound had internalised. FM4-64 fluorescence within the cell was more likely due to compromised membrane integrity due to SSA **70**, consequently allowing FM4-64 into the cytoplasm.

3.6.2. Fluorescence Anisotropy and membrane binding

After confirming membrane lipid binding, the next step was the investigation of the specific lipids these molecules were interacting with, as this would further verify their mode of action. Consequently, fluorescence anisotropy assays were conducted using SSAs **69** and **70** as described in section **2.6.4** of the materials and methods. Fluorescence anisotropy is a measurement of the changing orientation of a fluorescent molecule in space through the use of fluorescence absorption and emission events. When a fluorophore is excited by polarised light, the emitted light is also polarised (Figure 59).[190]

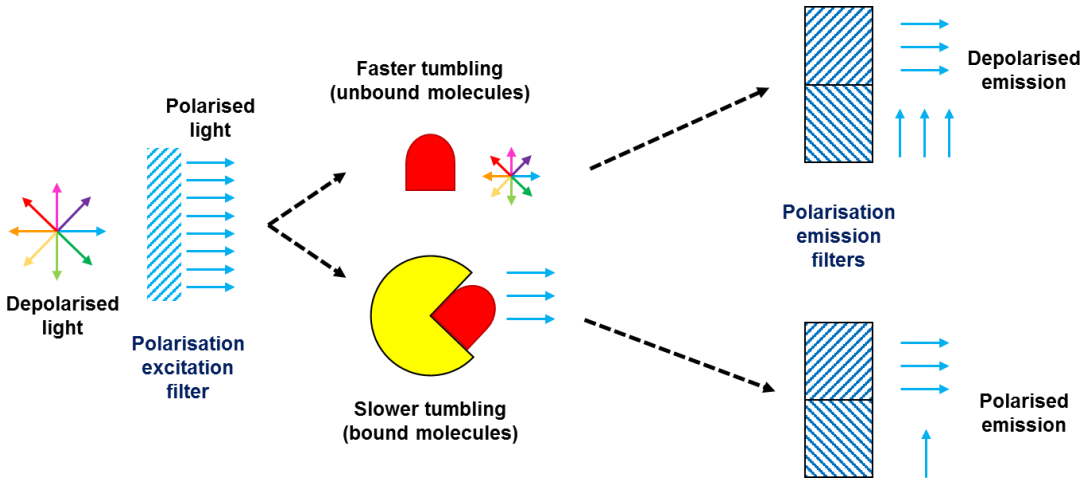

Figure 59. Diagram showing the principles of fluorescence anisotropy.

Free unbound ligands when excited with polarised light emit depolarised light due to faster rotational diffusion, whereas bound molecules emit polarised light due to slower rotational diffusion. Adapted from Cheow et al., 2014.[191]

Anisotropy (*r*) measurements allow for the observation of the angular displacement of a fluorophore that occurs between the absorption and subsequent emission of polarised light. The extent of depolarised emission is reliant on the rotational diffusion of the

molecule, which in turn is reliant on the shape and size of the molecule or the viscosity of the solvent.[150,192,193]

Smaller molecules undergo more rapid rotation and therefore depolarise the polarised light to a greater extent. Conversely, larger molecules have a lower rotational diffusion rate, and therefore maintain polarisation to a greater extent.[150,192,193] Changes in the shape and size of a fluorescent molecule result in changes in anisotropy, as the size of bound molecules is larger than the size of the free molecules in solution. Thus, fluorescence anisotropy measurements provide a way of monitoring binding events, as fluorescence anisotropy can detect the changes in mass between the free and bound states.[150,192,193]

Fluorescent anisotropy experiments within this study were conducted by exciting fluorescent SSAs using polarized light, then measuring the extent of polarisation of the fluorescent molecule alone compared to that of the molecule in the presence of the liposomes.[190] The final anisotropy values (*r*) represent the average polarisations of individual molecules in the solution.[150,192,193] Typically, the fluorescent component is kept constant and the binding partner is titrated against it. It is equally correct to titrate the fluorescent component against a non-labelled binding partner.[190,193–195]

Due to the intrinsic fluorescence of SSA **69** and **70**, SSAs were titrated against non-fluorescent liposomes, while liposomes were kept at a constant concentration. In anisotropy experiments where the fluorescent molecule concentration is maintained, any changes to anisotropy values will be a result of binding activities. The anisotropy values recorded within this system are a measure of the sum of individual anisotropies in solution; bound and unbound. Thus, an increase in fluorescent protein concentration would result in increasing anisotropy values due to the additional molecules, until a saturation point is reached. However, anisotropy values were seen to decrease with increasing SSA concentration (Figure 60A & 60B), and fluorescence intensity increased with increasing SSA, as expected (Figure 60C & 60D).

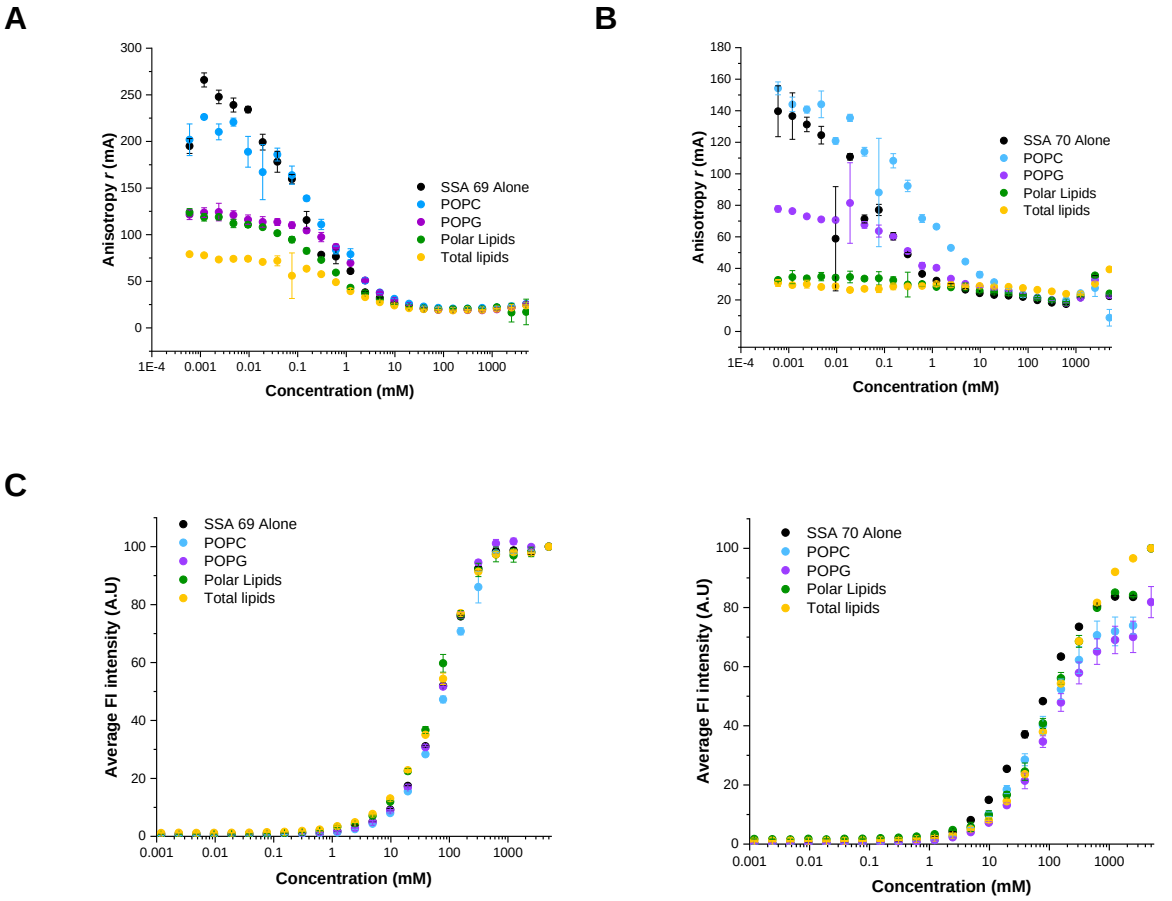

Figure 60. Fluorescence anisotropy and intensity measurements.

Anisotropy measurements using **(A)** SSA **69** and **(B)** SSA **70** and corresponding intensity values of **(C)** SSA **69** and **(D)** SSA **70** in the absence and presence of POPC, POPG, *E. coli* total and *E. coli* polar lipids obtained from Avanti polar lipids. Data points are an average of 3 independent experiments, the standard deviation used as the error value.

The SSAs have been shown to self-associate into larger aggregates, thus multiple interactions could be taking place within this experiment, not solely lipid binding. As such, any observations from this anisotropy experiment cannot determine absolute binding and can only suggest binding activities of these molecules. Furthermore, as it was hypothesised that multiple interactions could be occurring in the experiment, meaning multiple factors could impact the anisotropy results observed, disassociation constants could not be calculated.

The anisotropy data suggests comparatively stronger binding of SSA **69** to *E. coli* total lipids; anisotropy values were significantly lower than those of the other lipids. Binding to *E. coli* polar lipids and POPG is also observed with SSA **69**, however, this is to a lesser extent. Minimal binding was observed with POPC (Figure 60A), as the anisotropy values measured mirrored those of the SSA alone. Similarly, these data suggest SSA **70** binding strongly to *E. coli* total lipids, however stronger binding was observed with *E. coli* polar lipids compared to SSA **69**. This was consistent with the microscopy images observed, as SSA **70** exhibited brighter membrane fluorescence indicating stronger binding to *E. coli* membranes than SSA **69** (Figure 46). similar to SSA **69,** comparatively weaker binding to POPG was also observed, and minimal binding was observed with POPC (Figure 60B). In order to understand the binding observed, the profiles of the phospholipids present in the *E. coli* total and polar extracts were obtained from the Avanti Polar Lipids website[196], shown in Table 11, and compared.

Table 11. Phospholipid profiles.[196]

Phospholipid profiles obtained from the Avanti website, for the *E. coli* total and polar lipid extracts used in the fluorescence anisotropy assay, [a] unspecified lipids.

Phospholipid Profiles for *E. coli* lipid extracts	
Polar lipid extract	PE (67.0%)
	PG (23.2%)
	CL (9.8%)
Total lipid extract	PE (57.5%)
	PG (15.1%)
	CL (9.8%)
	other [a] (17.6%)

As binding was observed with PG for both molecules, it was determined that this would account for a portion of the binding observed with the *E. coli* polar and total liposomes. However, as both compounds bound to PG lipids to a lesser extent than *E. coli* total and polar, it was determined that binding to the other lipids present in these extracts may also have been taking place. The exception to this was SSA **69**, which exhibited similar

binding to *E. coli* polar lipids and PG, suggesting PG present within the *E. coli* polar liposomes accounted for all the binding observed with **69**.

As PE and CL were present in both samples, this suggested binding to either one or both of these lipids in addition to PG. Furthermore, PE made up a larger proportion of the total and polar lipid extracts, and as tight binding was observed with liposomes created from these extracts, it was hypothesised that binding was occurring with PE lipids to some extent. SSA **69** exhibited tighter binding to total lipids than polar lipids, indicating the unspecified lipids in the total lipid extract may also influence binding to liposomes made from this extract, as they were not present in the polar lipid extract. These initial studies allow for the hypothesis of specific lipid binding by SSAs **69** and **70** to PG, PE, and CL lipids. Further analysis using the single lipids, particularly PE and CL lipids, would be required to further understand these lipid binding processes. Additionally, the use of fluorescent lipids would allow us to conduct this experiment more robustly, however, due to time and COVID-19, those experiments were not possible to complete.

3.7. Summary

Statement	Evidence
Maintaining amphiphilicity through the use of specific functionalities and counter cations integral to the antimicrobial activity	TEA cation present in SSA **41** disrupted hydrophilicity at the sulfonate region of the molecule, decreasing antimicrobial efficacy.
	The use of hydrophilic R-groups, such as the NH_2 and NO_2 functionalities present in SSAs **50** and **53** respectively, on the phenyl ring decreased antimicrobial activity.
	Comparatively hydrophobic cations were not soluble under experimental conditions, as seen with SSAs **43** and **44**.
The formation of self – associated structures, for example, dimers, was essential to antimicrobial activity	Intramolecular bonds observed with SSAs **33** and **69** disrupted dimerisation which led to reduced antimicrobial activity.
	SSA **61** had a comparatively higher association constant, suggesting the formation of higher order structures, and also exhibited greater activity against *E. coli.*
The acidity of the thio(urea) amine groups contributed to effective antimicrobial activity	Electron withdrawing R-groups associated to the phenyl ring, such as the CF_3 present in SSAs **32,** drastically improved activity, whereas those that were electron-donating such as the NH_2 and MeO functionalities in SSAs **50** and **51**, reduced antimicrobial activity.
The coordination and hydrophilicity of the counter cation influenced the antimicrobial efficacy observed	The TBA counter cation was less coordinating in comparison to the Na^+, TMA, TEA, and TPA cations. SSAs with the TBA cation produced the highest efficacy against *E. coli.*
	Pyridinium counter cation present in SSAs **39** and **48** produced the highest MRSA activity.
	SSA **41** which disrupted hydrophilicity, decreased antimicrobial activity.
Multiple binding modes exhibited by the SSAs	Growth stages and bacterial species impacted in different ways by SSAs, as shown by the growth

	curves and types of inhibition observed.
	A decline in bacterial growth at the later stages of growth was only observed with *E. coli* and not with MRSA.
	Some functionalities that promoted *E. coli* activity (e.g., SSAs **34** and **61**) were different from those that promoted MRSA activity, (e.g. SSAs **32, 39,** and **48**).
SSAs confirmed to bind to bacterial membrane lipids	Bacterial membrane fluorescence was observed after incubation with SSAs **69** and **70.**
	Drastic reduction in the fluorescence of FM4-64, a non-specific lipid binding molecule, in the presence of SSA **70** demonstrated lipid binding.
	Significantly differing fluorescence anisotropy values in the presence of different lipids suggested specific lipid binding.
Secondary binding target once SSAs internalise	Brighter regions observed in both *E. coli* and MRSA after SSA **70** internalisation, indicating compound accumulation at a specific region/target.
SSA gel matrix allows for the diffusion of other antimicrobial molecules without hindering activity,	The activity of ampicillin was not greatly hindered when co-formulated with the SSA **70** gel, as zones of inhibition measured with/without SSA **70** were not significantly different.
Specific SSAs can be used in combination with other therapeutic agents with specific structures	1:1 heterogenous mixes with SSA **66** produced drastically lower MIC_{50} values than those obtained for the independent SSA solutions. Antagonistic effects observed with SSAs **67** and **68** indicated specific structures would need to be selected for combination therapies.

Summary

The data presented in this chapter provides evidence that the determination of structure-activity relationships can be utilised in the development and optimisation of more potent therapeutics. It was also determined that more complex interactions were taking place, as SSAs **35** and **68** exhibited comparatively stronger hydrogen-bonded complex formation, however antimicrobial activity was weaker. Furthermore, the replacement of the TBA counter cation to a TEA counter cation produced varying results, as the thiourea-based molecule exhibited increased activity whereas the urea-based molecule exhibited a reduction in activity. The use of further computational analysis may allow for a more thorough investigation into these more complex interactions.

The SSAs presented in this chapter were shown to bind to the bacterial membrane, through the use of microscopy using SSA **70**, which outcompeted the lipid binding molecule FM4-64, suggesting lipid binding. The fluorescence anisotropy assay conducted on SSAs **69** and **70** suggested specific phospholipid binding to *E. coli* total and polar lipids, the predominant lipids present in these extracts being PG and PE. This suggested binding of SSAs **69** and **70** to PG, and CL lipids and to some extent PE lipids. Both CL and PG have a net negative charge, CL being more negative than PG.[104] It is therefore hypothesised that the cationic component participates in electrostatic interactions with these lipids initially, then the lipophilic component on the anionic component can interact with the phospholipid tails. This may result in pore formation in the bacterial membranes leading to a loss in membrane integrity and resulting in cell death.

In conclusion, the stepwise modifications to SSA **32** revealed how the geometry of the SSAs impacted self-associated structures, and the disruption of those structures resulted in a reduction of antimicrobial activity.

Chapter 4: The characterisation and optimisation of novel antimicrobial compounds

4.1. Introduction

The optimisation of lead molecules is an essential step in antimicrobial drug design, and it is dependent on the nature of each molecule. QSAR data exploring the relationships between chemical structure and biological activity enable the design of new molecules that exhibit desired properties.[142,197,198] Analyses of the structure-activity relationships and associated activities of molecules are often utilised to make stepwise structural modifications.[142] These modifications can improve specific biological or physicochemical properties exhibited by the molecules, such as amphiphilicity, toxicity, potency, or solubility.[198] Moreover, stepwise structural modifications allow for the determination of the impact that functional group placement has on desired activities, and for the removal of nonessential functional groups. Optimisation through the use of stepwise modification tends to be unidirectional; each molecular modification is tested, then the physicochemical properties are explored, thus refining any hypotheses previously made.[142,143,198] Structural variation influences biological activity, binding selectivity, and affinity; thus, it is important for every modification made to a molecule to be thoroughly explored and understood to ensure these properties are not significantly reduced.[142,198] Furthermore, if molecules are to be used in combinatory therapies, it is vital to ensure that the modifications made are not antagonistic to the chosen complementary molecule.[68,199] Experimental approaches to optimisation are typically used, however, they may be utilised for the prediction of future molecules through the use of computational methods.[200]

4.1.1. Aim of studies

These studies aim to utilise the structure-activity relationships presented in chapter 3 to produce more effective antimicrobial molecules and further understand the behaviour of these molecules by determining the physicochemical properties. Furthermore, the aims of

these studies are also utilise the gelation properties of SSA **70** to synthesise novel gelating SSAs and investigate the impact of salt solution on these properties.

4.2. Molecular Design

In designing the next generation of molecules, we sought to improve efficacy against gram-negative bacteria, modelled here by *E. coli*. Additionally, we sought to incorporate the gelation and fluorescent properties exhibited by SSA **70** to aid in visualisation and provide additional methods of administration. From the study of structure-activity relationships in Chapter 3, the key changes that improved *E. coli* activity were increasing the length of the alkyl chain between the sulfonate and the NH groups and the use of the carboxylate functional group. In order to adopt the fluorescent and gelation properties into the new molecules, a benzothiazole functional group was preferred. On the basis of these findings and requirements, we designed SSAs **82 - 85** (Figure 61).

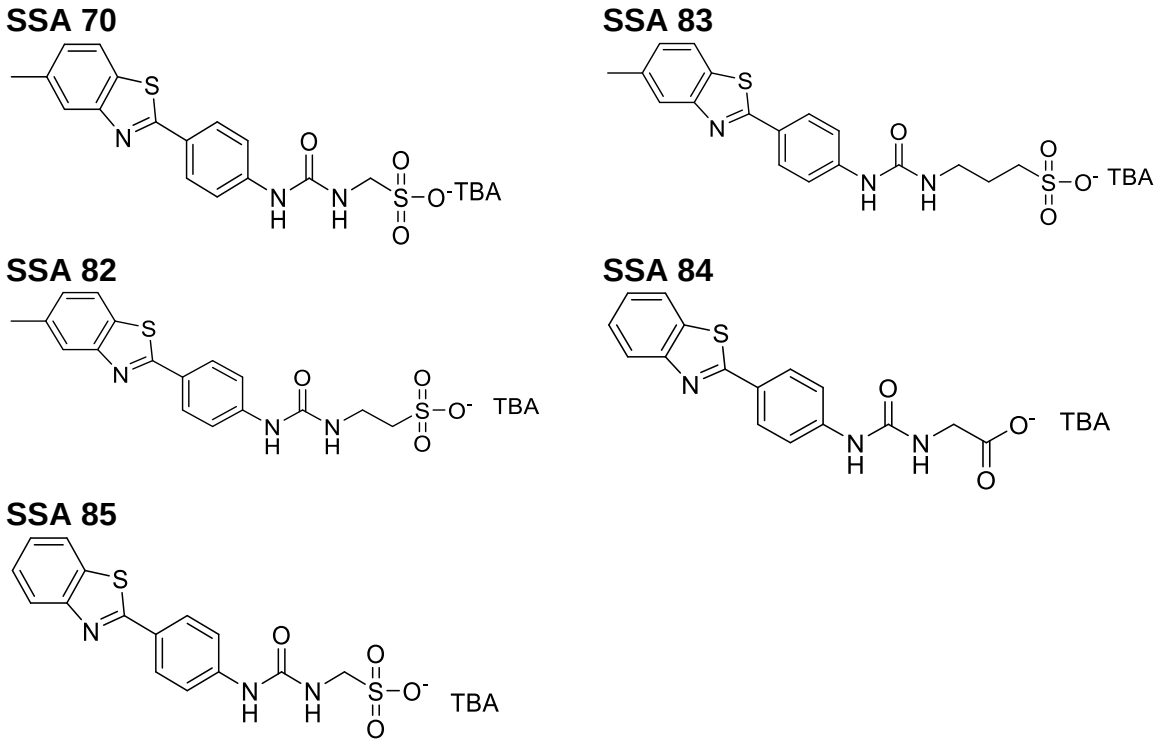

Figure 61. Structures of molecules discussed within this chapter.

SSAs **70**, **82** – **85** are next-generation molecules designed using the structure-activity relationships established in chapter 3.

4.3. Physicochemical Studies

Physicochemical analysis, first introduced in 1919 by Kurnakov, can be defined as a branch of chemistry concerned with the relationships between the composition of a molecule and its resulting properties.[201–203] Knowledge of physicochemical properties is required in understanding the self-associative properties and biological interactions of the SSAs, which can then inform any further optimisation and molecule design.

In this section, the methods used for determining the physicochemical properties of SSAs **82** and **83** are described. These will enable a deeper understanding of their interactions with bacterial membranes and aid in the prediction of future molecules. The physicochemical properties of **84** and **85** were conducted separately from SSAs **82** and **83** and are therefore not discussed in this section.

4.3.1. Low level *in silico* modelling

Electrostatic potential maps are computational models in three dimensional space that can be used to visualize the regions of electron excess and electron deficiency.[204,205] Negative electron potential values, which are red on electrostatic potential maps, correlate with concentrated electron density, and positive electron potential values, which are blue, correlate with low electron densities.[204–206] Hunter (2004) utilised computationally derived electrostatic potential maps to produce E_{min} (minimum in electrostatic potential) and E_{max} (maximum in electrostatic potential) surface values which he proposed would correlate with those derived from experimental data.[204]

Electrostatic potential maps can also be utilised to visualise hydrogen bonding sites and directionality in complexes and to predict the behaviour and subsequent interactions of complex molecules.[206,207] An example of this is seen with the studies conducted by Sathyamurthy et al. (2007), who investigated hydrogen bonding using electrostatic potential maps and found that hydrogen bond strength and stability increases linearly with increasing electron density at the hydrogen bonding critical point.[206] It has been hypothesised by Hiscock et al. (2018) that the increased acidity of the HBD groups within the anionic component of the SSAs increases the hydrogen bonded complex strength,

which may increase antimicrobial activity.[154] Furthermore, through their studies, E_{max} values were shown to correlate with dimerisation constants, which suggested increased HBD acidity of SSAs would increase their propensity to form dimers. The data obtained in Chapter 3 suggests the involvement of multiple factors, including the strength of the complex formed, in the observed antimicrobial activity.

Consequently, low-level theoretically derived electrostatic potential maps were generated for SSAs **82** and **83**; described as low-level due to the simplicity of the method used. This would enable the prediction of favourable HBA and HBD sites and hydrogen bonding strengths in the resulting complexes formed. Drawing on research conducted by Hunter (2004), low-level electrostatic potential maps were generated using Spartan 16' software to identify primary hydrogen bond donating and accepting sites in SSAs **82** and **83**.[204,208–210] E_{min} and E_{max} values were calculated using semi-empirical PM6 methods after energy minimisation calculations and PM6 was used over AM1 in line with studies conducted by Stewart.[208,209,211] Computational modelling and electrostatic potential maps were generated by Rebecca Ellaby, however, the interpretation was conducted by myself. The electrostatic potential map for SSA **82** is presented in Figure 62.

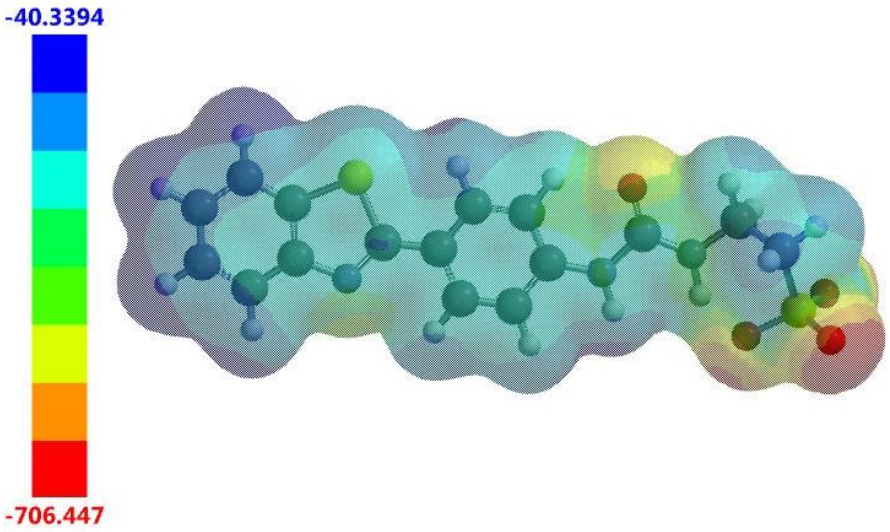

Figure 62. Electrostatic potential map calculated for SSA 82.

The E_{max} (-40.3394 kJ/mol) and E_{min} (-706.447 kJ/mol) correspond to the most positively and negatively charged points on the surface of the molecule, respectively.

The electrostatic potential map in Figure 62 can also support the evidence for the formation of intramolecular bond formation, as was previously reported with SSA **33**. The cyclisation of the sulfonate group to the alkyl NH was observed with SSA **82**, suggesting a preference for intramolecular hydrogen bonding. It was therefore hypothesised that the interactions and properties exhibited by SSA **33** would be comparable to those of SSA **82**. The electrostatic potential map for SSA **83** is presented in Figure 63.

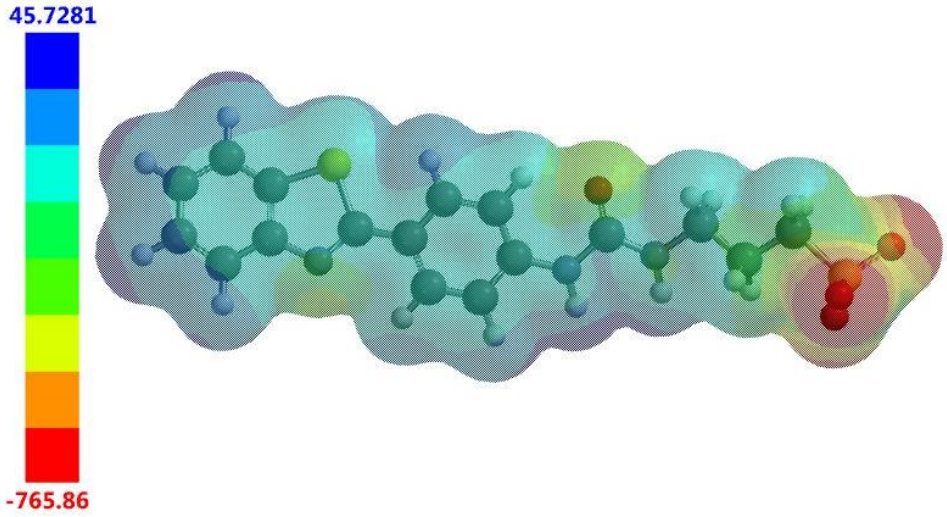

Figure 63. Electrostatic potential maps calculated for SSA 83.

The E_{max} (-45.7281 kJ/mol) and E_{min} (-765.86 kJ/mol) correspond to the most positively and negatively charged points on the surface of the molecule, respectively.

A planar structure was observed for SSA **83**, which suggested the formation of the intramolecular hydrogen bond was no longer favourable. Furthermore, a higher E_{max} value was observed with SSA **83**, suggesting higher acidity in comparison to SSA **82**. Therefore, drawing on the work conducted by Hiscock et al. (2018), it was hypothesised SSA **83** would form complexes with comparatively stronger hydrogen bonds than those of SSA **83**.[154] The electrostatic potential maps and E_{min}/E_{max} values were compared to the subsequent experimental data.

4.3.2. Synthesis

IR, ^{1}H and ^{13}C NMR spectroscopy and melting point experiments were conducted as described in sections **2.7.3, 2.7.6** and **2.7.7**, respectively, in the materials and methods. ^{1}H and ^{13}C NMR spectroscopy and synthesis were conducted by me; IR and melting points were obtained in collaboration with Jess Boles.

For the synthesis of SSA **82**, Tetrabutylammonium (TBA) hydroxide (1N) in methanol (4 mL, 4 mM) was added to 2-aminoethane-1-sulfonic acid (0.25 g, 2.0 mM) and taken to dryness. Triphosgene (0.31 g, 1 mM) was added to a stirring solution of 4-(6-methylbenzothiazol)aniline (0.50 g, 2 mM) in ethyl acetate (30 mL) and the mixture heated at reflux for 4 hours. The TBA salt was then dissolved in ethyl acetate (10 mL) and added to the reaction mixture and heated at reflux overnight, filtered and the solid washed with ethyl acetate (10 mL). Impurities were removed through precipitation in methanol with ethyl acetate, the solids filtered, and the filtrate taken to dryness to give the pure product as a pale-yellow solid in a 54.5 %, (0.69g, 1.09 mM). Melting point: >200°C; ^{1}H NMR (298K, 400 MHz, DMSO-d_6): δ; 0.93 (t, J = 7.32 Hz, 12H), 1.32 (m, 8H), 1.56 (m, 8H), 2.45 (s, 3H), 2.58 (t, J = 6.10 Hz, 2H), 3.16 (m, 8H), 3.39 (t, J = 6.4 Hz, 2H), 6.51 (t, J = 10.12 Hz, 1H), 7.32 (d, J = 10.12 Hz, 1H), 7.59 (d, J = 8.64 Hz, 2H), 7.89 (dd, J_1 = 8.72 Hz , J_2 = 8.56 Hz, 4H), 9.30 (s, 1H); $^{13}C\{^{1}H\}$ NMR (100 MHz, 298K, DMSO-d_6): δ; 13.4 (CH_3), 19.2 (CH_2), 21.0 (CH_3), 23.0 (CH_2), 36.1 (CH_2), 51.0 (CH_2), 57.5 (CH_2), 117.5 (ArCH), 121.7 (ArCH), 121.9 (ArCH), 125.4 (ArC), 127.8 (ArCH), 134.3 (ArC), 134.6 (ArC), 143.9 (ArC), 151.9 (ArC), 154.7 (ArC), 166.3 (C=O); IR (film): v (cm^{-1}) = 2961 (NH stretch), 1685, 1179, 1163, 1037, 841;HRMS for the sulfonate-urea ion (ESI): m/z: act: 404.88 $[M+H+CH3]^-$ cal: 390.45 $[M]^-$

For the synthesis of SSA **83**, Tetrabutylammonium (TBA) hydroxide (1N) in methanol (4 mL, 4.00 mM) was added to 3-aminopropane-1-sulfonic acid (0.28 g, 2.00 mM) and taken to dryness. Triphosgene (0.31 g, 1.00 mM) was added to a stirring solution of 4-(6-methylbenzothiazol) aniline (0.50 g, 2 mM) in chloroform (30 mL) and the mixture heated at reflux for 4 hours. The TBA salt was then dissolved in chloroform (10 mL) and added to

the reaction mixture and heated at reflux overnight, filtered and the solid washed with chloroform (10 mL). Impurities were removed by precipitation in methanol with chloroform, the solids filtered, and the filtrate taken to dryness to give the pure product as a pale-yellow solid in a 58 %, (0.753g, 1.16 mM). Melting point: >200°C; ^{1}H NMR (298K, 400 MHz, DMSO-d_6): δ: 0.91 (t, J = 7.44 Hz, 12H), 1.28 (m, 8H), 1.53 (m, 8H), 1.80 (m, 2H), 2.43 (s, 3H), 2.57 (t, J = 7.64, 2H), 3.16 (t, J = 6.04 Hz, 10H), 6.74 (t, J = 5.60 Hz, 1H), 7.30 (d, J = 8.24 Hz, 1H), 7.62 (d, J = 8.84 Hz, 2H), 7.87 (dd, J_1 = 8.80 Hz , J_2 = 9.88 Hz, 4H), 9.12 (s, 1H); ^{13}C{^{1}H} NMR (100 MHz, 298K, DMSO-d_6): δ; 13.5 (CH_3), 19.2 (CH_2), 21.0 (CH_3), 23.0 (CH_2), 26.1 (CH_2), 38.2 (CH_2), 49.1 (CH_2), 57.5 (CH_2), 117.5 (ArCH), 121.6 (ArCH), 121.9 (ArCH), 125.3 (ArC), 127.7 (ArCH), 127.8 (ArCH), 134.2 (ArC), 134.6 (ArC), 143.9 (ArC), 151.9 (ArC), 154.9 (ArC), 166.3 (C=O); IR (film): v (cm^{-1}) = 2963 (NH stretch), 1701, 1173, 1036, 847; HRMS for the sulfonate-urea ion (ESI): m/z: act: 404.88 $[M]^-$ cal: 404.07 $[M]^-$

4.3.3. Single-crystal x-ray diffraction

Single crystal X-ray diffraction is a non-destructive analytical technique that can provide information on the binding modes of molecules in the solid state. This technique was utilised to investigate the self-associative properties of SSAs **82** and **83** in the solid state. Crystals were obtained from a slow evaporation process, as described in section **2.7.9** of the materials and methods and the crystallography data discussed within this section was obtained and refined by Dr. J Hiscock. The crystal structure of SSA 82 is presented in Figure 64.

Contrary to the electrostatic potential maps, an intramolecular bond was not observed forming between the alkyl chain NH and the sulfonate functionality of SSA **82**. The crystal structure for SSA **82** revealed dimerisation through the formation of four intermolecular bonds between the urea NH groups of one molecule and the sulfonate of the other molecule. This revealed a limitation of single molecule computational modeling methods undertaken. Previously published crystal structures of SSAs exhibiting this dimerisation by Hiscock et al., (2018) resulted in the hypothesis that SSA **82** is more likely to behave

more like SSA **32** than SSA **33**, as the dimers observed with SSA **82** were more similar to those observed with SSA **32** than SSA **33**.[154]

A

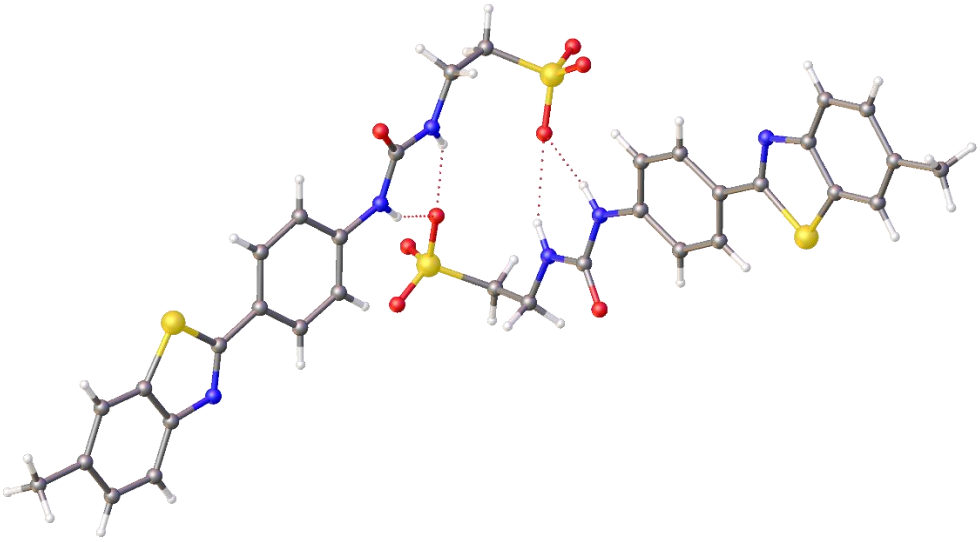

B

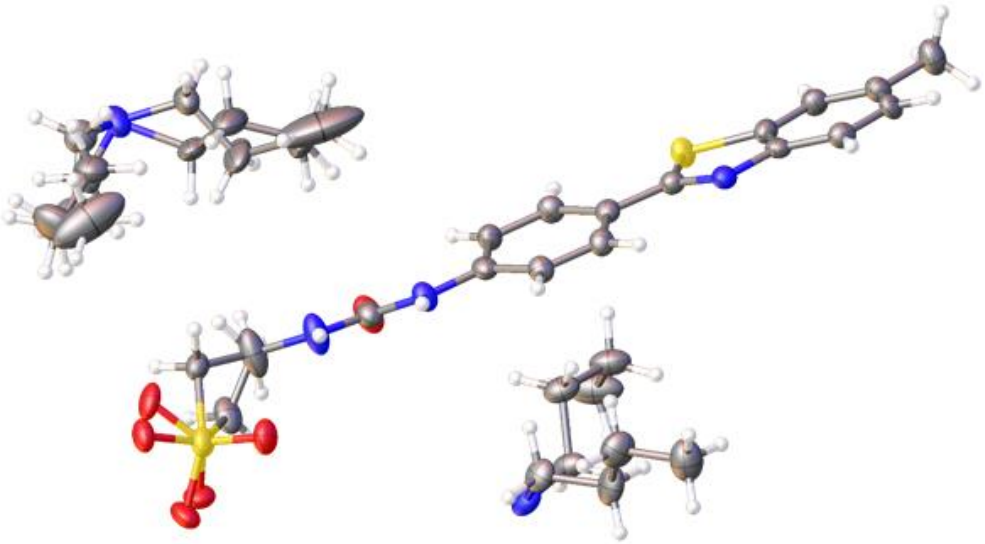

Figure 64. Single-crystal X-ray structures of SSA 82.

(A) Ball and stick representation of single crystals produced by SSA **82** illustrating the intermolecular hydrogen bond formation. TBA cation omitted for clarity. **(B)** Ellipsoid diagram of the crystal's unit cell. red = oxygen, yellow = sulphur, blue = nitrogen, white = hydrogen, grey = carbon.

The single-crystal structure of SSA **83** also reveals the formation of dimers, however secondary hydrogen bonds to water molecules were also observed, which acted as HBD bridges between dimers (Figure 65).

A

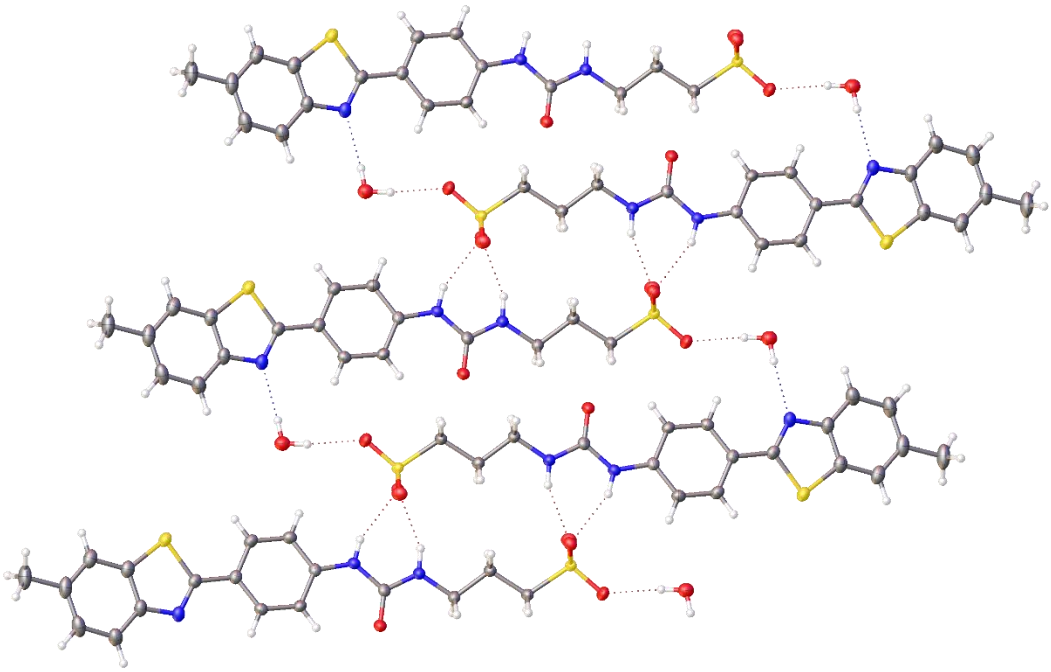

B

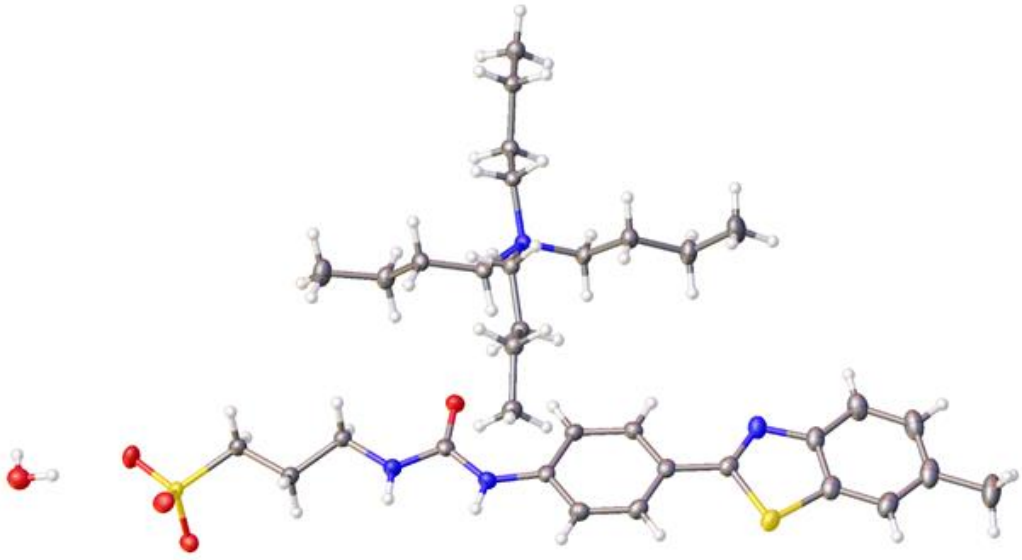

Figure 65. Single-crystal X-ray structures of SSA 83.

(A) Ball and stick representation of single crystals produced by SSA **83** illustrating the intermolecular hydrogen bond formation. TBA cation omitted for clarity; **(B)** Ellipsoid diagram of the crystal's unit cell; red = oxygen, yellow = sulphur, blue = nitrogen, white = hydrogen, grey = carbon.

It was hypothesised that while SSA **83** formed larger complexes, these would be comparatively weaker in comparison to those of SSA **82**, as the interactions with the competitive solvent interactions were not overcome.

The amino-sulfonate dimer had an interior dimerisation angle of 180.0° and was therefore planar in nature. Hydrogen bond angles were found to be 173.4 – 148.8 for SSA **82** and ranged between 154.6 – 173.5° for SSA **83**. Furthermore, hydrogen bond lengths from donor to acceptor (D – A) for SSA **82** were 2.839 and 2.995 Å, whereas for SSA **83** these ranged between 2.8719 – 2.9591 Å. The hydrogen bond distances and angles are reported in Table 12.

Table 12. Hydrogen bond angles and distances involved in hydrogen bonded self-association.

Hydrogen bond angles and distances calculated from single-crystal x-ray structures from Figures 64 and 65.

Hydrogen bond distances and angles				
	HBD	HBA	Hydrogen bond length (D•••A) (Å)	Hydrogen bond angle (D-H•••A) (°)
82	N2	O4	2.839 (4)	173.44 (7)
	N3	O4	2.995 (4)	148.8 (2)
83	N1	O2	2.9478 (17)	154.64 (9)
	N2	O1	2.9591 (17)	156.20 (9)
	O5	O3	2.8719 (18)	173.45 (9)
	O5	N3	2.9280 (19)	167.14 (10)

4.3.4. Gas-phase mass spectrometry

ESI-MS is a ‘soft’ analytical technique used for the identification and quantification of analytes using the mass-to-charge ratio (*m/z*) of ions generated from a sample. Generally, no fragmentation occurs upon ionization and the molecules retain minimal amounts of residual energy, thus this procedure can be utilised for the observation of non-covalent interactions which can be preserved in the gas phase. Consequently, ESI-MS experiments were conducted using SSAs **82** and **83** to determine whether the dimerisation or self-association observed in the solid state could also be observed in the gas phase. ESI-MS experiments were conducted by Rebecca Ellaby, however, the analysis of spectra obtained was conducted by me. The mass charge ratio prevents the

differentiation of monomeric [M]- and the dimeric $[M+M]^{2-}$ species, however, dimeric $[M+M+H]^{-}$ could be distinguished from monomeric species. CH_3 fragments are common impurities within the mass spectrometer used for these experiments.

ESI-MS spectra showed the presence of an SSA **82** anionic monomer $[M+H+CH_3]^{-}$ with an m/z of 404.8774, and also dimeric [M+M+H]- species with an m/z of 775.9959 (Figure 66).

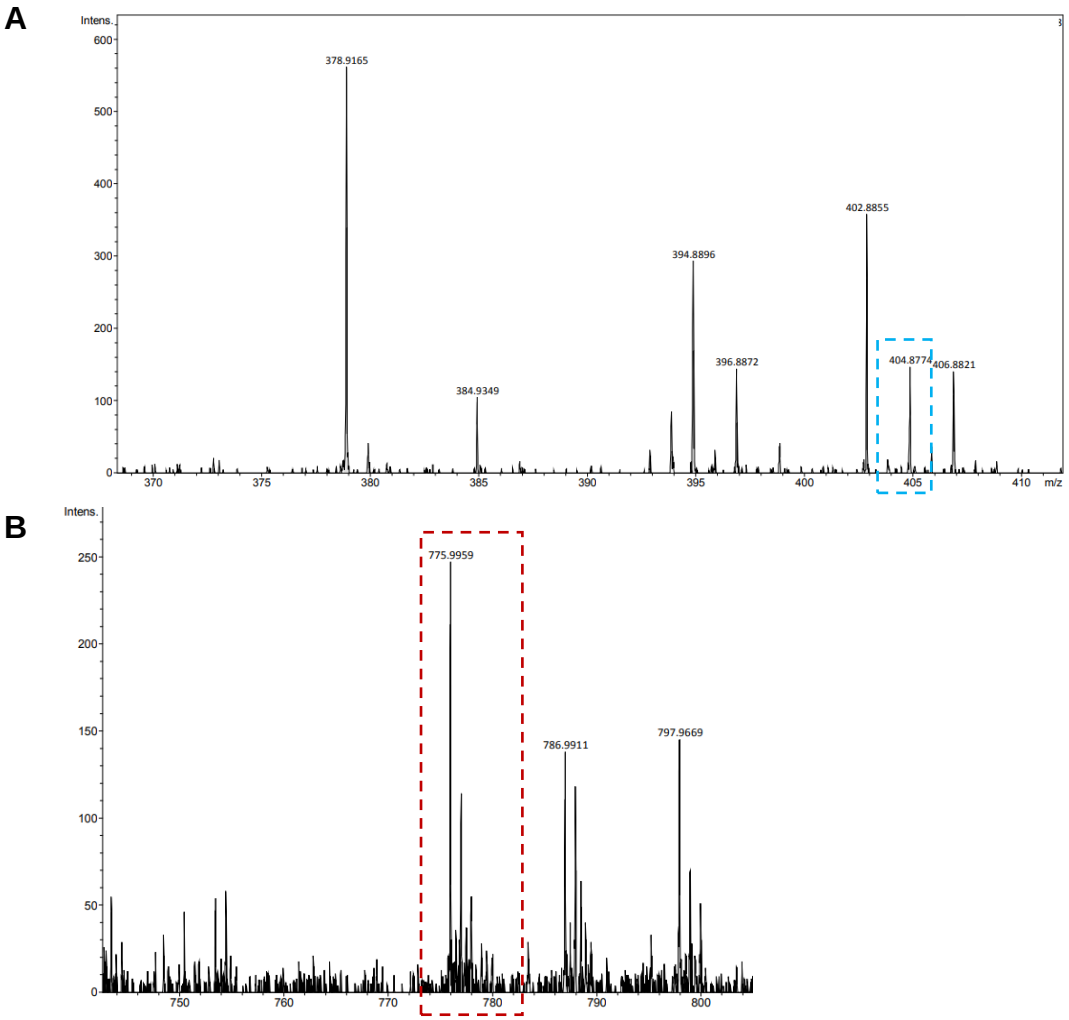

Figure 66. High-resolution ESI spectra of SSA 82

Spectra showing **(A)** the monomeric $[M+H+CH_3]^{-}$ species, highlighted in blue, and **(B)** the dimeric $[M+M+H]^{-}$ species, highlighted in red.

However, dimeric [M+M+H]- were not observed on ESI-MS spectra of SSA **83**, only the monomeric $[M]^{-}$ species with an m/z of 404.8818 were observed (Figure 67).

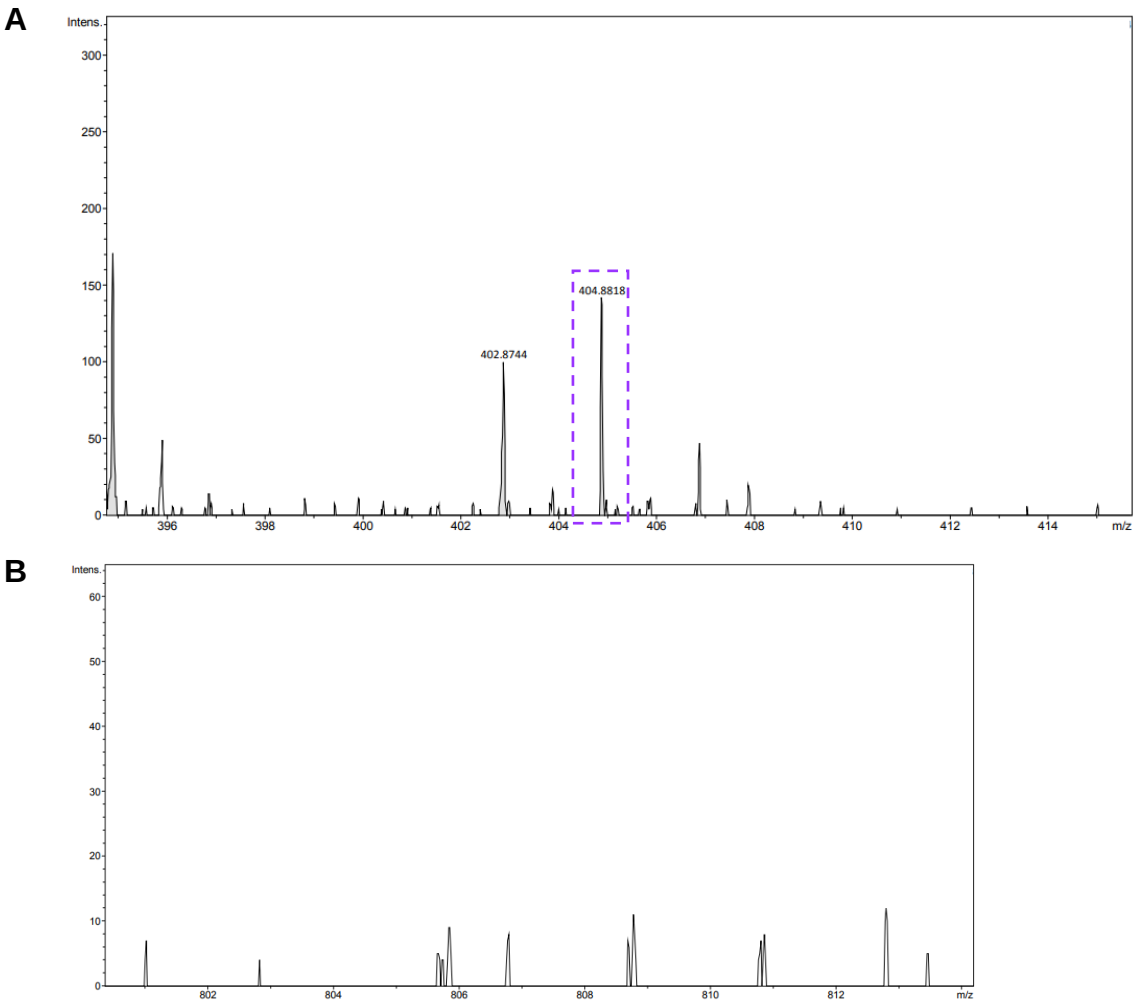

Figure 67. High-resolution ESI spectrum of SSA 83

Spectrum showing **(A)** monomeric $[M]^-$ species, highlighted in purple; **(B)** dimeric $[M+M+H]^-$ species were not observed in the gas phase.

These data suggests the presence of self-associated SSA **82** dimers in the gas phase but not of SSA **83**, despite dimeric species of its analogues SSA **34** and **70** being observed in the gas phase.[153] It is worth noting that gas phase experiments can be subject to experimental conditions, and therefore, solution state studies were employed to further investigate the intermolecular interactions.

4.3.5. Solution state studies

Self-associating molecules dissolved in solvents containing HBD/HBA groups are subject to competing solvent-solute interactions, which must be overcome for self-associated

complex formation. Solution state studies allow for the analysis of these interactions and the events leading up to aggregate formation. Furthermore, solution-state studies allow for the observation of molecular interactions in an environment representative of physiological conditions. As such, dynamic light scattering, surface tension, and zeta potential measurements as well as ^{1}H NMR DOSY, q^{1}HNMR, and ^{1}H NMR dilution studies and were utilised to observe the behaviour of SSAs **82** and **83** in different solvent environments.

4.3.5.1. Dynamic Light Scattering (DLS)

The specific properties of molecules in solution can be observed through the use of light scattering measurements.[212] This versatile technique can be utilised to observe a variety of particles and characterise their diffusion behaviour in different scientific disciplines.[213–215] Brownian motion, established by Einstein in 1905, is the random motion of particles in solution as a result of collision with surrounding solvent molecules.[216,217] Sir George Stokes in 1845 suggested that the radius and viscosity of solvent are proportional to the friction exerted by a moving particle.[218] Einstein utilised this discovery and developed what is now known as the Einstein-stokes equation (Equation 1), through which we can calculate the hydrodynamic diameter (d_H) of a particle.[218,219]

$$d_H = \frac{k_B T}{3\pi\eta D}$$

Equation 4. The Stokes-Einstein equation.

d_H – hydrodynamic diameter, k_B – Boltzmann's constant, T= thermodynamic temperature, η = dynamic viscosity, and D = translational diffusion constant.

Larger molecules tend to diffuse more slowly and therefore overall motion is minimal, whereas smaller particles do not adopt specific positions as they are able to diffuse faster. Therefore, monitoring the movement of particles in solution provides information on the size of the macromolecules in a given solution.[212] In DLS, particles encounter monochromatic light, which is then scattered due to the Brownian motion of the particles, and the scattered light signal is then appropriately detected.[212] The d_H calculated is based

on the assumption that the particles in solution are spherical, and therefore can only provide an indicative size of the aggregate.

As the SSAs have been previously shown to aggregate, DLS was utilised in these studies to investigate the size of the aggregates, if any, created by SSAs **82** and **83**.[153,155,156] Refractive index of these novel SSAs are yet to be explored, and therefore the number and volume distributions could not be obtained in these experiments. The polydispersity index (PDI) of particles in solution is reported instead, which will provide information concerning the width of the particle size distribution, where the number of particles at that size are weighted by size. Higher PDI values correspond to a wider range of aggregate sizes in solution.

DLS experiments were carried out on SSAs as described in section **2.7.4** of the materials and methods, in solutions of EtOH:H_2O (1:19). Samples underwent an annealing process whereby the SSA solutions were heated to 40°C then cooled to 25°C, thereby allowing any aggregates formed to achieve their thermodynamic minimum. As particle motion is dependent on temperature and accurate knowledge of the temperature is essential in DLS experiments, all experiments were conducted at 25°C.[212,220] Table 13 provides a summary of the peak maxima (nm) and the PDI (%) of SSAs **82** and **83** in a solution of EtOH:H_2O, (1:19) at 0.56 mM and 5.56 mM.

Table 13. DLS Data.

Peak maxima (nm) and PDI (%) obtained from an average intensity particle size distribution of SSAs **82** and **83** obtained at 0.56 mM and 5.56 mM in an EtOH: H_2O (1:19) system by DLS.

	DLS Data		
	Conc (mM)	Peak Maxima (nm)	PDI (%)
82	5.56	119.75 ± 5.30	24.44 ± 1.15
	0.56	108.41 ± 2.07	25.08 ± 0.78
83	5.56	410.80 ± 8.98	23.17 ± 0.91
	0.56	212.35 ± 9.52	27.90 ± 0.92

A broad range of aggregate sizes from ~ 1 nm to > 1000 nm were observed with SSA **82** at 5.56 mM, with a PDI of 24.44%. Smaller aggregates observed between 1 – 10 nm could be attributed to lower order structure formation, such as monomer, dimer, or trimer formation (Figure 68). These were classified as class 1 aggregates.

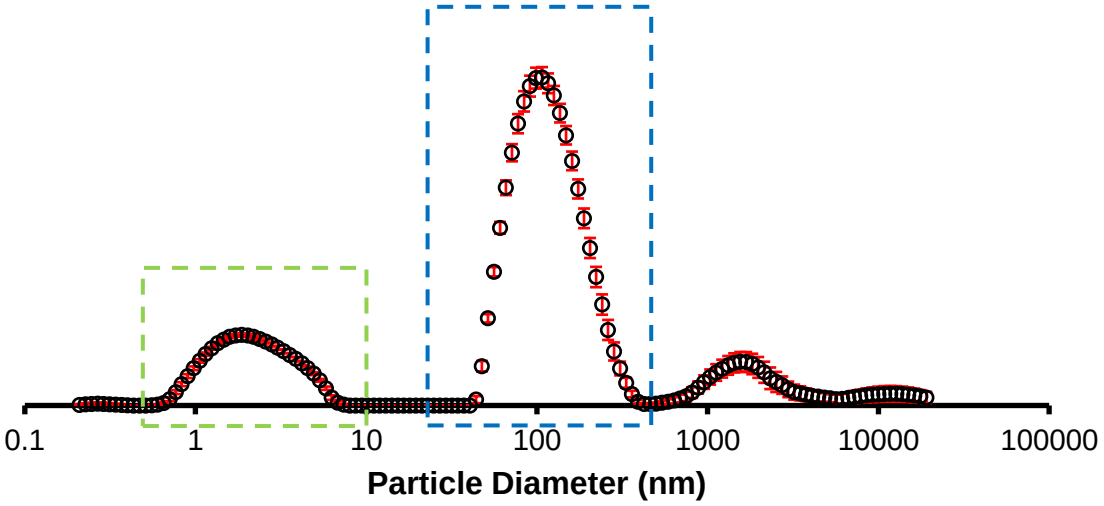

Figure 68. Average intensity particle size distribution.

Low order (green) and intermediate (blue) aggregates are highlighted. Aggregates > 1000 nm were above the limit of the experiment. The standard error of the mean (s.e.m) used as error values.

The solution predominantly contained aggregates of between 50 – 400 nm, the peak maxima being 119.75 nm. These aggregates were defined as intermediate class 2 aggregates. Aggregates observed below 1 nm were below the size limit of the experimental method, as particles of that size are too small to scatter sufficient light to be detected. Furthermore, aggregates > 1000 nm exceeded the limitations of the instrument and may be attributed to the combination of smaller structures.

Class 2 aggregates of SSA **82** persisted at 0.56 nm, with a peak maxima of 108.41 nm, suggesting the stability of these higher order complexes was not disrupted by competitive solvent interactions. Low-order structures (class 1) were also observed, as aggregates between 1-10 nm were recorded (Figure 69).

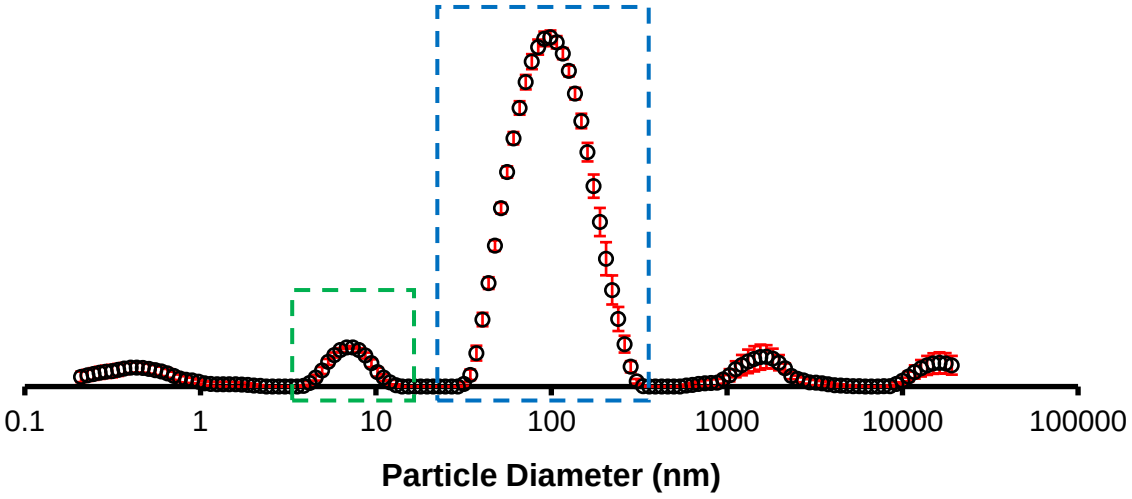

Figure 69. Average intensity particle size distribution.

Low order (green) and intermediate (blue) aggregates are highlighted. Aggregates > 1000 nm were above the limit of the experiment. The standard error of the mean (s.e.m) used as error values.

Comparatively larger aggerates with a peak maxima of 410 nm were observed in the solution of SSA **83** at 5.56 mM, which were defined as class 3 aggregates (Figure 70).

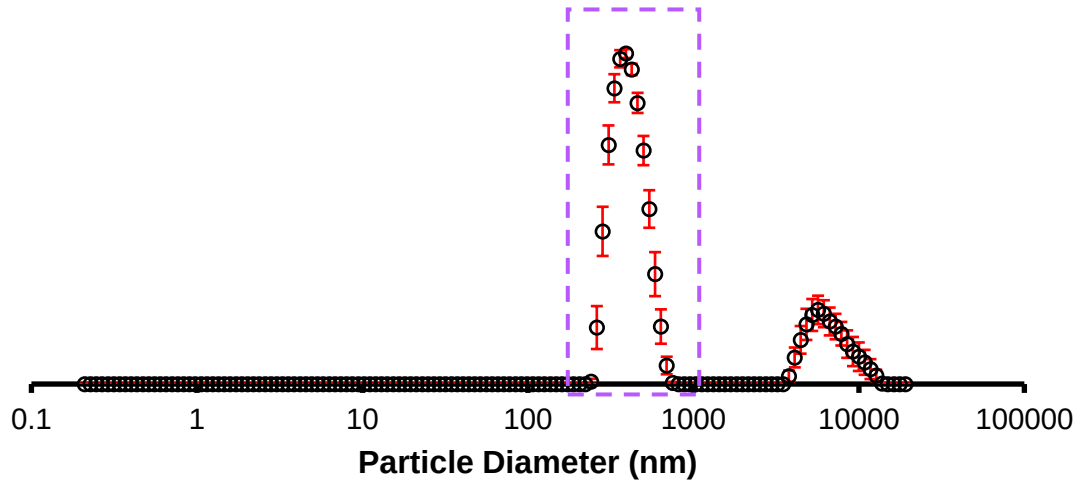

Figure 70. Average intensity particle size distribution.

Higher order aggregates are highlighted in purple. Aggregates > 1000 nm were above the limit of the experiment. The standard error of the mean (s.e.m) used as error values.

Lower order structures were not detected, which may suggest their presence at concentrations too low to be detected by DLS. Furthermore, the absence of multiple peaks suggested a comparatively more homogenous solution of SSA **83** aggregates in comparison to SSA 82 which had two definitive peaks. Unlike SSA **82**, these higher order structures exhibited by SSA **83** at 5.56 mM did not persist at 0.56 mM. Instead, class 2 aggregates with a peak maxima of 212.35 nm were observed (Figure 71).

This suggested that while the stability of the aggregates may be disrupted by solvent interactions, higher order complex formation was still preferable. Furthermore, the formation of comparatively larger aggregates even at 0.56 mM suggests more stable complexation, in comparison to SSA **82**. While aggregates > 1000 nm were recorded, as described before, these were above the limitations of the experiments and may be attributed to the amalgamation of smaller structures.

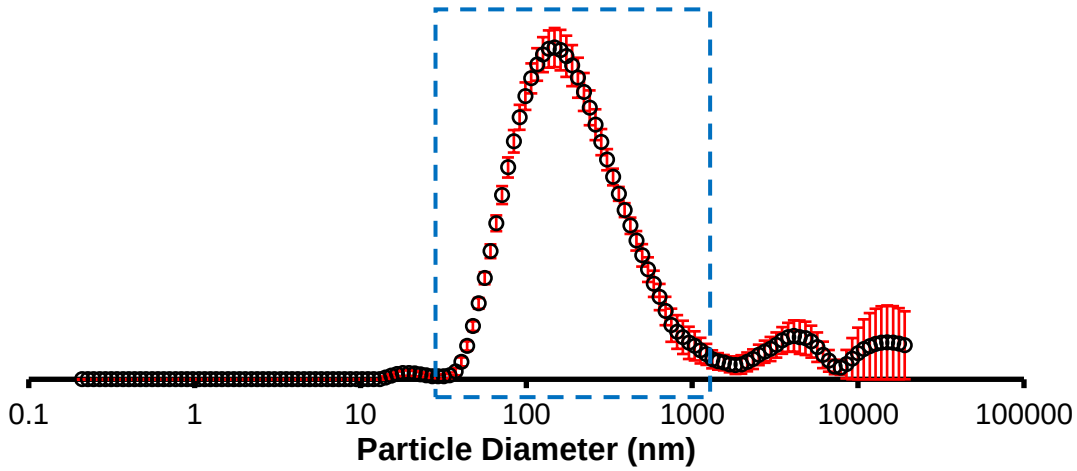

Figure 71. Average intensity particle size distribution.

Class 2 aggregates are highlighted in blue. Aggregates > 1000 nm were above the limit of the experiment. The standard error of the mean (s.e.m) used as error values.

4.3.5.2. Surface tension and CMC

As previously described, the critical micelle concentration (CMC) can be determined through multiple surface tension measurements of a serially diluted solution.[13] At lower concentrations, surface tension drops significantly, and as concentration increases, the surface tension continues to decrease due to the increased accumulation of molecules at

the water-air interface. When the surface is saturated with molecules, the surface tension no longer decreases, and the addition of more compound results in the formation of extended aggregates in solution. The concentration at which this occurs is the CMC.[13] The CMC of an antimicrobial molecule is hypothesised to be linked to antimicrobial activity.[156] It was therefore essential to determine the CMCs of SSAs **82** and **83**, in order to further define its relationship to the antimicrobial activity. Due to COVID restrictions, CMC experiments were conducted as stated in section **2.7.10** of the materials and methods by Kira Hilton, however, data analysis and CMC calculations were conducted by me. The CMC values and surface tension (σ) at CMC are reported in Table 14.

Table 14. Critical micelle concentrations.

CMCs (mM) of SSAs **82** and **83** and surface tension (σ) at the CMC.

	Critical Micelle Concentration	
	CMC (mM)	σ at CMC (mN/m)
82	1.92	56.24
83	14.77	45.16

The CMC obtained for SSA **82** (1.92 mM) was considerably lower than that of SSA **83** (14.77 mM). It was hypothesised previously that SSA **82** would produce a higher CMC value due to the hypothesised intramolecular hydrogen bond forming between the NH groups and the sulfonate, as was observed with its single ring analogue SSA 2. However, the increase from n=2 (SSA **82**) to n=3 (SSA **83**) significantly increased CMC. Lower CMC values were hypothesised to improve antimicrobial efficacy; thus, it could be hypothesised that SSA **82** would be more active in comparison to SSA **83**, despite the opposite being observed with their single ring analogues SSAs **32** and **33**, respectively.

4.3.5.3. ^{1}H DOSY NMR

Proton DOSY NMR can differentiate the NMR signals from a mixture of molecules based on their translational diffusion. DOSY experiments conducted by Hiscock et al., 2018 were able to show the formation of hydrogen bonded dimers in DMSO and also

demonstrated the hydrogen bonding mode could be manipulated through the addition of competitive HBA/HBD species.[154] Consequently, to investigate the aggregate formation observed in the DLS studies, a series of DOSY ^{1}H NMR studies were conducted at 55.56 mM in a DMSO-d_6 0.5% H_2O solution. The translational diffusion constants obtained were applied to Stokes-Einstein equation, thereby allowing for the determination of the d_H. DOSY experiments for SSA **83** were conducted by Kira Hilton due to COVID restrictions, however DOSY experiments for SSA **82** and data analysis for both molecules were conducted by me. The d_H calculated for SSAs **82** and **83** are reported in Table 15.

Table 15. Calculated d_H.

The d_H (nm) calculated for the anionic and cationic components of SSAs **82** and **83** in a DMSO-d_6 0.5% H_2O solution.

	Calculated d_H (nm)	
	Anionic component	Cationic component
82	1.54	1.25
83	1.77	1.28

The diffusion rate of the anionic component of SSA **82** (highlighted in blue in Figure 72) was different to that of the TBA counter-cation (red), which was also consistent with SSA **83** (provided in the supplementary information). This confirmed previous findings of the TBA cation not being strongly coordinated to the anionic component. The d_H of anionic components measured were 1.54 nm (SSA **82**) and 1.77 nm (SSA **83**), which suggested the presence of lower-order species (monomers or dimers) as opposed to higher order species in the DMSO-d_6 0.5% H_2O solution. However, the solution being predominantly composed of lower-order species supported the hypothesis that the larger aggregates (>100 nm) were combinations of lower-order complexes.

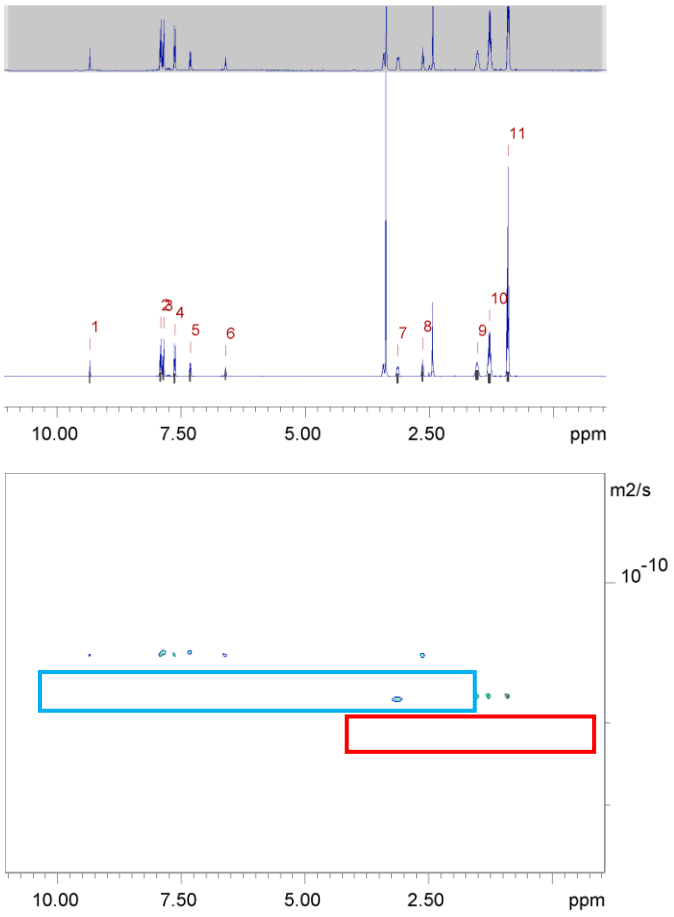

Figure 72. ^{1}H NMR DOSY.

Example ^{1}H DOSY NMR of SSA **82** at 55.56 mM in a DMSO-d_6 0.5% H_2O solution, conducted at 298.15 K. Anionic component highlighted in blue, counter cation (TBA) highlighted in red; d_H of the anionic component.

4.3.5.4. Quantitative NMR

Quantitative NMR studies are typically used to determine the concentrations and purity of low molecular weight molecules, such as the SSAs, through the use of an internal standard.[221,222] Within this study, q^{1}HNMR was utilised to confirm the presence of lower and higher order species observed in the DLS and ^{1}H DOSY NMR studies. Higher order species adopt solid-like properties, resulting in them becoming 'NMR-silent'.[153] The magnitude of the peak on an NMR spectrum is proportional to the nuclei present. Therefore, a comparative integration of the SSAs to a known internal standard allows for the percentage of compound apparently 'lost' – due to the formation of higher order

complexes – of SSAs to be calculated. Initially, q^{1}HNMR experiments were carried out on SSAs **82** and **83** in DMSO-d_6 0.5% H_2O solutions at 111.12 mM, using DCM (5 µL, 0.08 mM) as an internal standard due to its miscibility with DMSO and as the peaks for DCM could be differentiated from those of the SSAs. Relaxation rate was increased to 60s to ensure that the complete signal intensity was recorded. Complex formation at low concentrations could not be detected using this technique as this would fall below the detection limit of the NMR. The spectra obtained from these experiments are reported in Figure 73A and 73B.

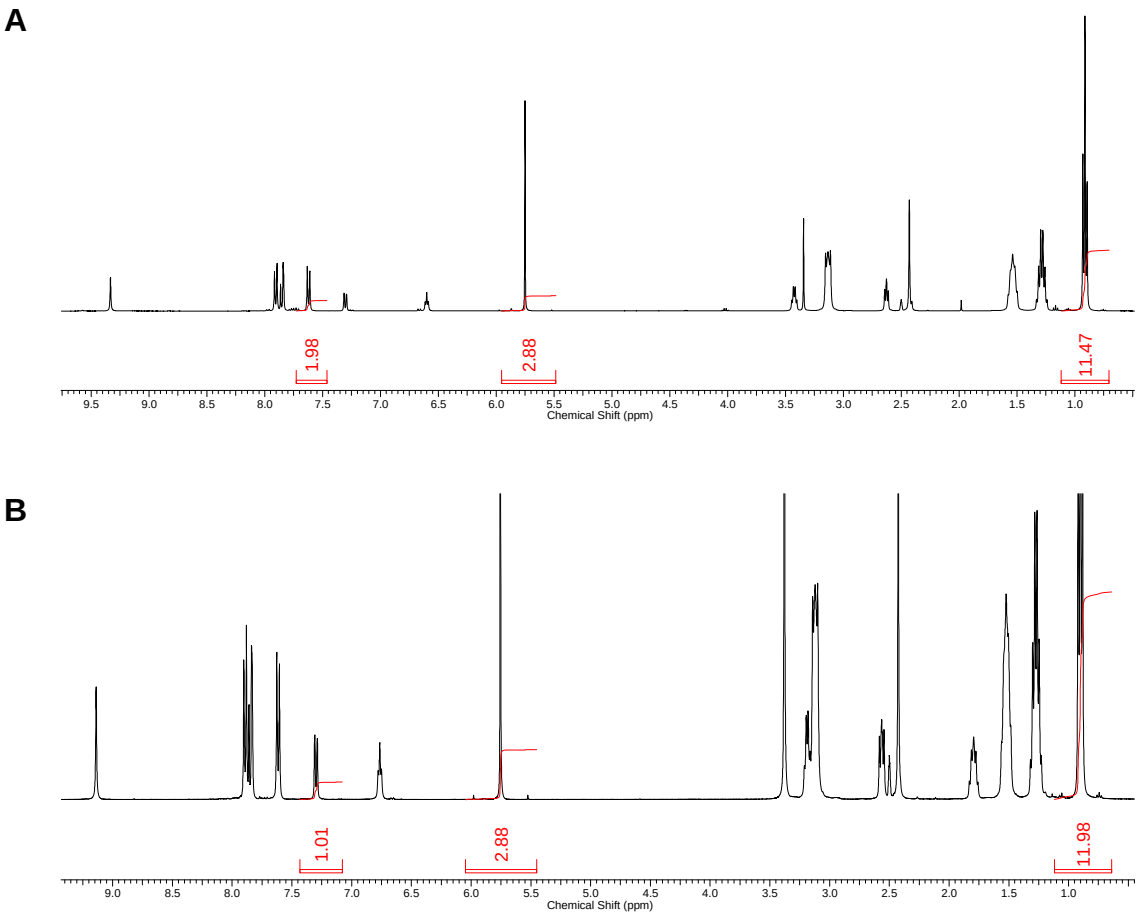

Figure 73. ^{1}HNMR spectra of (A) SSA 82 and (B) SSA 83 with a delay of 60 s. Quantitative ^{1}HNMR experiments were conducted in DMSO-d_6 0.5% H_2O solutions at 111.12 mM, using DCM (5 µL, 0.08 mM) as an internal standard.

While no apparent 'loss' of compound was observed for both SSAs in the DMSO-d_6 0.5% H_2O solution, DLS experiments had previously shown the presence of higher order species in DMSO solutions. This suggested the larger aggregates detected in the DLS

experiments (>100 nm) may have been present at too low concentrations or may have been tumbling too slowly to be resolved by q^1HNMR studies. Furthermore, this also suggests that the larger complexes observed were combinations of lower-order complexes. Following this, similar q^1HNMR experiments were conducted on SSAs **82** and **83** in solutions of EtOH:D_2O (1:19) at 5.56 mM, similar to the DLS conditions, with EtOH (25 µL) acting as the internal standard. The spectra obtained from those experiments are reported in Figures 74A and 74B, and the percentage 'loss' is reported in Table 16.

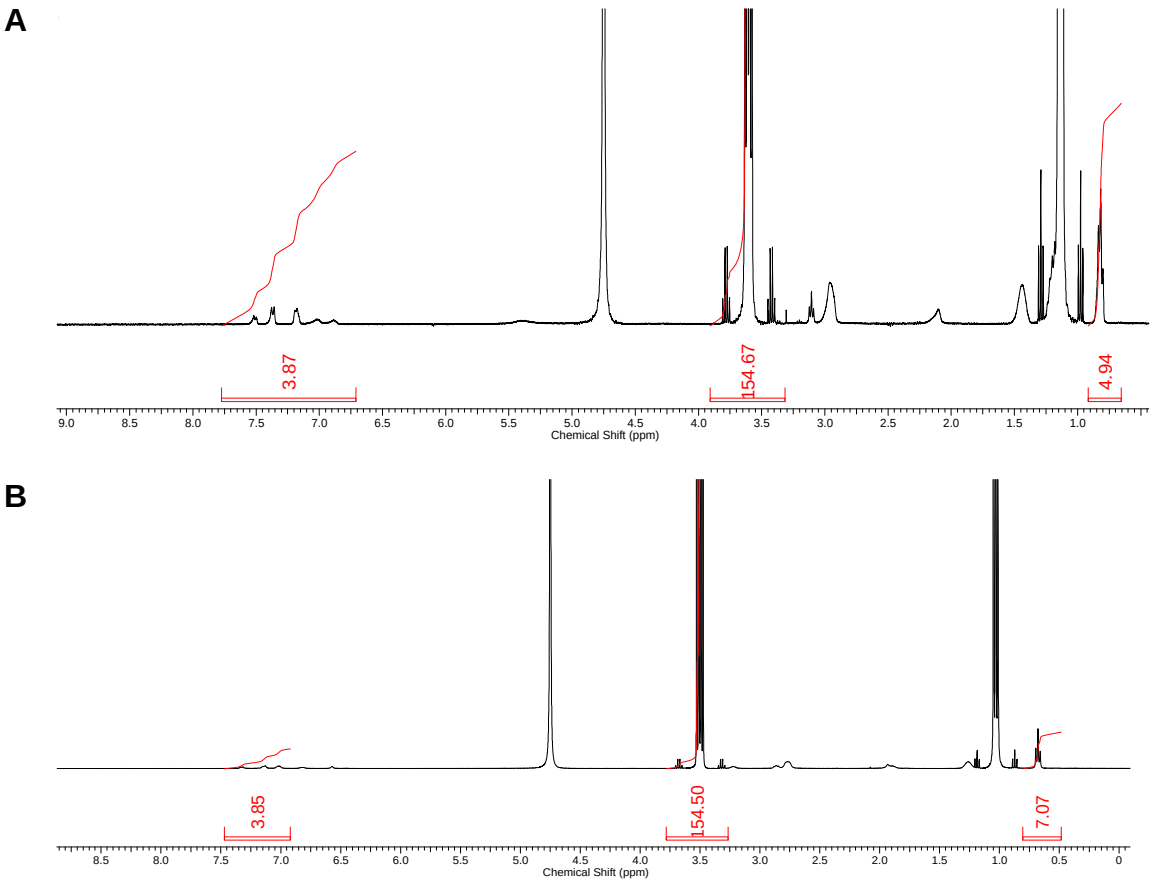

Figure 74. ^{1}HNMR spectra of (A) SSA 82 and (B) SSA 83 with a delay of 60 s.

Quantitative ^{1}HNMR experiments were conducted in EtOH:D_2O (1:19) solutions at 5.56 mM, using EtOH (25 µL, 0.43 mM) as an internal standard.

Table 16. Summary of the apparent percentage 'loss'.

Percentage 'loss' (%) values for the anionic and cationic components of SSAs **82** and **83** in EtOH:D_2O (1:19) solutions at 5.56 mM and in DMSO-d_6 0.5% H_2O solutions at 111.12 mM obtained from ^{1}HNMR experiments.

	Percentage 'loss' (%)			
	EtOH:D_2O (1:19)		DMSO-d_6 0.5% H_2O	
	Anionic	Cationic	Anionic	Cationic
82	45	59	0	0
83	36	41	0	0

Comparative integration against EtOH revealed a 45% 'loss' of the SSA 82 anion and a 36% 'loss' of the SSA **83** anion. Furthermore, a 59% 'loss' of the SSA **82** cation and a 41% 'loss' of the SSA **83** cation was observed, revealing the percentage of cation involved in aggregate formation. As mentioned previously, this apparent loss is attributed to the formation of higher-order complexes, as they can exhibit solid-like properties and are no longer observable by NMR, thus becoming signal silent. As these conditions mirror those of the DLS study in EtOH, this supports the observation of larger aggregates by both SSA **82** and SSA **83**. Strikingly, SSA **83** exhibiting a lower percentage 'loss', which suggested the incorporation of fewer molecules into the aggregate structures. The DLS studies conducted on SSA **83** revealed larger complex formation in comparison to SSA **82**. However, quantitative data obtained using these ^{1}H NMR studies suggest that this could be attributed to fewer larger complexes being formed by SSA **83** and multiple smaller complexes being formed in solutions of SSA **82**.

4.3.5.5. Zeta potential

Zeta potential experiments are used to define the stability of particles in solution, using well established guidelines.[223] Typically, a measurement more positive than + 30 mV and more negative than – 30 mV is considered stable. Liposomes, for example, are deemed stable when values fall between the range of – 10 mV and – 40 mV. Thus, zeta potential measurements were utilised to provide an indication of the stability of the higher order

aggregates formed by SSAs **82** and **83**. Zeta potential measurements were conducted as described in section **2.7.5** of the materials and methods, however briefly, solutions of SSA **82** and **83** (5.56 mM) in EtOH:H_2O (1:19) underwent an annealing process, similar to that of the DLS process, ensuring they had achieved their thermodynamic minimum. Following this, 10 consecutive zeta potential measurements were obtained, the average of values of which are reported in Table 17.

Table 17. Summary zeta potential measurements.

The final zeta potential value reported is an average of 10 consecutive experiments conducted with SSAs **82** and **83** and the standard error of the mean (s.e.m) used as the error value. Experiments were conducted in EtOH:H_2O (1:19) at 25°C.

Zeta Potential Summary	
	Zeta Potential (mV)
82	-30.22 ± 0.0025
83	-55.76 ± 0.0001

SSA **82** was observed forming stable aggregates, shown by the zeta potential value of -30.22 mV. Contrastingly, zeta potential experiments revealed the aggregates formed by SSA **83** were unstable, as shown by the zeta potential value of - 55.76 mV. An analysis of DLS studies supports these observations, as when the concentration of SSA **83** was decreased, the size of the resultant aggregates significantly decreased. This further solidifies the hypothesis that the aggregates formed by SSA **83** could be disrupted by the competing solvent environment, thus reducing the stability of these aggregates.

4.3.5.6. ^{1}H NMR Dilution studies

To quantify the strength of hydrogen-bonded complexes, a series of ^{1}H NMR dilution studies were carried out. Solutions of SSAs **82** and **52** were prepared in DMSO-d_6 0.5% H_2O at 112 mM, then serial dilutions were prepared from the same sample, obtaining a ^{1}HNMR spectra with each dilution. The downfield shift with increasing concentration of the HBD N-H resonances was measured and plotted against the concentration (Figure

75), then the data was fitted to two self-associative isotherms using BindFit v0.5[224]; the cooperative equal K (CoEK) model and the dimerisation / equal K (EK) model.[225] The CoEK model assumes the first self-associative event is different from successive interactions, whereas the EK model assumes all self-associative events occurring are equal.[154,224,225] Data fitted to both models allow for the derivation of self-association constants, which can be used to compare the strength of self-associative structures.

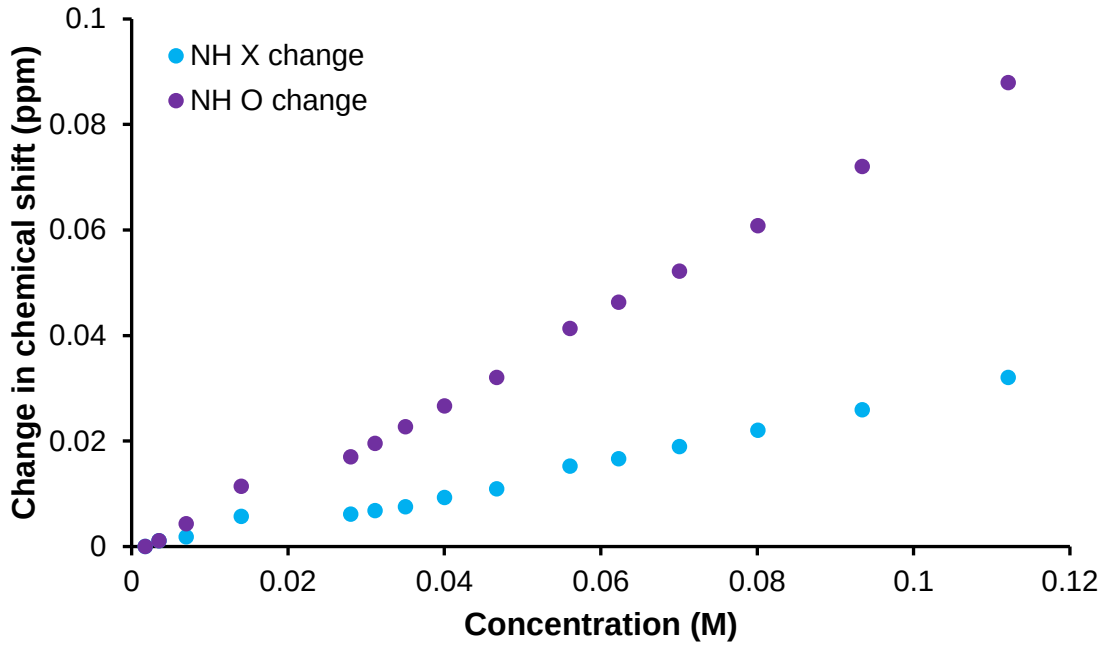

Figure 75. Downfield Chemical Shift Graph.

(A) SSA **82** was serially diluted, and the downfield chemical shift of the urea NH resonances with increasing concentration was recorded and plotted.[224,225]

A summary of the self-association constants calculated for SSAs **82** and **83** are reported in Table 18.

Table 18. Summary Self-association constants.

Self-association constants (M^{-1}) for SSAs **82** and **83** in a solution of DMSO-d_6 0.5% H_2O at 298 K, derived using the EK and CoEK binding models; K_e – aggregation constant, K_{dim} – association constant and ρ: cooperativity factor.[154,225,226]

Self-association constants					
	EK (M^{-1})		CoEK		
	K_e	K_{dim}	K_e (M^{-1})	K_{dim} (M^{-1})	ρ
82	1.83e-3 ± 2.31e-3	9.16e-4 ± 1.16e-3	-3.43 ± 4.10	-1.72 ± 2.05	0.75 ± 1.77
83	12.55 ± 2.04	6.28 ± 1.02	27.07 ± 2.27	13.54 ± 1.14	0.4 ± 11.09

A comparison of the errors produced by the EK and CoEK binding models reveals a preference to the dimerisation EK binding isotherm (K_{dim}), as such these association constants are used in the comparison. The association constants for both SSAs **82** and **83** were relatively low, with K_{dim} values < 15 M^{-1}. Additionally, the K_{dim} value of SSA **82** (K_{dim} = 9.16e-4 M^{-1}) was significantly lower than that of SSA **83** (K_{dim} = 6.28 M^{-1}). From these data, it can be concluded that the low-order structures formed are most like dimers, as the dimerisation EK binding isotherm was preferred, and SSA **83** has a greater propensity to dimerise and a higher binding strength in comparison to SSA **82**.

4.4. Antimicrobial studies

Following the physicochemical analysis, antimicrobial analyses were conducted using SSAs **82** – **85**. It was previously hypothesised that SSA **82** would possess higher antimicrobial efficacy, due to the higher stability exhibited by complexes, in comparison to SSA **83**, and SSA **84** would improve *E. coli* activity due to the carboxylate functionality.

4.4.5.1. Analysis of Growth dynamics and kinetics

To examine the antimicrobial efficacy of SSAs **82** – **85**, antimicrobial screening (described in sections **2.4.3** and **2.4.6** of the materials and methods) was conducted on *E. coli* DH10β and MRSA USA300. OD values were utilised to calculate the growth rate of the exponential phase, as described by Fattah et al., (2018) Stensjøen et al. (2015),

and the percentage change in growth (section in **2.4.9** materials and methods).[114,115] Similar to previous antimicrobial studies, SSAs that decreased bacterial growth by > 10% were deemed to have passed the antimicrobial screening and taken forward for MIC determination. The type of inhibition exhibited by the SSAs was determined qualitatively using the growth curves and categories previously described in Chapter 3. Screening results are summarised in Table 19.

Table 19: Growth parameters.

Average growth rates (*k*, mins), type of inhibition observed, and the percentage change in growth (%) of MRSA and *E. coli* in the presence of SSAs **82** - **85**. [a] - growth rate assumed to be zero due to lack of growth; [p] – passed the screening process (defined by a reduction in growth of > 10%); controls – growth rates of bacteria in the absence of compounds

Calculation of growth parameters						
	***k* (mins.)**		**Type of inhibition**		**Percentage change (%)**	
	E. coli	**MRSA**	***E. coli***	**MRSA**	***E. coli***	**MRSA**
82	247.66 ± 5.60	[a]	Partial/delayed	Complete	48.66 [p]	92.25 [p]
83	475.3 ± 193.55	[a]	Partial	Complete	70.02 [p]	98.86 [p]
84	435.44 ± 60.97	[a]	Partial	Complete	86.42 [p]	97.97 [p]
85	233.61 ± 28.71	[a]	Partial	Complete	45.74 [p]	101.73 [p]
Controls, *k* (mins): *E. coli* = 78.57 ± 7.61, MRSA = 65.10 ± 1.12						

All SSAs exhibited complete inhibition of MRSA, as no growth was detected throughout the growth period. An examination of MRSA growth curves produced by SSA **84** revealed OD values below those of the growth curve towards the end of the growth period, and a minimal increase in OD values was observed between 0 – 200 minutes. SSA **84** was observed to be unstable over time, which may be the cause of these observations, however, the growth curve produced in the presence of SSA **84** was not significantly different from the growth curves with the other SSAs (Figure 76).

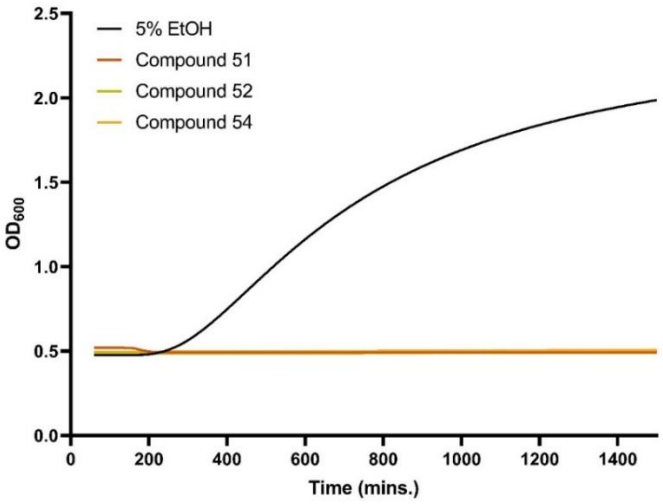

Figure 76. Example growth curves of MRSA demonstrating complete inhibition.
MRSA growth in the presence of SSAs **82** – **85** at 3.3 mM compared to the 5% EtOH growth control.

Although complete inhibition was observed, SSA **84** could not be taken forward for MIC_{50} calculations due to its instability over time.

While differences exist between the MRSA percentage decrease values for SSA **82**, **83**, and **85**, an examination of the growth curves revealed a minimal difference in growth effects (Figure 76). Furthermore, growth rates could not be calculated for SSAs **82** – **85** using the MRSA data, as no exponential phase was observed. As such, the following comparisons discuss the activity against *E. coli* only.

The data presented in Table 19 reveals higher activity by SSA **84** in comparison to all the molecules tested in this series of compounds. SSA **84** decreased growth by 86.42% and the growth rate of *E. coli* in the presence of this SSA was one of the slowest growth rates recorded for *E. coli*. The second most effective SSA in this series of molecules was SSA **83**, which decreased growth by 70.02%. While the growth rate produced by SSA **83** was numerically higher than SSA **84**, the errors associated with this growth rate value suggest no significant difference between the two values. Contrary to the earlier hypothesis, SSA **82** exhibited lower activity in comparison to SSA **83**, as it decreased bacterial growth by 48.66% and a faster growth rate (247.66 minutes) was observed in the presence of this compound. This suggested a lower impact on *E. coli* growth in comparison to SSA **83**. The delayed inhibition observed with SSA **34** was not observed with SSA **83**, instead, partial inhibition was observed, as shown in Figure 77.

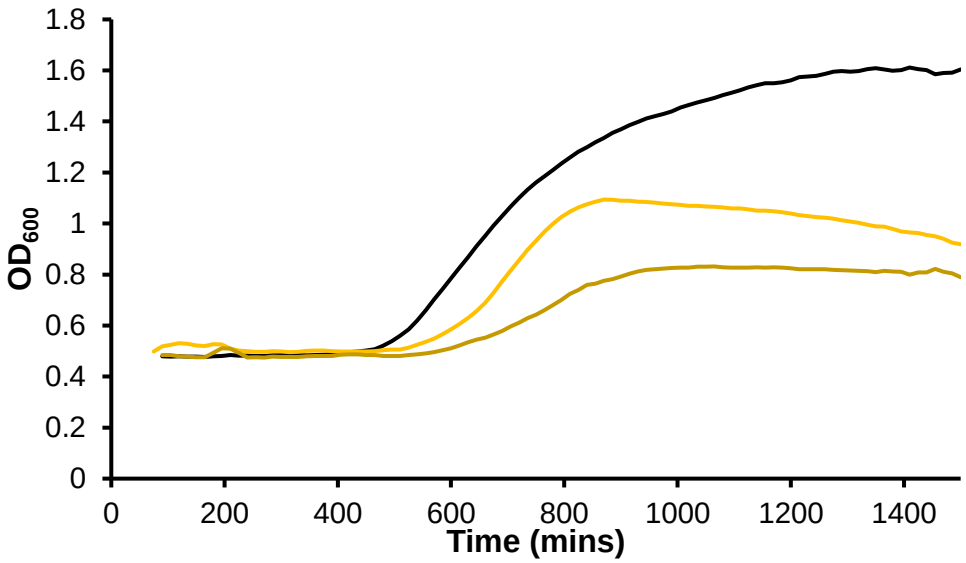

Figure 77. Example growth curves of *E. coli* demonstrating partial/delayed and partial inhibition of SSAs 82 and 83, respectively.

E. coli growth in the presence of SSAs **82** and **83** at 3.3 mM compared to the 5% EtOH growth control.

Furthermore, while delayed inhibition was exhibited in the presence of SSA **82**, this was more gradual in comparison to SSA **33**. This suggested differing impacts or interactions to the membrane in comparison to SSAs **33** and **34**. The weakest activity in this group of SSAs was SSA **85**, its only difference to SSA **70** being the removal of the CH_3 attached to the ring system (Figure 78).

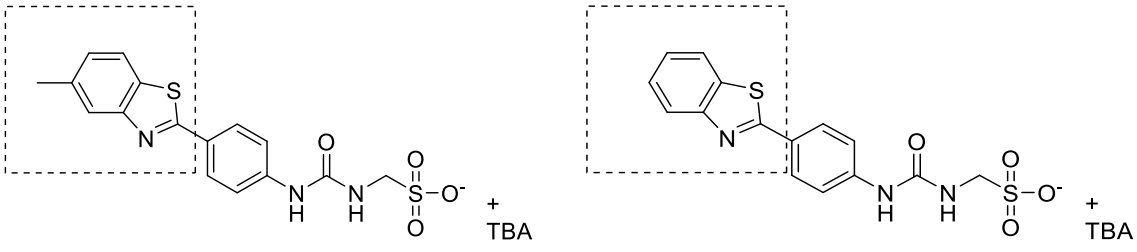

Figure 78. Comparison between the structures of SSAs (A) 70 and (B) 85.

Structures differ in the presence/absence of the CH_3 associated with the ring system (highlighted region).

Initial comparisons suggest a higher activity by SSA **85** in comparison to SSA **70**, as SSA **70** reduced *E. coli* growth by 27.12%, whereas SSA **85** decreased growth by 45.74%. However, further comparisons can be made through the use of MIC_{50} calculations.

4.3.1.1. MIC_{50} determination

As previously described, MIC_{50} values represent the concentration at which 50% of isolates in a test bacterial population are inhibited by an antimicrobial molecule.[167,168] Following the screening, MIC_{50} values were determined for SSAs that inhibited growth by > 10%, as defined by the screening parameters (sections **2.4.4**, **2.4.7,** and **2.4.8** of the materials and methods). MIC_{50} values are reported in Table 20, along with the MIC_{50} values for SSAs **34**, **61**, and **70** from the previous study.

Table 20: MIC_{50} values obtained for SSAs 82 – 85.

MIC_{50} values (mM) were calculated for SSAs that passed the screening. Most effective SSAs from prior studies are included to provide comparisons. [a] – unable to calculate MIC due to compound instability, [b] – unable to MIC_{50} due to crystallisation of compound, * - predicted endpoint used to calculate MIC_{50} due to solubility of SSA under experimental conditions.

	MIC_{50} values	
	MIC_{50} (mM)	
	E. coli	MRSA
82	2.16*	1.20
83	1.16*	0.59
84	[a]	[a]
85	3.38*	1.14
34	1.48*	[b]
61	1.25	1.14
70	5.00*	0.93

The data presented in Table 20 reveals a higher efficacy of SSAs **82** and **83** against *E. coli* in comparison to SSA **70**. The MIC_{50} value obtained for SSA **82** (2.16 mM) was significantly lower than that of SSA **70** (5.00 mM). Similarly, SSA **83** produced an MIC_{50} value of 1.16 mM, which was not only lower than that of SSA **70**, but the lowest MIC_{50}

obtained against *E. coli* for all the molecules tested so far. The previously lowest MIC_{50} values against *E. coli* were 1.25 mM (SSA **61**) and 1.48 mM (SSA **34**), as shown in Table 20. While it was predicted the MIC_{50} for SSA **84** would be lower than those obtained for SSAs **82** and **83**, its instability over time prevented MIC_{50} analysis. While SSA **85** exhibited improved *E. coli* activity in comparison to SSA **70**, it produced a higher MIC_{50} value (3.38 mM) in comparison to SSAs **82** and **83** and was, therefore, less effective. Thus, improved *E. coli* activity may be achieved through further optimisation to improve the stability of SSA **84** and through the use of the extended alkyl chain (n=3) in SSA **83**.

A comparison of the MIC_{50} values obtained against MRSA reveals a differing trend in activity. SSA **83** produced the lowest MIC_{50} value (0.59 mM) in this series of molecules. Furthermore, the incorporation of the benzothiazole ring system provided additional stability to SSA **83** in comparison to SSA **34**, as the crystallisation observed with SSA **34** that prevented accurate antimicrobial analysis was not observed with SSA **83**. This could be utilised in improving SSA stability. SSA **82**, however, was far less effective against MRSA in comparison to SSA **70**, as their MIC_{50} values were 1.20 mM and 0.93 mM, respectively. This was consistent with earlier observations, as SSA **70** was more effective against MRSA than SSA **34**, the single ring analogue to SSA **82**. The MIC_{50} value obtained for SSA **85** was 1.14 mM, which was higher than those of SSAs **83** and **70**, but lower than that of SSA **82**. It can therefore be concluded that the CH_3 associated with the aromatic ring contributed to the antimicrobial activity observed against MRSA and its removal, as seen in SSA **85**, decreased antimicrobial efficacy.

While the MIC_{50} value obtained for SSA **61** against MRSA was low in comparison to other SSAs tested, it was not the most effective within the first set of SSAs. Furthermore, other functionalities were observed to improve MRSA activity more than the carboxylate group present in SSA **61**. It was therefore hypothesised that while improved MRSA activity would be observed with SSA **84**, it would still not be as active as SSAs **36** and **39**, which obtained the lowest MIC_{50} values (0.25 mM and 0.35 mM respectively).

4.4. Gel Characterisation

Supramolecular gel formation is another self-assembly process that results in the formation of a soft solid-like material. Similar to the aggregates formed in solution, supramolecular gels are formed through reversible non-covalent interactions between molecules, which result in a network of fibres. Three main categories are typically used to characterise supramolecular gels, depending on the solution present. Organogels are gels that utilise non-polar and polar organic solvents, and ionogels are gels that utilise ionic liquids.[227–232]

The third type of gel is a hydrogel, which are the gels formed by the SSAs in this study. Supramolecular hydrogels are self-assembling polymeric networks of molecules that contain solvents predominantly made up of water.[232,233] Hydrogels are preferable particularly in drug design, due to their high biocompatibility and flexibility.[232,234,235] Furthermore, their reversible nature allows hydrogels to respond to external stimuli, such as pH, salt content, and temperature, therefore allowing their properties to be easily manipulated. However, hydrogels are diverse in structure, and their dynamic nature and the properties of the monomeric units endows them with unique properties.[155,233,235]

Characterisation of supramolecular gels provides information about the SSA-solvent interactions, enabling better manipulation and further optimisation of desired properties.[232,234] As such, the gels formed by SSAs **82** and **83** were characterised as described below. Due to COVID restrictions, the inversion tests were conducted by Lisa White, and rheometry experiments were conducted by Kira Hilton, however, data analysis, antimicrobial analysis, and microscopy studies were conducted by me. The gel characterisation of SSA **85** was conducted as part of a separate study and is therefore not reported below.

4.4.2. Inversion test and MGC

SSA **70** has been previously shown to gelate in the presence of various salt solutions. As such, six salt solutions were selected from the study conducted by Hiscock et al. (2020) to elucidate the impact of different salt solutions in an aqueous environment on gel fibre

formation.[155] Gelated materials were formed by dissolving SSA **82** and **83** (5 mg) in the appropriate sodium salt solutions (1 mL, 0.505 M), then heating these solutions at ~40°C and allowing them to cool to 25°C. The presence of a stable gel was determined by reproducible *n=3* inversion tests, in which the vials containing the SSA gels were upturned and the gel was characterised by the resistance to flow.[236] Inversion tests were utilised in the determination of the minimum gelation concentration (MGC), defined as the lowest gelator concentration required to form a stable gel. If the gel was able to retain its shape post inversion, then the MGC was determined. However, if the gel was not able to retain its shape, then the MGC was determined to be > 5 mg/mL and a further analysis was not conducted using inversion tests as gel processes could not be confirmed using MGC. A detailed description of this method is provided in in section **2.7.11** of the materials and methods. The minimum gelation concentrations of SSAs **82** and **83** are reported in Table 21.

Table 21: Minimum gelation concentrations obtained from inversion tests.

Minimum gelation Concentration (mg/mL)		
	SSA 82	**SSA 83**
NaCl	> 5	> 5
KCl	> 5	> 5
Na_2SO_4	> 5	> 5
NaH_2PO_4	> 5	> 5
$NaNO_3$	> 5	> 5
NaOBz	> 5	> 5

The inversion test revealed the gels formed by SSAs **82** and **83** were not stable, as they were not able to retain their shape when inverted in any of the sodium salt solutions. While the MGCs for SSAs **82** and **83** were all determined to be above 5 mg/mL, the effects of the different sodium salts on the observed gel strength can be compared.

NaCl and KCl differ in the anion-cation coordination; Na^+ is more strongly coordinating in comparison to K^+. SSA **70** was previously reported to form comparatively stronger gels when the salt solution used contained a weakly coordinating cation, as this enabled gel

formation. A similar trend is observed with SSA **82**, as gels were able to retain their shape more effectively with KCl present in comparison to NaCl (Figure 79A & 79B)

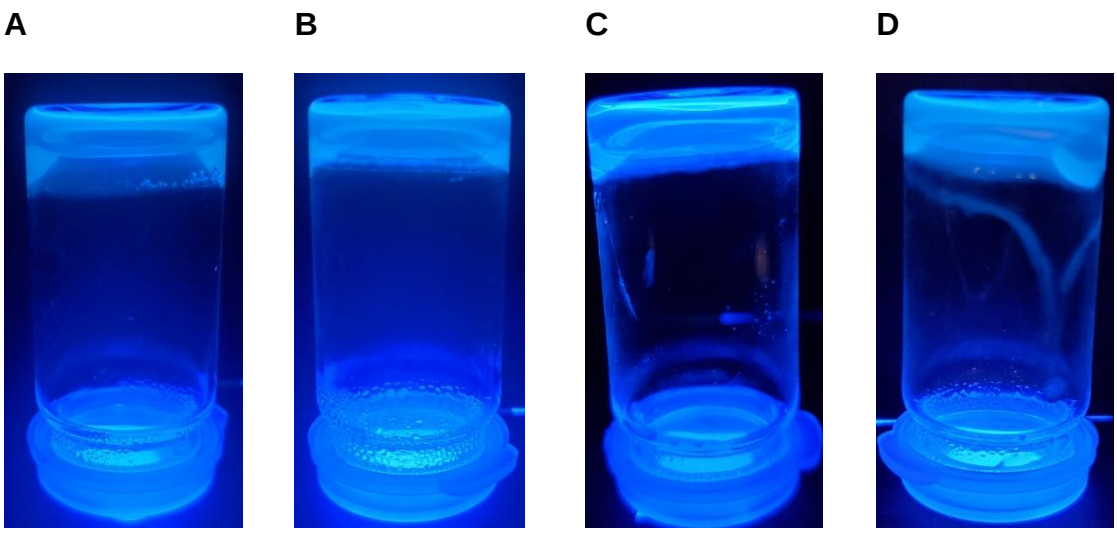

Figure 79. Results from the inversion tests.

Experiments conducted using SSA **82** (5 mg/mL) in **(A)** NaCl and **(B)** KCl and SSA **83** (5 mg/mL) in **(C)** NaCl and **(D)** KCl. Salt concentrations = 0.505 M, experiments conducted at 25°C.

This would support the hypothesis presented by Hiscock et al. (2020); that strong ion pair effects disrupt self-association events, leading to the instability of the gel structure. Conversely, the SSA **83** gels were able to retain their shape more effectively when NaCl was present, in comparison to KCl (Figure 79C & 79D). The strong ion-pair effects did not negatively impact the strength of the gel, suggesting differing gel fibre formation processes in comparison to SSA **82**. The inversion test results using SSA **82** gelated in $NaNO_3$ revealed more effective shape retention in comparison to NaCl (Figure 80).

Figure 80. Results from the inversion tests.

Experiments conducted using SSA **82** (5 mg/mL) and $NaNO_3$ (0.505 M). Experiments were conducted at 25°C.

A significantly weaker gel was observed with SSA **82** in NaH_2PO_4, as the resulting gel was unable to hold its shape (Figure 81A), in comparison to SSA **83** which was able to hold its shape in the presence of NaH_2PO_4 (Figure 81B).

A **B**

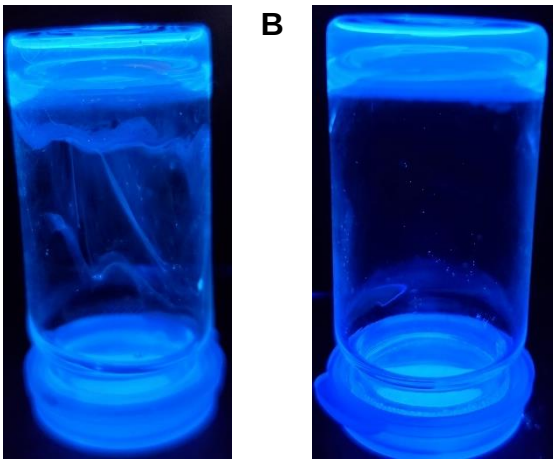

Figure 81. Results from the inversion tests.
Experiments conducted using **(A)** SSA **82** (5 mg/mL) and **(B)** SSA **83** (5 mg/mL) in NaH_2PO_4 (0.505 M). Experiments were conducted at 25°C.

The weakest gels were observed when SSAs were dissolved in NaOBz, as SSAs **82** and **83** were unable to retain their shape. Despite the resulting SSA **83** gel appearing more viscous in comparison to SSA **82**, both gels exhibited more liquid-like behaviour in comparison to those in NaCl (Figure 82).

A **B**

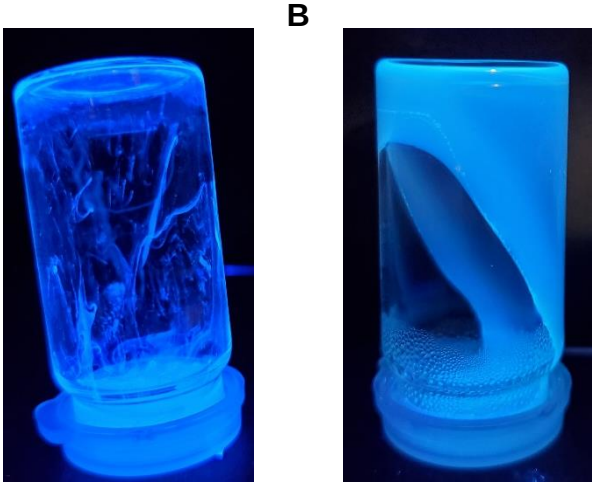

Figure 82. Results from the inversion tests.
Experiments conducted using **(A)** SSA **82** (5 mg/mL) and **(B)** SSA **83** (5 mg/mL) in NaOBz (0.505 M). Experiments were conducted at 25°C.

Minimal differences were observed between SSA **82** gels in NaCl and Na_2SO_4 (Figure 83A), and also between SSA **83** gels in NaCl, $NaNO_3$, and Na_2SO_4 (Figure 83B & 83C).

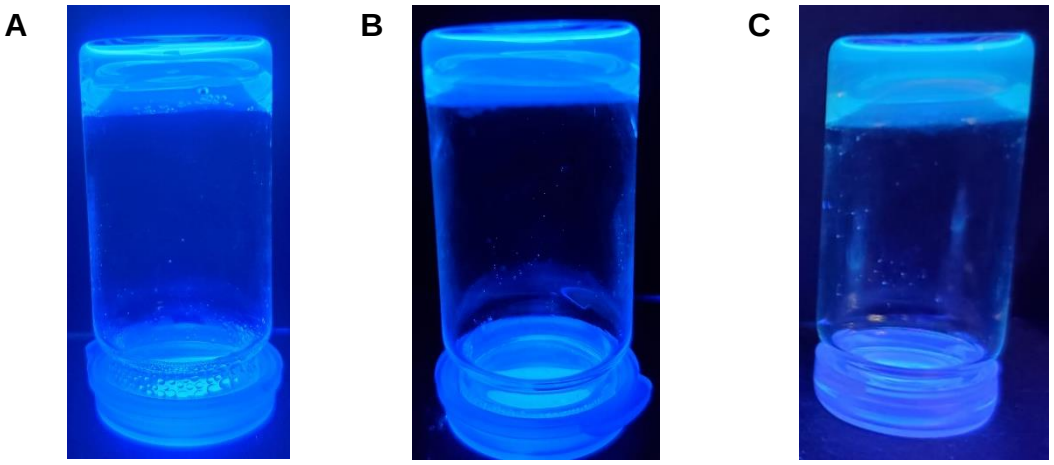

Figure 83. Results from the inversion tests.

(A) SSA **82** in Na_2SO_4 SSA **(B) 83** in $NaNO_3$, **(C)** SSA **83** in Na_2SO_4. Experiments were conducted at 25°C using SSAs at 5 mg/mL and salt solutions (1 mL) at 0.505 M.

4.4.3. Rheology

Information about the mechanical properties, structure, and assembling dynamics of a supramolecular gel can be determined using rheology.[155,237–241] In this technique, gelated materials are subjected to tensile and compressive stresses, and their deformation and flow behaviour are observed.[237–239]

The flow and deformation behaviour can be quantified by the elastic properties storage (G') and loss moduli (G''). The storage modulus is a measure of the energy stored during a strain cycle, whereas the loss modulus is a measure of the energy lost.[237–239] The dissipation factor (tan δ) is expressed by the ratio G''/G', which can assess the dominance of solid-like or liquid-like behaviour. When tan δ > 1 (G'' > G'), the material displays viscous liquid properties, and when tan δ < 1, (G'' < G'), the material displays more solid-like properties.[237–239]

Typically, these properties are independent of applied stress and behave as elastic materials (G'' > G') up to the yield point, where the material's behaviour is no longer linear. [155,238,239] At the yield point, G' decreases along with the structural strength of the material, down to a critical point known as the gel-sol transition point.[238] A graphical representation of these regions is presented in Figure 84.

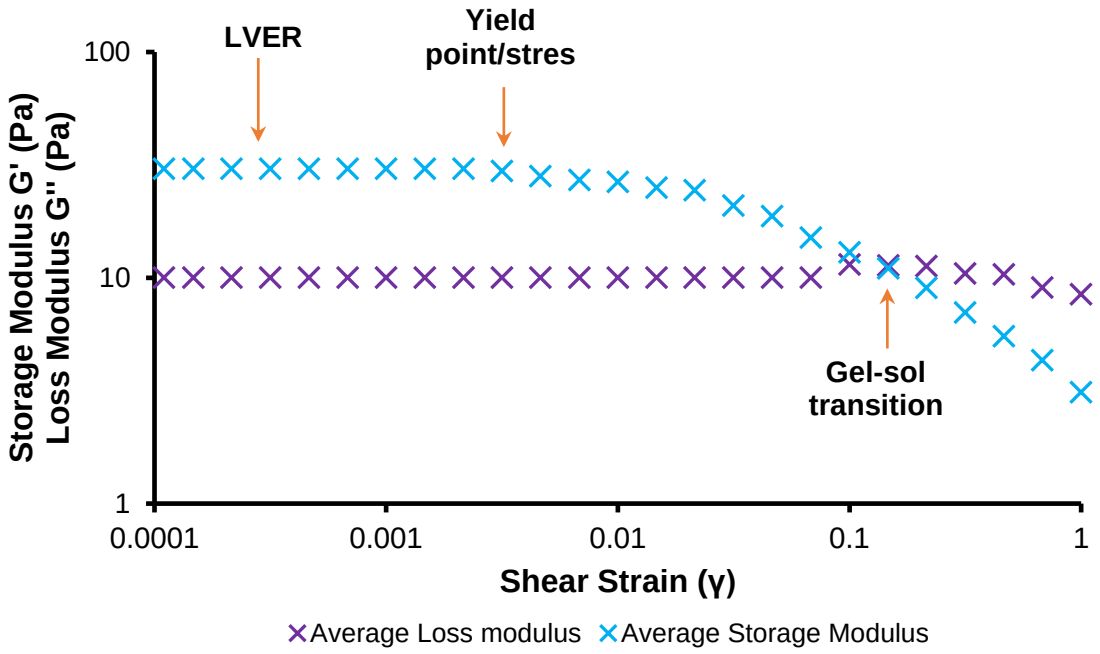

Figure 84. Graphical representation of the amplitude sweep experiments.

Graph showing the linear viscoelastic region (LVER), yield point, and the critical/flow point (gel-sol transition).

Amplitude sweep experiments are typically used as an initial evaluation of the stress dependence of G' and G'' and the linear viscoelastic region (LVER) can be established.[234,238,239] The LVER region is defined as the region where the material can undergo experimental procedures without a loss of structural integrity.[155,238] Below this point, the material is more solid-like and above this, the material is more fluid.[238,239]

Therefore, amplitude sweeps were conducted using SSA **82** and **83** gels in the six salt solutions tested in the inversion tests to determine their viscoelastic properties. In all of the salt solutions tested, gel-sol transition points were not observed when rheology experiments were conducted, as shown in Figure 85A. Furthermore, a gel-sol transition point was observed with SSA **82** in a solution of Na_2SO_4, the storage modulus was lower than the loss modulus (Figure 85B).

A

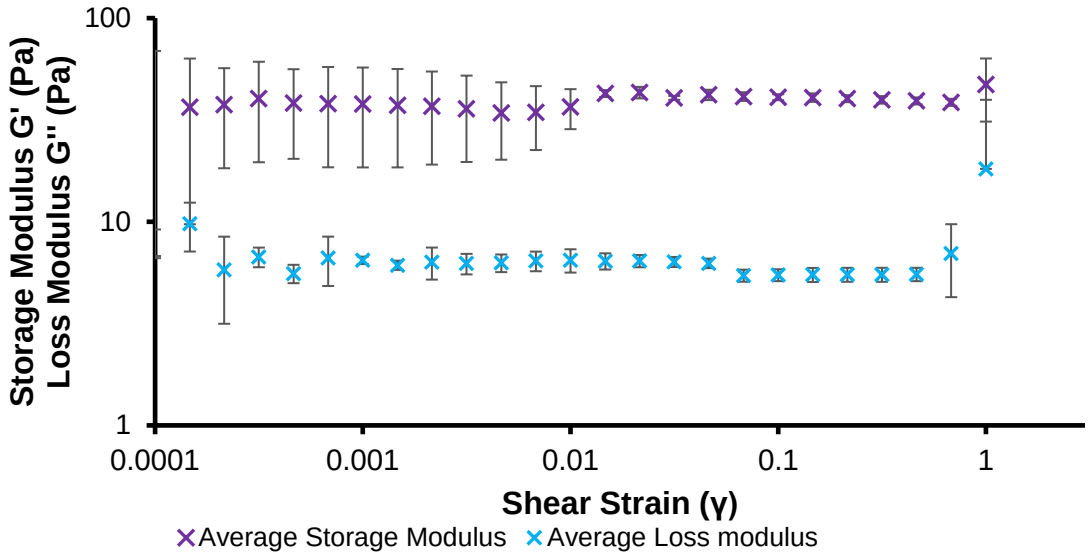

B

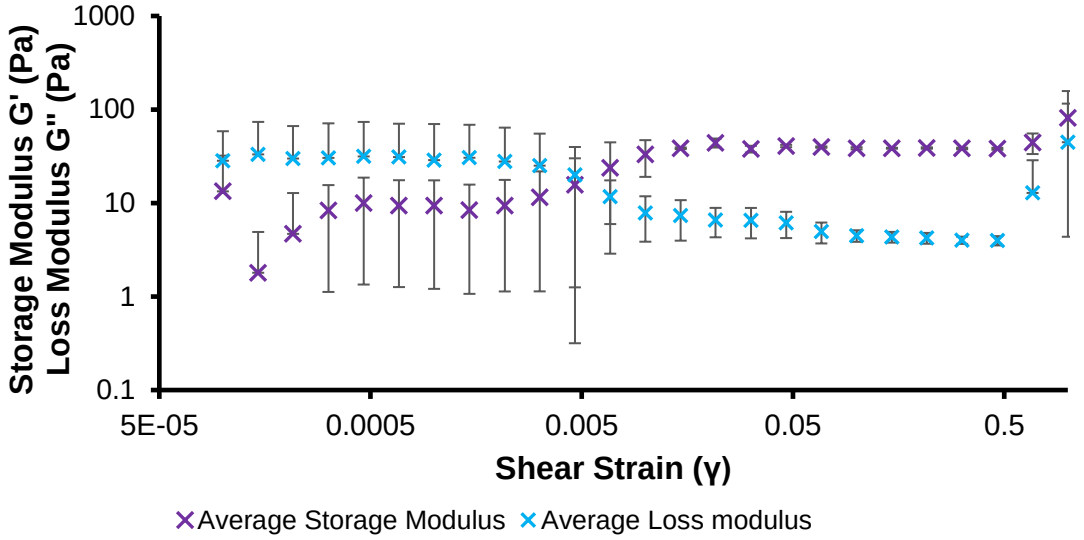

Figure 85. Example graph of amplitude sweep experiments conducted on SSA 82 (5 mg/mL) in (A) $NaNO_3$ and (B) in Na_2SO_4.

Data points are an average of 3 results, using the standard deviation as the error value; salt solutions at 0.505 M; experiments conducted at 25°C. 1 = 100%.

This indicated that the gel exhibited more fluid properties at the start of the experiment, and the transition into a solid material was likely induced by mechanical stress, in addition to the presence of the salt (Figure 85). The absence of a gel-sol transition point and fluid properties exhibited in Na_2SO_4 suggested a lack of homogeneity in the gels formed by

SSA **82**, thus further analysis using rheometry was not possible, as this is a requirement of this technique. Amplitude sweep experiments were also conducted on SSA **83** in NaCl, which had previously exhibited the most effective shape retention from the inversion tests (Figure 86).

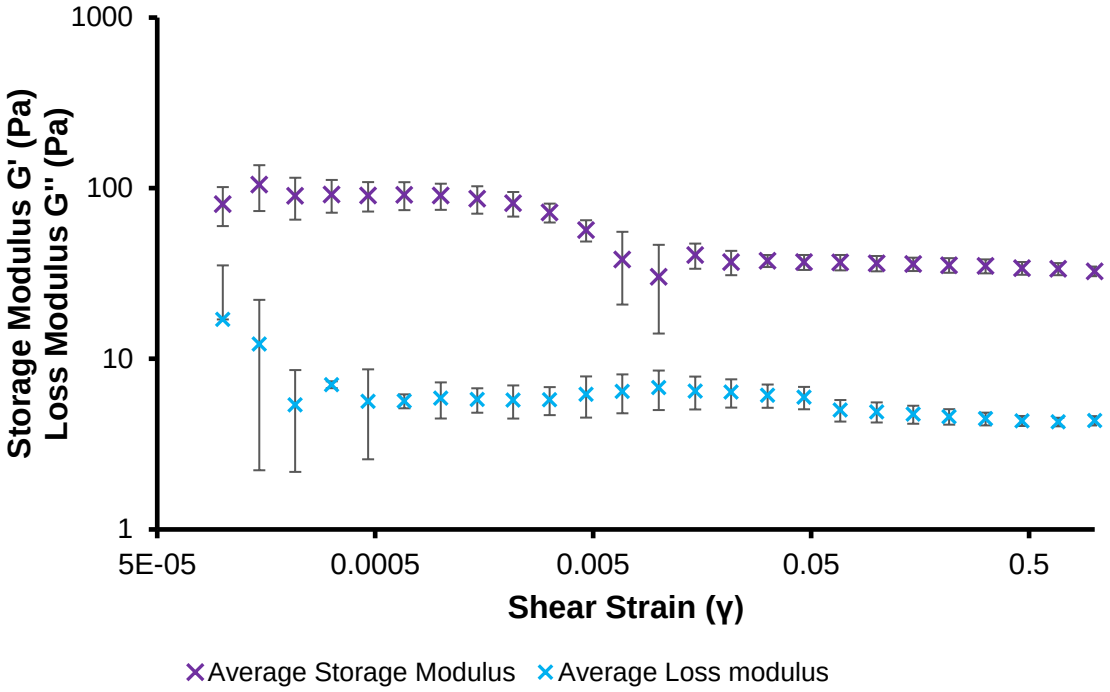

Figure 86. Example graph of amplitude sweep experiments conducted on SSA 83 (5 mg/mL) in NaCl.

Data points are an average of 3 results, using the standard deviation as the error value; salt solutions at 0.505 M; experiments conducted at 25°C. 1 = 100%.

However, due to the absence of a gel-sol transition point, amplitude sweep experiments were not conducted with SSA **83** in the presence of the other salts.

4.5. Microscopy studies

Scanning electron microscopy (SEM) is a microscopic technique that utilises a narrow electron beam to produce high-resolution images.[242,243] Typically, SEM is utilised in the examination of hydrogel microstructure, however, hydrogels must be dehydrated for this technique, bringing the fibres formed out of their native environment.[234,244] Furthermore, the formation of dehydrated hydrogels, known as xerogels, can be destructive and

produce artifacts in the final images observed.[234,244] Consequently, as SSAs **82**, **83**, and **85** were intrinsically fluorescent, widefield fluorescence microscopy was utilised to observe the gelation properties of SSAs **82**, **83**, and **85** in the six salt solutions tested previously. While this microscopic technique produces comparatively lower resolution images, the native fibre can be observed within the solvent environment without destruction of the gel.

Gel microscopy was carried out by first creating a chamber using a microscope slide and a coverslip, which were secured on three ends. Gel solutions were then prepared by dissolving SSAs (5 mg) in the appropriate sodium salt solution (1 mL) and heated to ~40°C. Molten gel solutions were then pipetted into the chamber and allowed to form on the microscope to enable imaging of the initial stages of gel formation. Further details of this method are provided in section **2.5.4** of the materials and methods.

4.5.1. Gel fibre characterisation

It was discovered that the time taken for gelated materials to form differed significantly, thus images were taken at differing time points depending on each gel solution. The time taken for the final gel structure to form – defined by no further changes occurring to the structure observed – was recorded and used in the comparison.

The microscopy images obtained using SSAs **82**, **83**, and **85** also revealed significantly varied gel fibre formation with differing salt solutions of the same SSA. Consequently, categories were created to characterise the gel fibres observed. Gel fibres were classified into the following categories; straight or curled; crosslinked or independent; short or long; densely packed, medium packing density or loosely packed; uniformly arranged or stochastically arranged; unidirectional fibres or multidirectional fibres.

To define gel fibre packing density, three categories were created. Gel fibres that close together with very little solvent was visible were classified as being densely packed (Figure 87A).

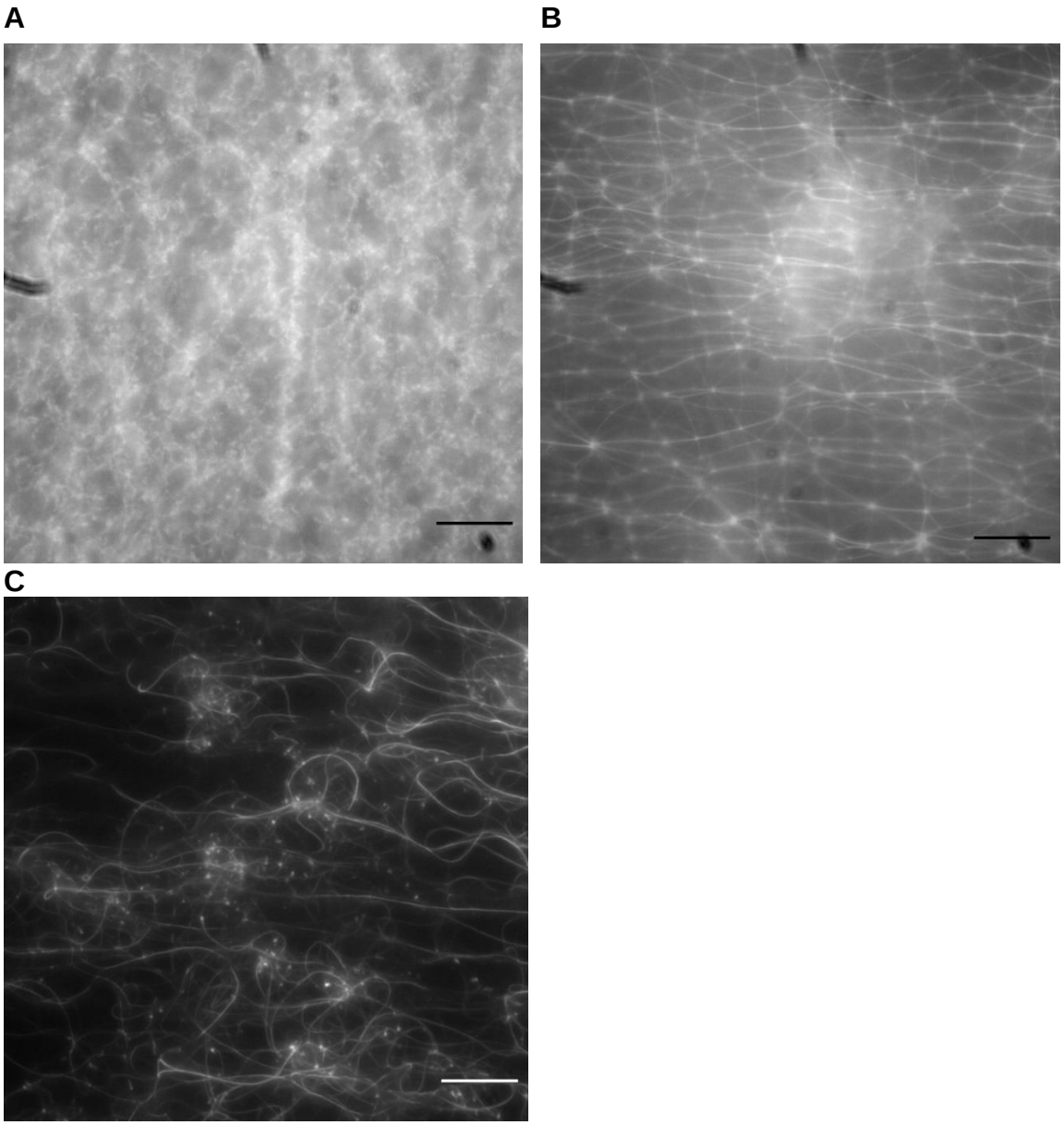

Figure 87. Example images used to define packing density of gel fibres.

(A) densely packed gel fibres; SSA **83** (5 mg) in an $NaNO_3$ solution (1 mL, 0.505 M), **(B)** medium packing density; SSA **82** (5 mg) in an NaCl solution (1 mL, 0.505 M) **(C)** loosely packed gel fibres; SSA **85** (5 mg) in an $NaNO_3$ solution (1 mL, 0.505 M). Scale = 15 µm.

Medium packing density was defined by gel fibres with larger amounts of solvent visible, but the fibres were held close together due to cross-linking (Figure 87B). Gel fibres with large amounts of visible solvent regions and easily discernible individual strands or independent strands that were not held together were defined as loosely packed (Figure 87C). Gel fibres were measured in order to determine whether they were long or short,

and all other categories were quantitatively determined. This provided a way to observe patterns between the salt solution present and the gel strand formed.

During the imaging process, some gels were observed to have large amounts of sol surrounding the resulting gel, which was not incorporated into the matrix. This resulted in gel movement on the microscope slide, thus, resulting gels were further categorised as either stationary or motile, depending on whether any movement was observed by microscopy.

4.5.2. Measurement of gel fibres

To measure gel fibre length, gel images were opened in ImageJ and the scale was set. Following this, the 'unsharp mask' filter (σ = 2.0) was applied to the images to create a sharper image, thus defining the gel fibres, as shown in Figure 88.[106,245]

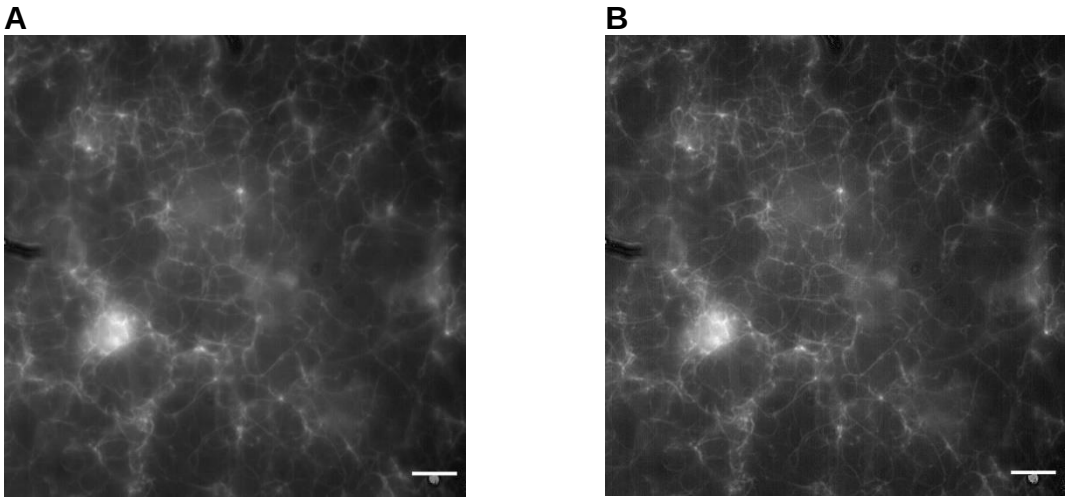

Figure 88. Example fluorescence microscopy images showing gel strand sharpening using the 'unsharp mask' filter.

(A) original, unedited image of gel strands **(B)** image with 'unsharp mask' filter. Scale = 15 µm.

The 'difference of gaussian' filter (DoG) is often used to define edges in a sample, removing background noise. The DoG filter was applied to the defined images (σ_1 = 1, σ_2 = 5), further enhancing the edges of the gel fibres and allowing specific layers of gel fibres to be observed.[245] This would enable fibre length measurement with less noise, as shown in Figure 89.

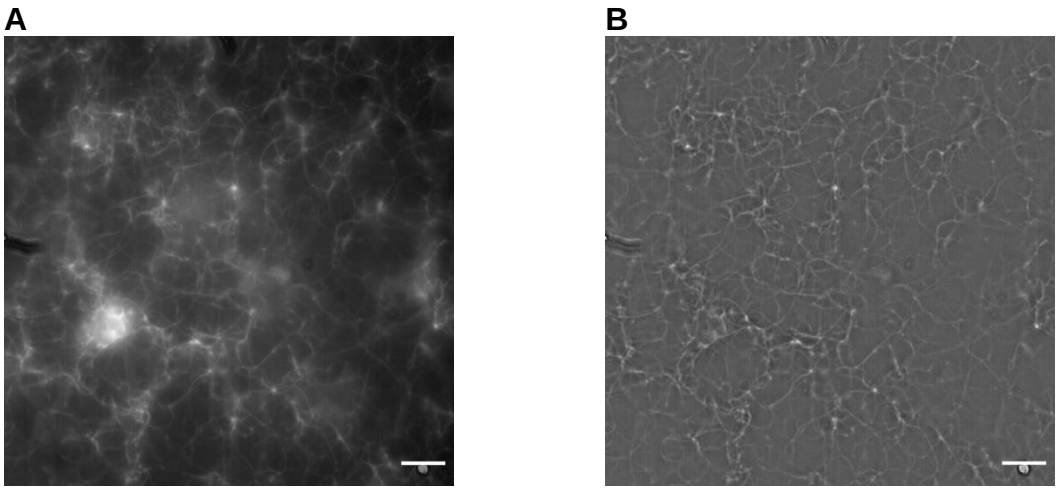

Figure 89. Example widefield fluorescence microscopy images showing further gel strand definition using the 'difference of gaussians' filter.

(A) the original, unedited image of gel strands **(B)** the image with 'difference of gaussians' filter, used in the final length determination. Scale = 15 µm.

The length of approximately 40 gel fibres from each condition (from multiple images) was measured using the segmented line tool and the measure length feature. The start and end points of gel fibres were determined in multiple ways. Firstly, if nodes (bright regions that appeared to be strand initiation sites) were present, these were determined to be the start of the strand. The strand was then followed along until it either branched to form multiple strands, it tapered off, or reached another node. These were determined to be the end points. Where nodes were not present, gel strands were measured either between tapered edges or from a tapered edge to the region where the strand branched to form multiple strands. Where the start and end points could not be determined, lengths were not measured. A full report of the averages of the lengths measured is reported in the appendix. Gel fibres were then classified as short if they were ≤ 20 µm in length and categorised as long if they were > 20 µm in length. Some gel fibres could not be measured as their length extended beyond the microscope camera's field of view; thus, a start and end point could not be accurately determined, and they could not be measured. These strands were classified as long fibres. A summary of the gel fibre formation is presented in Tables 22 and 23.

4.5.3. Microscopy summary Tables

Table 22. Gel fibres summary Table.

Approximate time taken for final gel formation of SSAs **82**, **83** and **85** – defined by no further changes being observed in the gel structure – and the motility of the resulting gel. Motility is defined as either stationary or motile. Salt concentration = 0.505 M. Approximately 50 µL of each sample was heated to ~ 40°C before being allowed to cool to ~18°C on the microscope stage. n/a = no gel fibre formation.

		Gel Sample Summary	
		Time for gel fibre formation at 5 mg / mL	Mobility of gel fibres within the sol
82	***KCl***	~ 1 hour	Stationary
	Na_2SO_4	< 1 minute	Stationary
	NaCl	~ 30 minutes	Stationary
	NaH_2PO_4	n/a	n/a
	$NaNO_3$	~ 30 minutes	Motile
	NaOBz	< 30 minutes	Stationary
83	***KCl***	~ 1 hour	Stationary
	Na_2SO_4	~ 2 hours	Motile
	NaCl	~ 30 minutes	Stationary
	NaH_2PO_4	n/a	n/a
	$NaNO_3$	~ 30 minutes	Stationary
	NaOBz	~ 5 hours	Motile
85	***KCl***	< 1 minute	Stationary
	Na_2SO_4	~ 30 minutes	Motile
	NaCl	< 1 minute	Stationary
	NaH_2PO_4	~ 2 hours	Motile
	$NaNO_3$	~ 2 hours	Motile
	NaOBz	~ 5 hours	Stationary

Table 23. Gel fibres summary Table.

Observed gel fibres formed by SSAs **82**, **83**, and **85** in various salt solutions. Strand formation of the final gel was defined by the following properties: straight (ST), curled (CL), crosslinked (LK), independent (IN), short (SH), long (LG), densely packed (DP), medium packing density (MP), loosely packed (LP), uniform arrangement (UF), stochastic arrangement (SC), unidirectional strands (UD), multidirectional strands (MD). [a] = larger than field of view, [b] = unable to discern individual fibres.

		Morphology of gel fibres												
		ST	**CL**	**LK**	**IN**	**SH**	**LG**	**DP**	**MP**	**LP**	**UF**	**SC**	**UD**	**MD**
82	***NaCl***	■		■		■			■		■			■
	KCl	■		■		■		■			■		■	
	NaH_2PO_4													
	Na_2SO_4	■	■	■		■			■		■			■
	$NaNO_3$		■		■		[a]	■			■		■	
	****NaOBz***	■	■	■			[b]			■		■		■
83	***NaCl***		■	■			■	■				■		■
	KCl	■		■		■			■		■			■
	NaH_2PO_4													
	Na_2SO_4		■	■			■		■		■			■
	$NaNO_3$	■	■	■			[b]	■				■		■
	NaOBz		■	■			[a]	■				■		■
85	***NaCl***		■				■		■			■		■
	KCl		■	■			■			■		■		■
	NaH_2PO_4			■			[b]					■		■
	Na_2SO_4		■	■			[a]	■				■		■
	$NaNO_3$		■	■			■			■		■		■
	NaOBz		■	■			■			■		■		■

4.5.4. The fibre formation of SSAs 82, 83, and 85 gels

The most common features of the gel fibres formed were multidirectional fibres and cross-linking between strands. Gel strand initiation and cross-linking appeared to start at bright regions of aggregated compound (nodes) and for the majority of gel fibres, strands formed in multiple directions between nodes. An example of this is seen with SSA **82** in NaCl (Figure 90)

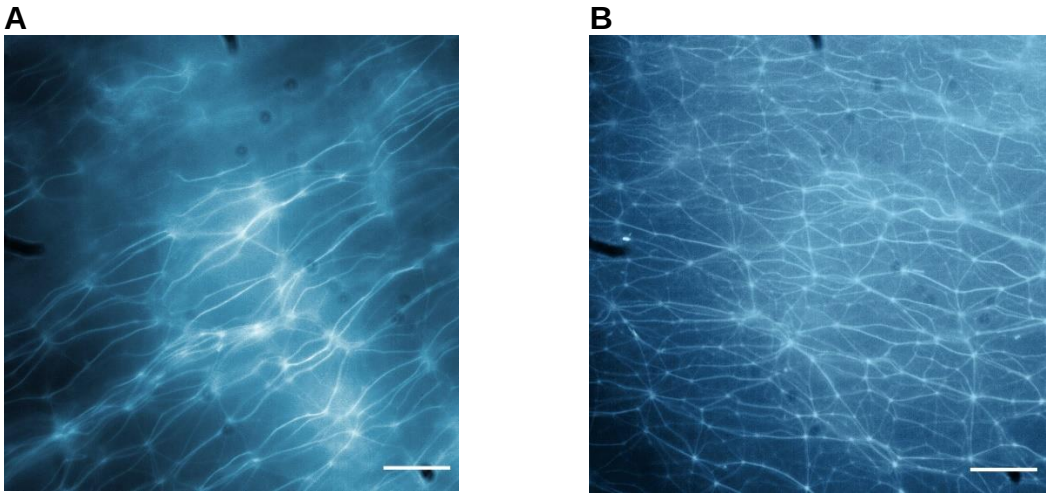

Figure 90. Widefield fluorescence microscopy.

Microscopy images showing the morphology gel strands formed by SSA **82** (5 mg/mL) in a NaCl solution (0.505 M). **(A)** early gel formation **(B)** after 30 minutes, when no further changes to the gel structure were observed. Scale = 15 µm.

During early gel formation (Figure 90A) cross-linking between nodes was observed, and the final gel structure observed (Figure 90B) was comprised of short, cross-linked fibres, with strands going in multiple directions from these nodes. As crosslinking between fibres was common in the majority of gel structures observed, it was hypothesised this was an integral feature in the gel strand formation process for this group of molecules. There were a couple of exceptions to this, however; SSA **82** in a $NaNO_3$ solution and SSA **82** in a KCl solution.

The strands in the gel formed by SSA **82** in a $NaNO_3$ solution appeared to develop independently, with no evidence of cross-linking between strands during early gel formation and 30 minutes later when the final gel structures had formed (Figure 91).

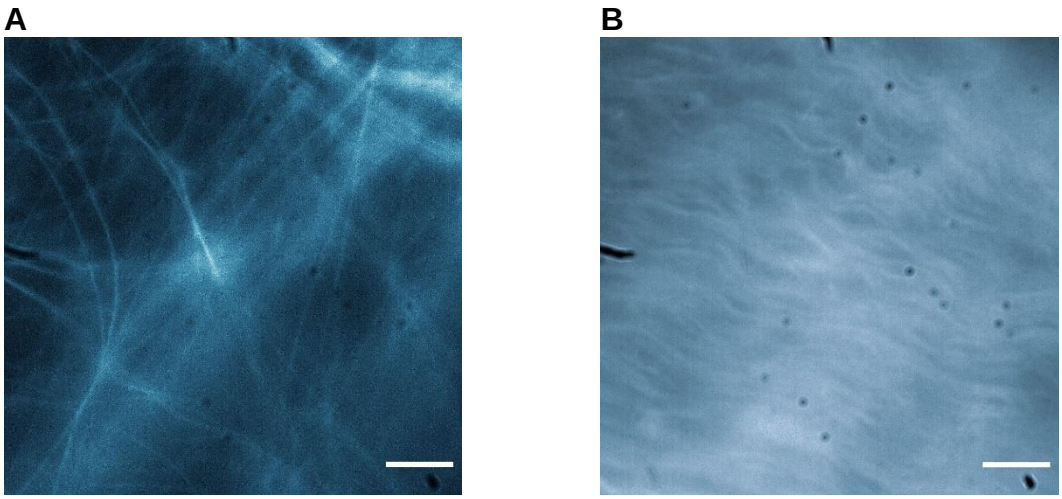

Figure 91. Widefield fluorescence microscopy.

Microscopy images showing the morphology gel strands formed by SSA **82** (5 mg/mL) in a $NaNO_3$ solution (0.505 M). **(A)** early gel formation **(B)** after 30 minutes, when no further changes to the gel structure were observed. Scale = 15 µm.

Additionally. while long, multidirectional strands were observed during early gel formation (Figure 91A), after 30 minutes, these strands had self-associated into compact regions of uniformly arranged, unidirectional fibres (Figure 91B). Strikingly, during early gel formation, gel fibres were straight, however, the final gel structure exhibited curled strands. However, the resulting gel was surrounded by large amounts of sol, causing the gel to be motile and fragile, and therefore the lack of cross-linked fibres may have reduced the stability of the resulting gel.

SSA **82** in a KCl solution produced fibres that were also unidirectional. However, unlike those observed in the $NaNO_3$ solution, strands remained straight, and cross-linking was observed from nodes (Figure 92). While the gel took longer to form, the gel matrix appeared to incorporate more sol, as there was no movement observed by microscopy. Thus, it was hypothesised that the cross-linking improved gel stability.

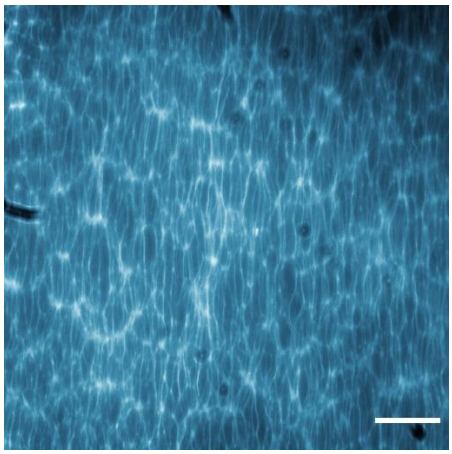

Figure 92. Widefield fluorescence microscopy. Microscopy image showing the morphology gel strands formed by SSA **82** (5 mg/mL) in a KCL solution (0.505 M). Scale = 15 µm.

Table 23 reveals a greater propensity for short strands to form uniform structures. Examples of this are seen with SSA **83** in KCl (Figure 93A), and SSA **82** in Na_2SO_4 (Figure 93B), whose short strands were arranged in a uniform, geometric pattern, cross-linking between nodes.

A **B**

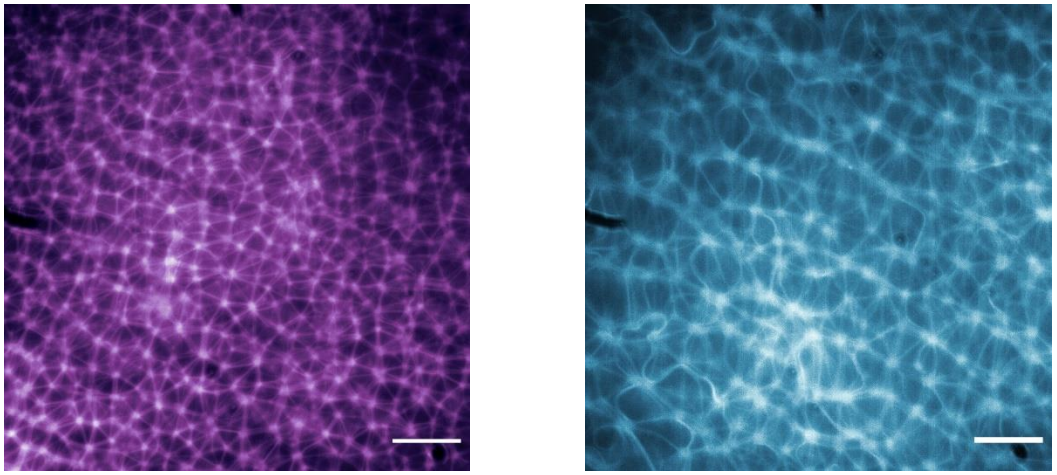

Figure 93. Widefield fluorescence microscopy.

Microscopy images showing the morphology gel strands formed by **(A)** SSA **83** in KCl and **(B)** SSA **82** in Na_2SO_4. SSAs at 5 mg/mL and salt solutions as 0.505 M. Scale = 15 µm.

Increasing the length of strands increased the greater propensity for curled fibres and also for stochastic arrangements. In Figure 93, the strands observed in KCl were shorter than those in Na_2SO_4, and curled fibres were observed randomly distributed in the gel with Na_2SO_4. Further evidence of this is provided in the images of SSA **85** in $NaNO_3$ (Figure 94).

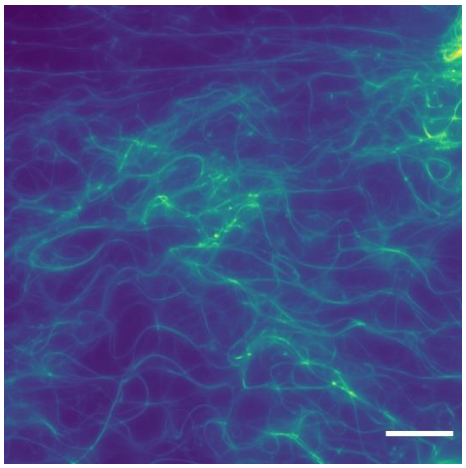

Figure 94. Widefield fluorescence microscopy. Microscopy image showing the morphology gel strands formed by SSA **85** (5 mg/mL) in $NaNO_3$ (0.505 M). Scale = 15 µm.

These fibres were longer than those of SSA **82** in KCl and Na_2SO_4 and were also curled with no uniform arrangement of fibres. Exceptions to this were SSAs **82** in $NaNO_3$ (Figure 91), which produced long, curled fibres that were uniformly arranged, and SSA **83** in Na_2SO_4 (Figure 95), which both produced comparatively shorter, straight fibres in a uniform arrangement.

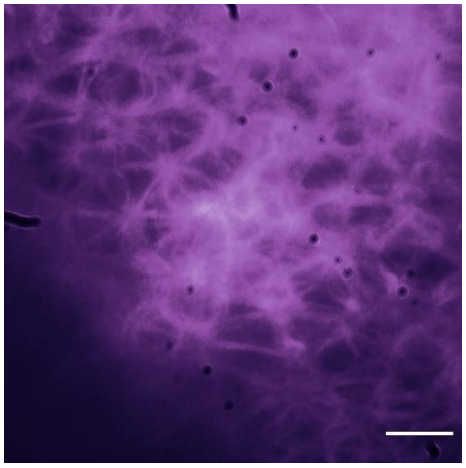

Figure 95. Widefield fluorescence microscopy. Microscopy image showing the morphology gel strands formed by SSA **83** (5 mg/mL) in Na_2SO_4 (0.505 M). Scale = 15 µm.

This suggests the formation of curled fibres is reliant on the length of the strands, and the formation of curled fibres increases the likelihood of stochastically arranged fibres. $NaNO_3$ molecules likely trigger the uniform arrangement of SSA **82**, as this was the only solution where long curled fibres were uniformly arranged.

SSA **82** had a high propensity to produce straight fibres in the salt solutions tested. Where curled fibres were present, they tended to make up a smaller proportion of the final gel structure, which was the case in Na_2SO_4 (Figure 96).

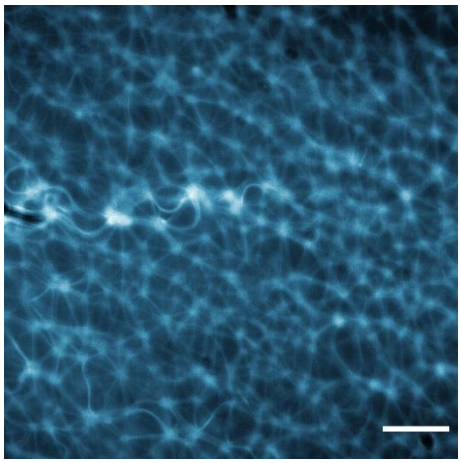

Figure 96. Widefield fluorescence microscopy. Microscopy image showing the morphology gel strands formed by SSA **82** (5 mg/mL) in Na_2SO_4 (0.505 M). Scale = 15 µm.

While fibres were predominantly short and straight fibres in a geometric arrangement, there were a few long curled fibres randomly distributed around the geometric matrix. These curled fibres made up a smaller proportion of the gel fibres observed. SSA **82** in Na_2SO_4 also provided evidence of a lack of homogeneity in these gels, as multiple types of fibres were observed in the same gel. This may lead to reduced stability, as was seen during the inversion tests and rheometry. Conversely, SSA **83** had a higher propensity to form curled fibres in the salt solutions tested. An example of this is seen with SSA **83** in a NaCl solution (Figure 97).

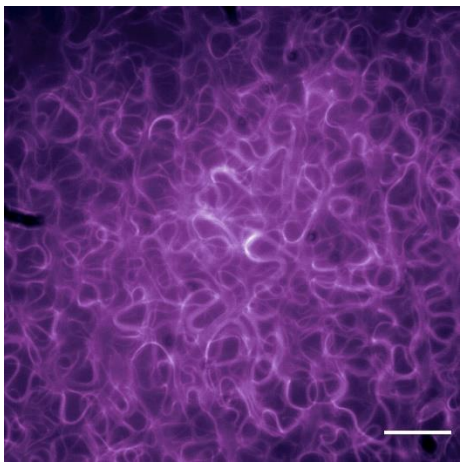

Figure 97. widefield fluorescence microscopy. Microscopy image showing the morphology gel strands formed by SSA **83** (5 mg/mL) in NaCl (0.505 M). Scale = 15 µm.

Despite producing long curled fibres, the gel produced by SSA **83** in NaCl was able to retain its shape just as effectively as SSA **82** in NaCl. This revealed another factor influencing stable gel formation: the packing density of gel fibres. It was hypothesised that closer packing of gel fibres resulted in more stable gel formation. Further evidence of this

was seen with the comparison between images obtained of SSAs **82** and **83** in NaOBz (Figure 98).

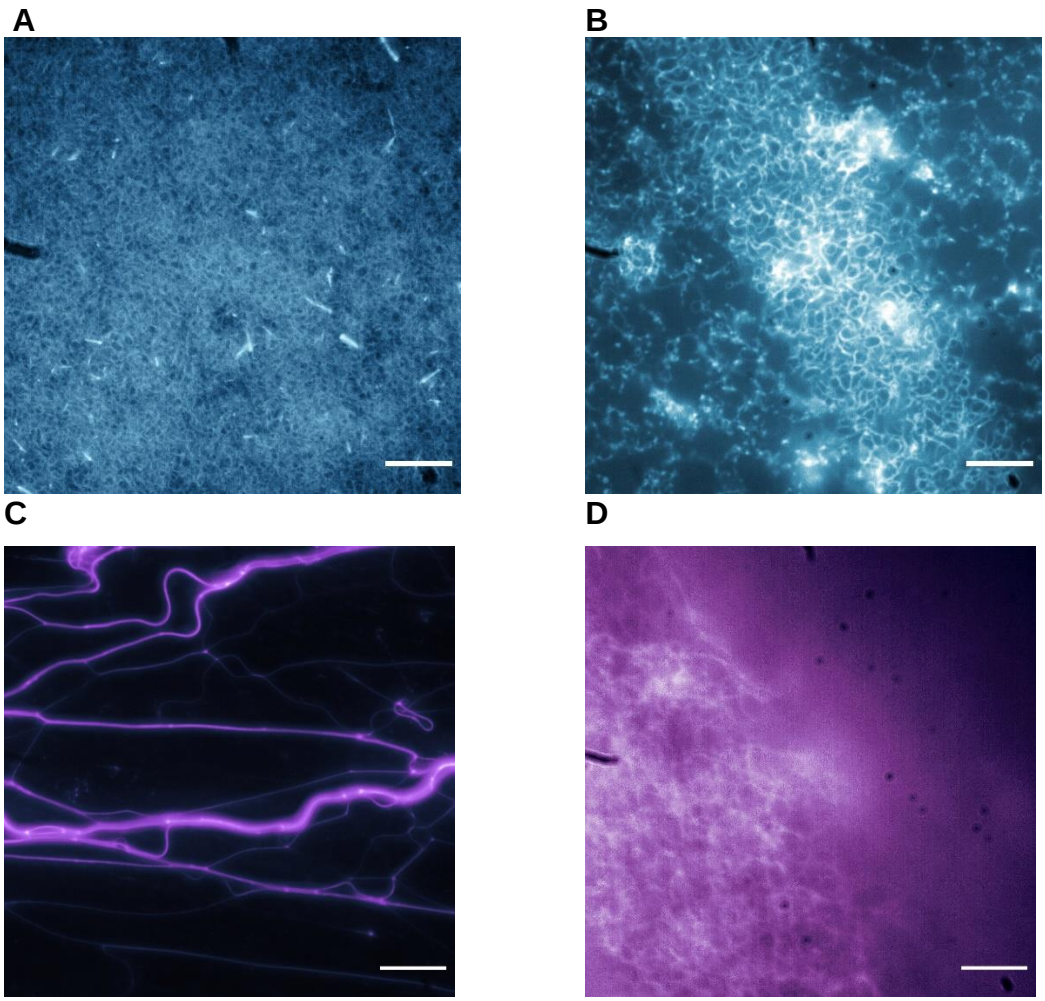

Figure 98. widefield fluorescence microscopy images.

Microscopy images showing the morphology gel strands formed by SSA **82** in NaOBz; **(A)** early gel fibre formation, **(B)** after 30 minutes when no further changes occurred to the gel and SSA **83** in NaOBz; **(A)** early gel fibre formation, **(B)** after 5 hours when no further changes occurred to the gel. SSAs at 5 mg/mL and salt solutions as 0.505 M; scale = 15 µm.

Early gel fibre formation of SSA **82** revealed curled fibre formation (Figure 98A) which then aggregated together to form densely packed regions and sparsely packed regions (Figure 98B). Similarly, SSA **83** exhibited long, curled strands initially (Figure 98C), which then packed together to form a densely packed gel surrounded by sol (Figure 98D).

During the inversion test, both gels were significantly less stable in comparison to the other salt solutions, as neither could retain their shape. However, the SSA **83** gel appeared to be more viscous in comparison to SSA **82** gel, which suggested greater stability. The SSA **82** gel observed by microscopy consisted of densely packed regions of curled fibres and parsley packed regions of curled fibres (Figure 98B). The SSAs **83** gel, however, consisted of densely packed curled fibres surrounded by sol, resulting in high motility (Figure 98D). The increased viscosity observed by SSA **83** may be attributed to the gel fibres being more densely packed together in comparison to SSA **82**, where the aggregates separated regions of fibres. Furthermore, although SSA **83** in $NaNO_3$ appeared to form a mix of curled and straight fibres initially (Figure 99A), the strands aggregated together resulting in a densely packed gel, which may have contributed to the comparative gel stability exhibited in the inversion test (Figure 99B).

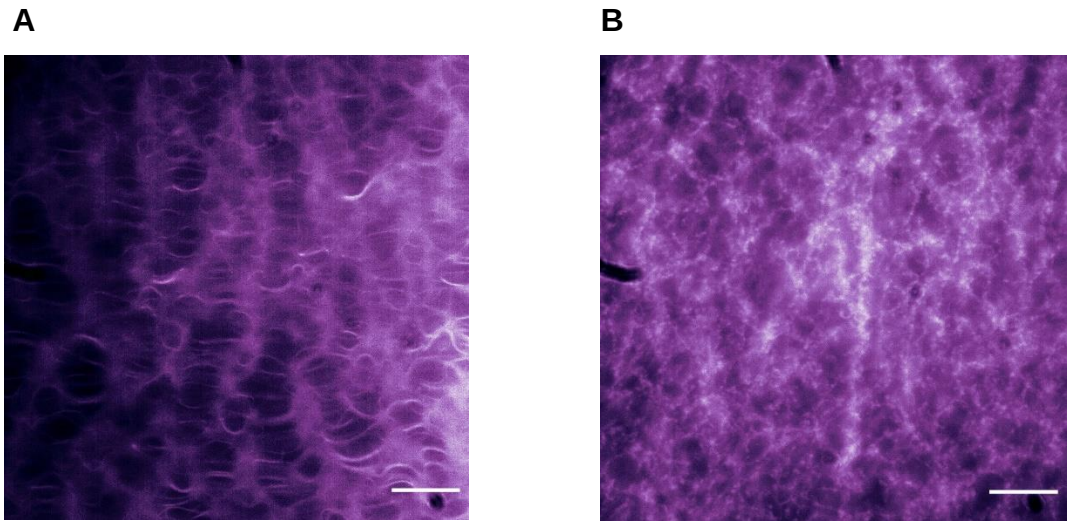

Figure 99. Widefield fluorescence microscopy.

Microscopy images showing the morphology gel strands formed by SSA **83** (5 mg/mL) in $NaNO_3$ (0.505 M). Scale = 15 µm.

The concentration of SSA **85** was reduced to 2.5 mg/mL, in an effort to slow the gelation process enough to visualize each step, and its gelation process in NaH_2PO_4 was observed. Initially, small aggregates were observed moving in the sol (Figure 100A), which were then observed to precipitate (Figure 100B). As more SSA precipitated from

the solution, the compounds aggregated together, forming large structures (Figures 100C and 100D).

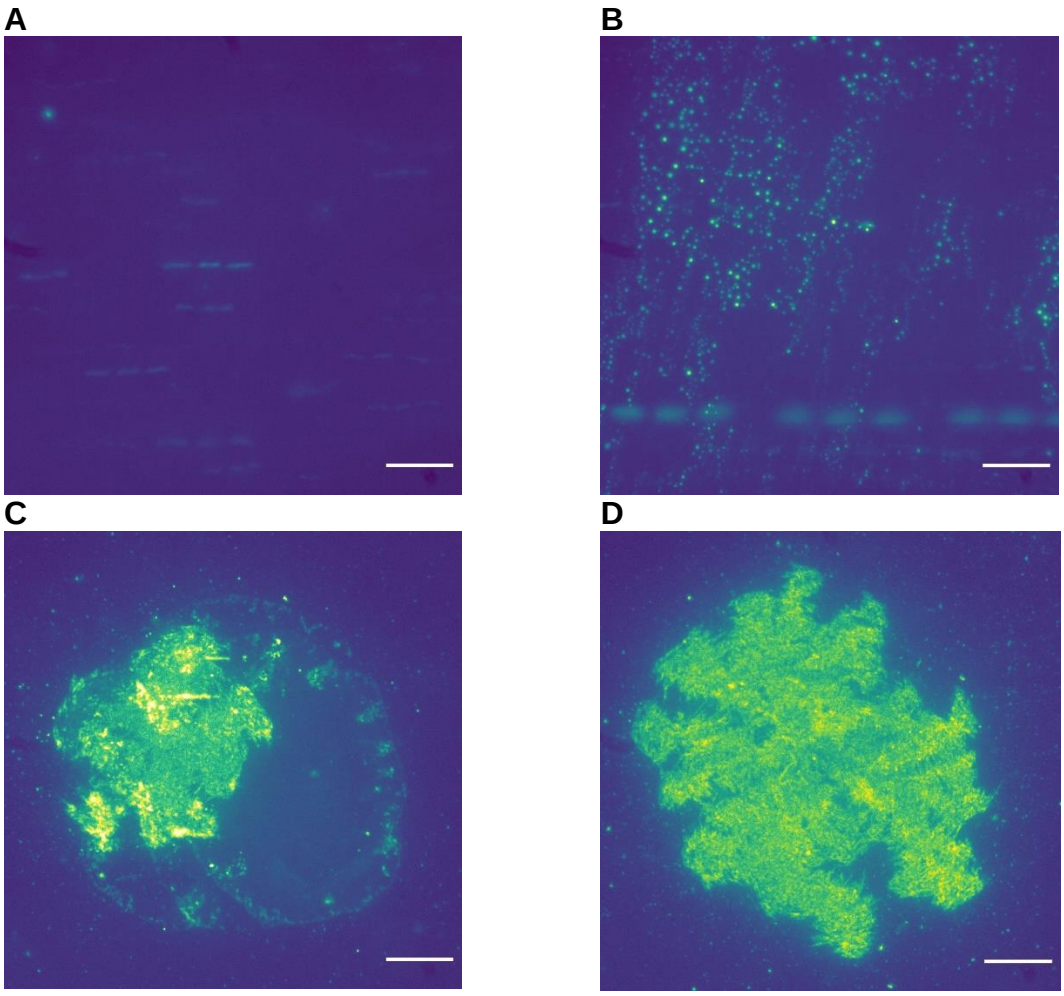

Figure 100. Widefield fluorescence microscopy.

Microscopy images showing the gel formation process of SSA **85** (2.5 mg/mL) in NaH_2PO_4 (0.505 M); **(A)** initial aggregate formation, **(B)** aggregate precipitation; **(C)** the initial morphology of large regions of aggregated compound formed by SSA **85** (2.5 mg/mL) in NaH_2PO_4 (0.505 M), **(D)** as time progressed, more compound was recruited into these structures. Scale = 15 µm.

Long, curled gel fibres started forming around the aggregated structures formed by SSA **85** (Figure 101 A), which were then elongated at nodes. As the number of gel fibres increased and the fibres continued to elongate, the aggregated structures became less visible. The resultant gel was made up of a mass of long, curled fibres surrounded by sol (Figure 101B).

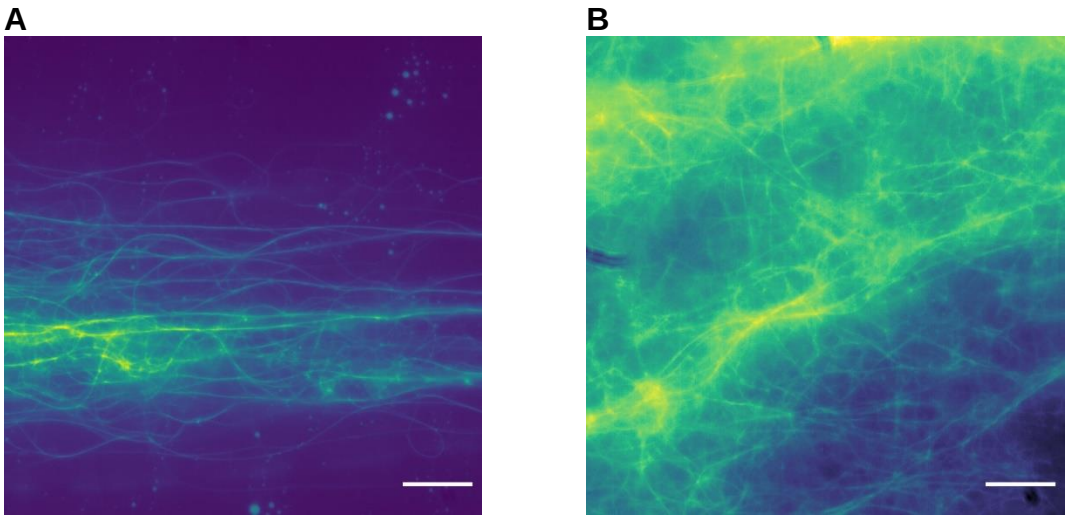

Figure 101. Widefield fluorescence microscopy.

Microscopy image showing the gel formation process of SSA **85** (2.5 mg/mL) in NaH_2PO_4 (0.505 M); **(A)** gel strands formed around precipitated compound and appeared to elongate at nodes; **(B)** the resultant gel formed, made up of long curled fibres. Aggregated structures were no longer visible. Scale = 15 µm.

The large regions of precipitated compound in Figure 100D were also observed when SSA **82** was in NaH_2PO_4 (Figure 102).

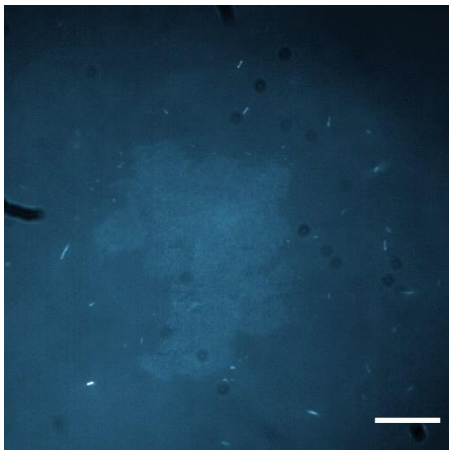

Figure 102. Widefield fluorescence microscopy. Microscopy image showing the large regions of precipitated compound formed by SSA **82** in NaH_2PO_4. Scale = 15 µm.

However, unlike SSA **85**, no gel fibres formed after 5 hours, despite observing gelation during the inversion test. Similarly, SSA **52** was observed in the inversion test to be forming gels, however, even after 5 hours, no gel strands or large structures were observed on the microscope. The experimental conditions may have elongated gelation time, which may have resulted in the fibres not forming in the time scale of these experiments, especially considering the instability shown by the SSA **82** gel during the

inversion test. A similar gelation process was also observed by SSA **85** in Na_2SO_4. Initial aggregate formation showed the initial stages of gel formation (Figure 103A), followed by large regions of aggregated compound (Figure 103B). Gel strands then formed around the aggregated structures (Figure 103C), and as the length of the gel strands increased, the aggregated structures became less visible until the final gel – made up of a mass of long, stochastic fibres surrounded by sol – was formed (Figure 103D).

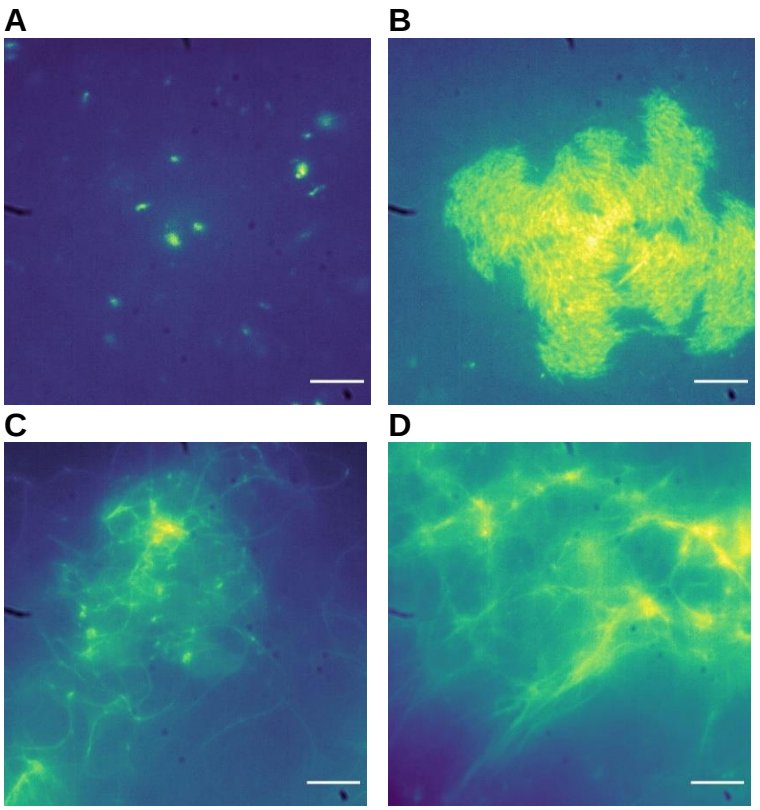

Figure 103. Widefield fluorescence microscopy. Microscopy image showing the gel formation process of SSA **85** (5 mg/mL) in Na_2SO_4 (0.505 M); **(A)** initial aggregate formation; **(B)** followed by the formation of large regions of precipitated compound; **(C)** gel strands then formed around precipitated compound structures; **(D)** the resultant gel was made up of long, stochastically arranged fibres surrounded by sol. Scale = 15 µm.

Gel strand initiation from the precipitated compound regions was also observed with SSA **85** in Na_2SO_4, providing further evidence of their role as gel fibre initiation sites (Figure 104).

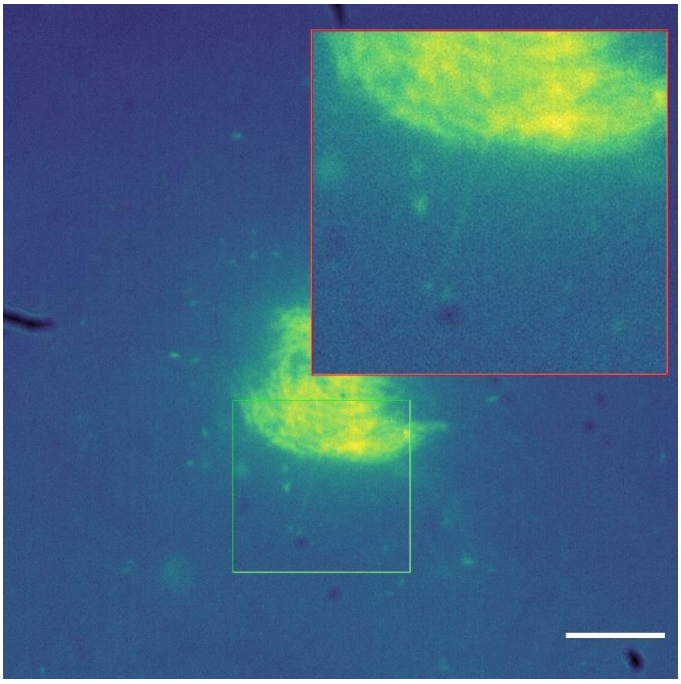

Figure 104. Widefield fluorescence microscopy.

Microscopy image of SSA **85** (5 mg/mL) in Na_2SO_4 highlighting gel strand initiation from aggregated compound regions with enlarged ROI in. Scale = 15 µm.

While different salt solutions were observed to produce different fibres, these data may provide insight into the gel formation processes for the gels that resulted in long, curled, stochastic fibres, which was the case for all SSA **85** gels. Further, the formation of the precipitated compound structures by SSA **82** in NaH_2PO_4 suggests a similar gel formation process to SSA **85** in NaH_2PO_4 and SSA **85** in Na_2SO_4.

The microscopy data presented demonstrates how different salt solutions can impact gel fibre morphology and formation processes, and thereby impacting the stability and properties of the resultant gels. For example, in salts that triggered the formation of longer strands, such as $NaNO_3$, reduced stability and increased motility was observed by the gels. Whereas salts that triggered shorter stand formation, such as KCl, tended to result in uniform arrangements that were thought to improve gel stability. Furthermore, salt solutions that allowed gel strands to pack closer together, such as $Na_2SO_4$and

$NaNO_3$ also exhibited more stable gels in comparison to those that did not, such as NaOBz.

A distinct feature of these gels was the formation of a gel mass surrounded by a large sol environment, which often resulted in motile gels that were difficult to image. This was more clearly seen with SSA **83** in NaOBz or SSA **82** in $NaNO_3$. Motile gels were often fragile and would easily break down. This was attributed to large amounts of the sol not being incorporated into the final gel structure, resulting in a comparatively weaker gel, as was observed with SSA **85** in NaH_2PO_4. This may have contributed to the unstable gel formation by all the gels formed, as the MGCs determined were all > 5 mg/mL. This also suggested the sol needed to be heavily incorporated into the gel matrix to create a more stable gel, as opposed to surrounding the gel. An additional factor influencing gel formation was the time taken for gels to form. NaOBz tended to trigger slower gel formation in SSAs **83** and **85** as the final gel structures were only observed after 5 hours. The resulting gel for SSA **83** displayed more liquid-like behaviour in the inversion test. Whereas gelation in NaCl was fairly rapid, by 30 minutes all final gel structures were observed, and SSA **82** and **83** in NaCl were more stable during the inversion test, in comparison to NaOBz.

While SSA **82**, **83**, and **85** were less stable gels in comparison to SSA **70**, we sought to determine how this would impact the antimicrobial activity when gelated.

4.5.4. Antimicrobial Studies

To determine the activities of SSAs **82**, **83**, and **85** in their gelated form, surface diffusion assays were performed, as described in section **2.4.12** of the materials and methods. After an 18-hour incubation at 37°C, SSA **82**, **83**, and **85** gels were found to dissolve into the agar plate, making it difficult to define the area of gel placement. However, reduced antimicrobial activity of SSAs **82**, **83**, and **85** was observed with *E. coli*, as no zones of inhibition or gel placement were observed (Figure 105).

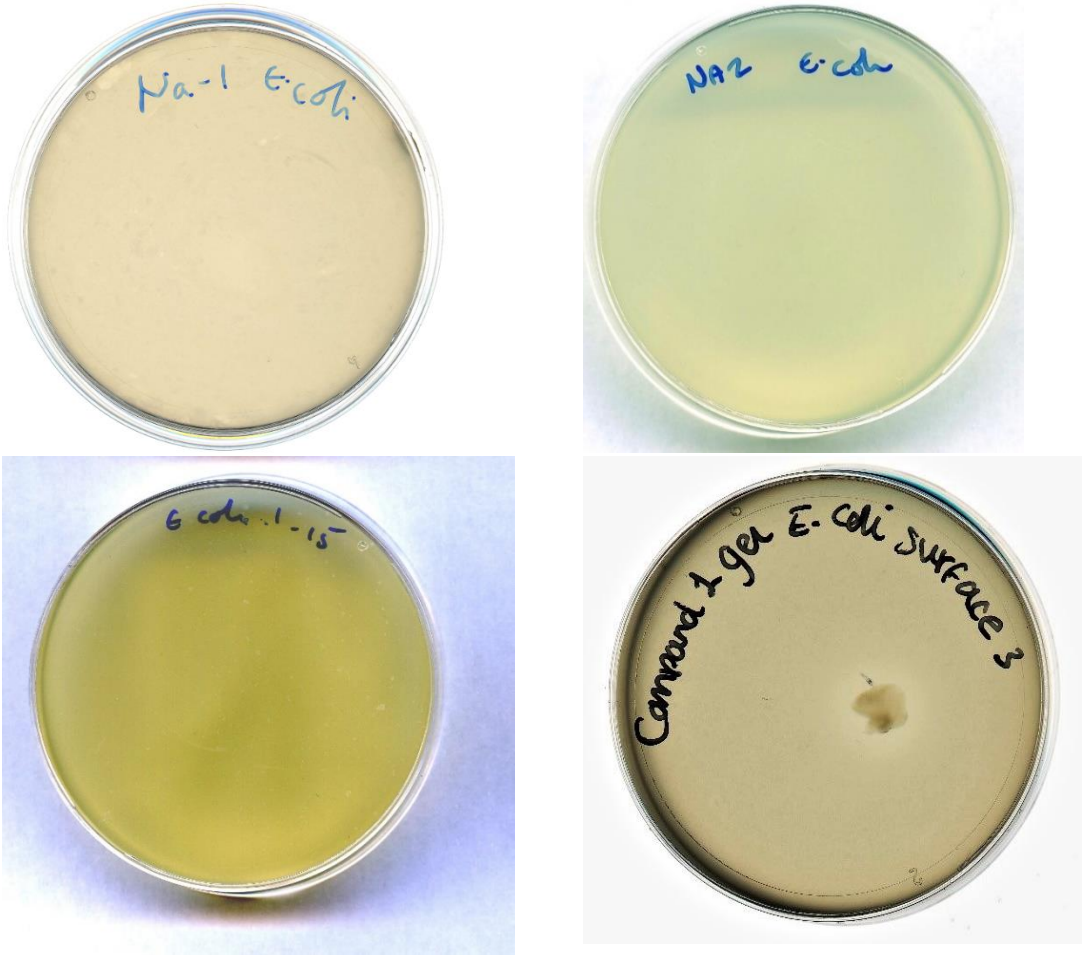

Figure 105. *E. coli* surface diffusion assay.

Agar plates showing reduced *E. coli* activity by SSAs **(A) 82, (B) 83, (C) 85** in comparison to SSA **(D) 70**.

This was surprising as in solution, SSAs **82**, **83**, and **85** had improved antimicrobial activity in comparison to SSA **70**, against *E. coli*, as shown by their lower MIC_{50} values.

Greater activity was observed against MRSA by SSA **82** and **83** gels. Despite the difficulty in defining the area of gel placement, zones of inhibition were still calculable for MRSA gel plate, as the zone of inhibition includes the area of gel placement. Zones of inhibition for SSAs **82**, **83**, and **85** were measured in ImageJ, as described in section **2.4.13** of the materials and methods, to ensure more accurate measurement as gel regions could not be defined. Furthermore, zones created by SSA **70** were measured again in ImageJ to provide an accurate comparison, as previously zones were measured manually.[106,246] The results are summarised in Table 24.

Table 24. Zones on inhibition measured using ImageJ.[106,246]

The zones of inhibition (mm) were measured for SSAs **70**, **82**, **83**, and **85** against MRSA using the surface diffusion assay; *n*=3 for all groups. Standard deviation (SD) is used as the error value.

	Zones of inhibition
	Diameter (mm)
70	10.59 ± 0.99
82	14.67 ± 1.66
83	19.15 ± 1.88
85	n/a

As seen in Table 24, the zone of inhibition measured by SSA **70** (*M* = 10.59 mm) in comparison to those of SSA **82** (*M* = 14.67 mm) and SSA **83** (*M* = 19.15 mm). A zone of inhibition was not observed for SSA **85**, thus had considerably lower activity in comparison to SSAs **82** and **83**, consistent with the MIC_{50} values obtained. While SSA **83** produced a numerically larger zone than SSA 82, to determine whether this difference was statistically significant, a between-groups ANOVA was conducted using the values for SSAs **70**, **82** and **83**.[247,248]

The between-groups one-way ANOVA is a statistical test used to determine whether any statistically significant differences exist between the means of three or more independent groups.[184] The one-way ANOVA uses F-tests to determine whether the differences observed between group means is larger than the variability observed within groups. A larger ratio, demonstrated by a high F-value, is indicative of high variability between group means, relative to the variation observed within each group. [184] In determining statistical significance, F-values must be used in combination with *p* values, as *p* values determine the significance or importance of F-values. Typically, *p* values ≤ .05, are considered significant whereas *p* values > .05 are considered not significant. [184]

Prior to conducting the ANOVA, the assumption of homogeneity of variances was tested and satisfied based on Levene's *F* test. The one-way between-groups ANOVA revealed a statistically significant effect; $F(2, 33) = 90.60$, $p = .000$, $\eta^2 = .846$. Therefore, the

calculated zones of inhibition means in the presence of each SSA were not equal to each other. While the one-way between-groups ANOVA can assess whether statistically significant differences exist between the means calculated, it does not provide information about where those differences lie. A posthoc test can be utilised to identify the means that are statistically significantly different from each other. Consequently, three Fisher's LSD posthoc tests were conducted to elucidate the nature of the differences.[184,247,248] A visual representation of the results is presented in Figure 106, however, the full analysis is provided in the appendix.

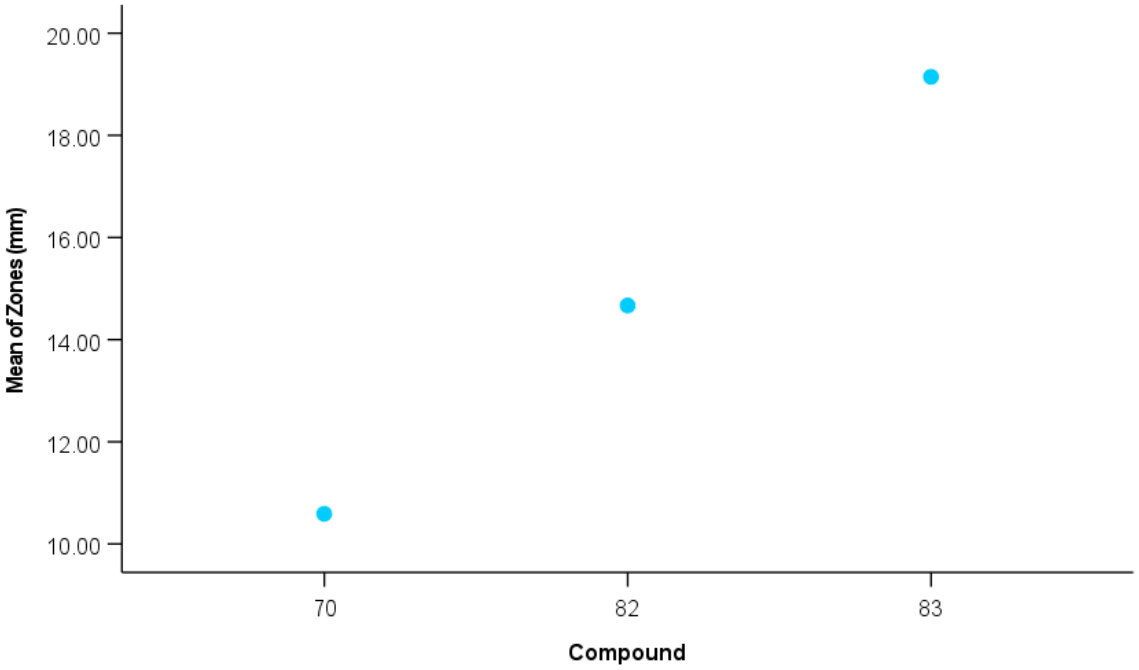

Figure 106. Means plot reporting the zones of inhibition for SSAs 70, 82 and 83 used in determining statical significance.

Fisher's LSD posthoc test (*p*-values): SSA **70** & SSA **82**; *p* = .000, SSA **70** & SSA **83**; *p* = .000, and SSA **82** and SSA **83**; *p* = .000. *n*= 3 for all groups.

The difference observed between zones measured with the SSA **70** and the SSA **82** gel was determined to be statistically significant, *t* (33) = -6.41, *p* =.000. Similarly, the differences observed between the SSA **70** gel and the SSA **83** gel were statistically significant; *t*(33) = -13.46, *p* = .000, as were the differences observed between SSA **82**

gel and the SSA **83**; $t(33) = -7.04$, $p = .000$. It can therefore be concluded that SSAs **82** and **83** were both more effective antimicrobials against MRSA in their gelated form, as they produced statistically significantly larger zones of inhibition in comparison to SSA **70**. Furthermore, SSA **83** was the most effective, as the gel made using this SSA produced the largest zones of inhibition which were statistically significantly higher than those of SSA **70** and **82**.

4.6. Summary

Statement	Evidence
SSAs **82** and **83** formed higher order complexes in EtOH:D_2O (1:19)	~ 50 – 500 nm aggregates observed by DLS.
	A 45% loss of SSA **82** and a 36% loss of SSA **83** in EtOH:D_2O (1:19).
SSA **83** formed larger complexes in comparison to SSA **82**	Comparatively larger aggerates with a peak maxima of 410 nm were observed in the solution of SSA **83** at 5.56 mM.
The complexes formed by SSA **82** were comparatively more stable as those of SSA **83** may be dependent on or be disrupted by solvent interactions	Peak maxima at 0.56 mM decreased to 212.35 nm for SSA **83**, whereas the peak maxima of SSA **82** did not significantly drop in the DLS experiments.
	Zeta potential for SSA was -30.22 mV, which was within the stable range for SSA **82**, whereas the zeta potential for SSA **83** was - 55.76, which was not.
Instability of the gels observed in the inversion test may have been a result of a lack of homogeneity and large amounts of sol not being incorporated into the gel matrix	Gel-sol transition points were not observed in the majority of rheology experiments, suggesting more fluid behaviour.
	Multiple types of fibres were observed in the same gel.

	A number of gels appeared to be surrounded by large amounts of sol, resulting in gel motility and fragility, for example, SSA **85** in NaH_2PO_4.
Gels were more stable when gel fibres were densely packed	salt solutions that allowed gel strands to pack closer together, such as Na_2SO_4 exhibited more stable gels in comparison to those that did not, such as NaOBz.
Longer strands had a greater propensity to curl, which reduced gel stability	An increase in the length of strands increased the propensity for curled fibres and also for stochastic arrangements, which may have contributed to instability
Cross-linking was an integral feature in the gel strand formation processes.	Cross-linked fibres were observed in the majority of gel structures.
	Lack of cross-linked fibres may have contributed to the reduced stability of the SSA **82** gel in the $NaNO_3$solution.
SSAs **82**, **83**, and **85** exhibited reduced *E. coli* activity when gelated	Discernible zones of inhibition were not observed with *E. coli.*
SSAs **82** and **83** exhibited improved *E. coli* activity in solution	SSAs **82** and **83** produced higher MIC_{50} values in comparison to SSA **70** against *E. coli.*
Improved *E. coli* activity may be achieved through the use of the extended alkyl	SSA **83** produced the lowest MIC_{50} value against *E. coli* (1.16 mM).

chain (n=3) in SSA **83** and through further optimisation of SSA **84** to improve stability.	SSA **84** decreased *E. coli* growth by 86.42%, which was the highest percentage observed with *E. coli*.
SSA **83** was the most effective against MRSA in this group of molecules	SSA **83** produced the lowest MIC_{50} value (0.59 mM) against *MRSA.*
	SSA **83** produced the largest zones of inhibition which were statistically significantly higher than those of SSA **70** and **82**.
The CH_3 associated with the aromatic ring contributed to the antimicrobial activity of SSA **70** against MRSA, and its removal (SSA **85**) decreased antimicrobial activity against MRSA.	The MIC_{50} obtained for SSA **85** against MRSA was 1.14 mM, which was higher than that of SSA **70**.
	A zone of inhibition was not observed for SSA **85** against MRSA.

Summary

The data presented within this chapter presents evidence for the optimisation of antimicrobial molecules through the use of stepwise modifications. The structure-activity relationships obtained in Chapter 3 were utilised to produce SSAs **82** – **85**. While the gelation properties were comparatively weaker than those of SSA **70**, SSAs 82 and **83** exhibited improved antimicrobial efficacy against MRSA.[155] Furthermore, SSA **83** was created in order to improve *E. coli* activity. While the activity of SSA **83** decreased when gelated, its activity in solution significantly increased in comparison to SSA **83**.[155] This provided further evidence for the hypothesis that increasing the alkyl chain could improve *E. coli* activity.

The physicochemical analysis conducted on SSA **82** and **83** provided insight into the behaviour of these molecules and allowed for the refinement of prior hypotheses. For example, the cyclisation predicted through the computational models was not observed in experimental data, highlighting a limitation of the computational approaches and a requirement for further improvement to these methods. Additionally, lower CMCs have been previously hypothesised to correlate with higher antimicrobial activity, however SSA **83** produced a higher CMC (14.77 mM) but exhibited higher antimicrobial efficacy in comparison to SSA **82** (CMC = 1.92 mM). This information can be utilised to further understand and optimise these molecules, and form more accurate hypotheses.

The microscopy data revealed characteristic features of resulting gels for each molecule, however the salt solution present could drastically alter the gelation process and properties of the resulting gel. A deeper investigation into the interactions between the sol components and the gelators is required in order to further understand the gelation processes of these SSAs. This will allow for the manipulation of gels so that they exhibit desired properties, which can then be utilised in a wide range of applications.

In conclusion, stepwise optimisation of the most effective SSAs presented in Chapter 3 resulted in the formation of SSAs that exhibited the desired improved antimicrobial efficacy. Further, the physicochemical and gelation analysis conducted on SSAs **82** – **85** provided an insight into the properties of these molecules, allowing for future optimisation and manipulation of desired properties.

Chapter 5: Exploring the lipid binding properties of membrane-related proteins

5.1. Introduction

Membranes contain a variety of lipids, to separate the internal contents of cells from the external environment, and define the functionally distinct compartments within the cell.[249] Many essential cell processes are reliant on membrane interactions with specific proteins, including cell-cell communication, endo/exocytosis, and regulation of the cytoskeleton. Furthermore, membrane lipids are also thought to regulate functional activity and induce oligomerisation of many proteins.[118] Many of these interactions are not yet fully understood. Membrane-binding proteins tend to be soluble and unstructured when cytosolic, however, upon interactions with membrane lipids, they undergo structural changes that are integral to their physiological function.[249] Characterisation of the lipid-protein interactions, and related conformational changes, is necessary for the determination of protein function. Further, a detailed investigation of specific interactions and protein function is imperative as misfolding or misregulation of these proteins can result in impaired binding and disease states.[249] An example of this can be observed with alpha synuclein.

Alpha synuclein (α-syn) is an aggregation-prone protein that is predominantly expressed in neuronal cells, preferentially found to localise to presynaptic terminals.[250,251] While the precise cellular function is unknown, α-syn is thought to regulate vesicle turnover at synaptic termini and thereby negatively control neurotransmitter release.[55,100] Aggregation of α-syn has been linked to a group of neurodegenerative diseases called synucleopathies, such as Parkinson's disease.[98,100,250–252] When cytosolic, α-syn is largely unstructured, however, upon interactions with certain lipid surfaces α-syn has been seen to adopt an alpha-helical structure.[98,100,250–252]

Eukaryotic cells possess up to six different amino-alpha-transferase complexes, called NAT A-F which conjugate acetyl groups onto the amino terminals of proteins. This

process is known as Nt-acetylation and has many implications on protein structure, function, and stability.[98,100] As mentioned previously, post-translational modifications, such as acetylation, are utilised in protein activity regulation. In the case of alpha-Synuclein, Nt-acetylation is thought to stabilise alpha-helical structure formation and modulate its subsequent membrane interactions.[98,100]

Thus, a detailed investigation into the specific lipid interactions and the impact Nt-acetylation on these activities will provide clarity on α-syn function and may allow for the prevention or treatment of disease states.

5.1.1. Aim of studies

We sought to determine the impact of Nt-acetylation on the membrane binding properties of α-Syn, to ascertain an understanding of its physiological function and regulation.

5.2. Recombinant protein synthesis and purification

Amino-terminal (Nt) acetylation of alpha synuclein is thought to regulate the stability of its alpha-helical structure, oligomerisation, and subsequent membrane interactions.[98] While Nt- acetylation occurs in bacteria, this is infrequent due to their lack of the NAT complexes required for acetylation. Researchers tend to use eukaryotic expression systems or post-purification acetylation reactions to generate acetylated recombinant proteins, which tend to be expensive and time consuming.[98] Consequently, Johnson et al. 2010 developed a novel method of creating Nt-acetylated recombinant proteins in bacterial expression systems, which were used in the production of acetylated proteins within this project.[98,253]

In an effort to understand the membrane binding capabilities of α-syn, we generated a plasmid coding for the first 38 amino acids from the N-terminus, which encompassed the hypothesised membrane binding domain. The resulting protein was also called the vesicle nucleating protein (VNp). VNp was tagged with the fluorescent protein, mNeonGreen (mNg), as well as 6 x histidine residues, to facilitate affinity chromatography purification using nickel resin.[254] We also produced the full length alpha synuclein protein, which contained a histidine tag and a mCerulean tag (mCer3).[255] The resulting proteins were termed either acetylated or unacetylated α-syn-mCer3, depending on the presence of amino-terminal modification.

Wild type α-syn-mCer3 and VNp-mNg proteins were expressed using BL21 DE3 competent cells co-expressing the fission yeast pNatB complex with a chloramphenicol selection marker, resulted in the production of Nt-acetylated isoforms. Successful protein expression and purification were verified using SDS PAGE and mass spectroscopy. After purification of the acetylated VNp-mNg protein, a clear strong band was present on the SDS PAGE gel between 85 – 100 kDa, which persisted throughout purification processes (Figure 107A). This band was hypothesised to be a result of VNp-mNg oligomerisation, which would create larger protein complexes and result in the higher band observed on the SDS PAGE gel. This was further investigated using western blot analysis, conducted

by Dr. Tara Eastwood, to confirm whether the second band was indeed oligomeric VNp-mNg. The western blot profile conducted on both acetylated and unacetylated VNp-mNg confirmed multiple α-syn species present when the protein was acetylated (Figure 107B) indicated by the detection of both bands.

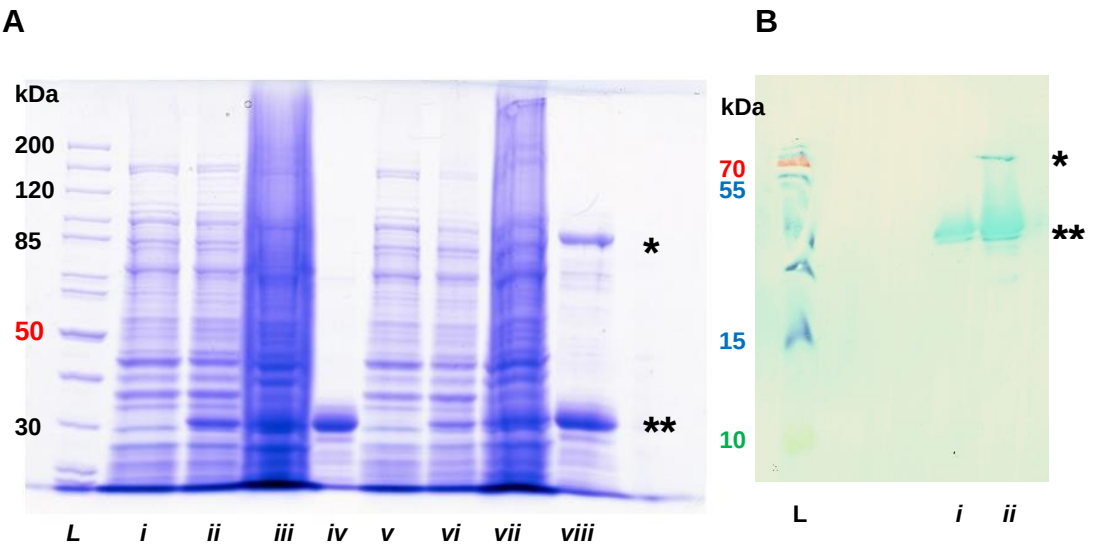

Figure 107. SDS PAGE gel showing the expression and purification of VNp-mNg.

(A) SDS-PAGE gel showing the expression and purification of unacetylated VNp-mNg: *(i)* pre induction, *(ii)* post induction, *(iii)* pre purification, *(iv)* post-purification, and acetylated VNp-mNg: *(v)* pre induction, *(vi)* post-induction, *(vii)* pre-purification, *(viii)* post purification. **(B)** Anti-His western blot of *(i)* unacetylated VNp-mNg and *(ii)* acetylated VNp-mNg. L = protein molecular weight marker, * - hypothesised oligomer formation band, ** - protein at ~ 32.3 kDa.

In contrast, only one band was detected for unacetylated VNp-mNg, consistent with the SDS PAGE gel. This suggested acetylation involvement in oligomerisation of VNp-mNg. acetylated and unacetylated α-syn-mCer3 were also expressed and purified (Figure 108A), and oligomer formation may also have been taking place with the acetylated protein, shown by the persisting band between ~100 and 80 kDa (Figure 108B).

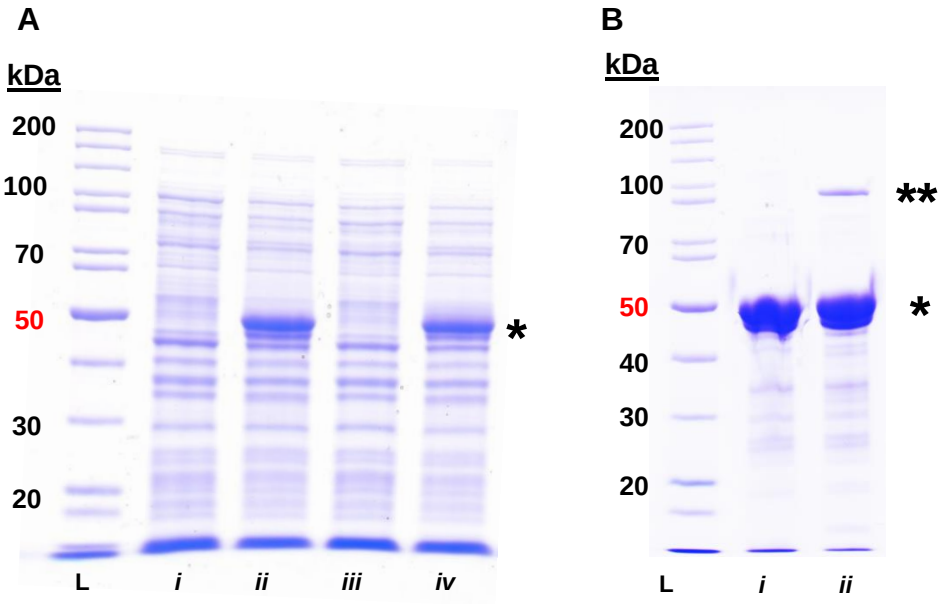

Figure 108. SDS PAGE gel showing the expression and purification α-syn-mCer3. **(A)** expression of α-syn-mCer3: *(i)* pre-induction unacetylated α-syn, *(ii)* post-induction unacetylated α-syn-mCer3, *(iii)* pre-induction acetylated α-syn-mCer3, *(iv)* post-induction acetylated α-syn-mCer3. **(B) Purified protein.** *(i)* unacetylated α-syn-mCer3 *(ii)* acetylated α-syn-mCer3. L = protein molecular weight markers; * - protein at ~ 42.6 kDa, ** - oligomer formation.

5.3. Fluorescence anisotropy

It was important to select an appropriate membrane binding assay that would allow the observation of specific lipid interactions. As such, liposomes were created using the following lipids, as described in section **2.6.1** of the materials and methods: POPA, POPC, POPG, and *E. coli* total and polar lipids. Further, a 1:3 molar ratio was made up using POPG: DPPE lipids respectively, which will be called PG: PE from this point forward.

The fusion of mNeongreen and mCerulean reporter proteins to VNp-mNg and α-syn-mCer3 respectively allowed fluorescence-based assays to be employed. An example of this is fluorescence anisotropy, which was utilised for an initial examination of the specific lipid interactions.

As described previously, fluorescence anisotropy is a measure of the changing orientation of a fluorescent molecule in space through the use of fluorescence absorption and emission events. Changes in the shape and size of a fluorescent molecule result in changes in anisotropy, as the size of bound molecules is larger than the size of the free molecules in solution. Thus, fluorescence anisotropy measurements provide a way of monitoring binding events, as fluorescence anisotropy can detect the changes in mass between the free and bound states.[150,192,193190] Determining and varying the concentration of proteins was more easily achievable in comparison to liposomes. Therefore, anisotropy experiments were conducted using a constant liposome concentration (1 mM) and varying fluorescent protein concentrations, as described in section **2.6.3** of the materials and methods.

The anisotropy values are a measure of the sum of individual anisotropies in solution, bound and unbound, and an increase in fluorescent protein concentration will result in a higher number of molecules in solution and therefore increased anisotropy values.[150,192,193] As such, anisotropy values of unbound protein were obtained and subtracted from anisotropy values with lipid present. This would remove the anisotropy values that were solely due to increased protein concentration and differences observed would be a result of binding activities (Figure 109). GraphPad Prism 9 software was used for subsequent data analysis.

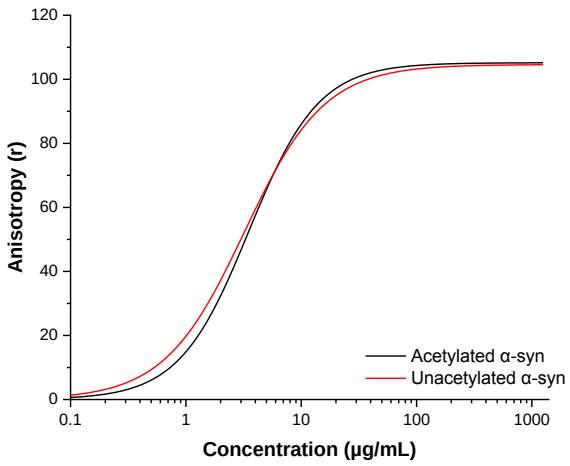

Figure 109. Background anisotropy curve.

Anisotropy values of unbound unacetylated and acetylated α-syn-mCer3 were subtracted from anisotropy values in the presence of liposomes to determine binding activities.

The graphs presented below represent the change in anisotropy when the liposomes were present compared to the anisotropy of the protein alone. As the protein concentration increased, the signal became more saturated, and the differences in anisotropy between the protein alone and liposome-protein solutions became less distinguishable. Thus, the anisotropy values at higher concentrations were similar to those of the protein alone differences were predominantly observed at lower concentrations.

The largest change was observed when unacetylated α-syn-mCer3 was in the presence of POPA. Anisotropy values started off significantly higher at low concentrations in comparison to the protein alone (Figure 110).

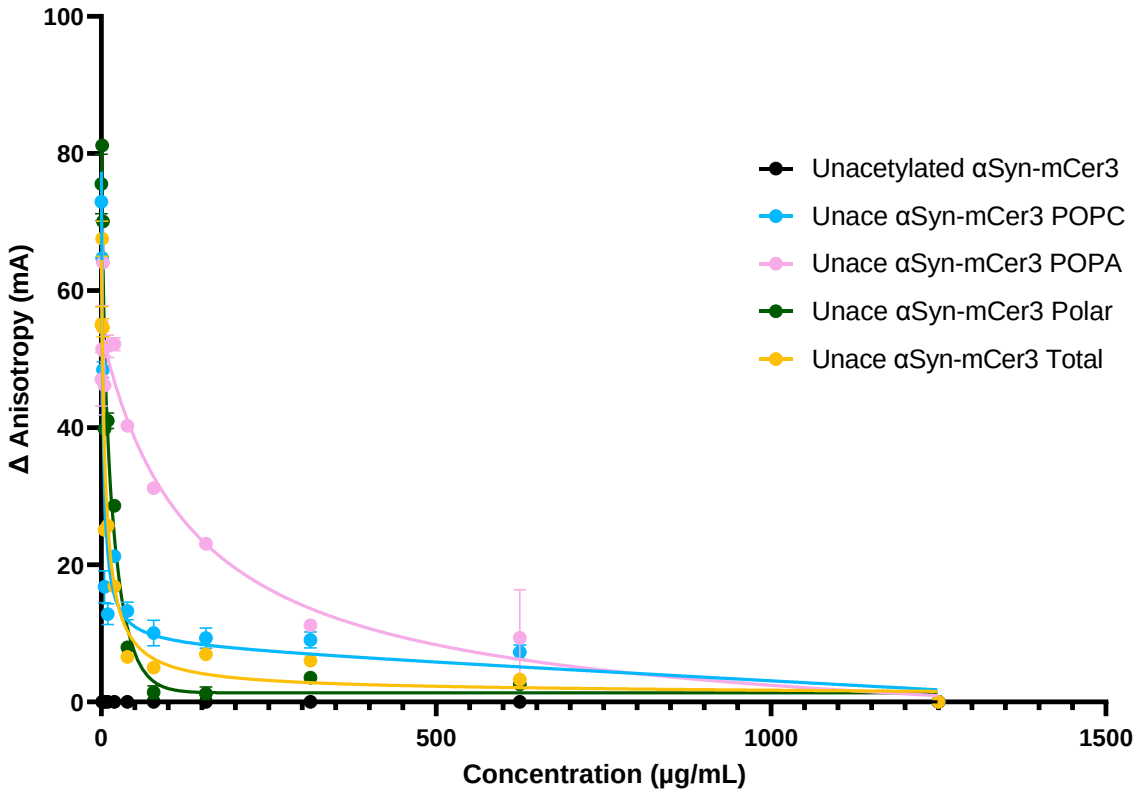

Figure 110. Unacetylated α-syn-mCer3 change in anisotropy curves.

Graph showing the change in anisotropy of unacetylated α-syn-mCer3 in the presence of POPA, POPC, *E. coli* polar and *E. coli* total lipids. Data points recorded are an average of three independent experiments and error bars represent the standard error of the mean (s.e.m).

The decrease observed with increasing protein concentration was far more gradual in comparison to POPC and *E. coli* total and polar lipids, which suggested a higher affinity to POPA in comparison to the other lipids. When POPC was present, two distinct phases were observed: a sudden initial decrease was observed, followed by a slower, more gradual decrease. Similarly, when *E. coli* total and *E. coli* polar lipids were present, an initial faster decrease in anisotropy was observed. However, the second more gradual phase occurred more rapidly in comparison to when POPC and POPA were present. This data suggests a lower affinity of unacetylated α-syn-mCer3 to POPC than with POPA, and a lower affinity to *E. coli* total and polar lipids than with POPC and POPA. Additionally, the presence of two phases may suggest multiple binding events occurring, however further investigation would be required to determine a definitive reason for these two phases. Similarly, α-syn-mCer3 in the presence of POPA produced significantly larger changes in anisotropy values at lower concentrations than with POPC. (Figure 111).

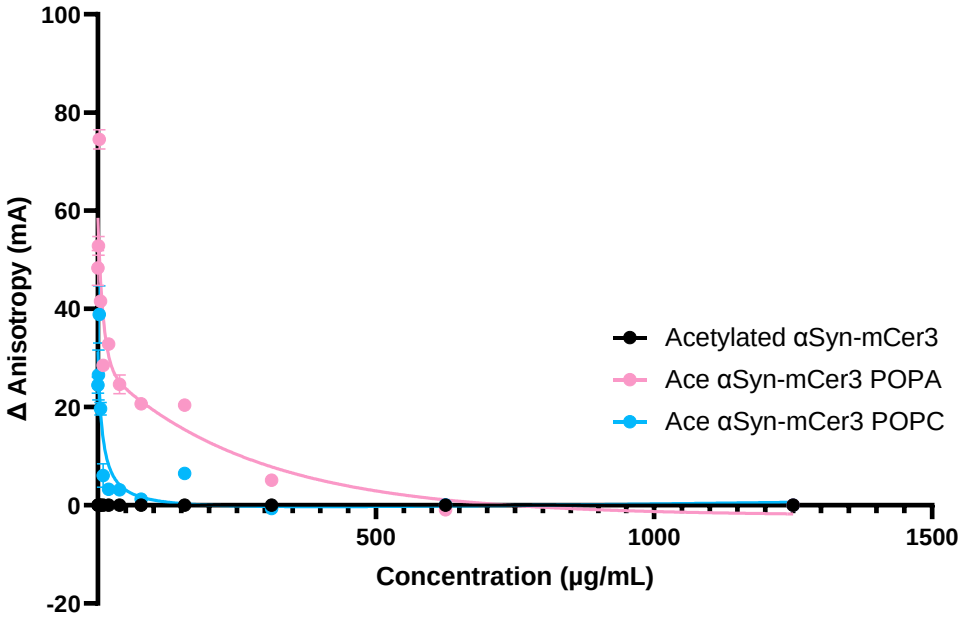

Figure 111. Acetylated α-syn-mCer3 anisotropy binding curves.

Graph showing the change in anisotropy of acetylated α-syn-mCer3 in the presence of POPA and POPC. Data points recorded are an average of three independent experiments and error bars represent the standard error of the mean (s.e.m).

Further, while initially there were higher anisotropy values were observed at lower concentrations in the presence of POPC, at concentrations above 100 ug/mL they were the same as the protein alone. This could suggest weaker interactions in comparison to those observed when POPA was present, as the anisotropy did not change to the same extent as when POPA was present, similar to the unacetylated protein.

Anisotropy values were seen to decrease below those of the protein controls in the presence of some liposomes, which resulted in a negative change in anisotropy. This was observed when acetylated α-Syn was in the presence of POPG, *E. coli* total and *E. coli* polar lipids (Figure 112).

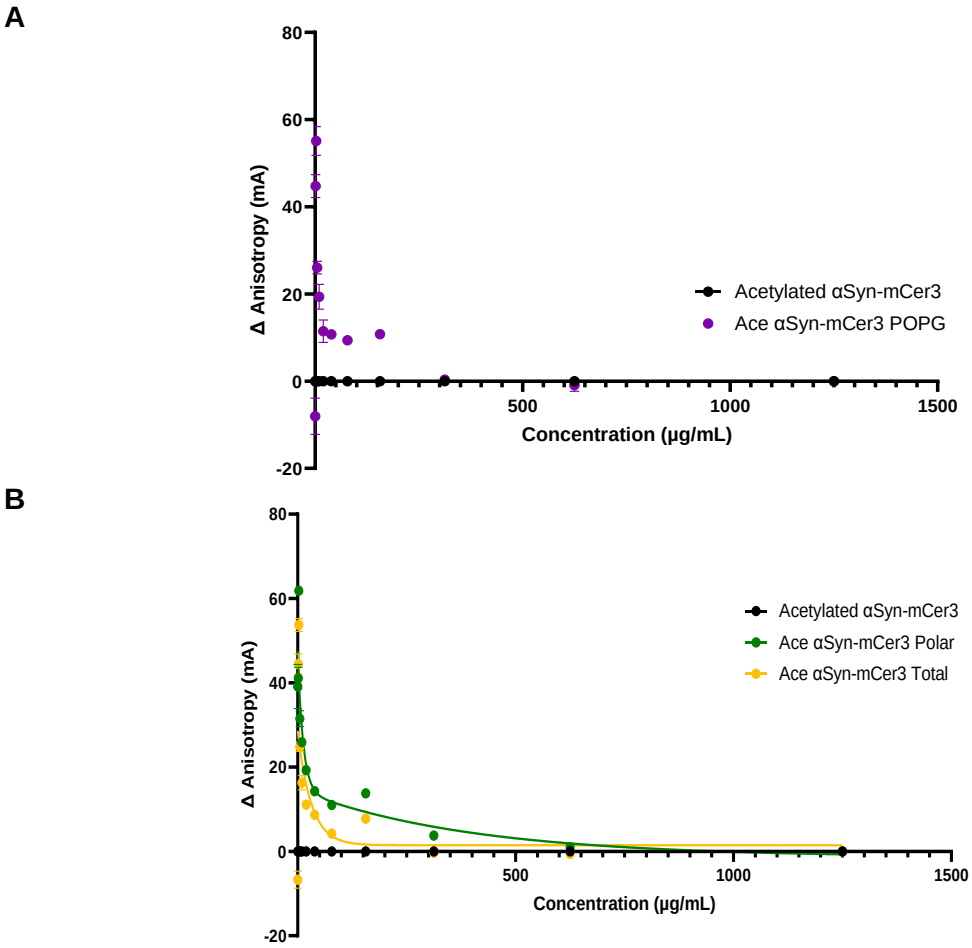

Figure 112. Acetylated α-syn-mCer3 anisotropy binding curves.

Graph showing the change in anisotropy of acetylated α-syn-mCer3 in the presence of **(A)** POPG and **(B)** *E. coli* total and *E. coli* polar lipids. Data points recorded are an average of three independent experiments and error bars represent the standard error of the mean (s.e.m).

For all three lipids, an initial decrease was observed at lower concentrations of protein, which was below that of the protein alone. Anisotropy values then followed a similar pattern as the other lipids after this initial decrease. This was also observed when both acetylated and unacetylated proteins were added to PG:PE lipids (Figure 113).

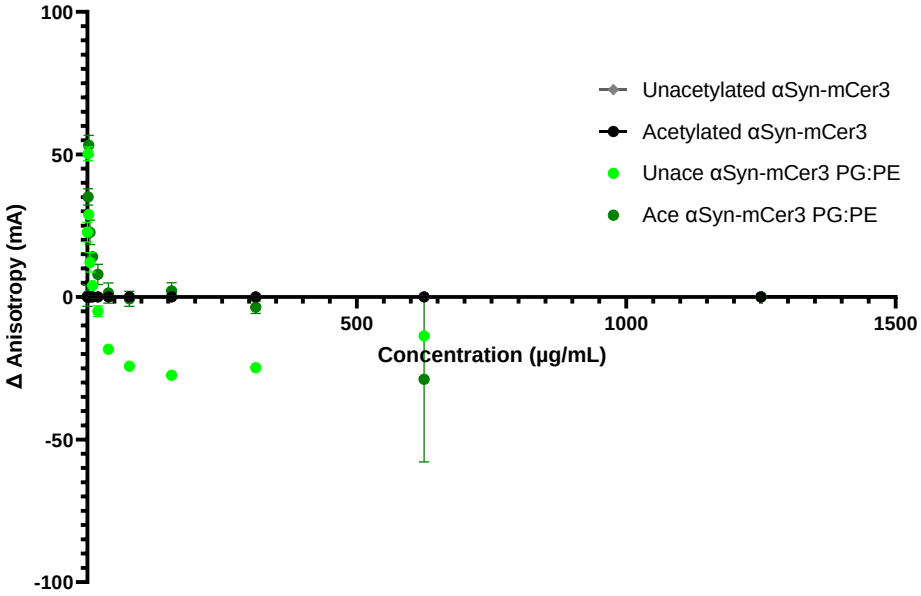

Figure 113. Acetylated α-syn-mCer3 Anisotropy binding curves.

Graph showing anisotropy curves of acetylated and unacetylated α-syn-mCer3 alone and in the presence of a 1:1 PG:PE mix. Data points recorded are an average of 3 independent experiments and error bars represent the standard error of the mean.

While initially, increased anisotropy values were observed, as the concentration increased, the anisotropy values decreased below those of the proteins alone. This was further observed when unacetylated α-Syn was added to POPG. However, in this case a significant decrease in anisotropy was observed at lower concentrations of protein, which then increased rapidly with increasing concentration of protein and then gradually decreased. (Figure 114).

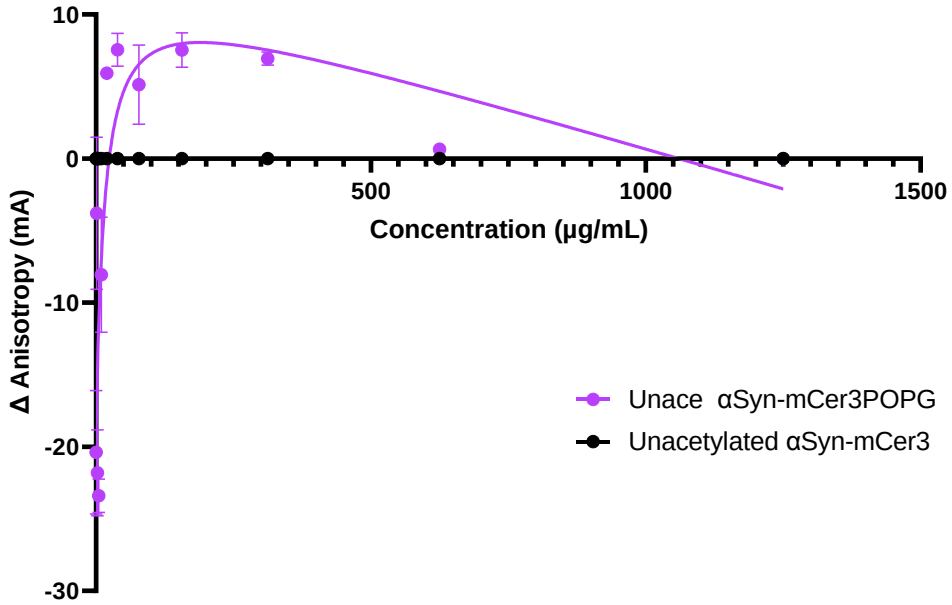

Figure 114. Anisotropy binding curves.

The change in anisotropy observed when unacetylated α-syn-mCer3 was added to POPG. Data points recorded are an average of 3 independent experiments and error bars represent the standard error of the mean.

The deceasing anisotropy values could indicate a change in the shape of either the proteins or the lipids upon interacting with one another. As previously mentioned, α-syn-mCer3 has been observed adopting an α-helical structure when interacting with anionic phospholipids, such as PG and CL, both of which are also present in the E. coli total and polar lipid mixes. Therefore, it was hypothesised that the decrease in anisotropy values may be attributed to an initial conformational change in the presence of POPG, polar, and total lipids. The subsequent increase observed with some of lipids, such as was seen with unacetylated α-Syn and POPG, may suggest secondary binding activities. However, further investigation would be required to clarify these observations.

A comparison of Figures 110 – 114 revealed reduced changed in anisotropy when acetylated α-syn-mCer3 was present in comparison to unacetylated α-Syn. This may suggest reduced binding activities when acetylated α-syn-mCer3 was present, which resulted in the hypothesis that acetylation may reduce lipid interactions, alluding to its regulatory role.

The binding activities of acetylated and unacetylated VNp-mNg were next investigated using fluorescence anisotropy experiments in the presence of POPC, POPG, and *E. coli* total and polar lipids. Comparisons of unacetylated VNp-mNg in the presence of either POPG or POPC revealed a higher affinity for POPG in comparison to POPC, as a significantly larger increase in anisotropy was observed with POPG than with POPC (Figure 115A).

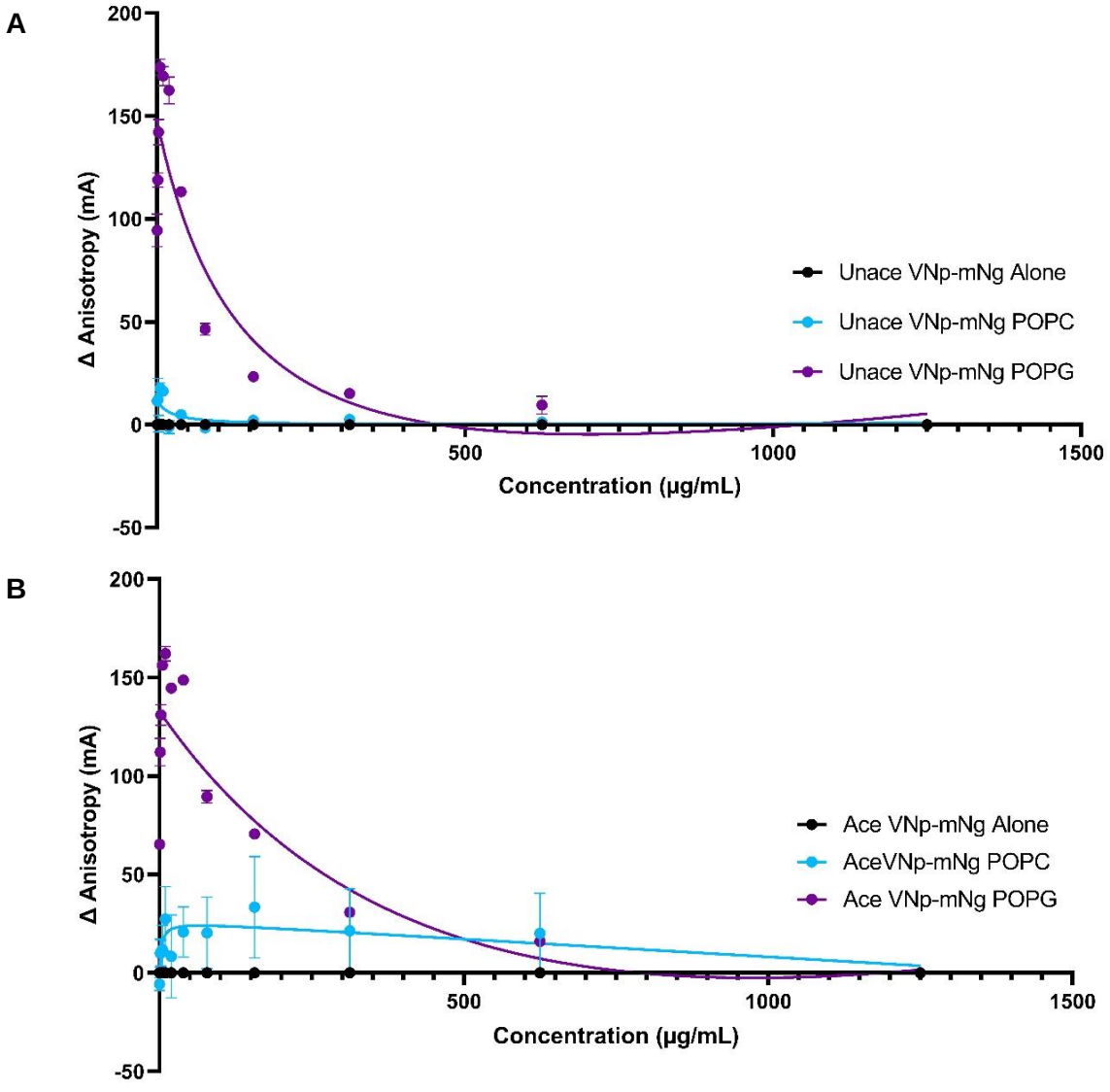

Figure 115. VNp-mNg anisotropy binding curves

Graph showing the change in anisotropy of **(A)** unacetylated and **(B)** acetylated VNp-mNg in the presence of POPC and POPG. Data points recorded are an average of 3 independent experiments and error bars represent the standard error of the mean (s.e.m).

Examination of the binding curves supports this, as anisotropy values were seen to drastically increase at lower protein concentrations when POPG was present. While an increase in anisotropy was observed with POPC, this was less than the increase observed in the presence of POPG. Similarly, acetylated VNp-mNg appeared to have a higher affinity for POPG than POPC, as significantly larger increases in anisotropy were observed (Figure 115B). A comparison of Figures 115A and 115B would suggest unacetylated VNp-mNg had a lower affinity for POPC in comparison to acetylated VNp-mNg. However, a larger variation in acetylated VNp-mNg anisotropy values was observed and therefore overall affinity for POPC may be similar for both proteins.

Aisotropy values that were lower than the protein alone were also observed with both VNp-mNg proteins in the presence of *E. coli* total lipids and when unacetylated VNp-mNg was in the presence of *E. coli* polar lipids (Figure 116). When unacetylated VNp-mNg was added to either *E. coli* polar or total lipids, anisotropy values at lower concentrations were seen to decrease below those of the protein alone with increasing protein concentration. Similarly, when acetylated VNp-mNg was added to *E. coli* polar lipids, an initial increase was observed, which was then followed by a decrease below the anisotropy values of the protein alone. As before, this was hypothesised to be either due to an initial conformational change in the protein, a change in shape or breakdown of the liposomes or a lack of binding. The binding activities observed with *E. coli* total and polar lipids between the α-Syn -mCer3 and VNp-mNg proteins appeared to differ, especially in the case of the unacetylated isoforms. This prompted the utilization of other binding assays to further characterise any interactions observed. Furthermore, while comparative affinities can be obtained by anisotropy, further analysis into the individual interactions was required to confirm the specific interactions.

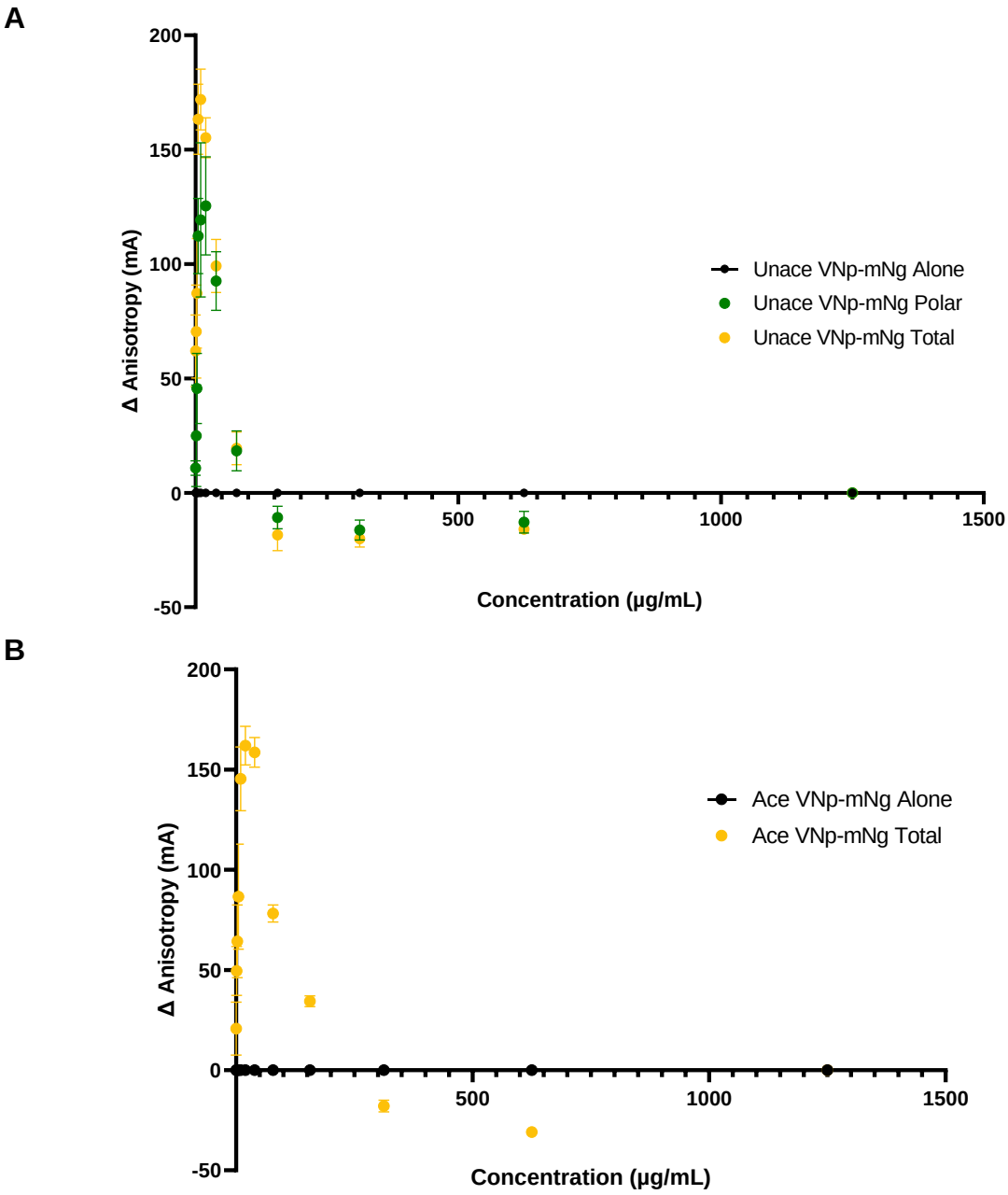

Figure 116. Anisotropy binding curves.

The change in anisotropy was observed for **(A)** unacetylated VNp-mNg and **(B)** acetylated VNp-mNg in the presence of E. coli total and polar lipids. Data points recorded are an average of 3 independent experiments and error bars represent the standard error of the mean (s.e.m).

5.4. Melting temperature

Following the anisotropy results, we sought to verify the binding activities exhibited by α-syn-mCer3 and further define the specific lipid interactions of α-syn. We, therefore, adapted the methodology presented by Hattori et al., 2012 and Nji et al., 2018 to perform thermal shift assays on acetylated and unacetylated α-syn-mCer3.[27,118] Thermal shift assays involve heating a fluorescently tagged protein at a range of temperatures in the presence and absence of liposomes, then comparing thermal denaturation to determine whether binding activities are taking place. The thermal shift assay is described in section **2.6.5** of the materials and methods. Briefly, mNeongreen and mCerulean fused proteins were incubated in the presence or absence of liposomes and with the non-ionic detergent octyl-Beta-D-glucoside (β-OG), as heat-induced aggregates precipitate with this detergent. Protein samples were then heated over a range of different temperatures and any resulting aggregates were sedimented by centrifugation. The fluorescence intensity of the supernatant was then recorded using a plate reader. As temperature increases, protein denaturation increases thereby decreasing the fluorescence intensity of the fluorescent tag. By plotting the fluorescence intensity against temperature, an apparent melting temperature (T_m) can be calculated. Increased thermostability of protein in the presence of lipid compared to the absence of lipid would indicate binding, thus a higher T_m would be observed.[27,118]

In order to determine whether the melting temperatures were statistically significantly different from one another, a between-groups ANOVA was performed. As the Levene's F test revealed that the homogeneity of variance assumption was not met, shown by *p*-values less than .05, Welch's *F* test was utilised. A series of Games-Howell multiple comparisons were performed to verify where the differences were if any. A full analysis is provided in the supplementary information. Initially, unacetylated and acetylated α-syn-mCer3 were heated at temperatures between 4°C and 100°C, then average fluorescence values were normalised and fitted to a sigmoidal curve and the Tm was calculated, as shown in Figure 117A.

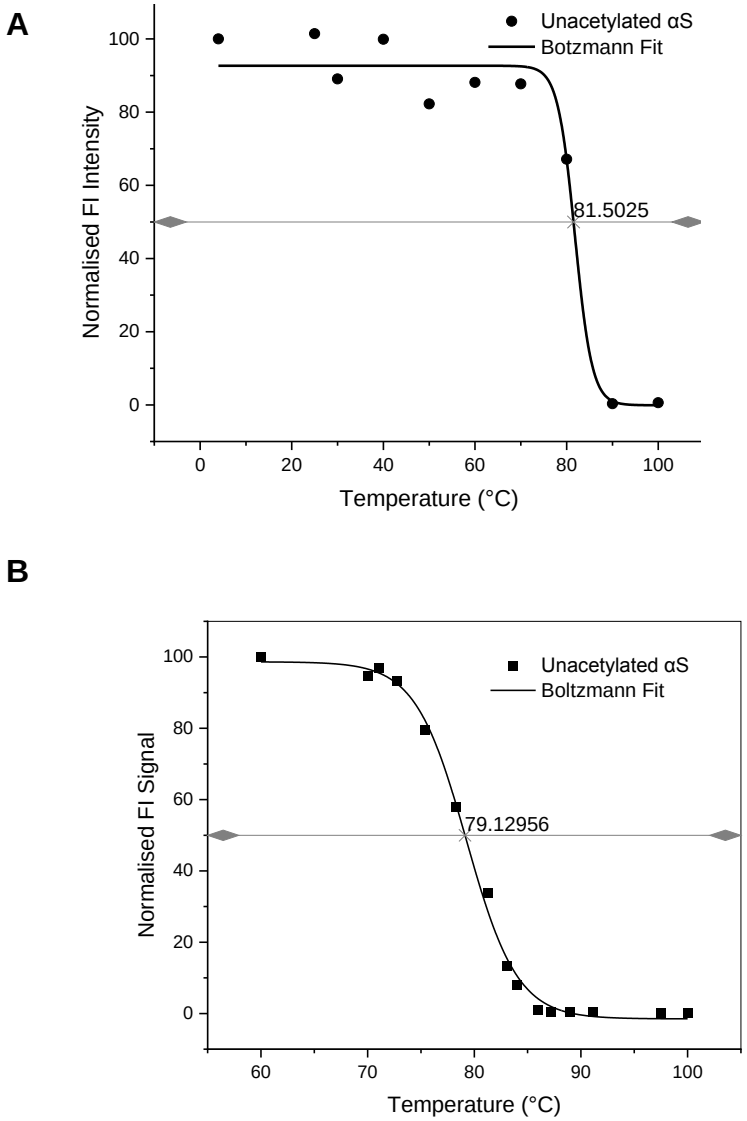

Figure 117. Melting curves of unacetylated α-syn-mCer3 alone.

(A) Initial melting curve used to determine the final temperature range. **(B)** final graph showing the temperature range used in melting temperature calculations. Average fluorescence values plotted are an average of three independent experiments.

From these initial melting curves, the optimal temperature range for analysis of the α-Syn -mCer3 proteins was determined to be between 60°C and 100°C. Following this, protein samples in the presence and absence of liposomes were heated at temperatures within that range and the individual melting temperatures were calculated, as demonstrated in Figure 117B. The final Tm values are reported in Table 26; each Tm reported uses average fluorescence intensity values from three independent experiments (mean ± SD).

The *p*-values obtained from the Games-Howell multiple comparisons post hoc test are recorded in Table 27.

Table 25. Thermal shift assay.

Melting temperatures calculated for unacetylated and acetylated α-Syn-mCer3 alone and in the presence of CL (cardiolipin), POPA, a 1:3 mix of PG:PE respectively, and *E. coli* total and polar lipids. [a] – unable to calculate a melting temperature. Standard deviation (SD) is used as the error value.

Melting Temperature (°C)		
	Unacetylated αSyn-mCer3	**Acetylated WT αS-FP-mCer3**
Protein alone	79.18 ± 0.48	77.86 ± 0.84
CL	[a]	[a]
POPA	82.16 ± 0.36*	82.48 ± 0.27*
PG:PE Mix	[a]	[a]
Polar lipids	79.46 ± 0.68**	77.59 ± 0.94**
Total lipids	81.75 ± 0.16*	81.80 ± 0.58*

*p <.05, **p >.05 in comparison to the respective protein alone

Table 26. Statistical analysis summary Table.

Summary of the Games-Howell posthoc test conducted on the melting temperatures of α-Syn-mCer3; *p*-values reported are a comparison to the protein alone. [a] – unable to calculate a melting temperature.

Games-Howell multiple comparisons posthoc summary		
	Unacetylated α-Syn-mCer3	**Acetylated α-Syn-mCer3**
CL	[a]	[a]
POPA	.000	.000
PC:PE Mix	[a]	[a]
Polar lipids	.966	.998
Total lipids	.000	.000

Both unacetylated and acetylated α-syn-mCer3 exhibited improved thermostability in the presence of POPA and Total lipids. Unacetylated α-syn-mCer3 produced significantly higher melting temperatures of 82.16°C and 81.75°C in the presence of POPA and Total lipids. Similarly, acetylated α-syn-mCer3 produced higher melting temperatures of

82.48°C and 81.80°C respectively, which again were statistically significantly different to the protein alone (p = .000 and p = .000 respectively). This improved thermostability suggested binding to these lipids. Strikingly, both acetylated and unacetylated α-syn-mCer3 in the presence of CL and the PC:PE mix appeared to exhibit significantly improved thermostability that minimal melting was observed in the presence of these lipids, thus no melting temperature could be calculated (Figure 118).

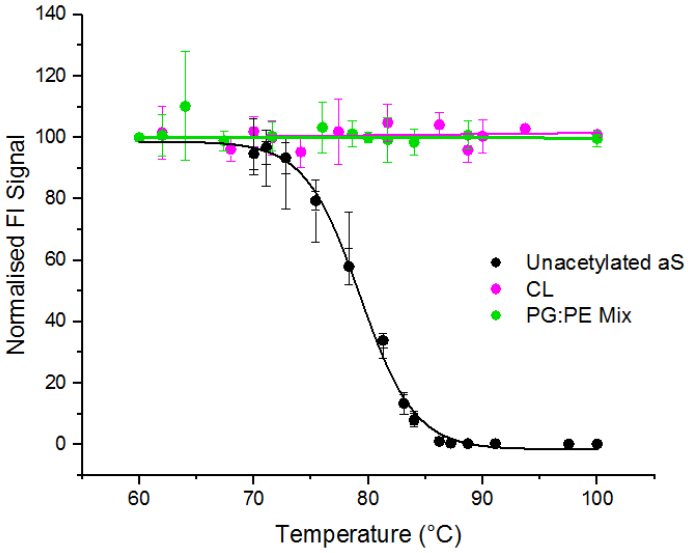

Figure 118. Thermal shift melting curves.

Melting curves were obtained for unacetylated α-syn-mCer3 alone and in the presence of Cardiolipin (CL) and a 1:3 PG:PE molar mix. Data points are an average of three independent experiments and standard deviation (SD) is used as the error value.

These results suggested stronger interactions with CL and the PC:PE mix in comparison to the other lipids, and binding activities with these lipids significantly improved thermostability, so much that no melting was observed (Figure 118).

Melting temperatures obtained in the presence of *E. coli* polar lipids were not statistically significantly different for both unacetylated (M = 79.46°C, SD = 0.68, p = .966) and acetylated (M = 77.59°C, SD = 0.94, p = .998) α-syn-mCer3 to those obtained for the proteins alone.

A comparison between the acetylated and unacetylated proteins revealed no difference in the binding activities, as both proteins exhibited binding to CL, POPA, PG:PE, and Total lipids, and no binding to polar lipids. However, the Tm value obtained for acetylated α-syn-mCer3 alone (*M* = 77.86°C, SD = 0.84) was lower than the Tm of unacetylated α-syn-mCer3 (*M* = 79.18°C, SD =0.48), which was found to be statistically significant (*p* = .020). Thus, acetylated α-syn-mCer3 appeared to be less stable in comparison to unacetylated α-syn-mCer3.

To further characterise and confirm binding, unacetylated and acetylated VNp-mNg were used in thermal shift assays. Similar to the α-syn-mCer3, the optimal temperature range was determined by heating protein samples at temperatures between 4°C and 100°C and plotting the fluorescence values against the temperature. The melting temperature range used was 55 - 80°C, which was expected as the VNp-mNg proteins were smaller in comparison to α-syn-mCer3 proteins. We also sought to investigate binding with other lipids, in particular, the PG:PE liposomes, to make further comparisons with the anisotropy data. Average fluorescence values from three independent experiments were used to calculate the T_m which is reported in Table 28 and a summary from the multiple comparisons posthoc test using the Games-Howell procedure is reported in Table 29.

Table 27. Thermal shift assay.

Melting temperatures calculated for acetylated and unacetylated VNp-mNg alone and in the presence of CL (cardiolipin), POPA, POPC, POPG, a 1:3 mix of PG:PE respectively, and *E. coli* total and polar lipids. Standard deviation (SD) is used as the error value.

Melting Temperature (°C)		
	Unace VNp-mNg	**Ace VNp-mNg**
None	65.43 ± 0.31	65.22 ± 0.43
CL	65.4 ± 0.30**	65.03 ± 0.14**
POPA	64.94 ± 0.18**	63.92 ± 0.61*
POPC	65.02 ± 0.29**	64.57 ± 0.33*
PC:PE Mix	66.84 ± 0.37*	65.68 ± 0.06**
POPG	65.2 ± 0.17**	64.44 ± 0.42*
Polar lipids	66.85 ± 0.11*	66.11 ± 0.25*
Total lipids	64.99 ± 0.60**	65.69 ± 0.57**

*p <.05, **p >.05 in comparison to the respective protein alone

Table 28. Statistical analysis summary Table

Summary of the Games-Howell Posthoc test conducted on the melting temperatures of VNp-mNg; p-values reported are a comparison to the protein alone; [a] – unable to calculate a melting temperature.

Games-Howell multiple comparisons posthoc test		
	Unace VNp-mNg	**Ace VNp-mNg**
CL	1.000	.991
POPA	.057	.007
POPC	.300	.112
PC:PE Mix	.000	.261
POPG	.822	.064
Polar lipids	.000	.007
Total lipids	.814	.802

Strikingly, the strong binding exhibited by unacetylated α-syn-mCer3 to CL was not observed with unacetylated VNp-mNg. In fact, the T_m value obtained for unacetylated

VNp-mNg in the presence of CL was not significantly different from the protein alone (p = 1.000). Similarly, the melting temperature obtained for acetylated VNp-mNg alone was not statistically significant to the Tm values obtained in the presence of CL and the PC:PE mix. While a less prominent effect was observed with unacetylated VNp-mNg in the presence of the PC:PE mix, the melting temperature was obtained was significantly higher than that of the protein alone (p = .000). Improved thermostability was observed with both acetylated and unacetylated VNp-mNg in the presence of polar lipids, as the melting temperature values (66.11°C and 66.85°C respectively) were statistically significantly higher than those of the proteins alone (65.22°C and 65.43°C respectively). The melting temperatures obtained for acetylated VNp-mNg in the presence of POPA, POPC, and POPG (63.92°C, 64.57°C, and 64.44°C respectively) were lower than the melting temperature of the protein alone (65.22°C). While numerically higher, the melting temperatures obtained with POPC and POPG were not statistically significantly different from that of the protein alone. The posthoc tests conducted using values of the protein alone and in the presence of POPA revealed that this lower temperature was statistically significant (p = .007).

It was hypothesised that lipid interactions may be induced by dimerisation of α-syn-mCer3, and VNp-mNg protein solutions may contain a mix of monomers and oligomers, resulting in less prominent binding being observed. As such, leucine zipper proteins were utilised. Leucine zippers are alpha helical protein-protein interaction domains consisting of amphipathic helices that dimerise in parallel and a series of leucine residues spaced seven residues apart.[256–259] Fusing proteins to leucine zippers provides a means of achieving guaranteed dimerisation of desired proteins in solution. Therefore, thermal shift assays were conducted using leucine zipper fused VNp-mNg.[257,259] This would allow us to determine whether dimerisation improved the binding activities of VNp-mNg observed. Acetylated and unacetylated isoforms were expressed and purified by Dr. Tara Eastwood and subsequent thermal shift assays were conducted by myself. Tabulated Tm values

presented in Table 30 are an average calculated from three independent experiments and three technical repeats (mean ± SD).

Table 29. Thermal shift assay.

Melting temperatures calculated for leucine zipper fused acetylated and unacetylated VNp-mNg alone and in the presence of CL (cardiolipin), *E. coli* polar, and total lipids. Standard deviation (SD) is used as the error value.

Melting Temperature (°C)		
	Unacetylated Lz VNp-mNg	**Acetylated Lz VNp-mNg**
None	63.42 ± 1.72	63.67 ± 1.81
CL	62.87 ± 0.21**	63.31 ± 0.29**
Polar lipids	64.06 ± 0.31**	64.39 ± 0.22**
Total lipids	63.75 ± 0.91**	64.42 ± 0.19**

*p <.05, **p >.05 in comparison to the respective protein alone

The multiple comparisons posthoc test using the Games-Howell procedure revealed that while the melting temperatures varied numerically, they did not vary statistically. This suggests a lack of lipid binding; however, this would be unusual as binding was observed with the full-length protein so that would be expected to translate when observing this membrane binding domain's interactions. If any lipid interactions were taking place, they did not impact the thermostability of both acetylated and unacetylated Leucine zipper fused-VNp-mNg enough to observe any differences in this assay. Furthermore, this suggests the involvement of other domains in lipid interactions within α-syn, as α-syn-mCer3 exhibited binding.

5.5. Myosin 1

Often model organisms are utilised in order to understand biological processes further, as a lot of these organisms contain homologs of bacterial genes and proteins and allow for the examination of these processes that are difficult to observe in humans.[260] One of

these model organisms is the nematode *Caenorhabditis elegans (C. elegans)*, often used as a simple model organism as they possess homologs of a majority of human genes. In particular, *C. elegans* encode at least 10 unconventional myosins, including the hum-1 gene, which encodes a *C. elegan* Myosin 1 homolog. Class 1 myosins are single headed motor proteins involved in a variety of membrane related functions, however, their specific lipid interactions are not fully characterised.[78,81,82,261] *C. elegan* myosin presents a typical class I structure, in that it contains an actin binding motor domain at the amino terminal, followed by a neck region and then finally a positively charged tail region, the focus of this study.[262] Within the tail region is a positively charged polybasic tail homology domain (TH1) which contains a pleckstrin homology domain, whose affinity to anionic membrane lipids has been documented in literature, however, regulation of these interactions is not well understood.[82] Phosphorylation, a mechanism employed to regulate protein function, is thought to be integral to Myosin 1 function. Potential phosphorylation sites have been identified within the TH1 domain and these are thought to be involved in regulating lipid interactions.[86] And while the TH1 domain has been suggested to cause Myosin 1 membrane binding, when phosphorylated and unphosphorylated, its specificity and affinity are yet to be fully characterised.

5.5.2. Aim of studies

Therefore, as the mechanisms behind lipid binding of myosin 1, in particular, the role of the TH1 domain is not well defined, we also sought to understand the specific lipid binding activities and the impact of phosphorylation on these binding activities.

5.5.3. Protein expression

In an effort to understand the membrane binding affinities of the TH1 domain in Myosin 1 and the role of phosphorylation in regulating these interactions, a recombinant wild type protein and also a phosphorylation mimic were generated from the *C. elegans* hum-1 TH1 domain. The phospho-mimic was created by replacing a serine residue (S734) with aspartic acid. After a variety of expression conditions and competent cell strains were

tested, it was determined that the use of BL21 PlysS DE3 competent cells significantly improved expression (Figure 119).

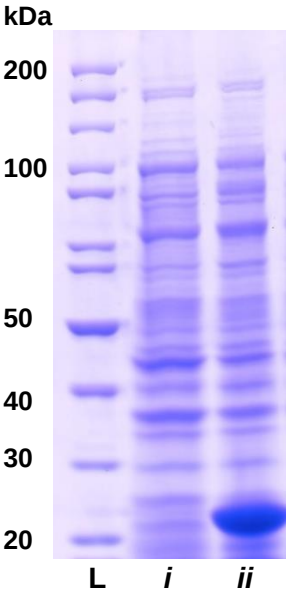

Figure 119. SDS PAGE expression gel.

Samples from wild type Hum-1 TH1 expression *(i)* pre-induction and *(ii)* post-induction in BL21 PlysS. L = protein molecular weight marker ***** - protein size ~ 23 kDa.

PlysS plasmids tend to be used for the expression of toxic genes, as they co-express a T7 polymerase inhibitor which reduces the background expression levels of target genes.[263] Ordinarily, expression of toxic genes in BL21 DE3 competent cells results in the selectivity of cells that do not produce the toxic gene, leading to varied, low, or a complete lack of protein expression, as was observed.[263] This led us to hypothesise that the Hum-1 TH1 protein may be toxic to the cells, leading to the complete lack of protein, and the use of the plysS plasmid allowed us to overcome this. Reduction of the IPTG concentration to 20 µg/ml and the induction temperature to 25°C further improved expression, further solidifying the hypothesis.

5.6. Hum-1 TH1 Purification and Refolding

The presence of hydrophobic residues within the PH domain of the TH1 protein reduced the solubility of the protein.[83] Purification under native conditions revealed a lack of binding to the nickel resin and the protein that was obtained in the final elutions precipitated out of solution (Figure 120A). As such, proteins were purified under denaturing conditions, through the use of urea which reversibly denatures and solubilises proteins, allowing effective purification. Protein refolding is typically achieved by dialysis

through the use of a linear urea gradient.[264,265] Proteins were successfully purified using denatured purification (Figure 120B), however during the dialysis process, the proteins were once again observed to precipitated fairly rapidly.

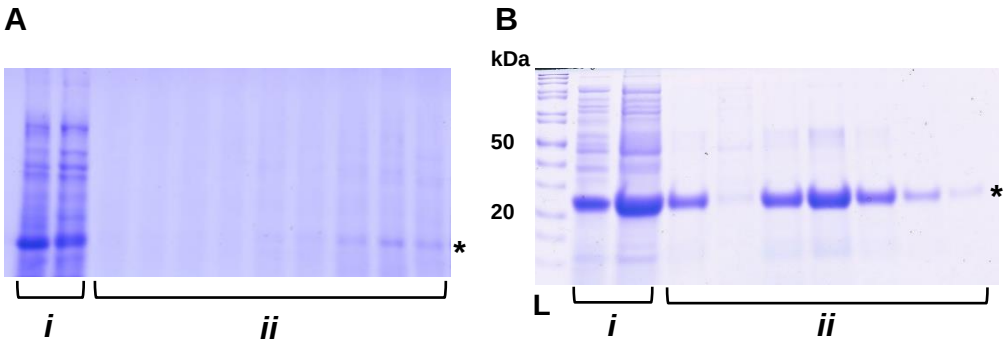

Figure 120. SDS PAGE purification gels.

(A) Native purification of Hum-1 TH1 S74D mutant: *(i)* pre-purification samples, *(ii)* post-purification elutions. **(B)** Denaturing purification of Hum-1 TH1 S734D: *(i)* pre-purification samples, *(ii)* post-purification elutions. L = protein molecular weight marker ***** - protein size ~ 23 kDa.

The use of chromatographic procedures, such as sephadex columns, has been previously used for the removal of molecules with small molecular weights, such as urea.[266,267] Sephadex is a gel filtration resin that allows the migration of larger molecules, such as proteins, but retains smaller molecules, such as urea, thereby separating them. Desalting was carried out as described in section **2.3.17** of the materials and methods, however briefly, protein post-purification samples were loaded onto a pre-calibrated Sephadex column and 1 mL elutions were taken from the column. Typically, urea would be eluted from the column between elutions 4 – 7, whereas the protein should elute in the first and second fractions. The use of the desalting column allowed for faster urea removal, in the hope that precipitation would not occur. Both the WT and S734 Hum-1 TH1 proteins were collected in the first 2 fractions (Figure 121), and no protein was observed in the urea fractions.

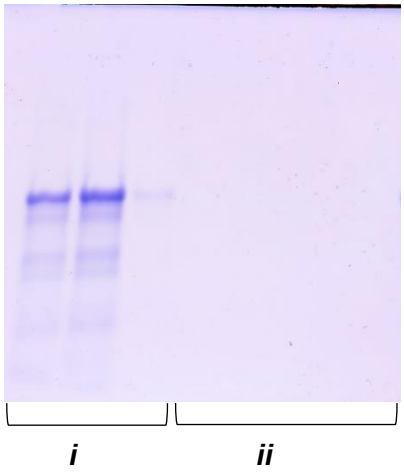

Figure 121. SDS PAGE desalting gels.

Elutions from the Sephadex desalting column of WT Hum-1 TH1 protein. Protein was observed in the urea fractions only. L = protein molecular weight marker ***** - protein size ~ 23 kDa.

Although the urea removal appeared to be successful (Figure 121), and proteins remained solubilised after the buffer exchange, initial co-sedimentation experiments conducted using revealed that the solubility observed with these proteins was short-lived, as proteins not only sedimented without lipid present but precipitated rapidly (Figure 122), which suggested impaired protein re-folding.

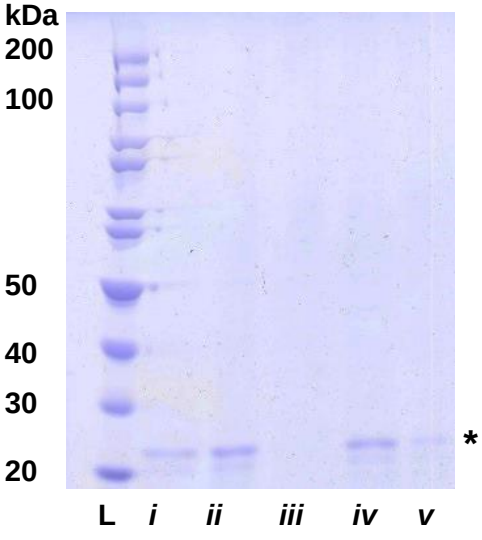

Figure 122. SDS PAGE of co-sedimentation experiments.

SDS-PAGE gel of pellet samples from initial co-sedimentation experiments: *(i)* S734D mutant alone, *(ii)* S734D mutant with PE lipid, *(iii)* Blank, *(iv)* WT protein and PE lipid, *(v)* WT protein alone. L = protein molecular weight marker; ***** - protein size ~ 23 kDa.

Consequently, the Hum-1 TH1 proteins were fused with reporter protein mNeonGreen resulting in a protein ~51 kDa in size. This drastically improved solubility, and though overall protein yield was reduced due to the protein sedimentation pre-purification, successful purification under native conditions was achieved with the solubilised protein (Figure 123).

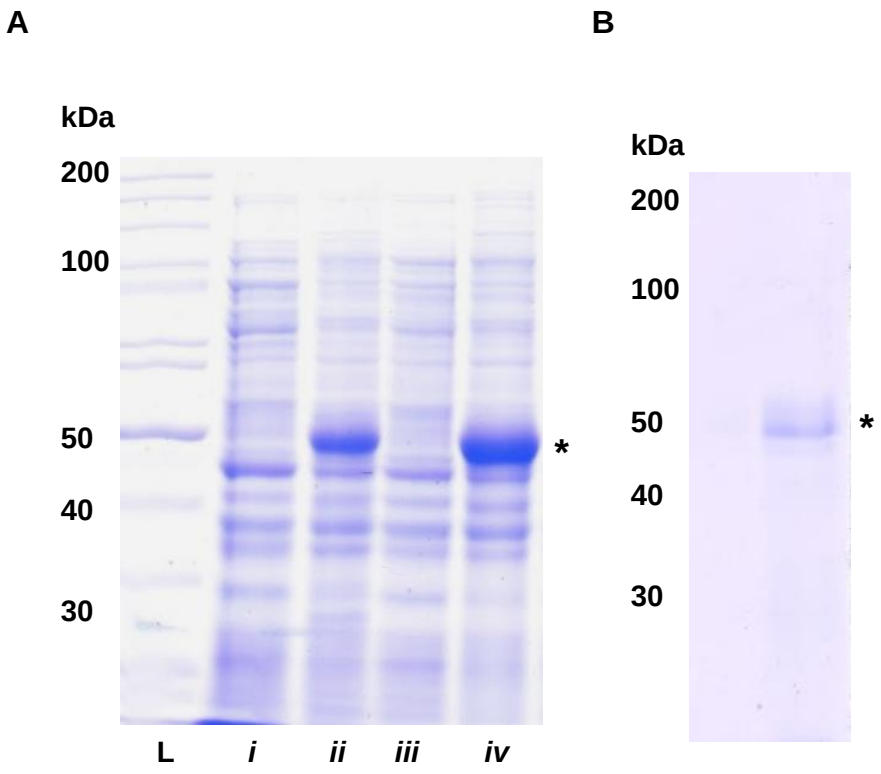

Figure 123. Hum-1 TH1-mNg SDS PAGE gels.

(A) WT Hum-1 TH1-mNg expression; *(i)* pre induction; *(ii)* post induction samples and S734D Hum-1 TH1 expression *(iii)* pre induction and *(iv)* post induction samples. **(B)** purified WT Hum-1 TH1-mNg. L = protein molecular weight marker; ***** - protein size ~ 51 kDa.

5.7. Hum-1 TH1 lipid binding

PIP strip arrays are nitrocellulose membranes with phospholipids noncovalently attached to the surface, which allow the lipid binding specificity of proteins to be observed even with low protein concentrations.[112,268] As the overall protein expression was low, these provided an opportunity to observe any differences in the lipid binding properties between the wild type TH1 and the S734D mutant. PIP strip analysis was conducted as described in section **2.3.19** of the materials and methods, Briefly, proteins were incubated with PIP strips, allowing the proteins to bind to the phospholipids, then unbound protein was washed off and western blot procedures were used for detecting bound protein, which would appear as a darker spot on the PIP strip, (Figure 124).

A

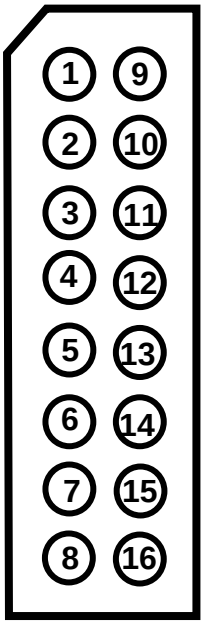

1. Lysophosphatidic acid
2. Lysophosphatidylcholine
3. Phosphatidylinositol (PtdIns)
4. PtdIns (3)P
5. PtdIns (4)P
6. PtdIns (5)P
7. Phosphatidylethanolamine
8. Phosphatidylcholine
9. Sphingosine 1-phosphate
10. PtdIns (3,4) P_2
11. PtdIns (3,5) P_2
12. PtdIns (4,5) P_2
13. PtdIns (3,4,5) P_3
14. Phosphatidic acid
15. Phosphatidylserine
16. Blank

B

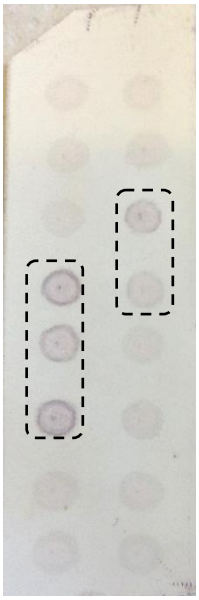

C

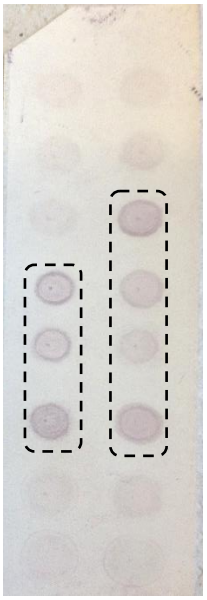

Figure 124. PIP Strip binding assay.

(A) Pip strip layout.[112,268] **(B)** PIP Strip conducted using WT Hum-1 TH1-mNg **(C)** PIP Strip conducted using Hum-1 TH1 S734D-mNg.

Similar binding was observed with both WT TH1 and the S734D mutant to PtdIns(3)P, PtdIns(4)P, and PtdIns(5)P. Interactions with these lipids by both Hum-1 isoforms suggested that phosphorylation did not impact binding to these lipids under these experimental conditions. While both proteins bound to PtdIns(3,5)P_2 and PtdIns(4,5)P_2, TH1 S734 exhibited stronger binding both lipids, indicated by the stronger detection. Additional S734D TH1 binding was observed to phosphatidic acid, which was not

observed WT TH1. Furthermore, there appeared to be weak binding of S734D TH1 to PtdIns(3,4,5)P_3. Stronger phosphatidic acid binding was observed with S734D TH1, which suggested phosphorylation-based regulation to this specific lipid, thus may impact specific processes within the cell.

Following these results, we sought to use liposomes to further characterise binding to these lipids, and confirm the results observed with the PIP strip experiments. Sedimentation assays had previously been shown to be ineffective with the TH1 proteins, as the proteins readily sedimented regardless of the presence of liposomes. Therefore, co-sedimentation assays under a density gradient were conducted, using the fluorescence of mNeonGreen to detect the presence of the protein and the addition of FM4-64 after centrifugation to detect the presence of the liposomes. Due to time constraints, only the WT TH1 was used in the following assay, thus only a confirmation of the binding observed in the above PIP strip could be conducted and a comparison could not be obtained using this assay. Co-sedimentation assays were carried out as described in section **2.6.2** of the materials and methods, briefly WT TH1 mNeongreen protein the presence and absence of liposomes underwent sucrose density centrifugation, with two repeats of each condition. Following this, three fractions were obtained (top, middle, and bottom) and the protein fluorescence in each fraction was determined by the mNeongreen fluorescence values obtained using a fluorescence detecting plate reader. FM4-64 was then added to each fraction, allowed to mix, and bind, then FM4-64 fluorescence was used to detect the presence of liposomes in each fraction. The average fluorescence intensity was calculated using the values from each repeat and a graphical representation of the fluorescence values is shown in Figure 125.

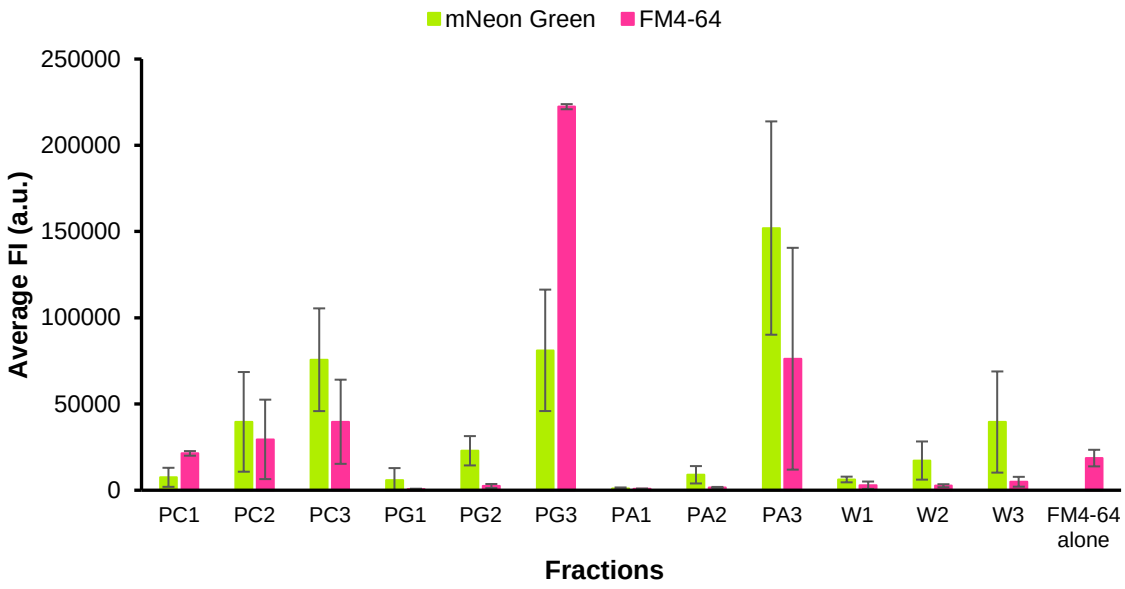

Figure 125. Average fluorescence intensity values obtained from the density gradient co-sedimentation assay.

PC – phosphatidylcholine, PG – phosphatidylglycerol, PA – phosphatidic acid, W – WT Hum-1 TH1, (1) – fraction 1, (2) – fraction 2, (3) – fraction 3. *n* = 2 for all groups. Standard deviation (SD) was used as the error value.

A series of multiple comparisons were performed using Games-Howell's posthoc test in order to determine whether the fluorescence values were equal to each other. A detailed description of the statistical analysis performed is provided in the supplementary information, however, a summary of relevant comparisons is reported in tables - below.

An initial comparison between the fractions obtained for the negative control (protein with no lipid present) reveals no statistically significant difference in the FM4-64 and mNeongreen fluorescence values (Table 31). This suggested an even distribution of protein between fractions for the controls, and no significant difference in FM4-64 fluorescence between fractions, thus any difference observed would be a result of the lipids.

Table 30. Summary of statistical analysis for the negative controls.

Summary Table using *p*-values obtained from the Games-Howell multiple comparisons posthoc test conducted from the on FM4-64 and mNg fluorescence values obtained for each fraction of WT Hum-1 TH1 protein alone; *p*-values reported. mNg – mNeongreen fluorescence, (1) – fraction 1, (2) – fraction 2, (3) – fraction 3.

Games-Howell multiple comparisons posthoc summary						
	FM4-64 (1)	**FM4-64 (2)**	**FM4-64 (3)**	**mNg (1)**	**mNg (2)**	**mNg (3)**
FM4-64 (1)	-	1.000	.987			
FM4-64 (2)	1.000	-	.701			
mNg (1)				-	.448	.314
mNg (2)				.448	-	.785

p > .05 – no statistically significant difference, *p* < .05 – statistically significant difference.

As shown in Table 32 below, any differences in FM4-64 fluorescence values obtained in the presence of PC between fractions 1 and 2 (*p* = .999), 1 and 3 (*p* = .731), and 2 and 3 (*p* = 1.000) were not statistically significantly different from one another. This indicated an even distribution of lipid.

Table 31. Statistical analysis comparing mean FM4-64 fluorescence values.

Summary Table using *p*-values obtained from the Games-Howell's multiple comparisons posthoc test conducted on FM4-64 fluorescence values obtained for each fraction of WT Hum-1 TH1 protein in the presence of **PC** (phosphatidylcholine), *n* = 2 for each group. (1) – fraction 1, (2) – fraction 2, (3) – fraction 3; *p*-values reported.

Games-Howell's Posthoc Test Summary			
	PC (1)	**PC (2)**	**PC (3)**
PC (1)	-	.999	.731
PC (2)	.999	-	1.000

p > .05 – no statistically significant difference
p < .05 – statistically significant difference.

However, the protein was observed predominantly in the second and third fractions. The mNeongreen fluorescence values obtained from the first fraction (Table 33) were statistically significantly lower than those of fraction 3 (p = .023), whereas no statistically significant difference was observed with fraction 2 in comparison to fractions 1 (p = .337) and 3 (p= .561).

Table 32. Statistical analysis comparing mean mNg fluorescence values.

Summary Table using *p*-values obtained from the Games-Howell's multiple comparisons posthoc test conducted on mNg fluorescence values obtained for each fraction of WT Hum-1 TH1 protein in the presence of **PC** (phosphatidylcholine), n = 2 for each group. (1) – fraction 1, (2) – fraction 2, (3) – fraction 3.

Games-Howell's Posthoc Test Summary			
	PC (1)	**PC (2)**	**PC (3)**
PC (1)	-	.337	.023
PC (2)	.337	-	.561

p < .05 – statistically significant difference.
p > .05 – no statistically significant difference

This suggested an increasing protein concentration from factions 1 – 3. Furthermore, as the lipid remained evenly dispersed but the protein sedimented, this indicated low binding to PC lipids, consistent with the PIP strip results.

Conversely, both PG lipids and WT TH1 were predominantly located in the third fraction together. The FM4-64 fluorescence intensity values obtained in the third fractions were found to be statistically significantly higher than those of fractions 1 (p = .000) and fraction 2 (p= .000) (Table 34). This suggested sedimentation of PG lipids, as the sedimentation of PG lipids was not observed with PC lipids. When mNeongreen fluorescence values were compared (Table 35), lower fluorescence values were obtained for fraction 1, which was found to be statistically significantly different from fraction 2 (p = .045) and fraction 3 (p = .047).

Table 33. Statistical analysis comparing mean FM4-64 fluorescence values.

Summary Table of the Games-Howell's multiple comparisons posthoc test conducted on FM4-64 fluorescence values obtained for each fraction of WT Hum-1 TH1 protein in the presence of **PG** (phosphatidylglycerol), *n* = 2 for each group. (1) – fraction 1, (2) – fraction 2, (3) – fraction 3.

Games-Howell's Posthoc Test Summary			
	PG (1)	**PG (2)**	**PG (3)**
PG (1)	-	.143	.000
PG (2)	.143	-	.000

p < .05 – statistically significant difference.
p > .05 – no statistically significant difference

Table 34. Statistical analysis comparing mean mNg fluorescence values.

Summary Table using *p*-values obtained from the Games-Howell's multiple comparison posthoc test conducted on mNeongreen fluorescence values obtained for each fraction of WT Hum-1 TH1 protein in the presence of **PG** (phosphatidylglycerol), *n* = 2 for each group. (1) – fraction 1, (2) – fraction 2, (3) – fraction 3.

Games-Howell's Posthoc Test Summary			
	PG (1)	**PG (2)**	**PG (3)**
PG (1)	-	.045	.047
PG (2)	.045	-	.131

p < .05 – statistically significant difference.
p > .05 – no statistically significant difference

However, while fluorescence values obtained for fraction 3 were higher than those of fraction 2, no statistical difference was observed between them (*p* = .131) This suggested predominant distribution of protein in fractions 2 and 3, which also indicated protein sedimentation. As lipid and protein appeared to sediment together, this suggested binding of PG lipids to WT Hum1 TH1.

The FM4-64 fluorescence values obtained in the presence of PA lipids suggested predominant localisation in fraction 3. The multiple comparisons posthoc test revealed no

statistically significant difference when compared to fraction 1 (p = .334) and fraction 2 (p = .343), as seen in Table 36.

Table 35. Statistical analysis comparing mean FM4-64 fluorescence values.

Summary Table using p-values obtained from the Games-Howell's multiple comparisons posthoc test conducted on FM4-64 fluorescence values obtained for each fraction of WT Hum-1 TH1 protein in the presence of **PA** (phosphatidic acid), n = 2 for each group. (1) – fraction 1, (2) – fraction 2, (3) – fraction 3.

Games-Howell's Posthoc Test Summary			
	PA (1)	**PA (2)**	**PA (3)**
PA (1)	-	.029	.334
PA (2)	.029	-	.343

p < .05 – statistically significant difference.
p > .05 – no statistically significant difference

This is more likely due to the large variation observed; thus no solid conclusion can be made from this value. An increase in FM4-64 fluorescence values obtained in fraction 2, which was found to be statistically significantly different from those of fraction 1 (p = .029). This suggested the lipid was most likely located in fractions 2 and 3. When mNeongreen fluorescence values were examined, no statistically significant difference was observed between the fluorescence values obtained (Table 37), despite higher fluorescence values being obtained in fractions 2 and 3.

Table 36. Statistical analysis comparing mean mNg fluorescence values.

Summary Table using p-values obtained from the Games-Howell's multiple comparisons posthoc test conducted on mNg fluorescence values obtained for each fraction of WT Hum-1 TH1 protein in the presence of **PA** (phosphatidic acid), n = 2 for each group. (1) – fraction 1, (2) – fraction 2, (3) – fraction 3.

Games-Howell's Posthoc Test Summary			
	PA (1)	**PA (2)**	**PA (3)**
PA (1)	-	.111	.062
PA (2)	.111	-	.076

p < .05 – statistically significant difference.
p > .05 – no statistically significant difference

Therefore, no solid conclusion could be made from these data, as these results from the multiple comparisons posthoc test were most likely a result of the large variation observed. An additional repeat may reduce the variation observed with these data.

A comparison of the PIP strip results and the density gradient co-sedimentation assay highlights the need for multiple lipid binding assays to gain a clearer picture of the protein binding properties. While the results with PC lipids were consistent in that minimal binding was observed in both assays, notably, while PG is not present on the PIP strip. However, a comparison could be made with the other anionic lipids present on the PIP strip, which were PI, PtdIns(4)P, PtdIns(4,5)P_2, and PtdIns(3,4,5)P_3, PS. These lipids contain 1, 3, 5, 7, and 1 net negative charges, respectively. From the PIP strip results, out of the anionic lipids, stronger binding of S734D, as suggested by the darker spots, was observed with PtdIns(4,5)P_2, which carried a net negative charge of -5. Phosphatidic acid (PA) carries a net negative charge of -2, and stronger binding was observed with S compared to the wild type. However, despite carrying a negative charge of -7, PtdIns(3,4,5)P_3 showed less binding in comparison to the other lipids, indicating lipid binding was not solely due to charge interactions. This was further observed with the binding of PtdIns(3,4)P_2, PtdIns(3)P, PtdIns(4)P, and PtdIns(5)P exhibited by both wild type and S734 TH1, despite holding weaker negative charges. Thus, while the density gradient co-sedimentation assay provided additional lipid binding information, further binding experiments would need to be carried out in order to confirm the binding properties of Hum-1 TH1.

5.8. Summary

Hypothesis	**Evidence**
Oligomerisation was observed with acetylated α-syn-mCer3 but not unacetylated α-syn-mCer3.	Two clear strong bands were observed for both acetylated VNp-mNg and α-syn-mCer3; one at the expected protein size and another at ~85-100 kDa on both SDS PAGE gels and western blots.
	A single band at the expected protein size was observed with unacetylated isoforms.
Unacetylated α-syn-mCer3 exhibited higher lipid binding affinities than acetylated α-syn-mCer3, therefore acetylation may reduce lipid interactions.	Larger increases in anisotropy were observed with unacetylated α-syn-mCer3 in comparison to the acetylated isoform.
	Decreasing anisotropy values were observed predominantly with acetylated α-syn-mCer3.
Unacetylated α-syn-mCer3 exhibited higher lipid binding affinities to *E. coli* polar lipids than *E. coli* total lipids, which suggests binding PE and PG lipids.	A larger increase in anisotropy were observed in the presence of polar lipids, which contained a higher PE and PG content than total lipids.
Highest affinity observed with POPA with both α-syn-mCer3 isoforms	Significantly larger increases in anisotropy were observed with POPA
The presence of CL, POPA, PG:PE, and *E. coli* total lipids improved the thermostability of both unacetylated and acetylated α-syn-mCer3.	Larger thermal shifts were observed when these lipids were present in comparison to the other lipids and the proteins alone.

Reduced binding activities were observed with both VNp-mNg isoforms.	The majority of melting temperatures calculated were not statistically significant to the protein alone.
Unacetylated VNp-mNg interacted with PG:PE liposomes.	Improved thermostability observed with the presence of PG:PE liposomes.
Interactions between leucine zipper fused VNp-mNg proteins and liposomes did not impact the thermostability of the proteins.	Melting temperatures obtained with leucine zipper fused VNp-mNg isoforms were not statistically significant whether lipid was present or absent.
Other domains may be involved in specific lipid interactions.	Overall reduced lipid interactions observed with VNp-mNg proteins when compared to the α-syn-mCer3.
	Dimerisation through the use of leucine zipper fused VNp-mNg isoforms did not improve lipid binding.
Suggested PA and PG binding of WT TH1	PG and PA lipids sedimented with the protein whereas PC lipids were generally evenly spread out.
	Increased fluorescence was also observed in the presence of these lipids, suggesting binding.

Summary

The anisotropy results suggest a higher affinity of α-syn-mCer3 to POPA liposomes, which was further solidified by the improved thermostability of both proteins whilst the lipid was present. While it was hypothesised that α-syn-mCer3 interactions with PG:PE liposomes were either minimal or unstable through the anisotropy results, the thermal shift assay revealed stronger binding in comparison to the other liposomes. The negative anisotropy results suggest a change in the shape of the protein or liposomes, which is known to occur with alpha synuclein upon interactions with liposomes. This may explain sudden changes in anisotropy observed with PG:PE liposomes and with total and polar liposomes. The thermostability of the VNp-mNg proteins was not greatly impacted by any interactions that may have been taking place. Conversely, the anisotropy data revealed lipid interactions, thus highlighting the need for multiple binding assays in defining the specific lipid interactions.

Through these studies, we were able to observe the impact of post-translational modifications on specific lipid interactions. A comparison between the acetylated and unacetylated proteins revealed reduced binding, making it possible to gain insight into the regulatory role of acetylation. The anisotropy results revealed lower lipid affinities with acetylated α-syn-mCer3 in comparison to unacetylated α-syn-mCer3, which suggests acetylation reducing lipid interactions. Furthermore, oligomerisation was observed with acetylated proteins but not with the unacetylated isoforms, which suggests a role in protein folding and conformation. A comparison of WT and S734D Hum 1 TH1 revealed phosphorylation increasing binding to specific lipids, in particular PA, which indicates a phosphorylation-based regulation. Further investigation, which was not possible due to COVID, would be required in order to further characterise these lipid interactions. Nonetheless, the data presented within this chapter aids in the understanding of post-translational regulation.

Chapter 6: Discussion

6.1. The development of multifunctional SSAs to tackle antimicrobial resistance

The studies described in chapter 3 sought to explore the relationship between the structure of an antimicrobial molecule and the bacterial activity exhibited, through stepwise molecular changes to SSA **32** and subsequent antimicrobial testing. In chapter 4, these structure-activity relationships were then utilised for the creation of second-generation SSAs that exhibited improved *E. coli* activity. While several functional groups were observed to improve activity, it is worth noting that simply incorporating these groups in molecules did not always improve activity. An example of this is observed with the TEA counter cation, which exhibited reduced activity when paired with a urea anion, but improved activity when paired with a thiourea anion. Thus, how the different functional groups interacted with one another, and the resulting structures observed also influenced the antimicrobial activity. Furthermore, improved antimicrobial activity may also be achieved by incorporating other functional groups that can achieve similar interactions.

As described previously, lipid interactions can occur through binding to the head group, the acyl chains, or both.[104] Thus, the improved activity observed with more amphiphilic molecules may be due to those SSAs having a higher likelihood to interact with both polar head groups and hydrophobic tails.

Overall, SSAs exhibited improved activity against MRSA in comparison to *E. coli*, the predominant cause of this most likely being the additional outer membrane present in *E. coli*. However, a comparison of the lipid composition may provide further insight into the higher activity exhibited against MRSA. The predominant lipids present in *E. coli* membranes are PE (~75%) and anionic lipids PG and CL (~20%), whereas MRSA predominantly contains PG (~50%), DAG (~ 20%), and other PG derivatives (~38%).[70,163,269,270] As the SSAs were observed interacting with membrane lipids through the FM4-64 competitive binding assay, and PG lipids are the most abundant MRSA membrane lipid, it is hypothesised that SSAs were interacting with PG lipids.

CL lipids are also present in MRSA membranes, however their relative proportion changes depending on growth stages. During the exponential phase, CL lipids make up ~ 1% of MRSA membranes, however as cells enter stationary phase this is estimated to increase six-fold.[70,269] Similarly, as *E. coli* cells enter stationary phase, PG lipids are converted to CL lipids resulting in a lower PG content and increased CL content. Some SSAs, such as SSA **34**, were characterised as producing delayed inhibition against *E. coli*, as a reduction in growth was not observed until the stationary phase.[70,271] Thus, interactions with both CL and PG lipids may produce the delayed inhibition exhibited by SSAs against *E. coli* as well as complete inhibition of MRSA. The anisotropy experiments provided further evidence of PG and CL binding, as SSAs **69** and **70** were both observed interacting with PG lipids and with *E. coli* total and polar lipids. The *E. coli* total and polar lipid extracts also contained PG lipids (15% and 23% respectively) and CL lipids (10% for both).[196] Thus, SSAs were hypothesised to interact with PG predominantly and CL to a lesser extent.

Targeting bacterial membranes is by no means simple, due to the diversity of lipid compositions, firstly between bacterial species and also between growth phases. However, if successful, membrane targeting can provide a way to target specific bacteria with high accuracy whilst also reducing mammalian toxicity. While the propensity to develop resistance is lower for membrane binding antimicrobials, bacteria may be able to redistribute membrane lipids as a mechanism of resistance. Thus, combination therapies become attractive options, as resistance is less likely to occur with multiple targets.[148] When SSA **66** was present in 1:1 heterogeneous mixtures with other SSAs, drastically lower MIC50 values were obtained against MRSA. Conversely, an antagonistic effect was exhibited when SSAs **67** and **68** were in a 1:1 heterogeneous mix. These data highlight the importance of investigating the intermolecular interactions between these molecules which can assist in the design of synergistic antimicrobial molecules.

The use of hydrogels can be an attractive option in antimicrobial drug design as they can be manipulated to exhibit desired properties and they tend to have high

biocompatibility.[272,273] Hydrogels can also be utilised for a wide range of applications, such as their use as drug delivery vehicles, as surface coatings for implants and wound dressings.[273,274] An example of their use in antimicrobial research is seen with the studies conducted by Zhou et al., 2011, who developed antimicrobial hydrogels that exhibited low toxicity and high bactericidal activity. Supramolecular hydrogels can also be utilised in combination therapies, as shown by Marchesan et al., 2013 who described a hydrogel that actively incorporated the antibiotic ciprofloxacin into its matrix and exhibited activity against *S. aureus, E. coli,* and a clinical strain of *K. pneumoniae*.[275] Similarly, ampicillin was incorporated into the gel matrix formed by SSA **70**, and the activity of ampicillin was not significantly reduced. Optimisation of the structure of SSA **70** may not only produce an effective drug delivery vehicle, but also a hydrogel that exhibits antimicrobial activity of its own, rendering it a better candidate for combination therapies.

The structure-activity relationships studies conducted were successfully utilised to develop second-generation SSAs **83** and **84**, which exhibited improved *E. coli* activity in solution. Furthermore, the physicochemical analysis of the second generation SSAs **82** – **85** provided further insight into the activities exhibited within the first generation of SSAs. For example, functional groups that promoted dimer formation within the first generation of molecules exhibited improved activity, such as the carboxylate functionality in SSA **61**. Additionally, disruption of these self-association processes resulted in reduced activity, as was observed with SSA **33**. However, in the second generation of molecules, SSA **83** exhibited weaker dimer formation, in comparison to SSA **82**, but improved antimicrobial activity. Therefore, improved antimicrobial activity was not solely due to dimerisation. It is uncertain whether SSAs interact with membrane lipids as dimers or as monomers. An investigation to determine this could provide information about the role of dimerisation in lipid interactions of SSAs, and their consequent antimicrobial activity.

The use of fluorescence microscopy enabled the visualisation of the gel fibre formation processes of SSAs **82**, **83**, and **85** in different salt solutions. The geometry of the anionic component was previously reported to influence gel formation by Hiscock et al., 2020.

Within these studies, the salt solution present was shown to impact gel fibre formation and the properties of the resulting gel due to the interactions between the SSAs and salt molecules.

Key observations included NaOBz promoting the formation of gels that exhibited fluid-like properties which may have been a result of its benzene ring and larger size in comparison to the other salts, which may have prevented closer packing of gel fibres. Additionally, two main types of gel stand formation were observed. One involved the formation of precipitated compound structures where long, curled fibre formation was initiated, which resulted in more fluid gels. The other involved the formation of SSA nodes followed by gel strand formation and cross-linking between nodes, which tended to produce straighter fibres and resulted in more rigid gels.

SSAs **82**, **83**, and **85** exhibited less stable gels overall, in comparison to the gels formed by SSA **70** as previously reported by Hiscock et al., 2020. This may be attributed to the sol not being fully incorporated into the gel matrix and the presence of multiple types of fibres in some gels, both of which were not observed in the stable gels reported by Hiscock et al., 2020.[155] The data obtained in these studies could not provide a specific reason for these observations, and a detailed investigation into the interactions between salt solutions and SSAs and also the influence of the anion geometry would be required to further understand.

6.2. Investigating the role of post-translational modifications on lipid interactions.

Post-translational modifications have been previously shown to be vital in the regulation of protein function, including protein-membrane interactions.[276] The studies conducted in Chapter 5 sought to investigate the role of post-translational modifications on lipid interactions, specifically Nt-acetylation and phosphorylation.

Oligomerisation was observed with acetylated α-Syn and VNp, but not with unacetylated α-Syn or VNp, which suggested a role in protein folding and conformation. Furthermore,

aggregated α-Syn has been observed in Lewy bodies, which are intracellular inclusions predominantly composed of α-Syn ; a pathological hallmark of Parkinson's disease (PD).[277] Therefore, this may also suggest impaired acetylation of α-Syn may have a role in the formation of Lewy bodies, and consequently the pathogenesis of PD.

α-Syn oligomers have been observed to disrupt a variety of membranes in PD, which has not been observed with native α-Syn in non-disease states. Further, the lipid composition of cell membranes and their physical properties have been shown to influence α-Syn membrane affinities. Thus, investigating the lipid interactions of α-Syn may provide further information concerning its physiological function and the role of the lipid interactions in PD pathogenesis. These studies also allowed for the exploration into the specific lipid interactions of acetylated and unacetylated α-Syn and VNp proteins to ascertain their physiological functions as well as the role of acetylation. Both acetylated and unacetylated α-Syn proteins exhibited higher binding affinities to POPA lipid in the anisotropy and thermal shift assays. POPA is an important signalling lipid that has been observed to recruit or activate specific proteins particularly in the central nervous system.[278,279] Therefore, the interactions observed with PA lipids suggest α-Syn may be one of the proteins recruited by POPA. This does not specify function but may provide insight into α-Syn localisation. Significantly higher thermostability was exhibited by both acetylated and unacetylated α-Syn -mCer3 proteins in the presence of CL and PG: PE liposomes. CL lipid is estimated to constitute ~10-20% of mitochondrial membrane phospholipids and is involved in processes such as energy conversion and respiration.[280–282] The research conducted by Shen et al., 2014, Devi et al., 2008, and Camilleri et al., 2013 provides evidence to suggest α-Syn interacts directly with the mitochondria, and more specifically with CL lipids.[280,283–285] It has thus been hypothesised that these interactions with CL may aid in the targeting of α-Syn oligomers to the mitochondria, resulting in membrane disruption of neuronal mitochondrial membranes.[280,281] Therefore, the strong interactions observed by both acetylated and unacetylated α-Syn with CL liposomes in the thermal shift assay provide further evidence to support these

hypotheses. Similarly, PE lipids in the central nervous system are particularly abundant in the inner mitochondrial membrane and play vital roles in membrane fusion events and interestingly in assisting membrane protein folding.[286,287] A reduction in PE consequently reduces membrane protein folding, resulting in the accumulation of toxic unfolded proteins. [286,287] Furthermore, a reduction in PE lipids has been observed in PD patients in studies conducted by Riekkinen et al., 1975 and Hattingen et al., 2009.[288,289] Thus, the strong interactions with PE lipids observed in thermal shift studies by α-Syn -mCer3 suggest PE involvement in α-Syn folding and its reduction may result in the accumulation of α-Syn that is observed in PD.

The increased interactions by unacetylated α-Syn to *E. coli* polar lipids in comparison to *E. coli* total lipids provides further evidence of PE binding, as the *E. coli* polar lipid extract contains a higher PE content. In addition to this, in the anisotropy experiments, a decrease in anisotropy values was observed when acetylated α-Syn -mCer3 was in the presence of POPG liposomes, which was then followed by an increase in anisotropy values. α-Syn has been observed adopting an alpha-helical conformation when in the presence of anionic lipids, which could explain these observations.[100,290] Lastly, unacetylated α-Syn -mCer3 exhibited increased lipid binding activities in comparison to acetylated α-Syn -mCer3. Acetylation of α-Syn has been reported in literature to modulate its lipid interactions by changing its affinity for specific lipids, thus, the data obtained suggests Nt-acetylation regulates α-Syn interactions by reducing its lipid interactions.[291,292]

Despite the VNp containing the proposed membrane binding domain, reduced binding activities were observed with VNp proteins in the thermal shift experiments and anisotropy experiments, in comparison to α-Syn -mCer3. This may suggest the involvement of other domains within α-Syn for lipid interactions that were not present in VNp. For example, the C-terminus of α-Syn has previously been reported to increase lipid binding of α-Syn through calcium binding.[293–295] Thus, its absence in the VNp protein may have resulted in reduced lipid interactions.

Phosphorylation of myosin-1 has previously been shown to regulate cellular localisation and ATPase activities.[296] However, the role of phosphorylation in the regulation of lipid interactions is not well known. In these studies, myosin 1 was not only observed to interact predominantly with anionic lipids, but phosphorylation was observed to increase binding to specific lipids, in particular PA. Thus, the data obtained in these studies suggests the lipid interactions may be positively regulated by phosphorylation. However, an extensive analysis of the individual interactions is required to confirm these observations, which could not be conducted due to COVID.

6.3. Conclusion

Biological membranes are dynamic and complex structures that provide cells with protection, define the cell compartments, control cell interactions, and perform vital cellular processes. The analysis of specific lipid interactions can provide vital information into complex membrane interactions, especially those that are not well characterised. These studies sought to investigate the lipid interactions of membrane-related proteins through the use of a variety of binding assays. Furthermore, these studies were able to show how information about specific lipid interactions can provide valuable information about the function, localisation, and regulation of proteins. Lastly, these studies enabled the optimisation of membrane binding antimicrobial compounds, which can then be used as tools in the fight against antimicrobial resistance.

4. Bibliography

1. Mora, C., Tittensor, D. P., Adl, S., Simpson, A. G. B. & Worm, B. How many species are there on earth and in the ocean? *PLoS Biol.* **9**, (2011).

2. Alberts, B. *et al. Molecular Biology of the Cell*. *Molecular Biology of the Cell* (2007). doi:10.1201/9780203833445.

3. Morgan, D. O. *The Cell Cycle*. (New Science Press Ltd, 2017).

4. Nanninga, N. Cell Structure, Organization, Bacteria and Archaea. in *Encyclopedia of Microbiology (Third Edition)* 357–374 (2009).

5. Lodish, H. *et al. Molecular Cell Biology*. (New York: W. H. Freeman, 2000).

6. Nicolson, G. L. The Fluid—Mosaic Model of Membrane Structure: Still relevant to understanding the structure, function and dynamics of biological membranes after more than 40 years. *Biochim. Biophys. Acta - Biomembr.* **1838**, 1451–1466 (2014).

7. Cooper, G. M. *The Cell: A Molecular Approach:2nd Edition*. (Sinauer Associates Inc. U.S., 2000).

8. Zhang, J., Drioli, E. & Giorno, L. *Encyclopedia of Membranes*. *Encyclopedia of Membranes* (2016). doi:10.1007/978-3-662-44324-8.

9. Ruiz, Y. *et al.* Biodegradation of Polyethoxylated Nonylphenols. *ISRN Microbiol.* **2013**, 1–9 (2013).

10. Song, S.-H., Koelsch, P., Weidner, T., Wagner, M. S. & Castner, D. G. Sodium Dodecyl Sulfate Adsorption onto Positively Charged Surfaces: Monolayer Formation With Opposing Headgroup Orientations. *Langmuir* **29**, (2013).

11. Ingalsbe, M. L., Denis, J. D. S., McGahan, M. E., Steiner, W. W. & Priefer, R. Development of a novel expression, ZIMAX/KZI, for determination of the counter-anion effect on the antimicrobial activity of tetrabutylammonium salts. *Bioorganic Med. Chem. Lett.* **19**, 4984–4987 (2009).

12. Wanderlingh, U. *et al.* Molecular dynamics of POPC phospholipid bilayers through the gel to fluid phase transition: An incoherent quasi-elastic neutron scattering study. *J. Chem.* **2017**, (2017).

13. Holmberg, K., Jönsson, B., Kronberg, B. & Lindman, B. *Surfactants and Polymers in Aqueous Solution, Second Edition*. (John Wiley & Sons, Ltd, 2002).

14. Anestopoulos, I. *et al.* Surface Active Agents and Their Health-Promoting Properties: Molecules of Multifunctional Significance. *Pharmaceutics* **12**, 688 (2020).

15. Laurén, S. What is critical micelle concentration? *Biolin Scientific* https://www.biolinscientific.com/blog/what-is-critical-micelle-concentration (2018).

16. Zhang, J., Li, X. & Li, X. Stimuli-triggered structural engineering of synthetic and biological polymeric assemblies. *Prog. Polym. Sci.* **37**, 1130–1176 (2012).

17. Israelachvili, J. *Intermolecular and Surface Forces*. *Intermolecular and Surface Forces* (Academic Press, 2011). doi:10.1016/C2009-0-21560-1.

18. Nakama, Y. Chapter 15 - Surfactants. in *Cosmetic Science and Technology* 231–244 (2017).

19. Frolov, V. A., Shnyrova, A. V. & Zimmerberg, J. Lipid polymorphisms and membrane shape. *Cold Spring Harb. Perspect. Biol.* **3**, (2011).

20. Cullis, P. R., Hope, M. J. & Tilcock, C. P. S. Lipid polymorphism and the roles of lipids in membranes. *Chem. Phys. Lipids* **40**, 127–144 (1986).

21. Harayama, T. & Riezman, H. Understanding the diversity of membrane lipid composition. *Nat. Rev. Mol. Cell Biol.* **19**, 281–296 (2018).

22. Hannun, Y. A. & Obeid, L. M. Sphingolipids and their metabolism in physiology and disease. *Nat. Rev. Mol. Cell Biol.* **19**, 175–191 (2018).

23. Berg, J. M., Tymoczko, J. L. & Stryer, L. There Are Three Common Types of Membrane Lipids. in *Biochemistry* (New York: W H Freeman, 2002).

24. LibreTexts. Fluid Mosaic Model. *Mind Touch* https://chem.libretexts.org/@go/page/12739 (2020).

25. Dufourc, E. J. Sterols and membrane dynamics. *J. Chem. Biol.* **1**, 1–4 (2008).

26. Miñones Jr, J., Pais, S., Miñones, J., Conde, O. & Dynarowicz-Łątk, P. Interactions between membrane sterols and phospholipids in model mammalian and fungi cellular membranes — A Langmuir monolayer study. *Biophys. Chem.* **140**, 69–77 (2009).

27. Takahashi, H. *et al.* Phosphatidylglucoside: Its structure, thermal behavior, and domain formation in plasma membranes. *Chem. Phys. Lipids* **165**, 197–206 (2012).

28. Cui, L. & Decker, E. A. Phospholipids in foods: prooxidants or antioxidants? *J. Sci. Food Agric.* **96**, 18–31 (2016).

29. Henry, S. A., Kohlwein, S. D. & Carman, G. M. Metabolism and Regulation of Glycerolipids in the Yeast Saccharomyces cerevisiae. *Genetics* **190**, 317–349

(2012).

30. Sodt, A. J. & Pastor, R. W. Molecular Modeling of Lipid Membrane Curvature Induction by a Peptide: More than Simply Shape. *Biophys. J.* **106**, 1958–1969 (2014).

31. Montealegre, C., Verardo, V., Marina, M. L. & Caboni, M. F. Analysis of glycerophospho- and sphingolipids by CE. *Electrophoresis* **35**, 779–792 (2014).

32. Brüning, B., Stehle, R., Falus, P. & Farago, B. Influence of charge density on bilayer bending rigidity in lipid vesicles: A combined dynamic light scattering and neutron spin-echo study. *Eur. Phys. J. E* **6**, (2013).

33. Shimanouchi, T. *et al.* Relationship between the mobility of phosphocholine headgroup and the protein-liposome interaction: A dielectric spectroscopic study. *Colloids Surfaces B Biointerfaces* **116**, 343–350 (2014).

34. LibreTexts. Lipid Headgroup Types. *Chem LibreTexts libraries* https://chem.libretexts.org/@go/page/864 (2020).

35. Kooijman, E. E. *et al.* Spontaneous Curvature of Phosphatidic Acid and Lysophosphatidic Acid. *Biochemistry* **44**, 2097–2102 (2005).

36. McMahon, H. T. & Boucrot, E. Membrane curvature at a glance. *J. Cell Sci.* **128**, 1065–1070 (2015).

37. Chen, I. & Lui, F. Neuroanatomy, Neuron Action Potential. in *StatPearls [Internet].* (Treasure Island (FL): StatPearls Publishing, 2020).

38. Tang, D. D. & Gerlach, B. D. The roles and regulation of the actin cytoskeleton, intermediate filaments and microtubules in smooth muscle cell migration.

Respir. Res. **18**, (2017).

39. Wickstead, B. & Gull, K. The evolution of the cytoskeleton. *J. Cell Biol.* **194**, 513–525 (2011).

40. W. Grogan, D. Chapter 50 - Physiology of Prokaryotic Cells. in *Cell Physiology Source Book (Fourth Edition)* 891–906 (2012).

41. Parker, J. Bacteria. in *Encyclopedia of Genetics* 146–151 (2001).

42. Salton, M., Kim, K., Peterson, J. & Baron, S. *Medical Microbiology. 4th edition.* (University of Texas Medical Branch at Galveston, 1996).

43. Parker, N., Schneegurt, M., Tu, A.-H. T., Lister, P. & Forster, B. M. *Microbiology*. (OpenStax, 2016).

44. Chien, A. C., Hill, N. S. & Levin, P. A. Cell size control in bacteria. *Curr. Biol.* **22**, 340–349 (2012).

45. Wang, L., Fan, D., Chen, W. & Terentjev, E. M. Bacterial growth, detachment and cell size control on polyethylene terephthalate surfaces. *Sci. Rep.* **5**, (2015).

46. Tan, S. Y. & Tatsumura, Y. Alexander Fleming (1881–1955): Discoverer of penicillin. *Singapore Med. J.* **56**, 366–367 (2015).

47. Fleming, A. On the antibacterial action of cultures of a penicillium, with special reference to their use in the isolation of B. influenzae. 1929. *Bull. World Health Organ.* **79**, 780–790 (2001).

48. Nicolaou, K. C., Chen, J. S., Edmonds, D. J. & Estrada, A. A. Recent Advances in the Chemistry and Biology of Naturally Occurring Antibiotics. *Angew. Chemie*

- *Int. Ed.* **48**, 660–719 (2009).

49. Kohanski, M. A., Dwyer, D. J. & Collins, J. J. How antibiotics kill bacteria: From targets to networks. *Nat. Rev. Microbiol.* **8**, 423–435 (2010).

50. Epand, R. M., Walker, C., Epand, R. F. & Magarvey, N. A. Molecular mechanisms of membrane targeting antibiotics. *Biochim. Biophys. Acta - Biomembr.* **1858**, 980–987 (2016).

51. Pandey, N. & Cascella, M. Beta Lactam Antibiotics. in *StatPearls [Internet]* (Treasure Island (FL): StatPearls Publishing, 2020).

52. O'NEIL, J. *TACKLING DRUG-RESISTANT INFECTIONS GLOBALLY: FINAL REPORT AND RECOMMENDATIONS*. *THE REVIEW ON ANTIMICROBIAL RESISTANCE* (2016).

53. O' Neil, J. *Review on Antibiotic resisitance. Antimicrobial Resistance : Tackling a crisis for the health and wealth of nations*. *Health and Wealth Nations* https://amr-review.org/sites/default/files/AMR Review Paper - Tackling a crisis for the health and wealth of nations_1.pdf (2014).

54. O'meara, S. Antimicrobial resistance. *Nat. Outlook* **586**, (2020).

55. Jackson, N., Czaplewski, L. & Piddock, L. J. V. Discovery and development of new antibacterial drugs: Learning from experience? *J. Antimicrob. Chemother.* **73**, 1452–1459 (2018).

56. Aminov, R. I. A brief history of the antibiotic era: Lessons learned and challenges for the future. *Front. Microbiol.* **1**, (2010).

57. Baker, S. J., Payne, D. J., Rappuoli, R. & Gregorio, E. De. Technologies to

address antimicrobial resistance. *Proc. Natl. Acad. Sci.* **115**, 12887–12895 (2018).

58. Bosch, F. & Rosich, L. The Contributions of Paul Ehrlich to Pharmacology: A Tribute on the Occasion of the Centenary of His Nobel Prize. *Pharmacology* **82**, 171–179 (2008).

59. Hibbing, M. E., Fuqua, C., Parsek, M. R. & Peterson, S. B. Bacterial competition: surviving and thriving in the microbial jungle. *Nat. Rev. Microbiol.* **8**, 15–25 (2010).

60. Geng, W.-C., Sessler, J. L. & Guo, D.-S. Supramolecular prodrugs based on host–guest interactions. *Chem. Soc. Rev.* **49**, 2303–2315 (2020).

61. Menger, F. M. Supramolecular chemistry and self-assembly. *Proc. Natl. Acad. Sci.* **99**, 4818–4822 (2002).

62. Koyasseril-Yehiya, T. M. *et al.* Supramolecular antibiotics: a strategy for conversion of broad-spectrum to narrow-spectrum antibiotics for Staphylococcus aureus. *Nanoscale* **12**, 20693–20698 (2020).

63. Qin, Z., Kreplak, L. & Buehler, M. J. Nanomechanical properties of vimentin intermediate filament dimers. *Nanotechnology* **20**, 425101 (2009).

64. Simonson, A. W., Aronson, M. R., Medina, S. H. & Guler, M. O. Supramolecular Peptide Assemblies as Antimicrobial Scaffolds. *Molecules* **25**, 2751 (2020).

65. El-Sheshtawy, H. S. *et al.* A Supramolecular Approach for Enhanced Antibacterial Activity and Extended Shelf-life of Fluoroquinolone Drugs with Cucurbit[7]uril. *Sci. Rep.* **8**, (2018).

66. Tyuleva, S. N. *et al.* A symbiotic supramolecular approach to the design of novel amphiphiles with antibacterial properties against MSRA. *Chem. Commun.* **55**, 95–98 (2019).

67. Prestinaci, F., Pezzotti, P. & Pantosti, A. Antimicrobial resistance: A global multifaceted phenomenon. *Pathog. Glob. Health* **109**, 309–318 (2015).

68. Park, K. S. *et al.* Potential strategies to combat antimicrobial resistance. *Res. J. Microbiol.* **11**, 153–156 (2016).

69. Miller, S. I. & Salama, N. R. The gram-negative bacterial periplasm: Size matters. *PLoS Biol.* **16**, (2018).

70. Sohlenkamp, C. & Geiger, O. Bacterial membrane lipids: Diversity in structures and pathways. *FEMS Microbiol. Rev.* **40**, 133–159 (2015).

71. Segura, A. *et al.* Membrane Composition and Modifications in Response to Aromatic Hydrocarbons in Gram Negative Bacteria. in *Handbook of Hydrocarbon and Lipid Microbiology* 1595–1603 (2010).

72. Spang, A. *et al.* Complex archaea that bridge the gap between prokaryotes and eukaryotes. *Nature* **521**, 173–179 (2015).

73. Fededa, J. P. & Gerlich, D. W. Molecular control of animal cell cytokinesis. *Nat. Cell Biol.* **14**, 440–447 (2012).

74. Norbury, C. & Nurse, P. Animal cell cycles and their control. *Annu. Rev. Biochem.* **61**, 441–470 (1992).

75. Vermeulen, K., Bockstaele, D. R. Van & Berneman, Z. N. The cell cycle: a review of regulation, deregulation and therapeutic targets in cancer. *Cell Prolif.*

36, 131–149 (2003).

76. Chou, S. Z. & Pollard, T. D. Mechanism of actin polymerization revealed by cryo-EM structures of actin filaments with three different bound nucleotides. *Proc. Natl. Acad. Sci.* **116**, 4265–4274 (2019).

77. Dominguez, R. & Holmes, K. C. Actin Structure and Function. *Annu. Rev. Biophys.* **40**, 169–186 (2011).

78. Lodish, H. *et al.* Section 18.3 Myosin: The Actin Motor Protein. in *Molecular Cell Biology. 4th edition.* (New York: W. H. Freeman, 2000).

79. Garrod, D. & Chidgey, M. Desmosome structure, composition and function. *Biochim. Biophys. Acta* **1778**, 572–587 (2008).

80. Hoyt, M. A., Hyman, A. A. & Bähler, M. Motor proteins of the eukaryotic cytoskeleton. *Proc. Natl. Acad. Sci.* **94**, 12747–12748 (1997).

81. McIntosh, B. B. & Ostap, E. M. Myosin-I molecular motors at a glance. *J. Cell Sci.* **129**, 2689–2695 (2016).

82. Mazerik, J. N., Kraft, L. J., Kenworthy, A. K. & Tyska, M. J. Motor and tail homology 1 (TH1) domains antagonistically control myosin-1 dynamics. *Biophys. J.* **106**, 649–658 (2014).

83. Lenoir, M., Kufareva, I., Abagyan, R. & Overduin, M. Membrane and Protein Interactions of the Pleckstrin Homology Domain Superfamily. *Membranes (Basel).* **5**, 646–663 (2015).

84. Lemmon, M. A. Pleckstrin Homology (PH) domains and phosphoinositides. *Biochem. Soc. Symp.* **74**, 81–93 (2007).

85. Amatya, N. *et al.* Lipid-targeting pleckstrin homology domain turns its autoinhibitory face toward the TEC kinases. *Proc. Natl. Acad. Sci.* **116**, 21539–21544 (2019).

86. Feeser, E. A., Ignacio, C. M. G., Krendel, M. & Ostap, E. M. Myo1e binds anionic phospholipids with high affinity. *Biochemistry* **49**, 9353–9360 (2010).

87. Chen, X.-W., Leto, D., Chiang, S.-H., Wang, Q. & Saltiel, A. R. Activation of RalA is required for insulin-stimulated Glut4 trafficking to the plasma membrane via the exocyst and the motor protein Myo1c. *Dev. Cell* **13**, 391–404 (2007).

88. Donaudy, F. *et al.* Multiple Mutations of MYO1A, a Cochlear-Expressed Gene, in Sensorineural Hearing Loss. *Am. J. Hum. Genet.* **72**, 1571–1577 (2003).

89. Conner, S. D. & Schmid, S. L. Regulated portals of entry into the cell. *Nature* **422**, 37–44 (2003).

90. Schmid, S. L. Reciprocal regulation of signaling and endocytosis: Implications for the evolving cancer cell. *J. Cell Biol.* **216**, 2623–2632 (2017).

91. Mettlen, M., Chen, P.-H., Srinivasan, S., Danuser, G. & Schmid, S. L. Regulation of Clathrin-Mediated Endocytosis. *Annu. Rev. Biochem.* **87**, 871–896 (2018).

92. Wang, Y.-C., Peterson, S. E. & Loring, J. F. Protein post-translational modifications and regulation of pluripotency in human stem cells. *Cell Res.* **24**, 143–160 (2013).

93. Lee, D. Y., Teyssier, C., Strahl, B. D. & Stallcup, M. R. Role of Protein Methylation in Regulation of Transcription. *Endocr. Rev.* **26**, 147–170 (2005).

94. Clarke, S. G. Protein methylation at the surface and buried deep: thinking outside the histone box. *Trends Biochem. Sci.* **38**, 243–252 (2013).

95. Nestler, E. J. & Greengard., P. Protein Phosphorylation is of Fundamental Importance in Biological Regulation. in *Basic Neurochemistry: Molecular, Cellular and Medical Aspects. 6th edition.* (eds. Siegel, G. J., Agranoff, B. W., Albers, R. W., Fisher, S. K. & Uhler, M. D.) (Philadelphia: Lippincott-Raven, 1999).

96. Ardito, F., Giuliani, M., Perrone, D., Troiano, G. & Muzio, L. Lo. The crucial role of protein phosphorylation in cell signaling and its use as targeted therapy (Review). *Int. J. Mol. Med.* **40**, 271–280 (2017).

97. Rhind, N. & Russell, P. Signaling Pathways that Regulate Cell Division. *Cold Spring Harb. Protoc.* **4**, (2012).

98. Eastwood, T. A., Baker, K., Brooker, H. R., Frank, S. & Mulvihill, D. P. An enhanced recombinant amino-terminal acetylation system and novel in vivo high-throughput screen for molecules affecting α-synuclein oligomerisation. *FEBS Lett.* **591**, 833–841 (2017).

99. Xia, C., Tao, Y., Li, M., Che, T. & Qu, J. Protein acetylation and deacetylation: An important regulatory modification in gene transcription (Review). *Exp. Ther. Med.* **20**, 2923–2940 (2020).

100. Outeiro, T. Alpha-Synuclein. in *Reference Module in Neuroscience and Biobehavioral Psychology* (Elsevier, 2017).

101. Kouli, A., Torsney, K. M. & Kuan., W.-L. Parkinson's Disease: Etiology, Neuropathology, and Pathogenesis. in *Parkinson's Disease: Pathogenesis and*

Clinical Aspects [Internet]. (eds. Stoker, T. & Greenland, J.) (Brisbane (AU): Codon Publications, 2018).

102. Stefanis, L. α-Synuclein in Parkinson's Disease. *Cold Spring Harb. Protoc.* **2**, (2012).

103. Zhang, J., Li, X. & Li, J.-D. The Roles of Post-translational Modifications on α-Synuclein in the Pathogenesis of Parkinson's Diseases. *Front. Neurosci.* **13**, (2019).

104. L.Yeagle, P. Non-covalent binding of membrane lipids to membrane proteins. *Biomembranes* **1838**, 1548–1559 (2014).

105. Johannes Schindelin, Ignacio Arganda-Carreras, Erwin Frise, Verena Kaynig, Mark Longair, Tobias Pietzsch, Stephan Preibisch, Curtis Rueden, Stephan Saalfeld, Benjamin Schmid, Jean-Yves Tinevez, Daniel James White, Volker Hartenstein, Kevin Eliceiri, Pavel, A. C. Fiji: an open-source platform for biological-image analysis. *Nat. Methods* **9**, 676–682 (2012).

106. Rueden, C. T. *et al.* ImageJ2: ImageJ for the next generation of scientific image data. *BMC Bioinformatics* **18**, (2017).

107. Sheldrick, G. M. SHELXT - Integrated space-group and crystal-structure determination. *Acta Crystallogr. Sect. A Found. Adv.* **71**, 3–8 (2015).

108. Sheldrick, G. M. A short history of SHELX. *Acta Crystallogr. Sect. A Found. Adv.* **64**, 112–122 (2008).

109. Dolomanov, O. V., Bourhis, L. J., Gildea, R. J., Howard, J. A. K. & Puschmann, H. OLEX2: A complete structure solution, refinement and analysis program. *J. Appl. Crystallogr.* **42**, 339–341 (2009).

110. Willcott, M. R. MestRe Nova. *J. Am. Chem. Soc.* **131**, 13180–13180 (2009).

111. Brynn Hibbert, D. & Thordarson, P. The death of the Job plot, transparency, open science and online tools, uncertainty estimation methods and other developments in supramolecular chemistry data analysis. *Chem. Commun.* **52**, 12792–12805 (2016).

112. Constans, A. PIP, PIP, Hooray! Echelon Biosciences' PIP Array and PIP Strips facilitate studies of lipid-protein interactions. (Lab Consumer). *Sci.* **16**, 48 (2002).

113. Andrews, J. M. Determination of minimum inhibitory concentrations. *J. Antimicrob. Chemother.* **48**, 5–16 (2001).

114. Abdul Fattah, S. S. *et al.* Short-chain fructo-oligosaccharides produced by enzymatic hydrolysis enhance the growth of probiotics isolated from cultured milk drinks. *Malays. J. Microbiol.* **14**, 497–502 (2018).

115. Stensjøen, A. L. *et al.* Growth dynamics of untreated glioblastomas in vivo. *Neuro. Oncol.* **17**, 1402–1411 (2015).

116. Phe. UK Standards for Microbiology Investigations Inoculation of culture media for bacteriology. *Quality Guidance* 1–22 https://assets.publishing.service.gov.uk/government/uploads/system/uploads/attachment_data/file/583859/Q_5i2.pdf (2017).

117. Mulvihill, D. P. Live cell imaging in fission yeast. *Cold Spring Harb. Protoc.* **2017**, 761–773 (2017).

118. Nji, E., Chatzikyriakidou, Y., Landreh, M. & Drew, D. An engineered thermal-shift screen reveals specific lipid preferences of eukaryotic and prokaryotic

membrane proteins. *Nat. Commun.* **9**, 4253 (2018).

119. Bock, L. J., Hind, C. K., Sutton, J. M. & Wand, M. E. Growth media and assay plate material can impact on the effectiveness of cationic biocides and antibiotics against different bacterial species. *Lett. Appl. Microbiol.* **66**, 368–377 (2018).

120. Rahman, M. A. *et al.* Macromolecular-clustered facial amphiphilic antimicrobials. *Nat. Commun.* **9**, (2018).

121. Brown, E. D. & Wright, G. D. Antibacterial drug discovery in the resistance era. *Nature* **529**, 336–343 (2016).

122. McGowan, J. E. Economic impact of antimicrobial resistance. *Emerg. Infect. Dis.* **7**, 286–292 (2001).

123. Smith, R. *The economic burden of antimicrobial resistance: why it is more serious than current studies suggest*. *London School of Hygiene & Tropical Medicine, London.* vol. 44 http://researchonline.lshtm.ac.uk/639028/ (2012).

124. WHO. *Antimicrobial resistance: global report on surveillance*. *World Health Organization* (2014).

125. Uchil, R. R., Kohli, G. S., Katekhaye, V. M. & Swam, O. C. Strategies to Combat Antimicrobial Resistance. *J. Clin. Diagnostic Res. Dr.* **8**, (2014).

126. Van Katwyk, S. R., Hoffman, S. J., Mendelson, M., Taljaard, M. & Grimshaw, J. M. Strengthening the science of addressing antimicrobial resistance: A framework for planning, conducting and disseminating antimicrobial resistance intervention research. *Heal. Res. Policy Syst.* **18**, (2020).

127. Barbosa, M. A. *et al. Comprehensive Biomaterials II*. (2017).

128. Dan, N. Chapter 2 - Core–shell drug carriers: liposomes, polymersomes, and niosomes. in *Nanostructures for Drug Delivery* 63–105 (2017).

129. Findlay, B., Zhanel, G. G. & Schweizer, F. Cationic amphiphiles, a new generation of antimicrobials inspired by the natural antimicrobial peptide scaffold. *Antimicrob. Agents Chemother.* **54**, 4049–4058 (2010).

130. Hancock, R. E. W. & Sahl, H. G. Antimicrobial and host-defense peptides as new anti-infective therapeutic strategies. *Nat. Biotechnol.* **24**, 1551–1557 (2006).

131. Chrom, C. L., Renn, L. M. & Caputo, G. A. Characterization and antimicrobial activity of amphiphilic peptide ap3 and derivative sequences. *Antibiotics* **8**, 20 (2019).

132. Garton, M., Mackinnon, S. S., Malevanets, A. & Wodak, S. J. Interplay of self-association and conformational flexibility in regulating protein function. *Philos. Trans. R. Soc. B Biol. Sci.* **373**, (2018).

133. Calabrese, M. F., Eakin, C. M., Wang, J. M. & Miranker, A. D. A regulatable switch mediates self-association in an immunoglobulin fold. *Nat. Struct. Mol. Biol.* **15**, 965–971 (2008).

134. Piljić, A. & Schultz, C. Annexin A4 self-association modulates general membrane protein mobility in living cells. *Mol. Biol. Cell* **17**, 3318–3328 (2006).

135. Marzahn, M. R. *et al.* The Role of Protein Disorder and Self-Association in the Formation of Cellular Bodies. *Biophys. J.* **108**, 6a (2015).

136. Yu, G., Jie, K. & Huang, F. Supramolecular Amphiphiles Based on Host-Guest Molecular Recognition Motifs. *Chem. Rev.* **115**, 7240–7303 (2015).

137. Nartowski, K. P. *et al.* The Plot Thickens: Gelation by Phenylalanine in Water and Dimethyl Sulfoxide. *Cryst. Growth Des.* **17**, 4100–4109 (2017).

138. Scozzafava, A., Mastrolorenzo, A. & Supuran, C. T. Antimycobacterial activity of 3,4-dichlorophenyl-ureas, N,N-diphenyl-ureas and related derivatives. *J. Enzyme Inhib.* **16**, 425–432 (2001).

139. Hiscock, J. R., Wells, N. J., Ede, J. A., Gale, P. A. & Sambrook, M. R. Biasing hydrogen bond donating host systems towards chemical warfare agent recognition. *Org. Biomol. Chem.* **14**, 9560–9567 (2016).

140. Zhou, X. *et al.* Self-assembling subnanometer pores with unusual mass-transport properties. *Nat. Commun.* **3**, (2012).

141. Chevalier, Y. New surfactants: New chemical functions and molecular architectures. *Curr. Opin. Colloid Interface Sci.* **7**, 3–11 (2002).

142. Guha, R. On Exploring Structure Activity Relationships 2013.pdf. *Methods Mol. Biol.* **993**, 81–94 (2013).

143. Cruz-Monteagudo, M., Borges, F. & Cordeiro, M. N. D. S. Desirability-based multiobjective optimization for global QSAR studies: Application to the design of novel NSAIDs with improved analgesic, antiinflammatory, and ulcerogenic profiles. *J. Comput. Chem.* **29**, 2445–2459 (2008).

144. Tyers, M. & Wright, G. D. Drug combinations: a strategy to extend the life of antibiotics in the 21st century. *Nat. Rev. Microbiol.* **17**, 141–155 (2019).

145. Silver, L. L. Multi-targeting by monotherapeutic antibacterials. *Nat. Rev. Drug Discov.* **6**, 41–55 (2007).

146. Besnard, J. *et al.* Automated design of ligands to polypharmacological profiles. *Nature* **492**, 215–220 (2012).

147. Wallace, S. J., Nation, R. L., Li, J. & Boyd, B. J. Physicochemical aspects of the coformulation of colistin and azithromycin using liposomes for combination antibiotic therapies. *J. Pharm. Sci.* **102**, 1578–1587 (2013).

148. Ahmed, A., Azim, A., Gurjar, M. & Baronia, A. K. Current concepts in combination antibiotic therapy for critically ill patients. *Indian J. Crit. Care Med.* **18**, 310–314 (2014).

149. Ganewatta, M. S. *et al.* Facially amphiphilic polyionene biocidal polymers derived from lithocholic acid. *Bioact. Mater.* **3**, 186–193 (2018).

150. Beer, P. D. & Gale, P. A. Anion recognition and sensing: The state of the art and future perspectives. *Angew. Chemie - Int. Ed.* **40**, 486–516 (2001).

151. Busschaert, N., Caltagirone, C., Van Rossom, W. & Gale, P. A. Applications of Supramolecular Anion Recognition. *Chem. Rev.* **115**, 8038–8155 (2015).

152. Gale, P. A. & Caltagirone, C. Anion sensing by small molecules and molecular ensembles. *Chem. Soc. Rev.* **44**, 4212–4227 (2015).

153. White, L. J. *et al.* Towards quantifying the role of hydrogen bonding within amphiphile self-association and resultant aggregate formation. *Chem. Sci.* **8**, 7620–7630 (2017).

154. White, L. J. *et al.* Towards the Prediction of Global Solution State Properties for

Hydrogen Bonded, Self-Associating Amphiphiles. *Chem. - A Eur. J.* **24**, 7761–7773 (2018).

155. White, L. J. *et al.* Controllable hydrogen bonded self-association for the formation of multifunctional antimicrobial materials. *J. Mater. Chem. B* **8**, 4694–4700 (2020).

156. Allen, N. *et al.* Towards the Prediction of Antimicrobial Efficacy for Hydrogen Bonded, Self-Associating Amphiphiles. *ChemMedChem* **15**, (2020).

157. Simpson, D. H. & Scott, P. Chapter Seven – Antimicrobial Metallodrugs. in *Inorganic and Organometallic Transition Metal Complexes with Biological Molecules and Living Cells* 205–243 (2017).

158. Hughes, D. & Karlén, A. Discovery and preclinical development of new antibiotics. *Ups. J. Med. Sci.* **119**, 162–169 (2014).

159. Buchanan, R. L., Whiting, R. C. & Damert, W. C. When is simple good enough: A comparison of the Gompertz, Baranyi, and three-phase linear models for fitting bacterial growth curves. in *Food Microbiology* vol. 14 313–326 (1997).

160. Hall, B. G., Acar, H., Nandipati, A. & Barlow, M. Growth rates made easy. *Mol. Biol. Evol.* **31**, 232–238 (2014).

161. Martínez, J. L. Effect of antibiotics on bacterial populations: A multi-hierachical selection process. *F1000Research* **6**, (2017).

162. Cronan, J. E. Phospholipid alterations during growth of Escherichia coli. *J. Bacteriol.* **95**, 2054–2061 (1968).

163. Gidden, J., Denson, J., Liyanage, R., Ivey, D. M. & O.Lay, J. J. Lipid

Compositions in Escherichia coli and Bacillus subtilis During Growth as Determined by MALDI-TOF and TOF/TOF Mass Spectrometry. *Int. J. Mass Spectrom.* **283**, 178–184 (2009).

164. Brown, J. S. *et al.* Antibacterial isoamphipathic oligomers highlight the importance of multimeric lipid aggregation for antibacterial potency. *Commun. Biol.* **1**, (2018).

165. Umar, U., Uba, A. & Oyawoye, O. M. Antibiotic Susceptibilities, MIC50 and MIC90 of Clinical Isolates of Methicillin Resistant Staphylococcus aureus (MRSA). *African J. Microbiol. Res.* (2019).

166. Catania, S. *et al.* Evaluation of Minimum Inhibitory Concentrations for 154 Mycoplasma synoviae isolates from Italy collected during 2012-2017. *PLoS One* **14**, (2019).

167. Schwarz, S. *et al.* Editorial: Assessing the antimicrobial susceptibility of bacteria obtained from animals. *J. Antimicrob. Chemother.* **65**, 601–604 (2010).

168. Cockerill, F. R. *et al. Methods for Dilution Antimicrobial Susceptibility Tests for Bacteria That Grow Aerobically*. *M07-a9* vol. 32 (2012).

169. Wang, H. *et al.* Acclimation of culturable bacterial communities under the stresses of different organic compounds. *Front. Microbiol.* **9**, (2018).

170. Poole, K. Bacterial stress responses as determinants of antimicrobial resistance. *J. Antimicrob. Chemother.* **67**, 2069–2089 (2012).

171. Mohapatra, R. K. *et al.* Recent Advances in Ureaand Thiourea-Based Metal Complexes: Biological, Sensor, Optical, and Corroson Inhibition Studies. *Comments Inorg. Chem.* **39**, 127–187 (2019).

172. DONDAS, H. A., NURAL, Y., DURAN, N. & KILNER, C. Synthesis, Crystal Structure and Antifungal/Antibacterial Activity of Some Novel Highly Functionalized Benzoylaminocarbothioyl Pyrrolidines. *Turkish J. Chem.* **30**, 573 – 583 (2006).

173. Auwerx, J. *et al.* The Phenylmethylthiazolylthiourea Nonnucleoside Reverse Transcriptase (RT) Inhibitor MSK-076 Selects for a Resistance Mutation in the Active Site of Human Immunodeficiency Virus Type 2 RT. *J. Virol.* **78**, 7427–7437 (2004).

174. Singh, A., Raj, P., Kaur, N. & Singh, N. DETOXIFICATION AND SENSING OF ORGANOPHOSPHATE-BASED PESTICIDES AND PRESERVATIVES IN BEVERAGES. in *Preservatives and Preservation Approaches in Beverages* 467–510 (2019).

175. Ouellette, R. J. & Rawn, J. D. Structure of Organic Compounds. in *Principles of Organic Chemistry* 1–32 (2015). doi:10.1016/b978-0-12-802444-7.00001-x.

176. Santos, O. L., Fonseca, T. L., Sabino, J. R., Georg, H. C. & Castro, M. A. Polarization effects on the electric properties of urea and thiourea molecules in solid phase. *J. Chem. Phys.* **143**, (2015).

177. Pluta, T. & Sadlej, A. J. Electric properties of urea and thiourea. *J. Chem. Phys.* **114**, 136–146 (2001).

178. Gilkerson, W. R. & Srivastava, K. K. The dipole moment of urea. *J. Phys. Chem.* **64**, 1485–1487 (1960).

179. Kumler, W. D. & Fohlen, G. M. The Dipole Moment and Structure of Urea and Thiourea. *J. Am. Chem. Soc.* **64**, 3071 (1942).

180. Gilbert, P. & Moore, L. E. Cationic antiseptics: Diversity of action under a common epithet. *J. Appl. Microbiol.* **99**, 703–715 (2005).

181. Jiao, Y. *et al.* Quaternary ammonium-based biomedical materials: State-of-the-art, toxicological aspects and antimicrobial resistance. *Prog. Polym. Sci.* **71**, 53–90 (2017).

182. Simpkins, N. S., Nytko, F. E., DeShong, P., Vayer, M. & Maulide, N. Tetrabutylammonium Difluorotriphenylsilicate (TBAT). in *Encyclopedia of Reagents for Organic Synthesis* (2013). doi:10.1002/9780471264194.fos11924.

183. Blackholly, L. R., Shepherd, H. J. & Hiscock, J. R. 'Frustrated' hydrogen bond mediated amphiphile self-assembly – a solid state study. *CrystEngComm* **18**, 7021–7028 (2016).

184. Gardner, R. C. *Psychological Statistics Using SPSS for Windows*. vol. 8 (2001).

185. Morgan, W. A. A Test for the Significance of the Difference Between the Two Variances in a Sample From a Normal Bivariate Population. *Biometrika* **31**, 13 (1939).

186. PITMAN, E. J. G. a Note on Normal Correlation. *Biometrika* **31**, 9–12 (1939).

187. Snedecor, G. W. & Cochran, W. G. *Statistical Methods*. (Blackwell, 1989).

188. Burnham, B. R. Chapter 14: Paired Samples t-Test. in *Fundamental Statistics for the Behavioral Sciences* (2015).

189. Waters, J. C. Accuracy and precision in quantitative fluorescence microscopy. *J. Cell Biol.* **185**, 1135–1148 (2009).

190. Lakowicz, J. R. Fluorescence Anisotropy. in *Principles of Fluorescence*

Spectroscopy 353–382 (2006). doi:10.1007/978-1-4757-3061-6_10.

191. Cheow, L. F. *et al.* Multiplexed Analysis of Protein-Ligand Interactions by Fluorescence Anisotropy in a Microfluidic Platform. *Anal. Chem.* **86**, (2014).

192. Invitrogen. Fluorescence Polarization. in *Technical Resource Guide FOURTH EDITION* (2006).

193. Rossi, A. M. & Taylor, C. W. Analysis of protein-ligand interactions by fluorescence polarization. *Nat. Protoc.* **6**, 365–387 (2011).

194. Motulsky, H. J. & Neubig, R. R. Analyzing binding data. *Curr. Protoc. Neurosci.* (2010) doi:10.1002/0471142301.ns0705s19.

195. NOSJEAN, O. *et al.* A Simple Theoretical Model for Fluorescence Polarization Binding Assay Development. *J. Biomol. Screen.* **11**, (2006).

196. Avanti. Avanti R Polar Lipids. https://avantilipids.com/product-category/phospholipids (2020).

197. Jones, J. A., Virga, K. G., Gumina, G. & Hevener, K. E. Recent Advances in the Rational Design and Optimization of Antibacterial Agents. *Medchemcomm* **7**, 1694–1715 (2017).

198. Klebe, G. Optimization of Lead Structures. in *Drug Design* 153–172 (Springer, Berlin, Heidelberg, 2013). doi:https://doi.org/10.1007/978-3-642-17907-5_8.

199. Pizzolato-Cezar, L. R., Okuda-Shinagawa, N. M. & Machini, M. T. Combinatory Therapy Antimicrobial Peptide-Antibiotic to Minimize the Ongoing Rise of Resistance. *Front. Microbiol.* (2019) doi:doi: 10.3389/fmicb.2019.01703.

200. Sliwoski, G., Kothiwale, S., Meiler, J. & Edward W. Lowe, J. Computational

Methods in Drug Discovery. *Pharmacol. Rev.* **66**, 334–395 (2014).

201. Kurnakov, N. S. *Introduction to Physicochemical Analysis*. *Izv. Akad. Nauk SSSR* (1940).

202. Kurnakov, N. Physikochemical Analysis. *Zadachi Inst.* **1**, 1–7 (1919).

203. Zlomanov, V. P., Khoviv, A. M. & Zavrazhnov, A. J. Physicochemical Analysis and Synthesis of Nonstoichiometric Solids. *Mater. Sci. - Adv. Top.* (2013) doi:10.5772/54815.

204. Hunter, C. A. Quantifying intermolecular interactions: Guidelines for the molecular recognition toolbox. *Angew. Chemie - Int. Ed.* **43**, 5310–5324 (2004).

205. Bottyan, T. Electrostatic potential maps. *Chem LibreTexts libraries* https://chem.libretexts.org/@go/page/1987 (2020).

206. Parthasarathi, R., Subramanian, V. & Sathyamurthy, N. Hydrogen bonding in protonated water clusters: An atoms-in-molecules perspective. *J. Phys. Chem. A* **111**, 13287–13290 (2007).

207. Kollman, P., McKelvey, J., Johansson, A. & Rothenberg, S. Theoretical Studies of Hydrogen-Bonded Dimers. Complexes Involving HF, H2O, NH3, CHl, H2S, PH3, HCN, HNC, HCP, CH2NH, H2CS, H2CO, CH4, CF3H, C2H2, C2H4, C6H6, F- and H3O+. *J. Am. Chem. Soc.* **97**, 955–965 (1975).

208. Wavefunction, I. Spartan’16.

209. Shao, Y. *et al.* Advances in methods and algorithms in a modern quantum chemistry program package. *Phys. Chem. Chem. Phys.* **8**, 3172–3191 (2006).

210. Hehre, W. J. *A Guide to Molecular Mechanics and Quantum Chemical*

Calculations. (2003).

211. Stewart, J. J. P. Optimization of parameters for semiempirical methods V: Modification of NDDO approximations and application to 70 elements. *J. Mol. Model.* **13**, 1173–1213 (2007).

212. Stetefeld, J., McKenna, S. A. & Patel, T. R. Dynamic light scattering: a practical guide and applications in biomedical sciences. *Biophys. Rev.* **8**, 409–427 (2016).

213. Strutt, J. W. LVIII. On the scattering of light by small particles . *London, Edinburgh, Dublin Philos. Mag. J. Sci.* **41**, 447–454 (1871).

214. Strutt, J. W. XXXVI. On the light from the sky, its polarization and colour . *London, Edinburgh, Dublin Philos. Mag. J. Sci.* **41**, 274–279 (1871).

215. Tyndall, J. IV. On the blue colour of the sky, the polarization of skylight, and on the polarization of light by cloudy matter generally. *Proc. R. Soc. London* **17**, (1869).

216. Floyd, K. A., Eberly, A. R. & Hadjifrangiskou, M. 3 - Adhesion of bacteria to surfaces and biofilm formation on medical devices. in *Biofilms and Implantable Medical Devices* 47–95 (2017).

217. Einstein, A. Über einen die Erzeugung und Verwandlung des Lichtes betreffenden heuristischen Gesichtspunkt. *Ann. Phys.* **322**, 132–148 (1905).

218. Stokes, G. G. On the theories of the internal friction in fluids in motion, and of the equilibrium and motion of elastic solids. *Trans. Cambridge Philos. Soc.* (1845).

219. Einstein, A. Zur Theorie der Brownschen Bewegung. *Ann. Phys.* **324**, 371–381 (1906).

220. Harding, S. E. & Jumel, K. Light Scattering. in *Current Protocols in Protein Science* vol. 11 7.8.1-7.8.14 (1998).

221. Bharti, S. K. & Roy, R. Quantitative 1H NMR spectroscopy. in *TrAC Trends in Analytical Chemistry* 5–26 (2012).

222. Simmler, C., Napolitano, J. G., McAlpine, J. B., Chen, S.-N. & Pauli, G. F. Universal Quantitative NMR Analysis of Complex Natural Samples. *Curr. Opin. Biotechnol.* **25**, 51–59 (2015).

223. Patel, V. R. & Agrawal, Y. K. Nanosuspension: An approach to enhance solubility of drugs. *J. Adv. Pharm. Technol. Res.* **2**, 81–87 (2011).

224. Supramolecular. Binding Constant Calculators. *Supramolecular.org* http://app.supramolecular.org/bindfit/ (2020).

225. Martin, R. B. Comparisons of Indefinite Self-Association Models. *Chem. Rev.* **96**, 3043–3064 (1996).

226. Wu, X. *et al.* Tetraurea Macrocycles: Aggregation-Driven Binding of Chloride in Aqueous Solutions. *Chem* **5**, 1210–1222 (2019).

227. Santos-López, G. *et al.* Aerogels from Chitosan Solutions in Ionic Liquids. *Polymers (Basel).* **9**, 722 (2017).

228. Jamart-Grégoire, B. *et al.* Monolithic organic aerogels derived from single amino-acid based supramolecular gels: physical and thermal properties. *RSC Adv.* **6**, (2016).

229. Vioux, A., Viau, L., Volland, S. & Bideau, J. Le. Use of ionic liquids in sol-gel; ionogels and applications. *Comptes Rendus Chim.* **13**, 242–255 (2010).

230. Liu, X., Bin He, Z. W., Tang, H., Su, T. & Wang, Q. Tough Nanocomposite Ionogel-based Actuator Exhibits Robust Performance. *Nat. Sci. Reports* **4**, (2014).

231. Esposito, C. L., Kirilov, P. & Roullin, V. G. Organogels, promising drug delivery systems: an update of state-of-the-art and recent applications. *J. Control. Release* **217**, 1–20 (2018).

232. Sangeetha, N. M. & Maitra, U. Supramolecular gels: Functions and uses. *Chem. Soc. Rev.* **34**, 821–836 (2005).

233. Rajbhandary, A. & Nilsson, B. L. Chapter 9: Self-Assembling Hydrogels. in *Gel's handbook* 219–250 (2016).

234. Yu, G., Yan, X., Han, C. & Huang, F. Characterization of supramolecular gels. *Chem. Soc. Rev.* **42**, 6697–6722 (2013).

235. Caló, E. & Khutoryanskiy, V. V. Biomedical applications of hydrogels: A review of patents and commercial products. *Eur. Polym. J.* **65**, 252–267 (2015).

236. Jones, C. D. & Steed, J. W. Gels with sense: supramolecular materials that respond to heat, light and sound. *Chem. Soc. Rev.* **45**, 6546–6596 (2016).

237. Dawn, A. & Kumari, H. Low Molecular WeightSupramolecularGels Under Shear:Rheologyasthe Tool for Elucidating Structure–FunctionCorrelation. *Chem. - A Eur. J.* **24**, 762–776 (2018).

238. Picout, D. R. & Ross-Murphy, S. B. Rheology of Biopolymer Solutions and

Gels. *Sci. World J.* **3**, 105–121 (2003).

239. Ikeda, S. & Foegeding, E. A. Measurement of Gel Rheology: Dynamic Tests. *Curr. Protoc. Food Anal. Chem.* **7**, (2003).

240. Dörr, D., Kuhn, U. & Altstädt, V. Rheological Study of Gelation and Crosslinking in Chemical Modified Polyamide 12 Using a Multiwave Technique. *Polymers (Basel).* **12**, 1–10 (2020).

241. Weng, L., Chen, X. & Chen, W. Rheological Characterization of in situ Crosslinkable Hydrogels Formulated from Oxidized Dextran and N-Carboxyethyl Chitosan. *Biomacromolecules* **8**, 1109–1115 (2008).

242. Singh, A. K. Chapter 4 - Experimental Methodologies for the Characterization of Nanoparticles. in *Engineered Nanoparticles: Structure, Properties and Mechanisms of Toxicity* 125–170 (2016).

243. Van de Ven, A. L., Mack, A., Dunner Jr., K., Ferrari, M. & Serda, R. E. Chapter one - Preparation, Characterization, and Cellular Associations of Silicon Logic-Embedded Vectors. *Methods Enzymol.* **508**, 1–16 (2012).

244. Foster, J. A. *et al.* Anion-switchable supramolecular gels for controlling pharmaceutical crystal growth. *Nat. Chem.* **2**, 1037–1043 (2010).

245. Bankhead, P. *Analyzing fluorescence microscopy images with ImageJ*. (Nikon Imaging Center, Heidelberg University, 2013).

246. Alonso, C. A. *et al.* Antibiogramj: A tool for analysing images from disk diffusion tests. *Comput. Methods Programs Biomed.* **143**, 159–169 (2017).

247. Howell, D. C. *Statistical Methods for Psychology*. (Belmont, CA : wadsworth,

2006).

248. Hayter, A. J. The Maximum Familywise Error Rate of Fisher's Least Significant Difference Test. *J. Am. Stat. Assoc.* **81**, 1000–1004 (1986).

249. Tuzi, S., Uekama, N., Okada, M. & Yagisawa, H. Structure of Membrane-Binding Proteins Revealed by Solid-State NMR. in *Modern Magnetic Resonance* (2008).

250. Liberski, P. P. & Ironside, J. W. Chapter 23 – Prion Diseases. in *Neurobiology of Brain Disorders* 356–374 (2015).

251. Guennewig, B. & A.Cooper, A. Chapter Seven - The Central Role of Noncoding RNA in the Brain. in *International Review of Neurobiology* 153–194 (2014).

252. Shahnawaz, M. *et al.* Discriminating α-synuclein strains in Parkinson's disease and multiple system atrophy. *Nature* **578**, 273–277 (2020).

253. Johnson, M., Coulton, A. T., Geeves, M. A. & Mulvihill, D. P. Targeted amino-terminal acetylation of recombinant proteins in E. coli. *PLoS One* **5**, (2010).

254. Shaner, N. C. *et al.* A bright monomeric green fluorescent protein derived from Branchiostoma lanceolatum. *Nat. Methods* **10**, 407–409 (2013).

255. Ml, M. *et al.* An Improved Cerulean Fluorescent Protein with Enhanced Brightness and Reduced Reversible Photoswitching. *PLoS One* **6**, (2011).

256. Moll, J. R., Ruvinov, S. B., Pastan, I. & Vinson, C. Designed heterodimerizing leucine zippers with a ranger of pIs and stabilities up to 10−15 M. *Protein Sci.* **10**, 649–655 (2001).

257. Behncken, S. N. *et al.* Growth Hormone (GH)-independent Dimerization of GH

Receptor by a Leucine Zipper Results in Constitutive Activation. *J. Mol. Biol.* **275**, (2000).

258. Roca-Pinilla, R. *et al.* Exploring the use of leucine zippers for the generation of a new class of inclusion bodies for pharma and biotechnological applications. *Microb. Cell Fact.* **19**, (2020).

259. Katz, B.-Z. *et al.* Green Fluorescent Protein Labeling of Cytoskeletal Structures—Novel Targeting Approach Based on Leucine Zippers. *Biotechniques* **25**, 298–304 (1998).

260. Taormina, G. *et al.* Longevity: Lesson from Model Organisms. *Genes (Basel).* **10**, (2019).

261. Greenberg, M. J., Lin, T., Shuman, H. & Ostap, E. M. Mechanochemical tuning of myosin-I by the N-terminal region. *Proc. Natl. Acad. Sci.* **112**, (2015).

262. Baker, J. P. & Titus, M. A. A family of unconventional myosins from the nematode Caenorhabditis elegans. *J. Mol. Biol.* **272**, 523–535 (1997).

263. Pan, S. H. & Malcolm, B. A. *Reduced background expression and improved plasmid stability with pET vectors in BL21 (DE3)*. *BioTechniques* vol. 29 https://www.future-science.com/doi/pdf/10.2144/00296st03 (2000).

264. Schlager, B., Straessle, A. & Hafen, E. Use of anionic denaturing detergents to purify insoluble proteins after overexpression. *BMC Biotechnol.* **12**, 95 (2012).

265. Palmer, I. & Wingfield, P. T. Preparation and extraction of insoluble (Inclusion-body) proteins from Escherichia coli. in *Current Protocols in Protein Science* vol. 1 (2004).

266. Werner, M. H., Clore, G. M., Gronenborn, A. M., Kondohb, A. & Fisher, R. J. Refolding proteins by gel filtration chromatography. *FEBS Lett.* **345**, 125–130 (1994).

267. Li, M., Su, Z. G. & Janson, J. C. In vitro protein refolding by chromatographic procedures. *Protein Expr. Purif.* **33**, 1–10 (2004).

268. Shirey, C. M., Scott, J. L. & Stahelin, R. V. Notes and Tips for Improving Quality of Lipid-Protein Overlay Assays. *Anal. Biochem.* **512**, 9–12 (2018).

269. Delekta, P. C., Shook, J. C., Lydic, T. A., Mulks, M. H. & Hammer, N. D. Staphylococcus aureus Utilizes Host-Derived Lipoprotein Particles as Sources of Fatty Acids. *Am. Soc. Microbiol.* **200**, (2018).

270. Young, S. A., Desbois, A. P., Coote, P. J. & Smith, T. K. Characterisation of Staphylococcus aureus lipids by nanoelectrospray ionisation tandem mass spectrometry (nESI-MS/MS). (2019).

271. John E. Cronan, J. Phospholipid Alterations During Growth of Escherichia coli. *J. Bacteriol.* **95**, 2054–2061 (1968).

272. Veiga, A. S. & Schneider, J. P. Antimicrobial hydrogels for the treatment of infection. *Biopolymers* **100**, 637–644 (2013).

273. Veiga, A. S. *et al.* Arginine-Rich Self-Assembling Peptides as Potent Antibacterial Gels. *Biomaterials* **33**, 8907–8916 (2012).

274. Salick, D. A., Kretsinger, J. K., Pochan, D. J. & Schneider, J. P. Inherent Antibacterial Activity of a Peptide-Based β-Hairpin Hydrogel. *J. Antimicrob. Chemother.* **129**, 14793–14799 (2007).

275. Marchesan, S. *et al.* Self-assembly of ciprofloxacin and a tripeptide into an antimicrobial nanostructured hydrogel. *Biomaterials* **4**, 3678–3687 (2013).

276. Su, M.-G. *et al.* Investigation and identification of functional post-translational modification sites associated with drug binding and protein-protein interactions. *BMC Syst. Biol.* **11**, (2017).

277. Lewis, P. A. & Spillane, J. E. Chapter 3 - Parkinson's Disease. in *The Molecular and Clinical Pathology of Neurodegenerative Disease* 83–121 (2019).

278. Emamzadeh, F. N. Alpha-synuclein structure, functions, and interactions. *J. Res. Med. Sci.* **21**, (2016).

279. Tanguy, E., Wang, Q., Moine, H. & Vitale1*, N. Phosphatidic Acid: From Pleiotropic Functions to Neuronal Pathology. *Front. cell Neurosci.* **13**, (2019).

280. Ghio, S. *et al.* Cardiolipin Promotes Pore-Forming Activity of Alpha-Synuclein Oligomers in Mitochondrial Membranes. *ACS Chem. Neurosci.* **10**, 3815–3829 (2019).

281. Ghio, S., Kamp, F., Cauchi, R., Giese, A. & Vassallo, N. Interaction of α-synuclein with biomembranes in Parkinson's disease —role of cardiolipin. *Prog. Lipid Res.* **61**, 73–82 (2016).

282. Dudek, J. Role of Cardiolipin in Mitochondrial Signaling Pathways. *Front. Cell Dev. Biol.* **5**, (2017).

283. Shen, J. *et al.* α-Synuclein amino terminus regulates mitochondrial membrane permeability. *Brain Res.* **1591**, 14–26 (2014).

284. Devi, L., Raghavendran, V., Prabhu, B. M., Avadhani, N. G. &

Anandatheerthavarada, H. K. Mitochondrial import and accumulation of alpha-synuclein impair complex I in human dopaminergic neuronal cultures and Parkinson disease brain. *J. Biol. Chem.* **283**, 9089–9100 (2008).

285. Camilleri, A. *et al.* Mitochondrial membrane permeabilisation by amyloid aggregates and protection by polyphenols. *Biochim. Biophys. Acta - Biomembr.* **1828**, 2532–2543 (2013).

286. Patel, D. & Witt, S. N. Ethanolamine and Phosphatidylethanolamine: Partners in Health and Disease. *Oxid. Med. Cell. Longev.* (2017).

287. Calzada, E., Onguka, O. & Claypool, S. M. Phosphatidylethanolamine Metabolism in Health and Disease. *Int. Rev. Cell Mol. Biol.* **321**, 29–88 (2017).

288. Riekkinen, P., Rinne, U. K., Pelliniemi, T. T. & Sonninen, V. Interaction between dopamine and phospholipids. Studies of the substantia nigra in Parkinson disease patients. *Arch. Neurol.* **32**, 25–27 (1975).

289. Hattingen, E. *et al.* Phosphorus and proton magnetic resonance spectroscopy demonstrates mitochondrial dysfunction in early and advanced Parkinson's disease. *Brain* **132**, 3285–3297 (2009).

290. Stöckl, M., Fischer, P., Wanker, E. & Herrmann, A. Alpha-synuclein selectively binds to anionic phospholipids embedded in liquid-disordered domains. *J. Mol. Biol.* **375**, 1394–1404 (2007).

291. Runfola, M., Simone, A. De, Vendruscolo, M., Dobson, C. M. & Fusco, G. The N-terminal Acetylation of α-Synuclein Changes the Affinity for Lipid Membranes but not the Structural Properties of the Bound State. *Sci. Rep.* **10**, (2020).

292. Viennet, T. *et al.* Structural insights from lipid-bilayer nanodiscs link α-Synuclein

membrane-binding modes to amyloid fibril formation. *Commun. Biol.* **1**, (2018).

293. Lautenschläger, J. *et al.* C-terminal calcium binding of α-synuclein modulates synaptic vesicle interaction. *Nat. Commun.* **8**, (2018).

294. Kim, T. D., Paik, S. R. & Yang, C.-H. Structural and Functional Implications of C-Terminal Regions of α-Synuclein. *Biochemistry* **41**, 13782–13790 (2002).

295. Gurnev, P. A. *et al.* Alpha-Synuclein Lipid-Dependent Membrane Binding and Translocation through the α-Hemolysin Channel. *Biophys. J.* **106**, 556–565 (2014).

296. Greenberg, M. J. & Ostap, E. M. Regulation and Control of Myosin-I by the Motor and Light Chain Binding Domains. *Trends Cell Biol.* **23**, 81–89 (2014).

Appendix

Development and characterisation of novel therapeutic and biotechnological molecules

Nyasha Allen

Contents

Screening growth curves **296**

***Escherichia coli* (*E. coli*)** **296**

USA 300 Methicillin-resistant Staphylococcus aureus (MRSA) **302**

MIC_{50} Growth Curves ..... **Error! Bookmark not defined.**

***Escherichia coli* (*E. coli*)** ..... Error! Bookmark not defined.

USA 300 Methicillin-resistant *Staphylococcus aureus* (MRSA) ..... Error! Bookmark not defined.

Antimicrobial gel plates **308**

Quantitative Microscopy Analysis **312**

***E. coli* at 30 minutes** **313**

***E. coli* at 4 hours** **326**

MRSA at 30 minutes **342**

MRSA at 4 hours **352**

Physicochemical studies conducted on second generation SSAs **367**

Gelation studies **376**

Antimicrobial gel plates: second generation SSAs **383**

Lengths of gel fibres used to determine long and short strands **385**

Gel fluorescence microscopy images **386**

Statistics **404**

Zones of inhibition **404**

WT ANOVA **406**

VNp ANOVA **409**

Lz ANOVA **417**

Hum1 Fluorescence **420**

Screening growth curves

Escherichia coli (*E. coli*)

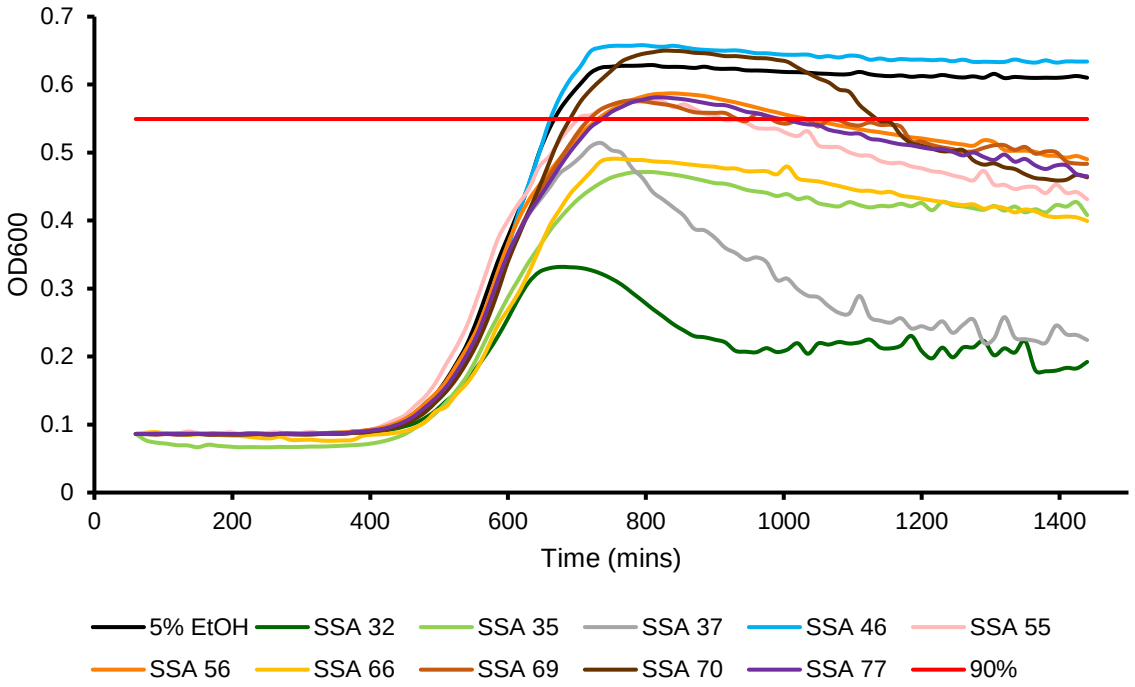

Figure S126 - E. coli DH10B growth curves created from an average of 6 absorbance readings in the presence of SSAs **32, 35**, **37**, **46**, **55**, **56**, **66**, **69, 70** and **77**.

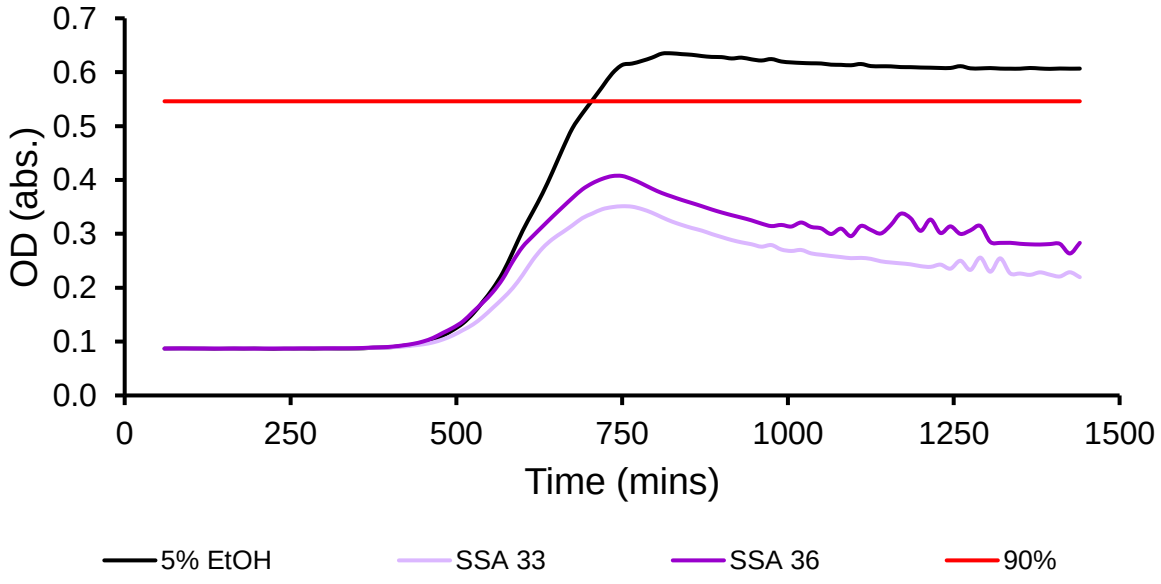

Figure S127 - *E. coli* DH10B growth curves created from an average of 6 absorbance readings in the presence of SSAs **33** and **36.**

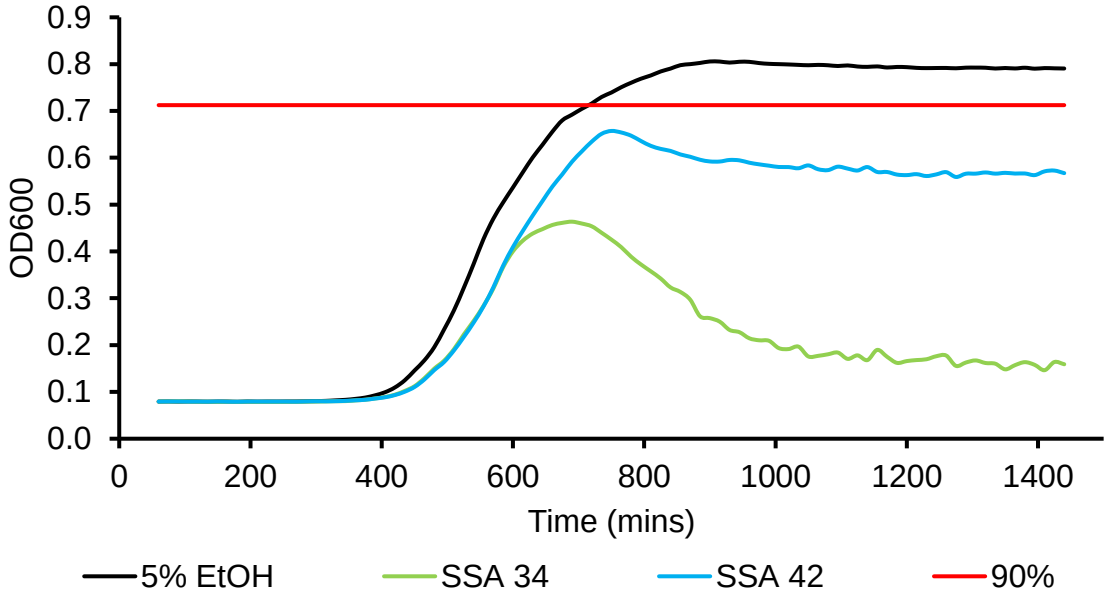

Figure S128 - *E. coli* DH10B growth curves created from an average of 6 absorbance readings in the presence of SSAs **34** and **42.**

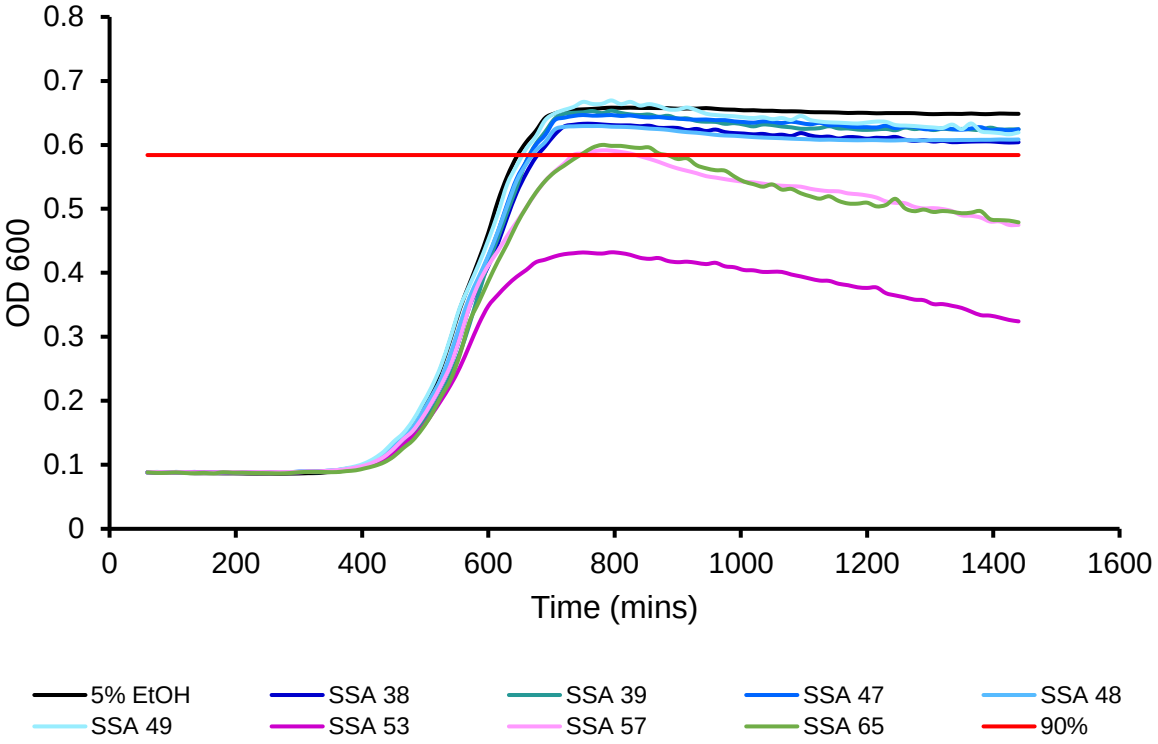

Figure S129 **-** *E. coli* DH10B growth curves created from an average of 6 absorbance readings in the presence of SSAs **38**, **39**, **47**, **48**, **49**, **53**, **57** and **65**.

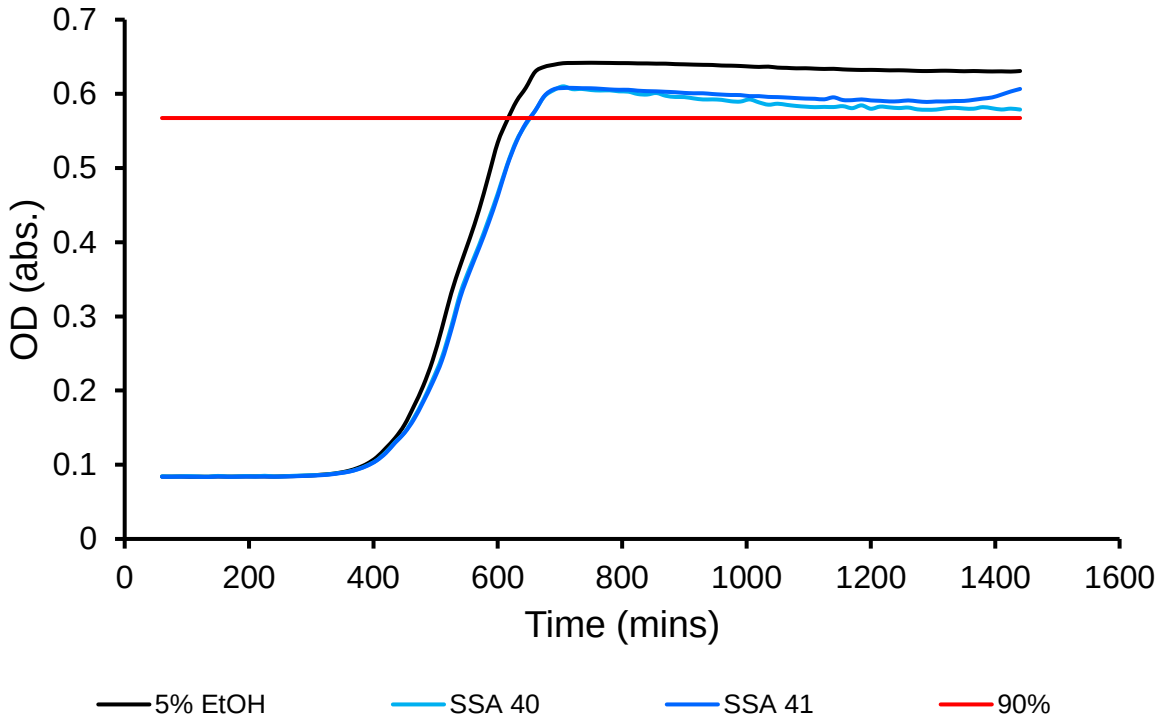

Figure S130 - *E. coli* DH10B growth curves created from an average of 6 absorbance readings in the presence of SSAs **40** and **41.**

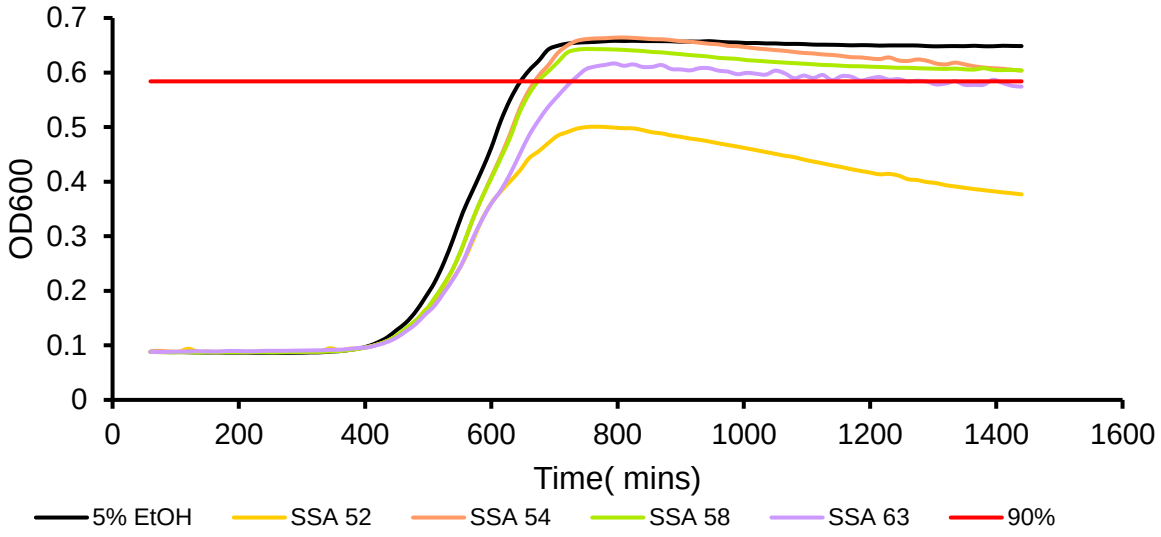

Figure S131 - *E. coli* DH10B growth curves created from an average of 6 absorbance readings in the presence of SSAs **52**, **52**, **58**, and **63**.

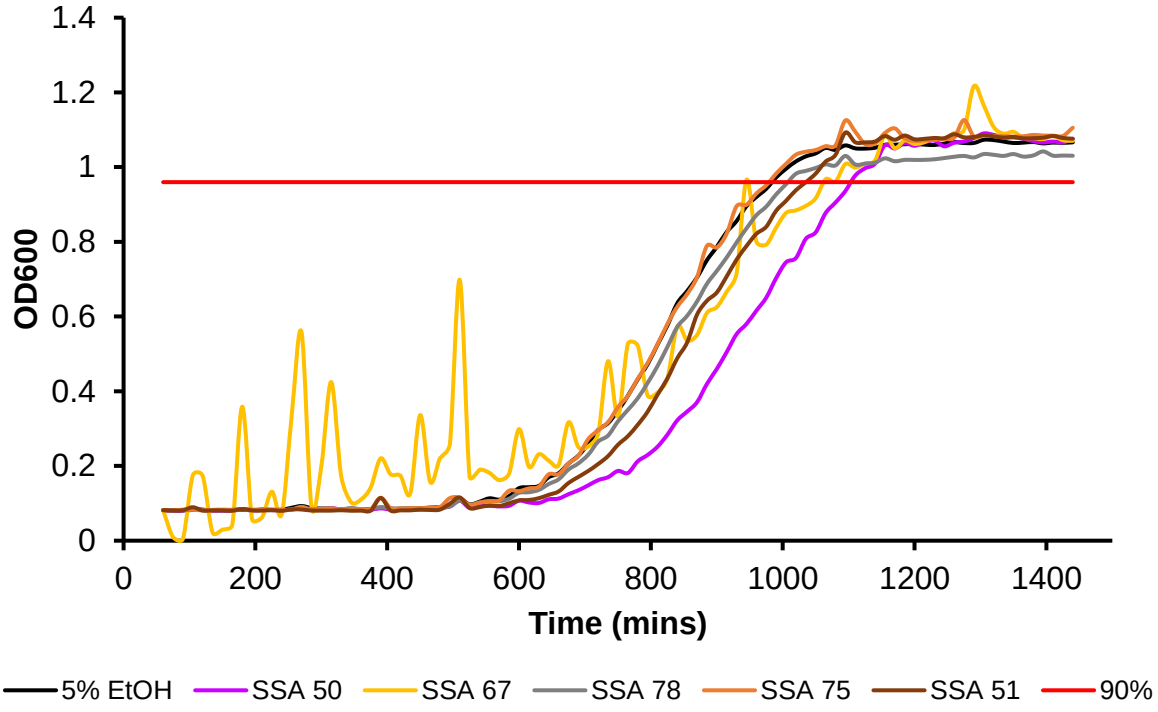

Figure S132 - *E. coli* DH10B growth curves created from an average of 6 absorbance readings in the presence of SSAs **50**, **67**, **78**, **75** and **51.**

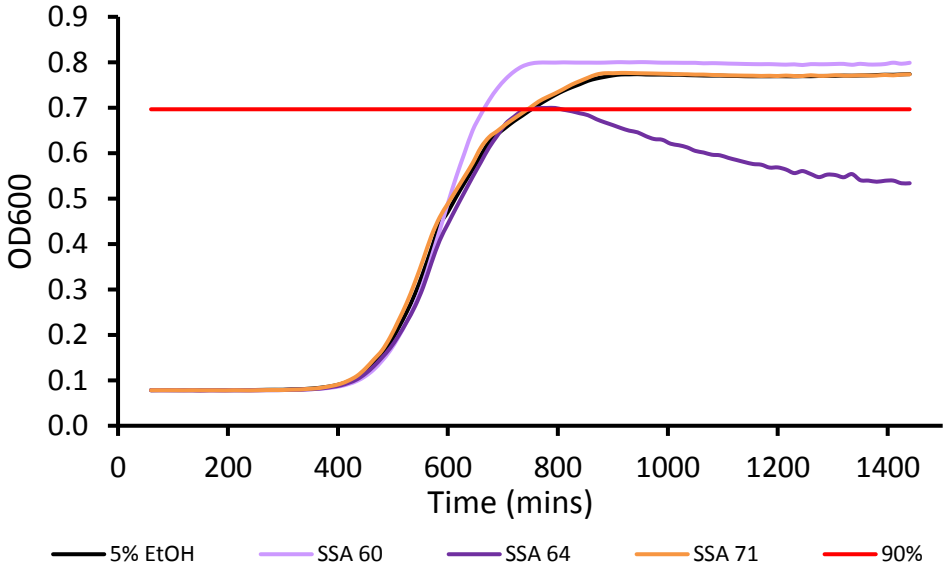

Figure S133 - *E. coli* DH10B growth curves created from an average of 6 absorbance readings in the presence of SSAs **60, 64** and **71.** MIC not calculated for compound **33** due to solubility of compound.

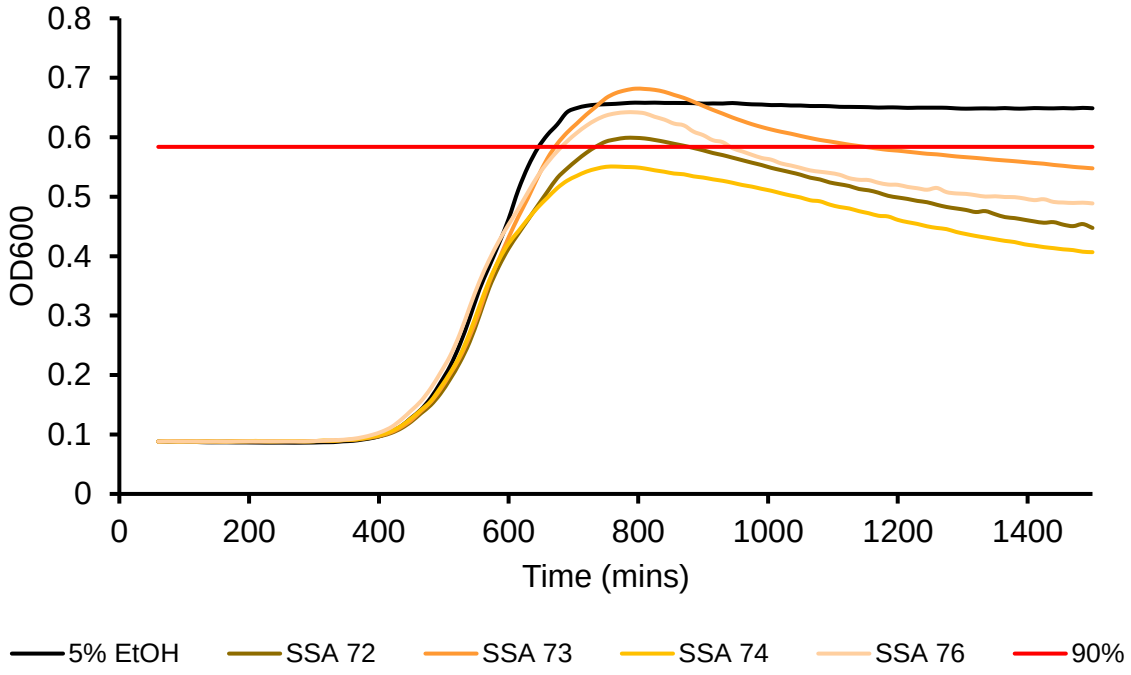

Figure S134 **-** *E. coli* DH10B growth curves created from an average of 6 absorbance readings in the presence of SSAs **72**, **73**, **74** and **76**.

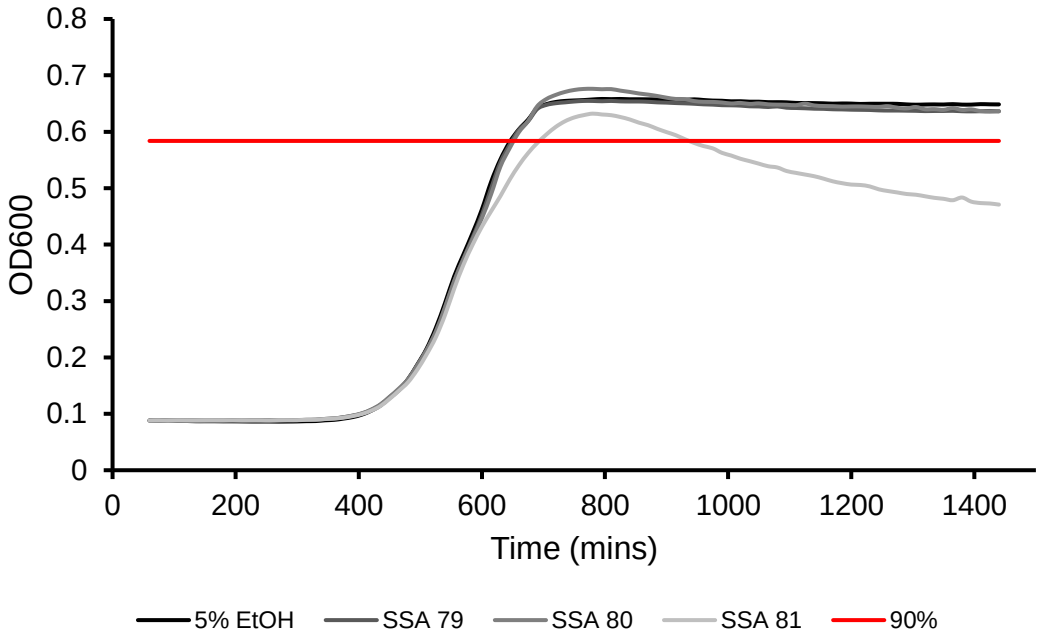

Figure S135 - *E. coli* DH10B growth curves created from an average of 6 absorbance readings in the presence of SSAs **79**, **80** and **81**.

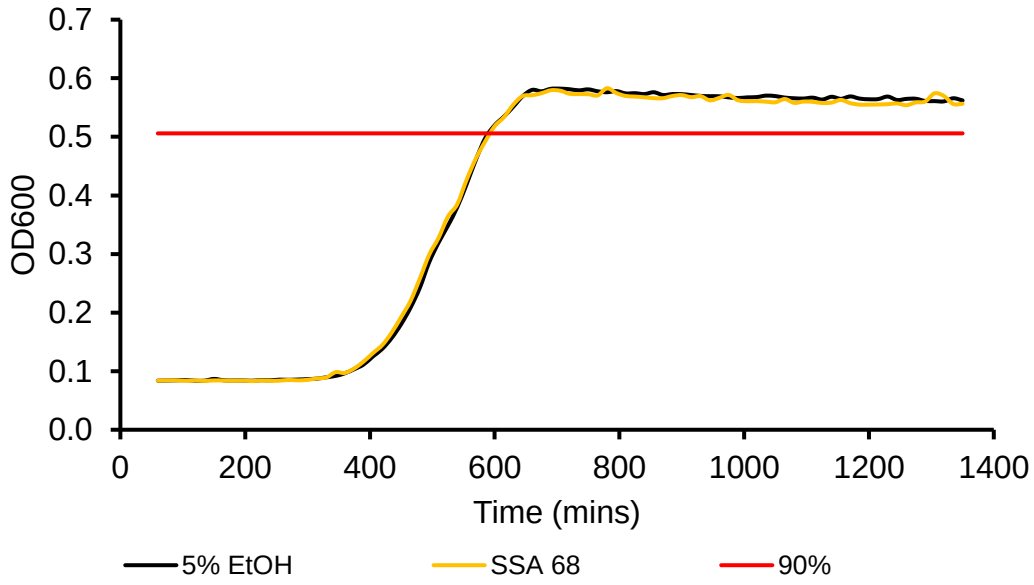

Figure S136 - *E. coli* DH10B growth curves created from an average of 6 absorbance readings in the presence of SSA **68**.

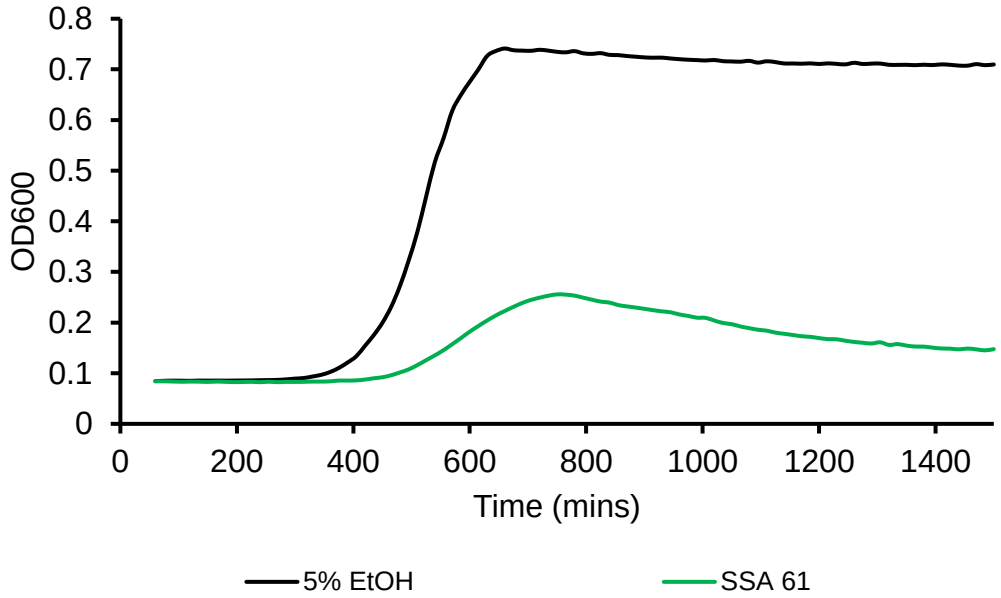

Figure S137 - *E. coli* DH10B growth curves created from an average of 6 absorbance readings in the presence of SSA **61**.

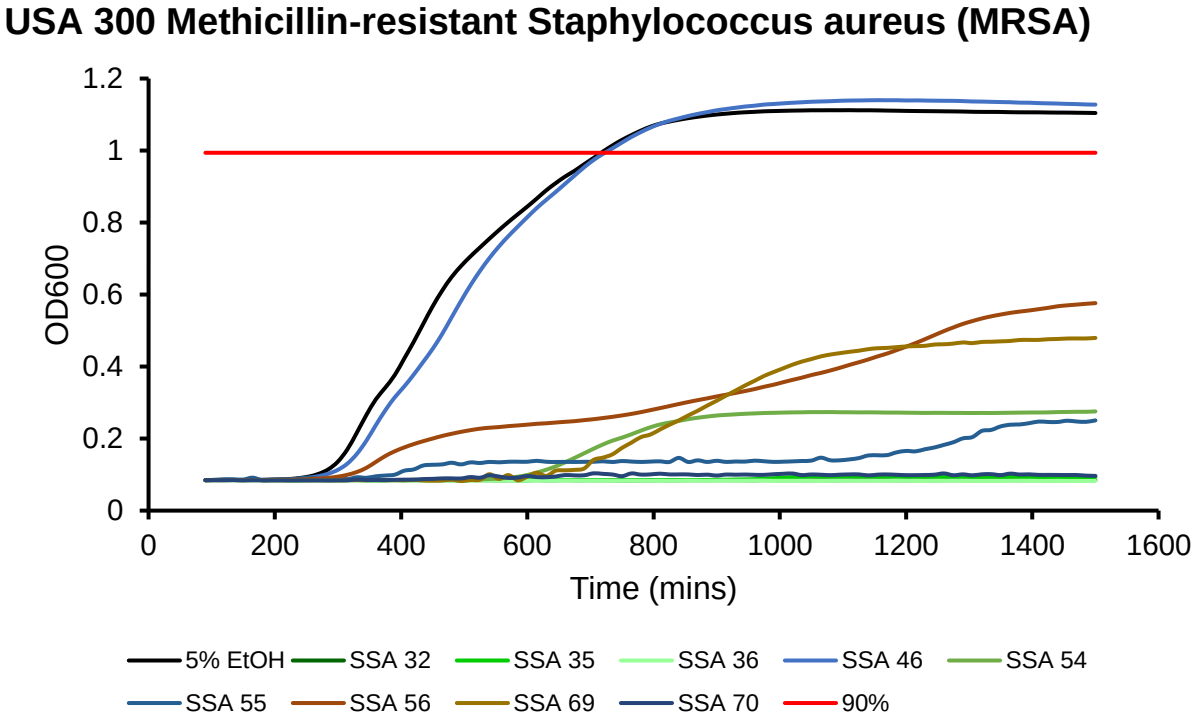

Figure S138 - MRSA growth curves created from an average of 6 absorbance readings in the presence of SSAs **32, 35**, **36**, **46**, **54**, **55**, **56**, **69** and **70**.

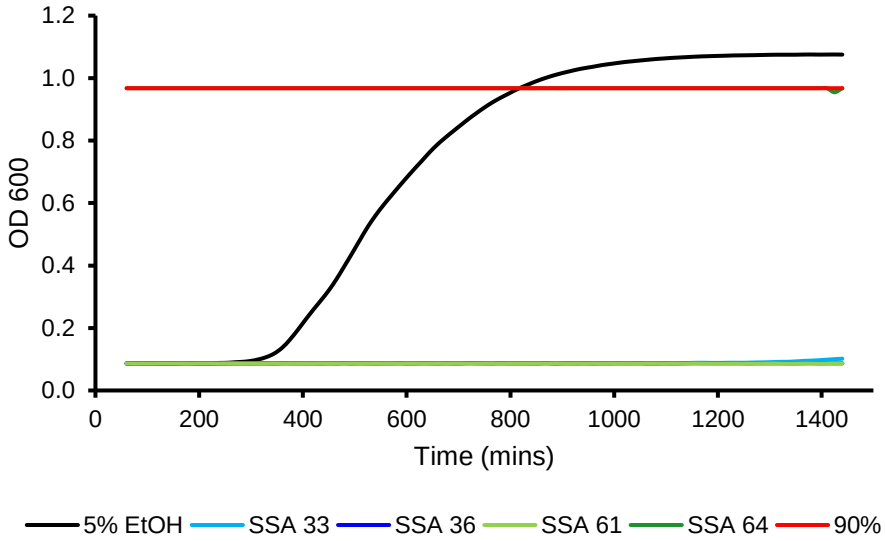

Figure S139 **-** MRSA growth curves created from an average of 6 absorbance readings in the presence of SSAs **33, 36,** and **61** and **64**.

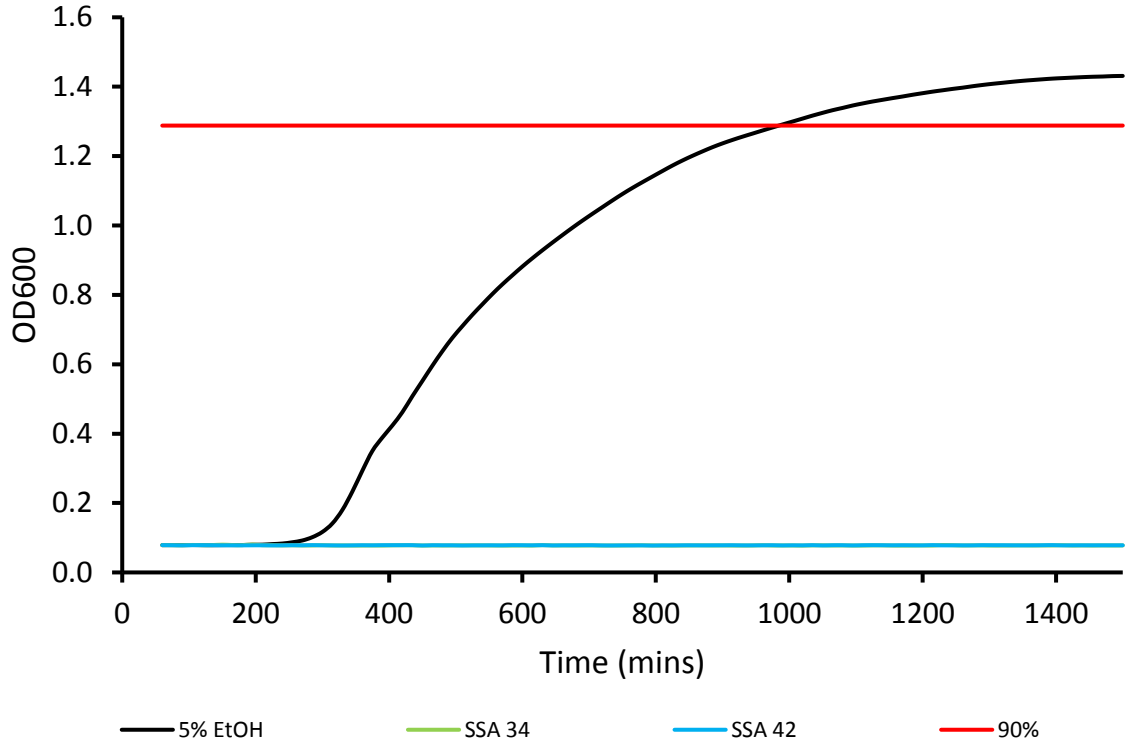

Figure S140 **-** MRSA growth curves created from an average of 6 absorbance readings in the presence of SSAs **34** and **42.**

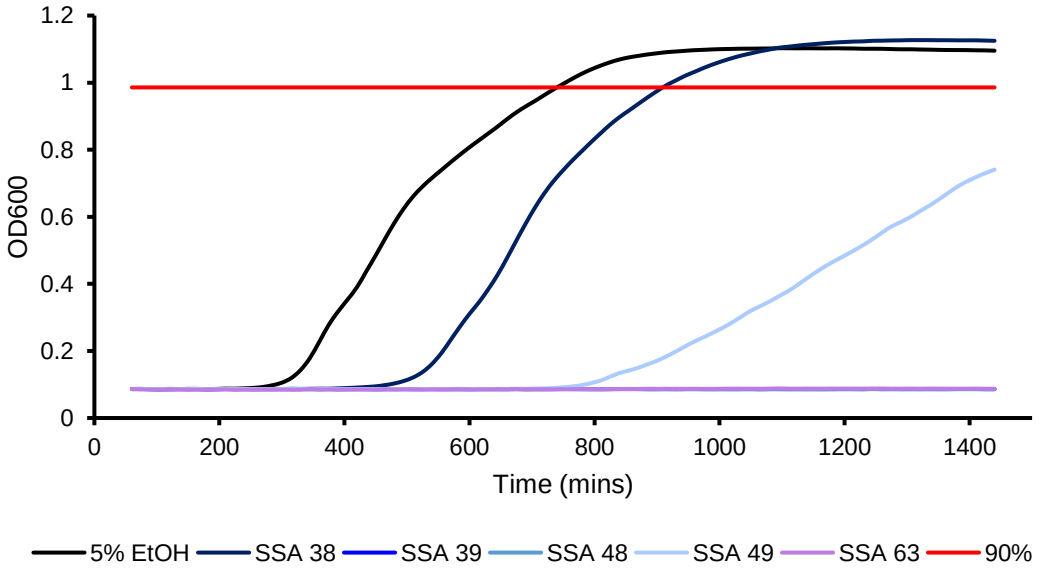

Figure S141 - MRSA growth curves created from an average of 6 absorbance readings in the presence of SSAs **38**, **39**, **48**, **49,** and **63**.

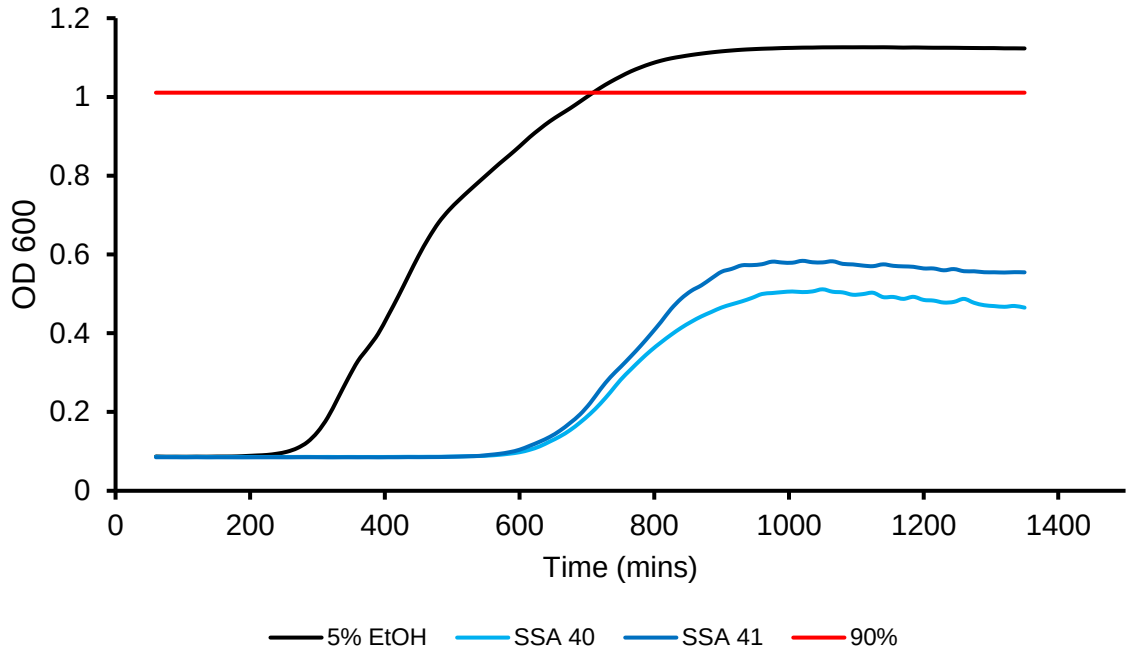

Figure S142 **-** MRSA growth curves created from an average of 6 absorbance readings in the presence of SSAs **40 and 41**.

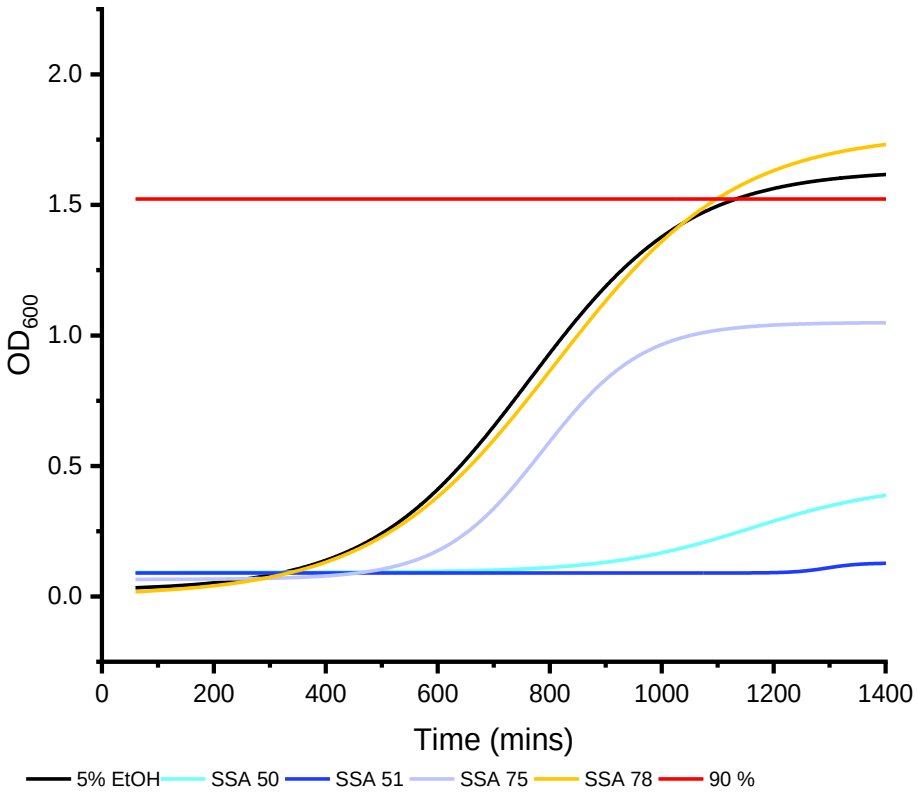

Figure S143 **-** MRSA growth curves created from an average of 6 absorbance readings in the presence of SSAs **19, 20, 44** and **47**.

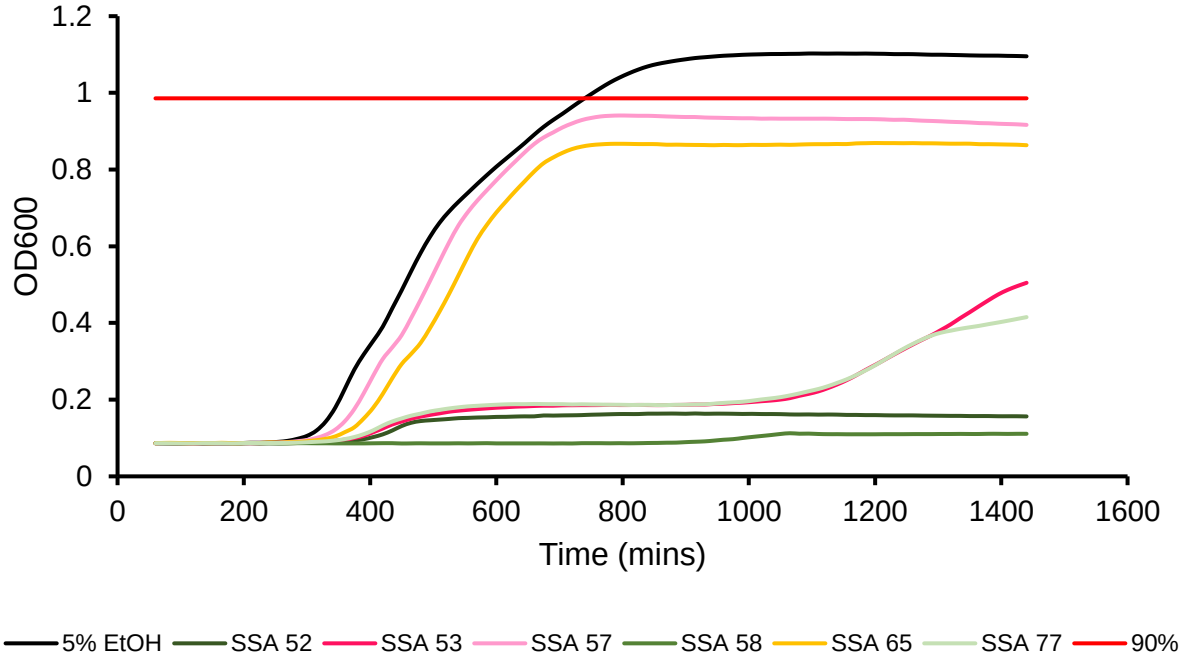

Figure S144 **-** MRSA growth curves created from an average of 6 absorbance readings in the presence of SSAs **52**, **53**, **57**, **58**, **68** and **77**.

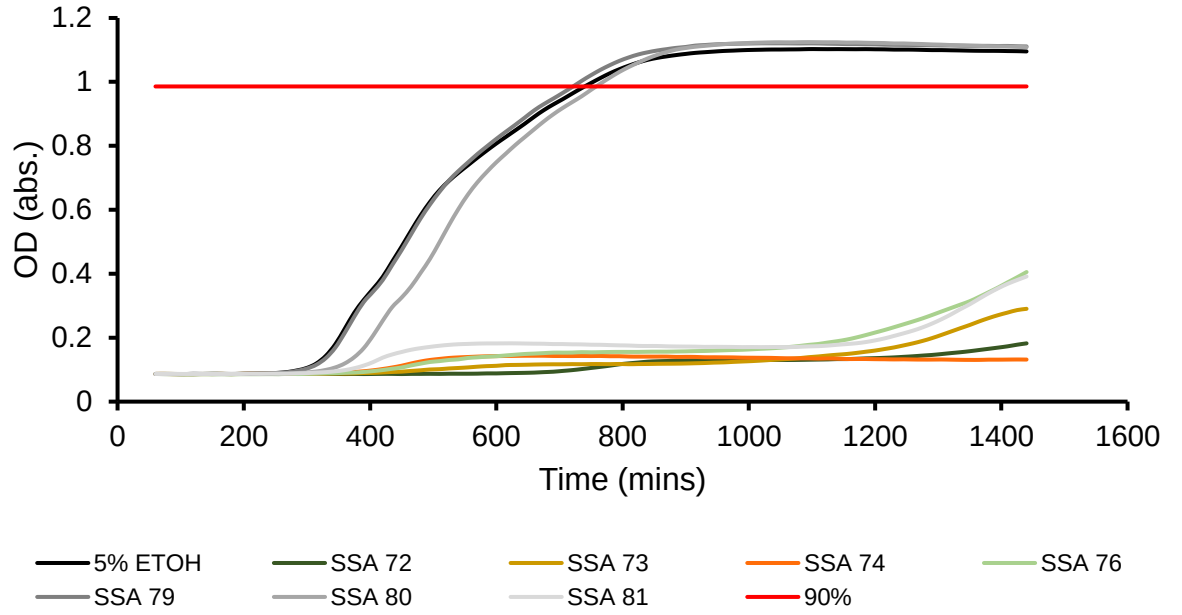

Figure S145 **-** MRSA growth curves created from an average of 6 absorbance readings in the presence of SSAs **72**, **73**, **74**, **76**, **79**, **80** and **81**.

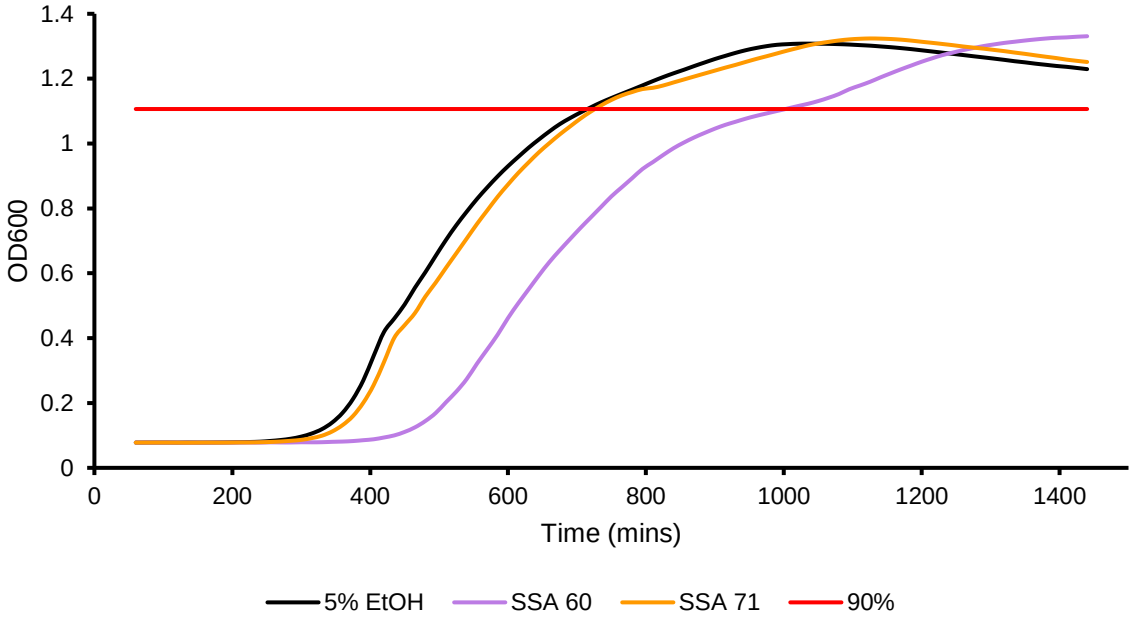

Figure S146 **-** MRSA growth curves created from an average of 6 absorbance readings in the presence of SSAs **60** and **71**.

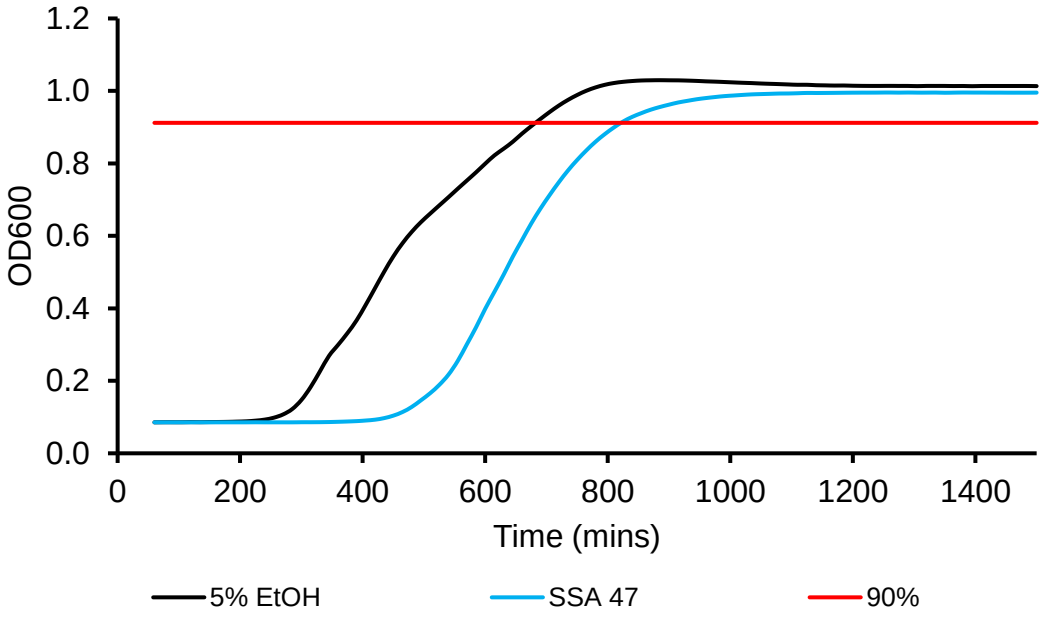

Figure S147 - MRSA growth curves created from an average of 6 absorbance readings in the presence of SSA **47**.

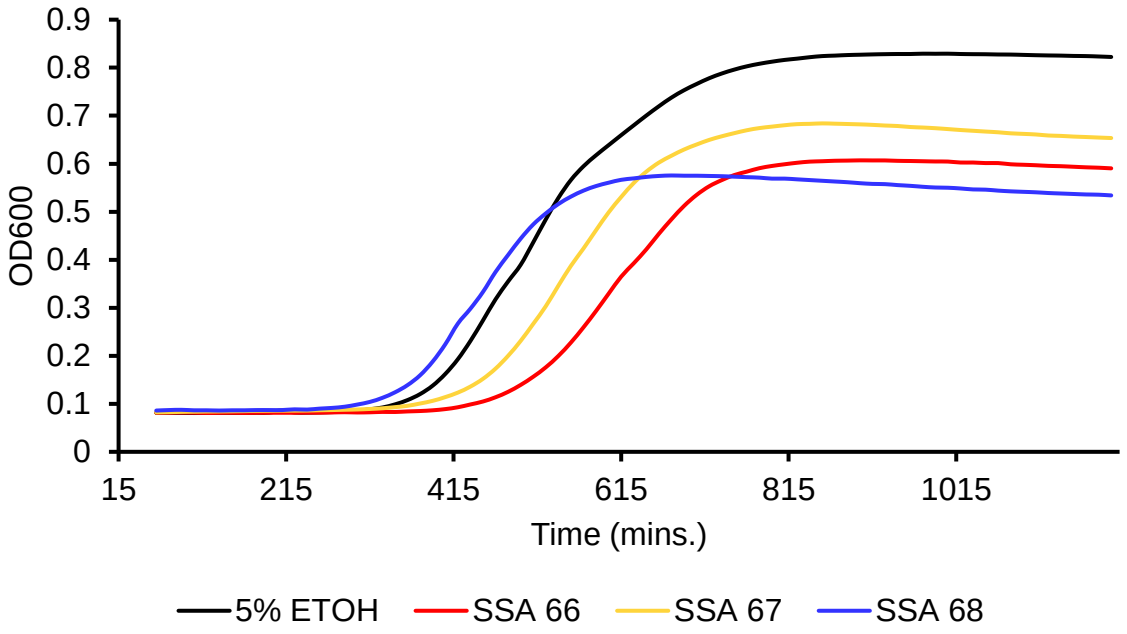

Figure S148 **-** MRSA growth curves created from an average of 6 absorbance readings in the presence of SSAs **66**, **67** and **68**. Screening conducted at 3.75 mM as part of a separate study.

Antimicrobial gel plates

Figure S149 – Surface diffusion assay using the SSA **70** (5 mg/mL) gel on MRSA inoculated agar plates.

Figure S150 – Surface diffusion assay using the SSA **70** (5 mg/mL) gel on *E. coli* inoculated agar plates.

Figure S151 – Well diffusion assay using the SSA **70** (5 mg/mL) gel on MRSA inoculated agar plates.

Figure S152 – Well diffusion assay using the SSA **70** (5 mg/mL) gel on *E. coli* inoculated agar plates.

Figure S153 – Well diffusion assay using the Ampicillin (5 mg/mL) on MRSA inoculated agar plates.

Figure S154 – Well diffusion assay using Ampicillin (5 mg/mL) gel on *E. coli* inoculated agar plates.

Figure S155 – Surface diffusion assay using the co-formulated SSA **70** and ampicillin gel (5 mg/mL) on MRSA inoculated agar plates.

Figure S156 – Well diffusion assay using the co-formulated SSA **70** and ampicillin gel (5 mg/mL) on MRSA inoculated agar plates.

Figure S157 – Surface diffusion assay using the co-formulated SSA **70** and ampicillin gel (5 mg/mL) on *E. coli* inoculated agar plates.

Figure S158 – Well diffusion assay using the co-formulated SSA **70** and ampicillin gel (5 mg/mL) on *E. coli* inoculated agar plates.

Quantitative Microscopy Analysis

Table S37**.** Fluorescence intensities (FI) of *E. coli* at T=30 min and T= 4 hours under various conditions. Cells n_{total} = total number of cells analyzed for that condition. DAPI (450 nm) and mCherry (605 nm) filters used.

	Peak Wavelength examined (T = 30 min)		**Cells n_{total} (T = 30min)**	**Peak Wavelength examined (T = 4 hrs.)**		**Cells n_{total} (T = 4hrs)**
	450 nm	605 nm		450 nm	605 nm	
Solvent alone	21.15 ± 1.59	4.28 ± 0.74	54	22.68 ± 1.96	4.46 ± 0.48	72
SSA *70*	104.35 ± 10.86	5.41 ± 0.43	69	264.58 ± 35.65	5.55 ± 4.02	74
FM 4-64	22.23 ± 0.91	32.66 ± 11.68	79	5.92 ± 1.11	80.36 ± 15.14	70
SSA 70 and FM 4-64	88.30 ± 17.49	6.60 ±1.60	67	559.61 ± 75.45	29.07 ± 24.68	74

Table S38. Fluorescence intensities (FI) of MRSA at T=30 min and T= 4 hours under various conditions. Cells n_{total} = total number of cells analyzed for that condition. DAPI (450 nm) and mCherry (605 nm) filters used.

	Peak Wavelength examined (T = 30 min)		**Cells n_{total} (T = 30min)**	**Peak Wavelength examined (T = 4 hrs.)**		**Cells n_{total} (T = 4hrs)**
	450 nm	605 nm		450 nm	605 nm	
Solvent Alone	22.46 ± 3.20	6.95 ± 1.87	73	23.38 ± 0.11	5.66 ± 0.57	78
SSA 70	133.98 ± 16.90	4.28 ± 1.91	69	297.77 ± 87.37	4.65 ± 2.95	66
FM 4-64	26.81 ± 1.04	53.24 ± 8.35	32	27 ± 1.36	22.05 ± 2.52	64
SSA 70 and FM 4-64	187.11 ± 19.30	7.20 ± 3.02	86	268.05 ± 45.99	6.68 ± 2.07	76

E. coli at 30 minutes

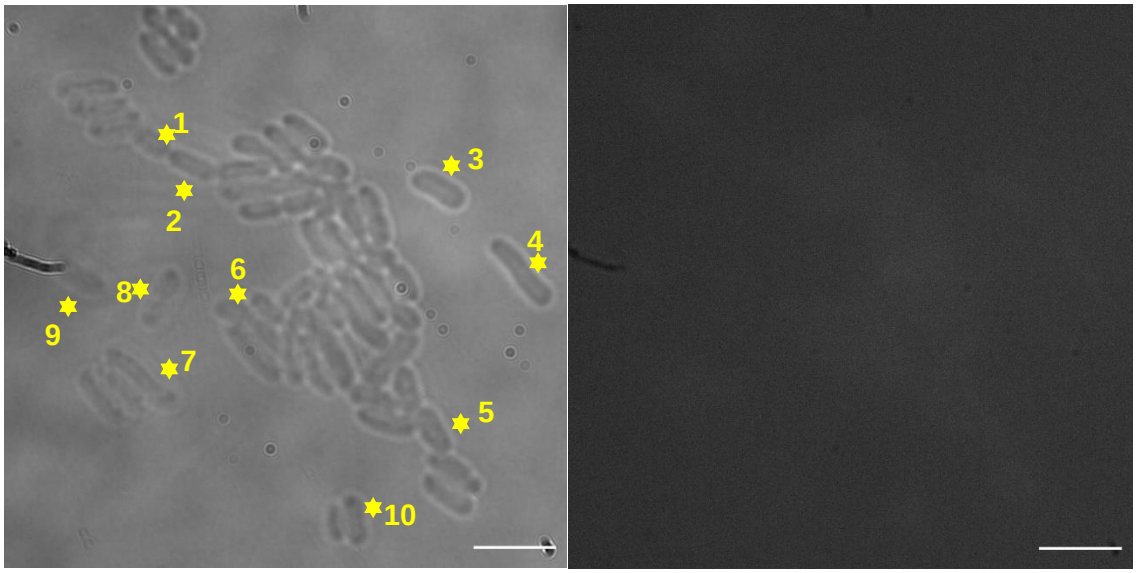

Figure S159 – *E. coli* transmitted image and fluorescence image at 450 nm used in fluorescence intensity calculations in the absence of both SSA **70** and FM4-64 at T = 30 minutes. Transmitted image used to locate cells on fluorescence image. Scale bar = 10 µM.

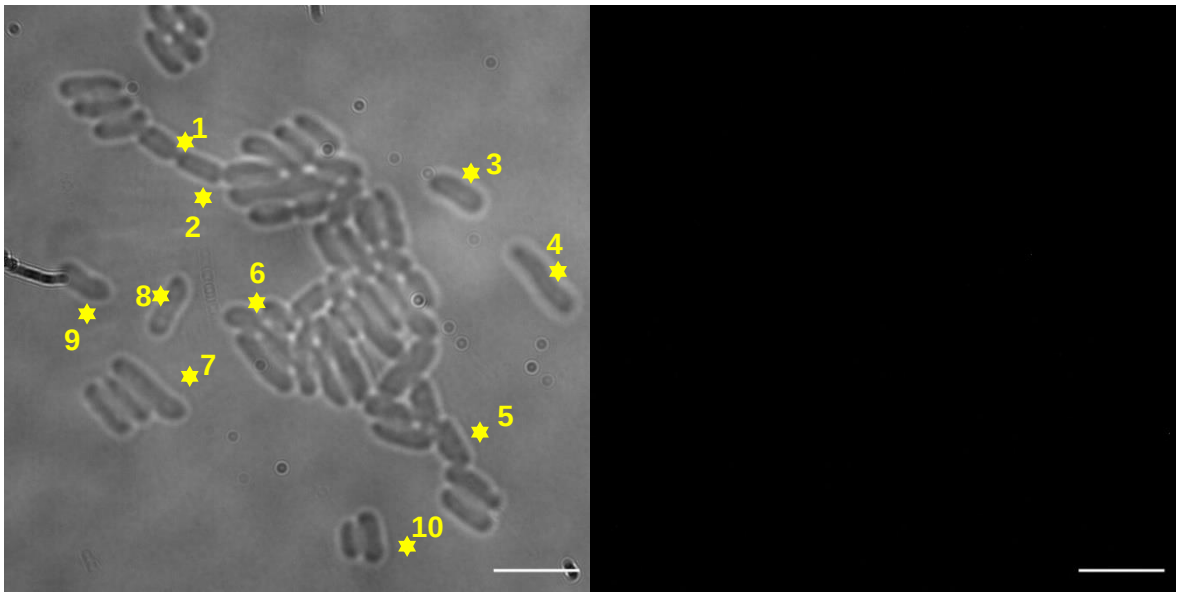

Figure S160 – *E. coli* transmitted image and fluorescence image at 605 nm used in fluorescence intensity calculations in the absence of both SSA **70** and FM4-64 at T = 30 minutes. Transmitted image used to locate cells on fluorescence image. Scale bar = 10 µM.

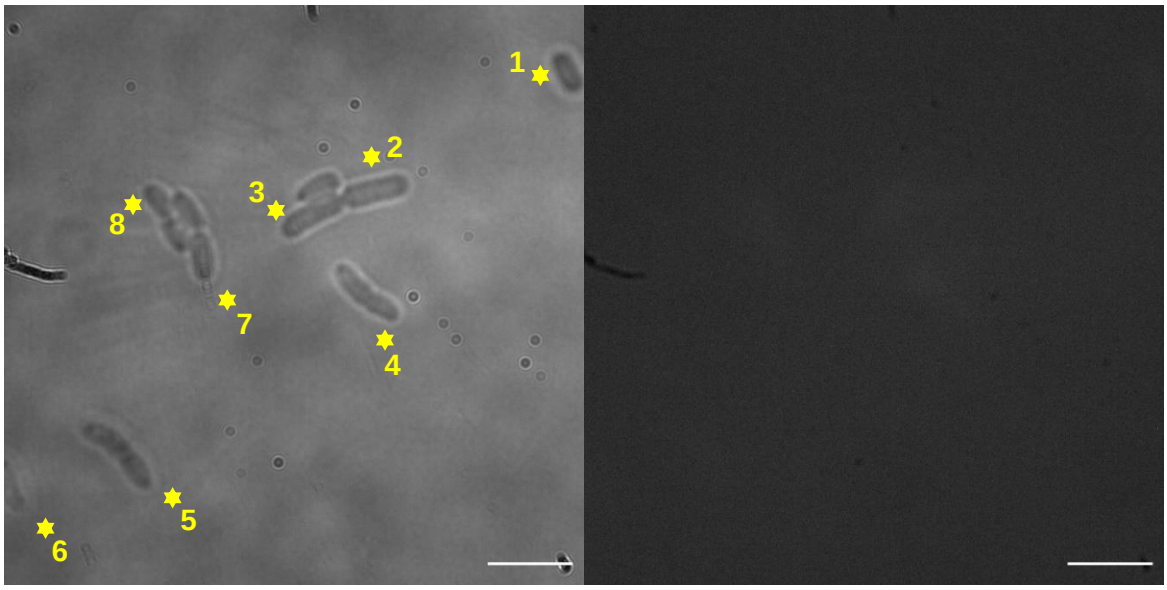

Figure S161 – *E. coli* transmitted image and fluorescence image at 450 nm images used in fluorescence intensity calculations in the absence of both SSA **70** and FM4-64 at T = 30 minutes. Transmitted image used to locate cells on fluorescence image at 450 nm. Scale bar = 10 µM.

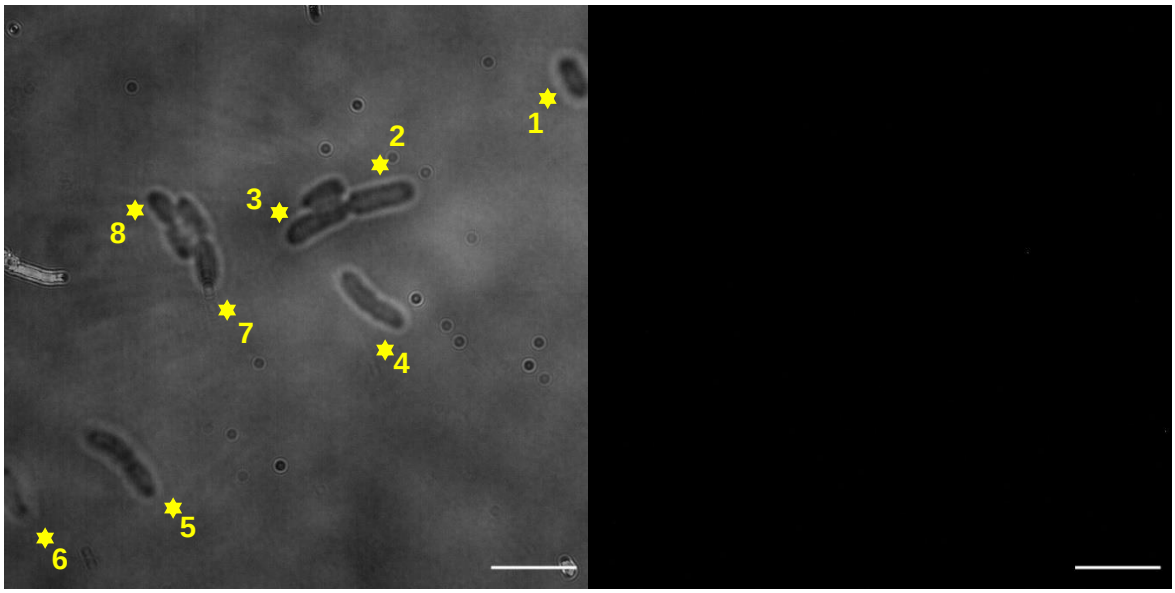

Figure S162 – *E. coli* transmitted image and fluorescence image at 605 nm used in fluorescence intensity calculations in the absence of both SSA **70** and FM4-64 at T = 30 minutes. Transmitted image used to locate cells on fluorescence image. Scale bar = 10 µM.

.

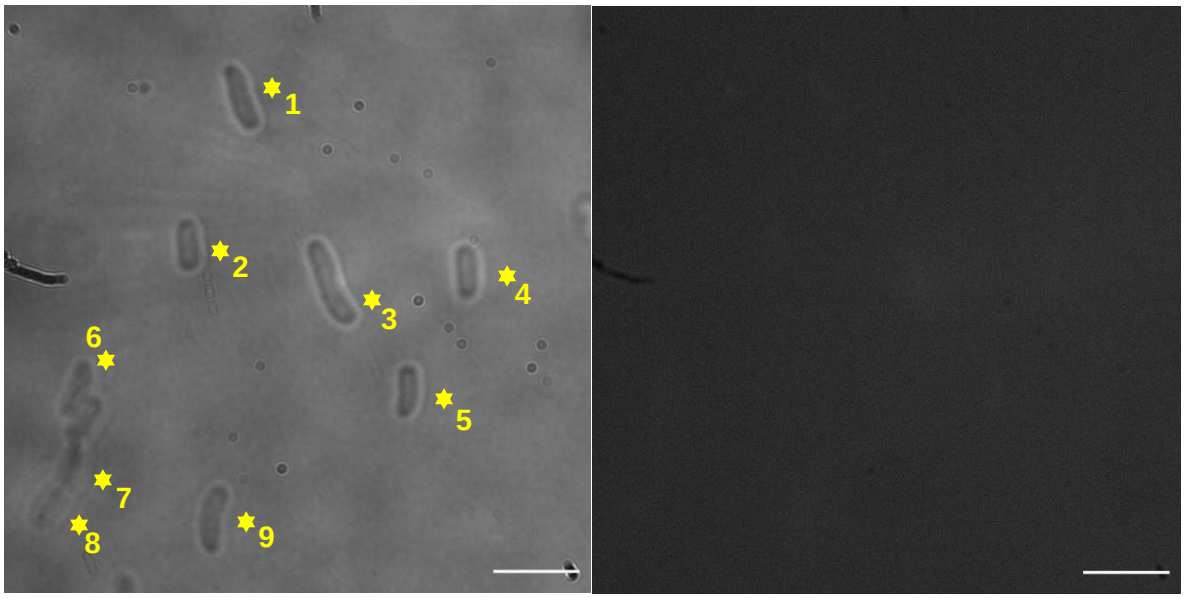

Figure S163 – *E. coli* transmitted image and fluorescence image at 450 nm used in fluorescence intensity calculations in the absence of both SSA **70** and FM4-64 at T = 30 minutes. Transmitted image used to locate cells on Fluorescence image at 450 nm. Scale bar = 10 µM.

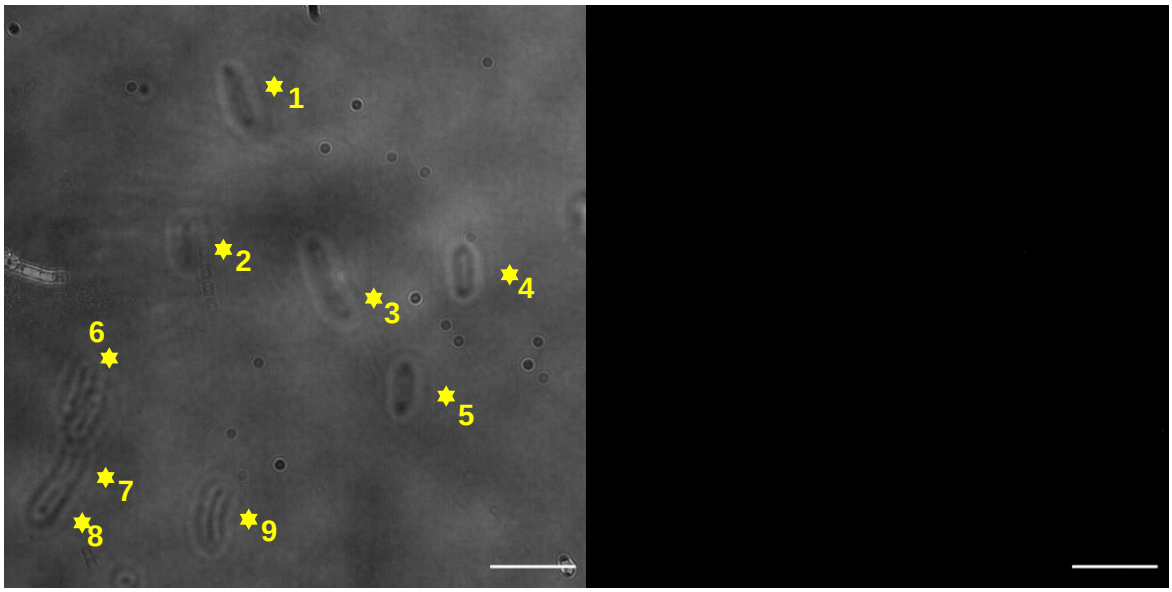

Figure S164 – *E. coli* transmitted image and fluorescence image at 605 nm used in fluorescence intensity calculations in the absence of both SSA **70** and FM4-64 at T = 30 minutes. Transmitted image used to locate cells on fluorescence image. Scale bar = 10 µM.

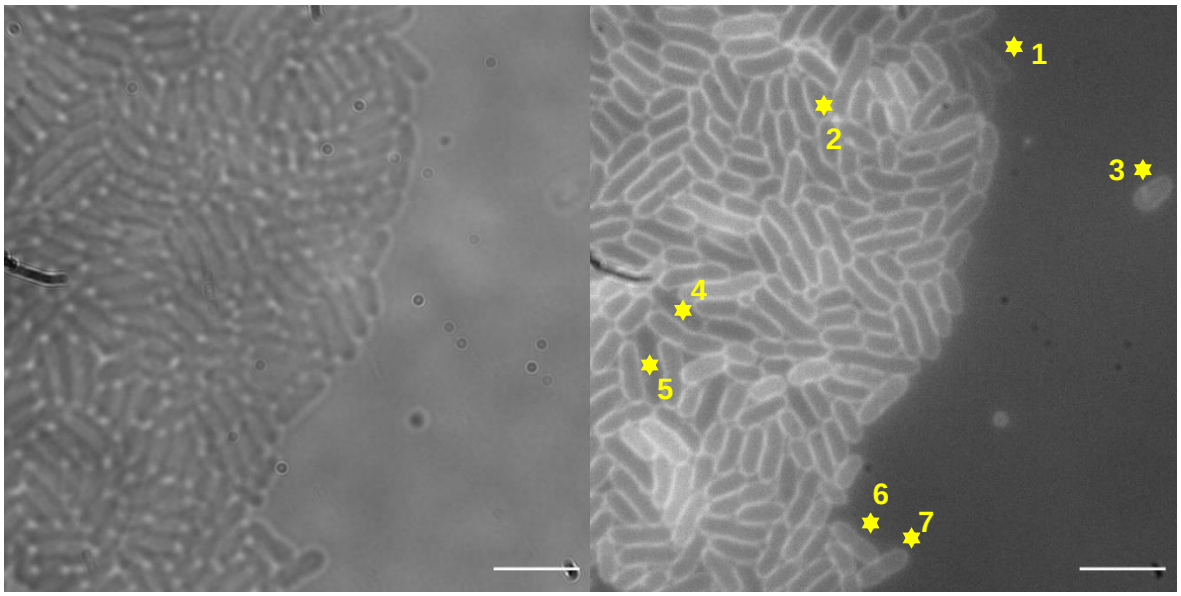

Figure S165 – *E. coli* transmitted image and fluorescence image at 450 nm used in fluorescence intensity calculations in the presence of SSA **70** at T = 30 minutes. Scale bar = 10 µM.

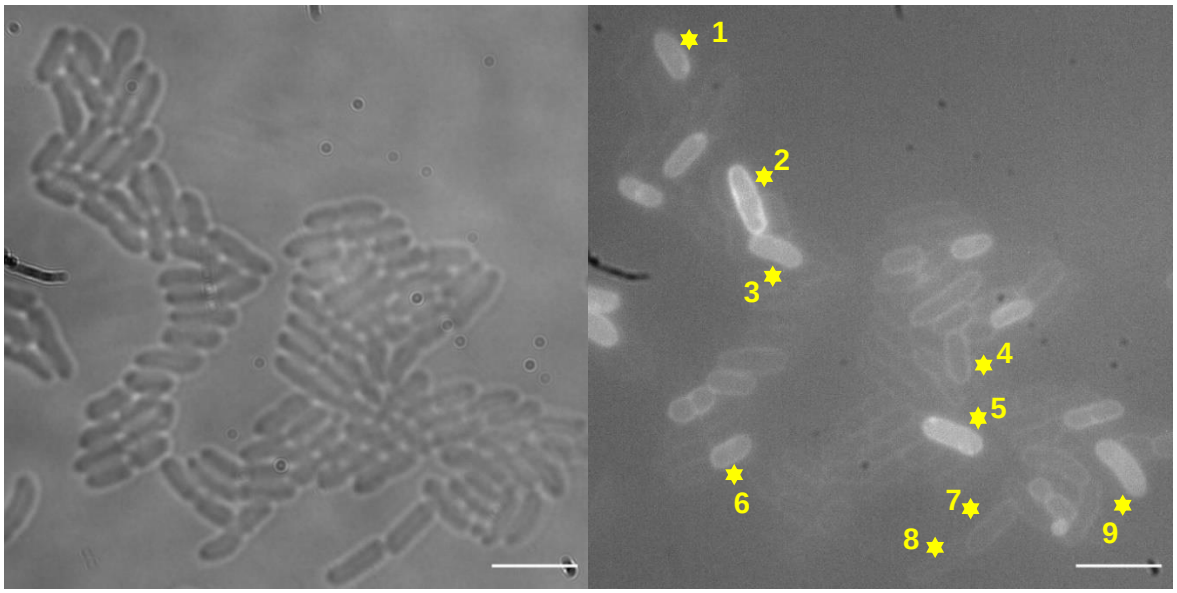

Figure S166 – *E. coli* transmitted image and fluorescence image at 450 nm used in fluorescence intensity calculations in the presence of SSA **70** at T = 30 minutes. Scale bar = 10 µM.

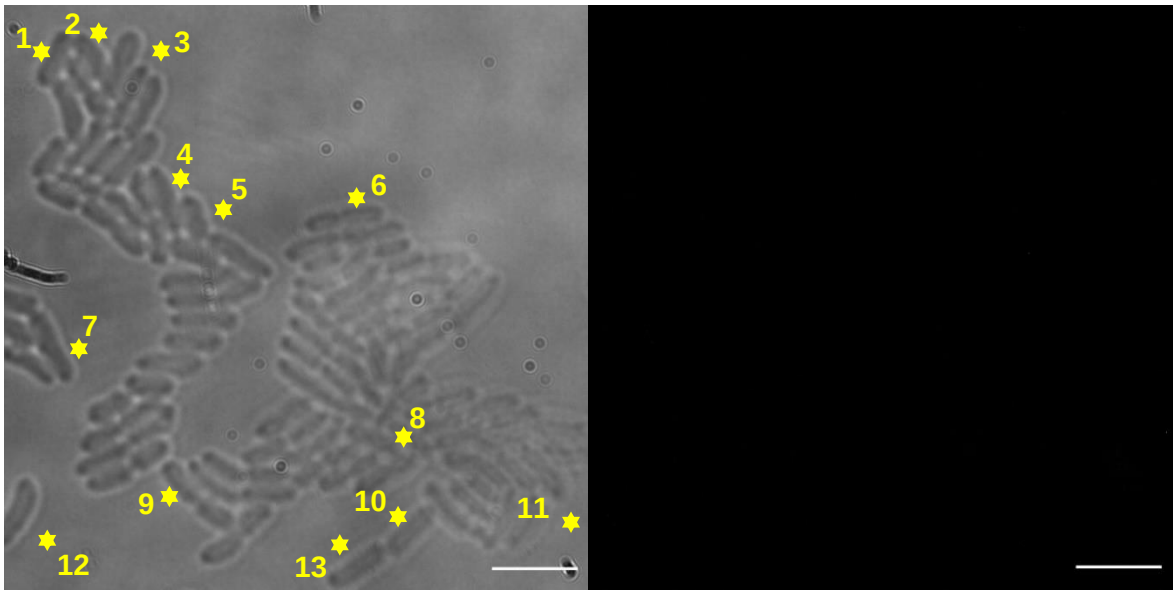

Figure S167 – *E. coli* transmitted image and fluorescence image at 605 nm used in fluorescence intensity calculations in the presence of SSA **70** at T = 30 minutes. Scale bar = 10 µM.

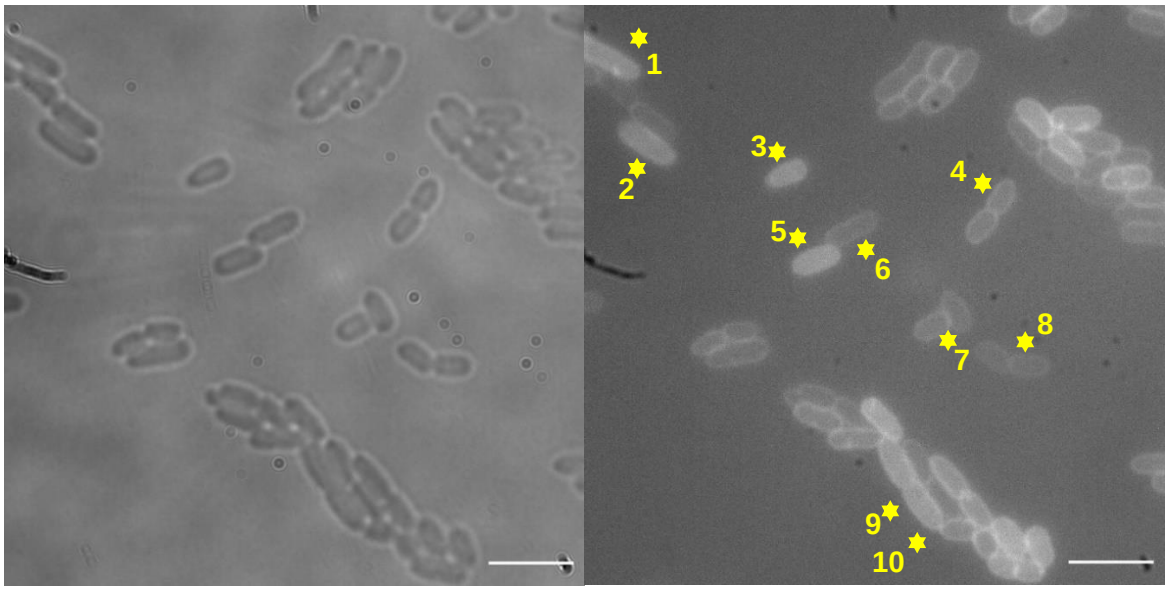

Figure S168 – *E. coli* transmitted image and fluorescence image at 450 nm used in fluorescence intensity calculations in the presence of SSA **70** at T = 30 minutes. Scale bar = 10 µM.

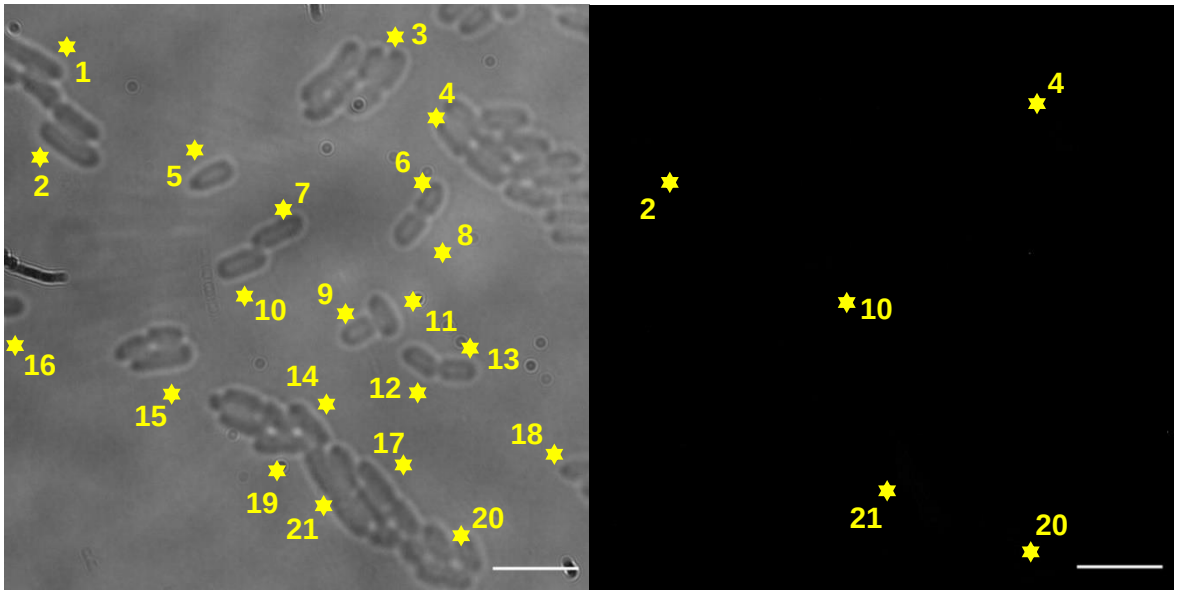

Figure S169 – *E. coli* transmitted image and fluorescence image at 605 nm used in fluorescence intensity calculations in the presence of SSA **70** at T = 30 minutes. Scale bar = 10 µM.

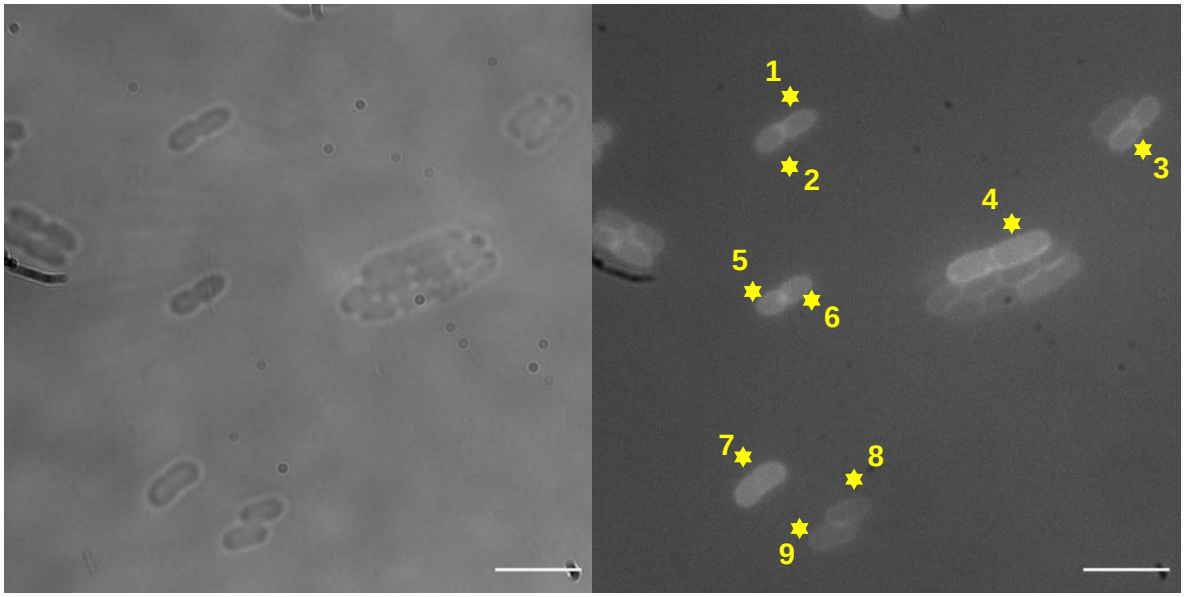

Figure S170 – *E. coli* transmitted image and fluorescence image at 450 nm used in fluorescence intensity calculations in the presence of SSA **70** at T = 30 minutes. Scale bar = 10 µM.

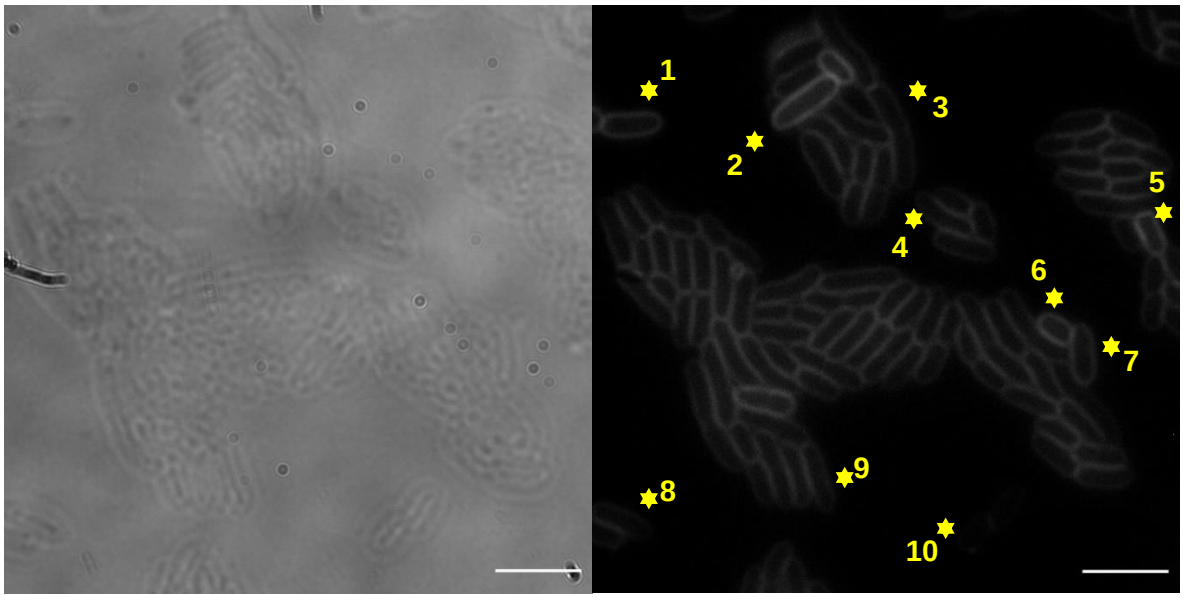

Figure S171 – *E. coli* transmitted image and fluorescence image at 605 nm used in fluorescence intensity calculations in the presence of FM4-64 at T = 30 minutes. Scale bar = 10 µM.

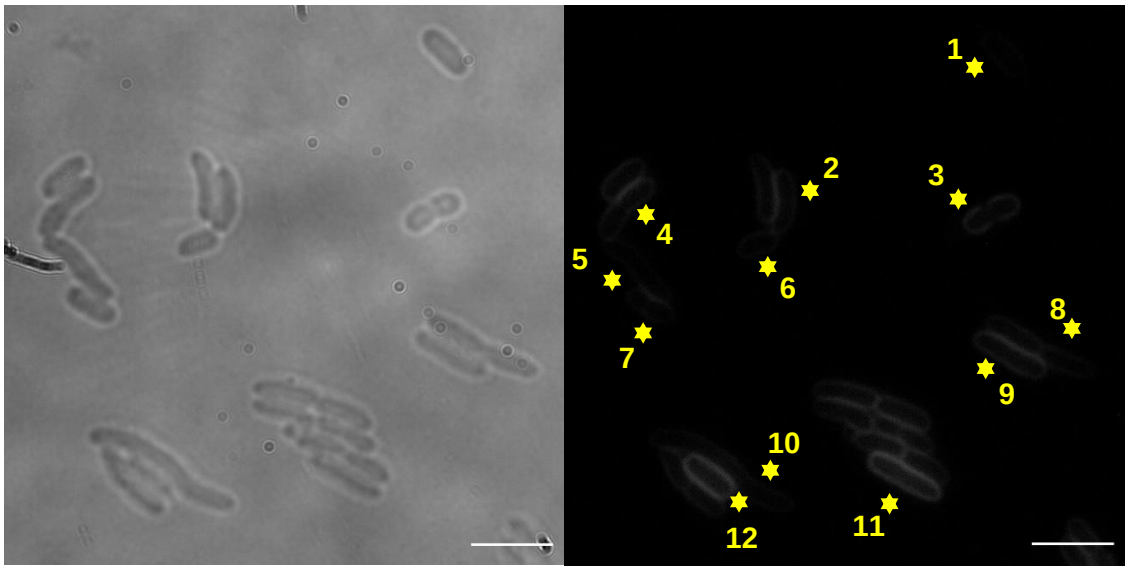

Figure S172 – *E. coli* transmitted image and fluorescence image at 605 nm used in fluorescence intensity calculations in the presence of FM4-64 at T = 30 minutes. Scale bar = 10 µM.

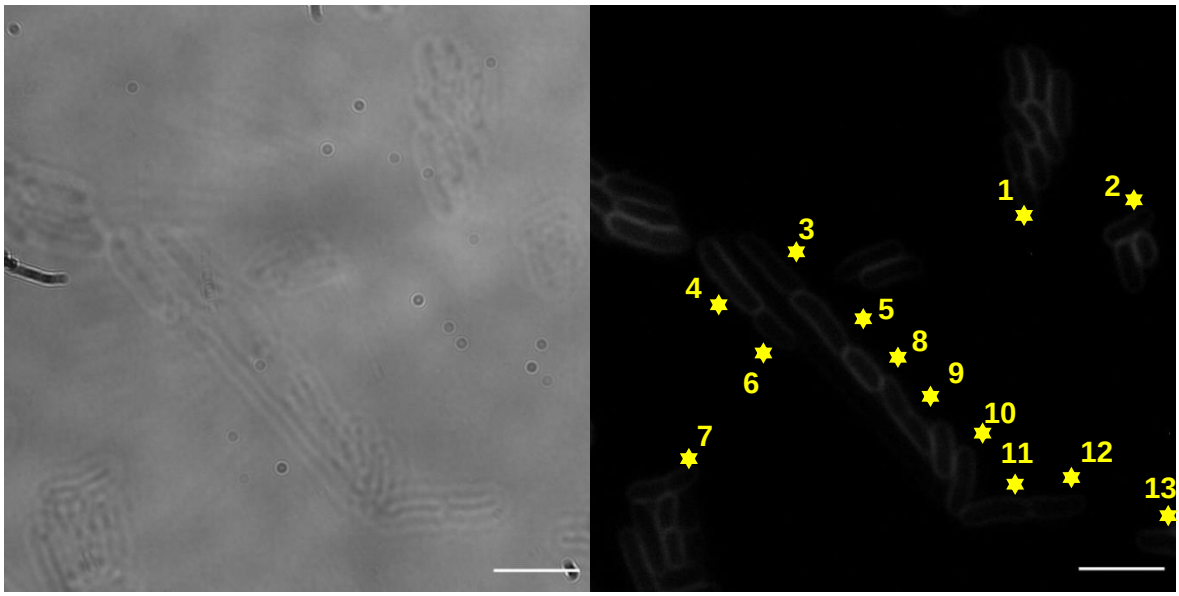

Figure S173 – *E. coli* transmitted image and fluorescence image at 605 nm used in fluorescence intensity calculations in the presence of FM4-64 at T = 30 minutes. Scale bar = 10 µM.

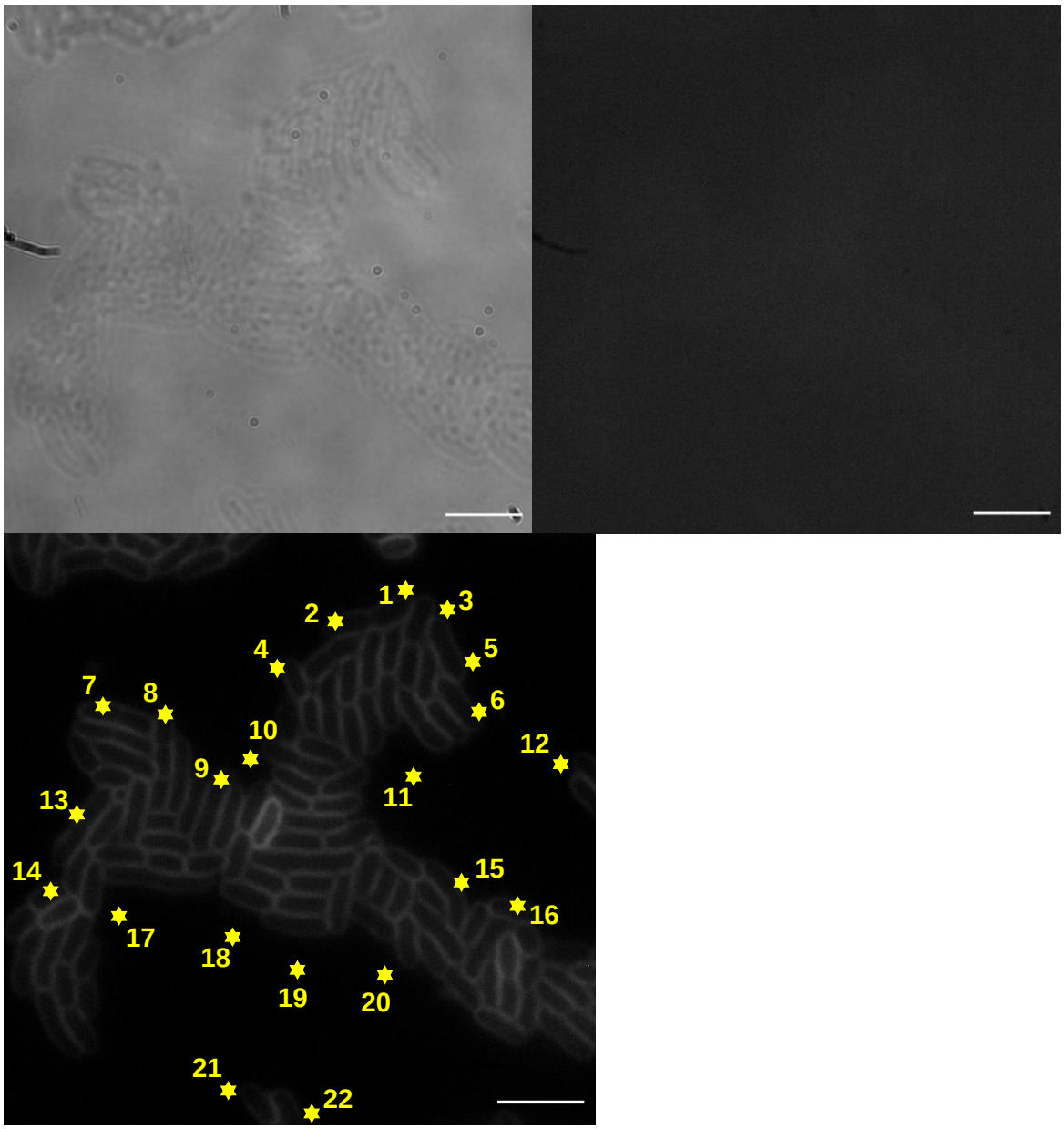

Figure S174 – *E. coli* transmitted image and fluorescence image at 450 nm used in fluorescence intensity calculations in the presence of FM4-64 at T = 30 minutes. Fluorescence image at 605 nm used to locate cells on fluorescence image at 450 nm. Scale bar = 10 µM.

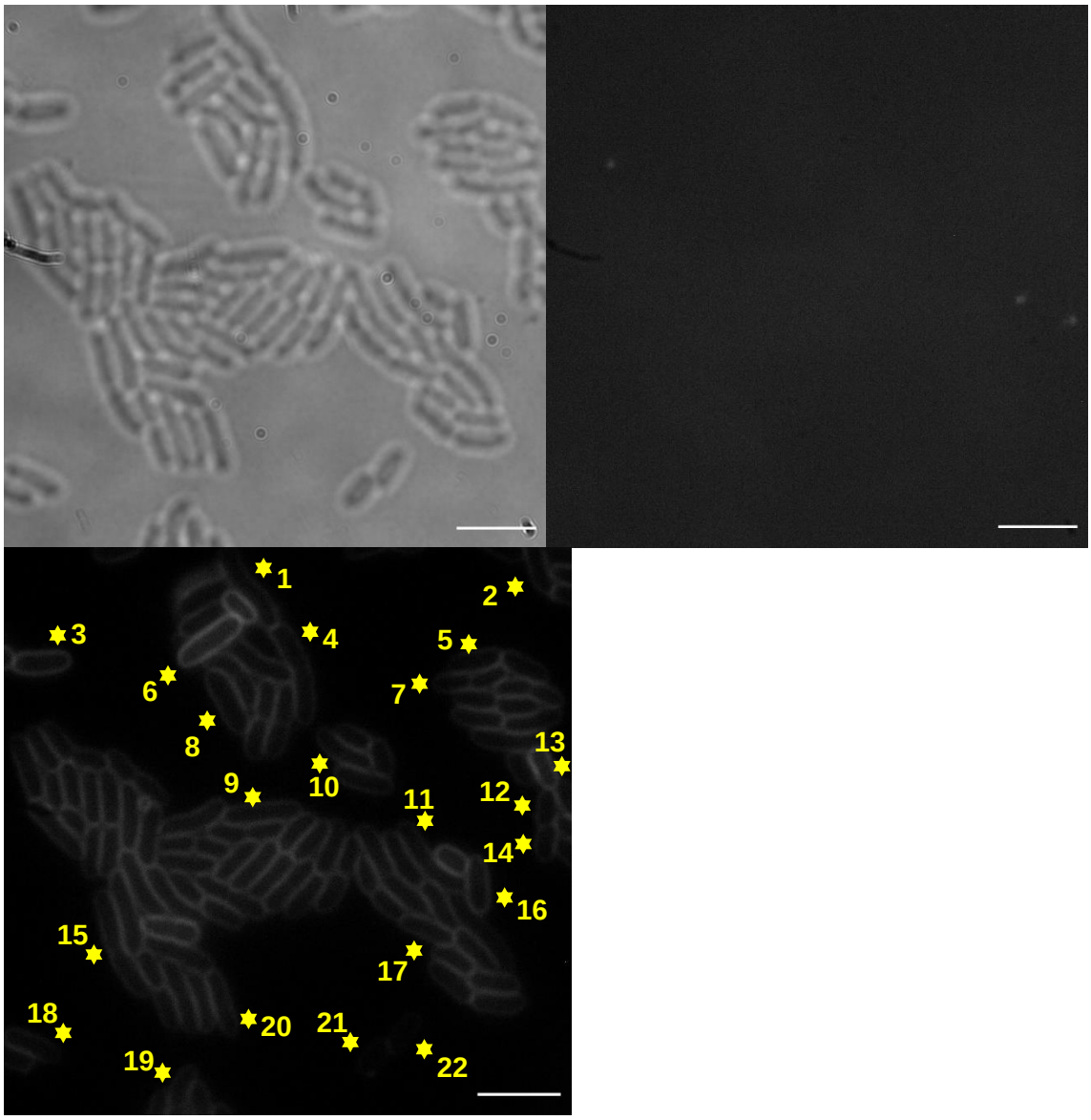

Figure S175 – *E. coli* transmitted image and fluorescence image at 450 nm used in fluorescence intensity calculations in the presence of FM4-64 at T = 30 minutes. Fluorescence image at 605 nm used to locate cells on fluorescence image at 450 nm. Scale bar = 10 µM.

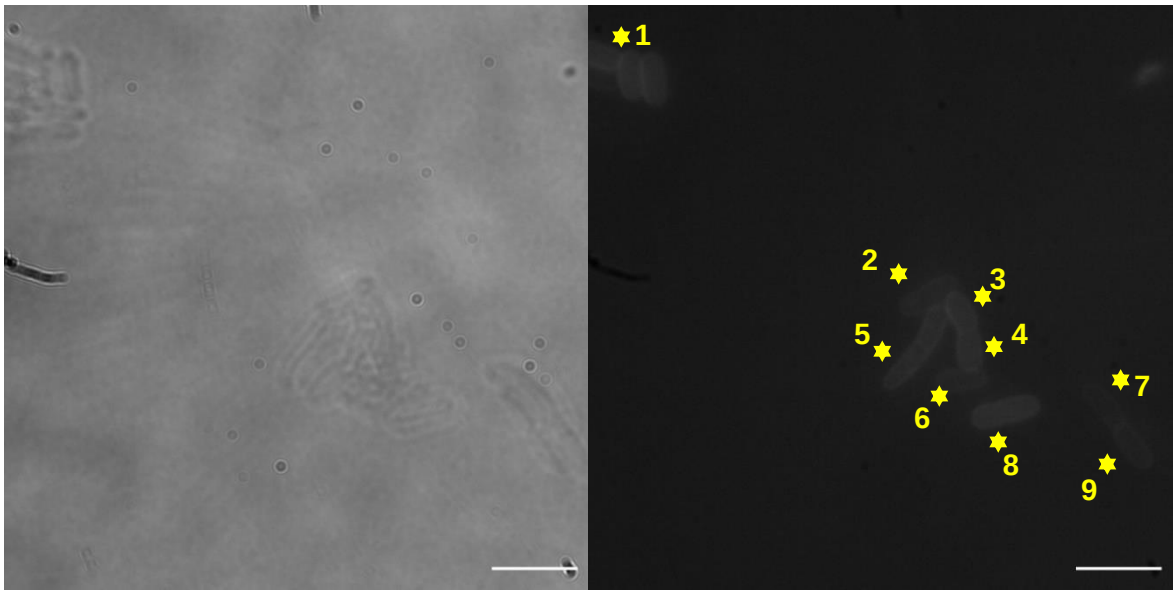

Figure S176 – *E. coli* transmitted image and fluorescence image at 450 nm used in fluorescence intensity calculations in the presence of both SSA **70** and FM4-64 at T = 30 minutes. Scale bar = 10 µM.

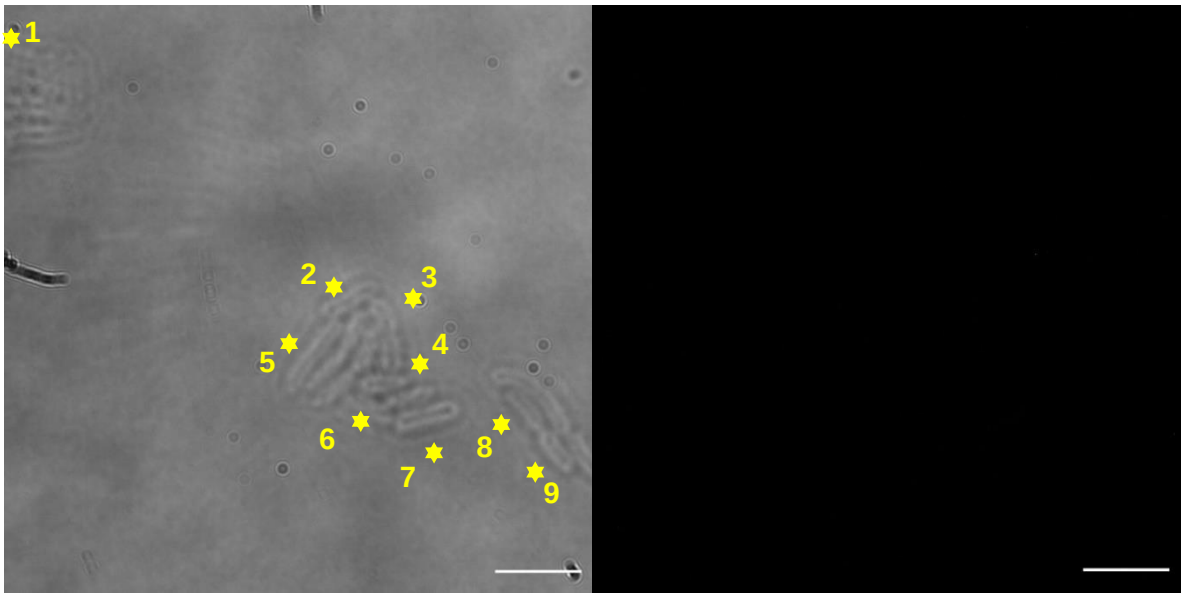

Figure S177 – *E. coli* transmitted image and fluorescence image at 605 nm used in fluorescence intensity calculations in the presence of both SSA **70** and FM4-64 at T = 30 minutes. Fluorescence image at 450 nm and transmitted image used to locate cells on fluorescence image at 605 nm. Scale bar = 10 µM.

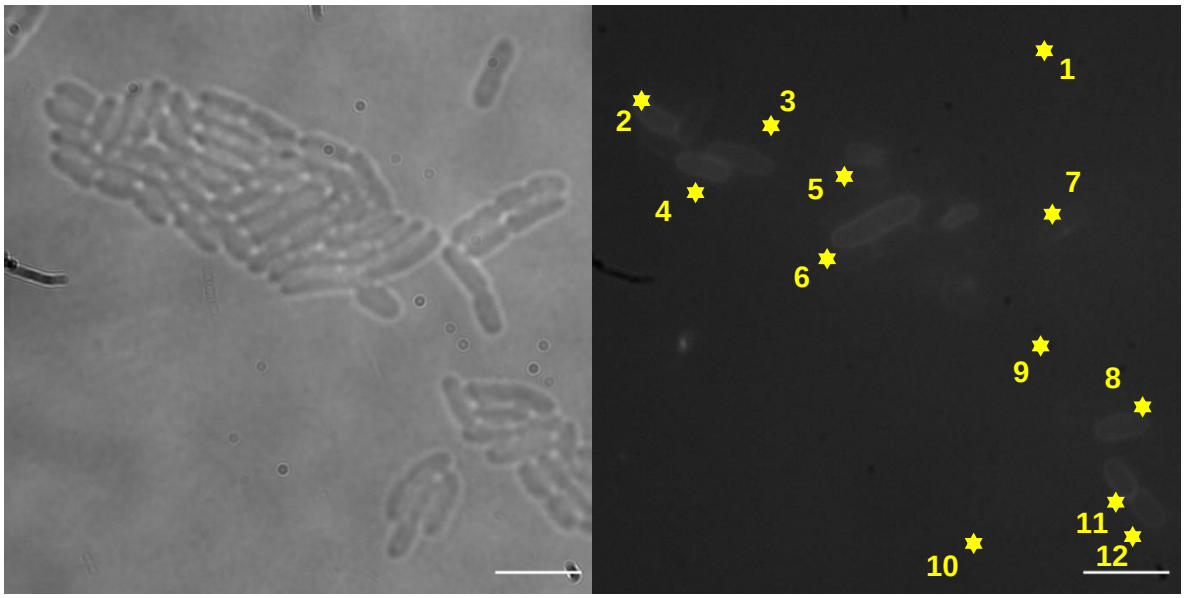

Figure S178 – *E. coli* transmitted image and fluorescence image at 450 nm used in fluorescence intensity calculations in the presence of both SSA **70** and FM4-64 at T = 30 minutes. Scale bar = 10 µM.

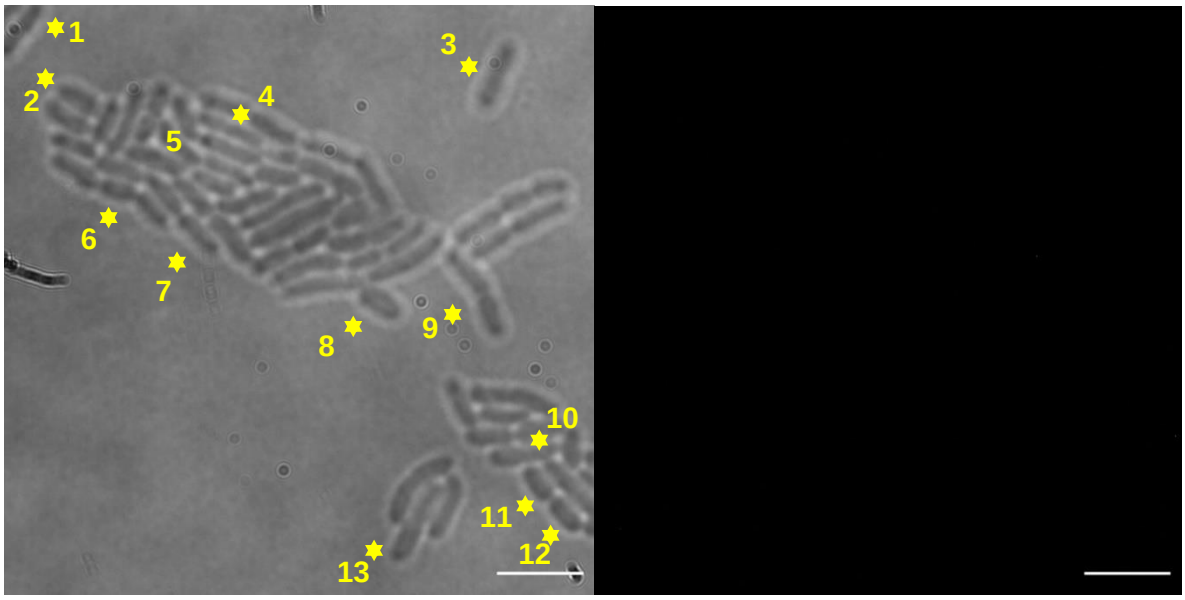

Figure S179 – *E. coli* transmitted image and fluorescence image at 605 nm used in fluorescence intensity calculations in the presence of both SSA **70** and FM4-64 at T = 30 minutes. Fluorescence image at 450 nm and transmitted image used to locate cells on fluorescence image at 605 nm. Scale bar = 10 µM.

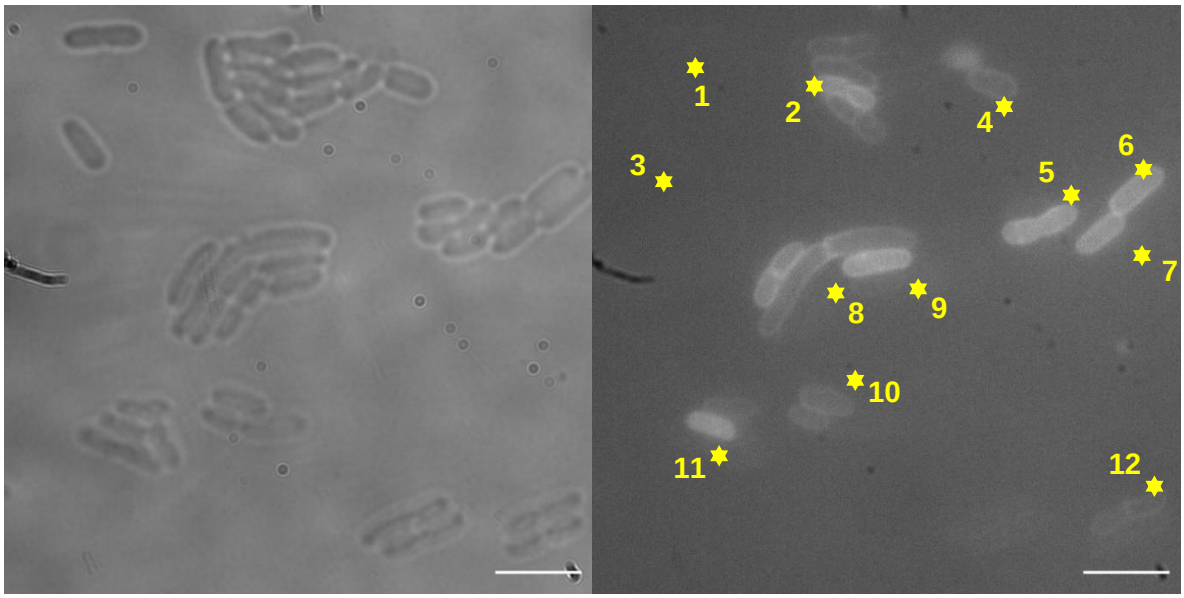

Figure S180 – *E. coli* transmitted image and fluorescence image at 450 nm used in fluorescence intensity calculations in the presence of both SSA **70** and FM4-64 at T = 30 minutes. Scale bar = 10 µM.

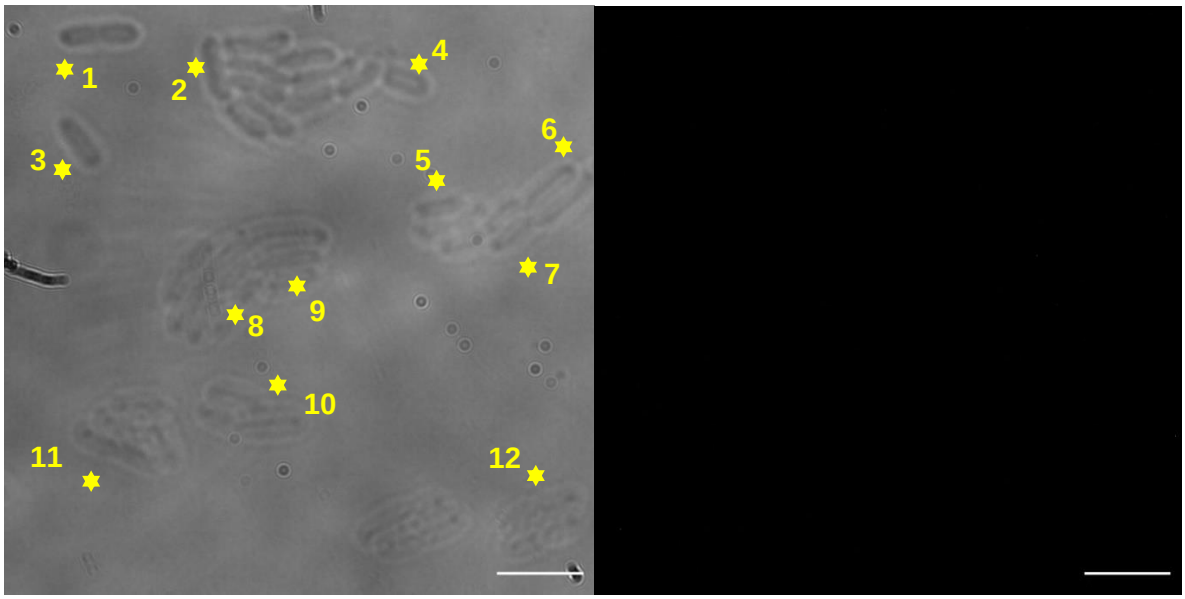

Figure S181 – *E. coli* transmitted image and fluorescence image at 605 nm used in fluorescence intensity calculations in the presence of both SSA **70** and FM4-64 at T = 30 minutes. Fluorescence image at 450 nm and transmitted image used to locate cells on fluorescence image at 605 nm. Scale bar = 10 µM.

E. coli at 4 hours

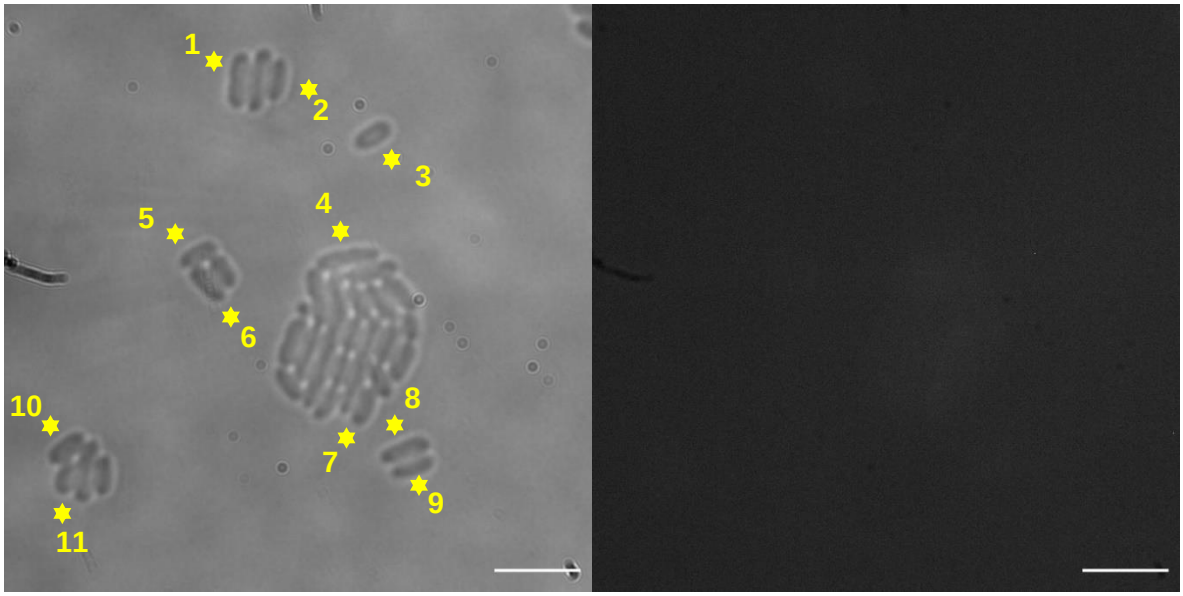

Figure S182 – *E. coli* transmitted image and fluorescence image at 450 used in fluorescence intensity calculations in the absence of both SSA **70** and FM4-64 at T = 4 hrs. Transmitted image used to locate cells on fluorescence image. Scale bar = 10µM.

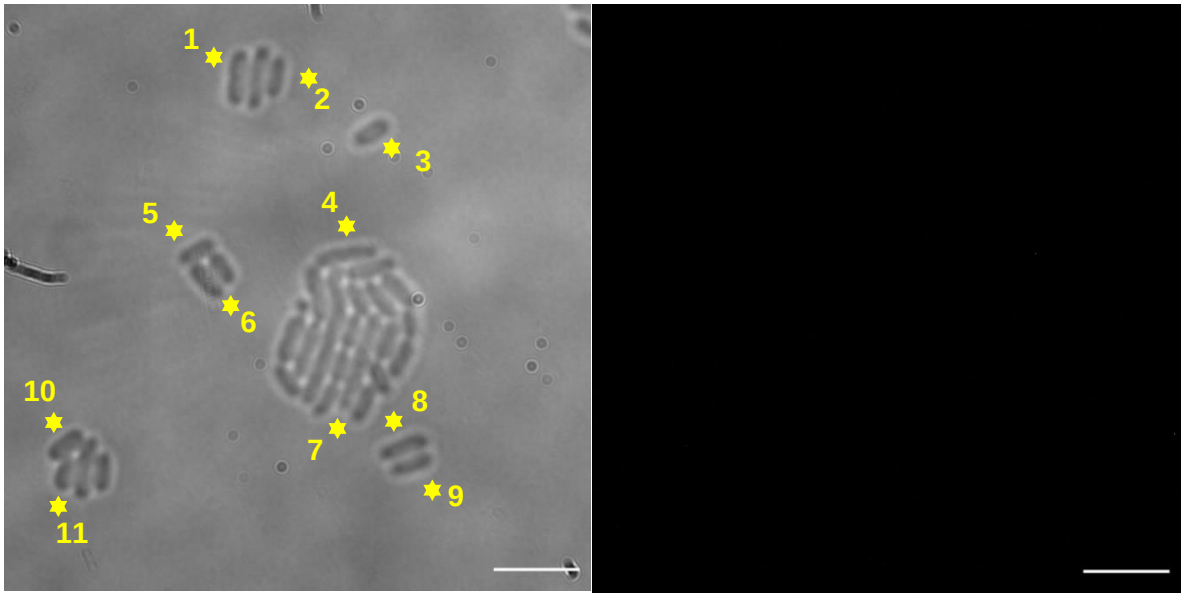

Figure S183 – *E. coli* transmitted image and fluorescence image at 605 nm used in fluorescence intensity calculations in the absence of both SSA **70** and FM4-64 at T = 4 hrs. Transmitted image used to locate cells on fluorescence image. Scale bar = 10µM.

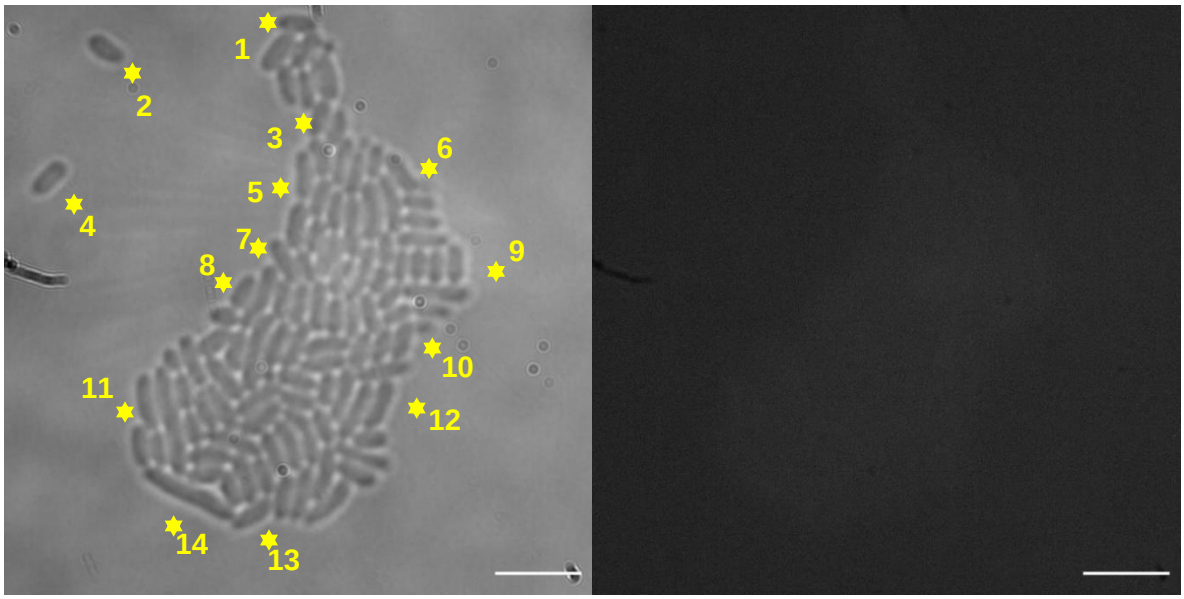

Figure S184 – *E. coli* transmitted image and Fluorescence image at 450 nm used in fluorescence intensity calculations in the absence of both SSA **70** and FM4-64 at T = 4 hrs. Transmitted image used to locate cells on fluorescence image. Scale bar = 10µM.

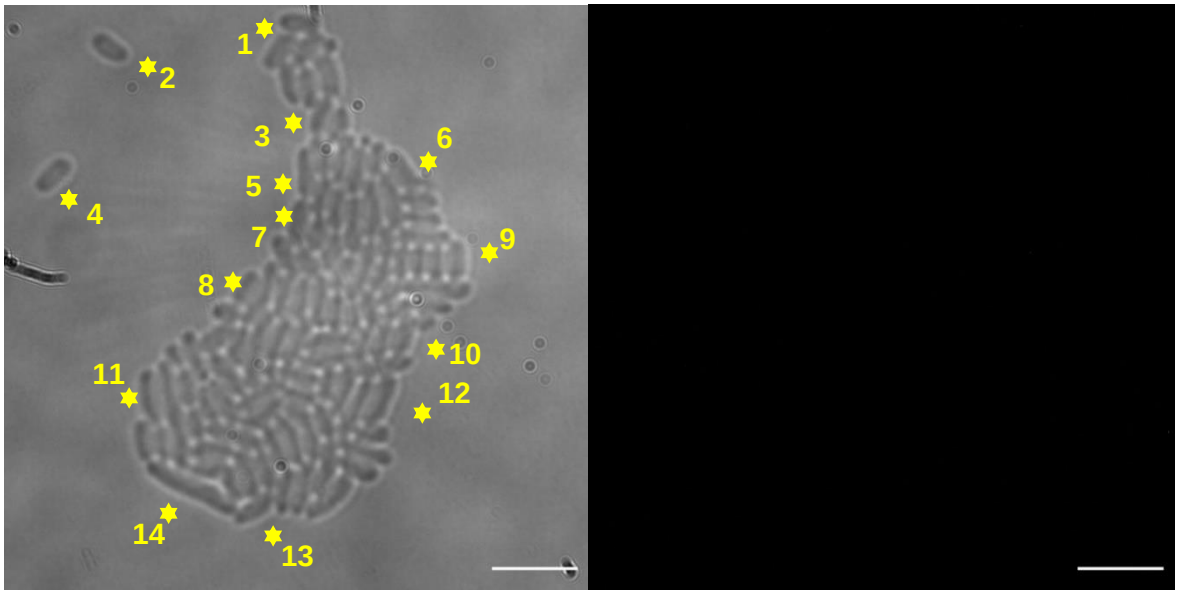

Figure S185 – *E. coli* transmitted image and fluorescence image at 605 nm used in fluorescence intensity calculations in the absence of both SSA **70** and FM4-64 at T = 4 hrs. Transmitted image used to locate cells on fluorescence image. Scale bar = 10µM.

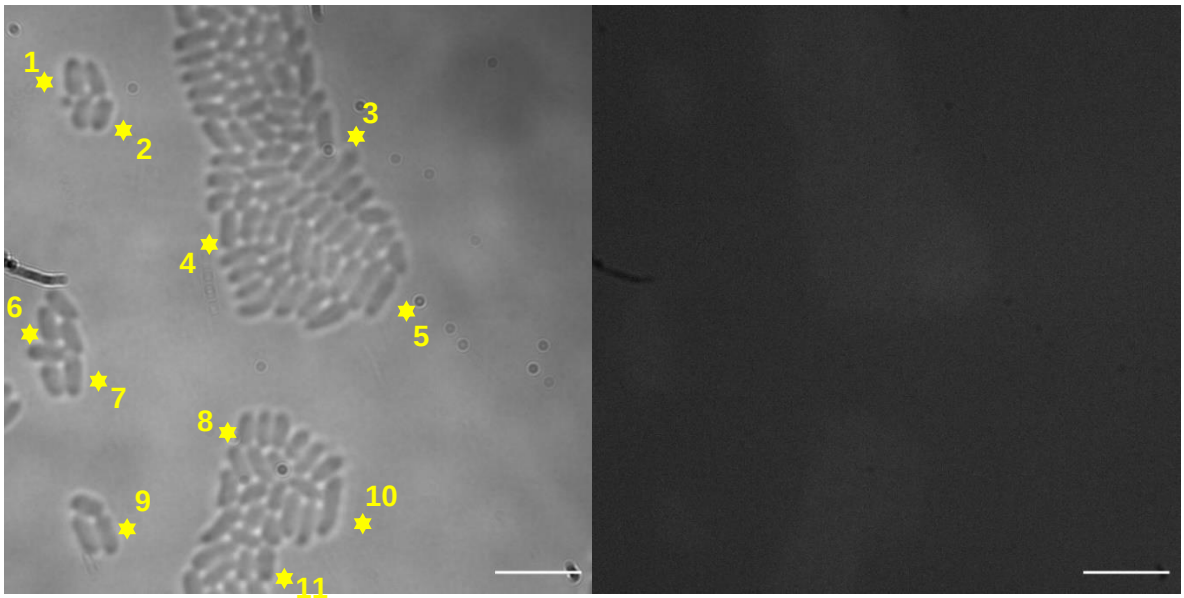

Figure S186 – *E. coli* transmitted image and fluorescence image at 450 nm used in fluorescence intensity calculations in the absence of both SSA **70** and FM4-64 at T = 4 hrs. Transmitted image used to locate cells on fluorescent image. Scale bar = 10µM.

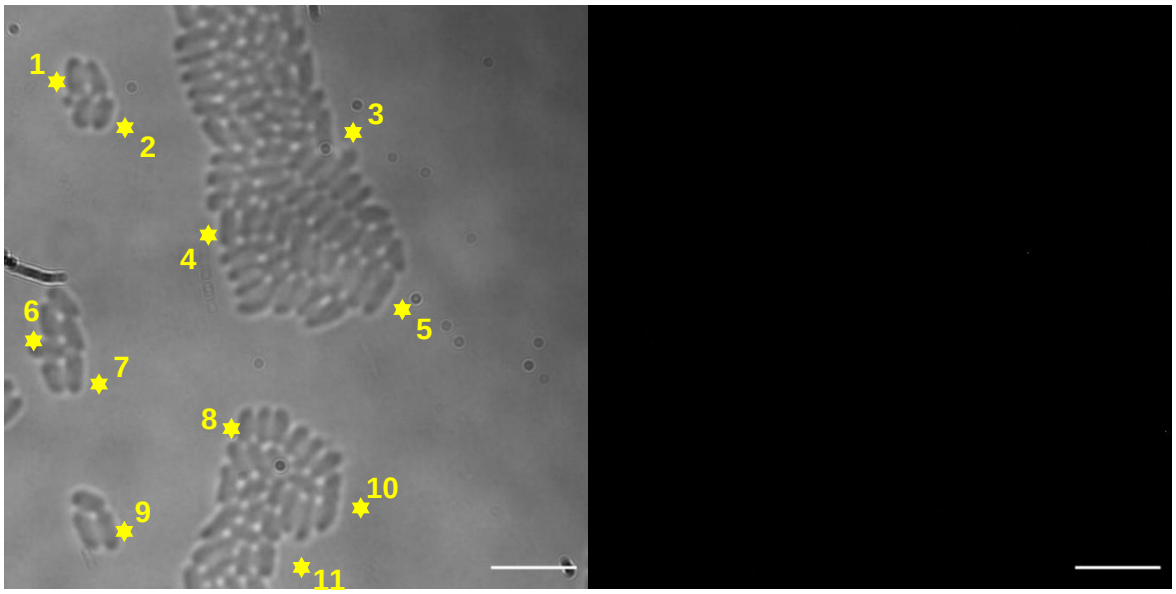

Figure S187 – *E. coli* transmitted image and fluorescence image at 605 nm used in fluorescence intensity calculations in the absence of both SSA **70** and FM4-64 at T = 4 hrs. Transmitted image used to locate cells on fluorescence image. Scale bar = 10µM.

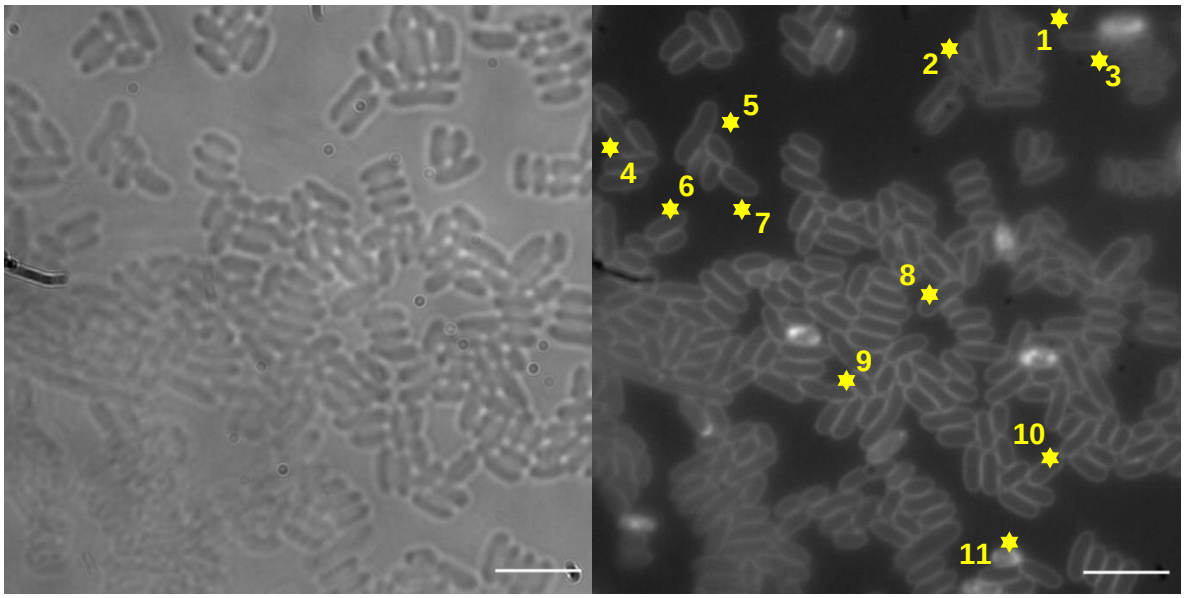

Figure S188 – *E. coli* transmitted image and fluorescence image at 450 nm used in fluorescence intensity calculations in the presence of SSA **70** at T = 4 hours. Scale bar = 10µM.

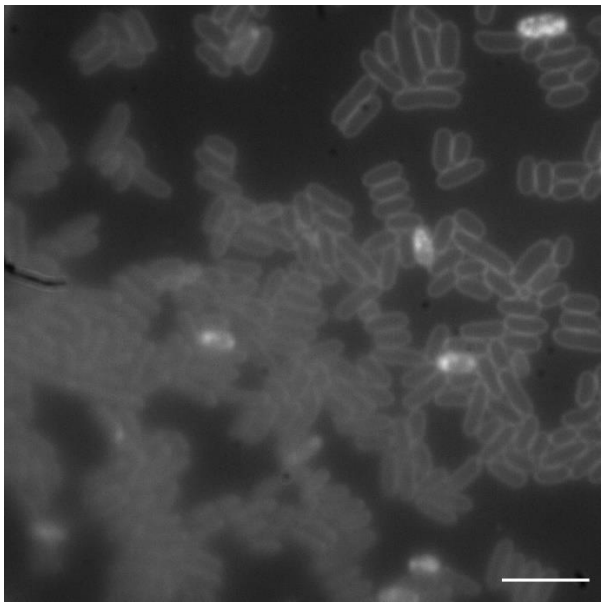

Figure S189 – Z-slice image used in combination with above figure to obtain more accurate fluorescence intensity calculations. Fluorescence image at 450 nm of *E. coli* in the presence of SSA **70** at T = 4 hours. Scale bar = 10µM.

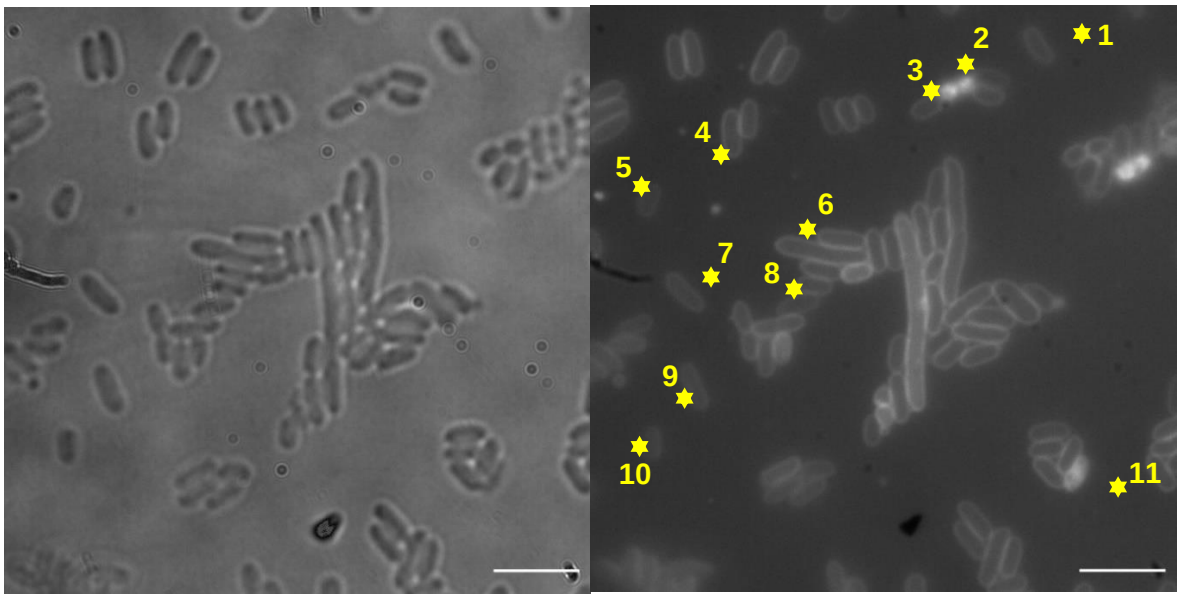

Figure S190 – *E. coli* transmitted image and fluorescence image at 450 nm used in fluorescence intensity calculations in the presence of SSA **70** at T = 4 hours. Scale bar = 10µM.

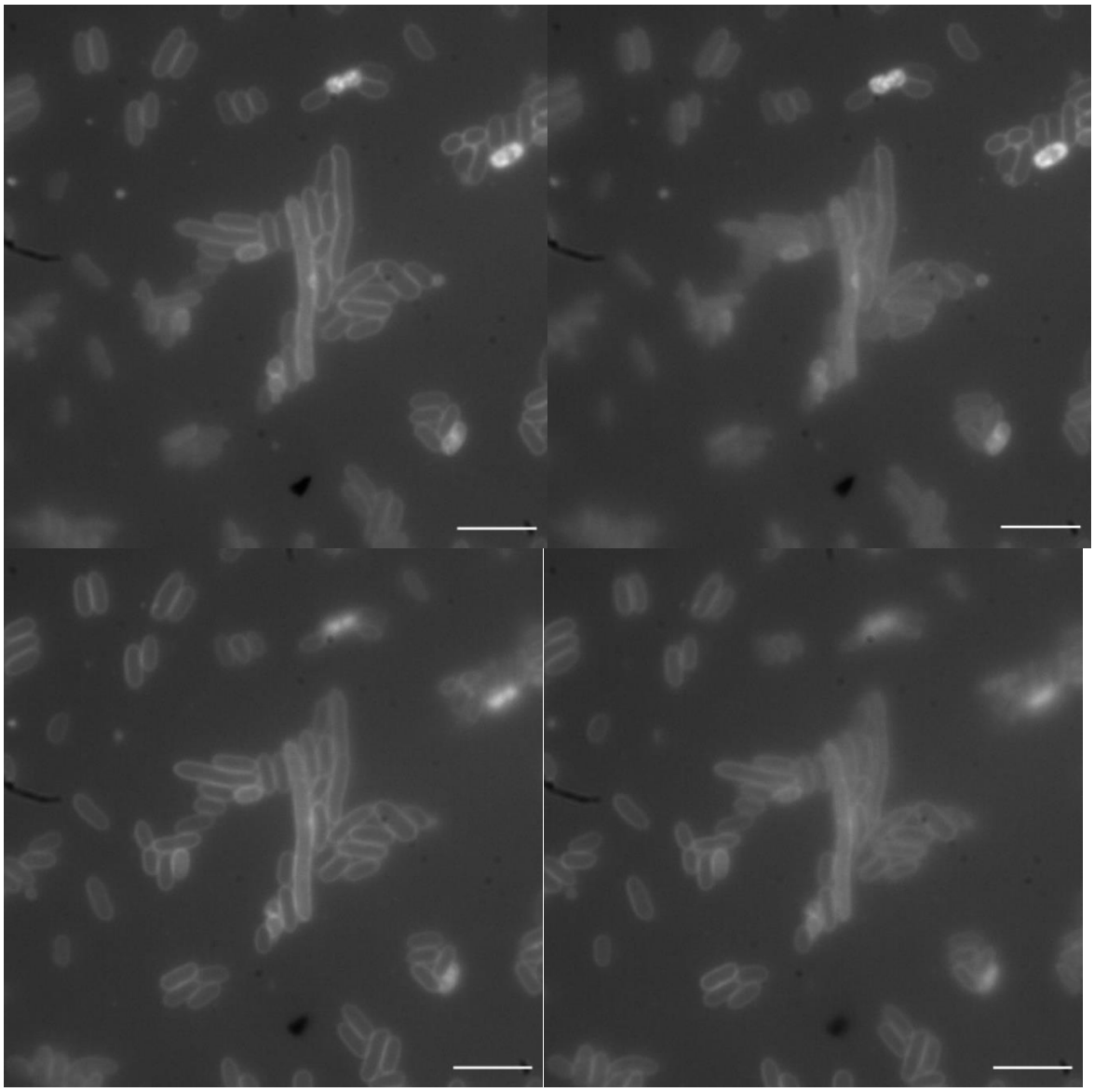

Figure S191 – Different z-slices used in combination with figure above to obtain more accurate fluorescence calculations. Fluorescence images at 450 nm of *E. coli* in the presence of SSA **70** at T = 4 hours. Scale bar = 10µM.

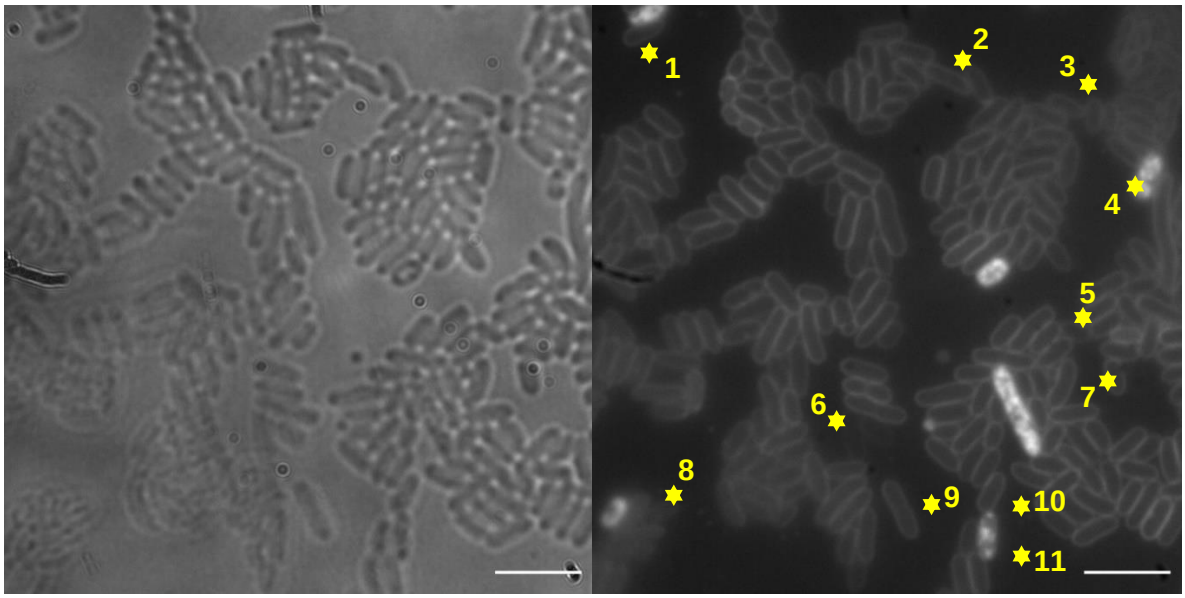

Figure S192 – *E. coli* transmitted image and fluorescence image at 450 nm used in fluorescence intensity calculations in the presence of SSA **70** at T = 4 hours. Scale bar = 10µM.

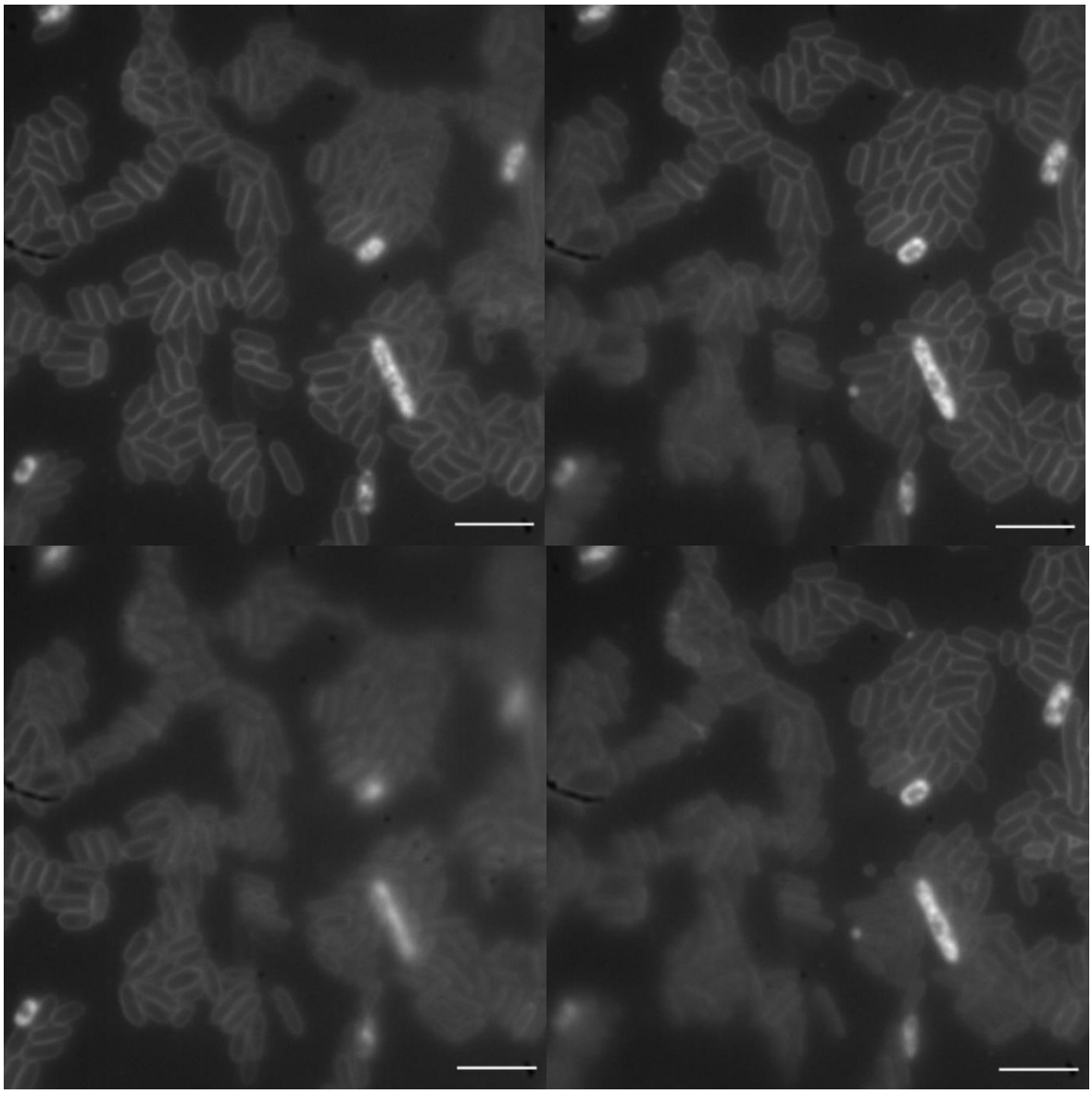

Figure S193 – Different z-slices used in combination to obtain more accurate fluorescence calculations. Fluorescence image at 450 nm of *E. coli* in the presence of SSA **70** at T = 4 hours. Scale bar = 10µM.

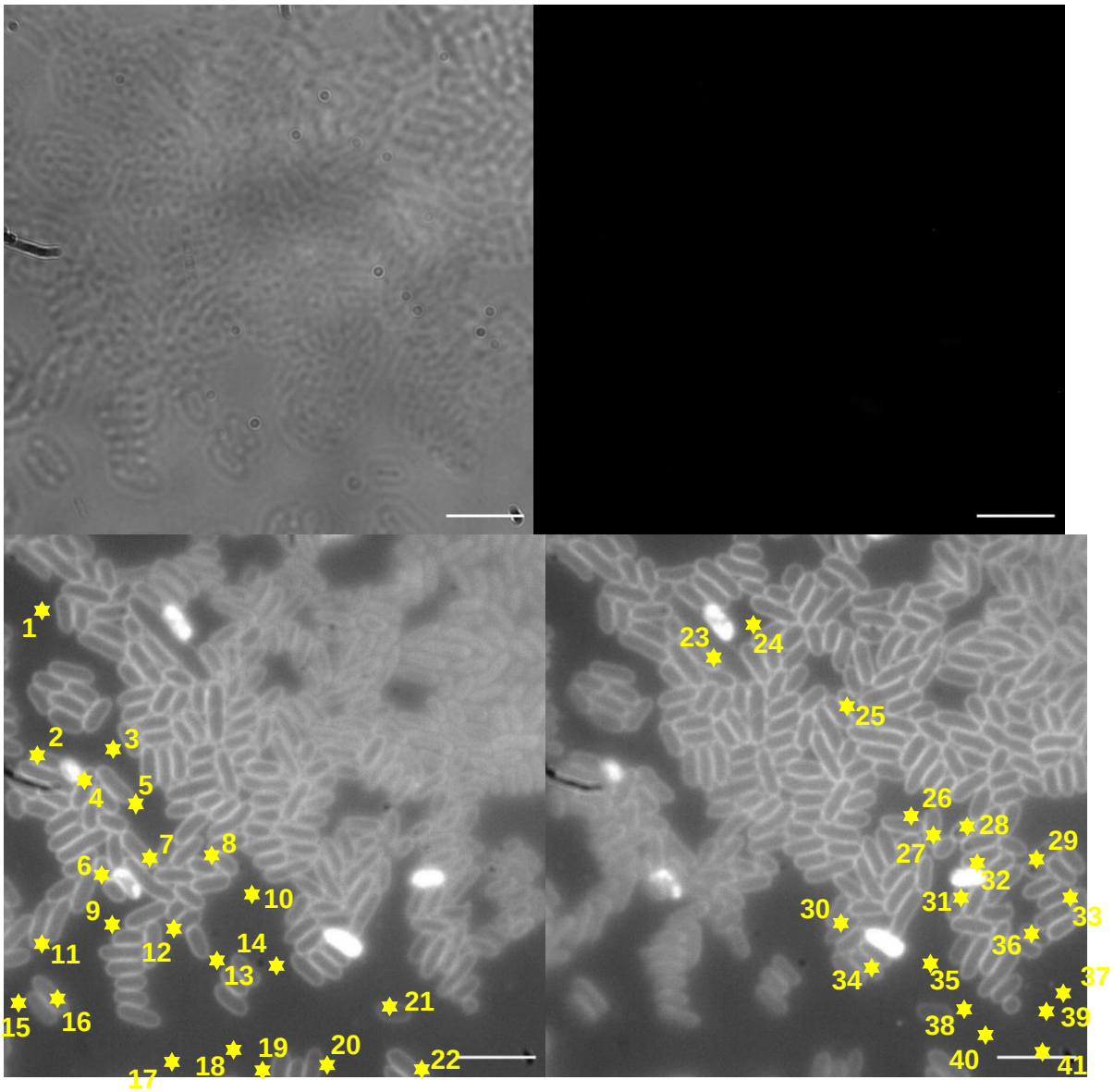

Figure S194 – (Above) *E. coli* transmitted image and fluorescence image at 605 nm used in fluorescence intensity calculations in the presence of SSA **70** at T = 4 hours. (Below) fluorescent images at 450 used in combination with transmitted images to locate cells on fluorescence image at 605 nm. Scale bar = 10μM.

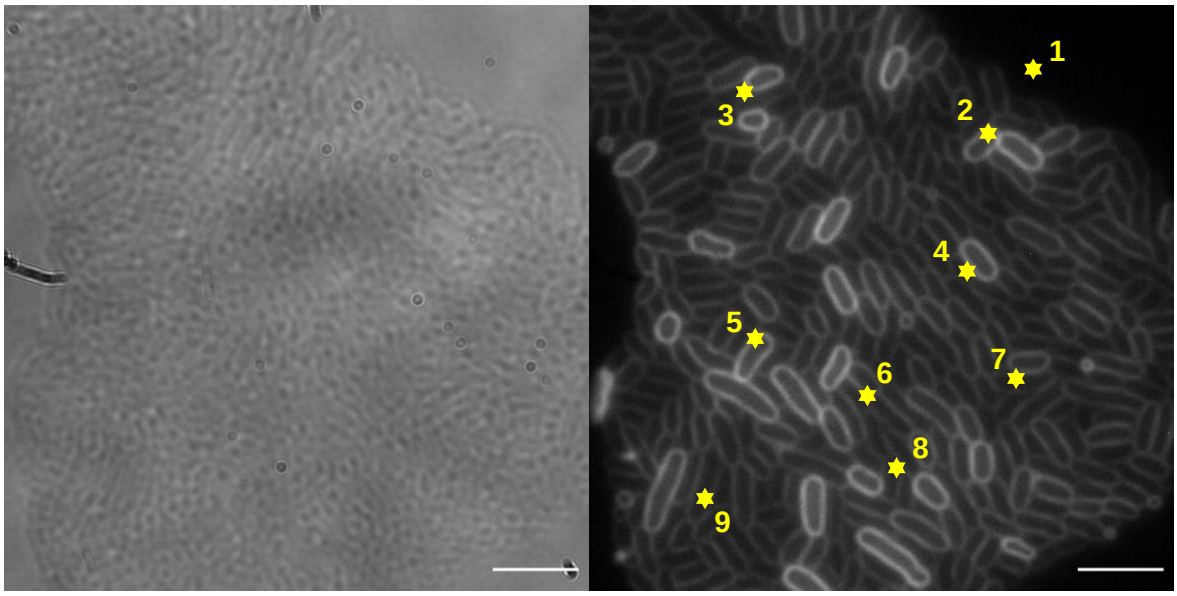

Figure S195 – *E. coli* transmitted image and fluorescence image at 605 nm used in fluorescence intensity calculations in the presence of FM4-64 at T = 4 hours. Scale bar = 10µM.

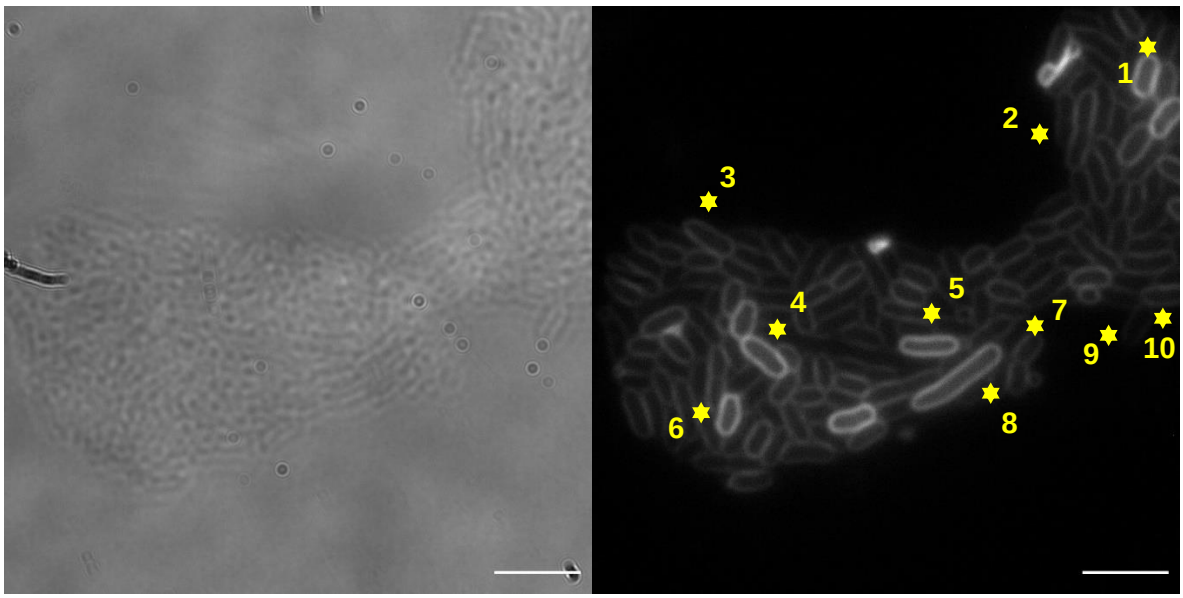

Figure S196 – *E. coli* transmitted image and fluorescence image at 605 nm used in fluorescence intensity calculations in the presence of FM4-64 at T = 4 hours. Scale bar = 10µM.

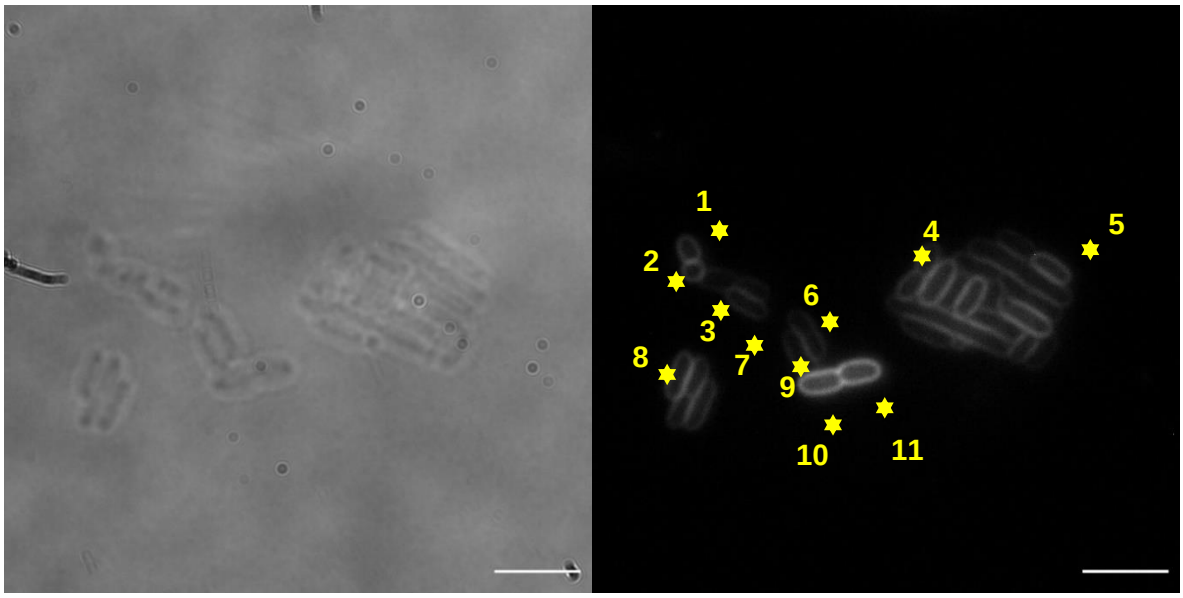

Figure S197 – *E. coli* transmitted image and fluorescence image at 605 nm used in fluorescence intensity calculations in the presence of FM4-64 at T = 4 hours. Scale bar = 10µM.

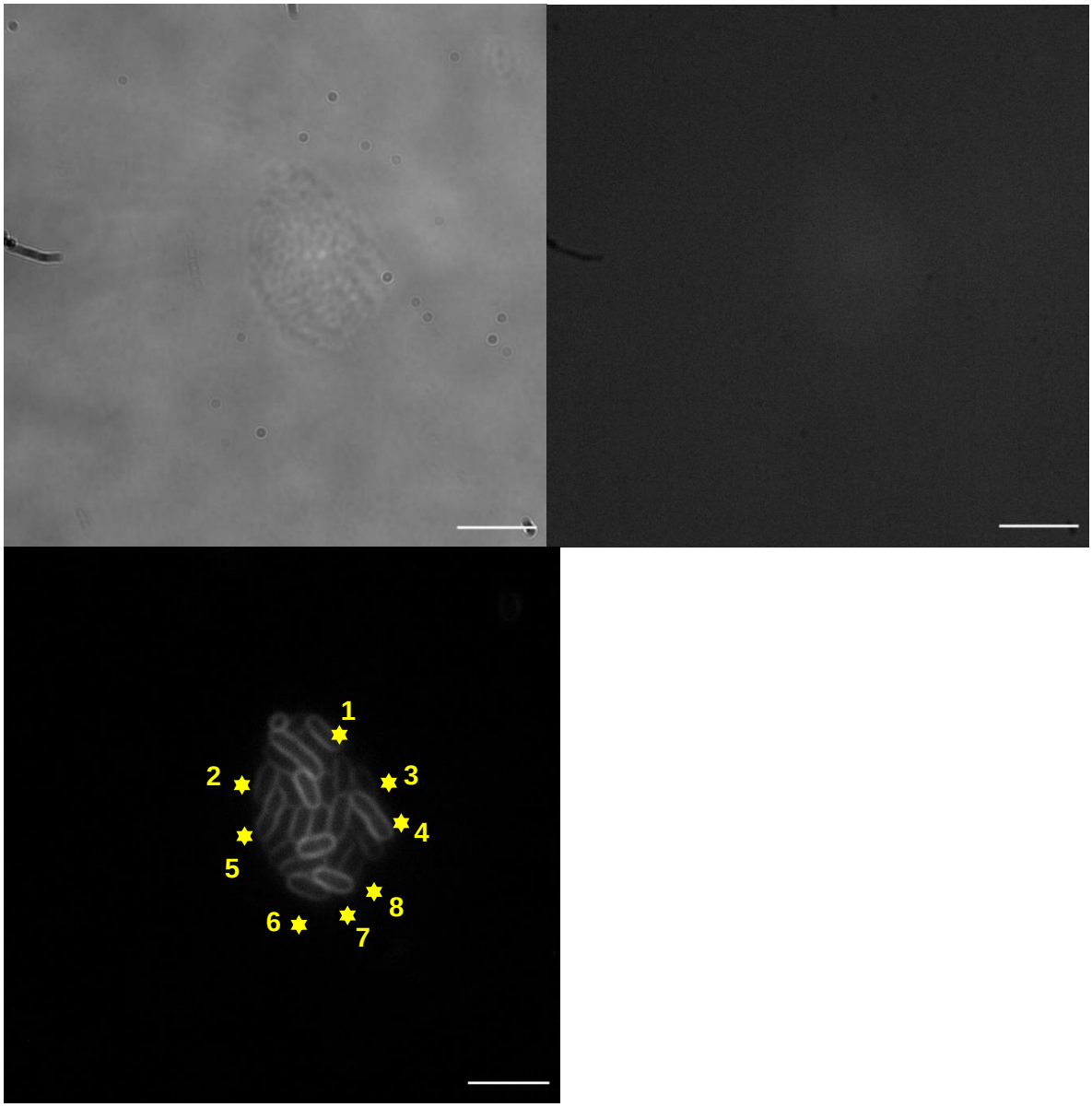

Figure S198 – (Above) *E. coli* transmitted image and fluorescence image at 450 nm used in fluorescence intensity calculations in the presence of FM4-64 at T = 4 hours. (Below) Fluorescence image at 605 nm used to locate cells on fluorescence image at 450 nm. Scale bar = 10µM.

.

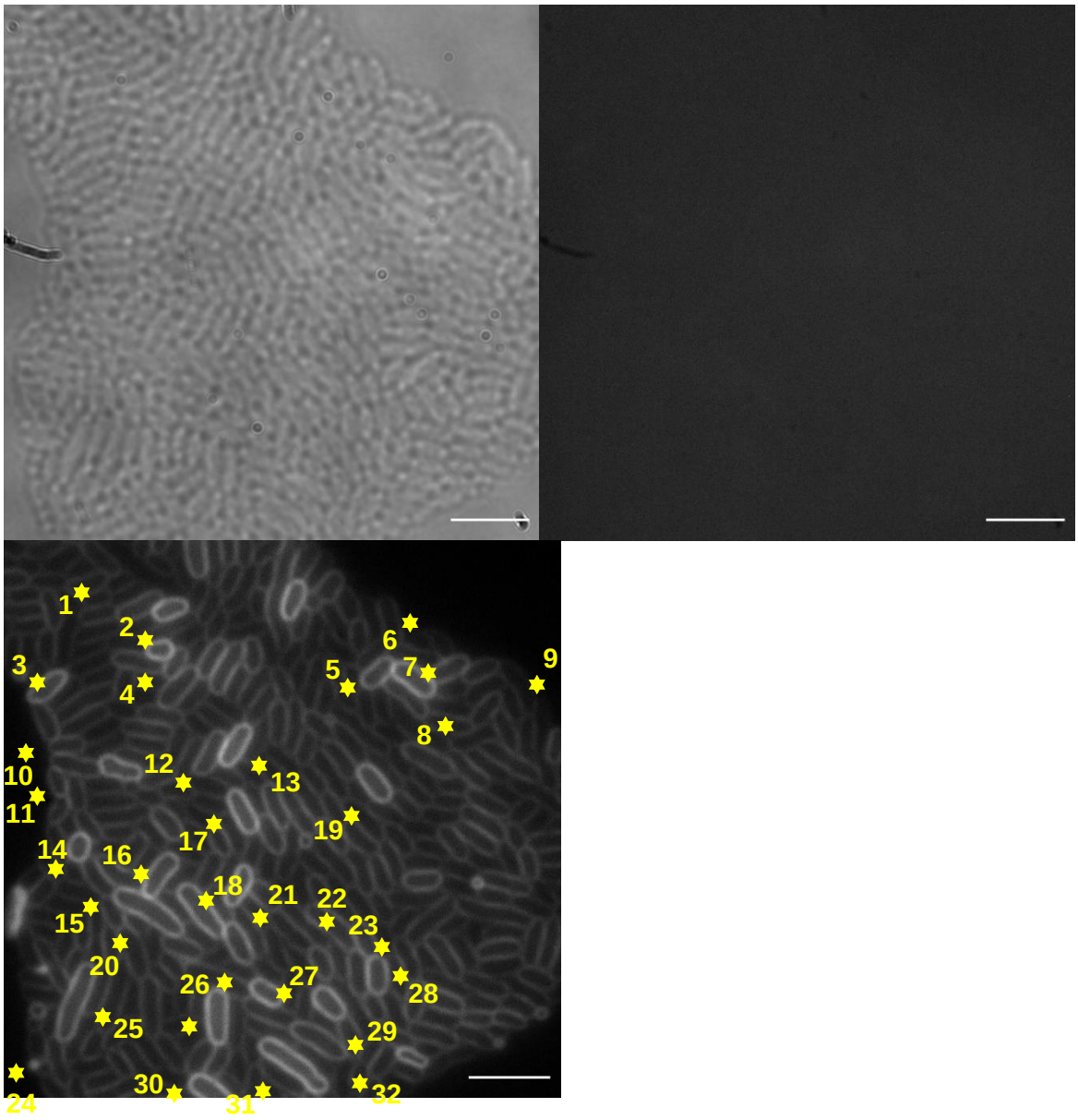

Figure S199 – (Above) *E. coli* transmitted image and fluorescence image at 450 nm used in fluorescence intensity calculations in the presence of FM4-64 at T = 4 hours. (Below) Fluorescence image at 605 nm used to locate cells on fluorescence image at 450 nm. Scale bar = 10µM.

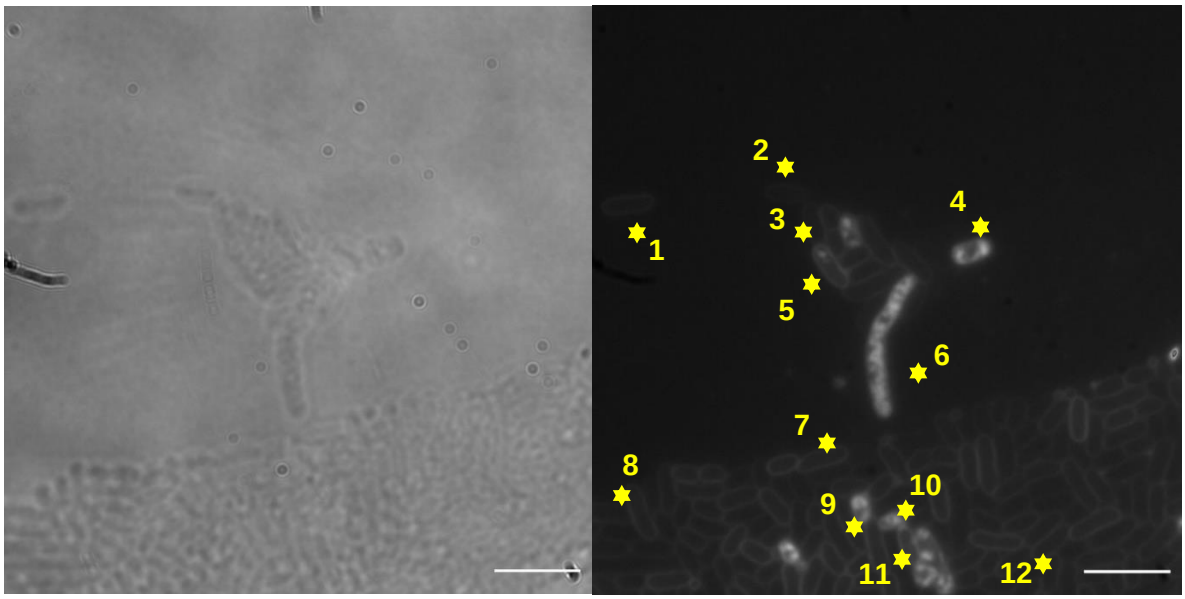

Figure S200 – *E. coli* transmitted image and fluorescence image at 450 nm used in fluorescence intensity calculations in the presence of both SSA **70** and FM4-64 at T = 4 hours. Scale bar = 10µM.

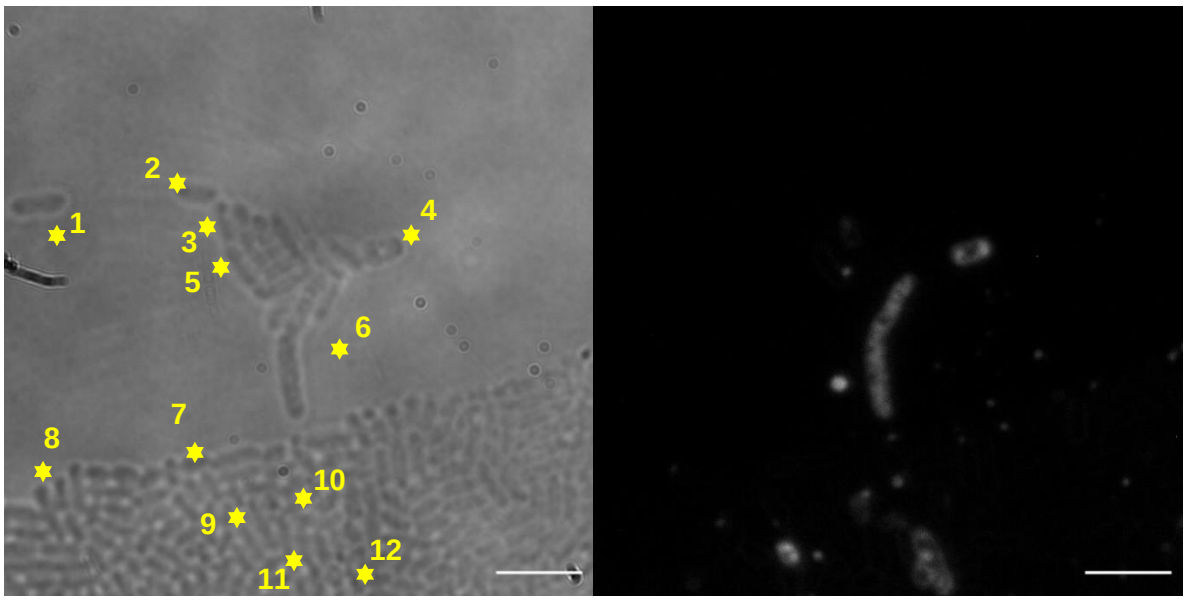

Figure S201 – *E. coli* transmitted image and fluorescence image at 605 nm used in fluorescence intensity calculations in the presence of both SSA **70** and FM4-64 at T = 4 hours. Fluorescence image at 450nm (Figure S658) and transmitted image used in combination with the fluorescence image at 605 nm to locate cells on fluorescence image at 605 nm. Scale bar = 10µM.

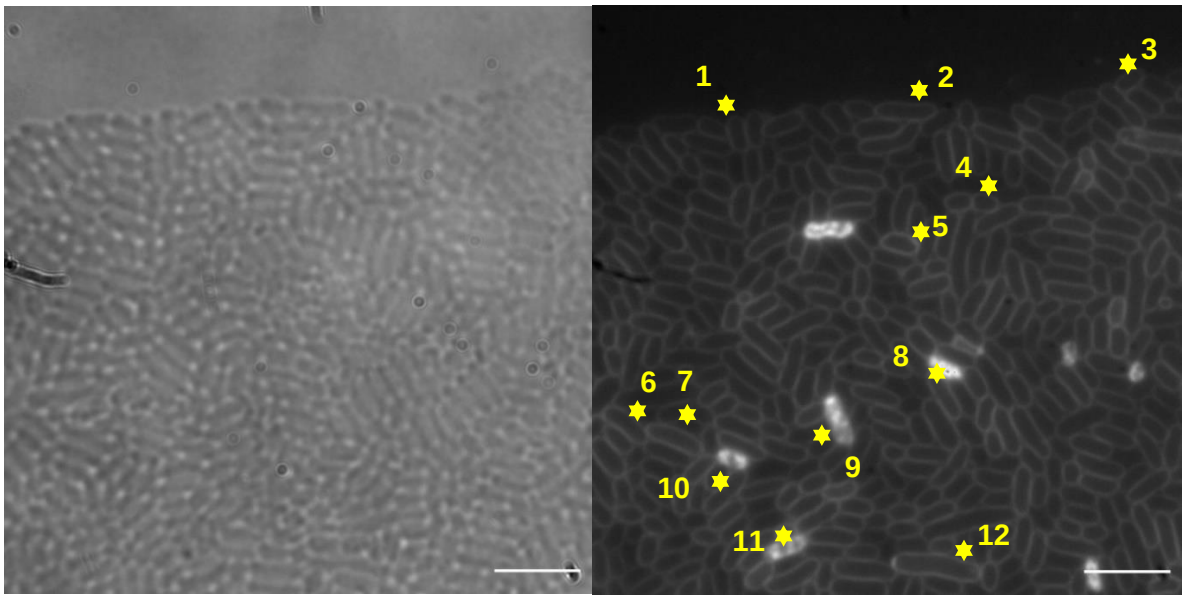

Figure S202 – *E. coli* transmitted image and fluorescence image at 450 nm used in fluorescence intensity calculations in the presence of both SSA **70** and FM4-64 at T = 4 hours. Scale bar = 10µM.

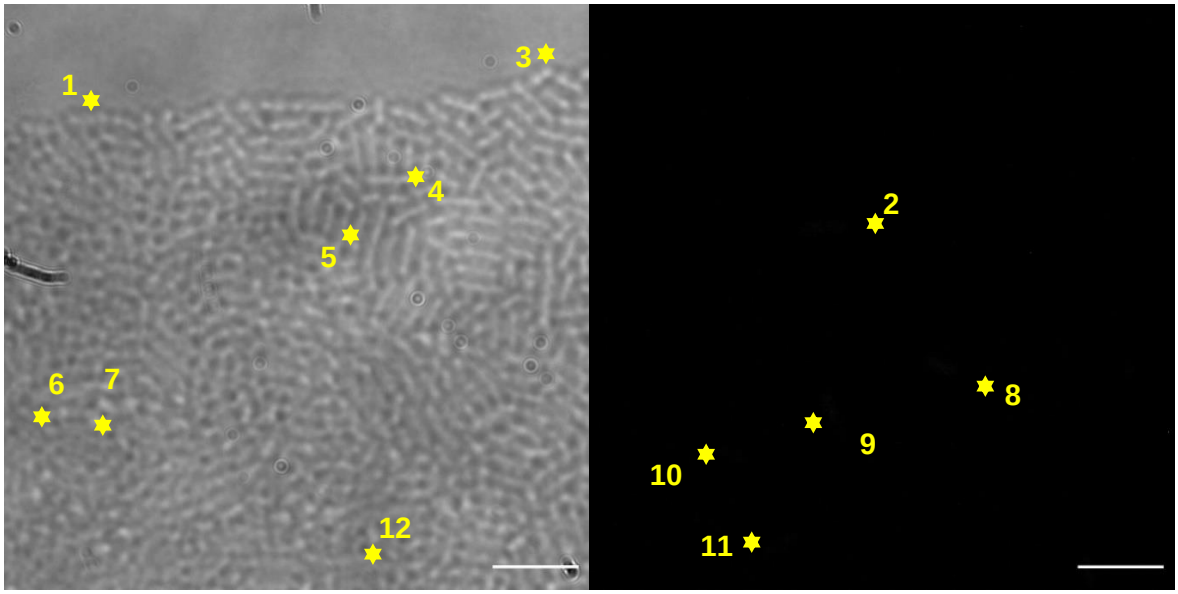

Figure S203 – *E. coli* transmitted image and fluorescence image at 605 nm used in fluorescence intensity calculations in the presence of both SSA **70** and FM4-64 at T = 4 hours. Fluorescence image at 450 nm (Figure S684) and transmitted images used to locate cells on fluorescence image at 605 nm. Scale bar = 10µM.

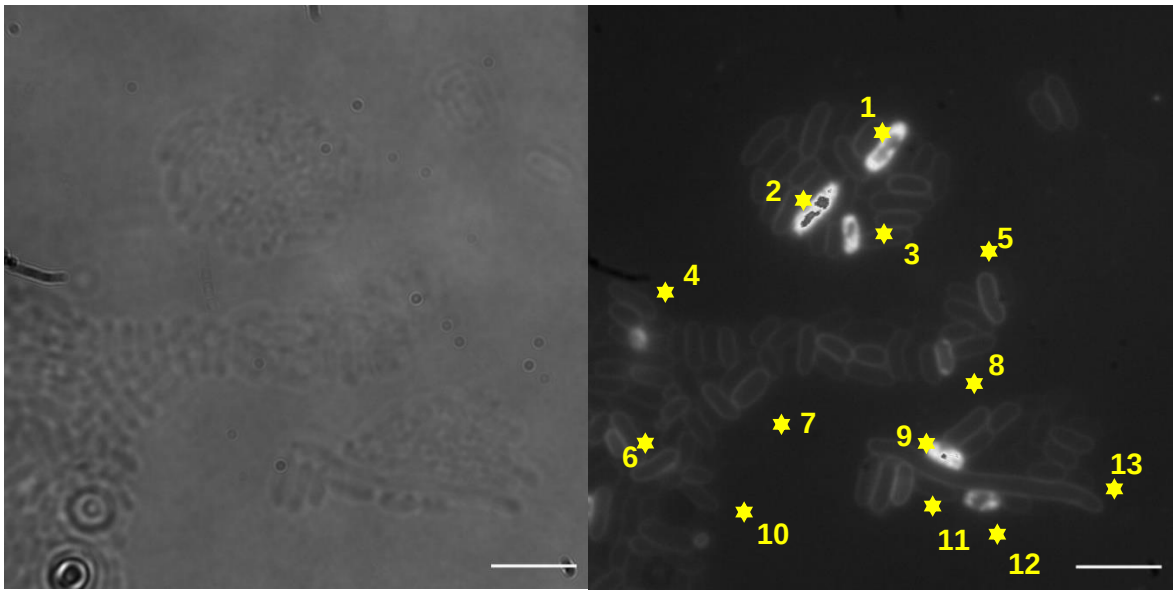

Figure S204 – *E. coli* transmitted image and fluorescence image at 450 nm used in fluorescence intensity calculations in the presence of both SSA **70** and FM4-64 at T = 4 hours. Scale bar = 10µM.

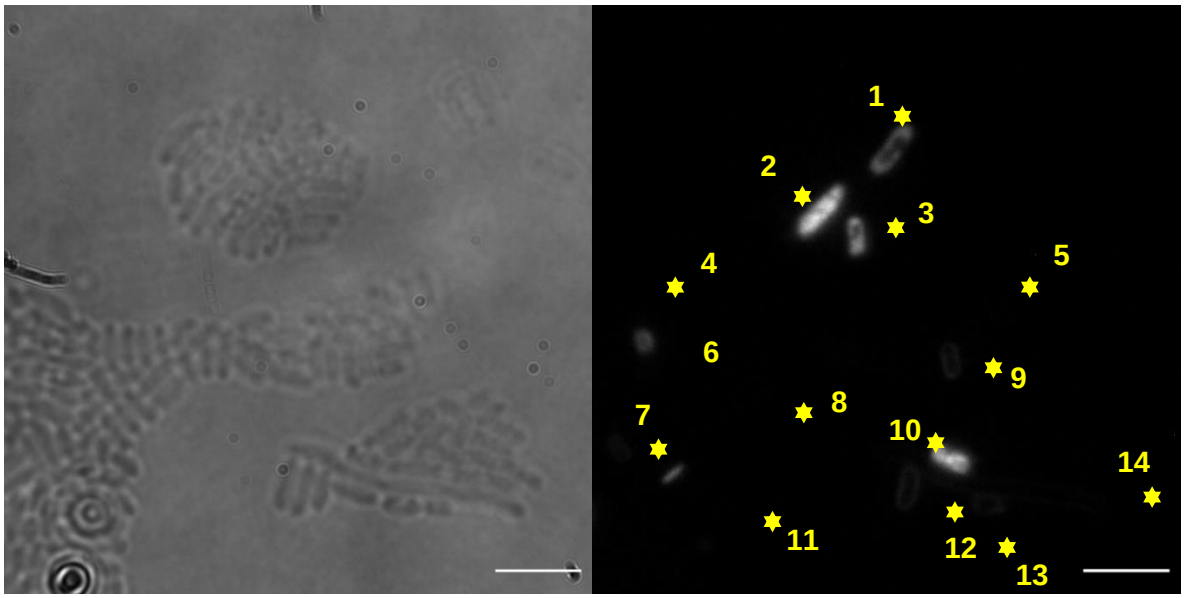

Figure S205 – *E. coli* transmitted image and fluorescence image at 605 nm used in fluorescence intensity calculations in the presence of both SSA **70** and FM4-64 at T = 4 hours. Figure S710 and transmitted images used in combination with fluorescence image at 605 nm for accurate fluorescence intensity calculations. Scale bar = 10µM.

MRSA at 30 minutes

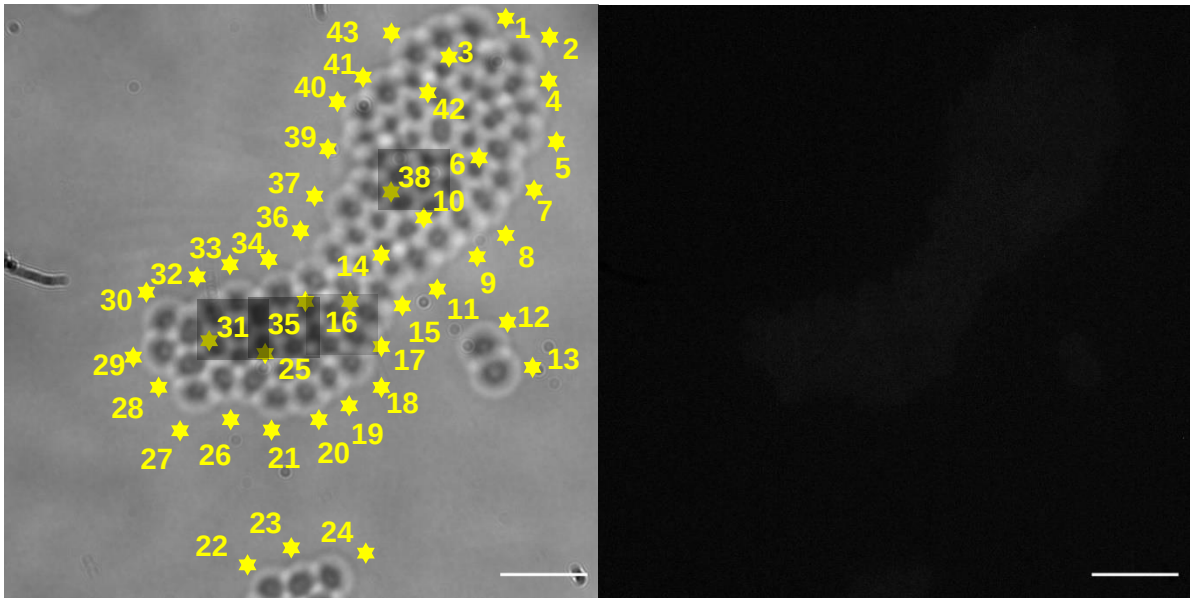

Figure S206 – MRSA transmitted image and fluorescence image at 450nm used in fluorescence intensity calculations in the absence of both SSA **70** and FM4-64 at T = 30 minutes. Transmitted image used to locate cells on fluorescence image. Scale bar = 10µM

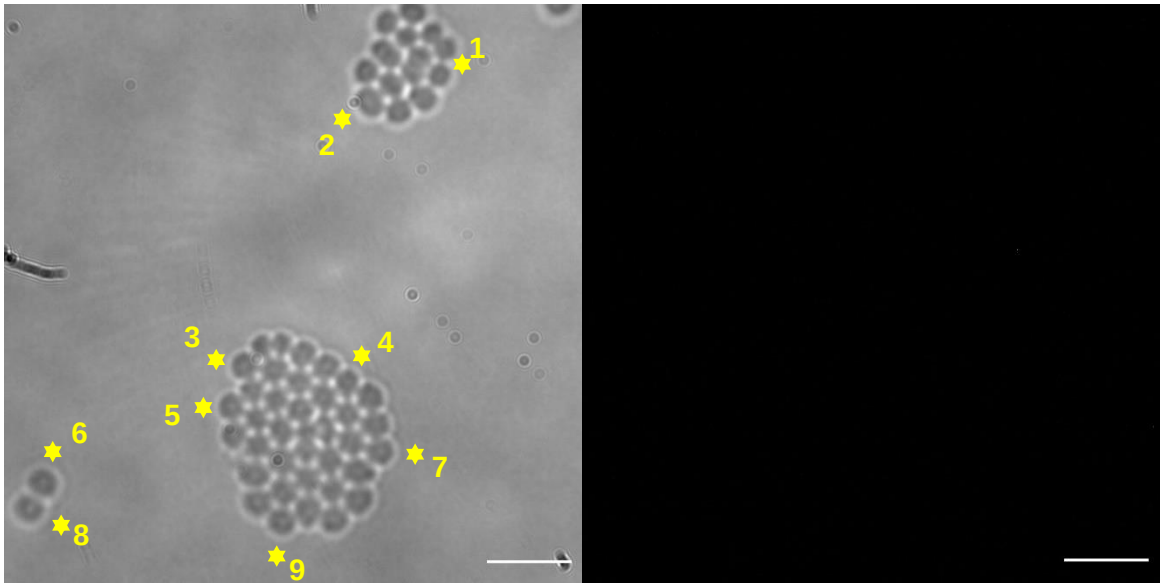

Figure S207 – MRSA transmitted image and fluorescence image at 605nm used in fluorescence intensity calculations in the absence of both SSA **70** and **FM4-64** at T = 30 minutes. Transmitted image used to locate cells on fluorescence image. Scale bar = 10µM

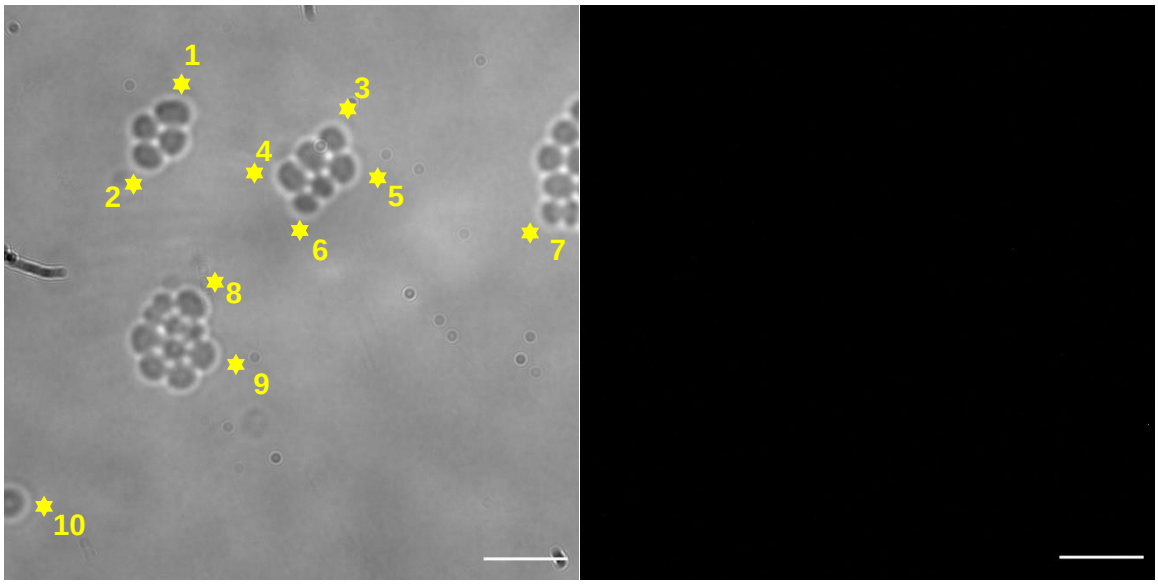

Figure S208 – MRSA transmitted image and fluorescence image at 605 nm used in fluorescence intensity calculations in the absence of both SSA **70** and **FM4-64** at T = 30 minutes. Transmitted image used to locate cells on fluorescence image. Scale bar = 10μM

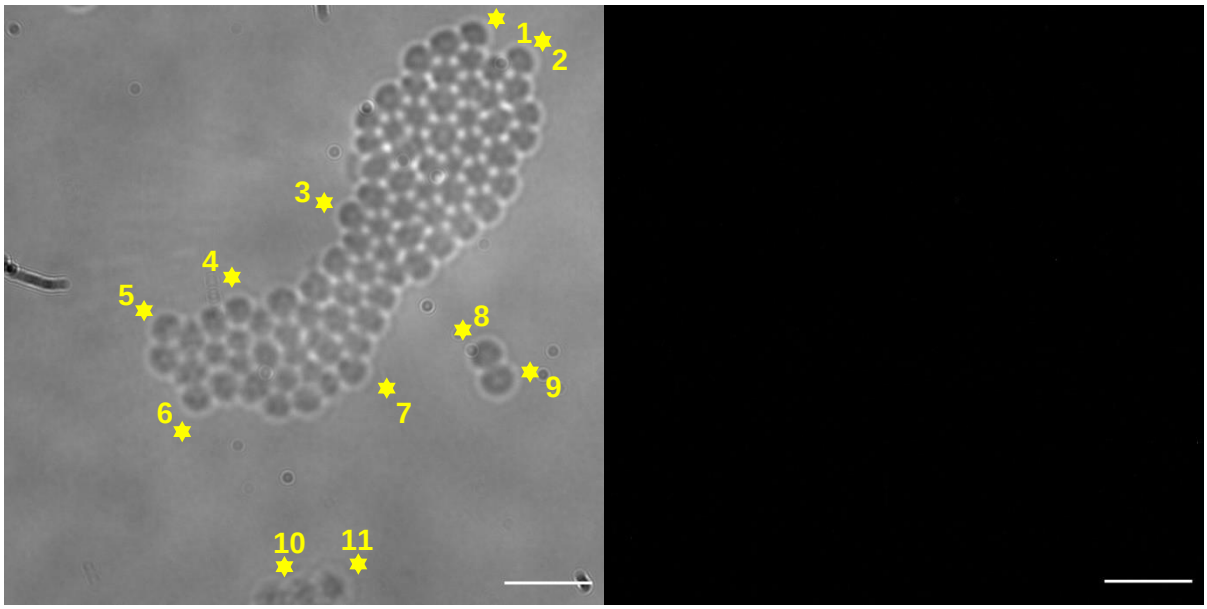

Figure S209 – MRSA transmitted image and fluorescence image at 605 nm used in fluorescence intensity calculations in the absence of both SSA **70** and **FM4-64** at T = 30 minutes. Transmitted image used to locate cells on fluorescence image. Scale bar = 10μM

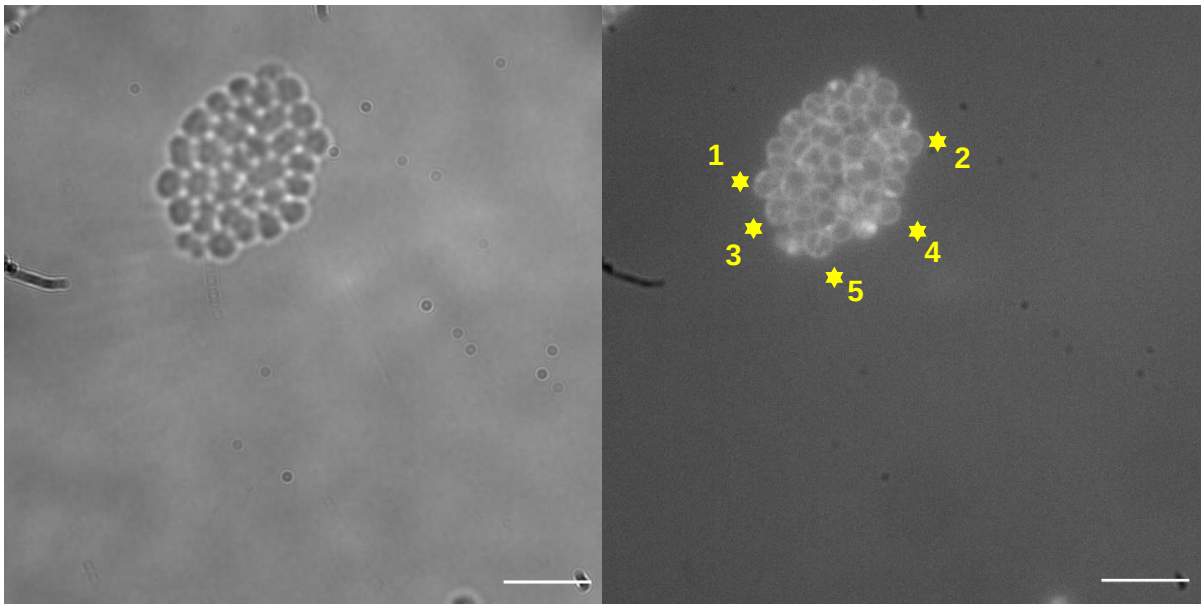

Figure S210 – MRSA transmitted image and fluorescence image at 450 nm used in fluorescence intensity calculations in the presence of SSA **70** only at T = 30 minutes. Scale bar = 10µM

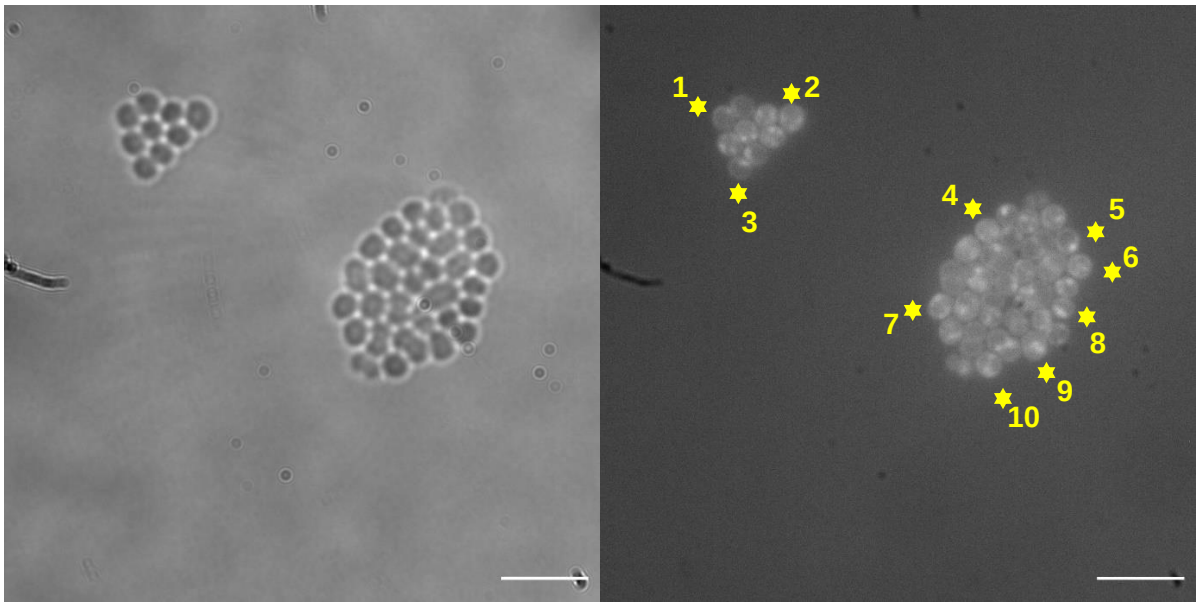

Figure S211 – MRSA transmitted image and fluorescence image at 450 nm used in fluorescence intensity calculations in the presence of SSA **70** only at T = 30 minutes. Scale bar = 10µM

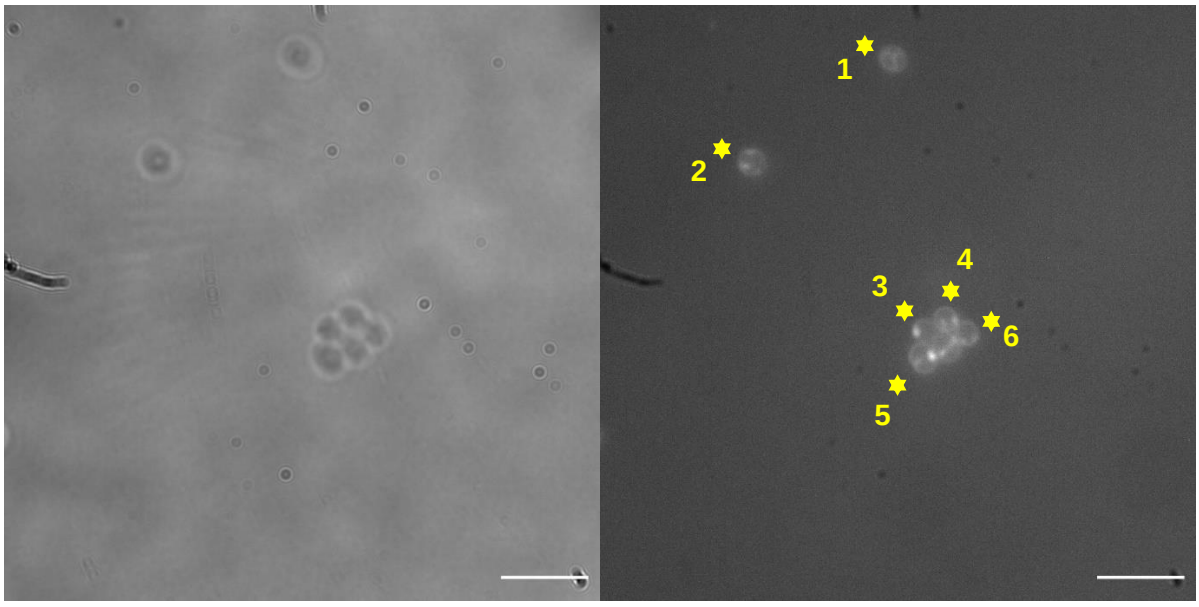

Figure S212 – MRSA transmitted image and fluorescence image at 450 nm used in fluorescence intensity calculations in the presence of SSA **70** only at T = 30 minutes. Scale bar = 10µM

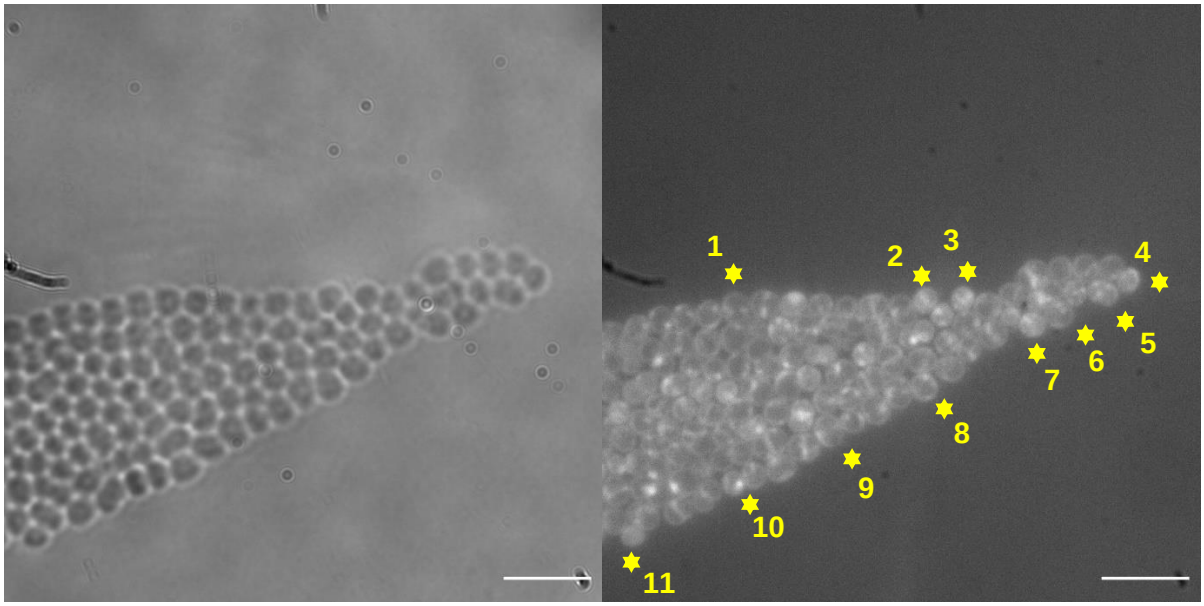

Figure S213 – MRSA transmitted image and fluorescence image at 450 nm used in fluorescence intensity calculations in the presence of SSA **70** only at T = 30 minutes. Scale bar = 10µM

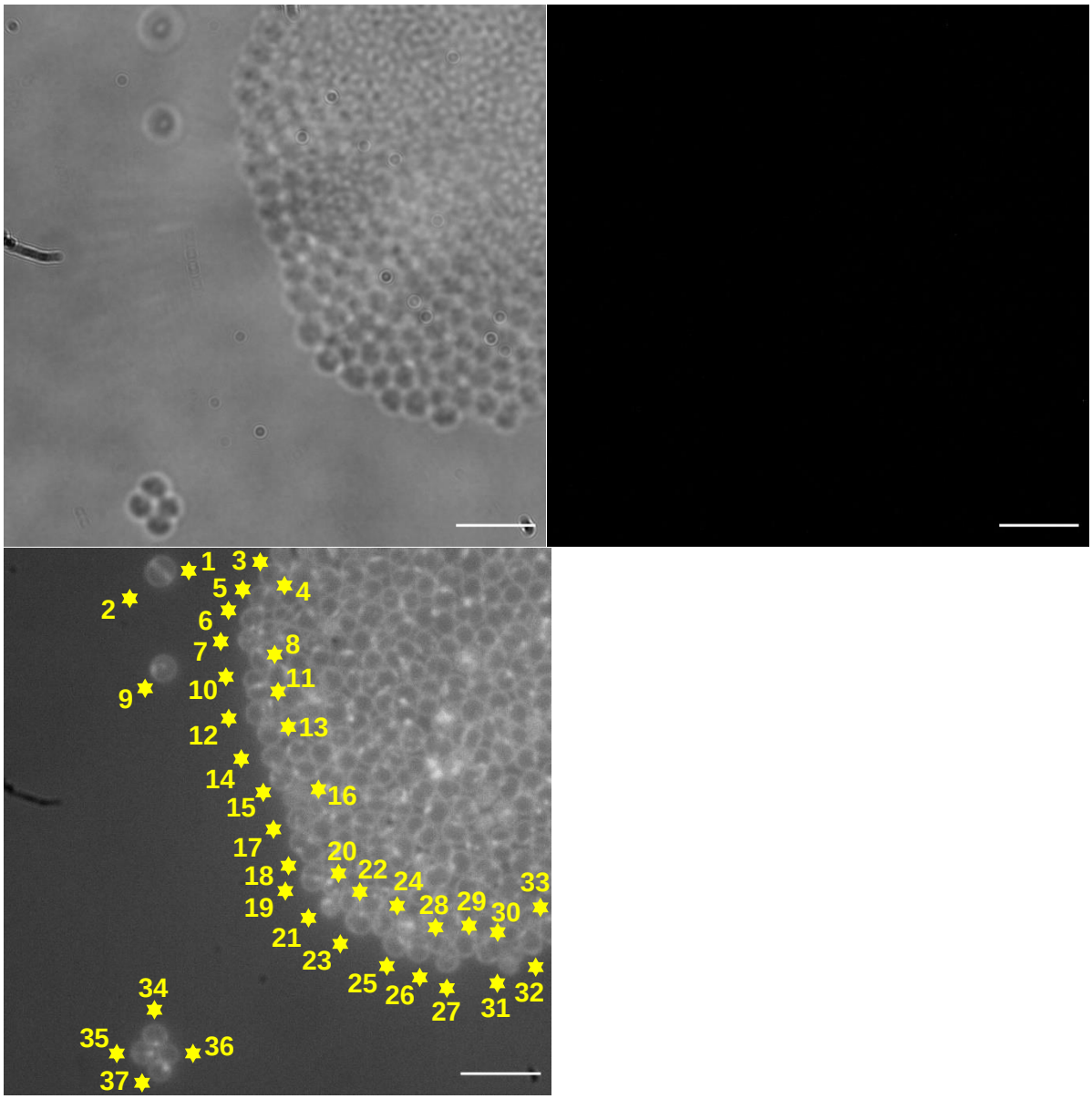

Figure S214 – MRSA transmitted image and fluorescence image at 605 nm used in fluorescence intensity calculations in the presence of SSA **70** only at T = 30 minutes. Fluorescence image at 450 nm used to locate cells on fluorescence image at 605 nm. Scale bar = 10μM

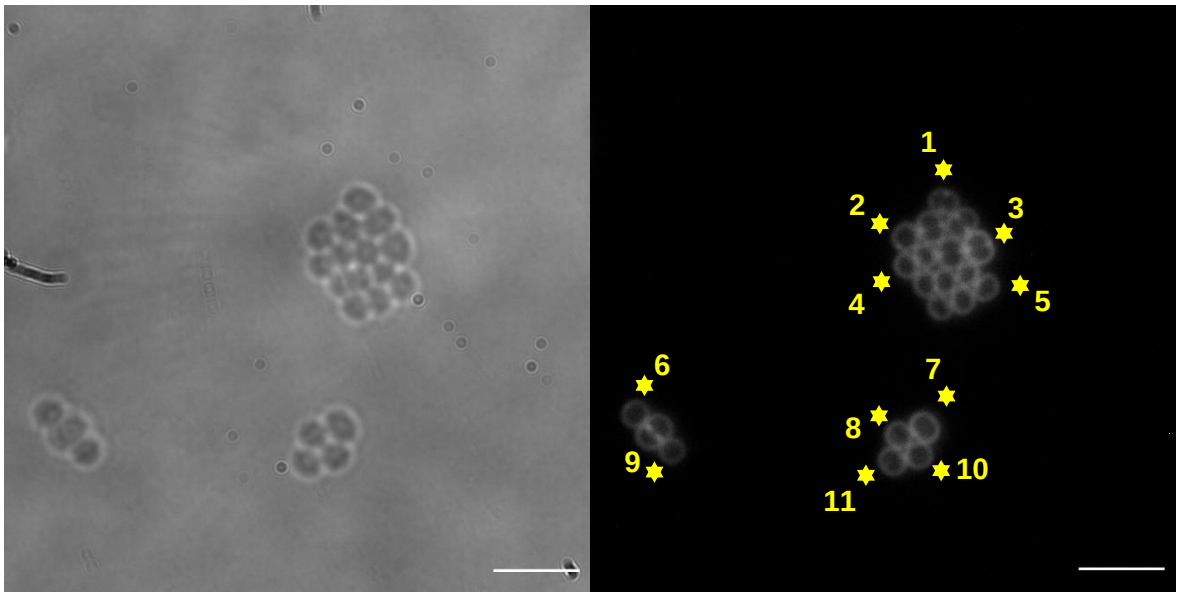

Figure S215 – MRSA transmitted image and fluorescence image at 605 nm used in fluorescence intensity calculations in the presence of **FM4-64** only at T = 30 minutes. Scale bar = 10µM

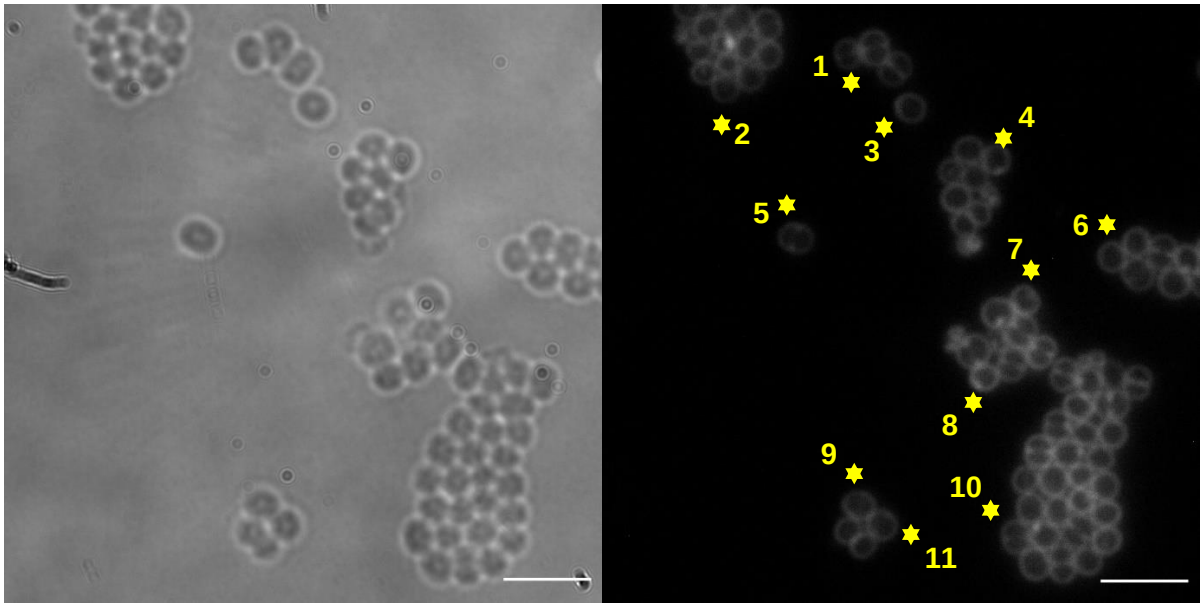

Figure S216 – MRSA transmitted image and fluorescence image at 605 nm used in fluorescence intensity calculations in the presence of **FM4-64** only at T = 30 minutes. Scale bar = 10µM

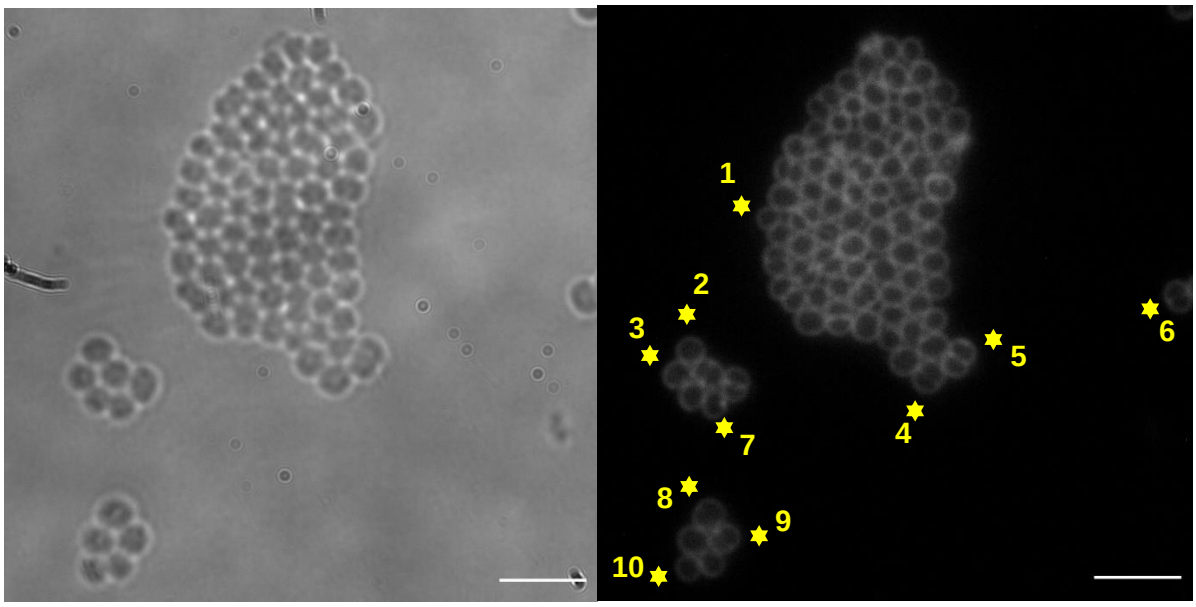

Figure S217 – MRSA transmitted image and fluorescence image at 605 nm used in fluorescence intensity calculations in the presence of **FM4-64** only at T = 30 minutes. Scale bar = 10µM

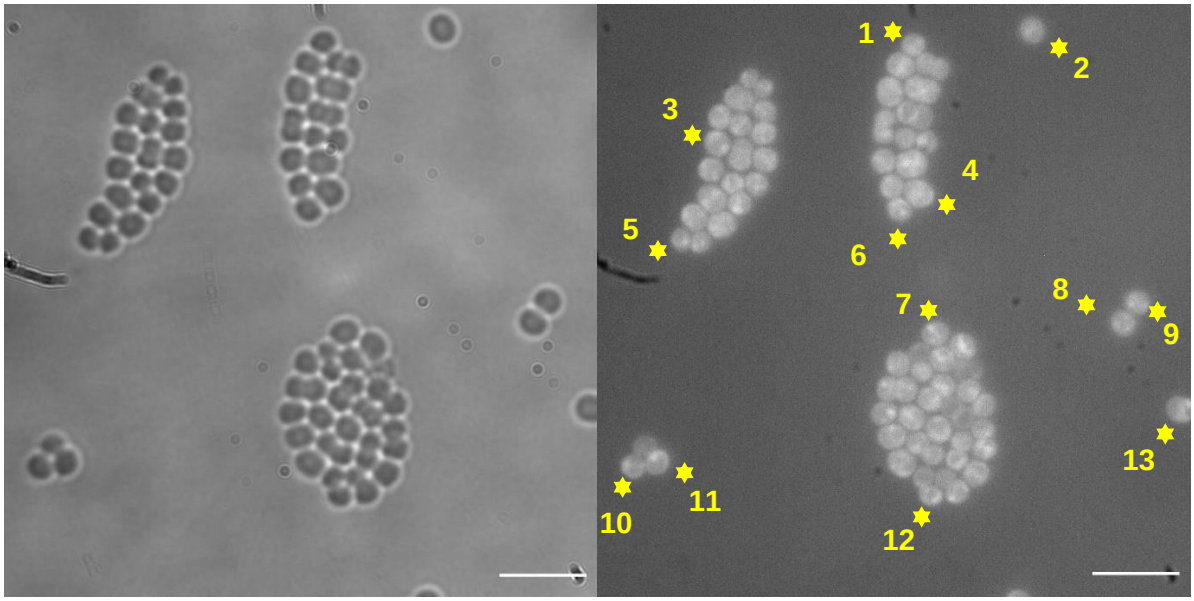

Figure S218 – MRSA transmitted image and fluorescence image at 450 nm used in fluorescence intensity calculations in the presence of both SSA **70** and **FM4-64** at T = 30 minutes. Scale bar = 10µM

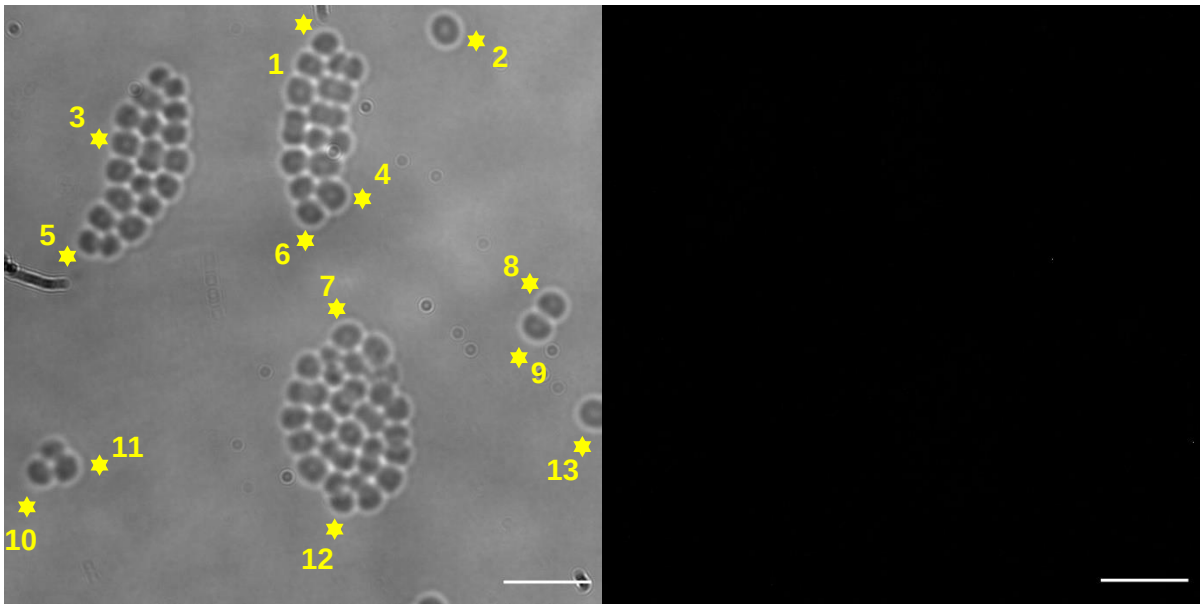

Figure S219 – MRSA transmitted image and fluorescence image at 605 nm used in fluorescence intensity calculations in the presence of both SSA **70** and **FM4-64** at T = 30 minutes. Transmitted image used to locate cells on fluorescence image. Scale bar = 10µM

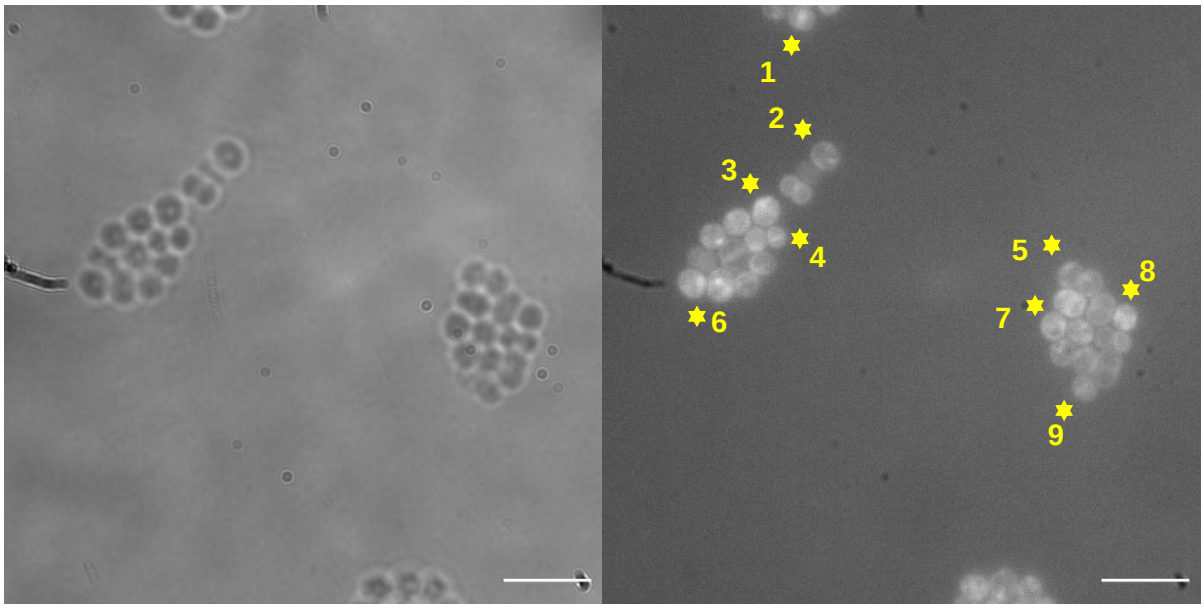

Figure S220 – MRSA transmitted image and fluorescence image at 450 nm used in fluorescence intensity calculations in the presence of both SSA **70** and **FM4-64** at T = 30 minutes. Scale bar = 10µM

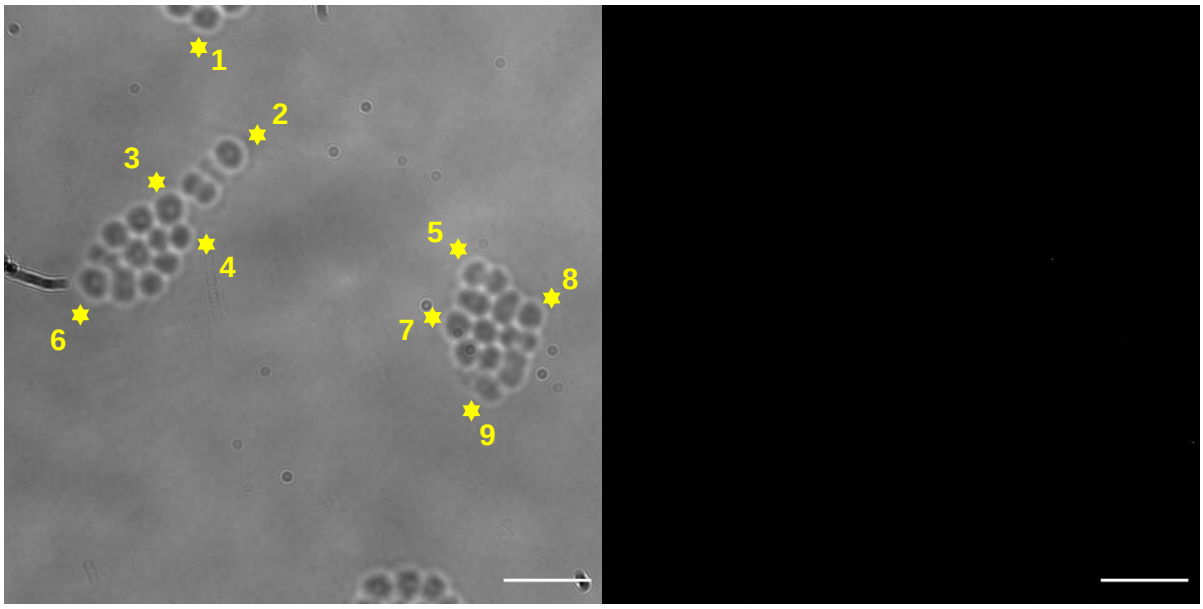

Figure S221 – MRSA transmitted image and fluorescence image at 605 nm used in fluorescence intensity calculations in the presence of both SSA **70** and **FM4-64** at T = 30 minutes. Transmitted image used to locate cells on fluorescence image. Scale bar = 10µM

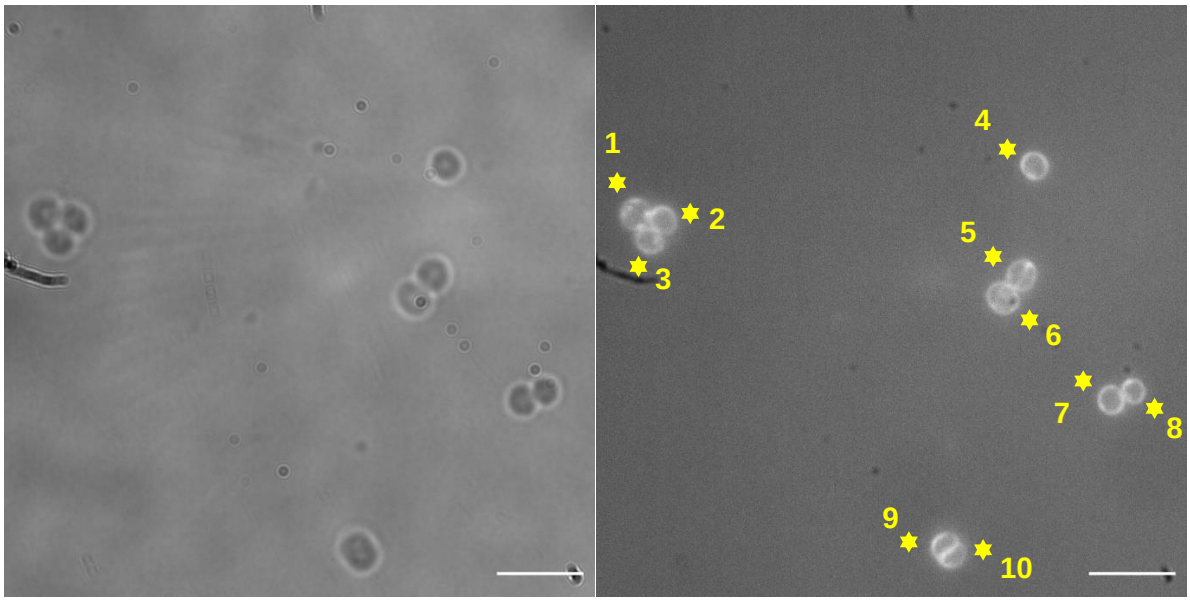

Figure S222 – MRSA transmitted image and fluorescence image at 450 nm used in fluorescence intensity calculations in the presence of both SSA **70** and **FM4-64** at T = 30 minutes. Scale bar = 10µM

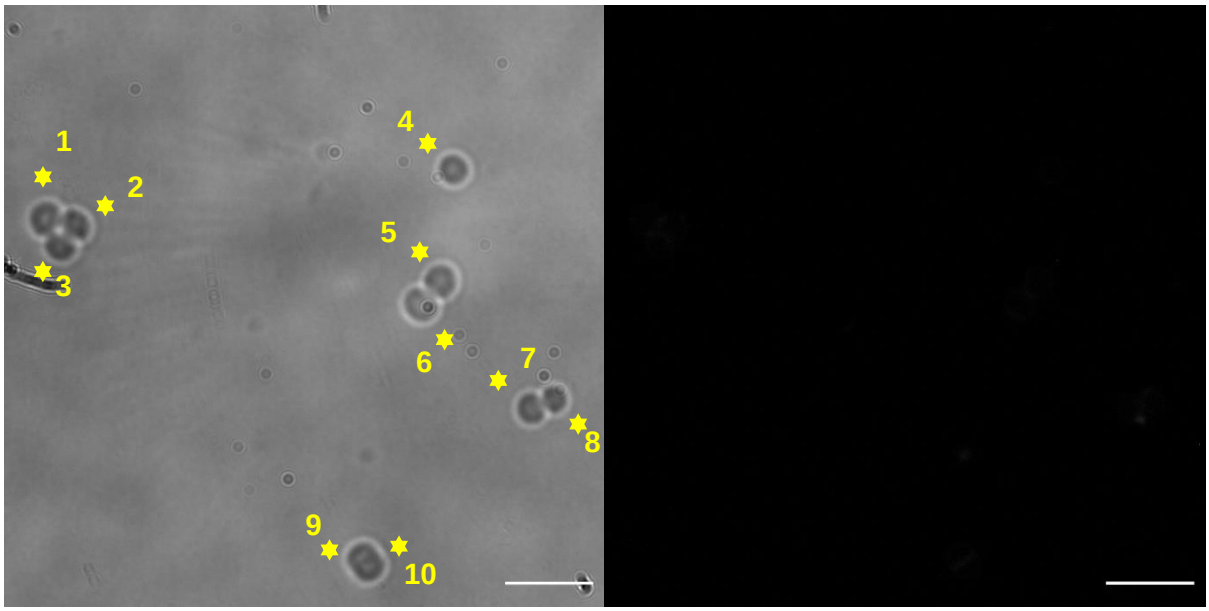

Figure S223 – MRSA transmitted image and fluorescence image at 605 nm used in fluorescence intensity calculations in the presence of both SSA **70** and **FM4-64** at T = 30 minutes. Transmitted image used to locate cells on fluorescence image. Scale bar = 10µM

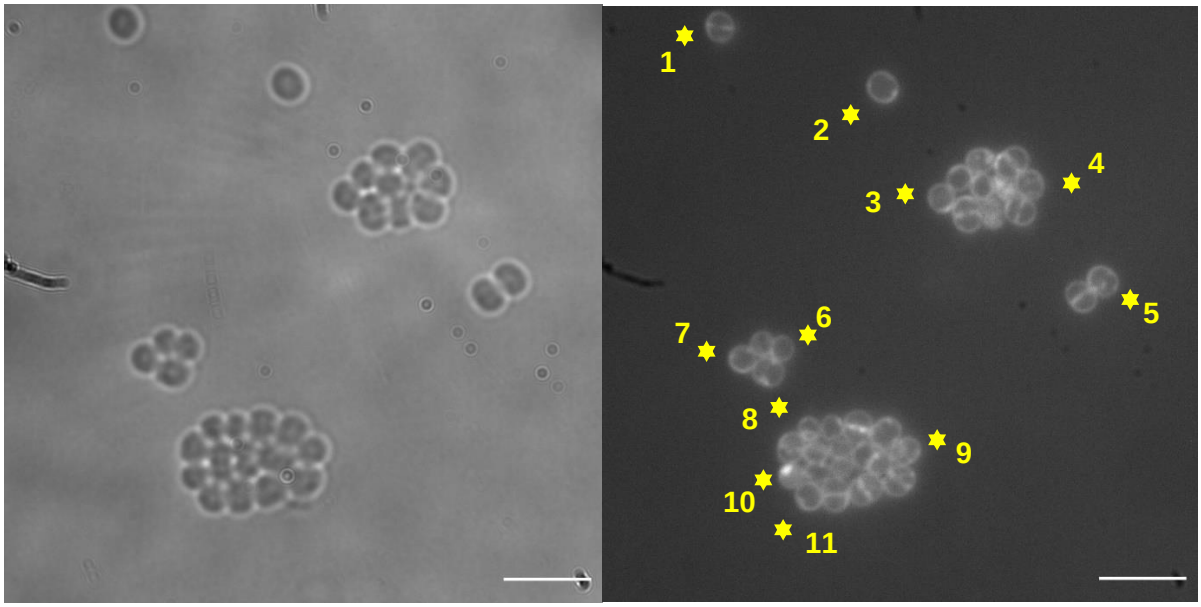

Figure S224 – MRSA transmitted image and fluorescence image at 450 nm used in fluorescence intensity calculations in the presence of both SSA **70** and **FM4-64** at T = 30 minutes. Scale bar = 10µM

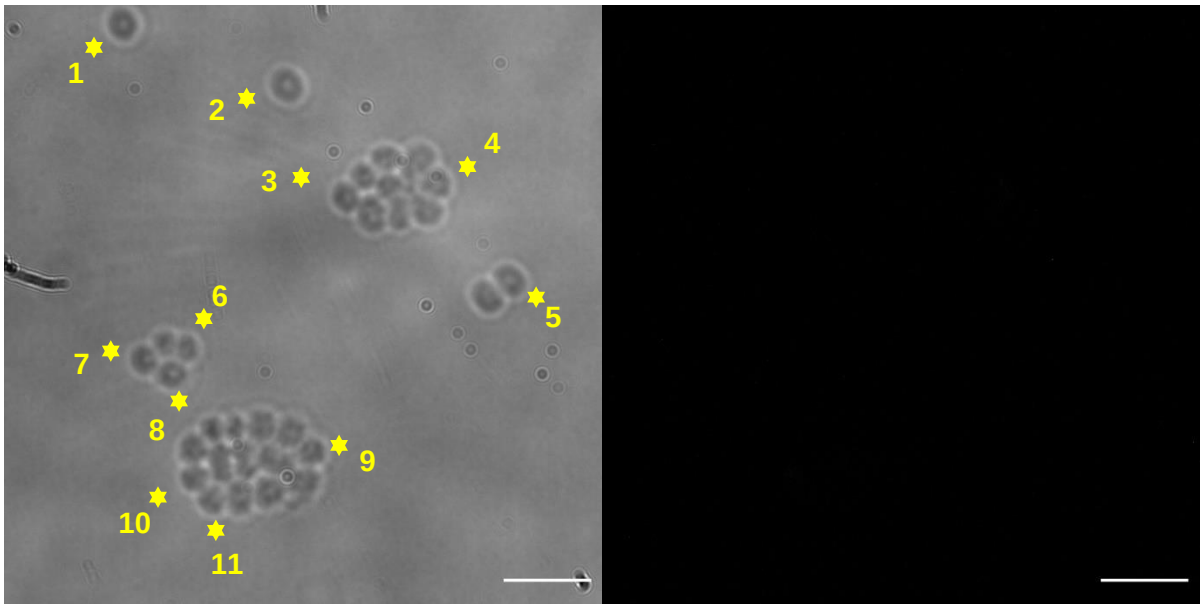

Figure S225 – MRSA transmitted image and fluorescence image at 605 nm used in fluorescence intensity calculations in the presence of both SSA **70** and **FM4-64** at T = 30 minutes. Transmitted image used to locate cells on fluorescence image. Scale bar = 10µM

MRSA at 4 hours

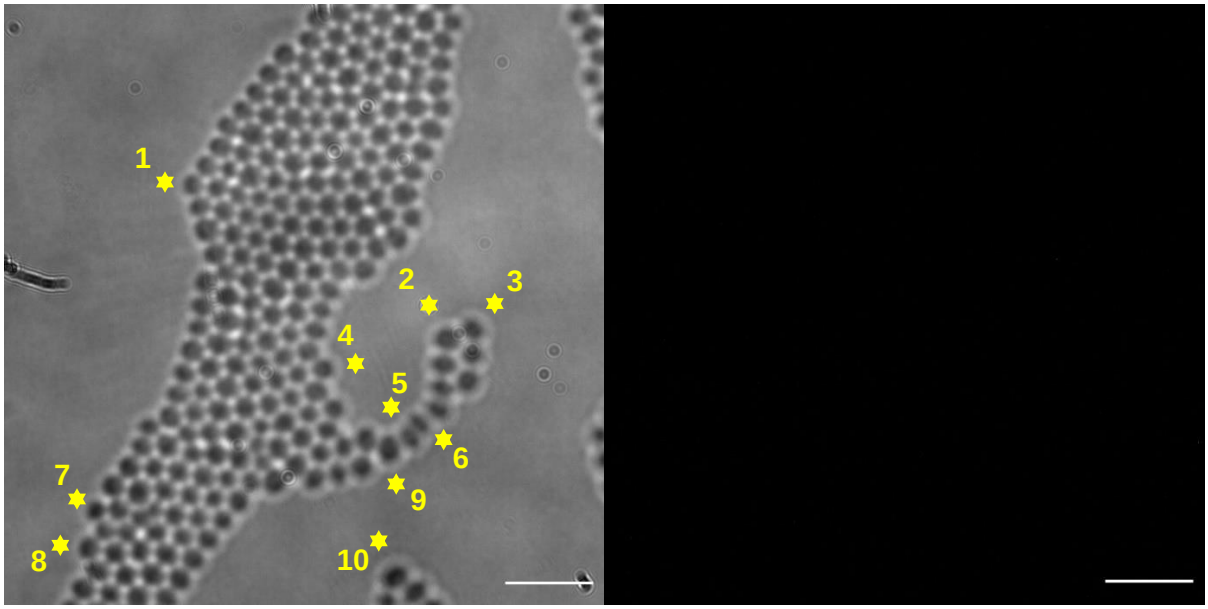

Figure S226 – MRSA transmitted image and fluorescence image at 605 nm used in fluorescence intensity calculations in the absence of both SSA **70** and **FM4-64** at T = 4 hours. Transmitted image used to locate cells on fluorescence image. Scale bar = 10µM

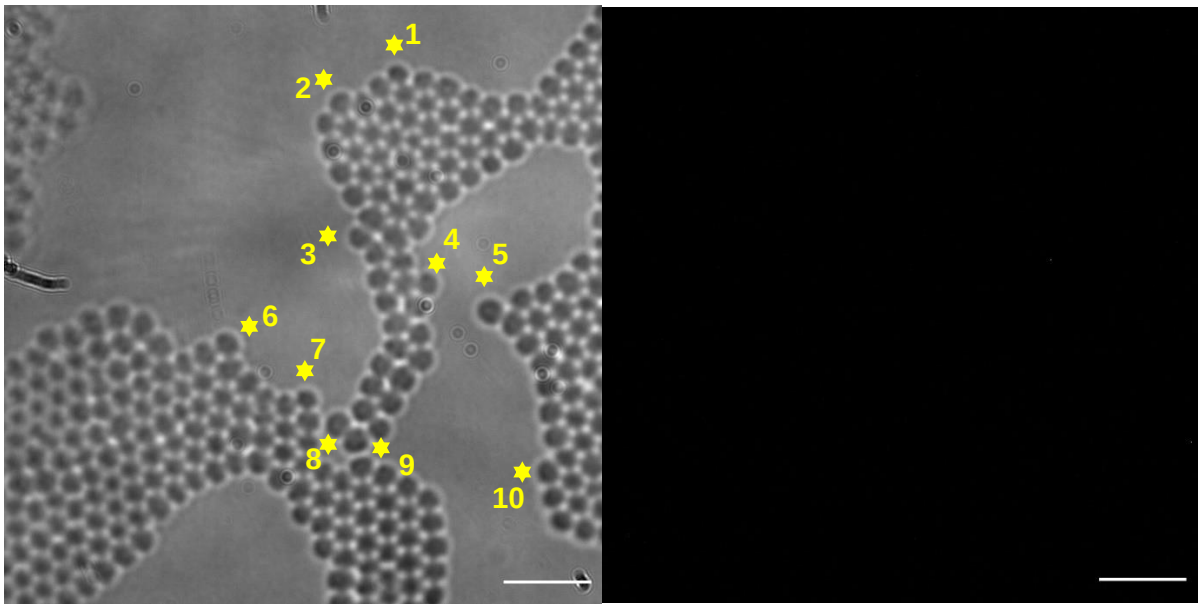

Figure S227 – MRSA transmitted image and fluorescence image at 605 nm used in fluorescence intensity calculations in the absence of both SSA **70** and **FM4-64** at T = 4 hours. Transmitted image used to locate cells on fluorescence image. Scale bar = 10µM

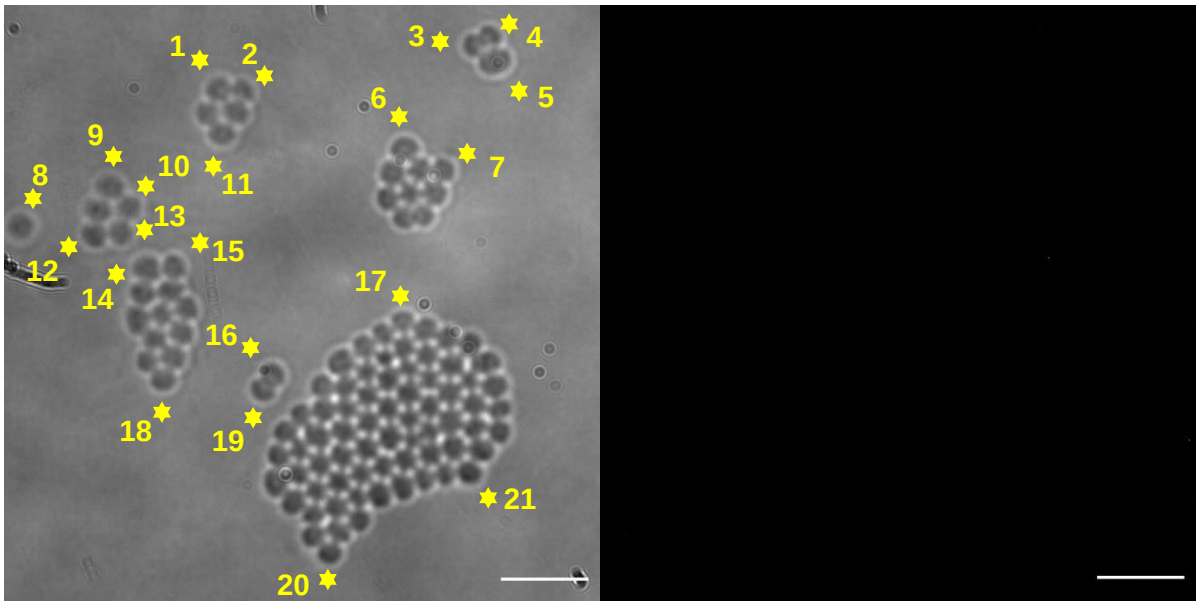

Figure S228 – MRSA transmitted image and fluorescence image at 605 nm used in fluorescence intensity calculations in the absence of both SSA **70** and **FM4-64** at T = 4 hours. Transmitted image used to locate cells on fluorescence image. Scale bar = 10µM

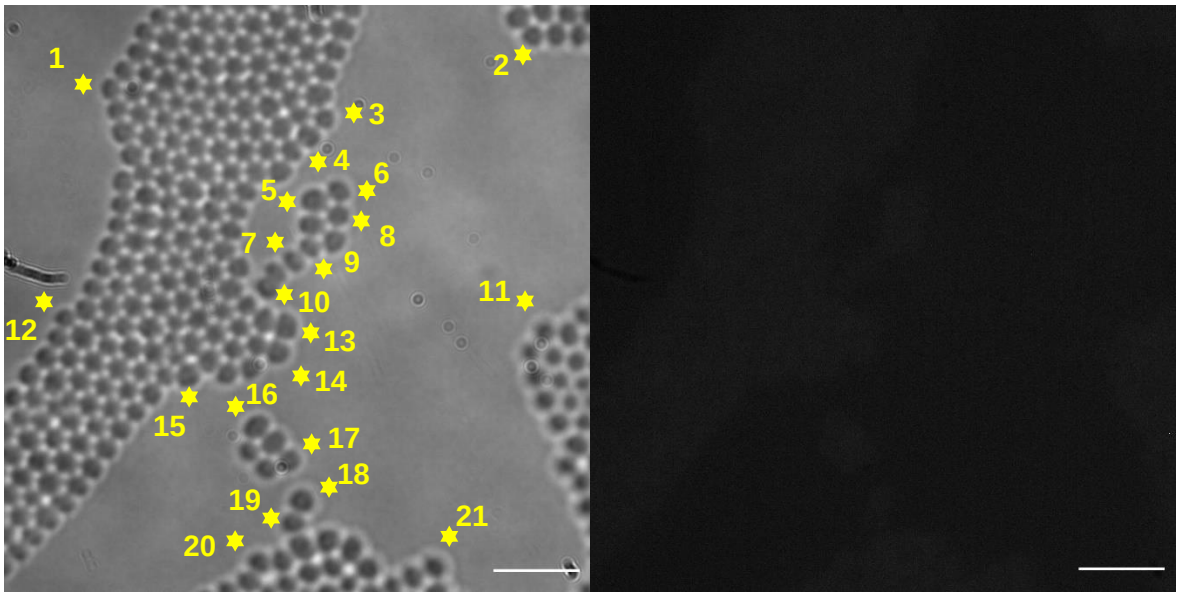

Figure S229 – MRSA transmitted image and fluorescence image at 450nm used in fluorescence intensity calculations in the absence of both SSA **70** and **FM4-64** at T = 4 hours. Transmitted image used to locate cells on fluorescence image. Scale bar = 10µM

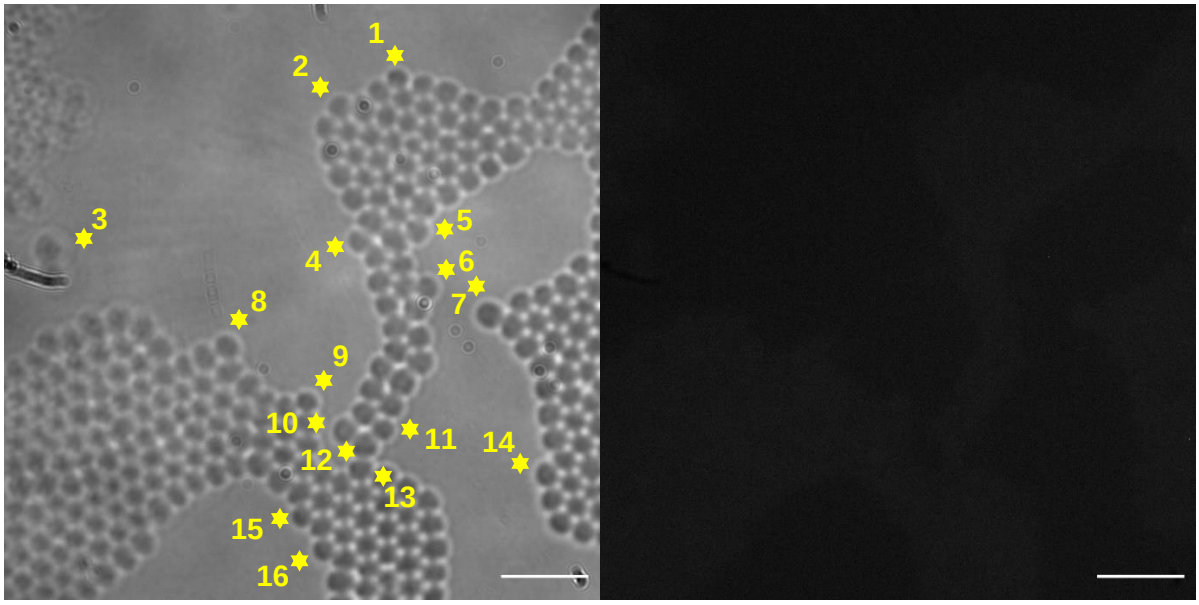

Figure S230 – MRSA transmitted image and fluorescence image at 450nm used in fluorescence intensity calculations in the absence of both SSA **70** and **FM4-64** at T = 4 hours. Transmitted image used to locate cells on fluorescence image. Scale bar = 10µM

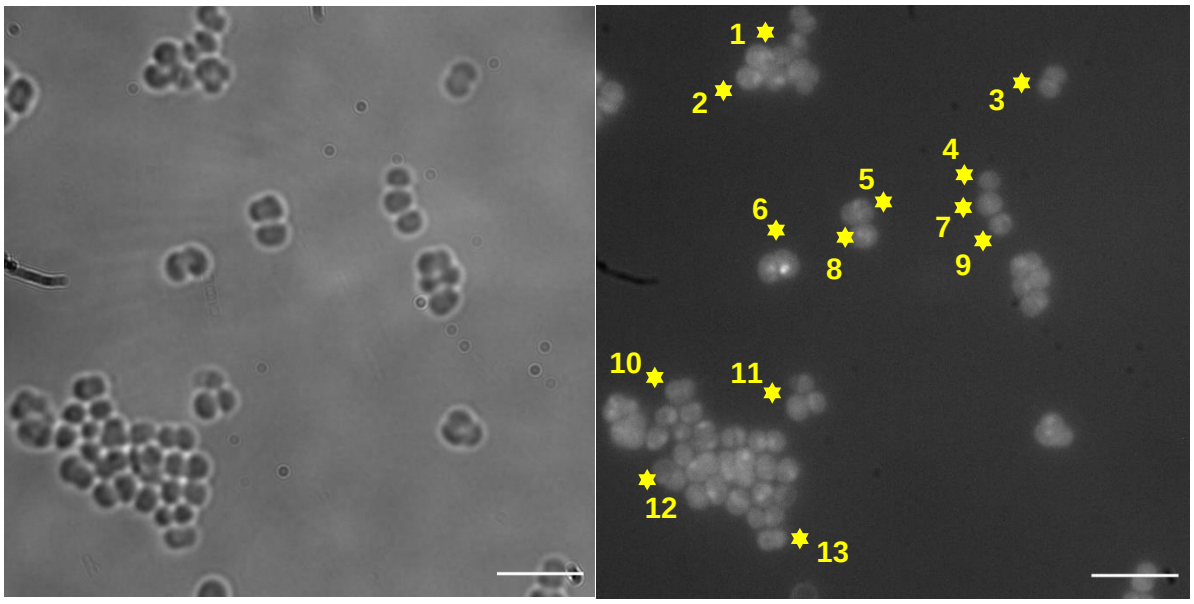

Figure S231 – MRSA transmitted image and fluorescence image at 450 nm used in fluorescence intensity calculations in the presence of SSA **70** only at T = 4 hours. Scale bar = 10µM

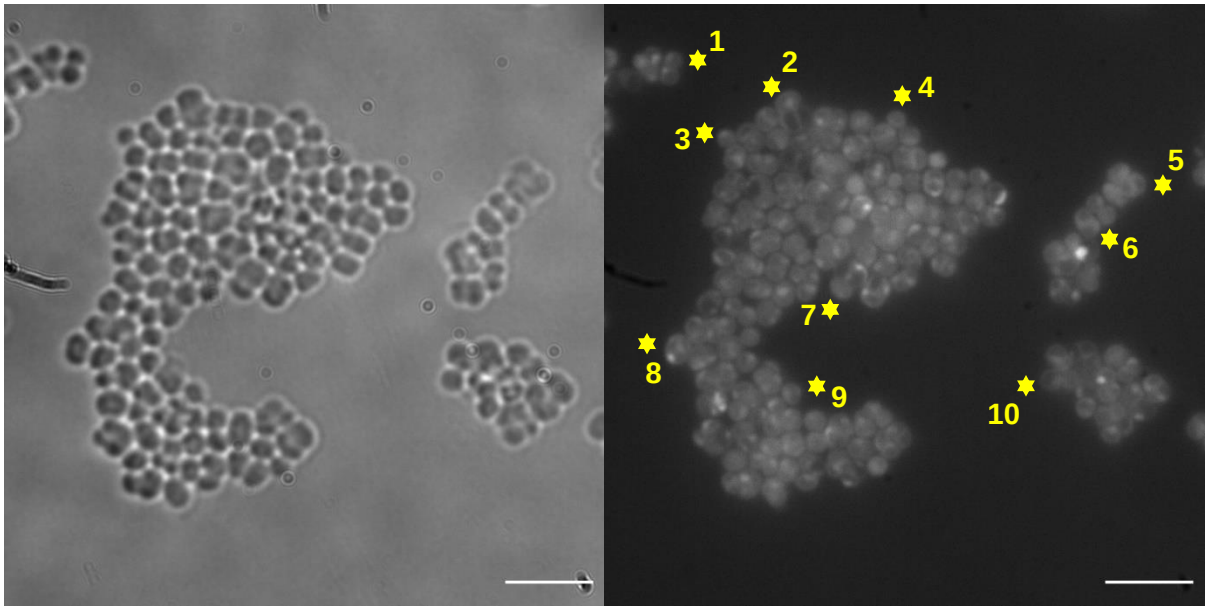

Figure S232 – MRSA transmitted image and fluorescence image at 450 nm used in fluorescence intensity calculations in the presence of SSA **70** only at T = 4 hours. Scale bar = 10µM

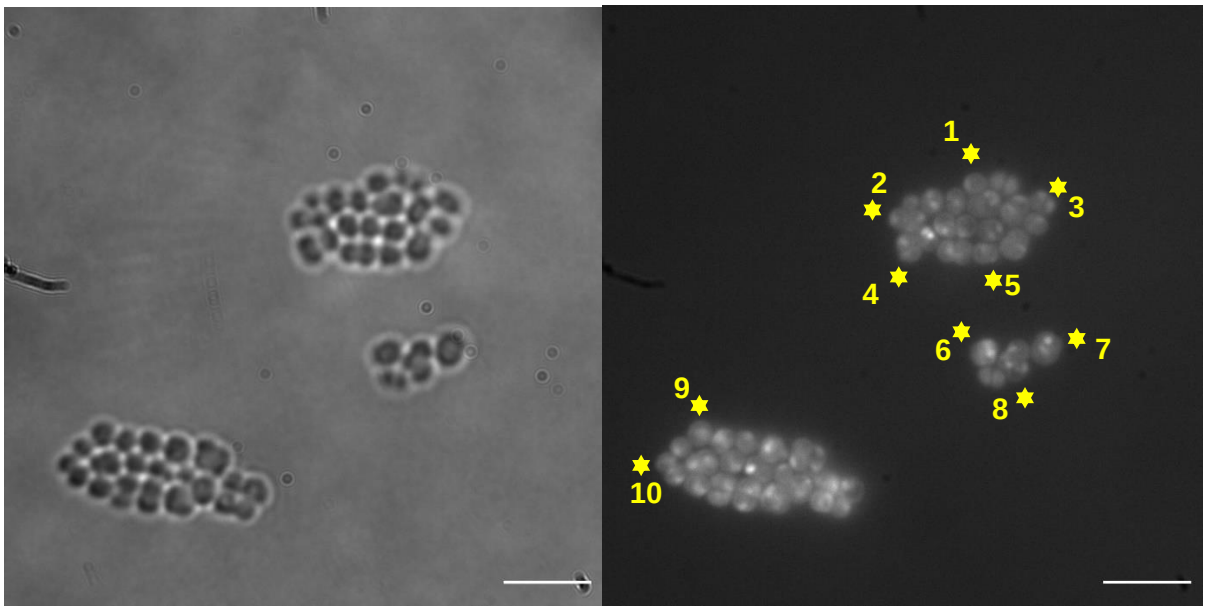

Figure S233 – MRSA transmitted image and fluorescence image at 450 nm used in fluorescence intensity calculations in the presence of SSA **70** only at T = 4 hours. Scale bar = 10µM

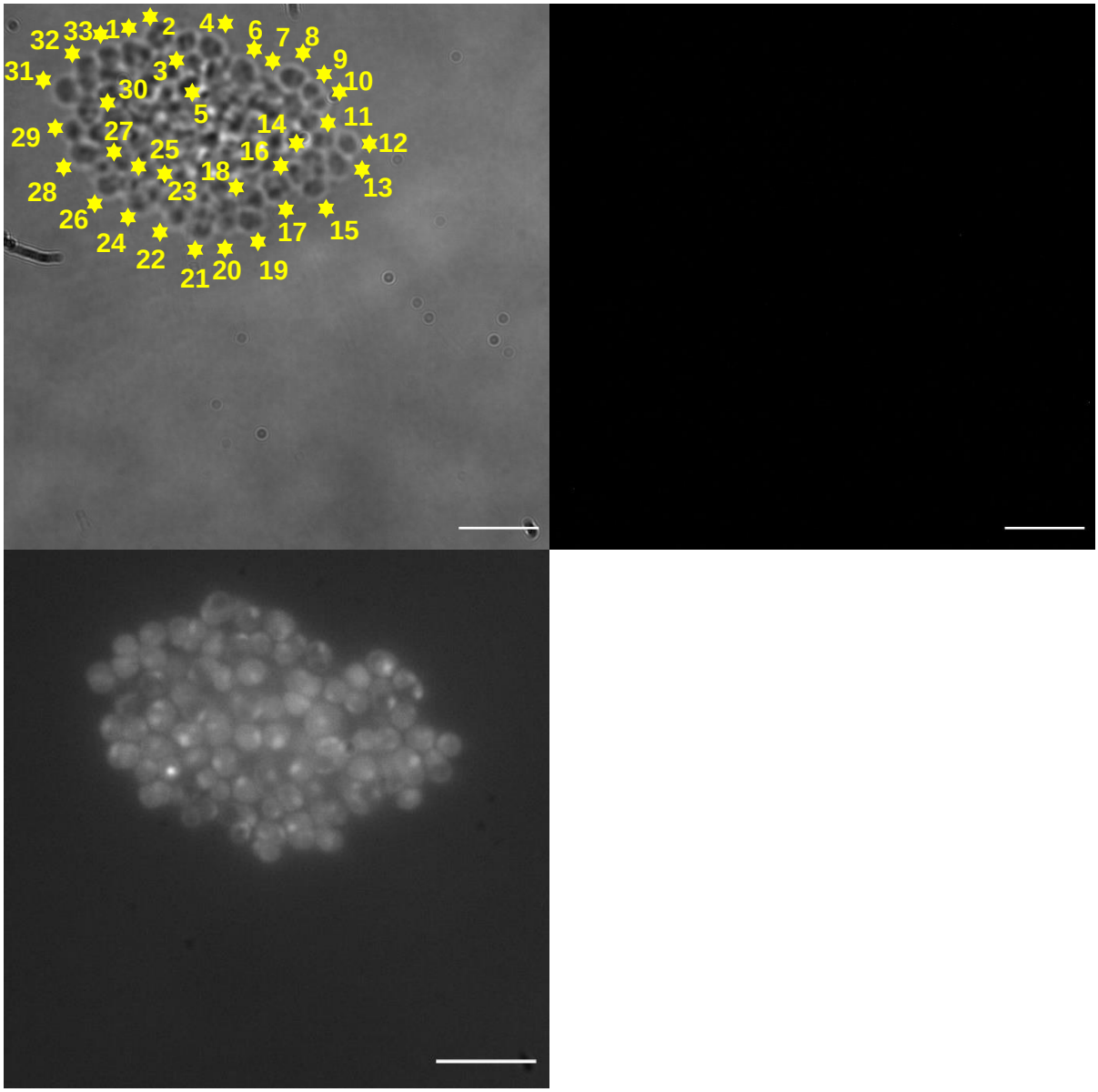

Figure S234 – MRSA transmitted image and fluorescence image at 605 nm used in fluorescence intensity calculations in the presence of SSA **70** only at T = 4 hours. Fluorescence image taken 450 nm used to locate cells on fluorescence image 605 nm. Scale bar = 10µM

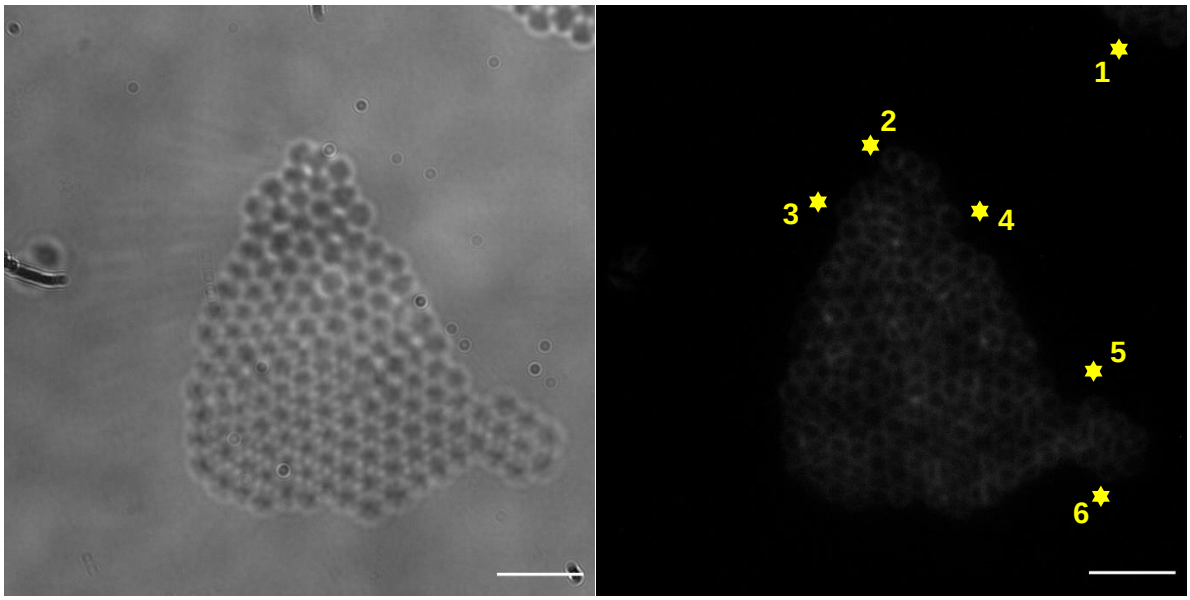

Figure S235 – MRSA transmitted image and fluorescence image at 605 nm used in fluorescence intensity calculations in the presence of **FM4-64** only at T = 4 hours. Scale bar = 10µM

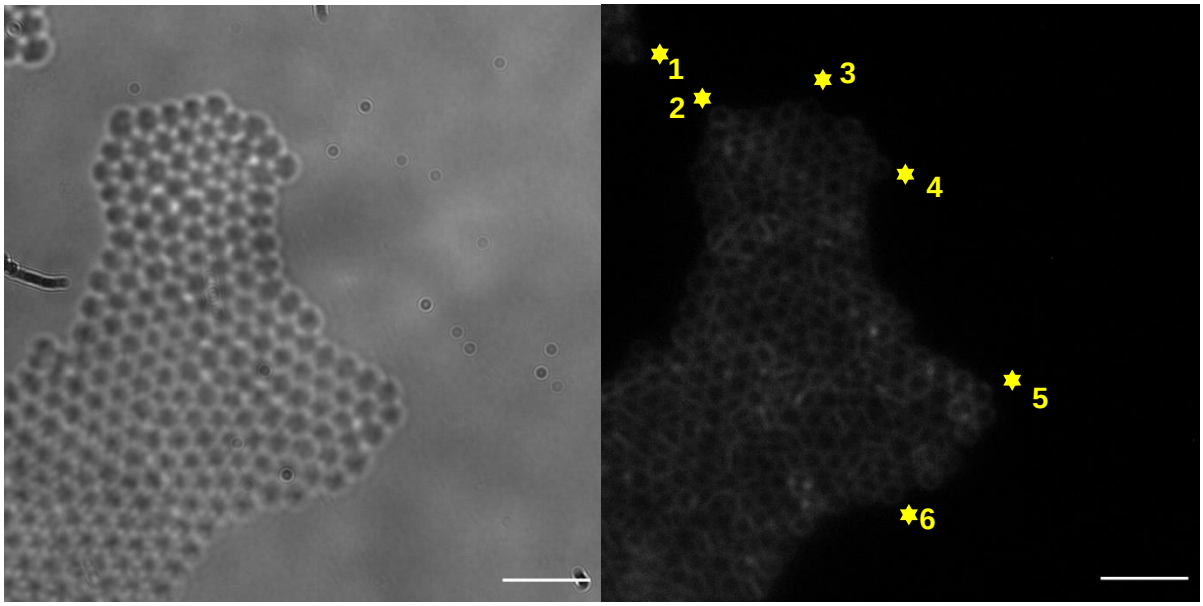

Figure S236 – MRSA transmitted image and fluorescence image at 605 nm used in fluorescence intensity calculations in the presence of **FM4-64** only at T = 4 hours. Scale bar = 10µM

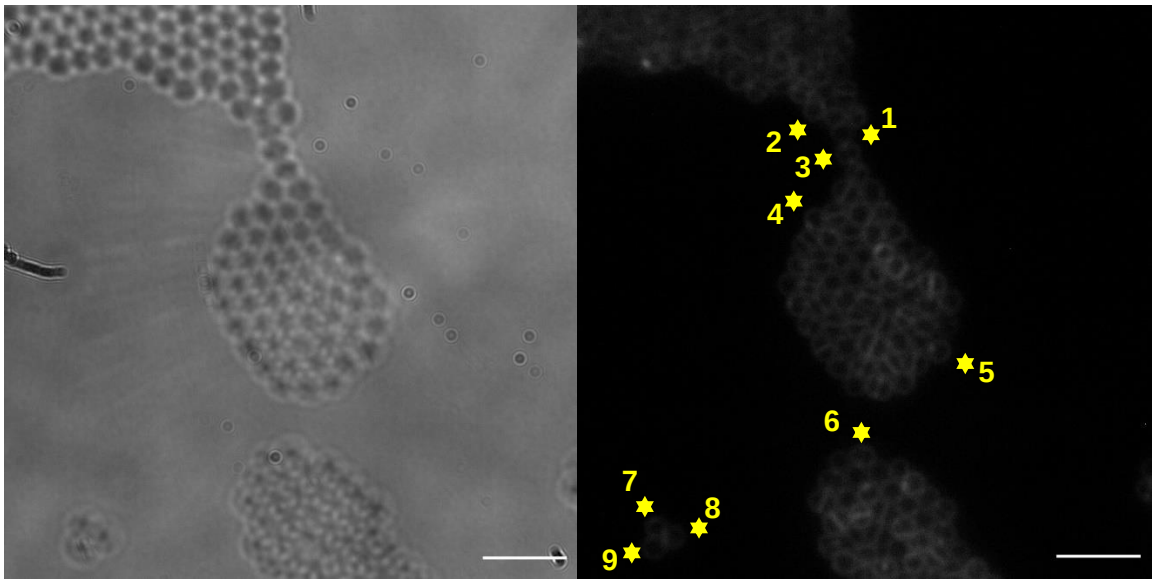

Figure S237 – MRSA transmitted image and fluorescence image at 605 nm used in fluorescence intensity calculations in the presence of **FM4-64** only at T = 4 hours. Scale bar = 10µM

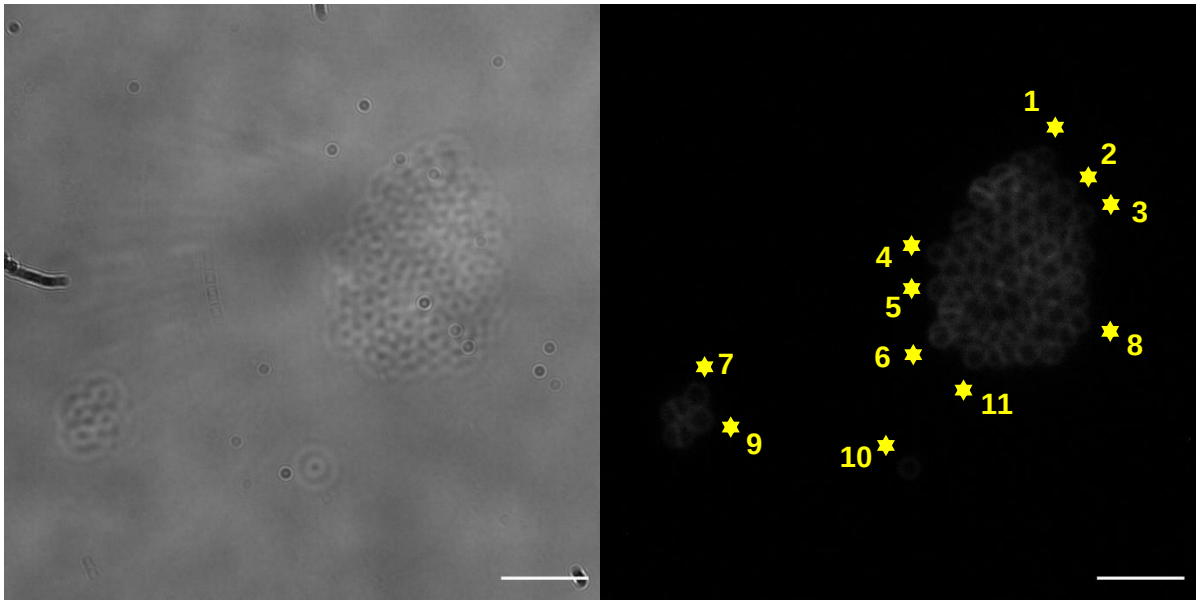

Figure S238 – MRSA transmitted image and fluorescence image at 605 nm used in fluorescence intensity calculations in the presence of **FM4-64** only at T = 4 hours. Scale bar = 10µM

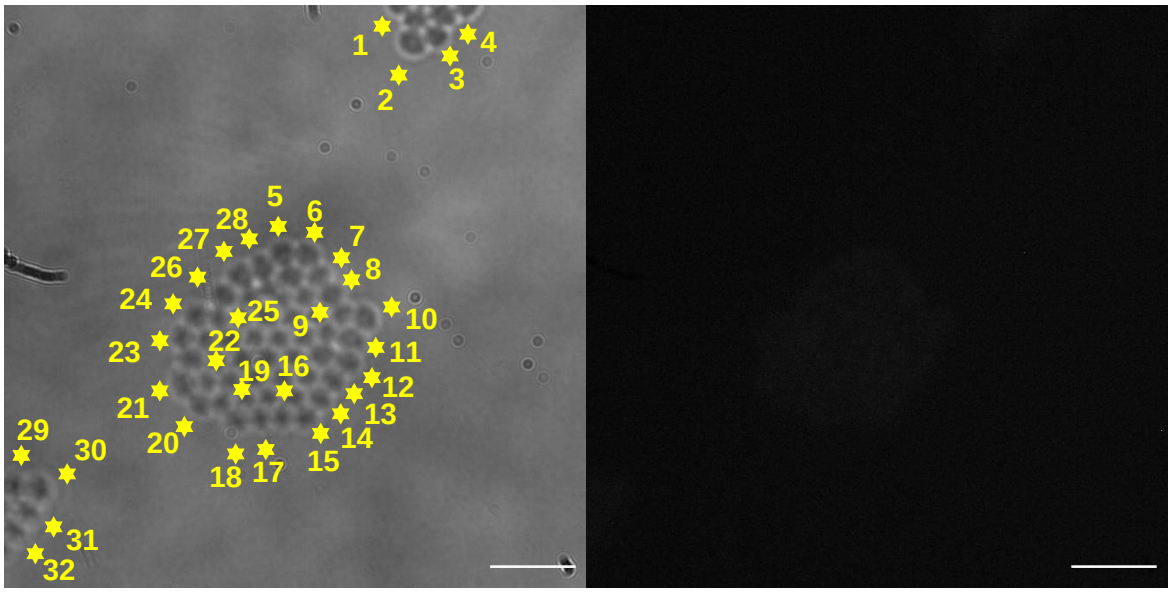

Figure S239 – MRSA transmitted image and fluorescence image at 450 nm used in fluorescence intensity calculations in the presence of **FM4-64** only at T = 4 hours. Transmitted image used to locate cells on fluorescence image. Scale bar = 10µM

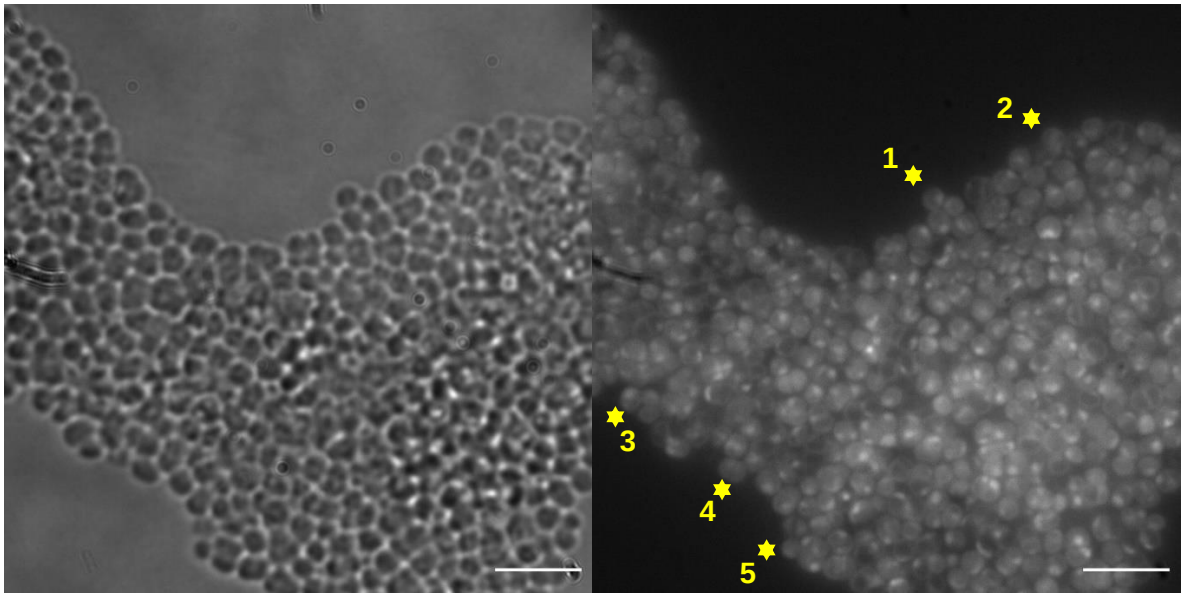

Figure S240 – MRSA transmitted image and fluorescence image at 450 nm used in fluorescence intensity calculations in the presence of both SSA **70** and **FM4-64** at T = 4 hours. Scale bar = 10µM

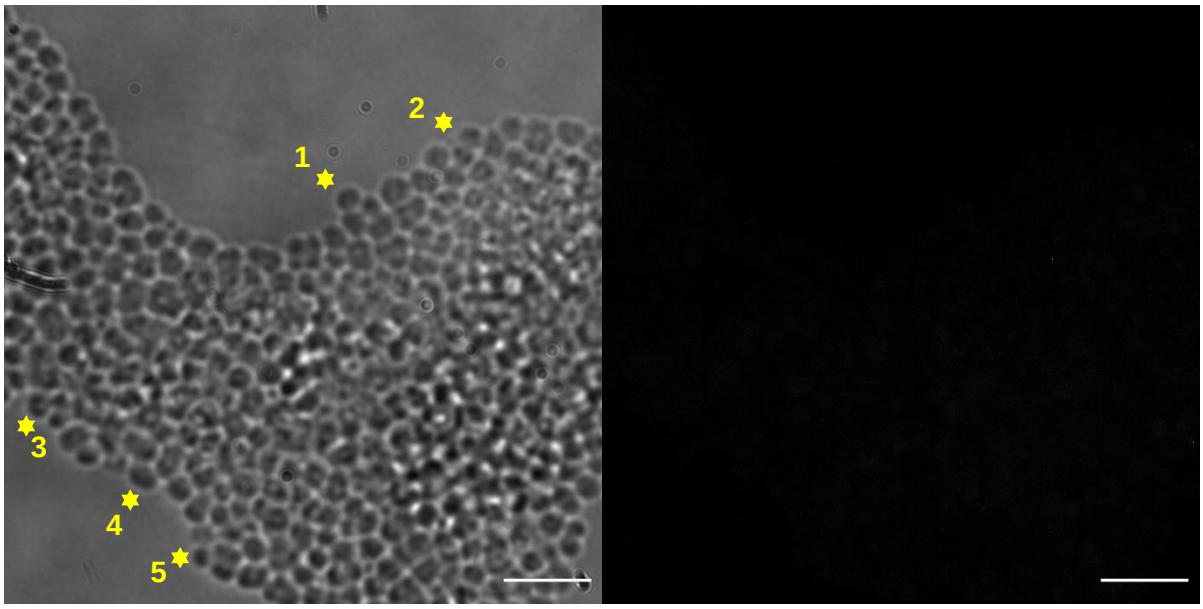

Figure S241 – MRSA transmitted image and fluorescence image at 605 nm used in fluorescence intensity calculations in the presence of both SSA **70** and **FM4-64** only at T = 4 hours. Transmitted image used to locate cells on fluorescence image. Scale bar = 10µM

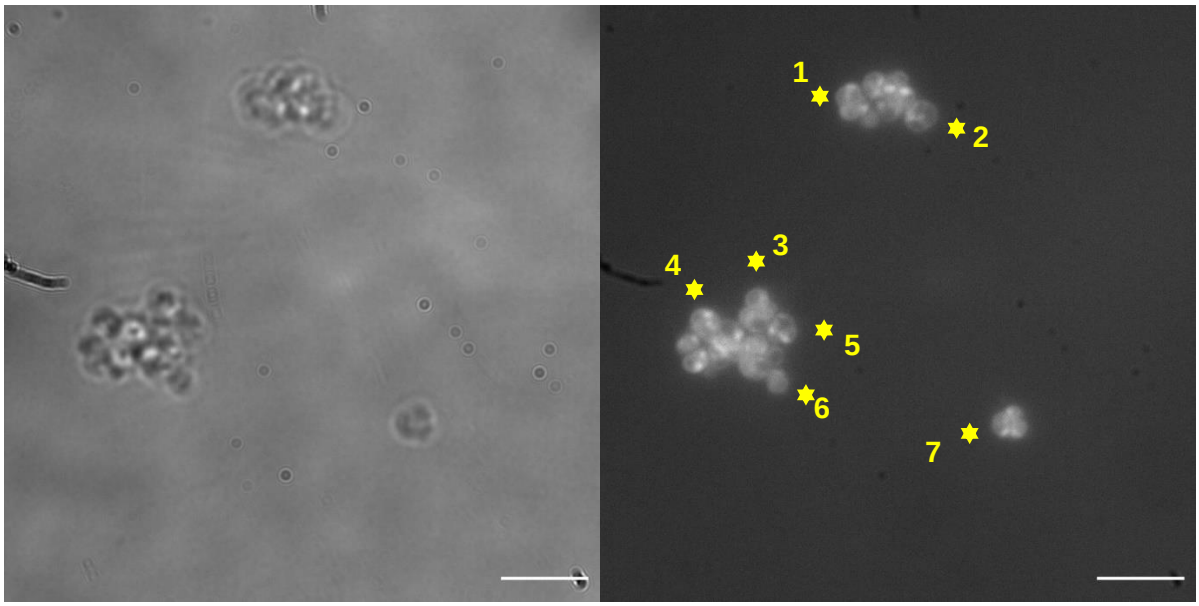

Figure S242 – MRSA transmitted image and fluorescence image at 450 nm used in fluorescence intensity calculations in the presence of both SSA **70** and **FM4-64** at T = 4 hours. Scale bar = 10µM

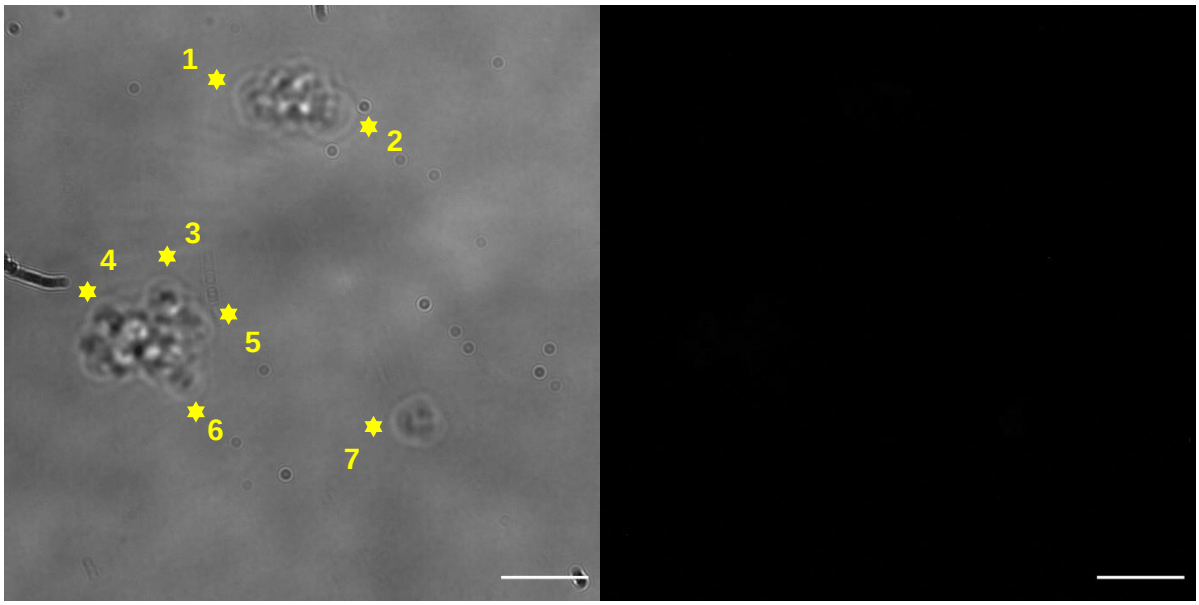

Figure S243 – MRSA transmitted image and fluorescence image at 605 nm used in fluorescence intensity calculations in the presence of both SSA **70** and **FM4-64** only at T = 4 hours. Transmitted image used to locate cells on fluorescence image. Scale bar = 10µM

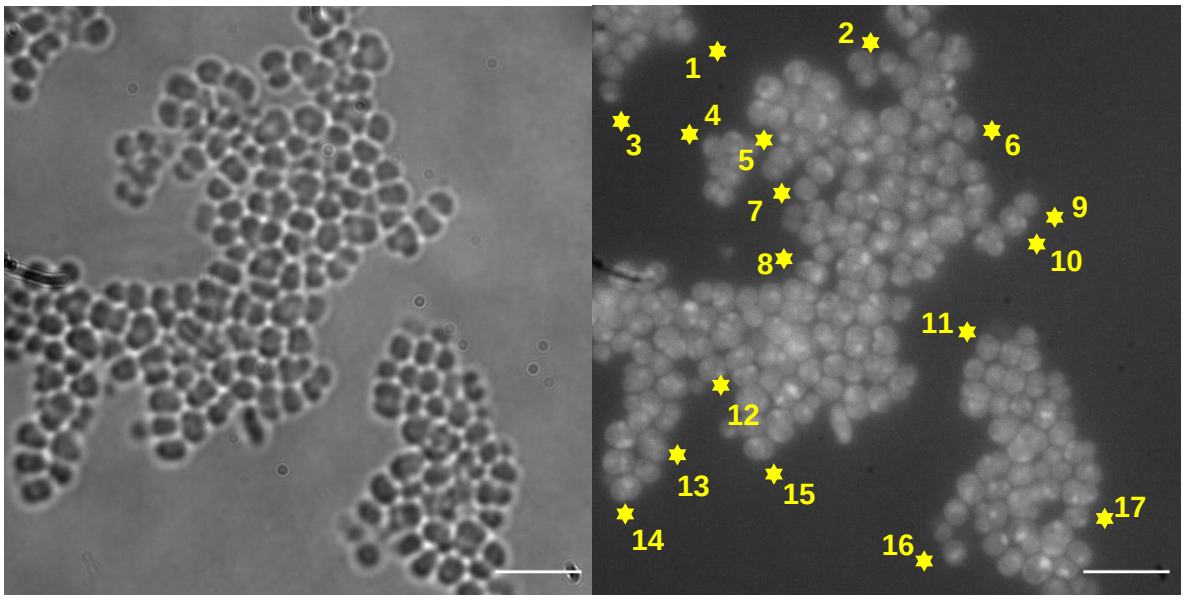

Figure S244 – MRSA transmitted image and fluorescence image at 450 nm used in fluorescence intensity calculations in the presence of both SSA **70** and **FM4-64** at T = 4 hours. Scale bar = 10µM

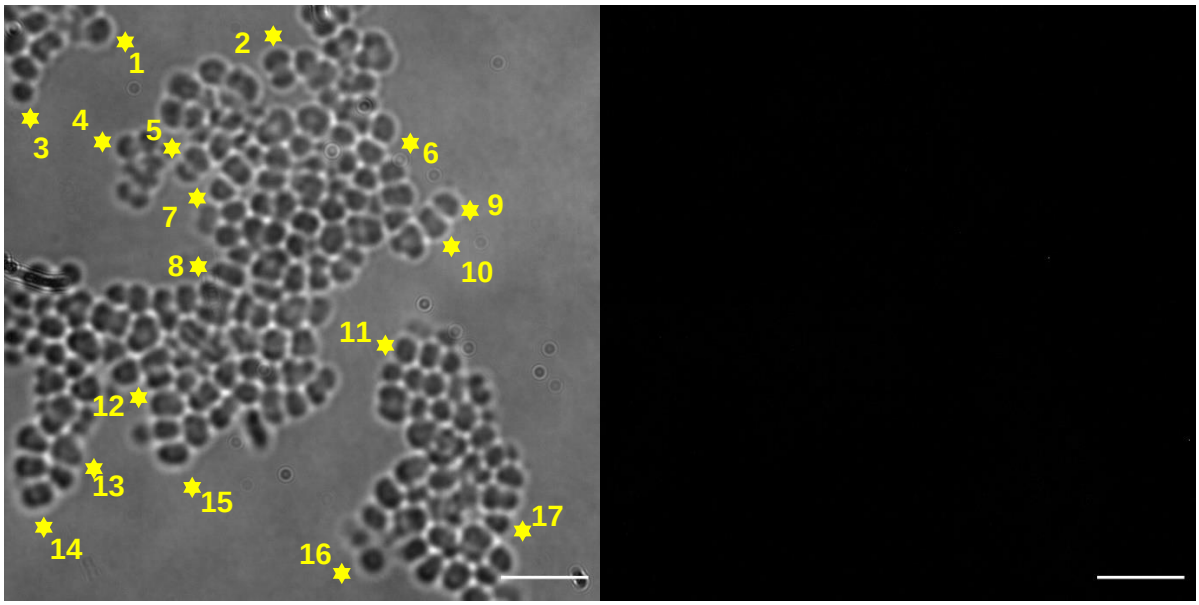

Figure S245 – MRSA transmitted image and fluorescence image at 605 nm used in fluorescence intensity calculations in the presence of both SSA **70** and **FM4-64** only at T = 4 hours. Transmitted image used to locate cells on fluorescence image. Scale bar = 10µM

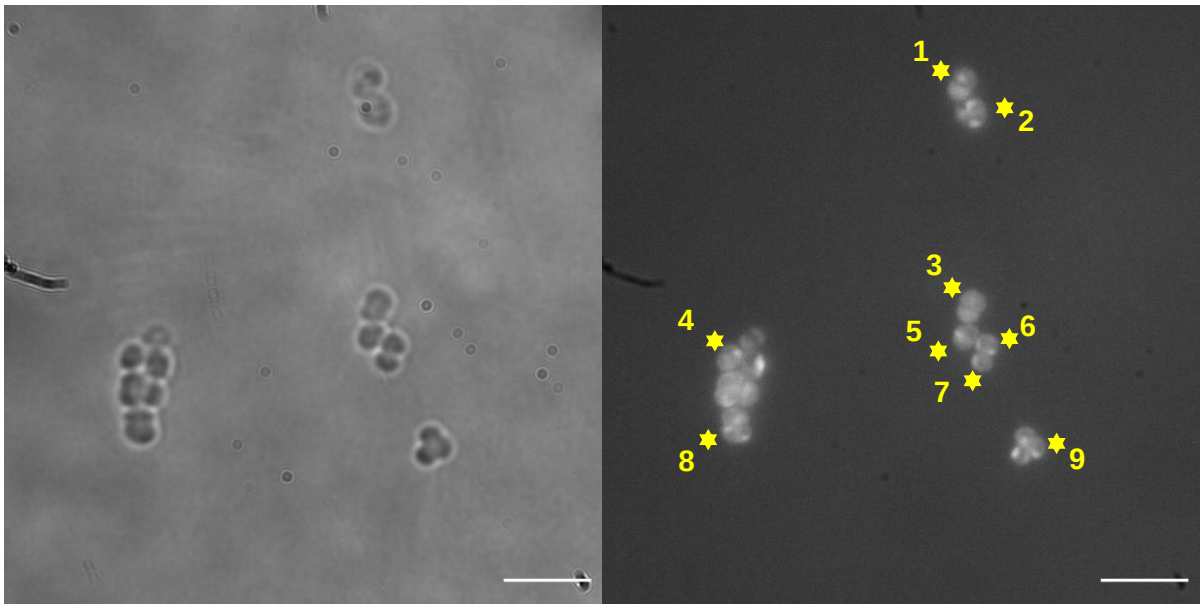

Figure S246 – MRSA transmitted image and fluorescence image at 450 nm used in fluorescence intensity calculations in the presence of both SSA **70** and **FM4-64** at T = 4 hours. Scale bar = 10µM

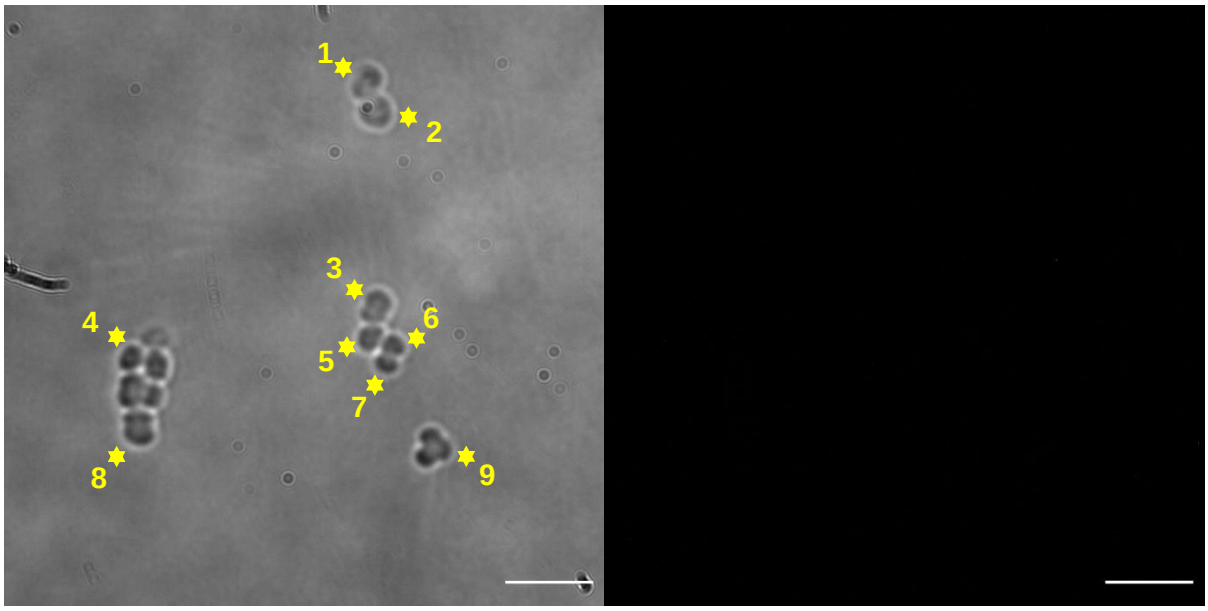

Figure S247 – MRSA transmitted image and fluorescence image at 605 nm used in fluorescence intensity calculations in the presence of both SSA **70** and **FM4-64** only at T = 4 hours. Transmitted image used to locate cells on fluorescence image. Scale bar = 10µM

Antimicrobial plates statistics

Ampicillin vs ampicillin co-formulated gel

Paired Samples Statistics

		Mean	N	Std. Deviation	Std. Error Mean
Pair 1	EAmpalone_well	52.6667	3	2.88675	1.66667
	EAmp70gel_well	53.3333	3	1.52753	.88192
Pair 2	MAmpalone_well	17.0000	3	1.00000	.57735
	MAmp70gel_well	15.3333	3	1.15470	.66667

Paired Samples Correlations

		N	Correlation	Sig.
Pair 1	EAmpalone_well & EAmp70gel_well	3	-.756	.454
Pair 2	MAmpalone_well & MAmp70gel_well	3	.000	1.000

Paired Samples Test

		Paired Differences			
		Mean	Std. Deviation	Std. Error Mean	95% Confidence Interval of the Difference Lower
Pair 1	EAmpalone_well – Eamp70gel_well	-.66667	4.16333	2.40370	-11.00896
Pair 2	MAmpalone_well – Mamp70gel_well	1.66667	1.52753	.88192	-2.12792

Paired Samples Test

		Paired Differences 95% Confidence Interval of the Difference Upper	t	df	Sig. (2-tailed)
Pair 1	EAmpalone_well - EAmp70gel_well	9.67562	-.277	2	.808
Pair 2	MAmpalone_well - MAmp70gel_well	5.46125	1.890	2	.199

Surface vs Well

Paired Samples Statistics

		Mean	N	Std. Deviation	Std. Error Mean
Pair 1	E.coli_Surface	15.0000	3	2.64575	1.52753
	E.coli_Well	17.6667	3	4.16333	2.40370
Pair 2	MRSA_Surface	15.6667	3	1.52753	.88192
	MRSA_Well	13.6667	3	1.15470	.66667
Pair 3	AmpE_Surface	59.3333	3	.57735	.33333
	AmpE_Well	53.3333	3	1.52753	.88192
Pair 4	AmpM_Surface	23.3333	3	1.52753	.88192
	AmpM_Well	17.0000	3	1.00000	.57735

Paired Samples Correlations

		N	Correlation	Sig.
Pair 1	E.coli_Surface & E.coli_Well	3	.817	.391
Pair 2	MRSA_Surface & MRSA_Well	3	.756	.454
Pair 3	AmpE_Surface & AmpE_Well	3	-.756	.454

Pair 4	AmpM_Surface & AmpM_Well	3	-.982	.121

Paired Samples Test

		Paired Differences			
		Mean	Std. Deviation	Std. Error Mean	95% Confidence Interval of the Difference Lower
Pair 1	E.coli_Surface - E.coli_Well	-2.66667	2.51661	1.45297	-8.91828
Pair 2	MRSA_Surface - MRSA_Well	2.00000	1.00000	.57735	-.48414
Pair 3	AmpE_Surface - AmpE_Well	6.00000	2.00000	1.15470	1.03172
Pair 4	AmpM_Surface - AmpM_Well	6.33333	2.51661	1.45297	.08172

Paired Samples Test

		Paired Differences 95% Confidence Interval of the Difference Upper	t	df	Sig. (2-tailed)
Pair 1	E.coli_Surface - E.coli_Well	3.58494	-1.835	2	.208
Pair 2	MRSA_Surface - MRSA_Well	4.48414	3.464	2	.074
Pair 3	AmpE_Surface - AmpE_Well	10.96828	5.196	2	.035
Pair 4	AmpM_Surface - AmpM_Well	12.58494	4.359	2	.049

Physicochemical studies conducted on second generation SSAs

Hydrogen bond donor	Hydrogen bond acceptor	Hydrogen bond length (D•••A) (Å)	Hydrogen bond angle (D-H•••A) (°)
N2	O4	2.839(4)	173.44(7)
N3	O4	2.995(4)	148.8(2)

Figure S248 – Hydrogen bond distances and angles observed for 3, calculated from the single-crystal X-ray structure shown of SSA **82**.

Information for Figure 64:

Single crystal X-ray structure of SSA **82**: red = oxygen; yellow = sulfur; blue = nitrogen; white = hydrogen; grey = carbon. CCDC 2023004, C33H52N4O4S2 (M = 632.90): monoclinic, space group P 2/n, a = 16.4865(13) Å, b = 10.4507(7) Å, c = 20.0106(17) Å, α = 90°, β = 94.596(7)°, γ = 90°, V = 3436.7(4) Å3, Z = 4, T = 100(1) K, CuK\α = 1.5418 Å, Dcalc = 1.223 g/cm3, 22331 reflections measured (7.238 ≤ 2Θ ≤ 133.202), 6083 unique (Rint = 0.1112, Rsigma = 0.1299) which were used in all calculations. The final R1 was 0.0622 (I > 2σ(I)) and wR2 was 0.1341 (all data).

Hydrogen bond donor	Hydrogen bond acceptor	Hydrogen bond length (D•••A) (Å)	Hydrogen bond angle (D-H•••A) (°)
N1	O2	2.9478 (17)	154.64 (9)
N2	O1	2.9591 (17)	156.20 (9)
O5	O3	2.8719 (18)	173.45 (9)
O5	N3	2.9280 (19)	167.14 (10)

Figure S249 – Hydrogen bond distances and angles observed for 3, calculated from the single crystal X-ray structure shown of SSA **83**.

Information for Figure 65:

Single crystal X-ray structure of **83**: red = oxygen; yellow = sulfur; blue = nitrogen; white = hydrogen; grey = carbon. CCDC 2033371, C34H56N4O5S2 (M = 664.94): triclinic, space group P -1, a = 9.2701(2) Å, b = 9.2791(3) Å, c = 21.7492(7) Å, α = 91.169(3)°, β = 96.234(2)°, γ = 103.561(2)°, V = 1805.87(9) Å3, Z = 2, T = 100(1) K, CuK\α = 1.5418 Å, Dcalc = 1.223 g/cm3, 12423 reflections measured (8.184 ≤ 2Θ ≤ 143.716), 6885 unique (Rint = 0.0271, Rsigma = 0.0402) which were used in all calculations. The final R1 was 0.0373 (I > 2σ(I)) and wR2 was 0.0950 (all data).

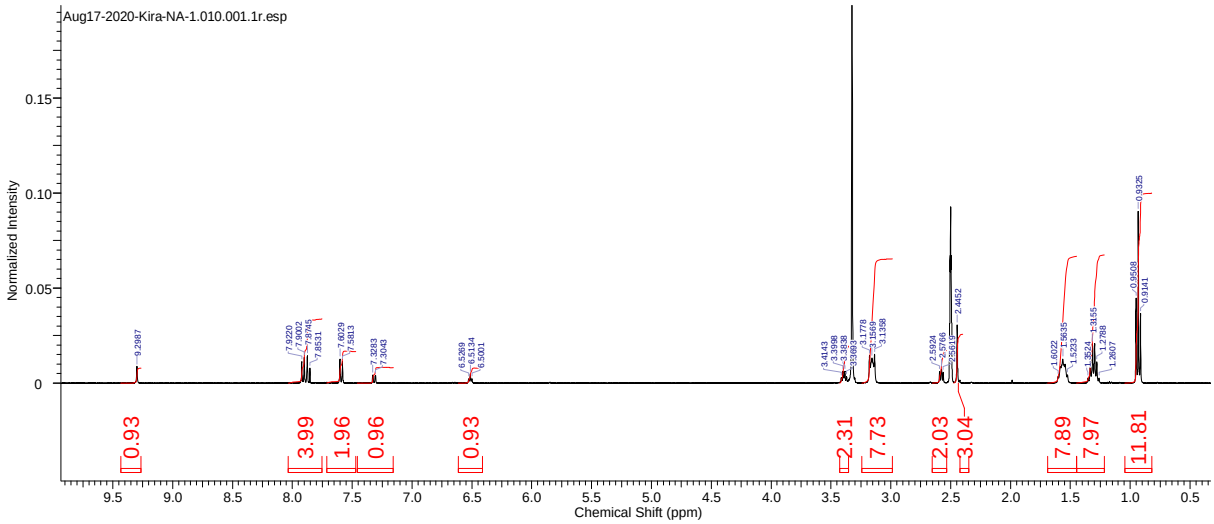

Figure S250 – ^{1}H NMR of SSA **82** in DMSO-d_6 conducted at 298.15 K.

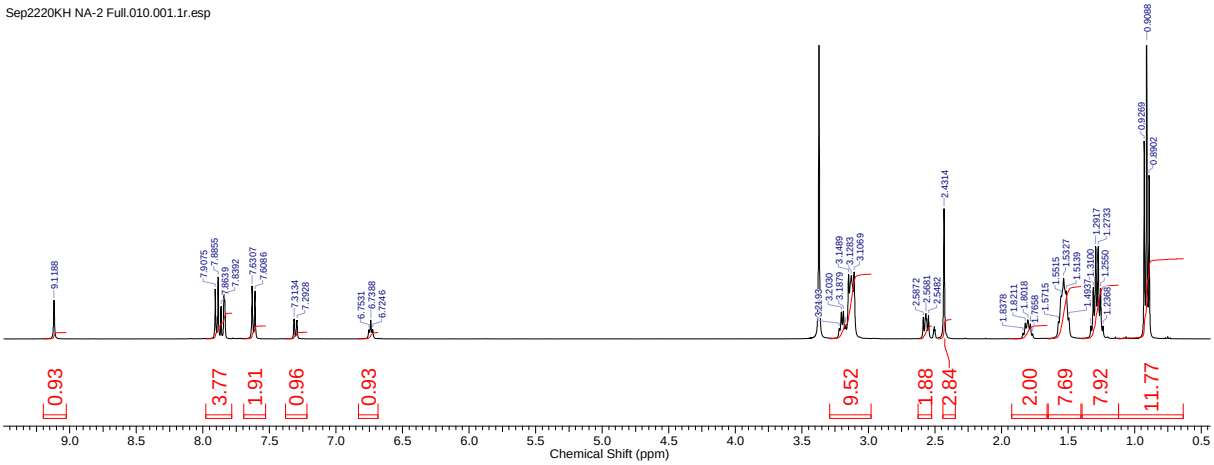

Figure S251 –^{1}H NMR of SSA **83** in DMSO-d_6 conducted at 298.15 K.

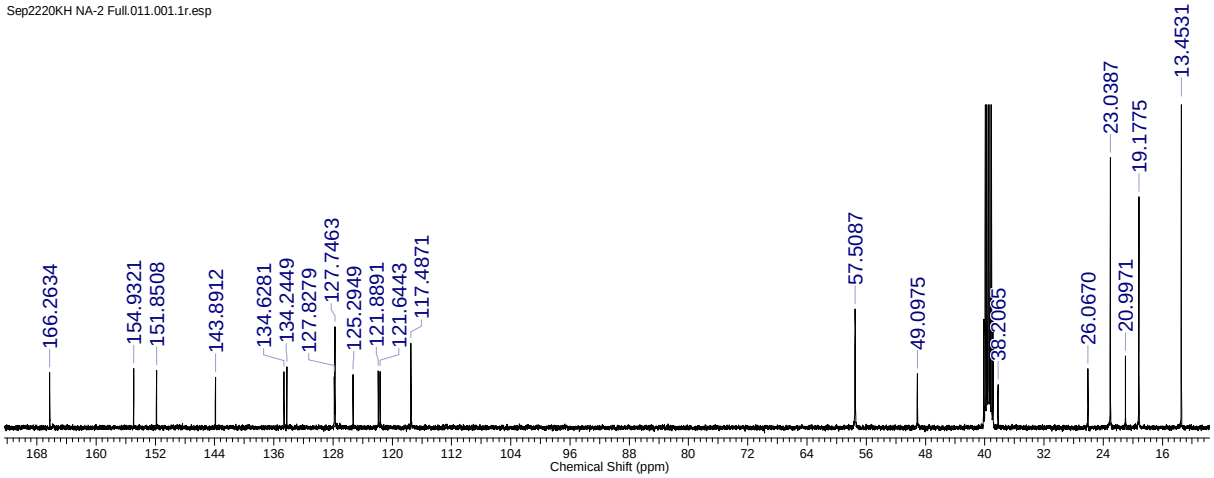

Figure S252 – ^{13}C NMR of SSA **82** in DMSO-d_6 conducted at 298.15 K.

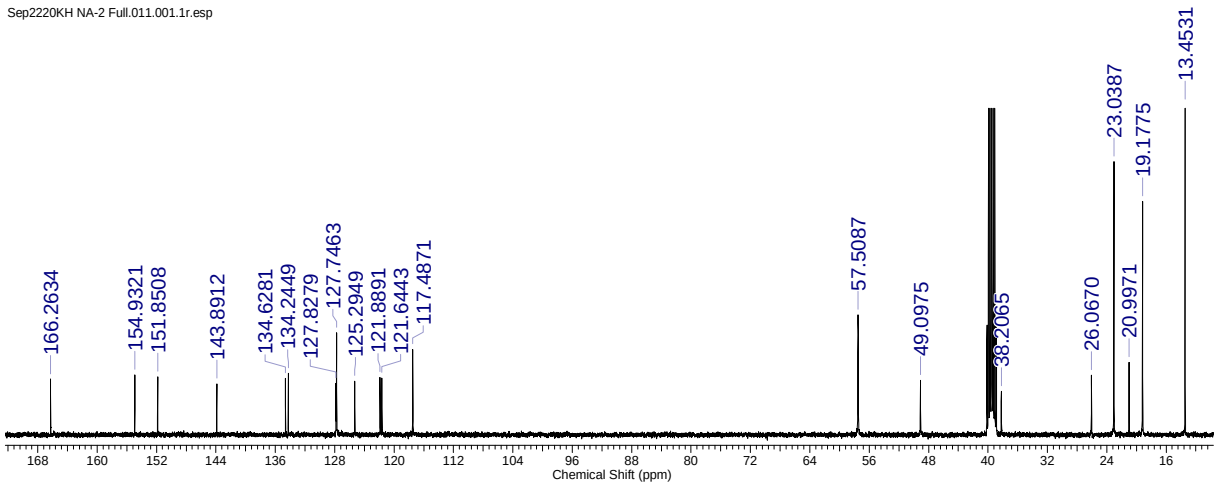

Figure S253 – ^{13}C NMR of SSA **83** in DMSO-d_6 conducted at 298.15 K.

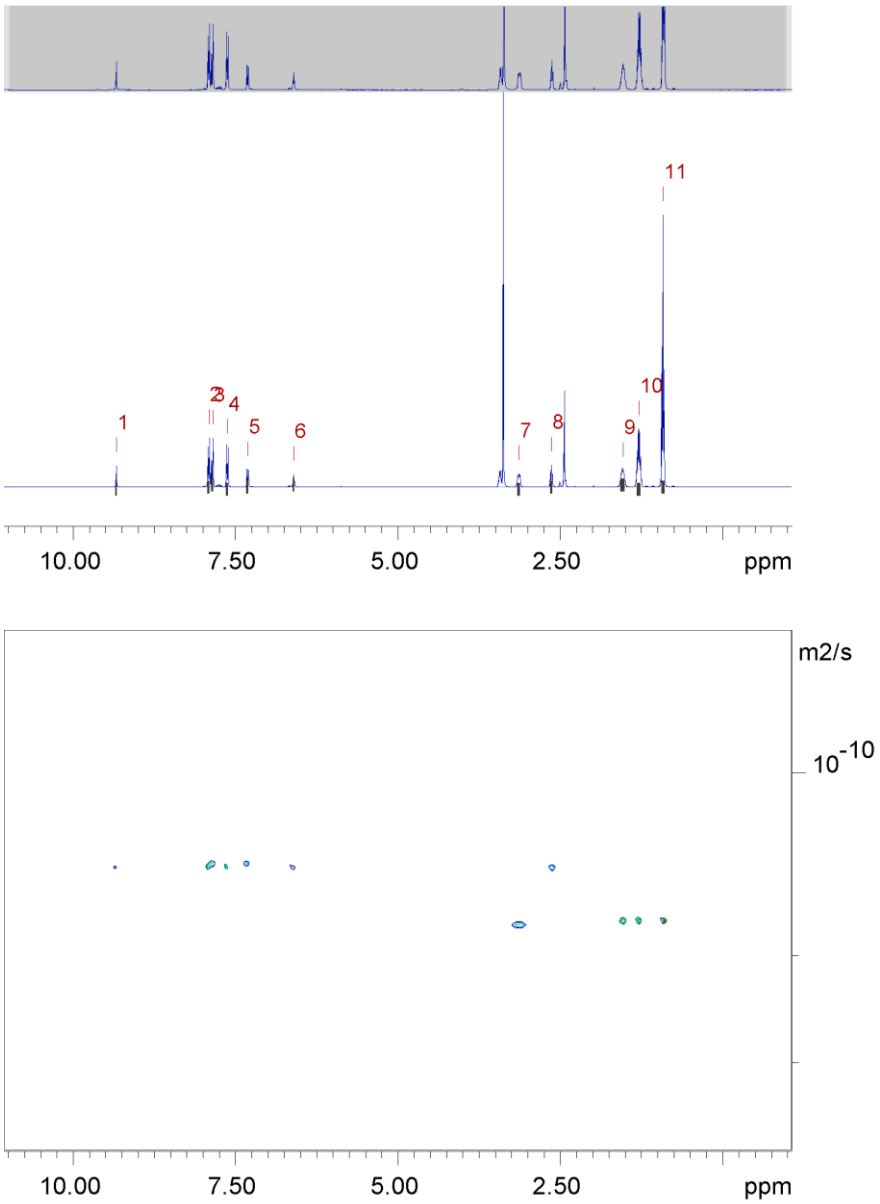

Peak name	F2 [ppm]	Io	error	D [m2/s]	error
1	9.335	1.70e+08	1.413e+04	1.42e-10	2.376e-14
2	7.914	5.43e+08	1.631e+04	1.42e-10	8.569e-15
3	7.854	4.99e+08	1.630e+04	1.42e-10	9.285e-15
4	7.626	6.11e+08	1.930e+04	1.42e-10	9.012e-15
5	7.314	2.91e+08	1.747e+04	1.42e-10	1.705e-14
6	6.605	1.42e+08	1.504e+04	1.42e-10	3.021e-14
7	3.138	4.01e+08	2.146e+04	1.77e-10	1.859e-14
8	2.636	3.23e+08	1.711e+04	1.42e-10	1.510e-14
9	1.535	7.55e+08	2.712e+04	1.76e-10	1.246e-14
10	1.288	1.61e+09	2.626e+04	1.76e-10	5.670e-15
11	0.914	3.40e+09	2.349e+04	1.76e-10	2.394e-15

Figure S254 – ^{1}H DOSY NMR spectrum of SSA **82** (55.56 mM) in DMSO-*d6* at 298 K and a table reporting the diffusion constants calculated for each peak used to determine the hydrodynamic diameter of the anionic and cationic components of SSA **82**.

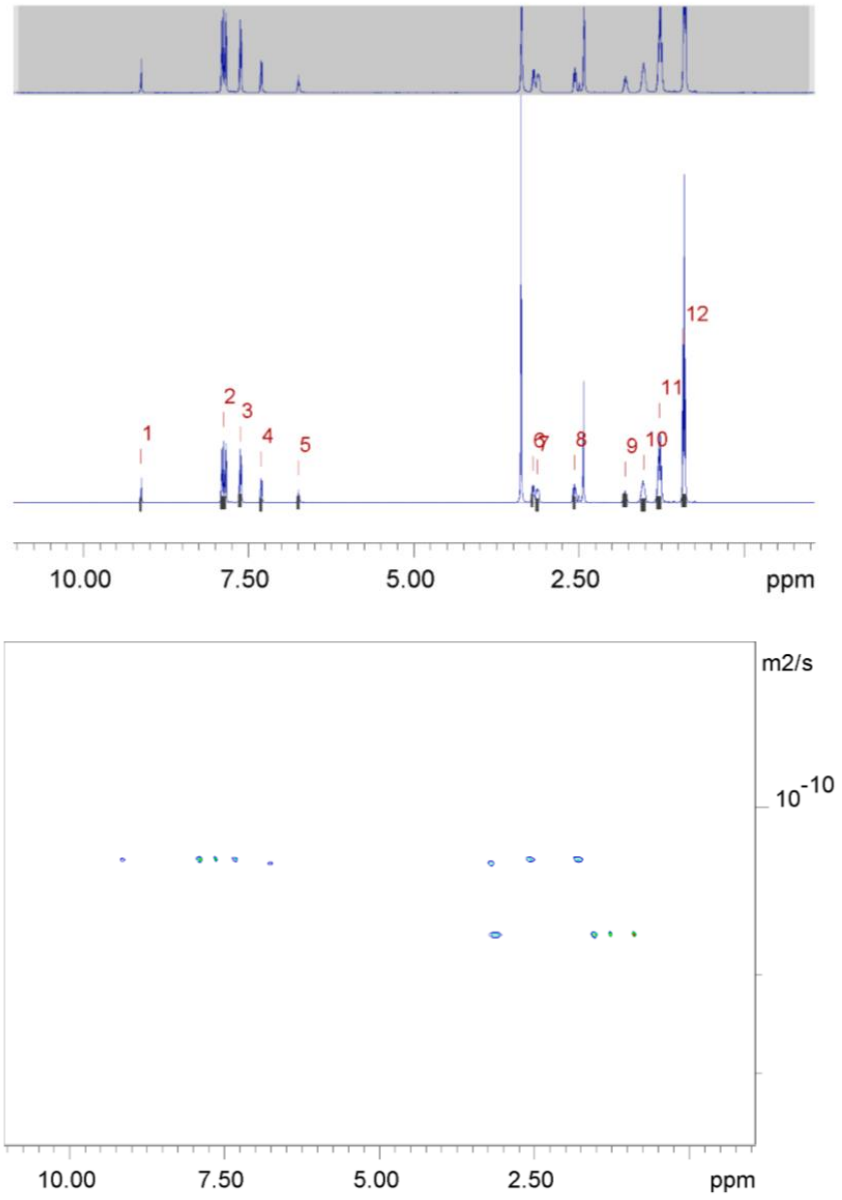

Peak name	F2 [ppm]	Io	error	D [m2/s]	error
1	9.129	1.55e+08	1.892e+04	1.23e-10	2.839e-14
2	7.883	1.09e+09	3.171e+04	1.23e-10	6.729e-15
3	7.623	5.92e+08	2.409e+04	1.24e-10	9.472e-15
4	7.309	2.98e+08	2.263e+04	1.24e-10	1.768e-14
5	6.747	1.45e+08	2.158e+04	1.26e-10	3.511e-14
6	3.203	2.42e+08	2.074e+04	1.25e-10	2.021e-14
7	3.132	3.24e+08	2.592e+04	1.70e-10	2.517e-14
8	2.569	2.75e+08	2.108e+04	1.24e-10	1.788e-14
9	1.804	2.88e+08	2.922e+04	1.24e-10	2.367e-14
10	1.527	6.34e+08	3.309e+04	1.70e-10	1.647e-14
11	1.284	1.50e+09	3.341e+04	1.70e-10	7.056e-15
12	0.905	3.26e+09	3.277e+04	1.70e-10	3.174e-15

Figure S255 – ^{1}H NMR spectrum of SSA **83** (55.56 mM) in DMSO-*d*6 at 298 K and a table reporting the diffusion constants calculated for each peak used to determine the hydrodynamic diameter of the anionic and cationic components of SSA **83**.

Figure S256 –^{1}H NMR stack plot of SSA **82** in DMSO-d_6 0.5 % H2O solution. Samples were prepared in series with an aliquot of the most concentrated solution undergoing serial dilution.

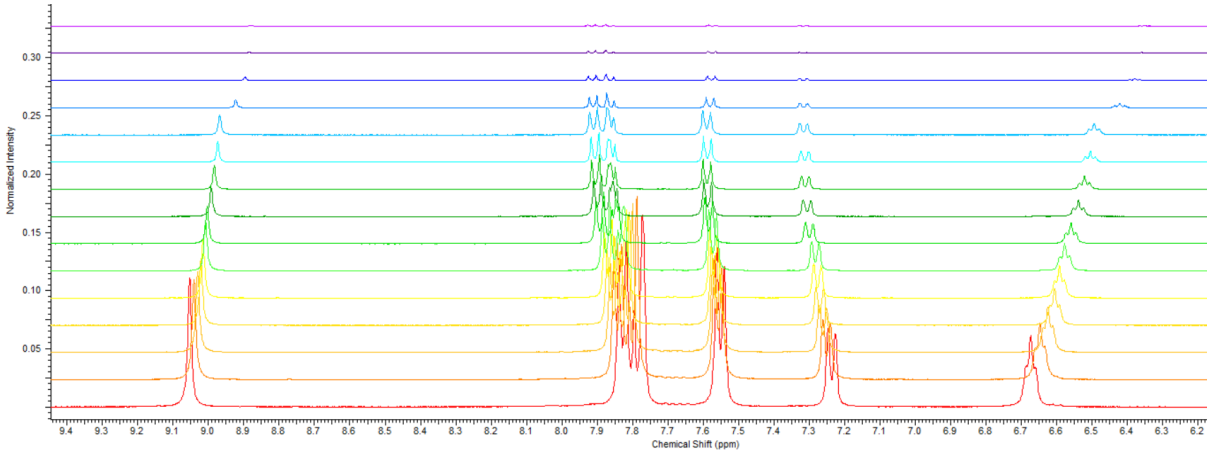

Figure S257 –1H NMR stack plot OF SSA **83** in DMSO-d_6 0.5 % H2O solution. Samples were prepared in series with an aliquot of the most concentrated solution undergoing serial dilution.

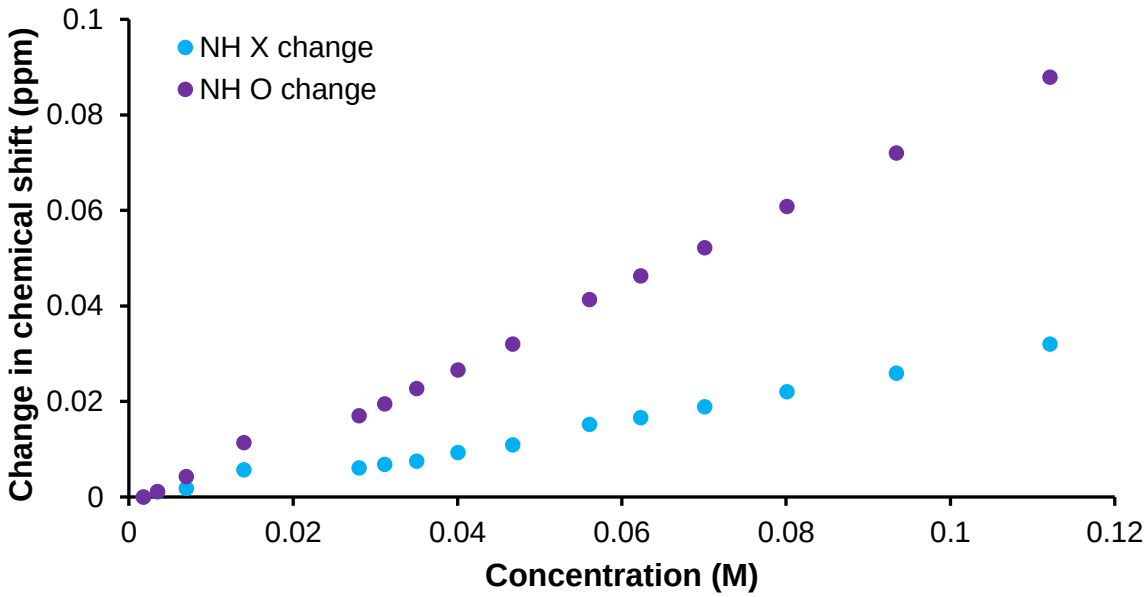

Figure S258 – Graph illustrating the ^{1}H NMR down-field change in chemical shift of urea NH resonances with increasing concentration of SSA **82** in DMSO-d_6 0.5 % H_2O (298.15 K). Equal K / dimerisation model: http://app.supramolecular.org/bindfit/view/e2d9a602-610c-4841-ae02-013b689f35c3 ; CoEK model: http://app.supramolecular.org/bindfit/view/ce54a853-3245-4e75-9754-66b20f4dd1e6

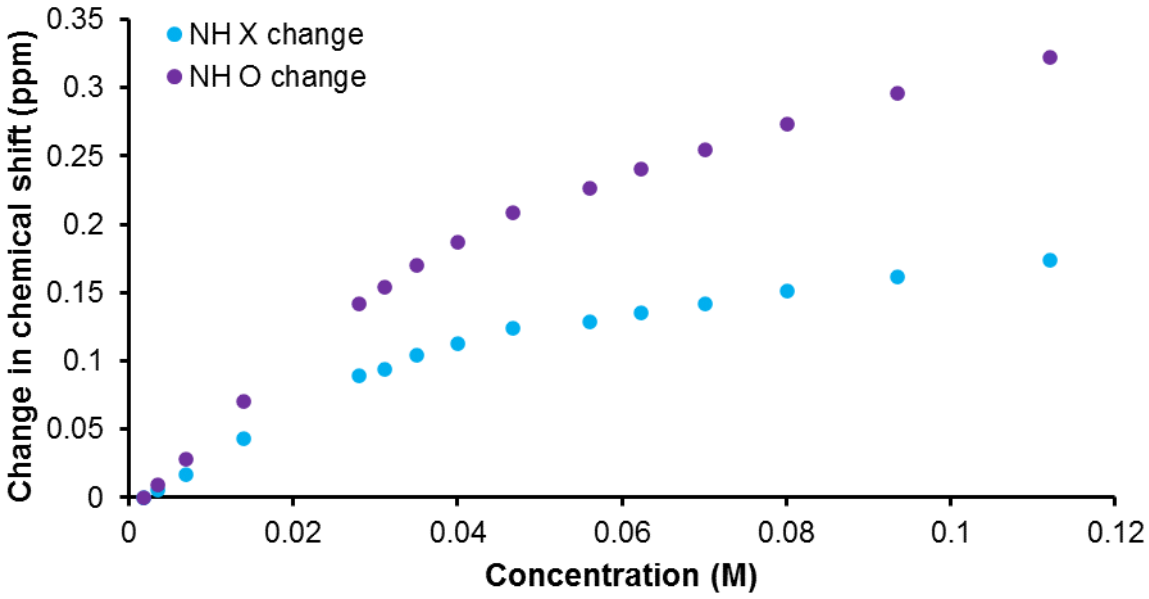

Figure S259 – Graph illustrating the ^{1}H NMR down-field change in chemical shift of urea NH resonances with increasing concentration of SSA **83** in DMSO-d_6 0.5 % H_2O (298.15 K). Equal K / dimerisation model: http://app.supramolecular.org/bindfit/view/38e6a72c-f700-47aa-b043-cfc3b3c3137e , CoEK model: http://app.supramolecular.org/bindfit/view/69d9124c-f2d4-4042-be5e-7fd0064909f8

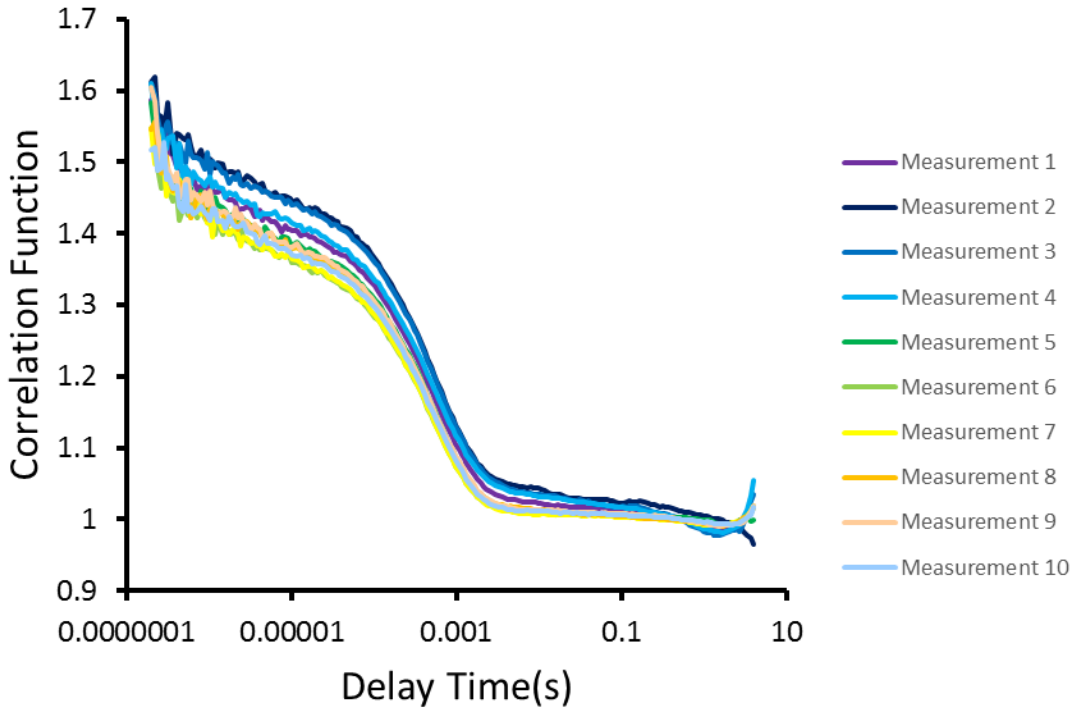

Figure S260 – Correlation function data for 10 DLS runs of SSA **82** (0.56 mM) in an EtOH:H2O (1:19) solution at 298 K.

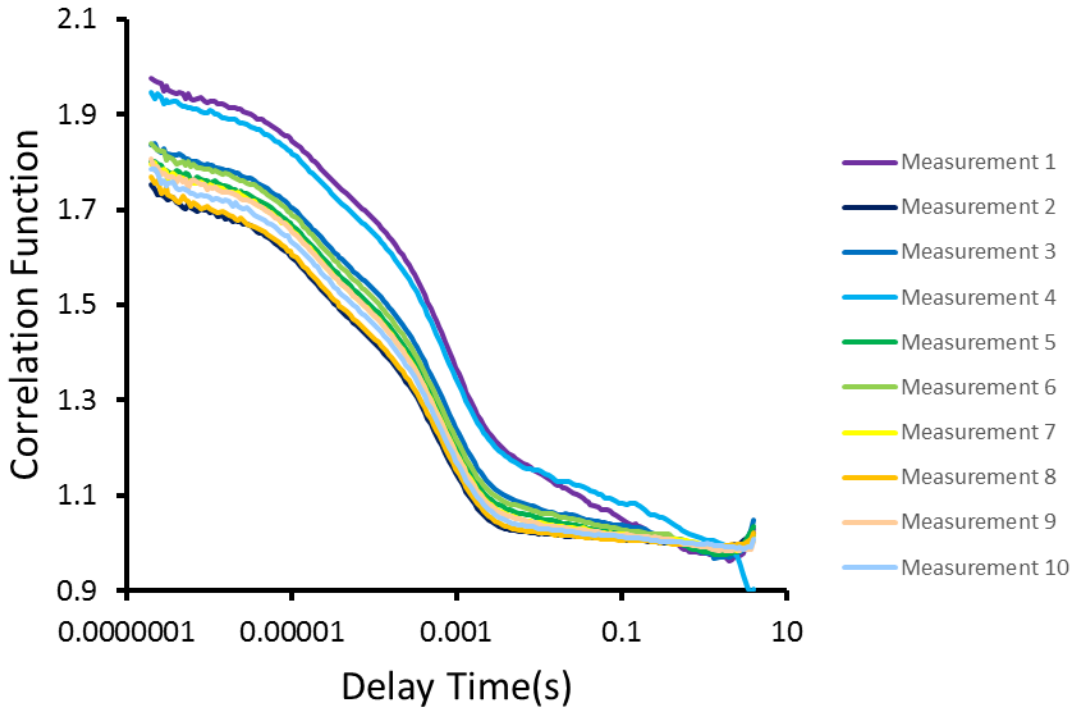

Figure S261 – Correlation function data for 10 DLS runs of SSA **82** (5.56 mM) in an EtOH:H2O (1:19) solution at 298 K.

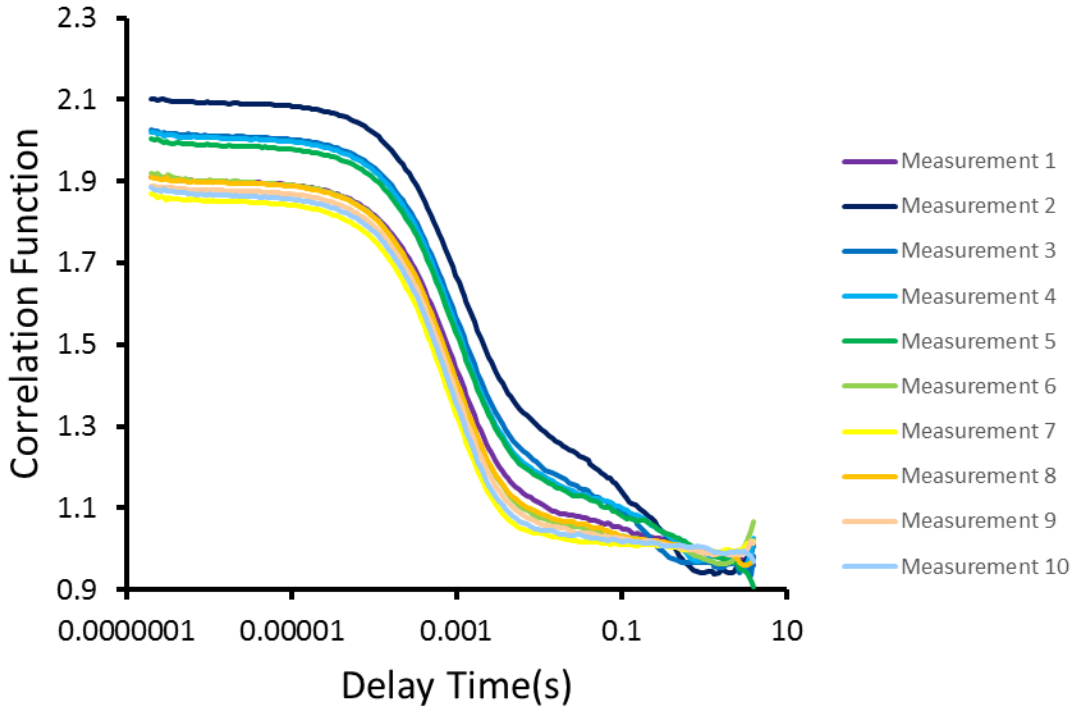

Figure S262 – Correlation function data for 10 DLS runs of SSA **83** (0.56 mM) in an EtOH:H2O (1:19) solution at 298 K.

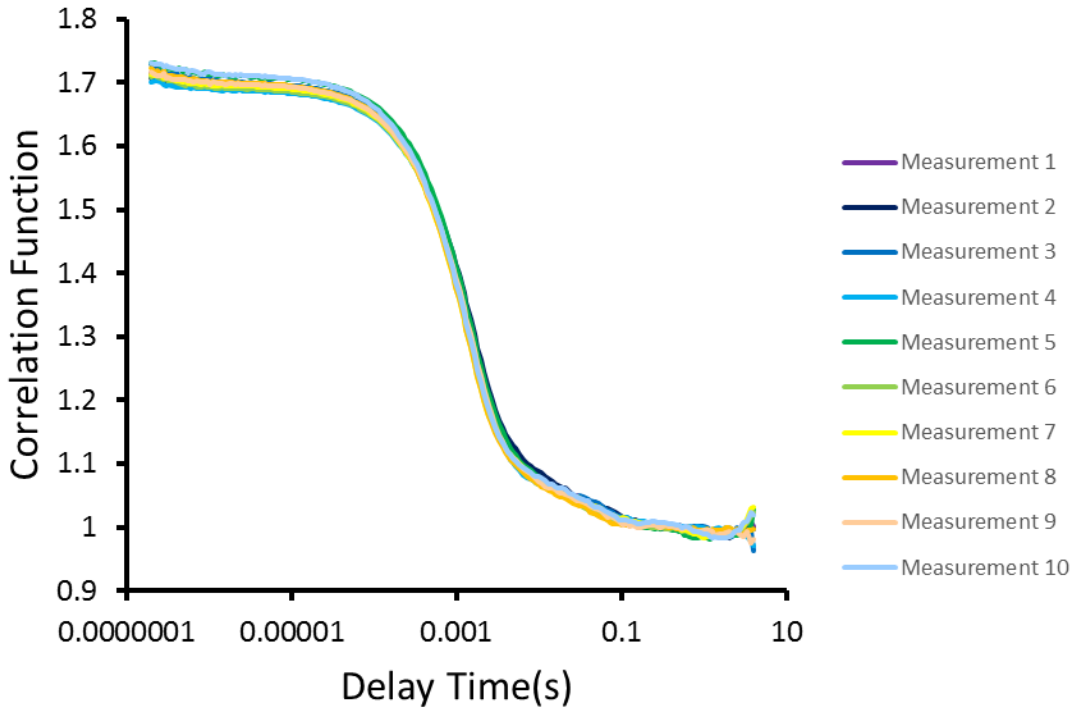

Figure S263 – Correlation function data for 10 DLS runs of SSA **83** (5.56 mM) in an EtOH:H2O (1:19) solution at 298 K.

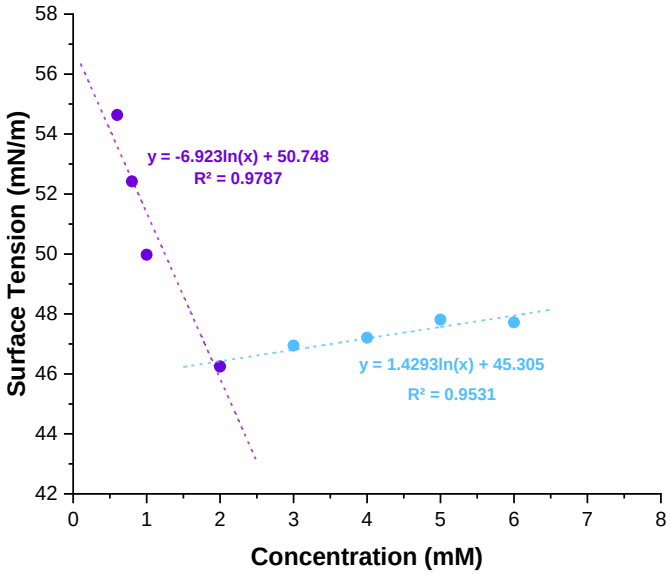

Figure S264 – Calculation of CMC (28.95 mM) for SSA **82** in an EtOH: H2O 1:19 mixture using surface tension measurements.

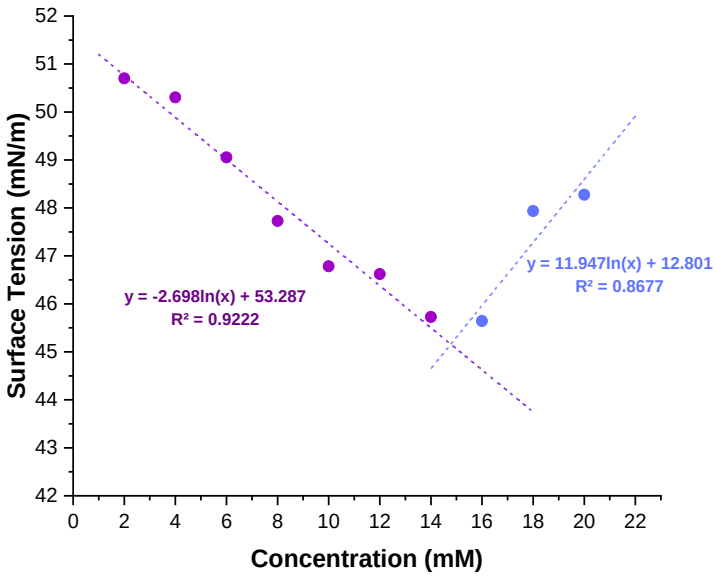

Figure S265 – Calculation of CMC (28.95 mM) for SSA **83** in an EtOH: H2O 1:19 mixture using surface tension measurements.

Gelation studies

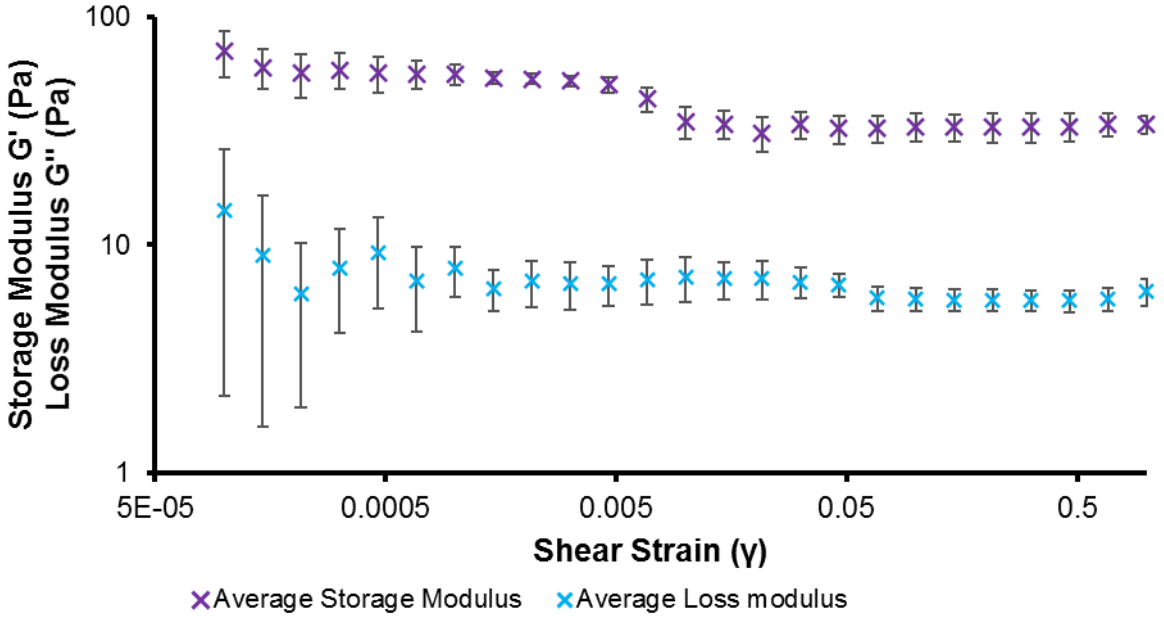

Figure S266 – Results of the amplitude sweep experiments. For SSA **82** in the presence of NaCl (0.505 M).

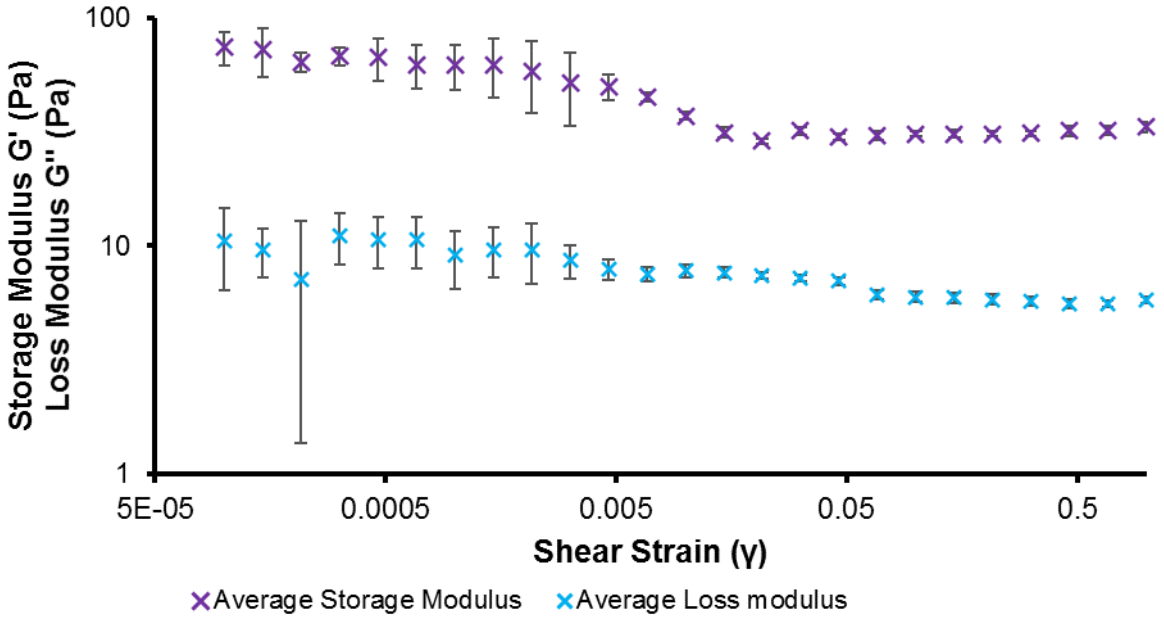

Figure S267 – Results of the amplitude sweep experiments. For SSA **82** in the presence of KCl (0.505 M).

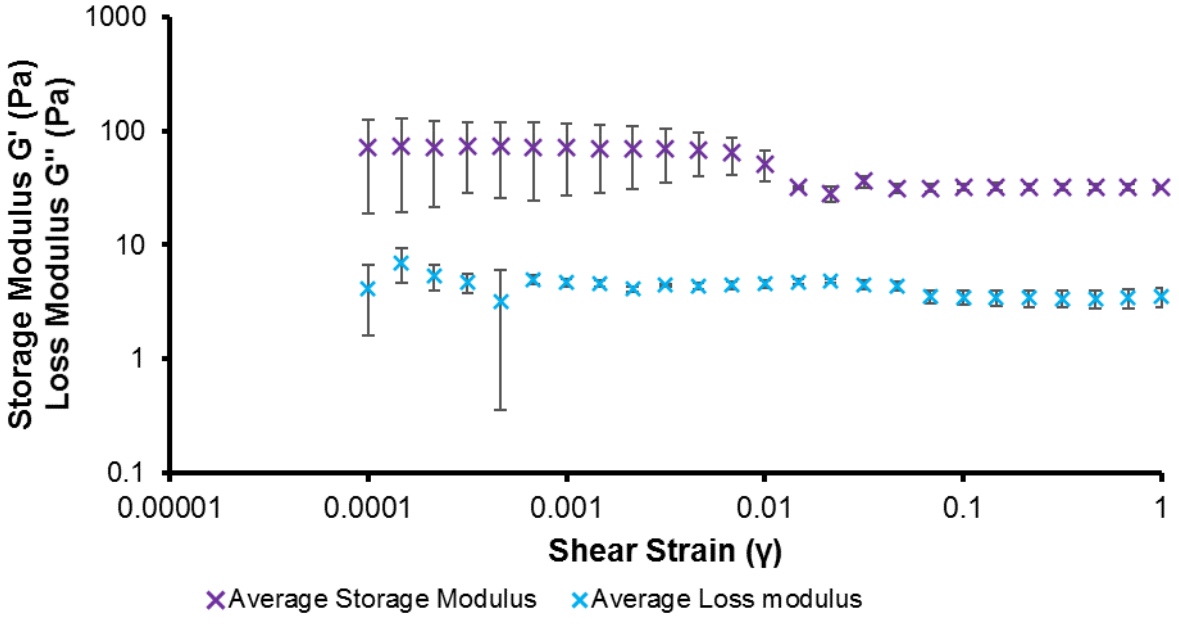

Figure S268 – Results of the amplitude sweep experiments. For SSA **82** in the presence of NaH_2PO_4 (0.505 M).

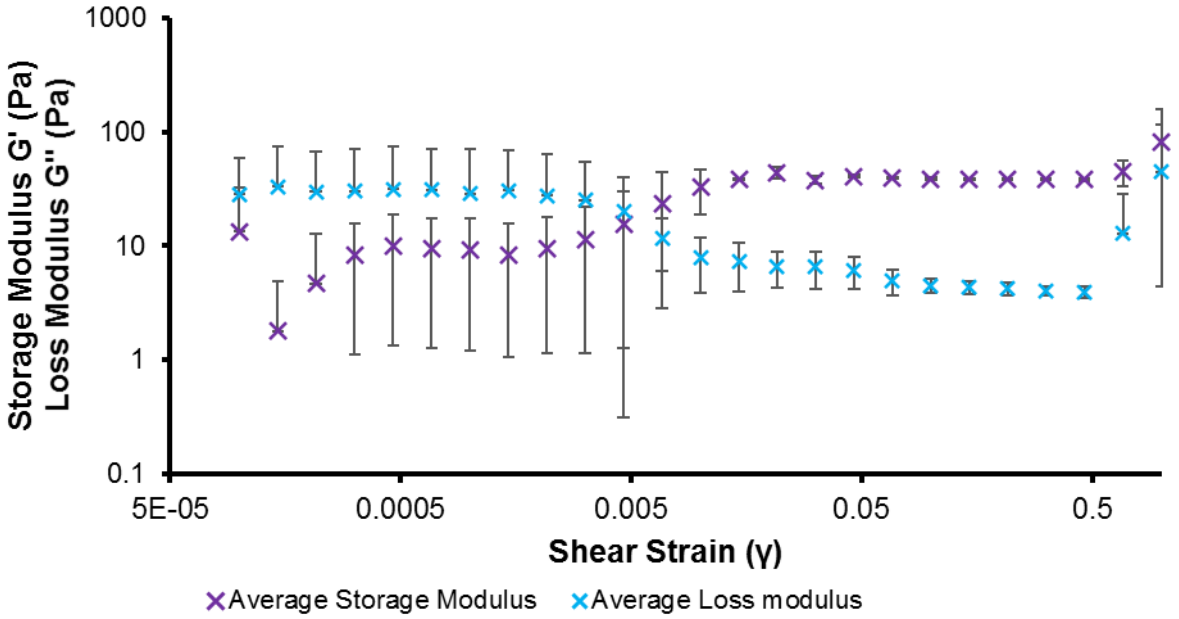

Figure S269 – Results of the amplitude sweep experiments. For SSA **82** in the presence of Na_2SO_4 (0.505 M). Sol to gel transition likely caused by experimental conditions.

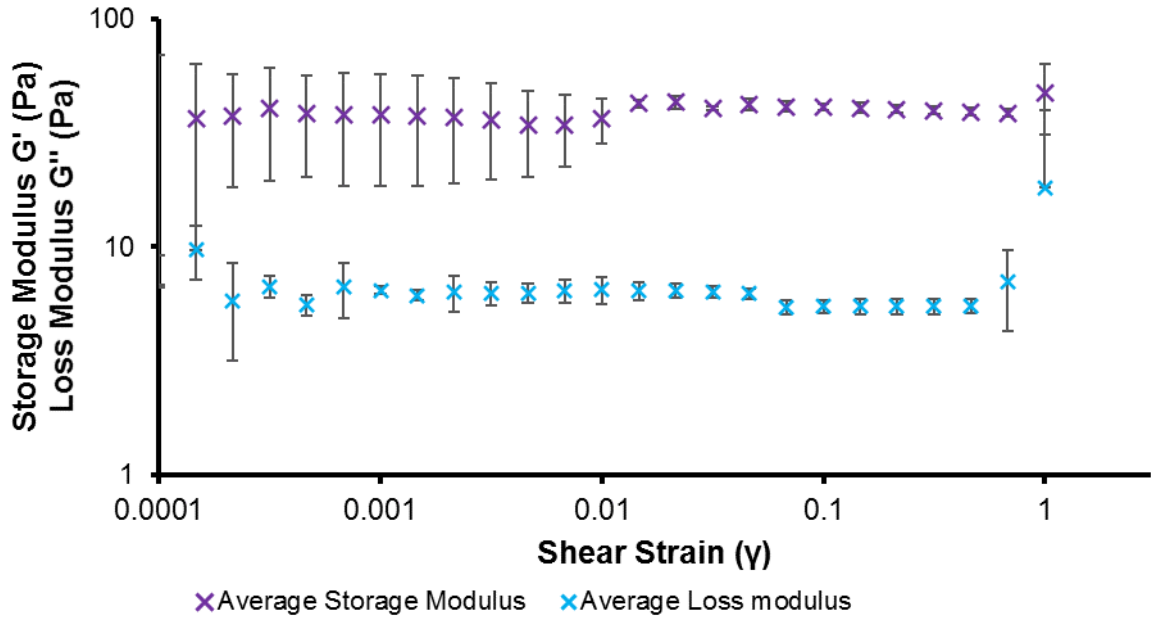

Figure S270 – Results of the amplitude sweep experiments. For SSA **82** in the presence of $NaNO_3$ (0.505 M).

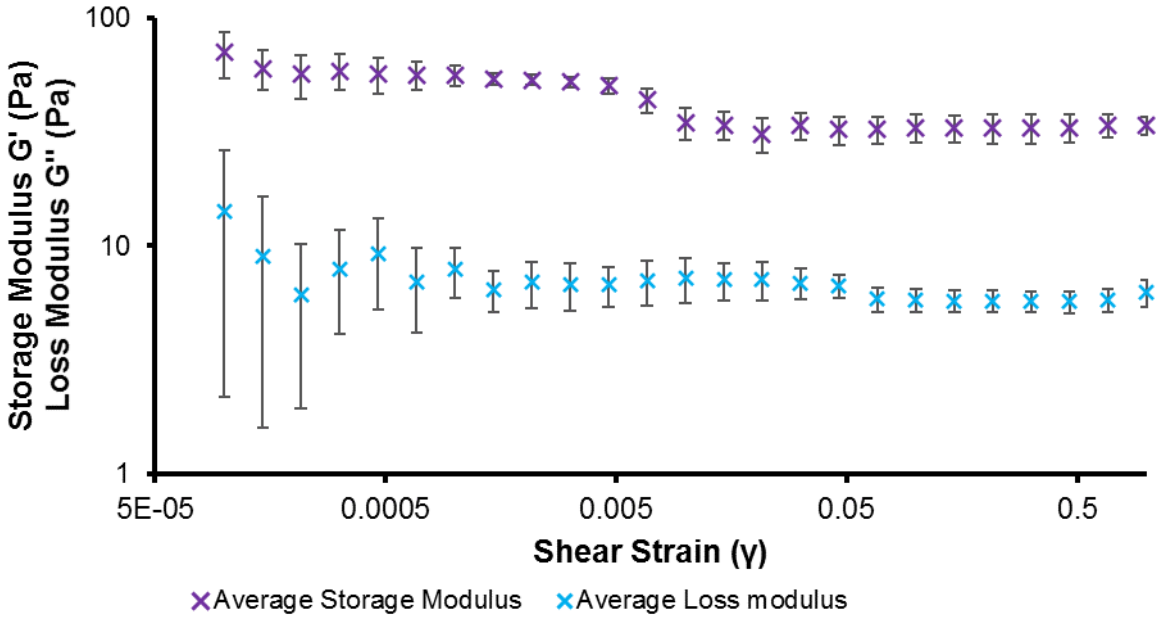

Figure S271 – Results of the amplitude sweep experiments. For SSA **82** in the presence of NaCl (0.505 M)

Figure S272 – SSA **82**(5 mg/mL) inversion test in the presence of NaCl (0.505 M).

Figure S273 – SSA **82**(5 mg/mL) inversion test in the presence of KCl (0.505 M).

Figure S274 – SSA **82**(5 mg/mL) inversion test in the presence of NaH_2PO_4 (0.505 M).

Figure S275 – SSA **82**(5 mg/mL) inversion test in the presence of Na_2SO_4 (0.505 M).

Figure S276 – SSA **82**(5 mg/mL) inversion test in the presence of $NaNO_3$ (0.505 M).

Figure S277 – SSA **82**(5 mg/mL) inversion test in the presence of NaOBz (0.505 M).

Figure S278 – SSA **83** (5 mg/mL) inversion test in the presence of NaCl (0.505 M).

Figure S279 – SSA **83** (5 mg/mL) inversion test in the presence of KCl (0.505 M).

Figure S280 – SSA **83** (5 mg/mL) inversion test in the presence of NaH_2PO_4 (0.505 M).

Figure S281 – SSA **83** (5 mg/mL) inversion test in the presence of Na_2SO_4 (0.505 M).

Figure S282 – SSA **83** (5 mg/mL) inversion test in the presence of $NaNO_3$ (0.505 M).

Figure S283 – SSA **83** (5 mg/mL) inversion test in the presence of NaOBz (0.505 M).

Antimicrobial gel plates: second generation SSAs

Figure S284 – Surface diffusion assay using the SSA **82** (5 mg/mL) gel on *E. coli* inoculated agar plates.

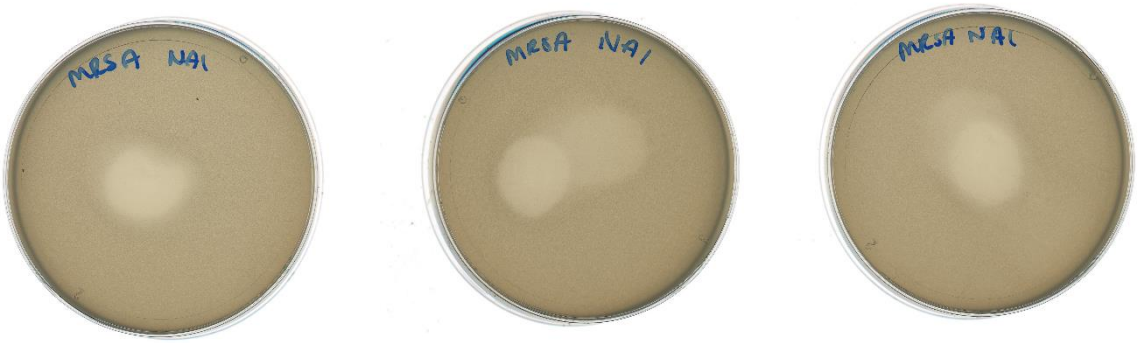

Figure S285 – Surface diffusion assay using the SSA **82** (5 mg/mL) gel on MRSA inoculated agar plates.

Figure S286 – Surface diffusion assay using the SSA **83** (5 mg/mL) gel on *E. coli* inoculated agar plates.

Figure S287 – Surface diffusion assay using the SSA **83** (5 mg/mL) gel on MRSA inoculated agar plates.

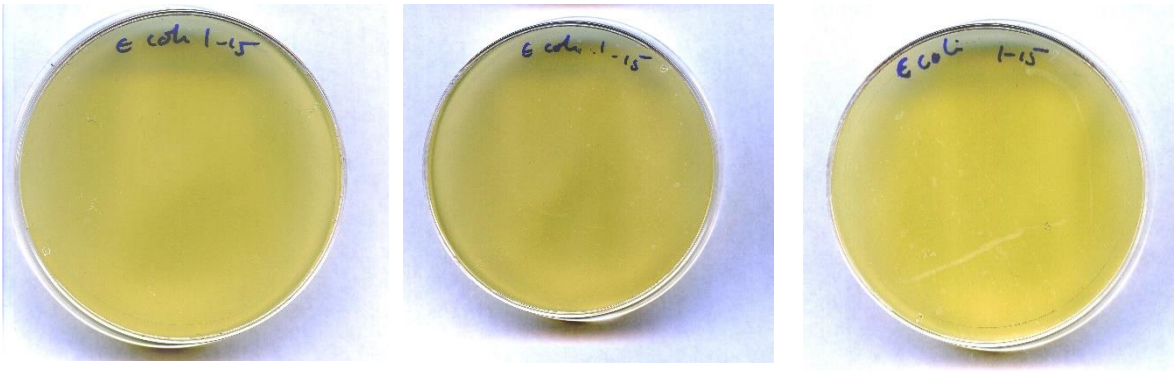

Figure S288 – Surface diffusion assay using the SSA 85 (5 mg/mL) gel on MRSA inoculated agar plates.

Figure S289 – Surface diffusion assay using the SSA 85 (5 mg/mL) gel on *E. coli* inoculated agar plates.

Lengths of gel fibres used to determine long and short strands

Table 39. [a] = larger than field of view, [b] = unable to discern individual fibres, [c] = no gel fibres observed

	length of fibres (µm)		
	82	**83**	**85**
NaCl	19.27 ± 7.43	34.47 ± 13.60	37.83 ± 15.81
KCl	18.98 ± 7.64	9.00 ± 1.52	25.84 ± 13.29
NaNO3	a	b	51.17 ± 28.07
Na2SO4	19.59 ± 12.38	23.79 ± 9.51	a
NaH2PO4	c	c	b
NaOBz	b	a, b	42.60 ± 18.76

Gel fluorescence microscopy images

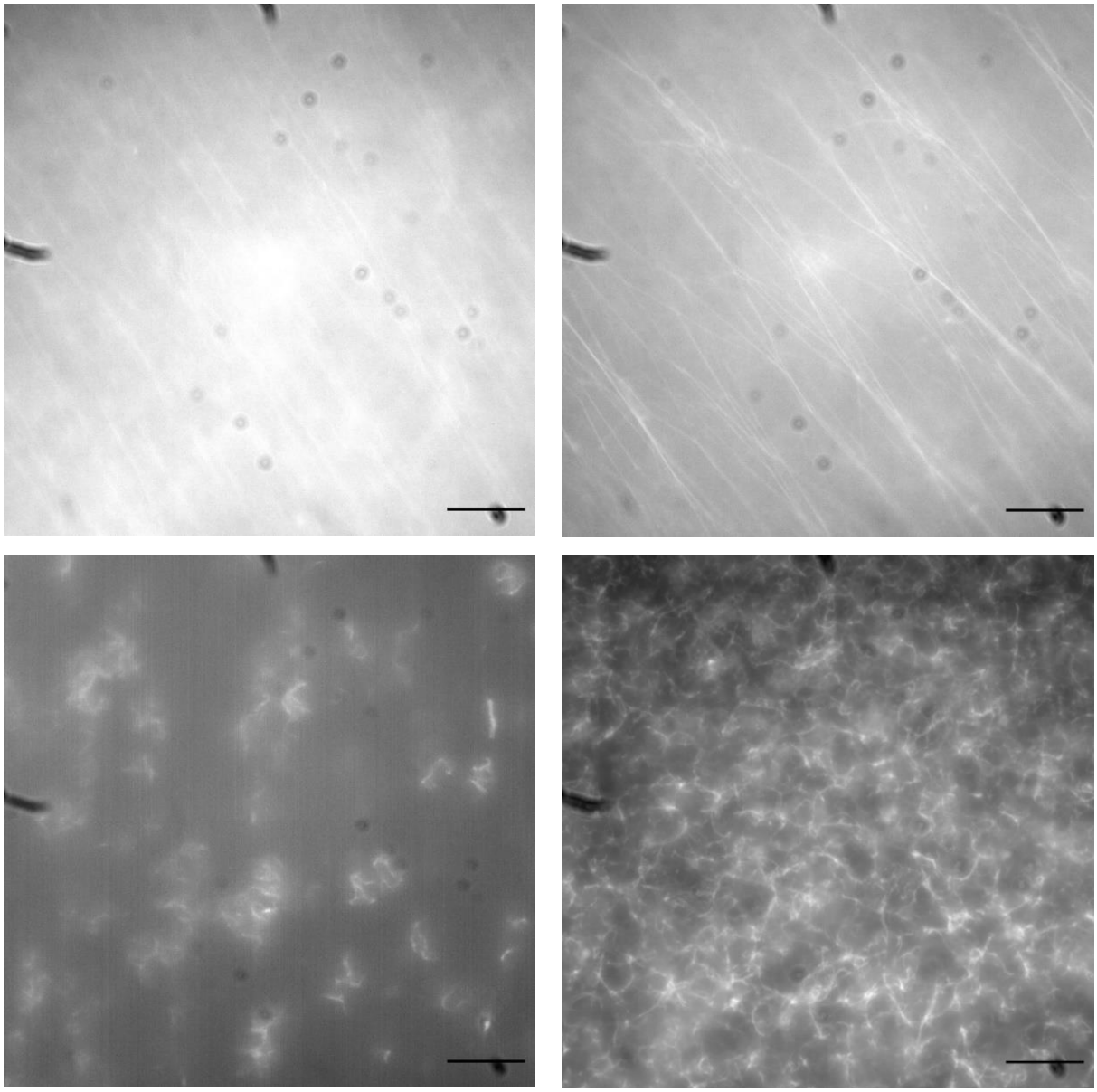

Figure S290. Fluorescence microscopy images showing the gel formation process of SSA **70** (5 mg/ mL) in NaCl (0.505 mM).

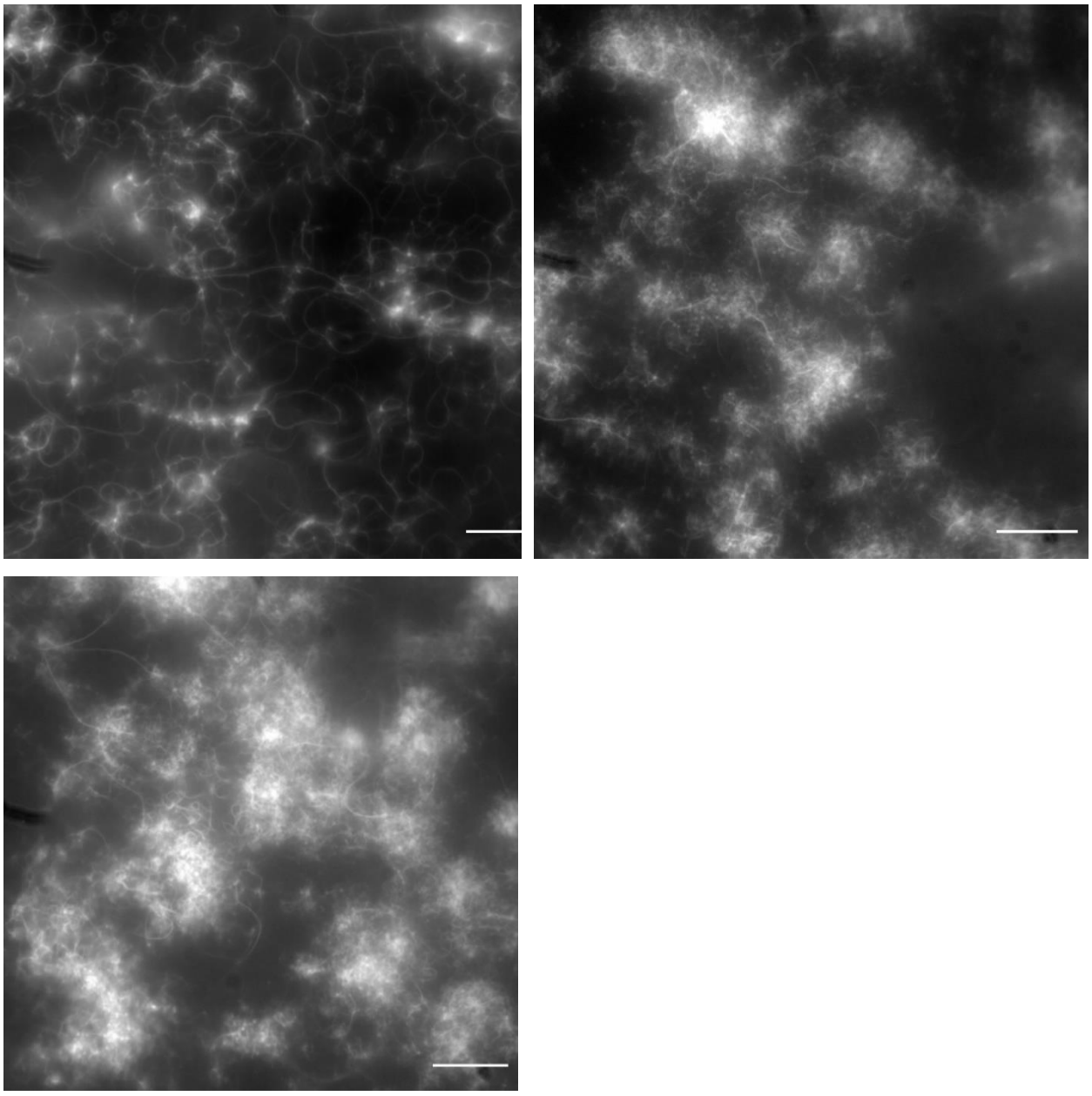

Figure S291 - Fluorescence microscopy images showing the gel formation process of compound **85** (5 mg/ mL) in NaCl (0.505 mM). Majority of strands formed were long, curled, and resultant gel was made up of layers of densely packed curled fibres and layers of loosely packed curled fibres.

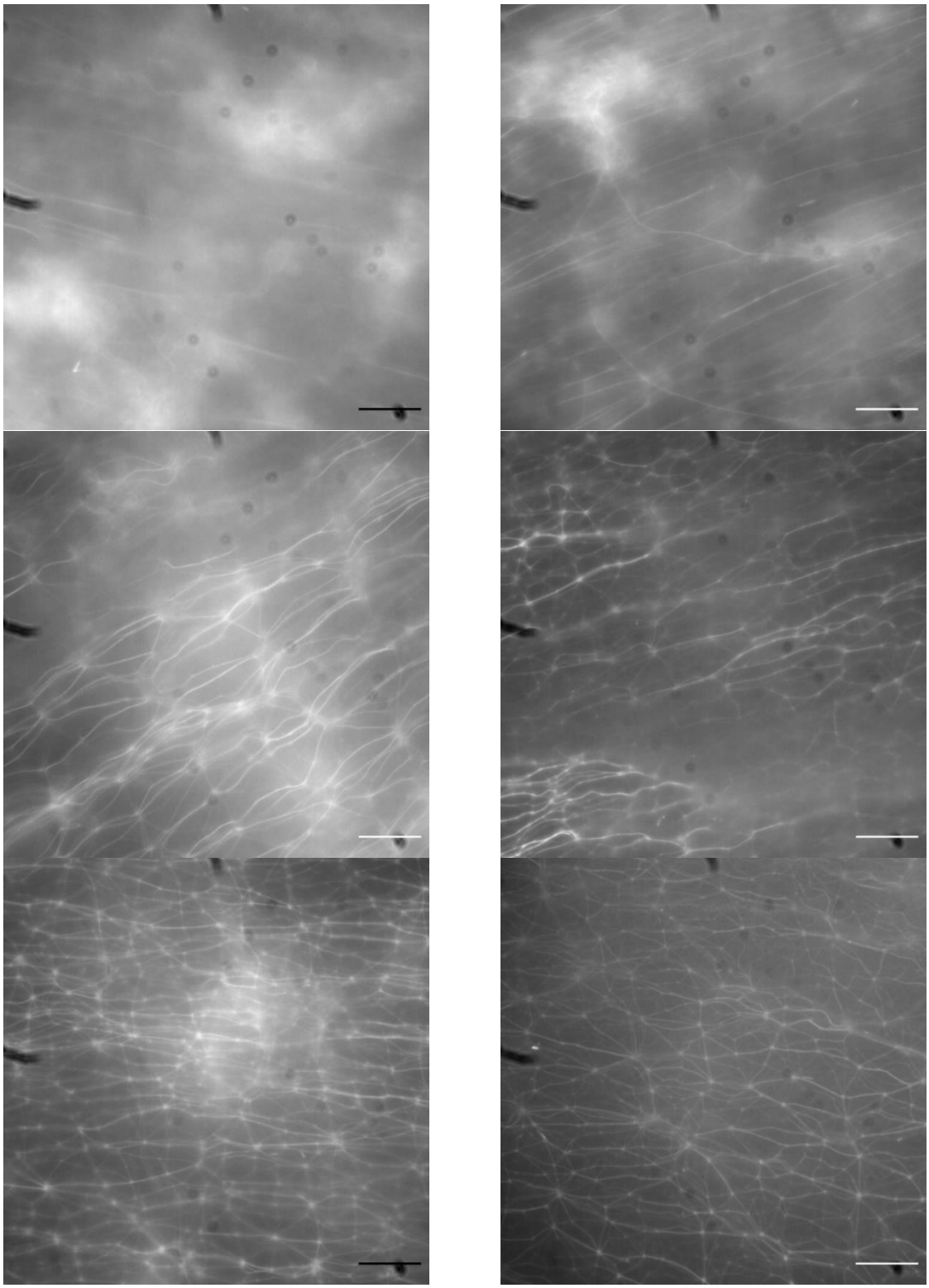

Figure S292 – Fluorescence microscopy images showing the gel formation process of compound **82** (5 mg/ mL) in NaCl (0.505 mM). Long straight strands form initially which then branch off at bright spots (nodes), and pack closer together. The resultant gel is made up of a network of straight, branching fibres.

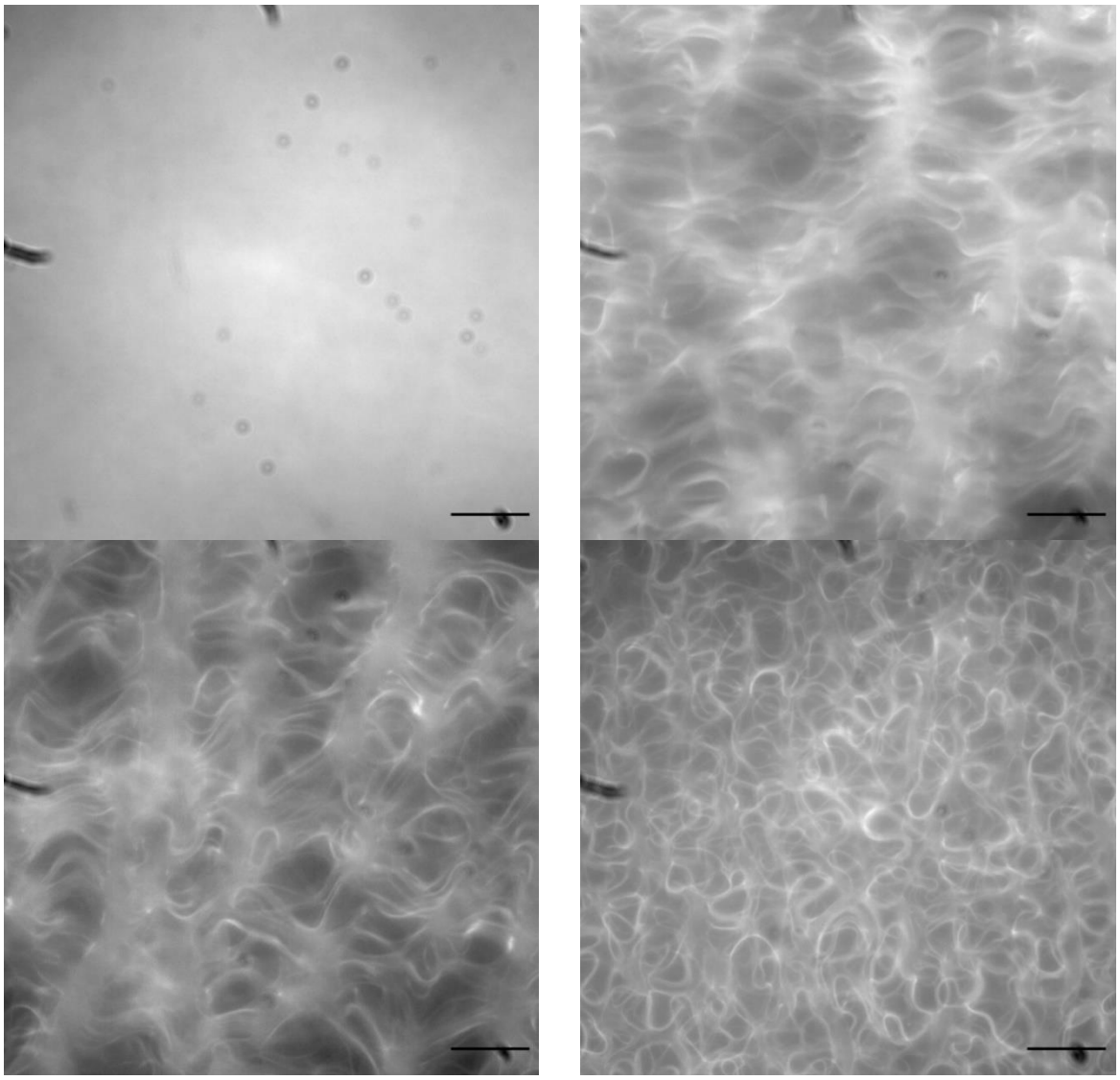

Figure S293 – Fluorescence microscopy images showing the gel formation process of compound **83** (5 mg/ mL) in NaCl (0.505 mM). Long strands formed and curled as they elongated, multiple strands branched off at bright spots (nodes). Gel fibres then aggregated together. The resultant gel was made up of densely packed non-uniform fibers.

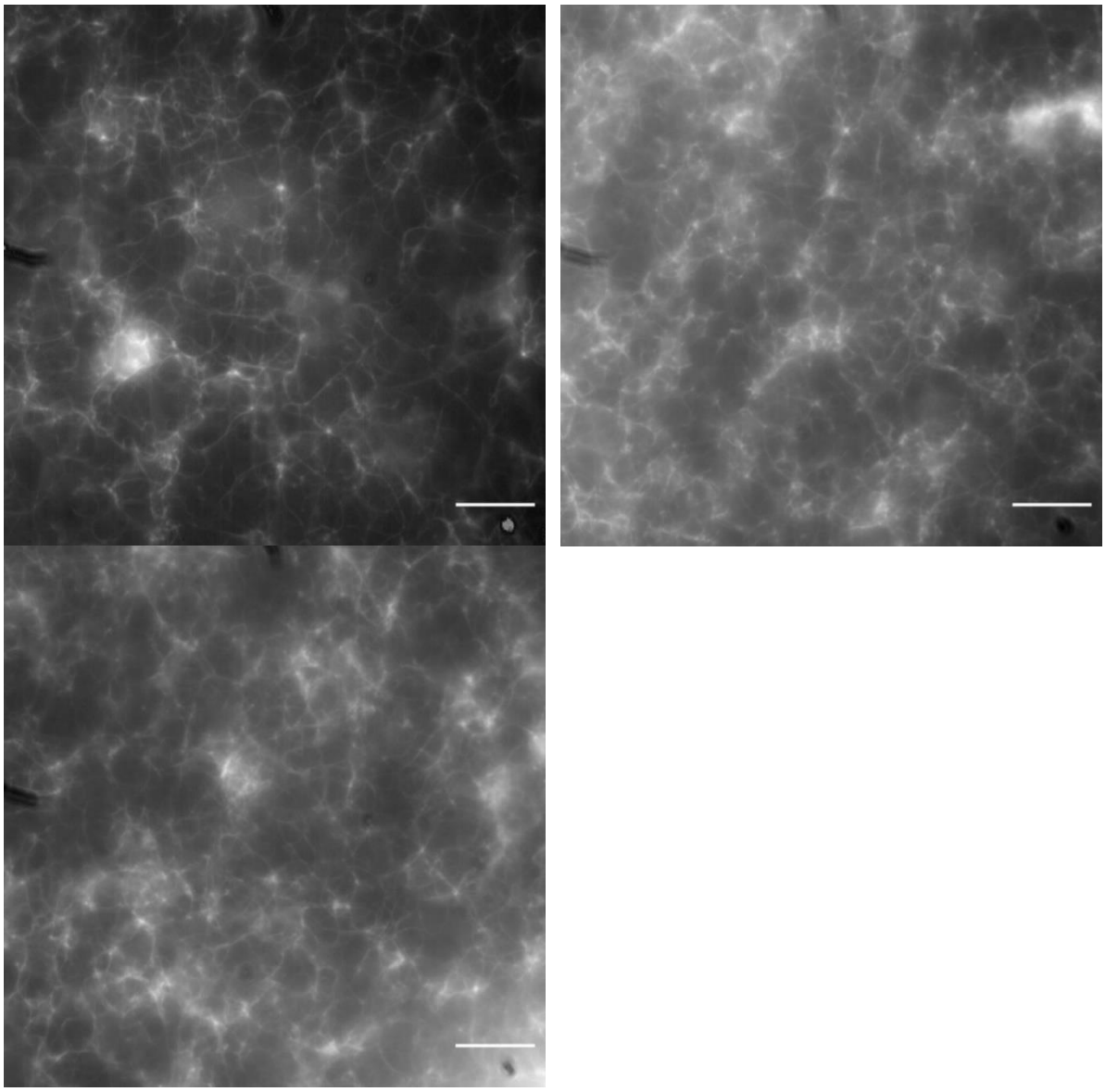

Figure S294 – Fluorescence microscopy images showing the gel formation process of compound **85** (5 mg/ mL) in KCl (0.505 mM). Branching strands, gel made up of long, non-uniform strands with layers that were loosely packed and layers that were more closely packed.

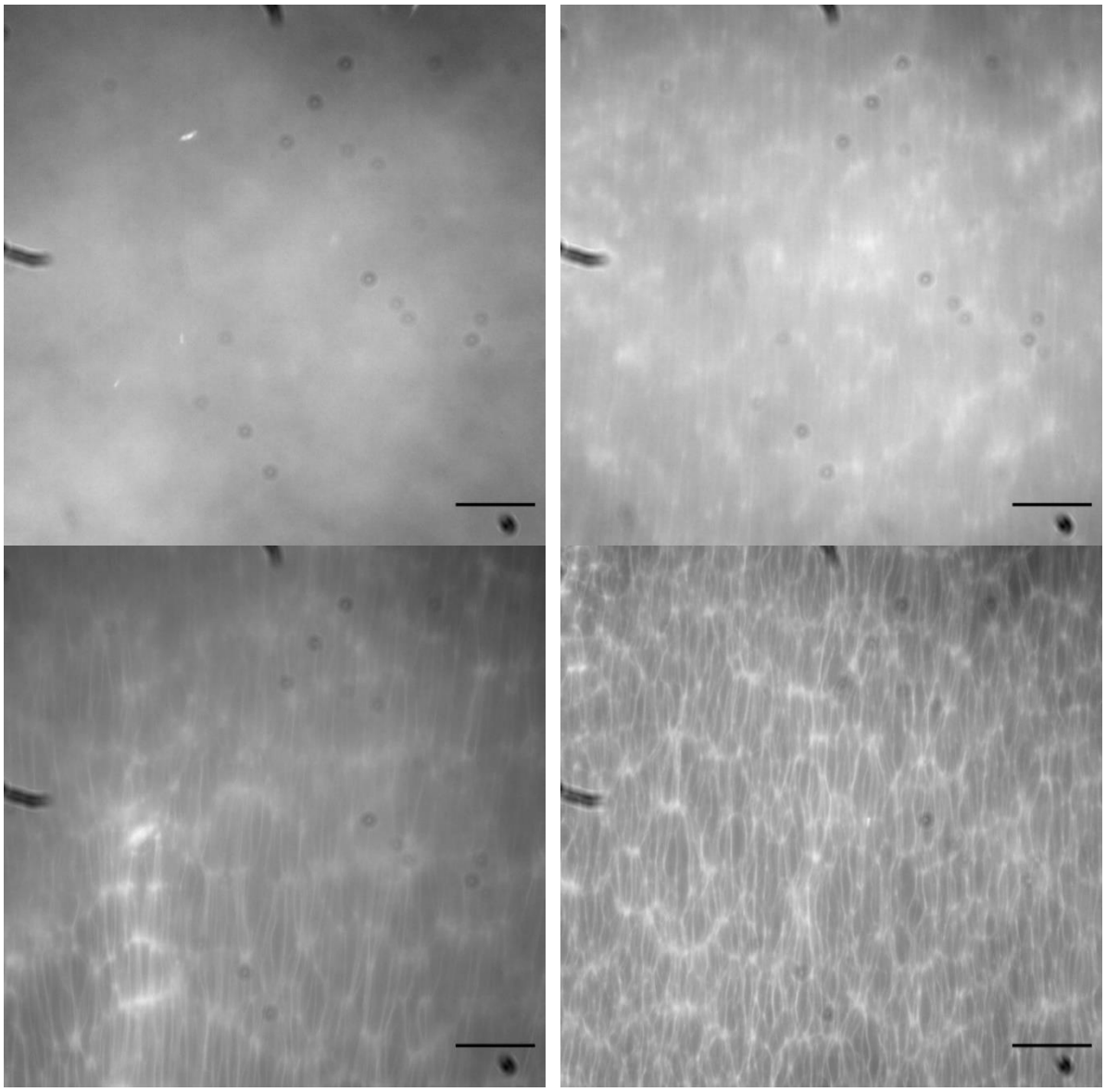

Figure S295 – Fluorescence microscopy images showing the gel formation process of compound **82** (5 mg/ mL) in KCl (0.505 mM). Long unidirectional strands that were straighter and branching/connecting at bright spots

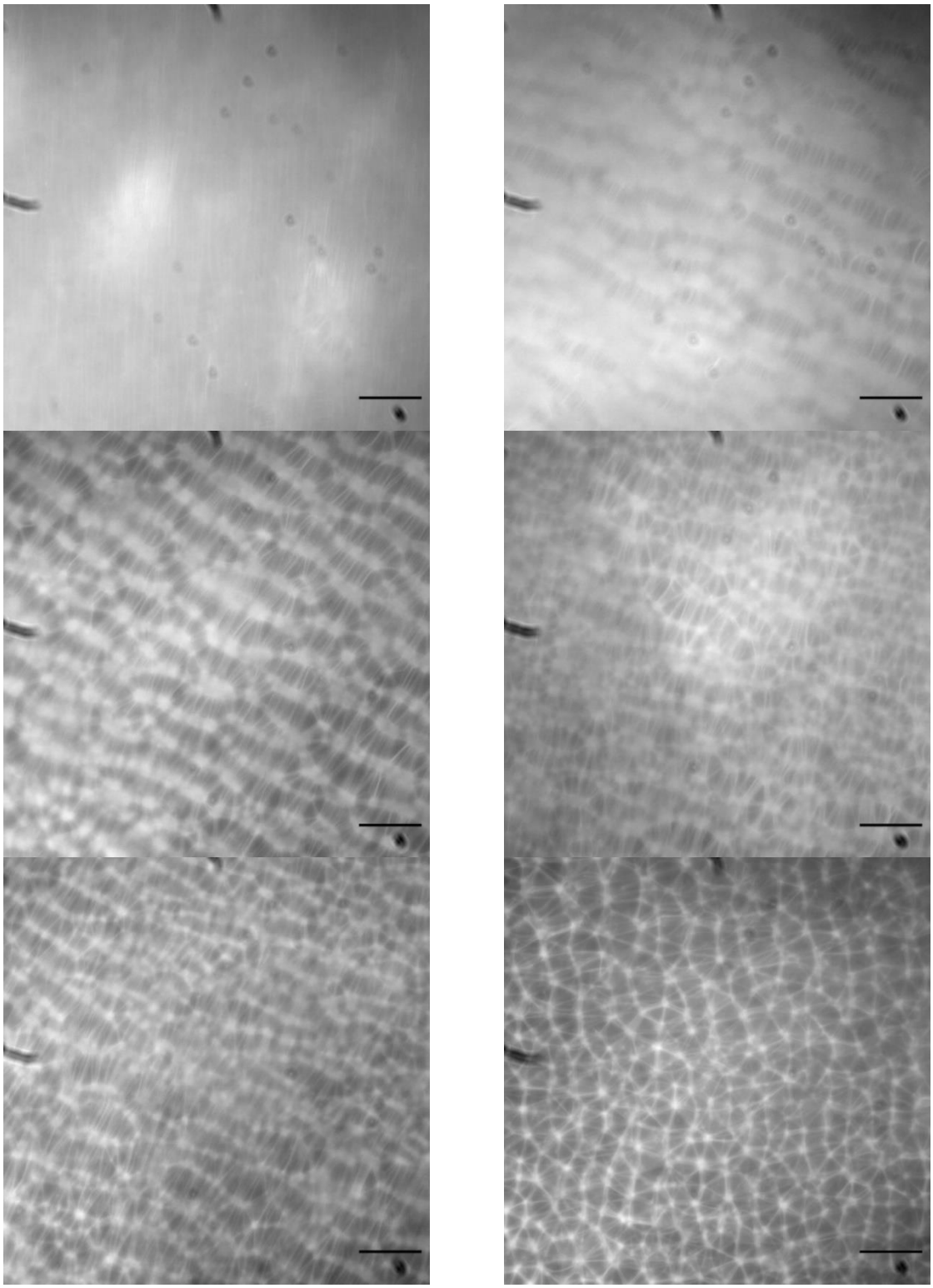

Figure S296 – Fluorescence microscopy images showing the gel formation process of compound **83** (5 mg/ mL) in KCl (0.505 mM). Regions of short straight fibres formed between regions of compound that hadn't formed strands yet. These regions of compound that hadn't formed strands yet became smaller over time, connecting the shorter strands together in multiple directions, resulting in a more geometric 'star' pattern.

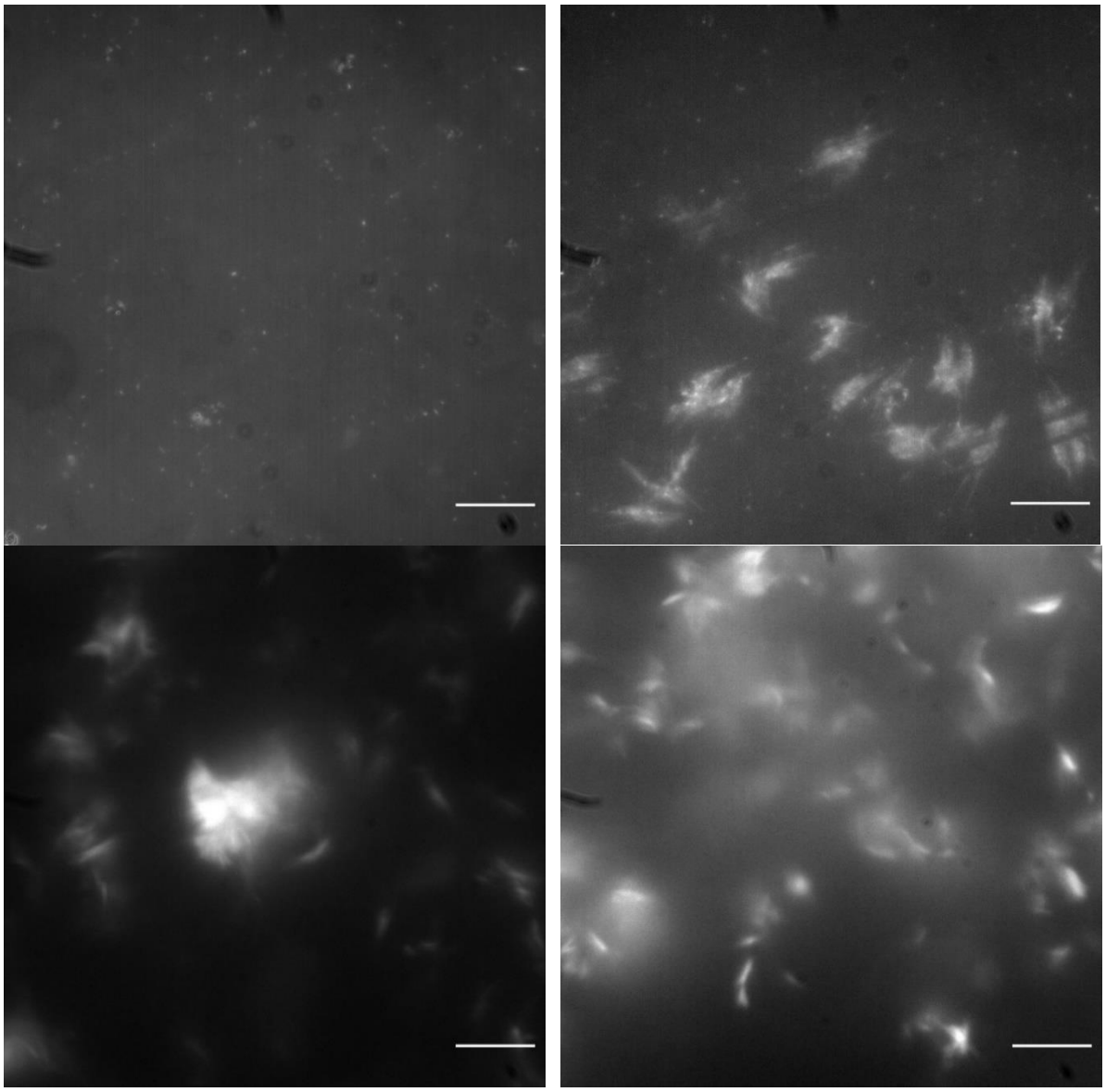

Figure S297 – Fluorescence microscopy images showing the gel formation process of compound **85** (5 mg/ mL) in NaH_2PO_4 (0.505 mM). However, at 5mg/mL, aggregates formed, and the structures formed quickly. Then, small, fragile gel clumps formed which easily broke up and the resulting structures were indiscernible. Due to movement of these clumps. (Some of the last images captured using the NDsnap feature)

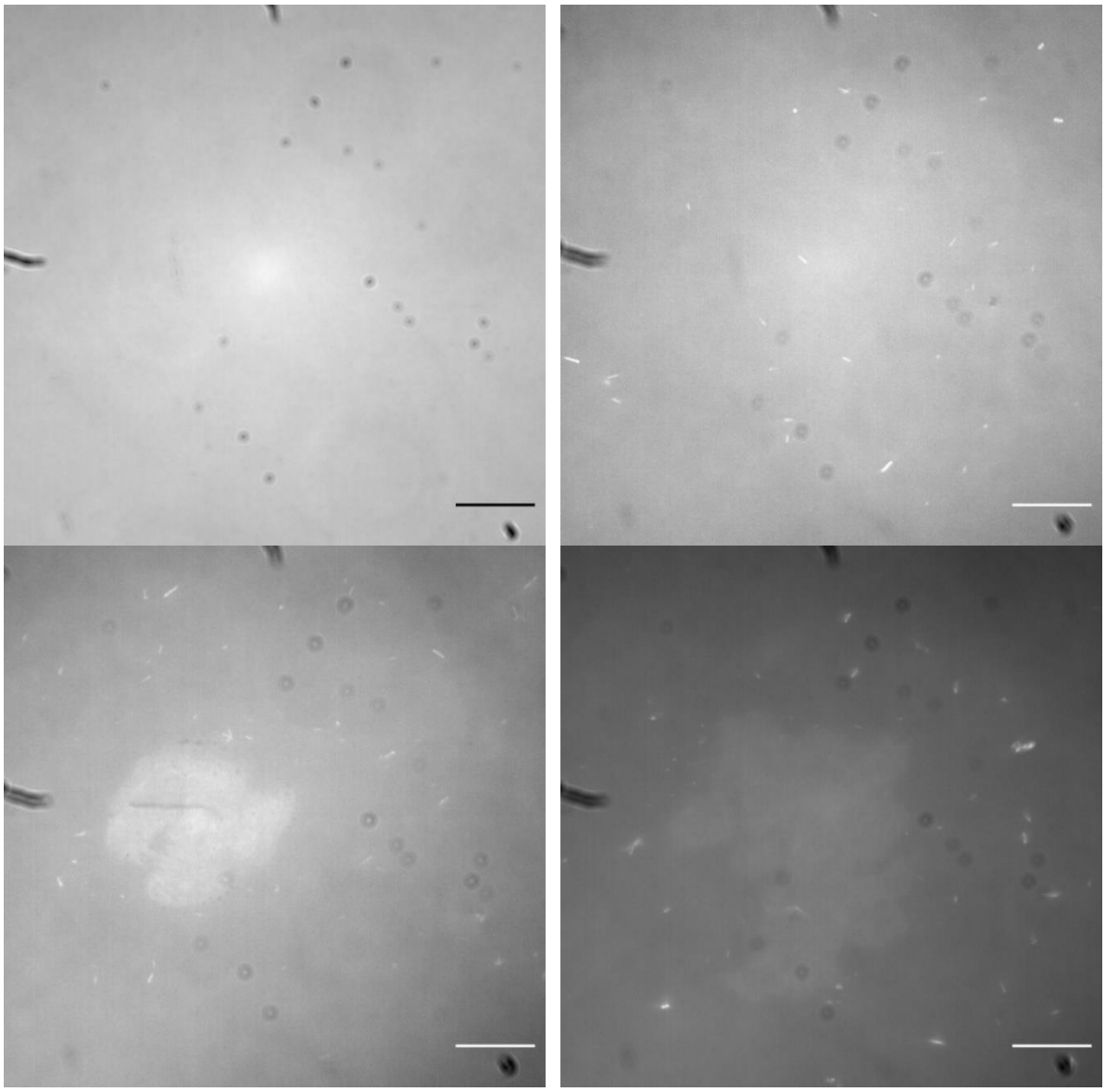

Figure S298 – Fluorescence microscopy images showing the gel formation process of compound **82** (5 mg/ mL) in NaH_2PO_4 (0.505 mM). Small aggregates formed and the larger structures formed, however no gel fibres formed.

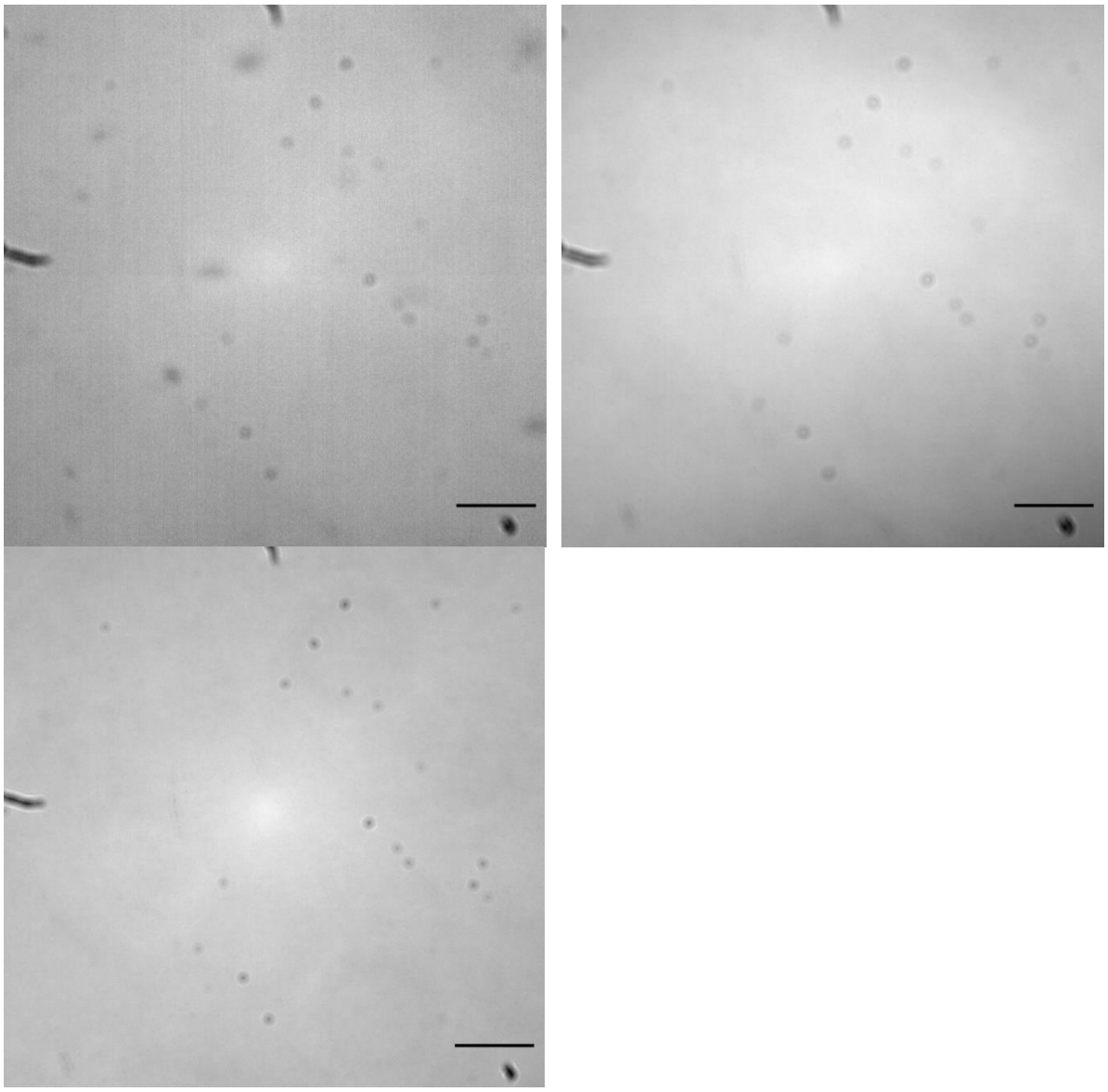

Figure S299 – Fluorescence microscopy images showing the gel formation process of compound **83** (5 mg/ mL) in NaH_2PO_4 (0.505 mM). No gel fibers observed

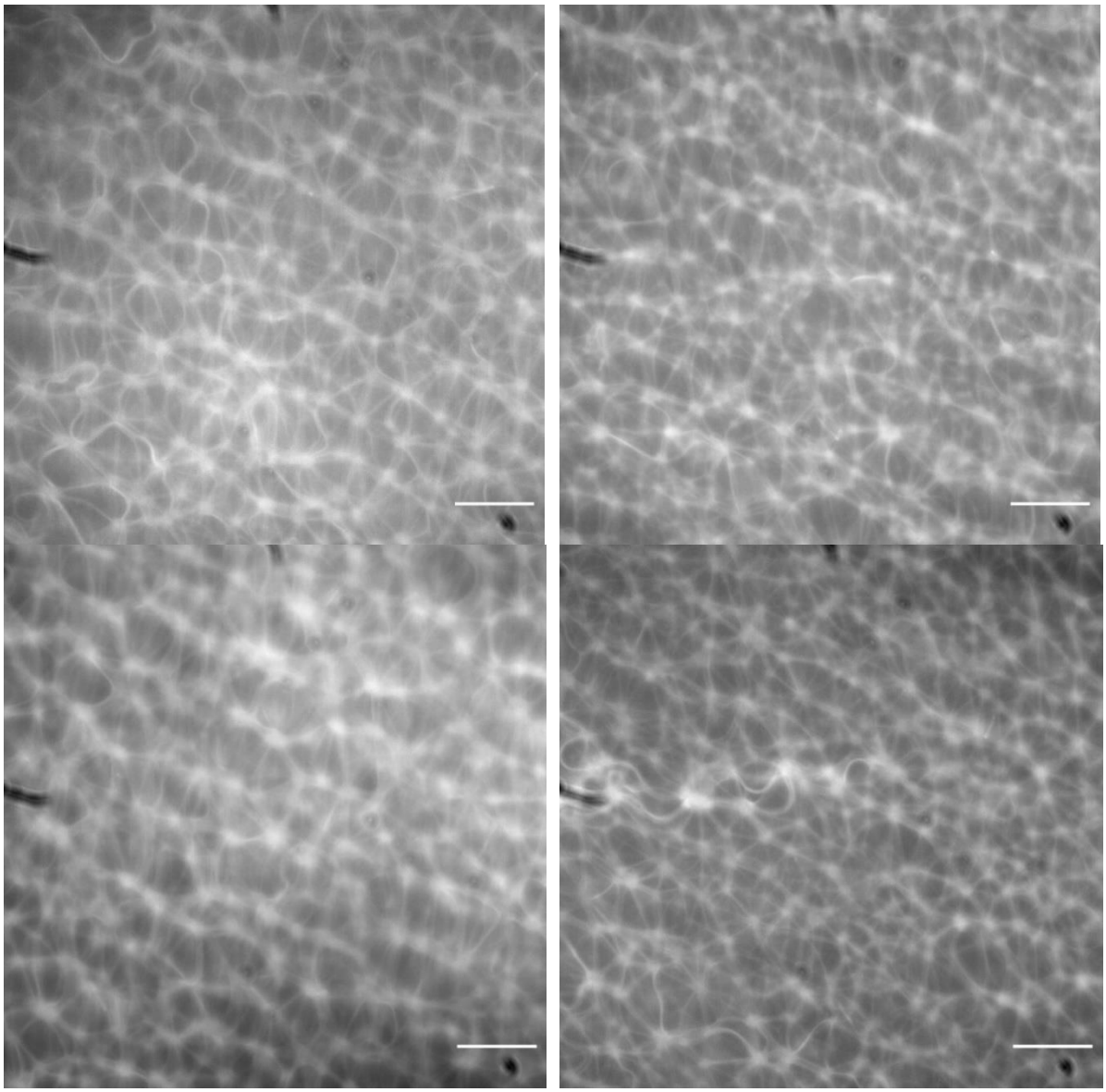

Figure S300 – Fluorescence microscopy images showing the gel formation process of compound **82** (5 mg/ mL) in Na_2SO_4 (0.505 mM). Majority of strands were short straight fibres in a geometric pattern, however random longer curled fibres were also present

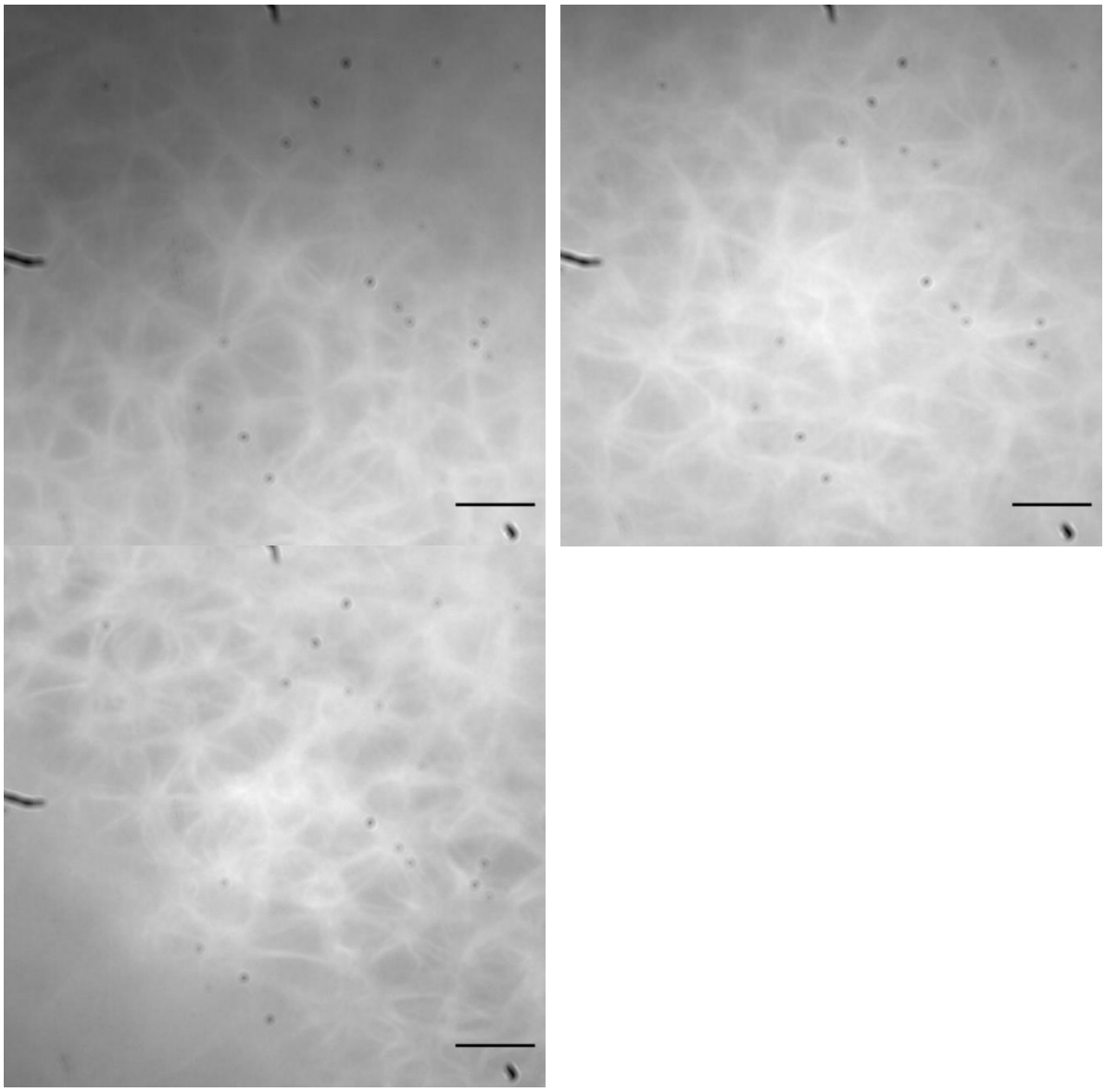

Figure S301 – Fluorescence microscopy images showing the gel formation process of compound **83** (5 mg/ mL) in Na_2SO_4 (0.505 mM). The long, curled strands from earlier form a more geometric pattern later on.

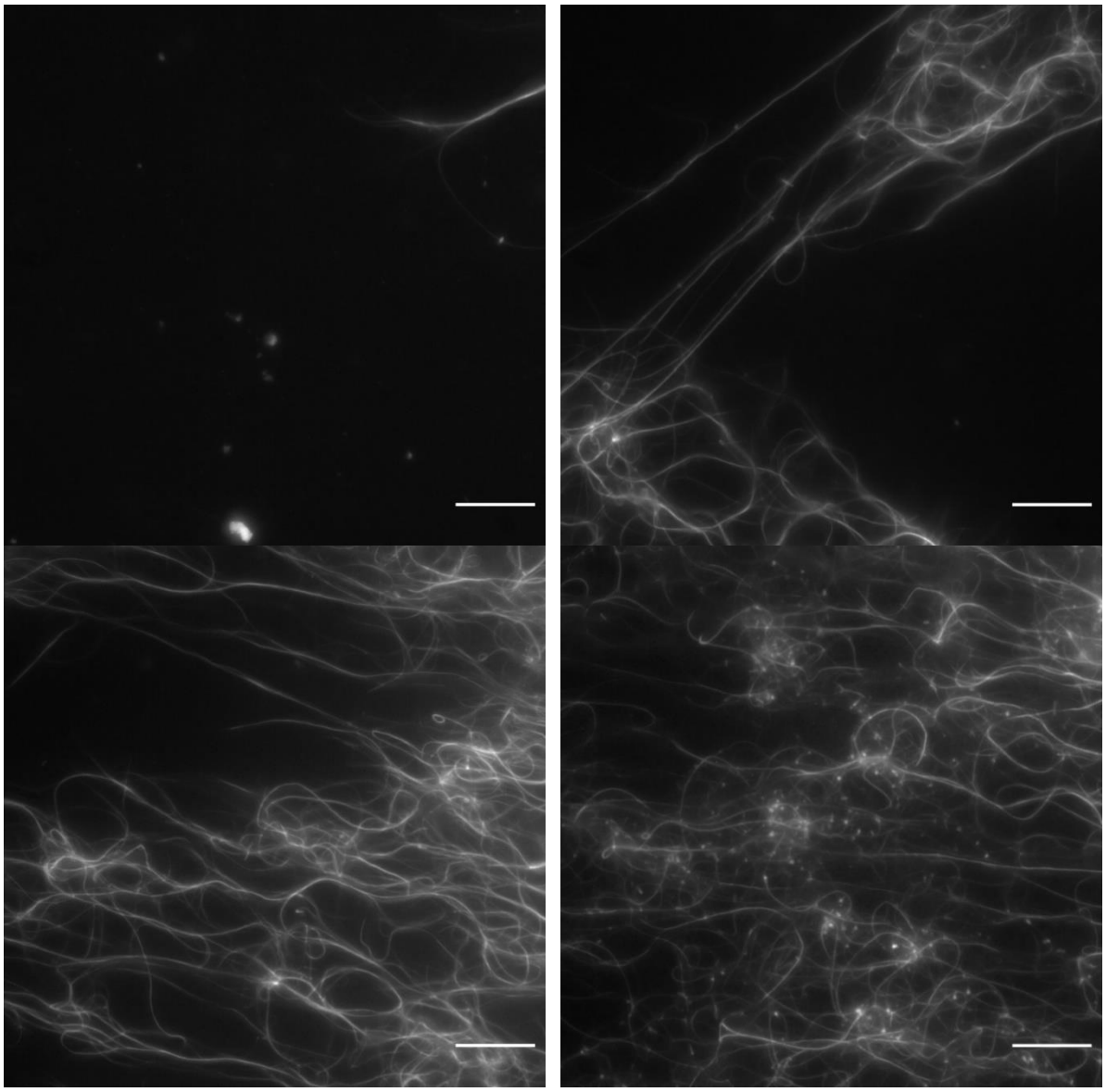

Figure S302 – Fluorescence microscopy images showing the gel formation process of compound **85** (5 mg/ mL) in $NaNO_3$ (0.505 mM). Compound aggregates formed then fibres, potentially using the aggregates to elongate. Resulting gel was made up of loosely packed, long, and curled strands

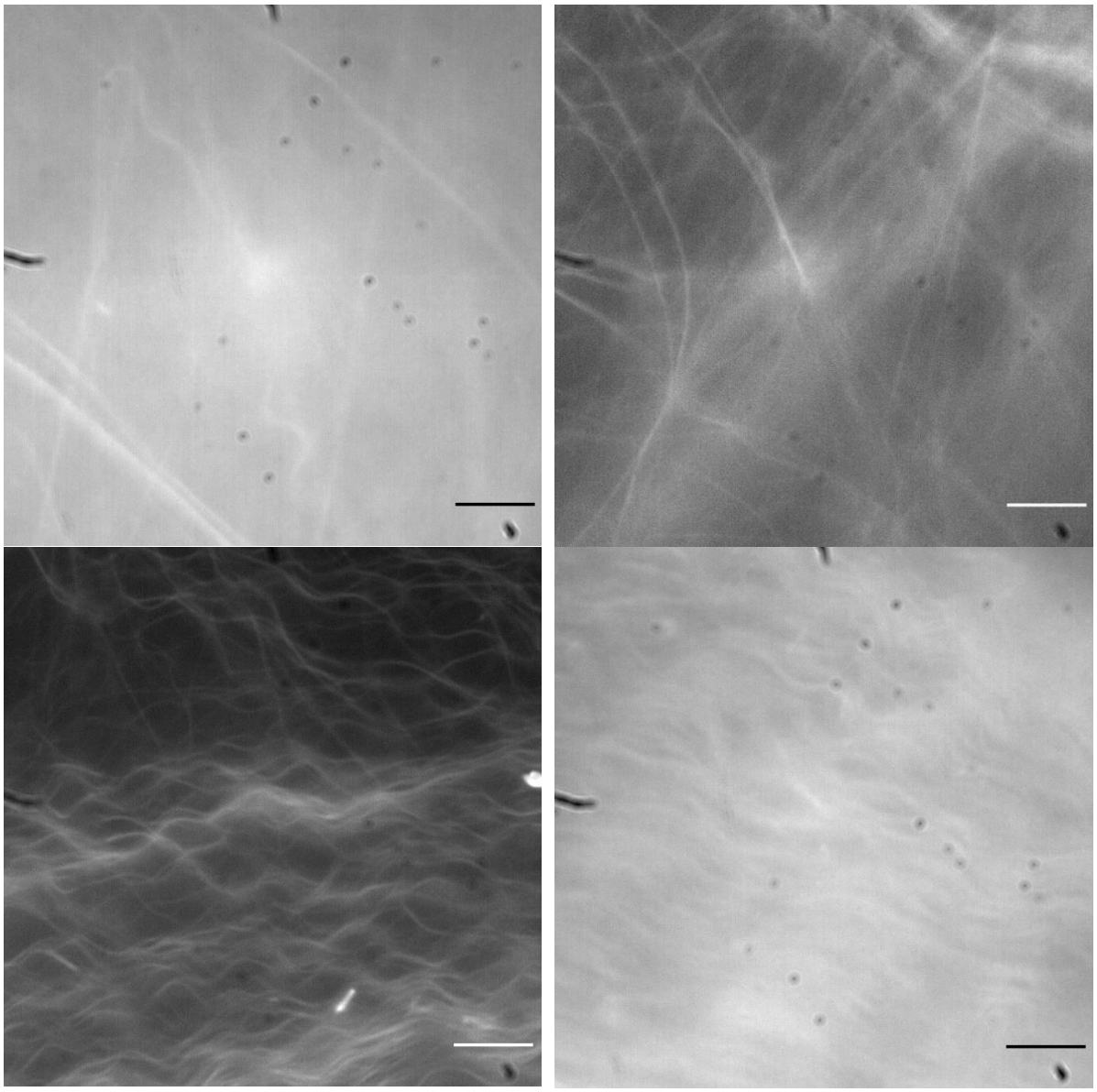

Figure S303 – Fluorescence microscopy images showing the gel formation process of compound **82** (5 mg/ mL) in $NaNO_3$ (0.505 mM). The final gel was made up of regions of densely packed gel fibres and regions of solvent. The resulting gel also ‘floated’ within the solvent.

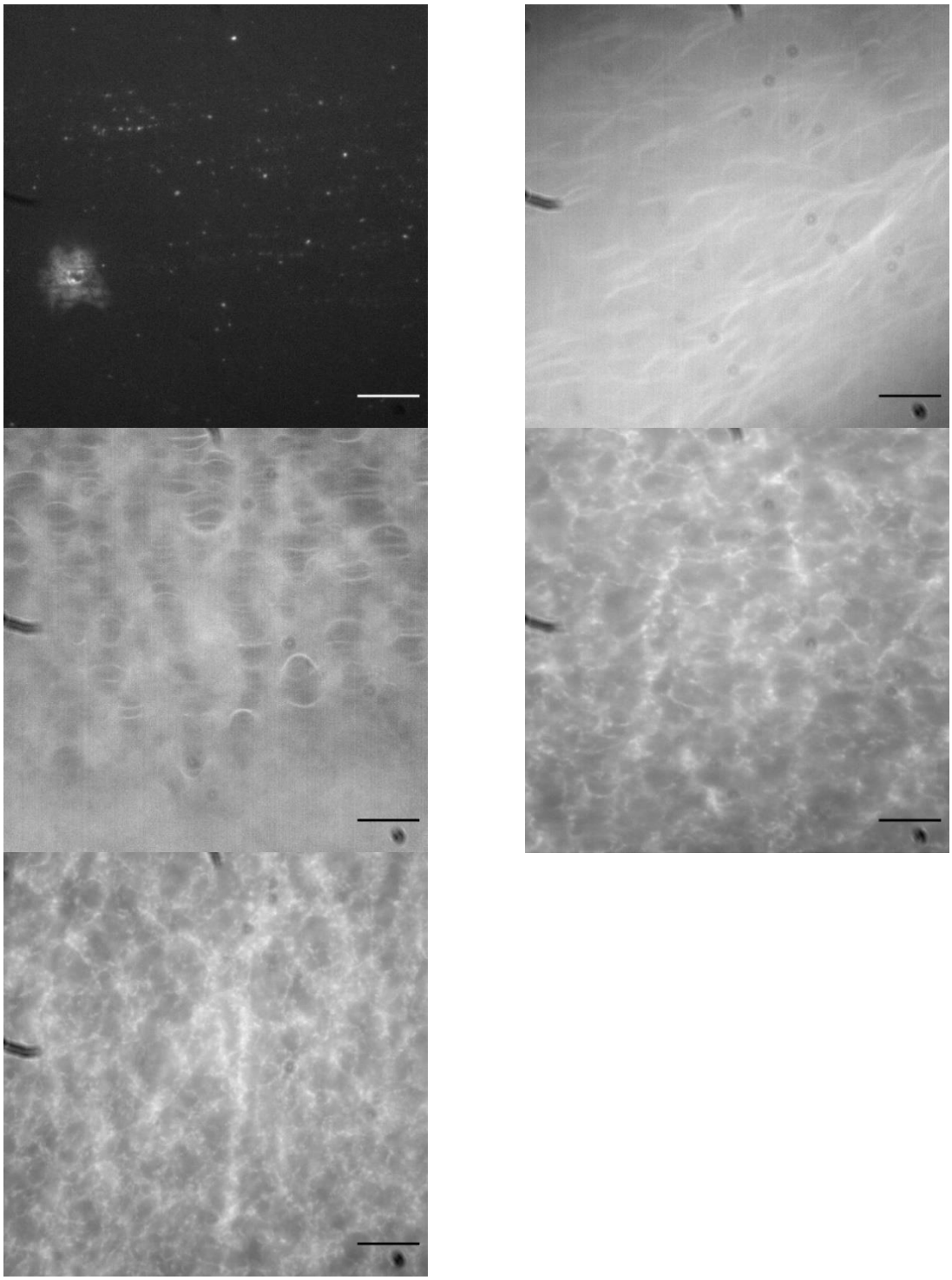

Figure S304 – Fluorescence microscopy images showing the gel formation process of compound **83** (5 mg/ mL) in $NaNO_3$ (0.505 mM). Initial aggregates, then short straight strands formed. The strands got longer, and as they were elongated, they began to curl into themselves. Aggregated together in an almost cross-hatched manner and became more and more densely packed

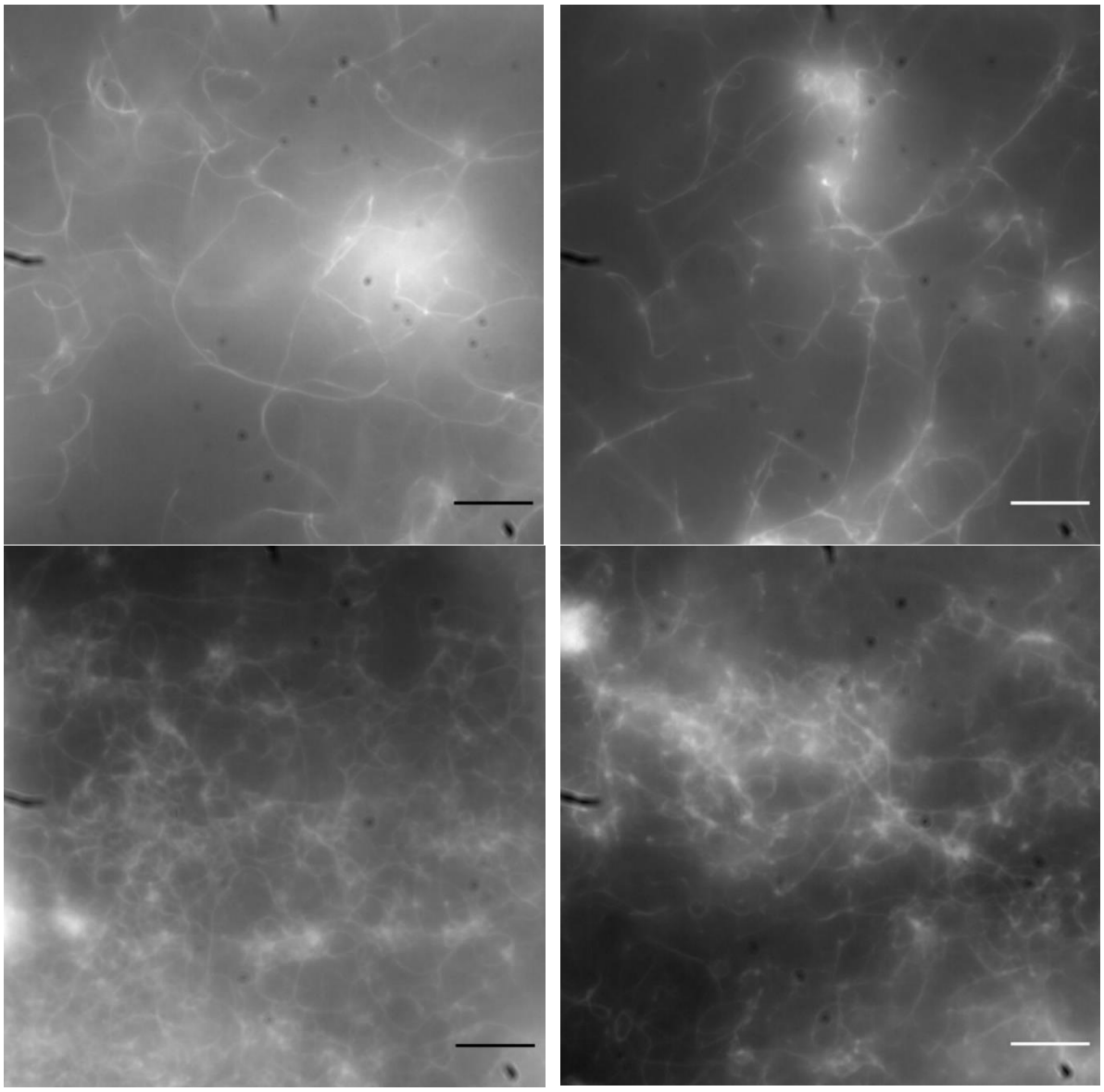

Figure S305 – Fluorescence microscopy images showing the gel formation process of compound **85** (5 mg/ mL) in NaOBz (0.505 mM). Strands formed quickly from bright spots (aggregates) and randomly. Resulting gel was made up of densely packed disorganised strands.

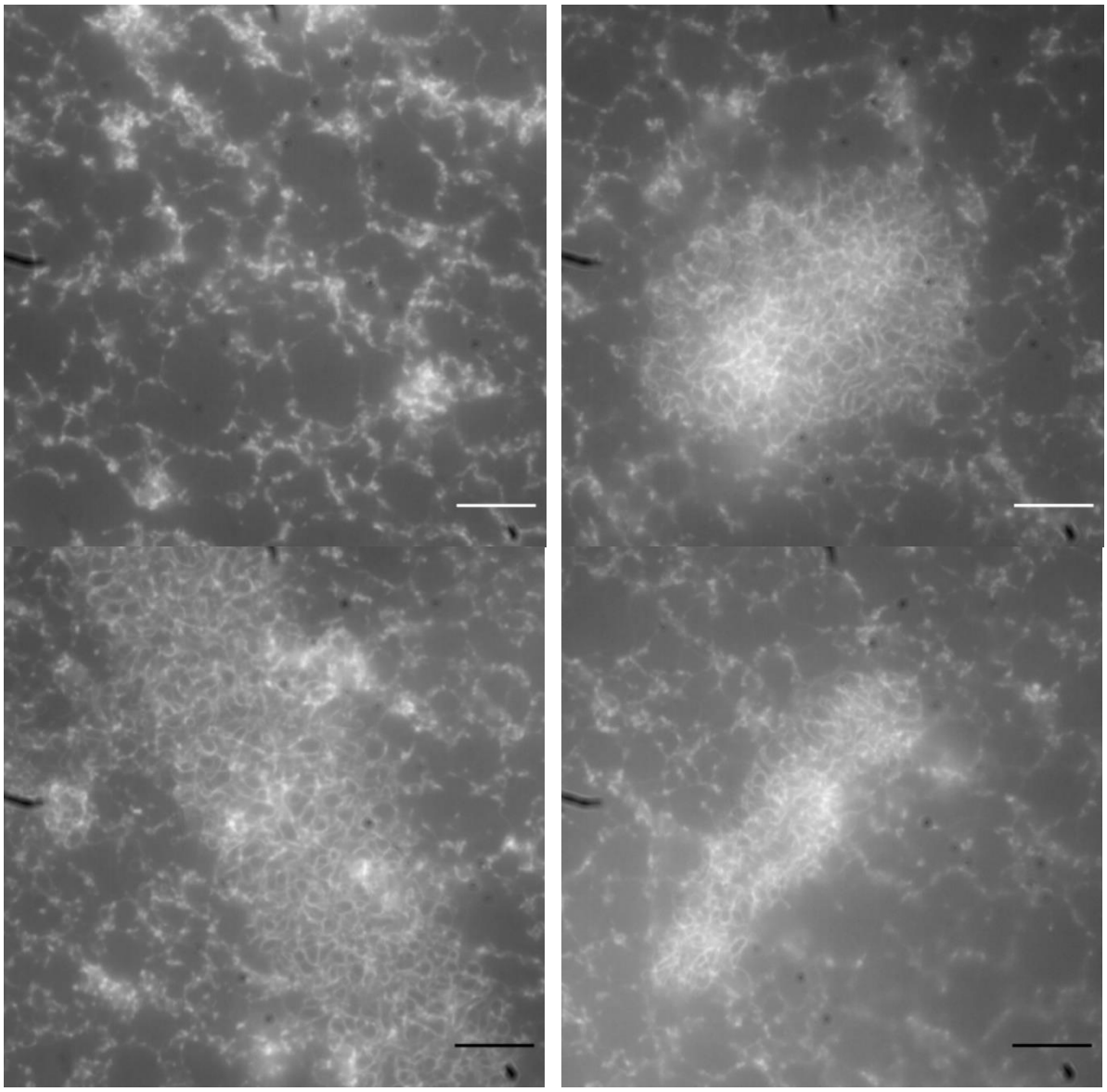

Figure S306 – Fluorescence microscopy images showing the gel formation process of compound **82** (5 mg/ mL) in NaOBz (0.505 mM). The resulting gel had regions of long curled strands and regions of shorter straighter strands separated by solvent

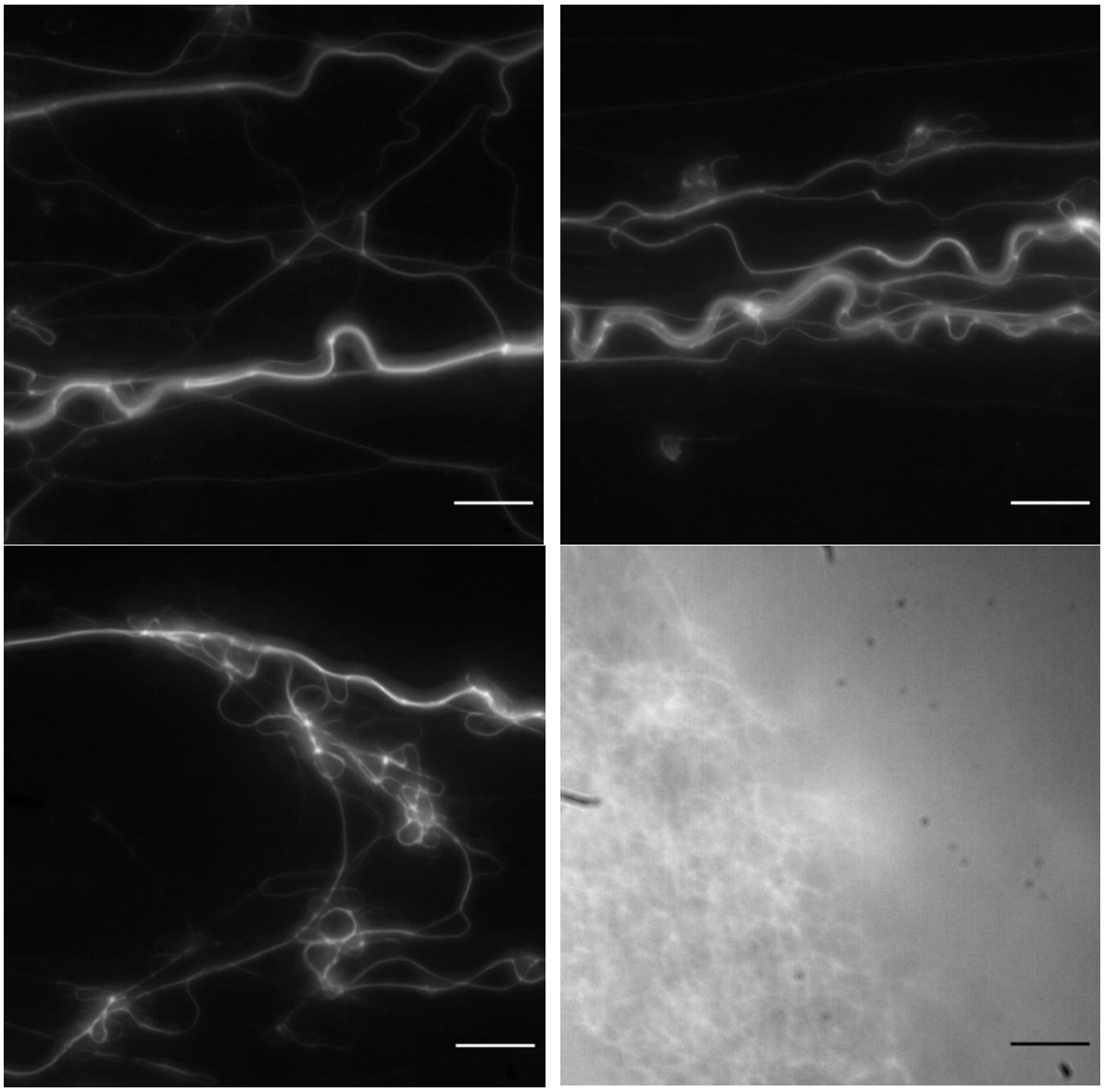

Figure S307 – Fluorescence microscopy images showing the gel formation process of compound **83** (5 mg/ mL) in NaOBz (0.505 mM). Initially long curled fibres formed, branching off at bright spots. The resulting gel was made up of regions of densely packed non-uniform gel strands ‘floating’ in solvent and constantly moving.

Statistics

Zones of inhibition

Descriptives

Zones

	N	Mean	Std. Deviation	Std. Error	95% Confidence Interval for Mean	
					Lower Bound	Upper Bound
70	12	10.5911	.98802	.28522	9.9633	11.2188
82	12	14.6700	1.66212	.47981	13.6139	15.7261
83	12	19.1475	1.88131	.54309	17.9522	20.3428
Total	36	14.8029	3.85320	.64220	13.4991	16.1066

Descriptives

Zones

	Minimum	Maximum	
70	8.76	12.15	
82	10.60	16.77	
83	15.92	21.83	
Total	8.76	21.83	

Tests of Homogeneity of Variances

		Levene Statistic	df1	df2	Sig.
Zones	Based on Mean	2.249	2	33	.121
	Based on Median	1.665	2	33	.205
	Based on Median and with adjusted df	1.665	2	27.851	.207
	Based on trimmed mean	2.218	2	33	.125

ANOVA

Zones

	Sum of Squares	df	Mean Square	F	Sig.
Between Groups	439.591	2	219.796	90.599	.000
Within Groups	80.059	33	2.426		
Total	519.651	35			

ANOVA Effect Sizes[a]

	Point Estimate	95% Confidence Interval	
		Lower	Upper

Zones	Eta-squared	.846	.719	.891
	Epsilon-squared	.837	.702	.885
	Omega-squared Fixed-effect	.833	.696	.882
	Omega-squared Random-effect	.713	.534	.789

a. Eta-squared and Epsilon-squared are estimated based on the fixed-effect model.

Robust Tests of Equality of Means

Zones

	Statistic[a]	df1	df2	Sig.
Welch	102.354	2	20.195	.000
Brown-Forsythe	90.599	2	27.600	.000

a. Asymptotically F distributed.

Contrast Coefficients

	Compound		
Contrast	70	**82**	**83**
1	1	0	-1

Contrast Tests

		Contrast	Value of Contrast	Std. Error	t	df
Zones	Assume equal variances	1	-8.5564	.63588	-13.456	33
	Does not assume equal variances	1	-8.5564	.61343	-13.949	16.639

Contrast Tests

		Contrast	Sig. (2-tailed)
Zones	Assume equal variances	1	.000
	Does not assume equal variances	1	.000

Contrast Effect Sizes

					95% Confidence Interval	
		Contrast	Standardizer[a]	Point Estimate	Lower	Upper
Zones	Cohen's d	1	1.55758	-5.493	-7.024	-3.938
	Hedges' correction	1	1.59413	-5.367	-6.863	-3.848

a. The denominator used in estimating the effect sizes. Cohen's d uses the pooled standard deviation for all the groups. Hedges' uses pooled standard deviation for all the groups, plus a correction factor.

Post Hoc Tests

Multiple Comparisons

Dependent Variable: Zones
LSD

(I) Compound	(J) Compound	Mean Difference (I-J)	Std. Error	Sig.	95% Confidence Interval Lower Bound
70	**82**	-4.07892*	.63588	.000	-5.3726
	83	-8.55642*	.63588	.000	-9.8501
82	**70**	4.07892*	.63588	.000	2.7852
	83	-4.47750*	.63588	.000	-5.7712
83	**70**	8.55642*	.63588	.000	7.2627
	82	4.47750*	.63588	.000	3.1838

Multiple Comparisons

Dependent Variable: Zones
LSD

(I) Compound	(J) Compound	95% Confidence Interval Upper Bound
70	**82**	-2.7852
	83	-7.2627
82	**70**	5.3726
	83	-3.1838
83	**70**	9.8501
	82	5.7712

*. The mean difference is significant at the 0.05 level.

WT ANOVA

Descriptives

Tm_WT

	N	Mean	Std. Deviation	Std. Error	95% Confidence Interval for Mean Lower Bound	95% Confidence Interval for Mean Upper Bound
Unace Alone	9	79.1822	.47715	.15905	78.8155	79.5490
Unace PA	9	82.1611	.35744	.11915	81.8864	82.4359
Unace Polar	9	79.4600	.67797	.22599	78.9389	79.9811
Unace Total	9	81.7511	.15957	.05319	81.6285	81.8738

Ace Alone	9	77.8567	.83911	.27970	77.2117	78.5017
Ace PA	9	82.4811	.26895	.08965	82.2744	82.6878
Ace Polar	9	77.5878	.93888	.31296	76.8661	78.3095
Ace Total	9	81.8044	.57544	.19181	81.3621	82.2468
Total	72	80.2856	1.96254	.23129	79.8244	80.7467

Descriptives

Tm_WT

	Minimum	Maximum	
Unace Alone	78.51	79.60	
Unace PA	81.82	82.63	
Unace Polar	78.65	80.26	
Unace Total	81.55	81.93	
Ace Alone	76.67	78.70	
Ace PA	82.17	82.80	
Ace Polar	76.38	78.80	
Ace Total	81.05	82.32	
Total	76.38	82.80	

Tests of Homogeneity of Variances

		Levene Statistic	df1	df2	Sig.
Tm_WT	Based on Mean	6.023	7	64	.000
	Based on Median	2.436	7	64	.028
	Based on Median and with adjusted df	2.436	7	40.268	.035
	Based on trimmed mean	5.773	7	64	.000

ANOVA

Tm_WT

	Sum of Squares	df	Mean Square	F	Sig.
Between Groups	250.825	7	35.832	101.307	.000
Within Groups	22.637	64	.354		
Total	273.462	71			

ANOVA Effect Sizes[a]

		Point Estimate	95% Confidence Interval	
			Lower	Upper
Tm_WT	Eta-squared	.917	.865	.932
	Epsilon-squared	.908	.850	.925
	Omega-squared Fixed-effect	.907	.848	.924

	Omega-squared Random-effect	.582	.444	.635

a. Eta-squared and Epsilon-squared are estimated based on the fixed-effect model.

Robust Tests of Equality of Means

Tm_WT

	Statistic[a]	df1	df2	Sig.
Welch	98.261	7	26.486	.000
Brown-Forsythe	101.307	7	38.407	.000

a. Asymptotically F distributed.

Post Hoc Tests

Multiple Comparisons

Dependent Variable: Tm_WT
Games-Howell

(I) WT_aS	(J) WT_aS	Mean Difference (I-J)	Std. Error	Sig.	95% Confidence Interval Lower Bound	95% Confidence Interval Upper Bound
Unace Alone	Unace PA	-2.97889*	.19873	.000	-3.6742	-2.2836
	Unace Polar	-.27778	.27635	.966	-1.2492	.6936
	Unace Total	-2.56889*	.16771	.000	-3.2011	-1.9367
	Ace Alone	1.32556*	.32176	.020	.1721	2.4790
	Ace PA	-3.29889*	.18258	.000	-3.9540	-2.6438
	Ace Polar	1.59444*	.35106	.011	.3214	2.8675
	Ace Total	-2.62222*	.24918	.000	-3.4889	-1.7556
Unace PA	Unace Alone	2.97889*	.19873	.000	2.2836	3.6742
	Unace Polar	2.70111*	.25548	.000	1.7782	3.6241
	Unace Total	.41000	.13048	.114	-.0694	.8894
	Ace Alone	4.30444*	.30402	.000	3.1823	5.4266
	Ace PA	-.32000	.14911	.432	-.8415	.2015
	Ace Polar	4.57333*	.33487	.000	3.3244	5.8223
	Ace Total	.35667	.22580	.754	-.4458	1.1592
Unace Polar	Unace Alone	.27778	.27635	.966	-.6936	1.2492
	Unace PA	-2.70111*	.25548	.000	-3.6241	-1.7782
	Unace Total	-2.29111*	.23217	.000	-3.1856	-1.3966
	Ace Alone	1.60333*	.35959	.008	.3510	2.8556
	Ace PA	-3.02111*	.24312	.000	-3.9245	-2.1177
	Ace Polar	1.87222*	.38603	.004	.5180	3.2264
	Ace Total	-2.34444*	.29642	.000	-3.3743	-1.3146
Unace Total	Unace Alone	2.56889*	.16771	.000	1.9367	3.2011
	Unace PA	-.41000	.13048	.114	-.8894	.0694
	Unace Polar	2.29111*	.23217	.000	1.3966	3.1856

	Ace Alone	3.89444*	.28471	.000	2.7880	5.0009
	Ace PA	-.73000*	.10424	.000	-1.1021	-.3579
	Ace Polar	4.16333*	.31745	.000	2.9254	5.4012
	Ace Total	-.05333	.19905	1.000	-.8135	.7068
Ace Alone	Unace Alone	-1.32556*	.32176	.020	-2.4790	-.1721
	Unace PA	-4.30444*	.30402	.000	-5.4266	-3.1823
	Unace Polar	-1.60333*	.35959	.008	-2.8556	-.3510
	Unace Total	-3.89444*	.28471	.000	-5.0009	-2.7880
	Ace PA	-4.62444*	.29372	.000	-5.7353	-3.5136
	Ace Polar	.26889	.41973	.998	-1.1867	1.7245
	Ace Total	-3.94778*	.33915	.000	-5.1425	-2.7531
Ace PA	Unace Alone	3.29889*	.18258	.000	2.6438	3.9540
	Unace PA	.32000	.14911	.432	-.2015	.8415
	Unace Polar	3.02111*	.24312	.000	2.1177	3.9245
	Unace Total	.73000*	.10424	.000	.3579	1.1021
	Ace Alone	4.62444*	.29372	.000	3.5136	5.7353
	Ace Polar	4.89333*	.32555	.000	3.6526	6.1341
	Ace Total	.67667	.21173	.103	-.0977	1.4510
Ace Polar	Unace Alone	-1.59444*	.35106	.011	-2.8675	-.3214
	Unace PA	-4.57333*	.33487	.000	-5.8223	-3.3244
	Unace Polar	-1.87222*	.38603	.004	-3.2264	-.5180
	Unace Total	-4.16333*	.31745	.000	-5.4012	-2.9254
	Ace Alone	-.26889	.41973	.998	-1.7245	1.1867
	Ace PA	-4.89333*	.32555	.000	-6.1341	-3.6526
	Ace Total	-4.21667*	.36706	.000	-5.5229	-2.9105
Ace Total	Unace Alone	2.62222*	.24918	.000	1.7556	3.4889
	Unace PA	-.35667	.22580	.754	-1.1592	.4458
	Unace Polar	2.34444*	.29642	.000	1.3146	3.3743
	Unace Total	.05333	.19905	1.000	-.7068	.8135
	Ace Alone	3.94778*	.33915	.000	2.7531	5.1425
	Ace PA	-.67667	.21173	.103	-1.4510	.0977
	Ace Polar	4.21667*	.36706	.000	2.9105	5.5229

*. The mean difference is significant at the 0.05 level.

VNp ANOVA

Descriptives

Tm_VNP

	N	Mean	Std. Deviation	Std. Error	95% Confidence Interval for Mean	
					Lower Bound	Upper Bound
Unace Alone	9	65.4289	.31106	.10369	65.1898	65.6680
Unace CL	9	65.4033	.29551	.09850	65.1762	65.6305
Unace PA	9	64.9389	.18435	.06145	64.7972	65.0806

Unace PC	9	65.0156	.28893	.09631	64.7935	65.2376
Unace PC:PE	9	66.8378	.37077	.12359	66.5528	67.1228
Unace PG	9	65.2011	.16811	.05604	65.0719	65.3303
Unace Polar	9	66.8489	.11084	.03695	66.7637	66.9341
Unace Total	9	64.9889	.60142	.20047	64.5266	65.4512
Ace Alone	9	65.2167	.42965	.14322	64.8864	65.5469
Ace CL	9	65.0322	.14060	.04687	64.9241	65.1403
Ace PA	9	63.9222	.60710	.20237	63.4556	64.3889
Ace PC	9	64.5744	.32600	.10867	64.3239	64.8250
Ace PC:PE	9	65.6789	.05968	.01989	65.6330	65.7248
Ace PG	9	64.4378	.42496	.14165	64.1111	64.7644
Ace Polar	9	66.1056	.24511	.08170	65.9171	66.2940
Ace Total	9	65.6867	.56591	.18864	65.2517	66.1217
Total	144	65.3324	.83711	.06976	65.1945	65.4703

Descriptives

Tm_VNP

	Minimum	Maximum	
Unace Alone	65.09	65.81	
Unace CL	65.08	65.78	
Unace PA	64.69	65.12	
Unace PC	64.79	65.40	
Unace PC:PE	66.47	67.32	
Unace PG	64.99	65.38	
Unace Polar	66.75	67.00	
Unace Total	64.18	65.47	
Ace Alone	64.93	65.96	
Ace CL	64.85	65.17	
Ace PA	63.11	64.42	
Ace PC	64.29	65.05	
Ace PC:PE	65.61	65.75	
Ace PG	63.95	64.94	
Ace Polar	65.85	66.42	
Ace Total	65.15	66.31	
Total	63.11	67.32	

Tests of Homogeneity of Variances

		Levene Statistic	df1	df2	Sig.
Tm_VNP	Based on Mean	11.757	15	128	.000
	Based on Median	1.745	15	128	.050
	Based on Median and with adjusted df	1.745	15	56.717	.068
	Based on trimmed mean	10.412	15	128	.000

ANOVA

Tm_VNP

	Sum of Squares	df	Mean Square	F	Sig.
Between Groups	83.529	15	5.569	42.733	.000
Within Groups	16.680	128	.130		
Total	100.209	143			

ANOVA Effect Sizes[a]		Point Estimate	95% Confidence Interval Lower	Upper
Tm_VNP	Eta-squared	.834	.759	.851
	Epsilon-squared	.814	.731	.834
	Omega-squared Fixed-effect	.813	.730	.833
	Omega-squared Random-effect	.225	.153	.250

a. Eta-squared and Epsilon-squared are estimated based on the fixed-effect model.

Robust Tests of Equality of Means

Tm_VNP

	Statistic[a]	df1	df2	Sig.
Welch	103.939	15	47.599	.000
Brown-Forsythe	42.733	15	70.087	.000

a. Asymptotically F distributed.

Post Hoc Tests

Multiple Comparisons

Dependent Variable: Tm_VNP

Games-Howell

(I) VNP	(J) VNP	Mean Difference (I-J)	Std. Error	Sig.	95% Confidence Interval Lower Bound	Upper Bound
Unace Alone	Unace CL	.02556	.14302	1.000	-.5473	.5984
	Unace PA	.49000	.12053	.057	-.0096	.9896
	Unace PC	.41333	.14152	.300	-.1537	.9804
	Unace PC:PE	-1.40889*	.16132	.000	-2.0577	-.7600
	Unace PG	.22778	.11786	.822	-.2659	.7215
	Unace Polar	-1.42000*	.11007	.000	-1.9021	-.9379
	Unace Total	.44000	.22570	.814	-.5102	1.3902
	Ace Alone	.21222	.17681	.995	-.5062	.9306

	Ace CL	.39667	.11379	.155	-.0898	.8831
	Ace PA	1.50667*	.22738	.001	.5484	2.4650
	Ace PC	.85444*	.15020	.002	.2529	1.4560
	Ace PC:PE	-.25000	.10558	.600	-.7308	.2308
	Ace PG	.99111*	.17555	.003	.2785	1.7037
	Ace Polar	-.67667*	.13201	.007	-1.2096	-.1438
	Ace Total	-.25778	.21525	.994	-1.1577	.6421
Unace CL	Unace Alone	-.02556	.14302	1.000	-.5984	.5473
	Unace PA	.46444	.11610	.061	-.0141	.9430
	Unace PC	.38778	.13776	.347	-.1638	.9394
	Unace PC:PE	-1.43444*	.15804	.000	-2.0720	-.7969
	Unace PG	.20222	.11333	.884	-.2697	.6741
	Unace Polar	-1.44556*	.10520	.000	-1.9041	-.9870
	Unace Total	.41444	.22337	.854	-.5315	1.3603
	Ace Alone	.18667	.17382	.998	-.5228	.8962
	Ace CL	.37111	.10908	.172	-.0925	.8347
	Ace PA	1.48111*	.22507	.002	.5270	2.4352
	Ace PC	.82889*	.14667	.002	.2408	1.4169
	Ace PC:PE	-.27556	.10049	.422	-.7322	.1811
	Ace PG	.96556*	.17254	.004	.2620	1.6691
	Ace Polar	-.70222*	.12798	.004	-1.2172	-.1872
	Ace Total	-.28333	.21281	.985	-1.1782	.6116
Unace PA	Unace Alone	-.49000	.12053	.057	-.9896	.0096
	Unace CL	-.46444	.11610	.061	-.9430	.0141
	Unace PC	-.07667	.11424	1.000	-.5465	.3931
	Unace PC:PE	-1.89889*	.13802	.000	-2.4826	-1.3152
	Unace PG	-.26222	.08316	.213	-.5956	.0712
	Unace Polar	-1.91000*	.07170	.000	-2.2067	-1.6133
	Unace Total	-.05000	.20968	1.000	-.9802	.8802
	Ace Alone	-.27778	.15584	.880	-.9478	.3922
	Ace CL	-.09333	.07728	.994	-.4060	.2194
	Ace PA	1.01667*	.21149	.031	.0778	1.9555
	Ace PC	.36444	.12484	.318	-.1558	.8847
	Ace PC:PE	-.74000*	.06459	.000	-1.0253	-.4547
	Ace PG	.50111	.15441	.218	-.1619	1.1642
	Ace Polar	-1.16667*	.10223	.000	-1.5808	-.7526
	Ace Total	-.74778	.19839	.118	-1.6236	.1280
Unace PC	Unace Alone	-.41333	.14152	.300	-.9804	.1537
	Unace CL	-.38778	.13776	.347	-.9394	.1638
	Unace PA	.07667	.11424	1.000	-.3931	.5465
	Unace PC:PE	-1.82222*	.15668	.000	-2.4552	-1.1892
	Unace PG	-.18556	.11142	.924	-.6484	.2773
	Unace Polar	-1.83333*	.10315	.000	-2.2820	-1.3847
	Unace Total	.02667	.22241	1.000	-.9176	.9709

	Ace Alone	-.20111	.17259	.996	-.9071	.5049
	Ace CL	-.01667	.10711	1.000	-.4707	.4374
	Ace PA	1.09333*	.22411	.020	.1408	2.0459
	Ace PC	.44111	.14520	.253	-.1415	1.0237
	Ace PC:PE	-.66333*	.09834	.004	-1.1098	-.2169
	Ace PG	.57778	.17129	.160	-.1222	1.2777
	Ace Polar	-1.09000*	.12630	.000	-1.5977	-.5823
	Ace Total	-.67111	.21180	.233	-1.5641	.2219
Unace PC:PE	Unace Alone	1.40889*	.16132	.000	.7600	2.0577
	Unace CL	1.43444*	.15804	.000	.7969	2.0720
	Unace PA	1.89889*	.13802	.000	1.3152	2.4826
	Unace PC	1.82222*	.15668	.000	1.1892	2.4552
	Unace PG	1.63667*	.13570	.000	1.0568	2.2166
	Unace Polar	-.01111	.12899	1.000	-.5844	.5622
	Unace Total	1.84889*	.23551	.000	.8769	2.8209
	Ace Alone	1.62111*	.18917	.000	.8613	2.3809
	Ace CL	1.80556*	.13218	.000	1.2300	2.3811
	Ace PA	2.91556*	.23712	.000	1.9359	3.8952
	Ace PC	2.26333*	.16457	.000	1.6028	2.9238
	Ace PC:PE	1.15889*	.12518	.000	.5856	1.7321
	Ace PG	2.40000*	.18799	.000	1.6453	3.1547
	Ace Polar	.73222*	.14815	.012	.1252	1.3393
	Ace Total	1.15111*	.22552	.009	.2262	2.0760
Unace PG	Unace Alone	-.22778	.11786	.822	-.7215	.2659
	Unace CL	-.20222	.11333	.884	-.6741	.2697
	Unace PA	.26222	.08316	.213	-.0712	.5956
	Unace PC	.18556	.11142	.924	-.2773	.6484
	Unace PC:PE	-1.63667*	.13570	.000	-2.2166	-1.0568
	Unace Polar	-1.64778*	.06712	.000	-1.9229	-1.3727
	Unace Total	.21222	.20816	.998	-.7174	1.1418
	Ace Alone	-.01556	.15379	1.000	-.6831	.6520
	Ace CL	.16889	.07305	.622	-.1250	.4628
	Ace PA	1.27889*	.20998	.007	.3406	2.2172
	Ace PC	.62667*	.12227	.012	.1118	1.1416
	Ace PC:PE	-.47778*	.05946	.001	-.7383	-.2172
	Ace PG	.76333*	.15234	.020	.1028	1.4238
	Ace Polar	-.90444*	.09907	.000	-1.3089	-.4999
	Ace Total	-.48556	.19678	.547	-1.3606	.3894
Unace Polar	Unace Alone	1.42000*	.11007	.000	.9379	1.9021
	Unace CL	1.44556*	.10520	.000	.9870	1.9041
	Unace PA	1.91000*	.07170	.000	1.6133	2.2067
	Unace PC	1.83333*	.10315	.000	1.3847	2.2820
	Unace PC:PE	.01111	.12899	1.000	-.5622	.5844
	Unace PG	1.64778*	.06712	.000	1.3727	1.9229
	Unace Total	1.86000*	.20385	.000	.9304	2.7896

	Ace Alone	1.63222*	.14791	.000	.9683	2.2961
	Ace CL	1.81667*	.05968	.000	1.5758	2.0576
	Ace PA	2.92667*	.20571	.000	1.9883	3.8650
	Ace PC	2.27444*	.11478	.000	1.7696	2.7793
	Ace PC:PE	1.17000*	.04196	.000	.9942	1.3458
	Ace PG	2.41111*	.14639	.000	1.7544	3.0678
	Ace Polar	.74333*	.08967	.000	.3600	1.1266
	Ace Total	1.16222*	.19222	.009	.2876	2.0368
Unace Total	Unace Alone	-.44000	.22570	.814	-1.3902	.5102
	Unace CL	-.41444	.22337	.854	-1.3603	.5315
	Unace PA	.05000	.20968	1.000	-.8802	.9802
	Unace PC	-.02667	.22241	1.000	-.9709	.9176
	Unace PC:PE	-1.84889*	.23551	.000	-2.8209	-.8769
	Unace PG	-.21222	.20816	.998	-1.1418	.7174
	Unace Polar	-1.86000*	.20385	.000	-2.7896	-.9304
	Ace Alone	-.22778	.24638	1.000	-1.2300	.7744
	Ace CL	-.04333	.20588	1.000	-.9726	.8859
	Ace PA	1.06667	.28485	.079	-.0738	2.2071
	Ace PC	.41444	.22803	.871	-.5404	1.3693
	Ace PC:PE	-.69000	.20146	.203	-1.6207	.2407
	Ace PG	.55111	.24547	.661	-.4484	1.5506
	Ace Polar	-1.11667*	.21648	.016	-2.0525	-.1809
	Ace Total	-.69778	.27527	.493	-1.8005	.4049
Ace Alone	Unace Alone	-.21222	.17681	.995	-.9306	.5062
	Unace CL	-.18667	.17382	.998	-.8962	.5228
	Unace PA	.27778	.15584	.880	-.3922	.9478
	Unace PC	.20111	.17259	.996	-.5049	.9071
	Unace PC:PE	-1.62111*	.18917	.000	-2.3809	-.8613
	Unace PG	.01556	.15379	1.000	-.6520	.6831
	Unace Polar	-1.63222*	.14791	.000	-2.2961	-.9683
	Unace Total	.22778	.24638	1.000	-.7744	1.2300
	Ace CL	.18444	.15069	.991	-.4805	.8494
	Ace PA	1.29444*	.24792	.007	.2852	2.3037
	Ace PC	.64222	.17978	.112	-.0855	1.3699
	Ace PC:PE	-.46222	.14459	.261	-1.1267	.2023
	Ace PG	.77889	.20144	.064	-.0276	1.5854
	Ace Polar	-.88889*	.16488	.007	-1.5753	-.2025
	Ace Total	-.47000	.23684	.802	-1.4286	.4886
Ace CL	Unace Alone	-.39667	.11379	.155	-.8831	.0898
	Unace CL	-.37111	.10908	.172	-.8347	.0925
	Unace PA	.09333	.07728	.994	-.2194	.4060
	Unace PC	.01667	.10711	1.000	-.4374	.4707
	Unace PC:PE	-1.80556*	.13218	.000	-2.3811	-1.2300
	Unace PG	-.16889	.07305	.622	-.4628	.1250

	Unace Polar	-1.81667*	.05968	.000	-2.0576	-1.5758
	Unace Total	.04333	.20588	1.000	-.8859	.9726
	Ace Alone	-.18444	.15069	.991	-.8494	.4805
	Ace PA	1.11000*	.20772	.018	.1719	2.0481
	Ace PC	.45778	.11834	.092	-.0507	.9663
	Ace PC:PE	-.64667*	.05091	.000	-.8658	-.4275
	Ace PG	.59444	.14921	.088	-.0634	1.2523
	Ace Polar	-1.07333*	.09419	.000	-1.4652	-.6815
	Ace Total	-.65444	.19437	.206	-1.5289	.2200
Ace PA	Unace Alone	-1.50667*	.22738	.001	-2.4650	-.5484
	Unace CL	-1.48111*	.22507	.002	-2.4352	-.5270
	Unace PA	-1.01667*	.21149	.031	-1.9555	-.0778
	Unace PC	-1.09333*	.22411	.020	-2.0459	-.1408
	Unace PC:PE	-2.91556*	.23712	.000	-3.8952	-1.9359
	Unace PG	-1.27889*	.20998	.007	-2.2172	-.3406
	Unace Polar	-2.92667*	.20571	.000	-3.8650	-1.9883
	Unace Total	-1.06667	.28485	.079	-2.2071	.0738
	Ace Alone	-1.29444*	.24792	.007	-2.3037	-.2852
	Ace CL	-1.11000*	.20772	.018	-2.0481	-.1719
	Ace PC	-.65222	.22970	.354	-1.6151	.3106
	Ace PC:PE	-1.75667*	.20334	.001	-2.6962	-.8171
	Ace PG	-.51556	.24702	.749	-1.5222	.4911
	Ace Polar	-2.18333*	.21824	.000	-3.1276	-1.2390
	Ace Total	-1.76444*	.27665	.001	-2.8729	-.6560
Ace PC	Unace Alone	-.85444*	.15020	.002	-1.4560	-.2529
	Unace CL	-.82889*	.14667	.002	-1.4169	-.2408
	Unace PA	-.36444	.12484	.318	-.8847	.1558
	Unace PC	-.44111	.14520	.253	-1.0237	.1415
	Unace PC:PE	-2.26333*	.16457	.000	-2.9238	-1.6028
	Unace PG	-.62667*	.12227	.012	-1.1416	-.1118
	Unace Polar	-2.27444*	.11478	.000	-2.7793	-1.7696
	Unace Total	-.41444	.22803	.871	-1.3693	.5404
	Ace Alone	-.64222	.17978	.112	-1.3699	.0855
	Ace CL	-.45778	.11834	.092	-.9663	.0507
	Ace PA	.65222	.22970	.354	-.3106	1.6151
	Ace PC:PE	-1.10444*	.11047	.000	-1.6083	-.6006
	Ace PG	.13667	.17853	1.000	-.5854	.8587
	Ace Polar	-1.53111*	.13596	.000	-2.0818	-.9804
	Ace Total	-1.11222*	.21770	.011	-2.0175	-.2070
Ace PC:PE	Unace Alone	.25000	.10558	.600	-.2308	.7308
	Unace CL	.27556	.10049	.422	-.1811	.7322
	Unace PA	.74000*	.06459	.000	.4547	1.0253
	Unace PC	.66333*	.09834	.004	.2169	1.1098
	Unace PC:PE	-1.15889*	.12518	.000	-1.7321	-.5856

	Unace PG	.47778*	.05946	.001	.2172	.7383
	Unace Polar	-1.17000*	.04196	.000	-1.3458	-.9942
	Unace Total	.69000	.20146	.203	-.2407	1.6207
	Ace Alone	.46222	.14459	.261	-.2023	1.1267
	Ace CL	.64667*	.05091	.000	.4275	.8658
	Ace PA	1.75667*	.20334	.001	.8171	2.6962
	Ace PC	1.10444*	.11047	.000	.6006	1.6083
	Ace PG	1.24111*	.14304	.001	.5839	1.8984
	Ace Polar	-.42667*	.08409	.025	-.8054	-.0479
	Ace Total	-.00778	.18968	1.000	-.8835	.8679
Ace PG	Unace Alone	-.99111*	.17555	.003	-1.7037	-.2785
	Unace CL	-.96556*	.17254	.004	-1.6691	-.2620
	Unace PA	-.50111	.15441	.218	-1.1642	.1619
	Unace PC	-.57778	.17129	.160	-1.2777	.1222
	Unace PC:PE	-2.40000*	.18799	.000	-3.1547	-1.6453
	Unace PG	-.76333*	.15234	.020	-1.4238	-.1028
	Unace Polar	-2.41111*	.14639	.000	-3.0678	-1.7544
	Unace Total	-.55111	.24547	.661	-1.5506	.4484
	Ace Alone	-.77889	.20144	.064	-1.5854	.0276
	Ace CL	-.59444	.14921	.088	-1.2523	.0634
	Ace PA	.51556	.24702	.749	-.4911	1.5222
	Ace PC	-.13667	.17853	1.000	-.8587	.5854
	Ace PC:PE	-1.24111*	.14304	.001	-1.8984	-.5839
	Ace Polar	-1.66778*	.16353	.000	-2.3477	-.9879
	Ace Total	-1.24889*	.23590	.006	-2.2045	-.2933
Ace Polar	Unace Alone	.67667*	.13201	.007	.1438	1.2096
	Unace CL	.70222*	.12798	.004	.1872	1.2172
	Unace PA	1.16667*	.10223	.000	.7526	1.5808
	Unace PC	1.09000*	.12630	.000	.5823	1.5977
	Unace PC:PE	-.73222*	.14815	.012	-1.3393	-.1252
	Unace PG	.90444*	.09907	.000	.4999	1.3089
	Unace Polar	-.74333*	.08967	.000	-1.1266	-.3600
	Unace Total	1.11667*	.21648	.016	.1809	2.0525
	Ace Alone	.88889*	.16488	.007	.2025	1.5753
	Ace CL	1.07333*	.09419	.000	.6815	1.4652
	Ace PA	2.18333*	.21824	.000	1.2390	3.1276
	Ace PC	1.53111*	.13596	.000	.9804	2.0818
	Ace PC:PE	.42667*	.08409	.025	.0479	.8054
	Ace PG	1.66778*	.16353	.000	.9879	2.3477
	Ace Total	.41889	.20557	.769	-.4640	1.3018
Ace Total	Unace Alone	.25778	.21525	.994	-.6421	1.1577
	Unace CL	.28333	.21281	.985	-.6116	1.1782
	Unace PA	.74778	.19839	.118	-.1280	1.6236
	Unace PC	.67111	.21180	.233	-.2219	1.5641

	Unace PC:PE	-1.15111*	.22552	.009	-2.0760	-.2262
	Unace PG	.48556	.19678	.547	-.3894	1.3606
	Unace Polar	-1.16222*	.19222	.009	-2.0368	-.2876
	Unace Total	.69778	.27527	.493	-.4049	1.8005
	Ace Alone	.47000	.23684	.802	-.4886	1.4286
	Ace CL	.65444	.19437	.206	-.2200	1.5289
	Ace PA	1.76444*	.27665	.001	.6560	2.8729
	Ace PC	1.11222*	.21770	.011	.2070	2.0175
	Ace PC:PE	.00778	.18968	1.000	-.8679	.8835
	Ace PG	1.24889*	.23590	.006	.2933	2.2045
	Ace Polar	-.41889	.20557	.769	-1.3018	.4640

*. The mean difference is significant at the 0.05 level.

Lz ANOVA

Descriptives

Tm_Lz

	N	Mean	Std. Deviation	Std. Error	95% Confidence Interval for Mean	
					Lower Bound	Upper Bound
Unace Alone	9	63.4167	1.72327	.57442	62.0920	64.7413
Unace CL	9	62.8733	.21154	.07051	62.7107	63.0359
Unace Polar	9	64.0600	.30777	.10259	63.8234	64.2966
Unace Total	9	63.7544	.90856	.30285	63.0561	64.4528
Ace Alone	9	63.6700	1.81424	.60475	62.2755	65.0645
Ace CL	9	63.3078	.29154	.09718	63.0837	63.5319
Ace Polar	9	64.3856	.22260	.07420	64.2144	64.5567
Ace Total	9	64.4178	.18687	.06229	64.2741	64.5614
Total	72	63.7357	1.04408	.12305	63.4903	63.9810

Descriptives

Tm_Lz

	Minimum	Maximum	
Unace Alone	61.11	64.64	
Unace CL	62.57	63.08	
Unace Polar	63.66	64.75	
Unace Total	62.17	64.41	
Ace Alone	61.25	65.05	
Ace CL	62.70	63.54	
Ace Polar	64.03	64.60	
Ace Total	64.17	64.75	
Total	61.11	65.05	

Tests of Homogeneity of Variances

		Levene Statistic	df1	df2	Sig.
Tm_Lz	Based on Mean	25.739	7	64	.000
	Based on Median	2.622	7	64	.019
	Based on Median and with adjusted df	2.622	7	20.318	.042
	Based on trimmed mean	21.161	7	64	.000

ANOVA

Tm_Lz

	Sum of Squares	df	Mean Square	F	Sig.
Between Groups	18.234	7	2.605	2.818	.013
Within Groups	59.164	64	.924		
Total	77.398	71			

ANOVA Effect Sizes[a,b]

		Point Estimate	95% Confidence Interval Lower	Upper
Tm_Lz	Eta-squared	.236	.013	.330
	Epsilon-squared	.152	-.095	.257
	Omega-squared Fixed-effect	.150	-.093	.255
	Omega-squared Random-effect	.025	-.012	.047

a. Eta-squared and Epsilon-squared are estimated based on the fixed-effect model.

b. Negative but less biased estimates are retained, not rounded to zero.

Robust Tests of Equality of Means

Tm_Lz

	Statistic[a]	df1	df2	Sig.
Welch	45.176	7	27.020	.000
Brown-Forsythe	2.818	7	21.495	.030

a. Asymptotically F distributed.

Post Hoc Tests

Multiple Comparisons

Dependent Variable: Tm_Lz

Games-Howell

(I) Leucine_Zipper	(J) Leucine_Zipper	Mean Difference (I-J)	Std. Error	Sig.	95% Confidence Interval	
					Lower Bound	Upper Bound
Unace Alone	Unace CL	.54333	.57873	.972	-1.7289	2.8155
	Unace Polar	-.64333	.58351	.940	-2.9155	1.6289
	Unace Total	-.33778	.64937	.999	-2.6837	2.0081
	Ace Alone	-.25333	.83407	1.000	-3.1420	2.6354
	Ace CL	.10889	.58258	1.000	-2.1632	2.3810
	Ace Polar	-.96889	.57920	.703	-3.2410	1.3033
	Ace Total	-1.00111	.57779	.672	-3.2734	1.2712
Unace CL	Unace Alone	-.54333	.57873	.972	-2.8155	1.7289
	Unace Polar	-1.18667*	.12449	.000	-1.6251	-.7482
	Unace Total	-.88111	.31095	.199	-2.0798	.3176
	Ace Alone	-.79667	.60884	.874	-3.1889	1.5955
	Ace CL	-.43444*	.12007	.041	-.8555	-.0134
	Ace Polar	-1.51222*	.10236	.000	-1.8667	-1.1577
	Ace Total	-1.54444*	.09409	.000	-1.8708	-1.2180
Unace Polar	Unace Alone	.64333	.58351	.940	-1.6289	2.9155
	Unace CL	1.18667*	.12449	.000	.7482	1.6251
	Unace Total	.30556	.31976	.971	-.8987	1.5098
	Ace Alone	.39000	.61339	.997	-2.0021	2.7821
	Ace CL	.75222*	.14131	.001	.2628	1.2417
	Ace Polar	-.32556	.12661	.241	-.7697	.1186
	Ace Total	-.35778	.12002	.132	-.7853	.0697
Unace Total	Unace Alone	.33778	.64937	.999	-2.0081	2.6837
	Unace CL	.88111	.31095	.199	-.3176	2.0798
	Unace Polar	-.30556	.31976	.971	-1.5098	.8987
	Ace Alone	.08444	.67634	1.000	-2.3719	2.5407
	Ace CL	.44667	.31806	.836	-.7561	1.6495
	Ace Polar	-.63111	.31181	.516	-1.8301	.5679
	Ace Total	-.66333	.30919	.456	-1.8615	.5349
Ace Alone	Unace Alone	.25333	.83407	1.000	-2.6354	3.1420
	Unace CL	.79667	.60884	.874	-1.5955	3.1889
	Unace Polar	-.39000	.61339	.997	-2.7821	2.0021
	Unace Total	-.08444	.67634	1.000	-2.5407	2.3719
	Ace CL	.36222	.61250	.998	-2.0298	2.7543
	Ace Polar	-.71556	.60928	.920	-3.1077	1.6766
	Ace Total	-.74778	.60794	.902	-3.1401	1.6445
Ace CL	Unace Alone	-.10889	.58258	1.000	-2.3810	2.1632
	Unace CL	.43444*	.12007	.041	.0134	.8555
	Unace Polar	-.75222*	.14131	.001	-1.2417	-.2628
	Unace Total	-.44667	.31806	.836	-1.6495	.7561
	Ace Alone	-.36222	.61250	.998	-2.7543	2.0298
	Ace Polar	-1.07778*	.12227	.000	-1.5050	-.6505
	Ace Total	-1.11000*	.11543	.000	-1.5190	-.7010

Ace Polar	Unace Alone	.96889	.57920	.703	-1.3033	3.2410
	Unace CL	1.51222*	.10236	.000	1.1577	1.8667
	Unace Polar	.32556	.12661	.241	-.1186	.7697
	Unace Total	.63111	.31181	.516	-.5679	1.8301
	Ace Alone	.71556	.60928	.920	-1.6766	3.1077
	Ace CL	1.07778*	.12227	.000	.6505	1.5050
	Ace Total	-.03222	.09688	1.000	-.3690	.3045
Ace Total	Unace Alone	1.00111	.57779	.672	-1.2712	3.2734
	Unace CL	1.54444*	.09409	.000	1.2180	1.8708
	Unace Polar	.35778	.12002	.132	-.0697	.7853
	Unace Total	.66333	.30919	.456	-.5349	1.8615
	Ace Alone	.74778	.60794	.902	-1.6445	3.1401
	Ace CL	1.11000*	.11543	.000	.7010	1.5190
	Ace Polar	.03222	.09688	1.000	-.3045	.3690

*. The mean difference is significant at the 0.05 level.

Hum1 Fluorescence

Descriptives

Fluorescence_Intensity

	N	Mean	Std. Deviation	Std. Error	95% Confidence Interval for Mean Lower Bound
mNg PC 1	6	7488.1667	4277.40793	1746.24447	2999.3023
mNg PC 2	6	39631.0000	22389.61007	9140.52004	16134.5452
mNg PC 3	6	75662.5000	23362.65825	9537.76529	51144.8938
mNg PG 1	6	5764.8333	5490.94008	2241.66690	2.4451
mNg PG 2	6	22881.6667	6606.99174	2697.29308	15948.0541
mNg PG 3	6	81110.3333	30405.62610	12413.04488	49201.5856
mNg PA 1	6	1095.5000	399.20008	162.97275	676.5652
mNg PA 2	6	8969.0000	3918.88556	1599.87833	4856.3818
mNg PA 3	6	152004.0000	64184.06874	26203.03634	84646.9508
mNg Alone 1	6	6230.5000	1284.85373	524.53934	4882.1287
mNg Alone 2	6	17214.6667	8591.58583	3507.50023	8198.3503
mNg Alone 3	6	39540.6667	22790.72443	9304.27429	15623.2682
FM4-64 PC 1	6	21363.3333	1181.64016	482.40258	20123.2780
FM4-64 PC 2	6	29483.0000	17843.53749	7284.59367	10757.3558
FM4-64 PC 3	6	39699.5000	18963.71123	7741.90269	19798.3056
FM4-64 PG 1	6	714.0000	127.41272	52.01602	580.2886
FM4-64 PG 2	6	2438.1667	920.35307	375.73257	1472.3154
FM4-64 PG 3	6	222371.6667	2900.83337	1184.26027	219327.4287
FM4-64 PA 1	6	847.5000	118.25185	48.27612	723.4023
FM4-64 PA 2	6	1584.5000	278.08110	113.52614	1292.6718

FM4-64 PA 3	6	76251.0000	52757.76360	21538.26680	20885.1226
FM4-64 WT 1	6	2914.6667	2291.29052	935.41544	510.1047
FM4-64 WT 2	6	2606.8333	684.82565	279.57890	1888.1529
FM4-64 WT 3	6	4912.6667	2211.57841	902.87311	2591.7575
FM4-64 Background	6	21363.3333	1181.64016	482.40258	20123.2780
Total	150	35365.7200	55153.15465	4503.23622	26467.2659

Descriptives

Fluorescence_Intensity

	95% Confidence Interval for Mean Upper Bound	Minimum	Maximum
mNg PC 1	11977.0310	3410.00	11586.00
mNg PC 2	63127.4548	18862.00	60439.00
mNg PC 3	100180.1062	51086.00	98220.00
mNg PG 1	11527.2216	719.00	11044.00
mNg PG 2	29815.2793	16592.00	29692.00
mNg PG 3	113019.0810	53586.00	124956.00
mNg PA 1	1514.4348	716.00	1503.00
mNg PA 2	13081.6182	5319.00	13116.00
mNg PA 3	219361.0492	88573.00	259933.00
mNg Alone 1	7578.8713	5009.00	7626.00
mNg Alone 2	26230.9830	9236.00	26016.00
mNg Alone 3	63458.0651	17478.00	63201.00
FM4-64 PC 1	22603.3886	20161.00	23178.00
FM4-64 PC 2	48208.6442	13053.00	46350.00
FM4-64 PC 3	59600.6944	21624.00	59501.00
FM4-64 PG 1	847.7114	580.00	842.00
FM4-64 PG 2	3404.0180	1502.00	3384.00
FM4-64 PG 3	225415.9046	218369.00	226359.00
FM4-64 PA 1	971.5977	729.00	1010.00

FM4-64 PA 2	1876.3282	1285.00	1918.00
FM4-64 PA 3	131616.8774	27109.00	152203.00
FM4-64 WT 1	5319.2286	1343.00	7208.00
FM4-64 WT 2	3325.5138	1928.00	3345.00
FM4-64 WT 3	7233.5759	2808.00	7008.00
FM4-64 Background	22603.3886	20161.00	23178.00
Total	44264.1741	580.00	259933.00

Tests of Homogeneity of Variances

		Levene Statistic	df1	df2
Fluorescence_Intensity	Based on Mean	17.532	24	125
	Based on Median	9.192	24	125
	Based on Median and with adjusted df	9.192	24	8.367
	Based on trimmed mean	16.216	24	125

Tests of Homogeneity of Variances

		Sig.
Fluorescence_Intensity	Based on Mean	.000
	Based on Median	.000
	Based on Median and with adjusted df	.001
	Based on trimmed mean	.000

ANOVA

Fluorescence_Intensity

	Sum of Squares	df	Mean Square	F	Sig.
Between Groups	401849337751.907	24	16743722406.329	40.728	.000
Within Groups	51389361944.333	125	411114895.555		
Total	453238699696.240	149			

ANOVA Effect Sizes[a]

		Point Estimate	95% Confidence Interval Lower	Upper
Fluorescence_Intensity	Eta-squared	.887	.824	.892
	Epsilon-squared	.865	.790	.872
	Omega-squared Fixed-effect	.864	.789	.871
	Omega-squared Random-effect	.209	.135	.219

a. Eta-squared and Epsilon-squared are estimated based on the fixed-effect model.

Robust Tests of Equality of Means

Fluorescence_Intensity

	Statistic[a]	df1	df2	Sig.
Welch	1209.079	24	44.514	.000
Brown-Forsythe	40.728	24	19.833	.000

a. Asymptotically F distributed.

Post Hoc Tests

Multiple Comparisons

Dependent Variable: Fluorescence_Intensity

Games-Howell

(I) Fractions	(J) Fractions	Mean Difference (I-J)	Std. Error	Sig.	95% Confidence Interval Lower Bound	95% Confidence Interval Upper Bound
mNg PC 1	mNg PC 2	-32142.83333	9305.83023	.337	-86790.5401	22504.8734
	mNg PC 3	-68174.33333*	9696.30530	.023	-125256.2718	-11092.3949
	mNg PG 1	1723.33333	2841.55596	1.000	-12009.3020	15455.9687
	mNg PG 2	-15393.50000	3213.21642	.061	-31339.5571	552.5571
	mNg PG 3	-73622.16667	12535.27235	.053	-148293.0075	1048.6742
	mNg PA 1	6392.66667	1753.83291	.296	-4159.5948	16944.9281
	mNg PA 2	-1480.83333	2368.32861	1.000	-12779.3312	9817.6645
	mNg PA 3	-144515.83333	26261.15921	.073	-303149.0463	14117.3796
	mNg Alone 1	1257.66667	1823.32424	1.000	-9028.0562	11543.3896
	mNg Alone 2	-9726.50000	3918.15360	.683	-30122.6627	10669.6627
	mNg Alone 3	-32052.50000	9466.72540	.356	-87703.7836	23598.7836
	FM4-64 PC 1	-13875.16667*	1811.65173	.012	-24193.9096	-3556.4237
	FM4-64 PC 2	-21994.83333	7490.97288	.500	-65258.0524	21268.3858
	FM4-64 PC 3	-32211.33333	7936.39887	.202	-78281.0424	13858.3758
	FM4-64 PG 1	6774.16667	1747.01901	.249	-3814.3339	17362.6672
	FM4-64 PG 2	5050.00000	1786.20960	.543	-5356.2644	15456.2644
	FM4-64 PG 3	-214883.50000*	2109.93889	.000	-225275.7520	-204491.2480
	FM4-64 PA 1	6640.66667	1746.91166	.264	-3948.4213	17229.7546

	FM4-64 PA 2	5903.66667	1749.93084	.367	-4669.0978	16476.4311
	FM4-64 PA 3	-68762.83333	21608.94043	.423	-199034.3776	61508.7109
	FM4-64 WT 1	4573.50000	1981.00273	.763	-5598.4644	14745.4644
	FM4-64 WT 2	4881.33333	1768.48357	.571	-5599.7017	15362.3684
	FM4-64 WT 3	2575.50000	1965.84577	.996	-7585.7763	12736.7763
	FM4-64 Background	-13875.16667*	1811.65173	.012	-24193.9096	-3556.4237
mNg PC 2	mNg PC 1	32142.83333	9305.83023	.337	-22504.8734	86790.5401
	mNg PC 3	-36031.50000	13210.52888	.561	-98963.5767	26900.5767
	mNg PG 1	33866.16667	9411.38550	.294	-20377.6492	88109.9825
	mNg PG 2	16749.33333	9530.18869	.940	-37127.2128	70625.8795
	mNg PG 3	-41479.33333	15415.34267	.582	-116499.5766	33540.9099
	mNg PA 1	38535.50000	9141.97280	.192	-16903.0701	93974.0701
	mNg PA 2	30662.00000	9279.47828	.381	-24098.8600	85422.8600
	mNg PA 3	-112373.00000	27751.54446	.186	-265825.9831	41079.9831
	mNg Alone 1	33400.50000	9155.55831	.297	-21964.2555	88765.2555
	mNg Alone 2	22416.33333	9790.38632	.766	-30935.0996	75767.7663
	mNg Alone 3	90.33333	13042.95314	1.000	-62020.4354	62201.1021
	FM4-64 PC 1	18267.66667	9153.24089	.867	-37109.5692	73644.9026
	FM4-64 PC 2	10148.00000	11688.21678	1.000	-46198.0439	66494.0439
	FM4-64 PC 3	-68.50000	11978.57102	1.000	-57490.5404	57353.5404
	FM4-64 PG 1	38917.00000	9140.66804	.186	-16528.7422	94362.7422
	FM4-64 PG 2	37192.83333	9148.23926	.215	-18211.4938	92597.1605
	FM4-64 PG 3	-182740.66667*	9216.91808	.000	-237791.1583	-127690.1750
	FM4-64 PA 1	38783.50000	9140.64752	.188	-16662.3551	94229.3551
	FM4-64 PA 2	38046.50000	9141.22501	.200	-17396.1788	93489.1788
	FM4-64 PA 3	-36620.00000	23397.56490	.977	-161992.2250	88752.2250
	FM4-64 WT 1	36716.33333	9188.25928	.224	-18477.1029	91909.7695

	FM4-64 WT 2	37024.16667	9144.79474	.218	-18398.9414	92447.2748
	FM4-64 WT 3	34718.33333	9185.00334	.266	-20491.7639	89928.4306
	FM4-64 Background	18267.66667	9153.24089	.867	-37109.5692	73644.9026
mNg PC 3	mNg PC 1	68174.33333*	9696.30530	.023	11092.3949	125256.2718
	mNg PC 2	36031.50000	13210.52888	.561	-26900.5767	98963.5767
	mNg PG 1	69897.66667*	9797.65468	.019	13215.9021	126579.4312
	mNg PG 2	52780.83333	9911.82913	.067	-3528.9822	109090.6488
	mNg PG 3	-5447.83333	15654.15759	1.000	-81221.9843	70326.3176
	mNg PA 1	74567.00000*	9539.15756	.017	16718.4012	132415.5988
	mNg PA 2	66693.50000*	9671.01739	.026	9500.6706	123886.3294
	mNg PA 3	-76341.50000	27884.90775	.572	-229556.9939	76873.9939
	mNg Alone 1	69432.00000*	9552.17820	.023	11654.2210	127209.7790
	mNg Alone 2	58447.83333*	10162.25982	.040	2698.3241	114197.3426
	mNg Alone 3	36121.83333	13324.35690	.569	-27333.6920	99577.3587
	FM4-64 PC 1	54299.16667	9549.95702	.064	-3490.5956	112088.9289
	FM4-64 PC 2	46179.50000	12001.42791	.169	-11955.4397	104314.4397
	FM4-64 PC 3	35963.00000	12284.38130	.467	-23147.1681	95073.1681
	FM4-64 PG 1	74948.50000*	9537.90713	.017	17093.0271	132803.9729
	FM4-64 PG 2	73224.33333*	9545.16326	.018	15408.5718	131040.0948
	FM4-64 PG 3	-146709.16667*	9611.00615	.001	-204183.8662	-89234.4672
	FM4-64 PA 1	74815.00000*	9537.88747	.017	16959.4189	132670.5811
	FM4-64 PA 2	74078.00000*	9538.44091	.018	16225.4631	131930.5369
	FM4-64 PA 3	-588.50000	23555.59176	1.000	-125865.5243	124688.5243
	FM4-64 WT 1	72747.83333*	9583.52591	.018	15134.9489	130360.7178
	FM4-64 WT 2	73055.66667*	9541.86204	.019	15221.8917	130889.4416
	FM4-64 WT 3	70749.83333*	9580.40430	.021	13120.8791	128378.7875
	FM4-64 Background	54299.16667	9549.95702	.064	-3490.5956	112088.9289
mNg PG 1	mNg PC 1	-1723.33333	2841.55596	1.000	-15455.9687	12009.3020

	mNg PC 2	-33866.16667	9411.38550	.294	-88109.9825	20377.6492
	mNg PC 3	-69897.66667*	9797.65468	.019	-126579.4312	-13215.9021
	mNg PG 2	-17116.83333*	3507.20123	.045	-33956.0390	-277.6277
	mNg PG 3	-75345.50000*	12613.83184	.047	-149659.4170	-1031.5830
	mNg PA 1	4669.33333	2247.58328	.840	-8896.7032	18235.3699
	mNg PA 2	-3204.16667	2754.02999	.999	-16665.0671	10256.7338
	mNg PA 3	-146239.16667	26298.74871	.069	-304674.0341	12195.7008
	mNg Alone 1	-465.66667	2302.21893	1.000	-13789.5352	12858.2018
	mNg Alone 2	-11449.83333	4162.64679	.555	-32152.5386	9252.8719
	mNg Alone 3	-33775.83333	9570.50628	.312	-89024.6241	21472.9574
	FM4-64 PC 1	-15598.50000*	2292.98555	.025	-28957.0395	-2239.9605
	FM4-64 PC 2	-23718.16667	7621.70424	.431	-66585.5149	19149.1816
	FM4-64 PC 3	-33934.66667	8059.90867	.169	-79600.7612	11731.4279
	FM4-64 PG 1	5050.83333	2242.27031	.775	-8543.8432	18645.5099
	FM4-64 PG 2	3326.66667	2272.93763	.982	-10115.6126	16768.9460
	FM4-64 PG 3	-216606.83333*	2535.25992	.000	-229658.6070	-203555.0596
	FM4-64 PA 1	4917.33333	2242.18667	.797	-8677.8019	18512.4686
	FM4-64 PA 2	4180.33333	2244.53975	.907	-9401.9903	17762.6570
	FM4-64 PA 3	-70486.16667	21654.60706	.400	-200521.6112	59549.2778
	FM4-64 WT 1	2850.16667	2429.00649	.999	-10203.2663	15903.5997
	FM4-64 WT 2	3158.00000	2259.03405	.988	-10349.5601	16665.5601
	FM4-64 WT 3	852.16667	2416.66099	1.000	-12213.0775	13917.4108
	FM4-64 Background	-15598.50000*	2292.98555	.025	-28957.0395	-2239.9605
mNg PG 2	mNg PC 1	15393.50000	3213.21642	.061	-552.5571	31339.5571
	mNg PC 2	-16749.33333	9530.18869	.940	-70625.8795	37127.2128
	mNg PC 3	-52780.83333	9911.82913	.067	-109090.6488	3528.9822
	mNg PG 1	17116.83333*	3507.20123	.045	277.6277	33956.0390

	mNg PG 3	-58228.66667	12702.71912	.131	-132179.1800	15721.8466
	mNg PA 1	21786.16667*	2702.21207	.015	5451.0619	38121.2714
	mNg PA 2	13912.66667	3136.08046	.097	-1890.2503	29715.5837
	mNg PA 3	-129122.33333	26341.49774	.111	-287336.5964	29091.9297
	mNg Alone 1	16651.16667*	2747.82305	.043	532.3735	32769.9598
	mNg Alone 2	5667.00000	4424.69748	.998	-15748.6859	27082.6859
	mNg Alone 3	-16659.00000	9687.35826	.948	-71538.3055	38220.3055
	FM4-64 PC 1	1518.33333	2740.09164	1.000	-14633.3172	17669.9838
	FM4-64 PC 2	-6601.33333	7767.92733	1.000	-49170.6533	35967.9866
	FM4-64 PC 3	-16817.83333	8198.31978	.858	-62158.8771	28523.2104
	FM4-64 PG 1	22167.66667*	2697.79459	.014	5808.5955	38526.7379
	FM4-64 PG 2	20443.50000*	2723.33710	.018	4215.4369	36671.5631
	FM4-64 PG 3	-199490.00000*	2945.82117	.000	-215180.7973	-183799.2027
	FM4-64 PA 1	22034.16667*	2697.72507	.014	5674.7138	38393.6195
	FM4-64 PA 2	21297.16667*	2699.68112	.016	4948.3994	37645.9339
	FM4-64 PA 3	-53369.33333	21706.50425	.693	-183145.2263	76406.5596
	FM4-64 WT 1	19967.00000*	2854.88914	.016	4167.3723	35766.6277
	FM4-64 WT 2	20274.83333*	2711.74378	.020	3989.5515	36560.1152
	FM4-64 WT 3	17969.00000*	2844.39270	.027	2148.1285	33789.8715
	FM4-64 Background	1518.33333	2740.09164	1.000	-14633.3172	17669.9838
mNg PG 3	mNg PC 1	73622.16667	12535.27235	.053	-1048.6742	148293.0075
	mNg PC 2	41479.33333	15415.34267	.582	-33540.9099	116499.5766
	mNg PC 3	5447.83333	15654.15759	1.000	-70326.3176	81221.9843
	mNg PG 1	75345.50000*	12613.83184	.047	1031.5830	149659.4170
	mNg PG 2	58228.66667	12702.71912	.131	-15721.8466	132179.1800
	mNg PA 1	80014.83333*	12414.11468	.039	4722.9672	155306.6995
	mNg PA 2	72141.33333	12515.72186	.058	-2623.7852	146906.4519
	mNg PA 3	-70893.66667	28994.53046	.700	-223222.5571	81435.2238

	mNg Alone 1	74879.83333	12424.12269	.051	-357.3344	150117.0011
	mNg Alone 2	63895.66667	12899.07907	.090	-9391.7740	137183.1073
	mNg Alone 3	41569.66667	15513.00110	.587	-33750.9695	116890.3028
	FM4-64 PC 1	59747.00000	12422.41504	.122	-15499.4563	134993.4563
	FM4-64 PC 2	51627.33333	14392.67133	.248	-21038.5589	124293.2256
	FM4-64 PC 3	41410.83333	14629.44771	.519	-31653.8879	114475.5546
	FM4-64 PG 1	80396.33333*	12413.15386	.038	5099.1827	155693.4840
	FM4-64 PG 2	78672.16667*	12418.73013	.042	3405.6044	153938.7289
	FM4-64 PG 3	-141261.33333*	12469.40879	.003	-216258.7709	-66263.8958
	FM4-64 PA 1	80262.83333*	12413.13875	.038	4965.5995	155560.0671
	FM4-64 PA 2	79525.83333*	12413.56400	.040	4230.9392	154820.7275
	FM4-64 PA 3	4859.33333	24859.21599	1.000	-121065.5281	130784.1948
	FM4-64 WT 1	78195.66667*	12448.24024	.042	3087.7420	153303.5913
	FM4-64 WT 2	78503.50000*	12416.19295	.042	3223.0445	153783.9555
	FM4-64 WT 3	76197.66667*	12445.83717	.047	1077.0259	151318.3074
	FM4-64 Background	59747.00000	12422.41504	.122	-15499.4563	134993.4563
mNg PA 1	mNg PC 1	-6392.66667	1753.83291	.296	-16944.9281	4159.5948
	mNg PC 2	-38535.50000	9141.97280	.192	-93974.0701	16903.0701
	mNg PC 3	-74567.00000*	9539.15756	.017	-132415.5988	-16718.4012
	mNg PG 1	-4669.33333	2247.58328	.840	-18235.3699	8896.7032
	mNg PG 2	-21786.16667*	2702.21207	.015	-38121.2714	-5451.0619
	mNg PG 3	-80014.83333*	12414.11468	.039	-155306.6995	-4722.9672
	mNg PA 2	-7873.50000	1608.15757	.111	-17534.4775	1787.4775
	mNg PA 3	-150908.50000	26203.54315	.062	-309853.7943	8036.7943
	mNg Alone 1	-5135.00000*	549.27373	.004	-8220.5788	-2049.4212
	mNg Alone 2	-16119.16667	3511.28437	.143	-37375.0579	5136.7246

	mNg Alone 3	-38445.16667	9305.70149	.205	-94877.2132	17986.8799
	FM4-64 PC 1	-20267.83333*	509.18794	.000	-23096.3486	-17439.3180
	FM4-64 PC 2	-28387.50000	7286.41648	.246	-72565.9601	15790.9601
	FM4-64 PC 3	-38604.00000	7743.61785	.107	-85557.0942	8349.0942
	FM4-64 PG 1	381.50000	171.07245	.789	-576.1743	1339.1743
	FM4-64 PG 2	-1342.66667	409.55473	.360	-3528.8406	843.5073
	FM4-64 PG 3	-221276.16667*	1195.42147	.000	-228402.4901	-214149.8432
	FM4-64 PA 1	248.00000	169.97264	.985	-712.4607	1208.4607
	FM4-64 PA 2	-489.00000	198.61596	.694	-1463.2393	485.2393
	FM4-64 PA 3	-75155.50000	21538.88337	.337	-205803.6158	55492.6158
	FM4-64 WT 1	-1819.16667	949.50627	.894	-7423.8115	3785.4782
	FM4-64 WT 2	-1511.33333	323.61162	.076	-3147.1861	124.5194
	FM4-64 WT 3	-3817.16667	917.46387	.190	-9222.5100	1588.1767
	FM4-64 Background	-20267.83333*	509.18794	.000	-23096.3486	-17439.3180
mNg PA 2	mNg PC 1	1480.83333	2368.32861	1.000	-9817.6645	12779.3312
	mNg PC 2	-30662.00000	9279.47828	.381	-85422.8600	24098.8600
	mNg PC 3	-66693.50000*	9671.01739	.026	-123886.3294	-9500.6706
	mNg PG 1	3204.16667	2754.02999	.999	-10256.7338	16665.0671
	mNg PG 2	-13912.66667	3136.08046	.097	-29715.5837	1890.2503
	mNg PG 3	-72141.33333	12515.72186	.058	-146906.4519	2623.7852
	mNg PA 1	7873.50000	1608.15757	.111	-1787.4775	17534.4775
	mNg PA 3	-143035.00000	26251.83277	.076	-301718.0645	15648.0645
	mNg Alone 1	2738.50000	1683.67223	.966	-6653.0321	12130.0321
	mNg Alone 2	-8245.66667	3855.14831	.830	-28639.9420	12148.6087
	mNg Alone 3	-30571.66667	9440.82257	.401	-86335.1819	25191.8486
	FM4-64 PC 1	-12394.33333*	1671.02451	.013	-21816.5399	-2972.1268

	FM4-64 PC 2	-20514.00000	7458.21129	.573	-63897.9365	22869.9365
	FM4-64 PC 3	-30730.50000	7905.48341	.235	-76919.8553	15458.8553
	FM4-64 PG 1	8255.00000	1600.72369	.094	-1445.2552	17955.2552
	FM4-64 PG 2	6530.83333	1643.40671	.215	-2977.2844	16038.9511
	FM4-64 PG 3	-213402.66667*	1990.49819	.000	-223082.9080	-203722.4254
	FM4-64 PA 1	8121.50000	1600.60653	.100	-1579.3955	17822.3955
	FM4-64 PA 2	7384.50000	1603.90113	.141	-2298.6436	17067.6436
	FM4-64 PA 3	-67282.00000	21597.60513	.445	-197613.2841	63049.2841
	FM4-64 WT 1	6054.33333	1853.27081	.346	-3308.7921	15417.4588
	FM4-64 WT 2	6362.16667	1624.12285	.233	-3223.0458	15947.3792
	FM4-64 WT 3	4056.33333	1837.06029	.807	-5285.4213	13398.0880
	FM4-64 Background	-12394.33333*	1671.02451	.013	-21816.5399	-2972.1268
mNg PA 3	mNg PC 1	144515.83333	26261.15921	.073	-14117.3796	303149.0463
	mNg PC 2	112373.00000	27751.54446	.186	-41079.9831	265825.9831
	mNg PC 3	76341.50000	27884.90775	.572	-76873.9939	229556.9939
	mNg PG 1	146239.16667	26298.74871	.069	-12195.7008	304674.0341
	mNg PG 2	129122.33333	26341.49774	.111	-29091.9297	287336.5964
	mNg PG 3	70893.66667	28994.53046	.700	-81435.2238	223222.5571
	mNg PA 1	150908.50000	26203.54315	.062	-8036.7943	309853.7943
	mNg PA 2	143035.00000	26251.83277	.076	-15648.0645	301718.0645
	mNg Alone 1	145773.50000	26208.28599	.071	-13145.7317	304692.7317
	mNg Alone 2	134789.33333	26436.74850	.094	-22952.0084	292530.6750
	mNg Alone 3	112463.33333	27805.91004	.186	-40889.0459	265815.7126
	FM4-64 PC 1	130640.66667	26207.47652	.107	-28283.0085	289564.3418
	FM4-64 PC 2	122521.00000	27196.77220	.133	-32278.6791	277320.6791
	FM4-64 PC 3	112304.50000	27322.81410	.184	-42135.4396	266744.4396
	FM4-64 PG 1	151290.00000	26203.08797	.061	-7657.7992	310237.7992
	FM4-64 PG 2	149565.83333	26205.73006	.064	-9367.4352	308499.1019

	FM4-64 PG 3	-70367.66667	26229.78432	.603	-229169.6036	88434.2703
	FM4-64 PA 1	151156.50000	26203.08081	.061	-7791.3386	310104.3386
	FM4-64 PA 2	150419.50000	26203.28226	.062	-8527.2299	309366.2299
	FM4-64 PA 3	75753.00000	33918.96298	.803	-87264.2805	238770.2805
	FM4-64 WT 1	149089.33333	26219.72760	.065	-9767.3018	307945.9684
	FM4-64 WT 2	149397.16667	26204.52781	.064	-9542.7113	308337.0446
	FM4-64 WT 3	147091.33333	26218.58679	.068	-11771.5256	305954.1922
	FM4-64 Background	130640.66667	26207.47652	.107	-28283.0085	289564.3418
mNg Alone 1	mNg PC 1	-1257.66667	1823.32424	1.000	-11543.3896	9028.0562
	mNg PC 2	-33400.50000	9155.55831	.297	-88765.2555	21964.2555
	mNg PC 3	-69432.00000*	9552.17820	.023	-127209.7790	-11654.2210
	mNg PG 1	465.66667	2302.21893	1.000	-12858.2018	13789.5352
	mNg PG 2	-16651.16667*	2747.82305	.043	-32769.9598	-532.3735
	mNg PG 3	-74879.83333	12424.12269	.051	-150117.0011	357.3344
	mNg PA 1	5135.00000*	549.27373	.004	2049.4212	8220.5788
	mNg PA 2	-2738.50000	1683.67223	.966	-12130.0321	6653.0321
	mNg PA 3	-145773.50000	26208.28599	.071	-304692.7317	13145.7317
	mNg Alone 2	-10984.16667	3546.50523	.448	-32062.4937	10094.1603
	mNg Alone 3	-33310.16667	9319.04832	.314	-89669.6629	23049.3295
	FM4-64 PC 1	-15132.83333*	712.63859	.000	-18532.0485	-11733.6182
	FM4-64 PC 2	-23252.50000	7303.45442	.423	-67339.0701	20834.0701
	FM4-64 PC 3	-33469.00000	7759.65197	.176	-80335.4166	13397.4166
	FM4-64 PG 1	5516.50000*	527.11212	.004	2348.3074	8684.6926
	FM4-64 PG 2	3792.33333*	645.22591	.016	640.2982	6944.3684
	FM4-64 PG 3	-216141.16667*	1295.22735	.000	-223029.3781	-209252.9552
	FM4-64 PA 1	5383.00000*	526.75621	.005	2212.9734	8553.0266
	FM4-64 PA 2	4646.00000*	536.68399	.008	1520.6941	7771.3059

	FM4-64 PA 3	-70020.50000	21544.65312	.404	-200636.9340	60595.9340
	FM4-64 WT 1	3315.83333	1072.44746	.413	-2144.1722	8775.8388
	FM4-64 WT 2	3623.66667*	594.39539	.019	568.7332	6678.6002
	FM4-64 WT 3	1317.83333	1044.18454	.998	-3963.7448	6599.4115
	FM4-64 Background	-15132.83333*	712.63859	.000	-18532.0485	-11733.6182
mNg Alone 2	mNg PC 1	9726.50000	3918.15360	.683	-10669.6627	30122.6627
	mNg PC 2	-22416.33333	9790.38632	.766	-75767.7663	30935.0996
	mNg PC 3	-58447.83333*	10162.25982	.040	-114197.3426	-2698.3241
	mNg PG 1	11449.83333	4162.64679	.555	-9252.8719	32152.5386
	mNg PG 2	-5667.00000	4424.69748	.998	-27082.6859	15748.6859
	mNg PG 3	-63895.66667	12899.07907	.090	-137183.1073	9391.7740
	mNg PA 1	16119.16667	3511.28437	.143	-5136.7246	37375.0579
	mNg PA 2	8245.66667	3855.14831	.830	-12148.6087	28639.9420
	mNg PA 3	-134789.33333	26436.74850	.094	-292530.6750	22952.0084
	mNg Alone 1	10984.16667	3546.50523	.448	-10094.1603	32062.4937
	mNg Alone 3	-22326.00000	9943.44397	.785	-76664.7539	32012.7539
	FM4-64 PC 1	-4148.66667	3540.51834	.998	-25255.3456	16958.0122
	FM4-64 PC 2	-12268.33333	8085.03945	.983	-54617.5252	30080.8586
	FM4-64 PC 3	-22484.83333	8499.38910	.610	-67502.8398	22533.1732
	FM4-64 PG 1	16500.66667	3507.88590	.132	-4773.7709	37775.1043
	FM4-64 PG 2	14776.50000	3527.56755	.192	-6394.0380	35947.0380
	FM4-64 PG 3	-205157.00000*	3702.03055	.000	-225723.3108	-184590.6892
	FM4-64 PA 1	16367.16667	3507.83244	.136	-4907.5648	37641.8981
	FM4-64 PA 2	15630.16667	3509.33698	.159	-5636.3206	36896.6539
	FM4-64 PA 3	-59036.33333	21821.99566	.593	-188267.0701	70194.4034
	FM4-64 WT 1	14300.00000	3630.09089	.218	-6453.2866	35053.2866
	FM4-64 WT 2	14607.83333	3518.62504	.199	-6608.8678	35824.5345

	FM4-64 WT 3	12302.00000	3621.84175	.346	-8477.8771	33081.8771
	FM4-64 Background	-4148.66667	3540.51834	.998	-25255.3456	16958.0122
mNg Alone 3	mNg PC 1	32052.50000	9466.72540	.356	-23598.7836	87703.7836
	mNg PC 2	-90.33333	13042.95314	1.000	-62201.1021	62020.4354
	mNg PC 3	-36121.83333	13324.35690	.569	-99577.3587	27333.6920
	mNg PG 1	33775.83333	9570.50628	.312	-21472.9574	89024.6241
	mNg PG 2	16659.00000	9687.35826	.948	-38220.3055	71538.3055
	mNg PG 3	-41569.66667	15513.00110	.587	-116890.3028	33750.9695
	mNg PA 1	38445.16667	9305.70149	.205	-17986.8799	94877.2132
	mNg PA 2	30571.66667	9440.82257	.401	-25191.8486	86335.1819
	mNg PA 3	-112463.33333	27805.91004	.186	-265815.7126	40889.0459
	mNg Alone 1	33310.16667	9319.04832	.314	-23049.3295	89669.6629
	mNg Alone 2	22326.00000	9943.44397	.785	-32012.7539	76664.7539
	FM4-64 PC 1	18177.33333	9316.77156	.881	-38194.4336	74549.1002
	FM4-64 PC 2	10057.66667	11816.71803	1.000	-47017.5710	67132.9043
	FM4-64 PC 3	-158.83333	12103.99014	1.000	-58267.8966	57950.2300
	FM4-64 PG 1	38826.66667	9304.41969	.198	-17612.4261	95265.7594
	FM4-64 PG 2	37102.50000	9311.85776	.229	-19295.8972	93500.8972
	FM4-64 PG 3	-182831.00000*	9379.33859	.000	-238880.9295	-126781.0705
	FM4-64 PA 1	38693.16667	9304.39953	.200	-17746.0370	95132.3703
	FM4-64 PA 2	37956.16667	9304.96686	.213	-18479.9165	94392.2499
	FM4-64 PA 3	-36710.33333	23462.02158	.977	-162038.4874	88617.8207
	FM4-64 WT 1	36626.00000	9351.17758	.239	-19564.8808	92816.8808
	FM4-64 WT 2	36933.83333	9308.47380	.232	-19483.0208	93350.6875
	FM4-64 WT 3	34628.00000	9347.97839	.282	-21579.2936	90835.2936
	FM4-64 Background	18177.33333	9316.77156	.881	-38194.4336	74549.1002
FM4-64 PC 1	mNg PC 1	13875.16667*	1811.65173	.012	3556.4237	24193.9096
	mNg PC 2	-18267.66667	9153.24089	.867	-73644.9026	37109.5692

	mNg PC 3	-54299.16667	9549.95702	.064	-112088.9289	3490.5956
	mNg PG 1	15598.50000*	2292.98555	.025	2239.9605	28957.0395
	mNg PG 2	-1518.33333	2740.09164	1.000	-17669.9838	14633.3172
	mNg PG 3	-59747.00000	12422.41504	.122	-134993.4563	15499.4563
	mNg PA 1	20267.83333*	509.18794	.000	17439.3180	23096.3486
	mNg PA 2	12394.33333*	1671.02451	.013	2972.1268	21816.5399
	mNg PA 3	-130640.66667	26207.47652	.107	-289564.3418	28283.0085
	mNg Alone 1	15132.83333*	712.63859	.000	11733.6182	18532.0485
	mNg Alone 2	4148.66667	3540.51834	.998	-16958.0122	25255.3456
	mNg Alone 3	-18177.33333	9316.77156	.881	-74549.1002	38194.4336
	FM4-64 PC 2	-8119.66667	7300.54911	.999	-52221.6882	35982.3549
	FM4-64 PC 3	-18336.16667	7756.91753	.731	-65217.1834	28544.8501
	FM4-64 PG 1	20649.33333*	485.19884	.000	17737.8361	23560.8305
	FM4-64 PG 2	18925.16667*	611.46317	.000	15970.0452	21880.2882
	FM4-64 PG 3	-201008.33333*	1278.74338	.000	-207908.5288	-194108.1379
	FM4-64 PA 1	20515.83333*	484.81216	.000	17602.3676	23429.2991
	FM4-64 PA 2	19778.83333*	495.58090	.000	16912.0955	22645.5711
	FM4-64 PA 3	-54887.66667	21543.66842	.657	-185509.4991	75734.1658
	FM4-64 WT 1	18448.66667*	1052.48007	.000	13005.8744	23891.4589
	FM4-64 WT 2	18756.50000*	557.56310	.000	15935.0420	21577.9580
	FM4-64 WT 3	16450.66667*	1023.66600	.000	11191.8635	21709.4698
	FM4-64 Background	.00000	682.22026	1.000	-3248.4905	3248.4905
FM4-64 PC 2	mNg PC 1	21994.83333	7490.97288	.500	-21268.3858	65258.0524
	mNg PC 2	-10148.00000	11688.21678	1.000	-66494.0439	46198.0439
	mNg PC 3	-46179.50000	12001.42791	.169	-104314.4397	11955.4397
	mNg PG 1	23718.16667	7621.70424	.431	-19149.1816	66585.5149
	mNg PG 2	6601.33333	7767.92733	1.000	-35967.9866	49170.6533
	mNg PG 3	-51627.33333	14392.67133	.248	-124293.2256	21038.5589

	mNg PA 1	28387.50000	7286.41648	.246	-15790.9601	72565.9601
	mNg PA 2	20514.00000	7458.21129	.573	-22869.9365	63897.9365
	mNg PA 3	-122521.00000	27196.77220	.133	-277320.6791	32278.6791
	mNg Alone 1	23252.50000	7303.45442	.423	-20834.0701	67339.0701
	mNg Alone 2	12268.33333	8085.03945	.983	-30080.8586	54617.5252
	mNg Alone 3	-10057.66667	11816.71803	1.000	-67132.9043	47017.5710
	FM4-64 PC 1	8119.66667	7300.54911	.999	-35982.3549	52221.6882
	FM4-64 PC 3	-10216.50000	10630.25692	1.000	-60880.4886	40447.4886
	FM4-64 PG 1	28769.00000	7284.77938	.236	-15418.4526	72956.4526
	FM4-64 PG 2	27044.83333	7294.27721	.284	-17090.8483	71180.5150
	FM4-64 PG 3	-192888.66667*	7380.22882	.000	-236598.0932	-149179.2401
	FM4-64 PA 1	28635.50000	7284.75364	.239	-15552.0942	72823.0942
	FM4-64 PA 2	27898.50000	7285.47824	.259	-16285.1103	72082.1103
	FM4-64 PA 3	-46768.00000	22736.80368	.855	-173049.8691	79513.8691
	FM4-64 WT 1	26568.33333	7344.40651	.300	-17309.7293	70446.3960
	FM4-64 WT 2	26876.16667	7289.95675	.289	-17282.9454	71035.2787
	FM4-64 WT 3	24570.33333	7340.33275	.371	-19327.7069	68468.3736
	FM4-64 Background	8119.66667	7300.54911	.999	-35982.3549	52221.6882
FM4-64 PC 3	mNg PC 1	32211.33333	7936.39887	.202	-13858.3758	78281.0424
	mNg PC 2	68.50000	11978.57102	1.000	-57353.5404	57490.5404
	mNg PC 3	-35963.00000	12284.38130	.467	-95073.1681	23147.1681
	mNg PG 1	33934.66667	8059.90867	.169	-11731.4279	79600.7612
	mNg PG 2	16817.83333	8198.31978	.858	-28523.2104	62158.8771
	mNg PG 3	-41410.83333	14629.44771	.519	-114475.5546	31653.8879
	mNg PA 1	38604.00000	7743.61785	.107	-8349.0942	85557.0942
	mNg PA 2	30730.50000	7905.48341	.235	-15458.8553	76919.8553
	mNg PA 3	-112304.50000	27322.81410	.184	-266744.4396	42135.4396
	mNg Alone 1	33469.00000	7759.65197	.176	-13397.4166	80335.4166

	mNg Alone 2	22484.83333	8499.38910	.610	-22533.1732	67502.8398
	mNg Alone 3	158.83333	12103.99014	1.000	-57950.2300	58267.8966
	FM4-64 PC 1	18336.16667	7756.91753	.731	-28544.8501	65217.1834
	FM4-64 PC 2	10216.50000	10630.25692	1.000	-40447.4886	60880.4886
	FM4-64 PG 1	38985.50000	7742.07743	.103	-7976.0575	85947.0575
	FM4-64 PG 2	37261.33333	7751.01491	.121	-9651.4536	84174.1202
	FM4-64 PG 3	-182672.16667*	7831.95567	.000	-229178.7017	-136165.6317
	FM4-64 PA 1	38852.00000	7742.05321	.104	-8109.6908	85813.6908
	FM4-64 PA 2	38115.00000	7742.73501	.112	-8842.9417	85072.9417
	FM4-64 PA 3	-36551.50000	22887.41999	.971	-162547.5463	89444.5463
	FM4-64 WT 1	36784.83333	7798.20872	.127	-9883.4986	83453.1653
	FM4-64 WT 2	37092.66667	7746.94918	.124	-9842.2066	84027.5399
	FM4-64 WT 3	34786.83333	7794.37214	.154	-11900.5675	81474.2341
	FM4-64 Background	18336.16667	7756.91753	.731	-28544.8501	65217.1834
FM4-64 PG 1	mNg PC 1	-6774.16667	1747.01901	.249	-17362.6672	3814.3339
	mNg PC 2	-38917.00000	9140.66804	.186	-94362.7422	16528.7422
	mNg PC 3	-74948.50000*	9537.90713	.017	-132803.9729	-17093.0271
	mNg PG 1	-5050.83333	2242.27031	.775	-18645.5099	8543.8432
	mNg PG 2	-22167.66667*	2697.79459	.014	-38526.7379	-5808.5955
	mNg PG 3	-80396.33333*	12413.15386	.038	-155693.4840	-5099.1827
	mNg PA 1	-381.50000	171.07245	.789	-1339.1743	576.1743
	mNg PA 2	-8255.00000	1600.72369	.094	-17955.2552	1445.2552
	mNg PA 3	-151290.00000	26203.08797	.061	-310237.7992	7657.7992
	mNg Alone 1	-5516.50000*	527.11212	.004	-8684.6926	-2348.3074
	mNg Alone 2	-16500.66667	3507.88590	.132	-37775.1043	4773.7709
	mNg Alone 3	-38826.66667	9304.41969	.198	-95265.7594	17612.4261
	FM4-64 PC 1	-20649.33333*	485.19884	.000	-23560.8305	-17737.8361

	FM4-64 PC 2	-28769.00000	7284.77938	.236	-72956.4526	15418.4526
	FM4-64 PC 3	-38985.50000	7742.07743	.103	-85947.0575	7976.0575
	FM4-64 PG 2	-1724.16667	379.31600	.143	-3984.9465	536.6132
	FM4-64 PG 3	-221657.66667*	1185.40206	.000	-228835.1694	-214480.1640
	FM4-64 PA 1	-133.50000	70.96654	.930	-471.8830	204.8830
	FM4-64 PA 2	-870.50000*	124.87534	.011	-1530.5700	-210.4300
	FM4-64 PA 3	-75537.00000	21538.32961	.332	-206188.1628	55114.1628
	FM4-64 WT 1	-2200.66667	936.86056	.737	-7867.0469	3465.7136
	FM4-64 WT 2	-1892.83333*	284.37656	.029	-3565.4232	-220.2434
	FM4-64 WT 3	-4198.66667	904.37023	.137	-9667.3680	1270.0347
	FM4-64 Background	-20649.33333*	485.19884	.000	-23560.8305	-17737.8361
FM4-64 PG 2	mNg PC 1	-5050.00000	1786.20960	.543	-15456.2644	5356.2644
	mNg PC 2	-37192.83333	9148.23926	.215	-92597.1605	18211.4938
	mNg PC 3	-73224.33333*	9545.16326	.018	-131040.0948	-15408.5718
	mNg PG 1	-3326.66667	2272.93763	.982	-16768.9460	10115.6126
	mNg PG 2	-20443.50000*	2723.33710	.018	-36671.5631	-4215.4369
	mNg PG 3	-78672.16667*	12418.73013	.042	-153938.7289	-3405.6044
	mNg PA 1	1342.66667	409.55473	.360	-843.5073	3528.8406
	mNg PA 2	-6530.83333	1643.40671	.215	-16038.9511	2977.2844
	mNg PA 3	-149565.83333	26205.73006	.064	-308499.1019	9367.4352
	mNg Alone 1	-3792.33333*	645.22591	.016	-6944.3684	-640.2982
	mNg Alone 2	-14776.50000	3527.56755	.192	-35947.0380	6394.0380
	mNg Alone 3	-37102.50000	9311.85776	.229	-93500.8972	19295.8972
	FM4-64 PC 1	-18925.16667*	611.46317	.000	-21880.2882	-15970.0452
	FM4-64 PC 2	-27044.83333	7294.27721	.284	-71180.5150	17090.8483
	FM4-64 PC 3	-37261.33333	7751.01491	.121	-84174.1202	9651.4536
	FM4-64 PG 1	1724.16667	379.31600	.143	-536.6132	3984.9465

	FM4-64 PG 3	-219933.50000*	1242.43605	.000	-226894.1685	-212972.8315
	FM4-64 PA 1	1590.66667	378.82126	.189	-672.5054	3853.8387
	FM4-64 PA 2	853.66667	392.50878	.810	-1358.9681	3066.3014
	FM4-64 PA 3	-73812.83333	21541.54385	.353	-204446.3253	56820.6586
	FM4-64 WT 1	-476.50000	1008.05605	1.000	-5928.8498	4975.8498
	FM4-64 WT 2	-168.66667	468.33676	1.000	-2444.7385	2107.4052
	FM4-64 WT 3	-2474.50000	977.93395	.662	-7732.3503	2783.3503
	FM4-64 Background	-18925.16667*	611.46317	.000	-21880.2882	-15970.0452
FM4-64 PG 3	mNg PC 1	214883.50000*	2109.93889	.000	204491.2480	225275.7520
	mNg PC 2	182740.66667*	9216.91808	.000	127690.1750	237791.1583
	mNg PC 3	146709.16667*	9611.00615	.001	89234.4672	204183.8662
	mNg PG 1	216606.83333*	2535.25992	.000	203555.0596	229658.6070
	mNg PG 2	199490.00000*	2945.82117	.000	183799.2027	215180.7973
	mNg PG 3	141261.33333*	12469.40879	.003	66263.8958	216258.7709
	mNg PA 1	221276.16667*	1195.42147	.000	214149.8432	228402.4901
	mNg PA 2	213402.66667*	1990.49819	.000	203722.4254	223082.9080
	mNg PA 3	70367.66667	26229.78432	.603	-88434.2703	229169.6036
	mNg Alone 1	216141.16667*	1295.22735	.000	209252.9552	223029.3781
	mNg Alone 2	205157.00000*	3702.03055	.000	184590.6892	225723.3108
	mNg Alone 3	182831.00000*	9379.33859	.000	126781.0705	238880.9295
	FM4-64 PC 1	201008.33333*	1278.74338	.000	194108.1379	207908.5288
	FM4-64 PC 2	192888.66667*	7380.22882	.000	149179.2401	236598.0932
	FM4-64 PC 3	182672.16667*	7831.95567	.000	136165.6317	229178.7017
	FM4-64 PG 1	221657.66667*	1185.40206	.000	214480.1640	228835.1694
	FM4-64 PG 2	219933.50000*	1242.43605	.000	212972.8315	226894.1685
	FM4-64 PA 1	221524.16667*	1185.24384	.000	214345.8043	228702.5291
	FM4-64 PA 2	220787.16667*	1189.68927	.000	213632.3402	227941.9932
	FM4-64 PA 3	146120.66667*	21570.79992	.031	15646.2934	276595.0399

	FM4-64 WT 1	219457.00000*	1509.13035	.000	212174.9207	226739.0793
	FM4-64 WT 2	219764.83333*	1216.81418	.000	212727.9466	226801.7201
	FM4-64 WT 3	217459.00000*	1489.17837	.000	210243.8468	224674.1532
	FM4-64 Background	201008.33333*	1278.74338	.000	194108.1379	207908.5288
FM4-64 PA 1	mNg PC 1	-6640.66667	1746.91166	.264	-17229.7546	3948.4213
	mNg PC 2	-38783.50000	9140.64752	.188	-94229.3551	16662.3551
	mNg PC 3	-74815.00000*	9537.88747	.017	-132670.5811	-16959.4189
	mNg PG 1	-4917.33333	2242.18667	.797	-18512.4686	8677.8019
	mNg PG 2	-22034.16667*	2697.72507	.014	-38393.6195	-5674.7138
	mNg PG 3	-80262.83333*	12413.13875	.038	-155560.0671	-4965.5995
	mNg PA 1	-248.00000	169.97264	.985	-1208.4607	712.4607
	mNg PA 2	-8121.50000	1600.60653	.100	-17822.3955	1579.3955
	mNg PA 3	-151156.50000	26203.08081	.061	-310104.3386	7791.3386
	mNg Alone 1	-5383.00000*	526.75621	.005	-8553.0266	-2212.9734
	mNg Alone 2	-16367.16667	3507.83244	.136	-37641.8981	4907.5648
	mNg Alone 3	-38693.16667	9304.39953	.200	-95132.3703	17746.0370
	FM4-64 PC 1	-20515.83333*	484.81216	.000	-23429.2991	-17602.3676
	FM4-64 PC 2	-28635.50000	7284.75364	.239	-72823.0942	15552.0942
	FM4-64 PC 3	-38852.00000	7742.05321	.104	-85813.6908	8109.6908
	FM4-64 PG 1	133.50000	70.96654	.930	-204.8830	471.8830
	FM4-64 PG 2	-1590.66667	378.82126	.189	-3853.8387	672.5054
	FM4-64 PG 3	-221524.16667*	1185.24384	.000	-228702.5291	-214345.8043
	FM4-64 PA 2	-737.00000*	123.36437	.029	-1397.7970	-76.2030
	FM4-64 PA 3	-75403.50000	21538.32090	.334	-206054.7108	55247.7108
	FM4-64 WT 1	-2067.16667	936.66036	.792	-7734.6263	3600.2930
	FM4-64 WT 2	-1759.33333*	283.71631	.041	-3434.7879	-83.8788
	FM4-64 WT 3	-4065.16667	904.16283	.154	-9534.9846	1404.6512

	FM4-64 Background	-20515.83333*	484.81216	.000	-23429.2991	-17602.3676
FM4-64 PA 2	mNg PC 1	-5903.66667	1749.93084	.367	-16476.4311	4669.0978
	mNg PC 2	-38046.50000	9141.22501	.200	-93489.1788	17396.1788
	mNg PC 3	-74078.00000*	9538.44091	.018	-131930.5369	-16225.4631
	mNg PG 1	-4180.33333	2244.53975	.907	-17762.6570	9401.9903
	mNg PG 2	-21297.16667*	2699.68112	.016	-37645.9339	-4948.3994
	mNg PG 3	-79525.83333*	12413.56400	.040	-154820.7275	-4230.9392
	mNg PA 1	489.00000	198.61596	.694	-485.2393	1463.2393
	mNg PA 2	-7384.50000	1603.90113	.141	-17067.6436	2298.6436
	mNg PA 3	-150419.50000	26203.28226	.062	-309366.2299	8527.2299
	mNg Alone 1	-4646.00000*	536.68399	.008	-7771.3059	-1520.6941
	mNg Alone 2	-15630.16667	3509.33698	.159	-36896.6539	5636.3206
	mNg Alone 3	-37956.16667	9304.96686	.213	-94392.2499	18479.9165
	FM4-64 PC 1	-19778.83333*	495.58090	.000	-22645.5711	-16912.0955
	FM4-64 PC 2	-27898.50000	7285.47824	.259	-72082.1103	16285.1103
	FM4-64 PC 3	-38115.00000	7742.73501	.112	-85072.9417	8842.9417
	FM4-64 PG 1	870.50000*	124.87534	.011	210.4300	1530.5700
	FM4-64 PG 2	-853.66667	392.50878	.810	-3066.3014	1358.9681
	FM4-64 PG 3	-220787.16667*	1189.68927	.000	-227941.9932	-213632.3402
	FM4-64 PA 1	737.00000*	123.36437	.029	76.2030	1397.7970
	FM4-64 PA 3	-74666.50000	21538.56599	.343	-205316.3620	55983.3620
	FM4-64 WT 1	-1330.16667	942.27927	.987	-6968.5679	4308.2346
	FM4-64 WT 2	-1022.33333	301.74914	.329	-2651.4604	606.7937
	FM4-64 WT 3	-3328.16667	909.98243	.291	-8768.0262	2111.6929
	FM4-64 Background	-19778.83333*	495.58090	.000	-22645.5711	-16912.0955
FM4-64 PA 3	mNg PC 1	68762.83333	21608.94043	.423	-61508.7109	199034.3776
	mNg PC 2	36620.00000	23397.56490	.977	-88752.2250	161992.2250
	mNg PC 3	588.50000	23555.59176	1.000	-124688.5243	125865.5243

	mNg PG 1	70486.16667	21654.60706	.400	-59549.2778	200521.6112
	mNg PG 2	53369.33333	21706.50425	.693	-76406.5596	183145.2263
	mNg PG 3	-4859.33333	24859.21599	1.000	-130784.1948	121065.5281
	mNg PA 1	75155.50000	21538.88337	.337	-55492.6158	205803.6158
	mNg PA 2	67282.00000	21597.60513	.445	-63049.2841	197613.2841
	mNg PA 3	-75753.00000	33918.96298	.803	-238770.2805	87264.2805
	mNg Alone 1	70020.50000	21544.65312	.404	-60595.9340	200636.9340
	mNg Alone 2	59036.33333	21821.99566	.593	-70194.4034	188267.0701
	mNg Alone 3	36710.33333	23462.02158	.977	-88617.8207	162038.4874
	FM4-64 PC 1	54887.66667	21543.66842	.657	-75734.1658	185509.4991
	FM4-64 PC 2	46768.00000	22736.80368	.855	-79513.8691	173049.8691
	FM4-64 PC 3	36551.50000	22887.41999	.971	-89444.5463	162547.5463
	FM4-64 PG 1	75537.00000	21538.32961	.332	-55114.1628	206188.1628
	FM4-64 PG 2	73812.83333	21541.54385	.353	-56820.6586	204446.3253
	FM4-64 PG 3	-146120.66667*	21570.79992	.031	-276595.0399	-15646.2934
	FM4-64 PA 1	75403.50000	21538.32090	.334	-55247.7108	206054.7108
	FM4-64 PA 2	74666.50000	21538.56599	.343	-55983.3620	205316.3620
	FM4-64 WT 1	73336.33333	21558.56996	.359	-57204.1803	203876.8470
	FM4-64 WT 2	73644.16667	21540.08127	.355	-56997.3615	204285.6948
	FM4-64 WT 3	71338.33333	21557.18248	.386	-59209.7180	201886.3846
	FM4-64 Background	54887.66667	21543.66842	.657	-75734.1658	185509.4991
FM4-64 WT 1	mNg PC 1	-4573.50000	1981.00273	.763	-14745.4644	5598.4644
	mNg PC 2	-36716.33333	9188.25928	.224	-91909.7695	18477.1029
	mNg PC 3	-72747.83333*	9583.52591	.018	-130360.7178	-15134.9489
	mNg PG 1	-2850.16667	2429.00649	.999	-15903.5997	10203.2663
	mNg PG 2	-19967.00000*	2854.88914	.016	-35766.6277	-4167.3723
	mNg PG 3	-78195.66667*	12448.24024	.042	-153303.5913	-3087.7420
	mNg PA 1	1819.16667	949.50627	.894	-3785.4782	7423.8115
	mNg PA 2	-6054.33333	1853.27081	.346	-15417.4588	3308.7921

	mNg PA 3	-149089.33333	26219.72760	.065	-307945.9684	9767.3018
	mNg Alone 1	-3315.83333	1072.44746	.413	-8775.8388	2144.1722
	mNg Alone 2	-14300.00000	3630.09089	.218	-35053.2866	6453.2866
	mNg Alone 3	-36626.00000	9351.17758	.239	-92816.8808	19564.8808
	FM4-64 PC 1	-18448.66667*	1052.48007	.000	-23891.4589	-13005.8744
	FM4-64 PC 2	-26568.33333	7344.40651	.300	-70446.3960	17309.7293
	FM4-64 PC 3	-36784.83333	7798.20872	.127	-83453.1653	9883.4986
	FM4-64 PG 1	2200.66667	936.86056	.737	-3465.7136	7867.0469
	FM4-64 PG 2	476.50000	1008.05605	1.000	-4975.8498	5928.8498
	FM4-64 PG 3	-219457.00000*	1509.13035	.000	-226739.0793	-212174.9207
	FM4-64 PA 1	2067.16667	936.66036	.792	-3600.2930	7734.6263
	FM4-64 PA 2	1330.16667	942.27927	.987	-4308.2346	6968.5679
	FM4-64 PA 3	-73336.33333	21558.56996	.359	-203876.8470	57204.1803
	FM4-64 WT 2	307.83333	976.30242	1.000	-5203.0178	5818.6845
	FM4-64 WT 3	-1998.00000	1300.06996	.987	-8190.3966	4194.3966
	FM4-64 Background	-18448.66667*	1052.48007	.000	-23891.4589	-13005.8744
FM4-64 WT 2	mNg PC 1	-4881.33333	1768.48357	.571	-15362.3684	5599.7017
	mNg PC 2	-37024.16667	9144.79474	.218	-92447.2748	18398.9414
	mNg PC 3	-73055.66667*	9541.86204	.019	-130889.4416	-15221.8917
	mNg PG 1	-3158.00000	2259.03405	.988	-16665.5601	10349.5601
	mNg PG 2	-20274.83333*	2711.74378	.020	-36560.1152	-3989.5515
	mNg PG 3	-78503.50000*	12416.19295	.042	-153783.9555	-3223.0445
	mNg PA 1	1511.33333	323.61162	.076	-124.5194	3147.1861
	mNg PA 2	-6362.16667	1624.12285	.233	-15947.3792	3223.0458
	mNg PA 3	-149397.16667	26204.52781	.064	-308337.0446	9542.7113
	mNg Alone 1	-3623.66667*	594.39539	.019	-6678.6002	-568.7332
	mNg Alone 2	-14607.83333	3518.62504	.199	-35824.5345	6608.8678

	mNg Alone 3	-36933.83333	9308.47380	.232	-93350.6875	19483.0208
	FM4-64 PC 1	-18756.50000*	557.56310	.000	-21577.9580	-15935.0420
	FM4-64 PC 2	-26876.16667	7289.95675	.289	-71035.2787	17282.9454
	FM4-64 PC 3	-37092.66667	7746.94918	.124	-84027.5399	9842.2066
	FM4-64 PG 1	1892.83333*	284.37656	.029	220.2434	3565.4232
	FM4-64 PG 2	168.66667	468.33676	1.000	-2107.4052	2444.7385
	FM4-64 PG 3	-219764.83333*	1216.81418	.000	-226801.7201	-212727.9466
	FM4-64 PA 1	1759.33333*	283.71631	.041	83.8788	3434.7879
	FM4-64 PA 2	1022.33333	301.74914	.329	-606.7937	2651.4604
	FM4-64 PA 3	-73644.16667	21540.08127	.355	-204285.6948	56997.3615
	FM4-64 WT 1	-307.83333	976.30242	1.000	-5818.6845	5203.0178
	FM4-64 WT 3	-2305.83333	945.16888	.701	-7617.6396	3005.9730
	FM4-64 Background	-18756.50000*	557.56310	.000	-21577.9580	-15935.0420
FM4-64 WT 3	mNg PC 1	-2575.50000	1965.84577	.996	-12736.7763	7585.7763
	mNg PC 2	-34718.33333	9185.00334	.266	-89928.4306	20491.7639
	mNg PC 3	-70749.83333*	9580.40430	.021	-128378.7875	-13120.8791
	mNg PG 1	-852.16667	2416.66099	1.000	-13917.4108	12213.0775
	mNg PG 2	-17969.00000*	2844.39270	.027	-33789.8715	-2148.1285
	mNg PG 3	-76197.66667*	12445.83717	.047	-151318.3074	-1077.0259
	mNg PA 1	3817.16667	917.46387	.190	-1588.1767	9222.5100
	mNg PA 2	-4056.33333	1837.06029	.807	-13398.0880	5285.4213
	mNg PA 3	-147091.33333	26218.58679	.068	-305954.1922	11771.5256
	mNg Alone 1	-1317.83333	1044.18454	.998	-6599.4115	3963.7448
	mNg Alone 2	-12302.00000	3621.84175	.346	-33081.8771	8477.8771
	mNg Alone 3	-34628.00000	9347.97839	.282	-90835.2936	21579.2936
	FM4-64 PC 1	-16450.66667*	1023.66600	.000	-21709.4698	-11191.8635
	FM4-64 PC 2	-24570.33333	7340.33275	.371	-68468.3736	19327.7069

	FM4-64 PC 3	-34786.83333	7794.37214	.154	-81474.2341	11900.5675
	FM4-64 PG 1	4198.66667	904.37023	.137	-1270.0347	9667.3680
	FM4-64 PG 2	2474.50000	977.93395	.662	-2783.3503	7732.3503
	FM4-64 PG 3	-217459.00000*	1489.17837	.000	-224674.1532	-210243.8468
	FM4-64 PA 1	4065.16667	904.16283	.154	-1404.6512	9534.9846
	FM4-64 PA 2	3328.16667	909.98243	.291	-2111.6929	8768.0262
	FM4-64 PA 3	-71338.33333	21557.18248	.386	-201886.3846	59209.7180
	FM4-64 WT 1	1998.00000	1300.06996	.987	-4194.3966	8190.3966
	FM4-64 WT 2	2305.83333	945.16888	.701	-3005.9730	7617.6396
	FM4-64 Background	-16450.66667*	1023.66600	.000	-21709.4698	-11191.8635
FM4-64 Background	mNg PC 1	13875.16667*	1811.65173	.012	3556.4237	24193.9096
	mNg PC 2	-18267.66667	9153.24089	.867	-73644.9026	37109.5692
	mNg PC 3	-54299.16667	9549.95702	.064	-112088.9289	3490.5956
	mNg PG 1	15598.50000*	2292.98555	.025	2239.9605	28957.0395
	mNg PG 2	-1518.33333	2740.09164	1.000	-17669.9838	14633.3172
	mNg PG 3	-59747.00000	12422.41504	.122	-134993.4563	15499.4563
	mNg PA 1	20267.83333*	509.18794	.000	17439.3180	23096.3486
	mNg PA 2	12394.33333*	1671.02451	.013	2972.1268	21816.5399
	mNg PA 3	-130640.66667	26207.47652	.107	-289564.3418	28283.0085
	mNg Alone 1	15132.83333*	712.63859	.000	11733.6182	18532.0485
	mNg Alone 2	4148.66667	3540.51834	.998	-16958.0122	25255.3456
	mNg Alone 3	-18177.33333	9316.77156	.881	-74549.1002	38194.4336
	FM4-64 PC 1	.00000	682.22026	1.000	-3248.4905	3248.4905
	FM4-64 PC 2	-8119.66667	7300.54911	.999	-52221.6882	35982.3549
	FM4-64 PC 3	-18336.16667	7756.91753	.731	-65217.1834	28544.8501
	FM4-64 PG 1	20649.33333*	485.19884	.000	17737.8361	23560.8305
	FM4-64 PG 2	18925.16667*	611.46317	.000	15970.0452	21880.2882

	FM4-64 PG 3	-201008.33333*	1278.74338	.000	-207908.5288	-194108.1379
	FM4-64 PA 1	20515.83333*	484.81216	.000	17602.3676	23429.2991
	FM4-64 PA 2	19778.83333*	495.58090	.000	16912.0955	22645.5711
	FM4-64 PA 3	-54887.66667	21543.66842	.657	-185509.4991	75734.1658
	FM4-64 WT 1	18448.66667*	1052.48007	.000	13005.8744	23891.4589
	FM4-64 WT 2	18756.50000*	557.56310	.000	15935.0420	21577.9580
	FM4-64 WT 3	16450.66667*	1023.66600	.000	11191.8635	21709.4698

*. The mean difference is significant at the 0.05 level.

Means Plots